Transactions of the ASME

Journal of Heat Transfer

Published Quarterly by The American Society of Mechanical Engineers

VOLUME 106 • NUMBER 1 • FEBRUARY 1984

The Journal of Heat Transfer (ISSN 0022-1481) is published quarterly for $90 per year by The American Society of Mechanical Engineers, 345 East 47th Street, New York, N Y 10017. Second class postage paid at New York, NY and additional mailing offices. POSTMASTER: Send address changes to The Journal of Heat Transfer, c/o THE AMERICAN SOCIETY OF MECHANICAL ENGINEERS, P.O. Box 3199, Grand Central Station, New York, NY 10163.

CHANGES OF ADDRESS must be received at Society headquarters seven weeks before they are to be effective. Please send old label and new address.

PRICES: To members, $36.00, annually; to nonmembers, $90.00. Single copies, $24.00 each. Add $6.00 for postage to countries outside the United States and Canada.

INDEXED by the Engineering Index, Inc.

ANNOUNCEMENTS

11 Mandatory excess-page charges announcement

19 Change of address form for subscribers

233 Errata on a previously published paper by P. Razelos

258 Information for authors

TECHNICAL PAPERS

5 Role of the Liquid Layer in Ice Accumulation Flat Surfaces (82-WA/HT-15)
P. M. Chung and R. Bywater

12 Heat Transfer During Melting From an Isothermal Vertical Wall
C.-J. Ho and R. Viskanta

20 Analysis of Two-Dimensional Melting in Rectangular Enclosures in Presence of Convection
A. Gadgil and D. Gobin

27 The Effect of Entrainmnet Temperature on Jet Impingement Heat Transfer
S. A. Striegl and T. E. Diller

34 Heat Transfer Characteristics for Jet Array Impingement With Initial Crossflow (83-GT-28)
L. W. Florschuetz, D. E. Metzger, and C. C. Su

42 Effect of Location in an Array on Heat Transfer to a Short Cylinder in Crossflow
R. J. Simoneau and G. J. Van Fossen, Jr.

49 Finite Difference Analysis of Laminar Separated Forced Convection in Cavities
A. Bhatti and W. Aung

55 Periodically Converging-Diverging Tubes and Their Turbulent Heat Transfer, Pressure Drop, Fluid Flow, and Enhancement Characteristics
P. Souza Mendes and E. M. Sparrow

64 Turbulent Heat Transport in Circular Ducts With Circumferentially Varying Heat Flux
J. W. Baughn, M. A. Hoffman, B. E. Lauder, and R. K. Takahashi

71 Heat Convection in a Horizontal Curved Pipe
L. S. Yao

78 A Finite Element Model for Temperature Induced Electrohydrodynamic Pumping in Horizontal Pipes (82-WA/HT-23)
B. S. Kuo, J. C. Chato, and J. M. Crowley

85 Heat Transfer in Large Particle Bubbling Fluidized Beds
R. L. Adams

91 Heat Transfer From Rough and Finned Horizontal Tubes in a Gas Fluidized Bed
I. Goel, S. C. Saxena, and A. F. Dolidovich

98 The Boundary Layer Natural Convection Regime in a Rectangular Cavity With Uniform Heat Flux From the Side
S. Kimura and A. Bejan

104 On the Existence of an Oscillatory Approach to Steady Natural Convection in Cavities
J. C. Patterson

109 An Experimental Study of Natural Convection in an Inclined Rectangular Cavity Filled With Water at Its Density Extremum
H. Inaba and T. Fukuda

116 Thermally Optimum Spacing of Vertical, Natural Convection Cooled, Parallel Plates
A. Bar-Cohen and W. M. Rohsenow

124 Enhancement of Natural Convection Heat Transfer From A Horizontal Cylinder Due to Vertical Shrouding Surfaces
E. M. Sparrow and D. R. Pfeil

131 Conductivity Models of Electrothermal Convection in a Plane Layer of Dielectric Liquid (82-WA/HT-21)
P. J. Martin and A. T. Richardson

137 Thermal Convective Instabilities in a Porous Medium
M. Kaviany

143 Higher-Order Approximations for Darcian Free Convective Flow About a Semi-Infinite Vertical Flat Plate
P. Cheng and C. T. Hsu

(Contents continued)

152 Natural Convection in a Rectangular Porous Cavity With Constant Heat Flux on One Vertical Wall
V. Prasad and F. A. Kulacki

158 Convective Heat Transfer in a Rectangular Porous Cavity—Effect of Aspect Ratio on Flow Structure and Heat Transfer
V. Prasad and F. A. Kulacki

166 Low Rayleigh Number Thermal Convection in a Saturated Porous Medium Bounded by Two Horizontal, Eccentric Cylinders
H. H. Bau

176 Dryout Heat Fluxes in Particulate Beds Heated Through the Base
S. W. Jones, M. Epstein, S. G. Bankoff, and D. R. Pedersen

184 Prediction of Nucleate Pool Boiling Heat Transfer Coefficients of Refrigerant-Oil Mixtures
M. K. Jensen and D. L. Jackman

191 The Effect of Vapor Velocity Profile Shape on Flow Film Boiling From Submerged Bodies
L. C. Witte and J. Orozco

198 A Nonequilibrium Vapor Generation Model for Flashing Flows
P. Saha, N. Abuaf, and B. J. C. Wu

204 Application of the Local Assumption for the Design of Compact Heat Exchangers for Boiling Heat Transfer
C. C. Chen and J. W. Westwater

210 Study of Heat and Mass Transfer in a Vertical-Tube Evaporative Cooler (82-WA/HT-75)
H. Perez-Blanco and W. A. Bird

216 The Representation of Regeneration Fluid Carryover by Bypass Flows
P. J. Banks

221 An Investigation of Steady Wall-Ceiling and Partial Enclosure Fires
C. P. Mao, A. C. Fernandez-Pello, and J. A. C. Humphrey

229 Effect of Free-Stream Velocity Vector and Aspect Ratio on the Output of a Free-Standing Circular Disk Heat Flux Gage
M. F. Young

TECHNICAL NOTES

234 The Accuracy of Perfect Contact Fin Analyses
M. Manzoor, D. B. Ingham, and P. J. Heggs

237 Solidification Interface Shape for Continuous Casting in an Offset Mold—Two Analytical Models
T. Siegel

240 Mixed Convection Over a Horizontal Plate
N. Afzal and T. Hussain

241 Natural Convection in a Volumetrically Heated Porous Layer
C. W. Somerton, J. M. McDonough, and I. Catton

244 Radiation View Factors Between Axisymmetric Subsurfaces Within a Cylinder With Spherical Centerbody
B. Mahbod and R. L. Adams

248 Determination of Angular Distribution of Radiation in an Isotropically Scattering Slab
Y. A. Cengel, M. N. Özisik, and Y. Yener

252 The Latent Heat of Vaporization of a Widely Diverse Class of Fluids
S. Torquato and P. Smith

DISCUSSION

255 Discussion of a previously published paper by
A. M. Kanury and D. J. Holve

256 Discussion of a previously published paper by
C. P. Hedderich, M. D. Kelleher, and G. N. Vanderplaats

256 Discussion of a previously published paper by
P. Razelos

Role of the Liquid Layer in Ice Accumulation on Flat Surfaces

P. M. Chung
University of Illinois at Chicago,
Chicago, Ill. 60680

R. Bywater
The Aerospace Corporation

Ice formation on a flat plate from humid air at above-freezing temperatures is studied. Condensations from both laminar-forced and natural convective boundary layers are considered. The governing equations are hyperbolic. One family of characteristics immediately coalesces to form a mathematical shock. Physically, the shock represents the extent to which the liquid layer has spread. Behind the shock, the thin liquid layer completely transforms the ice layer profile at near the shock speed. Various parameters affecting the shock speed and the condensate profile are discussed.

1 Introduction

Often, both in nature and man-made machines, condensation takes place on surfaces held at below the freezing temperature. As long as the entire condensate layer is at below the freezing temperature, it remains a solid, and the local rate of condensate accumulation is largely determined by the local mass transfer characteristics of the gas-phase boundary layer. When the gas temperature is above the freezing temperature, eventually a liquid layer appears at the gas-solid interface as its temperature rises above the melting point. The liquid layer flows along the solid surface driven by the gas-phase boundary layer or gravity until it meets a colder temperature and solidifies. The time-evolution of the solid-layer profile is then largely governed by the liquid-layer behavior rather than the distribution of the local mass transfer rate along the surface.

Usually, the heat and mass transfer rates vary substantially along a surface. A liquid layer, therefore, appears first in the region where the transfer rates are maximum provided that the refrigerated surface temperature is uniform. In the case of the gas-phase boundary layer flow over a flat plate, the maximum transfer rates exist at the leading edge, and the liquid layer appears immediately there. Accumulation of the solid condensate downstream is then greatly affected by the continuous process of condensation near the leading edge and transport of the excess liquid condensate to downstream where solidification occurs.

In the present paper, ice formation on the surface of a uniform-temperature flat plate is studied. Condensations from both laminar-forced and natural convective boundary layers are considered. Particular attention is given to the behavior of the liquid layer affecting the evolution of the ice layer profile along the plate.

The present problem is closely related to that studied by Im and Chung [1] who analyzed the problem of deposition of the molten ash (slag) droplets on cold surfaces and eventual solidification in coal-fired regenerative heat exchangers. The present problem is somewhat related to the problems of frost formation studied by many investigators including Trammel et al. [2], Thibaut et al. [3], Hayashi et al. [4], Chung and Algren [5], Varma, et al. [6], Reid et al. [7], and Cremers and Mehra [8]. All of these studies, however, were concerned with the frost formation and properties before the appearance of the liquid layer.

In the next section, the governing equations are formulated. The ice formation under forced-laminar boundary layer is analyzed, and the results are discussed in section 3. This analysis is then extended to the vertical plate problem in section 4.

2 Formulation

Frost and Ice. Before we begin description of the problem to be analyzed, it would be helpful to discuss briefly the general phenomenon of frost deposition and ice formation. Consider a surface refrigerated to a subfreezing temperature and in contact with a humid air stream at above the freezing temperature. The vapor condenses on the surface as frost, and the frost properties vary with time depending on the rate of condensation and the frost temperature. The frost-air interface temperature increases as the frost deposition proceeds until it reaches the melting point. Continued condensation is then accompanied by permeation of the water across the frost and transformation of the frost density and other properties toward those of the ice. More detailed descriptions of the foregoing phenomena are found elsewhere [2–5]. When conversion of the frost to ice is completed, a liquid layer begins to form above the ice that is now subject to fluid motion.

The present study is concerned with condensation involving the liquid layer. As has been stated, the solid phase is ice when the liquid layer forms. Also, the condensate accumulates at a given location because of the vapor diffusion from the air and advection of liquid from the adjacent region. Hence, the time required for condensate accumulation until the appearance of the liquid layer is, for all practical purposes, independent of the detials of conversion of frost to ice. In order not to unnecessarily complicate the analysis, the solid phase is assumed to be ice in the sections that follow.

Physical Problem. Consider that the temperature of a plate in contact with a laminar humid air stream is suddenly lowered to a subfreezing temperature and held there. The characteristic times associated with the condensate accumulation are much longer than those for establishment of the steady gas-phase thermal and diffusion boundary layers. We may, therefore, consider the gas-phase boundary layers to be in a steady state for the present transient analysis of the liquid and ice layers.

The mass transfer rate varies as $x^{-1/2}$ for the gas-phase boundary layer (see [9]). Therefore, the frost profile will tend to approximate $x^{-1/2}$ as shown in Fig. 1. Near the leading edge, however, the heat and mass transfer rates are extremely high. The high heat transfer melts the frost, and a liquid layer appears immediately. The shear stress applied by the air boundary layer is equally high in this region. The liquid is, therefore, continuously dragged downstream away from the

Contributed by the Heat Transfer Division and presented at the ASME Winter Annual Meeting, Phoenix, Arizona, November 14–19, 1982. Manuscript received by the Heat Transfer Division January 21, 1983. Paper No. 82-WA/HT-15.

neighborhood of the leading edge. Hence, the condensate[1] profile in the region affected by the liquid layer is expected to be fundamentally different from that in the other region as shown in Fig. 2. In fact, the present study is mainly concerned with this reshaping of the condensate profile by the liquid layer.

The phenomenon is essentially the same when a vertical plate is in contact with a quiescent humid air. The heat and mass transfer rates vary as $x^{-1/4}$ for the gas-phase natural convective boundary layer. Also, the liquid generated upstream is transported downstream by gravity rather than shear stress. At a given time, the condensate profile is expected to be as shown in Fig. 2 also.

Governing Equations for Condensate.

(Continuity)

$$\frac{\partial \delta}{\partial t} + \frac{\partial}{\partial x}\int_0^{\delta} u dy = \frac{\omega}{\rho} \tag{1}$$

(Momentum)

$$\frac{\partial}{\partial y}\left(\mu \frac{\partial u}{\partial y}\right) = -\rho g \tag{2}$$

(Energy)

$$k\frac{\partial T}{\partial y} = q_a \tag{3}$$

The transient and convection terms are neglected in equations (2) and (3) as usually justified for thin liquid layers (see, for instance, Im and Chung [1]). The initial and boundary conditions are specified as follows:

[1] By "condensate," we refer to the total condensate including both liquid and solid.

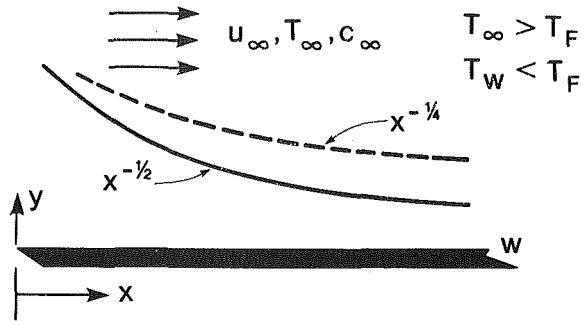

Fig. 1 Flow configuration and distribution of gas-phase mass transfer

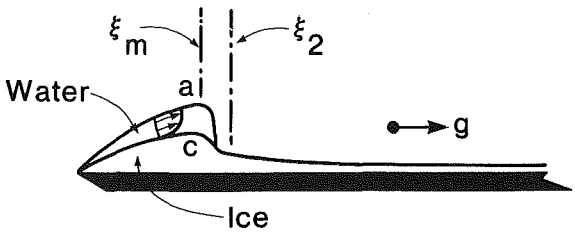

Fig. 2 Sketch of the ice and water layer formation

(Initial)

$$\delta = 0 \quad \text{for all } x \tag{4}$$

(Boundary)

At $x = 0$,

$$\delta = 0 \quad \text{for all } t \tag{5}$$

Nomenclature

A_1, A_{1l}, A_{1s}, A_2 = parameters defined in equations (21)
A_4 = constant defined in equations (27)
B = dimensionless ice thickness defined in equations (18)
B_1 = functions defined in equations (42)
b = ice thickness
c = mass fraction
c_p = constant pressure specific heat of air
D = vapor diffusion coefficient in air
EL = characteristic temperature given in equations (27)
F_1, F_2 = right-hand sides of equations (19) and (20), respectively
F_3 = function defined by equation (56)
g = gravitational acceleration
h_l^0 = heat of vaporization of water
h_s^0 = heat of fusion of ice
k = thermal conductivity
L = reference length of the plate
Pr = Prandtl number of air
q_a = total heat flux per unit area at the interface a
q_a' = sensible heat flux per unit area at the interface a
Sc = Schmidt number of air
T = absolute temperature
t = time
u = streamwise velocity
x = distance along the plate
y = distance normal to the plate
Δ = dimensionless total condensate thickness defined in equations (17)
δ = total condensate thickness
η = dummy variable
θ = dimensionless liquid layer thickness defined in equations (18)
θ_1 = function defined in equations (42)
μ = dynamic viscosity (refers to liquid with no subscript)
ν = kinematic viscosity (refers to liquid with no subscript)
ξ = x/L
ρ = density (refers to liquid with no subscript)
σ^+, σ^- = two characteristic directions defined by equations (30) and (31)
τ = dimensionless time defined in equations (17)
τ_a = shear stress at the interface a
ω = condensation rate per unit area at the interface a

Subscripts

a = gas-liquid or gas-solid interface
c = liquid-solid interface
F = freezing point
l = liquid
m = shock position
ml = immediately behind the shock
ms = immediately in front of the shock
s = solid
w = plate surface
∞ = undisturbed gas

At $y=0$,

$$u=0 \tag{6}$$

$$T=T_w \tag{7}$$

At $y=\delta(x,t)$,

$$\mu\frac{\partial u}{\partial y}=\tau_a \tag{8}$$

With expressions for the condensation velocity, ω/ρ, and heat flux, q_a, considered to be available elsewhere [9], equations (1-8) comprise a self-consistent set.

These equations will first be analyzed for the flat plate with forced convective gas-phase boundary layer. The solution will then be extended to vertical surface with natural convective gas-phase boundary layer.

3 Ice Formation by Laminar Boundary Layer

Equations. We consider the condensation on a flat plate from a laminar boundary layer of humid air. With the gravity set to zero, equation (2) is readily integrated to satisfy the boundary conditions (6) to (8), and there results for u,

$$u=\tau_a\int_0^y\frac{d\eta}{\mu} \tag{9}$$

Substitution of the foregoing expression into equation (1) gives, after a little manipulation,

$$\frac{\partial\delta}{\partial t}+\frac{\partial}{\partial x}\left[\tau_a\int_0^\delta\left(\frac{\delta-y}{\mu}\right)dy\right]=\frac{\omega}{\rho} \tag{10}$$

We assume for convenience that

$$\mu=\mu_l \quad\text{and}\quad k=k_l \quad\text{for}\quad b<y\le\delta$$
$$\mu=\infty \quad\text{and}\quad k=k_s \quad\text{for}\quad y\le b \tag{11}$$

where b denotes the thickness of the ice layer. Equation (10) then becomes

$$\frac{\partial\delta}{\partial t}+\frac{1}{2\mu_l}\frac{\partial}{\partial x}[\tau_a(\delta-b)^2]=\frac{\omega_a}{\rho_{l,s}} \tag{12}$$

where

$$\rho_{l,s}=\rho_l \quad\text{when}\quad \delta>b$$
$$\rho_{l,s}=\rho_s \quad\text{when}\quad \delta=b \tag{13}$$

With the division of the condensate into the liquid and solid layers by equations (11), we have introduced a new variable, b. The equation governing this variable is obtained by constructing a heat balance at the solid-liquid interface, c, as

$$\rho_s h_s^0\frac{\partial b}{\partial t}=k_s\left(\frac{T_s-T_w}{b}\right)-q_a \tag{14}$$

where equation (3) has been employed.

In order to proceed further, we make use of the well-known expressions [9]

$$\frac{\tau_a}{\rho_\infty u_\infty^2}=0.332\left(\frac{\nu_\infty}{u_\infty x}\right)^{1/2}$$

$$\frac{q_a'}{\rho_\infty u_\infty c_p(T_\infty-T_a)}=\mathrm{Pr}^{-2/3}\frac{\tau_a}{\rho_\infty u_\infty^2} \tag{15}$$

$$\frac{\omega_a}{\rho_\infty u_\infty(c_\infty-c_a)}=\mathrm{Sc}^{-2/3}\frac{\tau_a}{\rho_\infty u_\infty^2}$$

There are more accurate results available, which include the effect of mass transfer (suction) on the gas-phase boundary layer (see, for instance, [10-12]). In view of the other approximations involved, such as the constant properties for the frost and ice, equations (15) are sufficiently accurate for the present study.

Total heat transfer, q_a, is obtained from equations (15) as

$$\frac{q_a}{\rho_\infty u_\infty c_p(T_\infty-T_a)}=\frac{\tau_a}{\rho_\infty u_\infty^2}\mathrm{Pr}^{-2/3}\left[1+\left(\frac{\mathrm{Pr}}{\mathrm{Sc}}\right)^{2/3}\frac{h_l^0(c_\infty-c_a)}{c_p(T_\infty-T_a)}\right] \tag{16}$$

For convenience, we define the following dimensionless variables.

$$\xi=x/L$$
$$\tau=\left(\frac{\mu_\infty}{\mu_l}\frac{u_\infty}{L}\right)t \tag{17}$$
$$\Delta=(0.332)\left(\frac{u_\infty}{\nu_\infty L}\right)^{1/2}\delta$$
$$B=(0.332)\left(\frac{u_\infty}{\nu_\infty L}\right)^{1/2}b$$
$$\theta=\Delta-B \tag{18}$$

With the use of equations (15-18), equations (12) and (14) are manipulated into the following set of equations:

$$\frac{\partial\theta}{\partial\tau}+\frac{\theta}{\xi^{1/2}}\frac{\partial\theta}{\partial\xi}=\frac{A_1}{\xi^{1/2}}\left[\mathrm{Sc}^{-2/3}(c_\infty-c_a)+\frac{1}{4A_1}\frac{\theta^2}{\xi}\right]-\frac{\partial B}{\partial\tau} \tag{19}$$

$$\frac{\partial B}{\partial\tau}=A_2\frac{1}{B}\left\{1-\frac{k_\infty}{k_s}\mathrm{Pr}^{1/3}\left(\frac{T_\infty-T_a}{T_b-T_w}\right)\frac{B}{\xi^{1/2}}\left[1+\left(\frac{\mathrm{Pr}}{\mathrm{Sc}}\right)^{2/3}\frac{h_l^0(c_\infty-c_a)}{c_p(T_\infty-T_a)}\right]\right\}\frac{c_p(T_F-T_w)}{h_s^0} \tag{20}$$

In the foregoing equations

$$A_1=A_{1l}=(0.332)^2\left(\frac{\nu_l}{\nu_\infty}\right) \qquad \text{when } \theta>0$$

$$A_1=A_{1s}=(0.332)^2\left(\frac{\nu_l}{\nu_\infty}\right)\left(\frac{\rho_l}{\rho_s}\right) \quad \text{when } \theta=0 \tag{21}$$

$$A_2=(0.332)^2\left(\frac{\nu_l}{\nu_\infty}\right)\left(\frac{\rho_l}{\rho_s}\right)\left(\frac{k_s}{k_\infty}\right)\frac{1}{\mathrm{Pr}}$$

The energy equation, equation (3), is trivially integrated for the liquid and ice layers as

$$q_a=k_l\left(\frac{T_a-T_F}{\delta-b}\right) \qquad \text{when} \quad \delta>b \tag{22}$$

$$q_a=k_s\left(\frac{T_a-T_w}{b}\right) \qquad \text{when} \quad \delta=b \tag{23}$$

Combining equation (16) with equations (22) and (23) in tandem, and manipulating the resulting equations with the use of equations (15-18), we obtain

(when $\theta>0$)

$$\frac{\theta}{\xi^{1/2}}=\frac{\frac{k_l}{k_\infty}\left(\frac{T_a-T_F}{T_\infty-T_a}\right)}{\mathrm{Pr}^{1/3}\left[1+\left(\frac{\mathrm{Pr}}{\mathrm{Sc}}\right)^{2/3}\frac{h_l^0(c_\infty-c_a)}{c_p(T_\infty-T_a)}\right]} \tag{24}$$

(when $\theta=0$)

$$\frac{B}{\xi^{1/2}}=\frac{\frac{k_s}{k_\infty}\left(\frac{T_a-T_w}{T_\infty-T_a}\right)}{\mathrm{Pr}^{1/3}\left[1+\left(\frac{\mathrm{Pr}}{\mathrm{Sc}}\right)^{2/3}\frac{(h_l^0+h_s^0)(c_\infty-c_a)}{c_p(T_\infty-T_a)}\right]} \tag{25}$$

We have now reduced the original governing equations into the three equations, equations (19), (20), and either (24) or

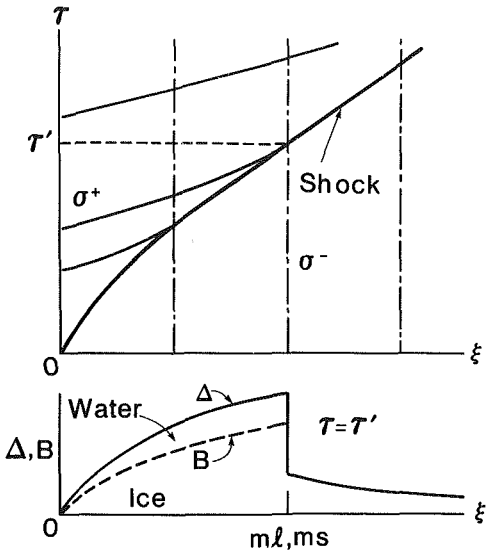

Fig. 3 Wave diagram and the corresponding condensate profile

(25). An additional relationship is needed since there are four unknown functions, θ, B, T_a, and c_a, in these equations. The Clapeyrons equation [13] relates the saturation mass function of the vapor, c_a, to the temperature, T_a. This equation can be written for the present temperature range as

$$c_a = A_4 \exp(-EL/T_a) \tag{26}$$

where

$$A_4 = 1{,}388{,}000$$

$$EL = 5386.5 \text{ K} \tag{27}$$

Equations (19), (20), (24) or (25), and (26) constitute a self-consistent set for the four variables, θ, B, T_a, and c_a. The initial and boundary conditions for equations (19) and (20) are those given by equations (4) and (5), and are written for $\theta(\xi, \tau)$ and $B(\xi, \tau)$ as

$$\theta(\xi,0) = B(\xi,0) = 0 \tag{28}$$

$$\theta(0,\tau) = B(0,\tau) = 0 \tag{29}$$

The general behavior of the equations and its physical implications will now be discussed. Solution of the equations will then follow.

General Behavior. Equations (19) and (20) are hyperbolic. Their behavior, therefore, can be best elucidated by the use of a wave diagram. The two characteristic directions [14, 15] of the equations are obtained as

$$\left(\frac{d\tau}{d\xi}\right)_{\sigma^+} = \xi^{1/2}/\theta \tag{30}$$

$$\left(\frac{d\tau}{d\xi}\right)_{\sigma^-} = \infty \tag{31}$$

Equations (19) and (20) become, along the characteristics,

$$\frac{d\theta}{d\sigma^+} = F_1 \tag{32}$$

$$\frac{dB}{d\sigma^-} = F_2 \tag{33}$$

where F_1 and F_2 represent the right-hand sides of equations (19) and (20), respectively.

The σ^--characteristics are sketched as vertical semi-broken lines in the wave diagram of Fig. 3.

Let us now consider the σ^+-characteristics given by equation (30). In the limit of $\xi \to 0$, θ is expected to behave as $\xi^{1/2}$ for all τ from the steady-state solutions [10–12]. Therefore, equation (30) gives

$$\lim_{\substack{\xi\to 0\\ \tau\to 0}} \left(\frac{d\tau}{d\xi}\right)_{\sigma^+} = \text{finite} \tag{34}$$

For $\xi > 0$, however, $\theta = 0$ for $\tau = 0$, and

$$\left(\frac{d\tau}{d\xi}\right)_{\sigma^+} \to \infty \tag{35}$$

Equations (34) and (35) show that the σ^+-characteristics will immediately coalesce for $\tau > 0$ and $\xi > 0$ to form a mathematical shock. The shock will emanate from the origin of the wave plane and create discontinuities of properties across it as shown by the Δ and B profiles sketched in Fig. 3.

In the region traversed by the shock, the wave represented by F_1 will travel in the ξ-direction through the liquid layer as seen by the direction of the σ^+-characteristics. Ahead of the shock, on the other hand, the two families of characteristics, as well as equations (32) and (33), collapse together and no wave motion in the ξ-direction is possible. No liquid layer exists there.

It is expected that integration of the governing equations will face numerical difficulty unless the shock is properly handled. Appropriate shock relationship will be derived below.

Shock Relationship. We first rewrite equation (19) as

$$\frac{\partial\theta}{\partial\tau} + \frac{1}{2}\frac{\partial}{\partial\xi}\left(\frac{\theta^2}{\xi^{1/2}}\right) = A_1 \frac{(c_\infty - c_a)}{\text{Sc}^{2/3}\xi^{1/2}} - \frac{\partial B}{\partial\tau} \tag{36}$$

We integrate the terms of this equation between ξ_m and ξ_2 (see Fig. 2), and let ξ_2 approach ξ_m without limit.

$$\lim_{\xi_2\to\xi_m}\left\{\frac{\partial}{\partial\tau}\int_{\xi_m}^{\xi_2}\theta d\xi - \theta(\tau,\xi_2)\frac{\partial\xi_2}{\partial\tau} + \theta(\tau,\xi_m)\frac{\partial\xi_m}{\partial\tau} + \frac{1}{2}[\theta^2(\tau,\xi_2)/\xi_2^{1/2} - \theta^2(\tau,\xi_m)/\xi_m^{1/2}]\right\}$$

$$= \lim_{\xi_2\to\xi_m}\left\{A_1\text{Sc}_\infty^{-2/3}\int_{\xi_m}^{\xi_2}\left(\frac{c_\infty - c_a}{\xi^{1/2}}\right)d\xi - \frac{\partial}{\partial\tau}\int_{\xi_m}^{\xi_2}Bd\xi + B(\xi_2)\frac{\partial\xi_2}{\partial\tau} - B(\xi_m)\frac{\partial\xi_m}{\partial\tau}\right\} \tag{37}$$

This equation reduces to

$$\frac{d\xi_m}{d\tau} = \frac{1}{2\xi_m^{1/2}}\frac{\theta_{ml}^2}{(\Delta_{ml} - \Delta_{ms})} \tag{38}$$

The foregoing equation relates the shock speed to the liquid and total condensate layer thicknesses behind the shock (ml) and the solid condensate layer thickness in front of the shock (ms).

Numerical Solutions. Equations (19) and (20) are integrated by a finite difference scheme to satisfy the initial conditions, equations (28) and (29), with the aid of the algebraic equations, equation (24) or (25) and equation (26), and the shock relationship, equation (38). Typical solutions are shown in Figs. 4 and 5. The results show that steady state is reached very quickly following the shock passage. This indicates that the σ^+-wave speed is much greater than the shock speed as sketched in Fig. 3.

The preceding findings suggest a much simpler approximate solution which utilizes the steady-state values for θ_{ml} and Δ_{ml} in equation (38).

Approximate Solution. Steady-state approximation of equations (19) and (20) is effected by setting

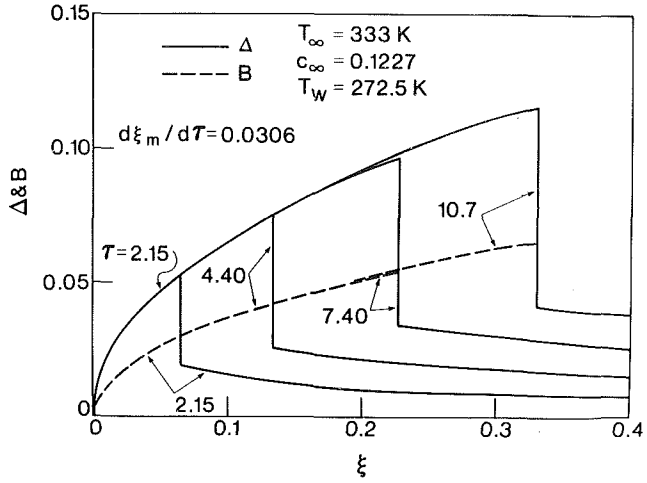

Fig. 4 Typical condensate profile computed by finite difference for T_w near T_F

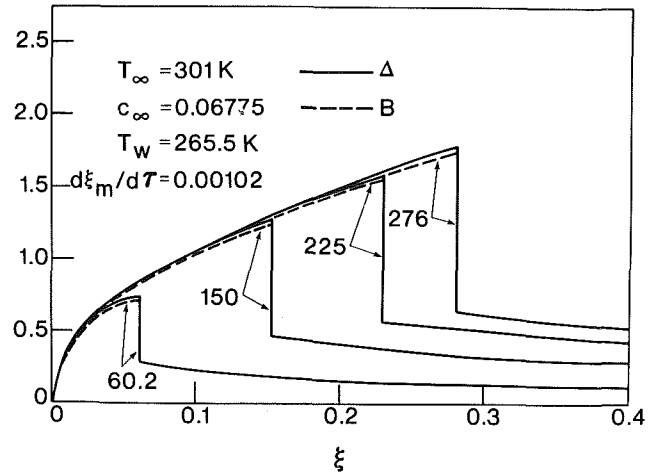

Fig. 5 Typical condensate profile computed by finite difference for T_w substantially below T_F

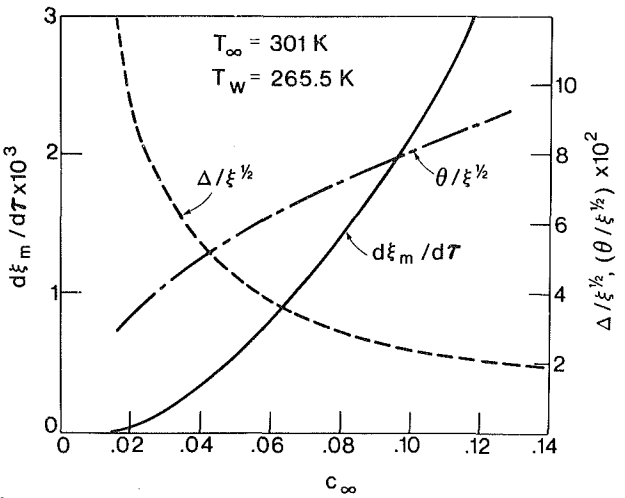

Fig. 6 Influence of c_∞ on ice accumulation computed by the approximate method

$$\frac{\partial\theta}{\partial\tau} = \frac{\partial B}{\partial\tau} = 0 \tag{39}$$

Equation (19) then becomes an ordinary differential equation, and equation (20) degenerates to an algebraic equation. The differential equation is integrated in closed form to satisfy the boundary condition, equation (29), as

$$\theta = \theta_1 \xi^{1/2} \tag{40}$$

The algebraic equation is rewritten as

$$B = B_1 \xi^{1/2} \tag{41}$$

In the foregoing

$$\theta_1 = 2[A_{1l}\mathrm{Sc}^{-2/3}(c_\infty - c_a)]^{1/2}$$

$$B_1 = \frac{k_s}{k_\infty}\mathrm{Pr}^{-1/3}\left(\frac{T_F - T_w}{T_\infty - T_a}\right)\Big/\left[1+\left(\frac{\mathrm{Pr}}{\mathrm{Sc}}\right)^{2/3}\frac{h_l^0(c_\infty - c_a)}{c_p(T_\infty - T_a)}\right] \tag{42}$$

Combining equation (40) with equation (24), we obtain

$$2\mathrm{Pr}^{1/3}[A_{1l}\mathrm{Sc}^{-2/3}(c_\infty - c_a)]^{1/2}\left[1+\left(\frac{\mathrm{Pr}}{\mathrm{Sc}}\right)^{2/3}\frac{h_l^0(c_\infty - c_a)}{c_p(T_\infty - T_a)}\right] = \frac{k_l}{k_\infty}\left(\frac{T_a - T_F}{T_\infty - T_a}\right) \tag{43}$$

Solution of the above nonlinear algebraic equation with the use of equation (26) results in T_a and c_a. Equations (40) and (41) then give θ and $\Delta(=\theta + B)$.

For Δ_{ms}, we consider the region $\xi \geq \xi_m$ where $\theta = 0$. Equations (19) and (20) are identical in this region and degenerate to

$$\frac{\partial\Delta}{\partial\tau} = \frac{\partial B}{\partial\tau} = A_{1s}\mathrm{Sc}^{-2/3}(c_\infty - c_{as})/\xi^{1/2} \tag{44}$$

Before the shock arrival, c_{as} deviates little from c_w. Within the accuracy of the approximate analysis, we replace c_{as} by c_w and trivially integrate equation (44) to obtain

$$\Delta_s = A_{1s}\mathrm{Sc}^{-2/3}(c_\infty - c_w)\tau/\xi^{1/2} \tag{45}$$

The quantities, θ_{ml}, Δ_{ml}, and Δ_{ms}, needed by the shock equation, equation (38), are now obtained from equations (40), (41), and (45) by setting $\xi = \xi_m$. Equation (38) is then integrated to satisfy the boundary condition, $\xi_m(\tau = 0) = 0$, resulting in the closed-form solution

$$\xi_m = \left[\frac{2A_{1l}(c_\infty - c_a) + A_{1s}(c_\infty - c_w)}{\mathrm{Sc}^{2/3}(\theta_1 + B_1)}\right]\tau \tag{46}$$

Discussion of Results. For all solutions shown on Figs. 4–8, the following property values of water and ice were employed

$k_l/k_\infty = 22.6$, $k_s/k_\infty = 88$, $\nu_l/\nu_\infty = .101$

$\mathrm{Pr} = .72$, $\mathrm{Sc} = .52$

$h_l^0/c_p = 2477$ K, $h_s^0/c_p = 330.83$ K, $c_p = .24$ Kcal/(Kg − K)

$\rho_l = 1000$ Kg/m^3, $\rho_s = 917$ Kg/m^3, $\rho_\infty = 1.2$ Kg/m^3

Solutions obtained by the approximate method were found to be within about 2–3 percent of the finite difference solutions for all cases computed. We shall, therefore, employ the approximate solutions in the following discussion, for convenience.

Equation (46) shows that the shock velocity is constant with respect to ξ and τ. For a given time, τ, equation (46) gives the shock position. The condensate profile is then obtained from equations (40) and (41) for $\xi \leq \xi_m$, and from equation (45) for $\xi \geq \xi_m$.

Equations (40–45) show that, for a given set of property values such as Pr and k_s/k_∞, the solution depends mainly on c_∞, T_∞, and T_w. The influence of these variables on the total condensate and liquid layer thicknesses for $\xi \leq \xi_m$ and the shock speed are illustrated in Figs. 6–8.

Figure 6 shows that the liquid layer thickens as c_∞ is increased. A thicker liquid layer facilitates flow, and the shock

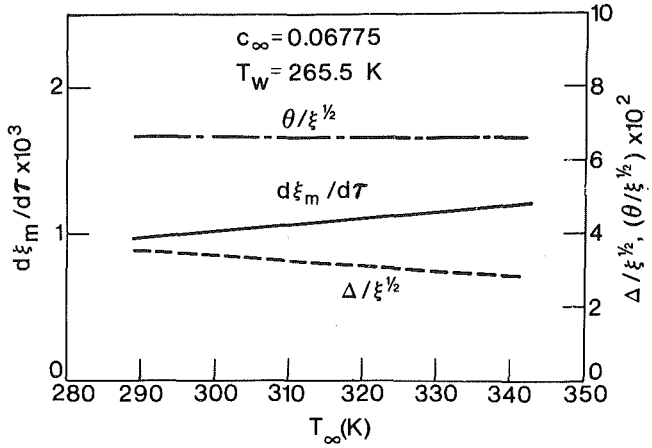

Fig. 7 Influence of T_∞ on ice accumulation computed by the approximate method

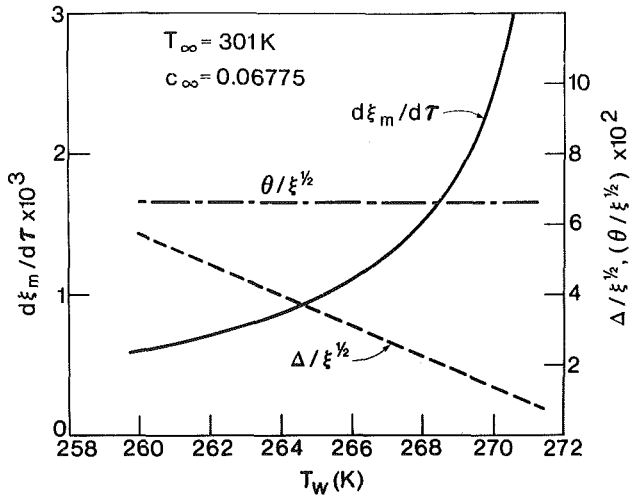

Fig. 8 Influence of T_W on ice accumulation computed by the approximate method

speed is greatly enhanced. Note that the shock represents the farthest distance to which the liquid has spread. Increased c_∞, however, results in the reduced total condensate thickness despite the thickened liquid layer. The greater deposition rate of heat of condensation accompanying the increased c_∞ reduces the ice layer thickness to such an extent that the overall condensate thickness is reduced even with the thickened liquid layer.

The influence of T_∞ is seen in Fig. 7. The liquid layer is immune to the T_∞ variation. The overall condensate thickness, however, is reduced as T_∞ is increased. This is caused by the enhanced heat transfer accompanying the higher T_∞, which reduces the ice layer thickness.

The shock speed increases with the decreasing condensate thickness, Δ. The reason for this is as follows. Physically, the shock speed, the speed at which the liquid layer spreads, is dictated by the time necessary for the liquid in the liquid layer immediately behind the shock to flow into the shock and fill it between the heights Δ_{ms} and B_{ml} (see Fig. 3). Until B_{ml} is reached, the liquid entering the shock will immediately solidify. As soon as B_{ml} is reached, however, liquid will appear there and the shock would have moved forward. Now, the smaller the Δ for a given θ, the smaller are the B_{ml} and the time required to fill the shock with ice. The smaller time requirement implies a greater shock speed. This explains the increased shock speed which usually accompanies decreased Δ.

The liquid layer is immune to T_w also, according to Fig. 8. The ice thickness is greatly reduced as T_w is increased resulting in the corresponding reduction in Δ. The shock speed increases as Δ is reduced, for the reason discussed in the preceding paragraph.

4 Extension to Ice Formation Under Gravitational Field

Analysis. We consider that a vertical plate in contact with a quiescent humid air at above freezing temperature is suddenly cooled to a subfreezing temperature. We then wish to describe the role of the liquid layer in the ice formation on the plate. The governing equations are those given in equations (1-8), with the interface shear stress, τ_a, set to zero in equation (8).

Following closely the procedure described in section 3, equations (1-8) are manipulated into

$$\frac{\partial \delta}{\partial t} + \frac{\rho g}{3\mu}\frac{\partial}{\partial x}(\delta - b)^3 = \frac{\omega}{\rho} \tag{47}$$

$$\frac{dx_m}{dt} = \frac{\rho g}{3\mu}\frac{[(\delta - b)^3]_{ml}}{\delta_{ml} - \delta_{ms}} \tag{48}$$

Expressions for ω/ρ and q_a given elsewhere [9] are employed, as

$$\frac{\omega}{\rho} = .508\, D_\infty \left[\frac{g(T_\infty - T_a)}{4\nu_\infty^2 T_\infty}\right]^{1/4} \frac{(c_\infty - c_a)}{x^{1/4}} \tag{49}$$

$$q_a' = \rho_\infty c_p \left(\frac{T_\infty - T_a}{c_\infty - c_a}\right)\frac{\omega}{\rho} \tag{50}$$

where both Pr and Sc are considered to be 0.733 for convenience.

The approximate method described in section 3 is expected to be as accurate for the present problem as for the forced boundary layer flow. Therefore, by setting $\partial\delta/\partial t = 0$, equations (47), and (48) and other auxiliary equations resulting from equations (1-8) are solved precisely in the manner described in the preceding section. The following relationships are then obtained:

$$(.508)\left[1 + \frac{h_l^0 (c_\infty - c_a)}{c_p (T_\infty - T_a)}\right]\left[.693\left(\frac{\nu_l}{\nu_\infty}\right)(c_\infty - c_a)\frac{T_\infty - T_a}{T_\infty}\right]^{1/3} = \frac{k_l}{k_\infty}\left(\frac{T_a - T_F}{T_\infty - T_a}\right) \tag{51}$$

For $x \le x_m$

$$\delta \cdot \left(\frac{g}{\nu_\infty^2}\right)^{1/4} = \left(\frac{4T_\infty}{T_\infty - T_a}\right)^{1/4}\left\{\left(\frac{1}{.508}\right)\frac{k_s}{k_\infty}\left(\frac{T_F - T_w}{T_\infty - T_a}\right) \Big/ \left[1 + \frac{h_l^0 (c_\infty - c_a)}{c_p (T_\infty - T_a)}\right] + \left[.693\left(\frac{\nu_l}{\nu_\infty}\right)(c_\infty - c_a)\frac{T_\infty - T_a}{T_\infty}\right]^{1/3}\right\} x^{1/4} \tag{52}$$

$$b \cdot \left(\frac{g}{\nu_\infty^2}\right)^{1/4} = \left(\frac{1}{.508}\right)\frac{k_s}{k_\infty}\left(\frac{T_F - T_w}{T_\infty - T_a}\right) \Big/ \left\{\left(\frac{T_\infty - T_a}{4T_\infty}\right)^{1/4}\left[1 + \frac{h_l^0 (c_\infty - c_a)}{c_p (T_\infty - T_a)}\right]\right\} x^{1/4} \tag{53}$$

For $x \ge x_m$

$$\delta \cdot \left(\frac{g}{\nu_\infty^2}\right)^{1/4} = (.693) g^{1/2} (c_\infty - c_w)\left(\frac{T_\infty - T_w}{4T_\infty}\right)^{1/4} \frac{t}{x^{1/4}} \tag{54}$$

Equation (26) relates c_a to T_a, or c_w to T_w.

The variables δ_{ml}, b_{ml}, and δ_{ms} are obtained from equations (52-54) by simply setting $x = x_m$. Substitution of these

variables into equation (48) results in the following shock equation.

$$x_m^{-1/2}\frac{dx_m}{dt}=F_3 \tag{55}$$

where

$$F_3=(.693)g^{1/2}(c_\infty-c_a)\left(\frac{T_\infty-T_a}{T_\infty}\right)^{1/2}$$

$$\left[\frac{3}{2}+\left(\frac{T_\infty-T_w}{T_\infty-T_a}\right)^{1/4}\left(\frac{c_\infty-c_w}{c_\infty-c_a}\right)\right]$$

$$\Big/\left\{\frac{k_s}{k_\infty}\left(\frac{T_F-T_w}{T_\infty-T_a}\right)\frac{1}{(.508)\left[1+\dfrac{h_l^0(c_\infty-c_a)}{c_p(T_\infty-T_a)}\right]}\right.$$

$$\left.+\left[(.693)\frac{\nu}{\nu_\infty}(c_\infty-c_a)\left(\frac{T_\infty-T_a}{T_\infty}\right)\right]^{1/3}\right\} \tag{56}$$

Integration of equation (55) gives

$$x_m=\frac{1}{4}F_3^2t^2 \tag{57}$$

Solution of the nonlinear algebraic equation, equation (51), together with equation (26) yields T_a and c_a. The shock velocity and position are then given by equations (55) and (57), respectively. The condensate profile is obtained from equations (52) and (53) for $x \le x_m$, and from equation (54) for $x \ge x_m$.

Comments. Equation (55) shows that the shock velocity increases as $x_m^{1/2}$, in contrast to the constant shock velocity given by equation (46) for the forced flow case. This means that the speed at which the liquid layer spreads accelerates when the gravity is responsible for the spread, whereas the speed is constant when it is the gas-phase boundary layer that drags the liquid.

5 Concluding Remarks

Ice formation on a flat plate caused by laminar boundary layer of humid air, at above freezing temperatures, was first analyzed. The analysis was then extended to the ice formation over a vertical plate in contact with a quiescent humid air.

The governing equations were hyperbolic. One family of characteristics immediately coalesced to form a mathematical shock. Physically, the shock represented the extent to which the liquid layer spread.

In the region not yet traversed by the shock, the solid condensate profile grew essentially as $x^{-1/2}$ for the forced boundary layer flow case and $x^{-1/4}$ for the vertical plate. These growth rates were mainly governed by the diffusion through the gas-phase boundary layers. Behind the shock, on the other hand, the thin liquid layer transformed the profile to $x^{1/2}$ and $x^{1/4}$ for the forced flow and vertical plate, respectively. This transfiguration took place at near shock speed such that the approximate solutions, based on certain steady-state properties behind the shock, were found to be sufficiently accurate.

The large heat and mass transfer rates near the leading edge of the plate quickly engendered a liquid layer there. The liquid then spread downstream. The spread was sustained by the continuous condensation upstream. The speed of spread was the shock speed. The shock traversed the plate in a much shorter time than that required for the local gas-phase diffusion to deposit a sufficient amount of frost to create a liquid layer on the top.

References

1 Im, K. H., and Chung, P. M., "Slag and Other Liquid Behavior on Vertical Surface at Near-Freezing Temperature," *AIAA Journal*, Vol. 18, Nov. 1980, pp. 1383–1389.

2 Trammell, G. J., Little, D. C., and Killgore, E. M., "A Study of Frost Formed on a Flat Plate Held at Sub-Freezing Temperatures," *ASHRAE Journal*, July 1968, pp. 42–47.

3 Brian, P. L. T., Reid, R. C., and Shah, Y. T., "Frost Deposition on Cold Surfaces," *Ind. Eng. Chem. Fundam.*, Vol. 9, No. 3, 1970, pp. 375–380.

4 Hayashi, Y., Aoki, A., Adachi, S., and Hori, K., "Study of Frost Properties Correlating with Frost Formation Types," ASME JOURNAL OF HEAT TRANSFER, Vol. 99, May 1977, pp. 239–245.

5 Chung, P. M., and Algren, A. B., "Frost Formation and Heat Transfer on a Cylinder Surface in Humid Air Cross Flow," *Heating, Piping and Air Conditioning*, pt. 1, Vol. 30, No. 9, 1958, pp. 171–178; and pt. 2, Vol. 30, No. 10, 1958, pp. 115–122.

6 Varma, H. K., Charan, V., and Soogappa, P., "Simultaneous Heat and Mass Transfer to Flat Plate in Humid Air Stream Under Frosting Conditions," *Letters in Heat and Mass Transfer*, Vol. 5, 1978, pp. 297–305.

7 Reid, R. C., Brian, P. L. T., and Weber, M. E., "Heat Transfer and Frost Formation Inside Liquid Nitrogen-Cooled Tube," *AIChE Journal*, Vol. 12, November 1966, pp. 1190–1195.

8 Cremers, C. J., and Mehra, V. K., "Frost Formation on Vertical Cylinders in Free Convection," ASME JOURNAL OF HEAT TRANSFER, Vol. 104, 1982, pp. 3–7.

9 Schlichting, H., *Boundary Layer Theory*, 6th ed., McGraw-Hill, New York, 1968.

10 Minkowycz, W. J., and Sparrow, E. M., "Condensation Heat Transfer in the Presence of Noncondensables, Interfacial Resistance, Superheating, Variable Properties, and Diffusion," *International Journal of Heat and Mass Transfer*, Vol. 9, 1966, pp. 1125–1144.

11 Koh, J. C. Y., Sparrow, E. M., and Hartnett, J. P., "The Two-Phase Boundary Layer in Laminar Film Condensation," *International Journal of Heat and Mass Transfer*, Vol. 2, 1961, pp. 69–82.

12 Sparrow, E. M., and Lin, S. H., "Condensation Heat Transfer in the Presence of a Noncondensable Gas," ASME JOURNAL OF HEAT TRANSFER, C86, 1964, pp. 430–436.

13 Lee, J., Sears, F., and Turcotte, D., *Statistical Thermodynamics*, ch. 11, Addison-Wesley, Inc., Reading, Mass., 1973.

14 Von Mises, R., *Mathematical Theory of Compressible Fluid Flow*, Academic Press, New York, 1958, pp. 100–134.

15 Courant, R., and Friedrichs, K. O., *Supersonic Flow and Shock Waves*, Pure and Applied Mathematics, Vol. 1, Interscience Publishers, Inc., New York, N.Y., 1948, Chapter 2.

Heat Transfer During Melting From an Isothermal Vertical Wall

C.-J. Ho[1]

R. Viskanta

Fellow ASME

School of Mechanical Engineering,
Purdue University,
West Lafayette, Ind. 47907

This paper reports basic heat transfer data during melting of n-octadecane from an isothermal vertical wall of a rectangular cavity. The shadowgraph technique was used to measure local heat transfr coefficents at the heat source surface and the solid-liquid interface motion during phase change was recorded photographically. Experimental results clearly showed that, except in the very early stages of melting, the rates of melting and of heat transfer were greatly affected by the buoyancy-driven convection in the liquid. Initial subcooling of the solid substanially impeded the phase change process. A numerical simulation of the corresponding two-dimensional melting in the presence of natural convection was performed, and the numerical predictions are compared with experimental data.

Introduction

Among the possible applications and designs of the latent heat-of-fusion energy storage systems, interest has been focused on the use of the latent-heat solar walls in passive solar heating of homes [1, 2]. These walls (or bricks) consist of a rectangular container or enclosure filled with a phase change material in which one of the external surfaces of the container is heated by direct exposure to solar irradiation. Fundamental understanding of heat transfer during melting which arises from heating of the walls is of practical importance for efficent design of the systems.

Due to their wide range of applications of the solid-liquid phase change heat transfer problems have attracted considerable research attention and have generated a great body of analytical literature during the past few decades. Mathematically, the problem of solid-liquid phase change belongs to the class of the so-called "moving boundary problems" due to the existence of moving phase-change boundary. Such problems are nonlinear, and therefore analytical solutions of the phase change problems are known only for a mere handful of physical situations with simple geometries and boundary conditions: e.g., a semi-infinite slab with a boundary condition of the first kind (constant temperature), commonly referred to as the Neumann problem [3], a semi-infinite solid with a boundary condition of the second kind (constant heat flux), and the freezing adjacent to plane wall cooled by forced convection [4]. Consequently, approximate analytical techniques and numerical methods have been extensively used in the literature [5]. It appears that solutions of one-dimensional transient heat conduction problems involving phase change have been well established. More recently, there has been considerable interest to extend the one-dimensional phase change analysis to multidimensional geometries by considering conduction to be the only mode of heat transfer [6–8]. Experiments have provided conclusive evidence that during melting from a vertical, isothermal wall natural convection heat transfer in the liquid controls the rate of melting and the shape of the solid liquid interface [9, 10]. Local heat transfer coefficents at the heat source have been determined with a Mach-Zehnder interferometer [10]. Unfortunately, the experimental results are restricted to small temperature differences between the heated wall and the solid-liquid interface because of the difficulties in interpreting the high interference fringe density produced by larger temperature differences. An extensive up to date review of literature is available [11], and there is no need to repeat it here.

The present paper reports on melting from a vertical wall of a rectangular cavity using n-octadecane as a phase change material. This configuration was chosen because of fundamental interest and numerous applications. The ojective of the present work is to extend the earlier investigations [9, 10] by performing basic heat transfer measurements along an isothermal, vertical wall. The experiments were started with the solid material in the cavity at a uniform temperature that was either very close to, or a preselected amount below, the fusion temperature of the material. To gain improved understanding of the phenomena and support the experiments, an analysis of two-dimensional melting from a vertical, isothermal wall has also been performed, and the theoretical predictions were compared with experimental data.

Experiments

Test Apparatus. The inner dimensions of the test cell used in the experiments were 130-mm high, 50-mm wide, and 50-mm deep. In order to accommodate the volume expansion associated with the phase change process from the solid to the liquid, a small air gap was maintained between the top of the material and the insulated top surface of the cavity. The front and back windows of the test cell were made of plexiglass. The right-hand-side vertical wall of the cavity could be heated by circulating a working fluid from a constant temperature bath through the channels milled inside the heated vertical plate. The other sidewalls of the cavity were insulated by a thick layer of Styrofoam insulation that was readily removable.

The local heat transfer coefficients at the heated wall were measured using a shadowgraph method. The experimental setup employed here is identical to the one described earlier [12], thereby obviating the need for detailed exposition. Experimentally, the shadowgraphic technique for heat transfer measurements involves identification of the heat source surface as a reference position as well as the recording of the deflection of the light beam on the screen after its passage through the test cell. To make the deflection of the light beam (which passes through the this region adjacent to the heat source surface) more visible against the dark background, a plate with a narrow aperture was placed between the collimating lens and the test cell. This aperture blocked off the light entering the test cell, except that which passed in the immediate vicinity of the heat source surface.

Test Procedure and Data Reduction. Research grade (99 percent pure) n-octadecane [$OH_3(CH_2)_{16}CH_3$] was used as the phase change material in the experiments. This paraffin is a desirable because its fusion temperature is near the ambient

[1] Currently at Deparment of Mechanical Engineering, National Cheng Kung University, Tainan, Republic of China.

Contributed by the Heat Transfer Division for publication in the JOURNAL OF HEAT TRANSFER. Manuscript recieved by the Heat Transfer Division January 26, 1983.

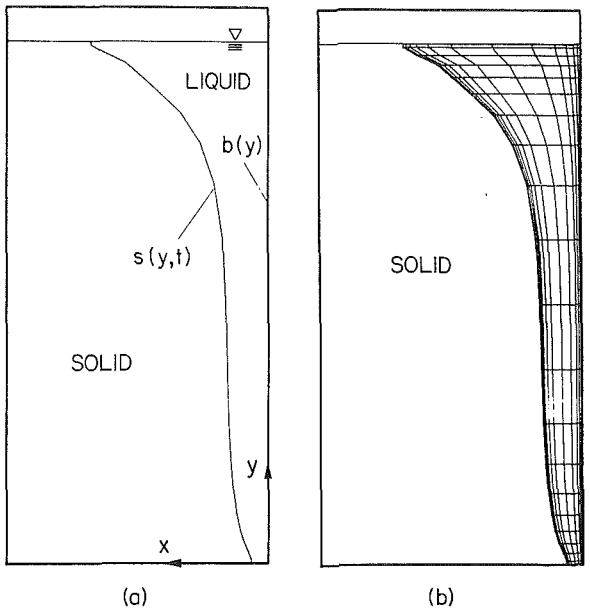

Fig. 1 (a) Schematic diagram and coordinate system for melting from a vertical wall in rectangular cavity, and (b) grid system (13 x 21) for numerical solution

laboratory temperature, which is conductive for reducing heat losses (or gains) to the ambient environment. Its liquid phase is transparent to the visible radiation, and this allows for the photographic observations and the optical measurements. In addition, the thermophysical properties of n-octadecane are reasonably well established.

The preparation for a test run always began with the degasification of the phase change material. The material was contained in a flask having a small side-opening and was heated well above its fusion temperature. Then, by connecting the side-opening of the flask to a vacuum pump, the flask was evacuated for about 3 to 4 hrs. The degasified liquid was then carefully syphoned into the test cell. The ambient air temperature was always controlled such that only a small temperature difference existed between the ambient and the fusion temperature of the material.

Once the test cell was filled with the liquid the shadowgraph system was aligned. A plastic foil marker with a grid network of the exact contour of the test cell was attached on the screen to identify the orientation of the heat source. Then, the liquid paraffin in the test cell was solidified by circulating cold (below the fusion temperature) working fluid through the channels milled inside the heat source. In the solidification process, the upper surface of the unfrozen material appeared to be concave as a result of the contraction associated with solidification. In order to obtain a rather flat upper surface of the solid, additional liquid PCM was syphoned into the test cell. After the solidification was completed the temperature of the circulating fluid was adjusted to a preselected value and maintained thereafter so as to establish an initial temperature condition in the solid for the melting experiments that followed. A uniform initial temperature in the solid was insured by circulating the coolant for a period of over 8 hrs. After all of these initial preparations, the melting experiment was started by switching on the second constant temperature bath circulating a hot (above the fusion temperature) working fluid through the heat source.

In the experiments, the surface temperatures of the heat source/sink were recorded at the preselected time intervals. The solid-liquid interface profiles as well as the shadowgraph images during the melting were photographed with a 35-mm Nikon FE camera. The contours of the solid-liquid interface were then traced from the photographs. The area of the unmelted solid PCM was evaluated with a planimeter. The accuracy of this device was estimated to be about ±5 percent for an area of one inch square (or 6.45 cm^2).

Analysis

Physical Model and Basic Equations. Two-dimensional melting of a solid from an isothermal, vertical wall was modeled mathematically. Initially, the solid was assumed to be at its fusion temperature, T_f. At time $t = 0$, the temperature of one of the vertical walls (right) of the cavity is (Fig. 1(*a*)) suddenly raised to a prescribed temperature, $T_w > T_f$. The bottom, the left wall of the cavity, the air-gap above the solid, and the two faces are assumed to be insulated. In the analysis, the following additional indealizations are made:

1 The thermophysical properties of the material undergoing phase change are independent of temperature and are evaluated at the film temperature.

2 The denstiy variation in the liquid is considered only insofar as it contributes to buoyancy, but is otherwise neglected, i.e., Boussinesq approximation is valid.

Nomenclature

b = location of heated boundary/wall (see Fig. 1)
c = specific heat
Fo = Fourier number, $\alpha t/H^2$
g = acceleration due to gravity
H = height of wall
h = heat transfer coefficient
Δh_f = latent heat of fusion
k = thermal conductivity
Nu = Nusselt number
Pr = Prandtl number, ν/α
Ra = Rayleigh number, $g\beta(T_w - T_m)H^3/\nu\alpha$
s = solid-liquid interface position (see Fig. 1)
S_c = subcooling parameter, $c_s(T_f - T_i)/\Delta h_f$
Ste = Stefan number, $c_l(T_w - T_f)/\Delta h_f$
T = temperature
t = time
u = velocity component in the x-direction
U = dimenionless velocity, uH/α
V = volume or dimensionless velocity, vH/α
v = velocity component in the y-direction
x = coordinate (see Fig. 1(*a*))
y = coordinate (see Fig. 1(*a*))
α = thermal diffusivity
B = dimensionless location of heated boundary, b/H
β = temperature coefficient of volume expansion
Γ = dimensionless solid-liquid interface position, s/H
ζ = dimensionless coordinate, x/H
η = transformation variable, see equation (1)
θ = dimensionless temperature, $(T-T_f)/(T_w-T_f)$
ν = kinematic viscosity
ξ = dimensionless coordinate, y/H
τ = dimensionless time, Fo Ste
Ψ = dimensionless stream function, ψ/α
ψ = stream function
Ω = dimensionless vorticity, $\omega/H^2\alpha$
ω = vorticity

Subscripts

f = fusion
i = initial
l = liquid phase
m = film temperature
s = solid
w = heated wall

3 Volume change due to solid-liquid phase change is negligible.

4 Liquid is assumed to be Newtonian.

5 Fluid motion in the melt is laminar and two-dimensional.

The basic conservation equations (not given here for the sake of brevity) modeling mathematically the moving boundary problem must be solved numerically. The Landau immobilization [6, 13] and the body-fitted orthogonal curvilinear time-dependent coordiante system [14] can be used to accomplish the transformation. However, the latter scheme inolves tedious mathematical manipulation to generate the orthogonal curvilinear coordinate system and increases the computational effort. Therefore, the Landau coordinate transformation

$$\eta=[x-s(y,t)]/[b(y)-s(y,t)] \tag{1}$$

is used in the present study. The main utility of this transformation is that the range of η in the transformed space ranges from zero to unity for all y during any time interval, i.e., the time-dependent physical domain occupied by the liquid has been transformed to a time-independent rectangular domain. The solid-liquid interface in the transformed space is stationary and defined by $\eta = 0$ during any given time interval. In dimensionless form the tranformed version of the governing equations can be written as:

Vorticity equation:

$$\frac{\partial\Omega}{\partial Fo}+\frac{\partial\eta}{\partial Fo}\frac{\partial\Omega}{\partial\eta}+\frac{\partial\eta}{\partial\zeta}\left[\frac{\partial\Psi}{\partial\eta}\frac{\partial\Omega}{\partial\xi}-\frac{\partial\Psi}{\partial\xi}\frac{\partial\Omega}{\partial\eta}\right]$$
$$=\mathrm{Ra\,Pr}\frac{\partial\eta}{\partial\zeta}\frac{\partial\theta}{\partial\eta}+\mathrm{Pr}\left\{\left[\left(\frac{\partial\eta}{\partial\zeta}\right)^2+\left(\frac{\partial\eta}{\partial\xi}\right)^2\right]\frac{\partial^2\Omega}{\partial\eta^2}$$
$$+2\frac{\partial\eta}{\partial\xi}\frac{\partial^2\Omega}{\partial\eta\partial\xi}+\frac{\partial^2\Omega}{\partial\xi^2}+\frac{\partial^2\eta}{\partial\xi^2}\frac{\partial\Omega}{\partial\eta}\right\} \tag{2}$$

Stream function equation:

$$-\Omega=\left[\left(\frac{\partial\eta}{\partial\zeta}\right)^2+\left(\frac{\partial\eta}{\partial\xi}\right)^2\right]\frac{\partial^2\Psi}{\partial\eta^2}+2\frac{\partial\eta}{\partial\xi}\frac{\partial^2\Psi}{\partial\eta\partial\xi}$$
$$+\frac{\partial^2\Psi}{\partial\xi^2}+\frac{\partial^2\eta}{\partial\xi^2}\frac{\partial\Psi}{\partial\eta} \tag{3}$$

Energy equation:

$$\frac{\partial\theta}{\partial Fo}+\frac{\partial\eta}{\partial Fo}\frac{\partial\theta}{\partial\eta}+\frac{\partial\eta}{\partial\zeta}\left[\frac{\partial\Psi}{\partial\eta}\frac{\partial\theta}{\partial\xi}-\frac{\partial\Psi}{\partial\xi}\frac{\partial\theta}{\partial\eta}\right]$$
$$=\left[\left(\frac{\partial\eta}{\partial\zeta}\right)^2+\left(\frac{\partial\eta}{\partial\xi}\right)^2\right]\frac{\partial^2\theta}{\partial\eta^2}+2\frac{\partial\eta}{\partial\xi}\frac{\partial^2\theta}{\partial\eta\partial\xi}$$
$$+\frac{\partial^2\theta}{\partial\xi^2}+\frac{\partial^2\eta}{\partial\xi^2}\frac{\partial\theta}{\partial\eta} \tag{4}$$

where

$$\frac{\partial\eta}{\partial Fo}=-\frac{\partial\Gamma}{\partial Fo}\left(\frac{1-\eta}{B-\Gamma}\right) \tag{5}$$

$$\frac{\partial\eta}{\partial\zeta}=\frac{1}{(B-\Gamma)} \tag{6}$$

$$\frac{\partial\eta}{\partial\zeta}=-\frac{1}{(B-\Gamma)}\left[\frac{\partial\Gamma}{\partial\zeta}+\eta\left(\frac{\partial B}{\partial\xi}-\frac{\partial\Gamma}{\partial\xi}\right)\right] \tag{7}$$

$$\frac{\partial^2\eta}{\partial\xi^2}=-\frac{1}{(B-\Gamma)}\left[\frac{\partial^2\Gamma}{\partial\xi^2}+2\frac{\partial\eta}{\partial\xi}\left(\frac{\partial B}{\partial\xi}-\frac{\partial\Gamma}{\partial\xi}\right)\right.$$
$$\left.+\left(\frac{\partial^2 B}{\partial\xi^2}-\frac{\partial^2\Gamma}{\partial\xi^2}\right)\right] \tag{8}$$

The conservation equations are subjected to the following boundary conditions:

$$\zeta=0;\ \frac{\partial\theta}{\partial\xi}=0,\ V=0,\ \Psi=0 \tag{9}$$

$$\zeta=1;\ \frac{\partial\theta}{\partial\xi}=0,\ U=V=0,\ \Psi=0 \tag{10}$$

$$\eta=0;\ \theta=0,\ U=V=0,\ \Psi=0 \tag{11}$$

$$\eta=1;\ \theta=1,\ U=V=0,\ \Psi=0 \tag{12}$$

The energy balance at the solid-liquid interface can be expressed as

$$\frac{\partial\Gamma}{\partial Fo}=-\mathrm{Ste}\frac{\partial\eta}{\partial\zeta}\frac{\partial\theta}{\partial\eta}\left[1+\left(\frac{\partial\Gamma}{\partial\xi}\right)^2\right] \tag{13}$$

Method of Solution. A finite difference method was used to solve the coupled governing equations (2–4) together with boundary conditions, equations (9–13). The equations were finite differenced and solved numerically. As a result of compromise between accuracy, stability, and computational time requried for obtaining solutions, a grid system of 13 in η-direction by 21 in ξ-direction was chosen after some trial and error. The nonuniform grid network having a smoothly varying grid spacing with a denser grid near the boundries of the liquid domain shown in Fig. 1(*b*) was constructed to account for the boundary layers near both the heated wall and the solid-liquid interface [15]. It should be noted that although the grid network in the physical space shown in Fig. 1(*b*) appears to be nonorthogonal, the grid system in the transformed space is orthogonal.

In solving the stream function equation a pseudo-transient approach was used by adding a time-dependent term, $\partial\Psi/\partial Fo$, to the left-hand side of equation (3). Then all of the governing equations may be written in a general form as follows:

$$\frac{\partial\Phi}{\partial Fo}=A_1\frac{\partial^2\Phi}{\partial\eta^2}+A_2\frac{\partial^2\Phi}{\partial\eta\partial\xi}+A_3\frac{\partial^2\Phi}{\partial\xi^2}$$
$$+A_4\frac{\partial\Phi}{\partial\eta}+A_5\frac{\partial\Phi}{\partial\xi}+S_\Phi \tag{14}$$

where the dependent variables Ω, Ψ, and θ are denoted by Φ and the relevant source terms are absorbed in S_Φ. The values of the coefficients A_i (i = 1,2, . . ,5) and S_Φ, corresponding to the appropriate dependent variables, are listed elsewhere [16].

The forward time and centered space difference scheme was used to obtain the algebraic finite difference representation of the partial derivatives in the governing equations. The alternating direction implicit (ADI) procedure [17] was employed to formulate the system of finite difference equations in the tridiagonal form. This allows for their rapid solution by utilizing the well knwon and efficient Thomas algorithm [18]. The "troublesome" cross-differential terms, $\partial^2\Phi/\partial\eta\partial\xi$, were treated as known quantities and evaluated from the values of the variables at the previous time step.

Examination of the transformed version of the governing equations and boundary conditions, equations (2–8), reveals that the fixed but unknown position of the solid-liquid interface, which is dependent on the unknown temperature field in the liquid, still presents special difficulties for the numerical procedure. An iterative procedure for evaluating this unknown interface has been used by Duda et al. [9] for a two-dimensional phase change of cylindrical system. However, this scheme is rather time consuming. A quasi-static approximation was adopted for the present study, i.e., no significant effect of the interface motion on the temperature and flow fields in the melt during short periods of melting was assumed. This assumption is valid for small Stefan numbers,

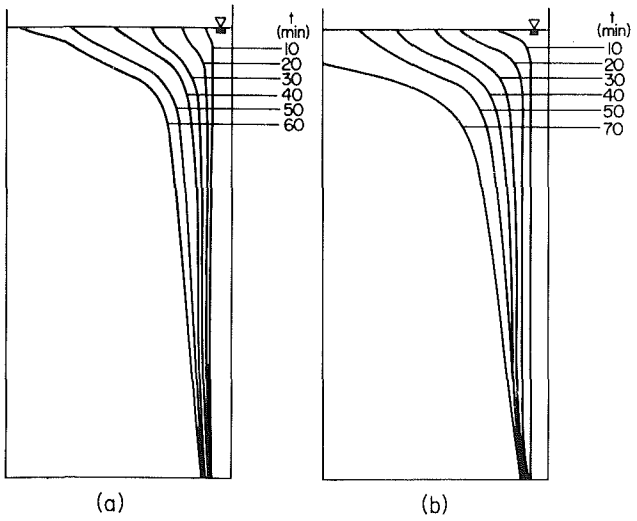

Fig. 2 Timewise motion of the melt front: (a) Ste = 0.090, S_c = 0.010, and (b) Ste = 0.137, S_c = 0.183

since the interface velocity is much slower than the velocity in the liquid. Two types of approximations, quasi-stationary and quasi-steady, can be inferred from the foregoing assumption. The quasi-stationary approximation can be made by simply neglecting the motion of the interface in calculating the flow and temperature fields in the melt, i.e., the interface is determined explicitly from the known temperature field at the previous time step. The quasi-steady approximation further simplifies the quasi-stationary assumption by neglecting the transient terms in the governing equations. In general, the quasi-stationary solution is more suitable for the initial melting period due to the rapid motion of the interface and the change of the temperature field with time so as to satisfy the appropriate initial condition. On the other hand, the quasi-steady approximation is ideally suited for long-time behavior in which the interface velocity as well as the temperature and flow fields vary slowly with time.

A combination of the approximations was adopted such that the quasi-stationary one was used for initial periods of time and quasi-steady one for late time. Under the quasi-stationary assumption, the problem reduces to one of transient natural convection with no phase change. The interface motion is determined from the energy balance condition across the interface, equation (13), based on the temperature distribution obtained at the previous time step. As for the quasi-steady solution, a sequence of steady natural convection states in the melt is determined over a number of larger quasi-static periods of time, during which the interface remains fixed within each of the time intervals. Typical dimensionless quasi-static period taken under quasi-steady assumption was $\Delta Fo = 5.0 \times 10^{-2}$, which depended on the Rayleigh number, grid size, etc. The time step employed in the computations was determined by stability considerations and depended primarily on the Rayleigh number. For example, for Ra = 10^8 a dimensionless time step $\Delta Fo = 10^{-6}$ was used. Even with a relatively crude grid the numerical computations were very time consuming, and therefore only two experiments were simulated. Simulation of one experiment required about 50,000 CPU s on a CDC 6500 digital computer.

To avoid potential computational difficulties at Fo = 0, (e.g., those associated with $1/(B - \Gamma) \rightarrow \infty$, in the governing equations), a very thin, uniform thickness melt layer parallel to the heated wall was assumed to exist initially. The value of Fo corresponding to the assumed melt thickness was determined from the relevant Neumann solution [3]. A typical

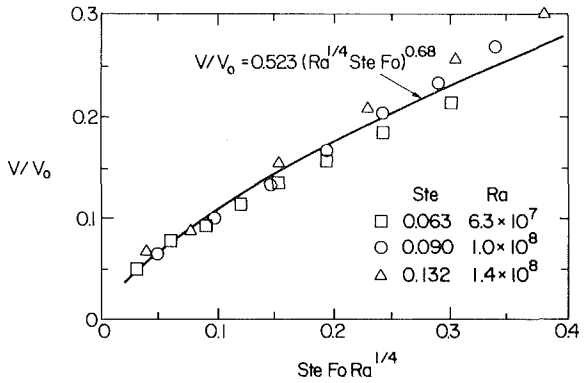

Fig. 3 Correlation of the experimental results for the molten volume fraction with negligible subcooling, $S_c \simeq 0$

initial melt layer thickness was chosen such that the molten volume fraction of the PCM was less than 5 percent. A linear initial temperature distribution across the melt layer was also assumed. The computational procedure using the ADI scheme is given elsewhere [16].

Results and Discussion

Experimental Results.

Melting Patterns. The solid-liquid interface in the direction perpendicular to the face of the test cell was found to be uniform, except in the immediate vicinity of the windows of the test cell where slightly more melting occurred. This edge effect is due to conduction along the plexiglass windows which have higher thermal conductivity than the solid. Typical progression of the solid-liquid interface with time, traced directly from the photographs, is shown in Fig. 2. At early times (t = 10 min) it is evident that heat transfer in the melt zone is predominated by conduction, since the molten region appears to be uniformly parallel to the vertical heated wall, except in the vicinity of the free surface where substantial more melting takes place. This earlier departure of the melting behavior at the top of the solid is attributed to the presence of the density-induced melt motion, resulting from the volume increase which accompanies the phase change. This phenomena forced the liquid to seek extra space to expand and thus overflow the top of the solid core. As the heating continued, the buoyancy-driven convection in the melt started to develop and continued to intensify as evidenced by the appearance of a nonuniform melt layer receding from the free surface to the bottom. As the melt moved upward adjacent to the heated vertical plate, it gained heat and reached the maximum temperature near the free surface. The heated liquid then took a 90 deg turn, deflecting away from the heated wall toward the solid-liquid interface. Consequently, significantly more melting occured in this region. It should be noted that the density-induced overflowing of the solid core by the liquid produces enhanced melting in the region. As the melt flowed downward along the solid-liquid interface, it lost heat and directly contributed to the melting of the solid; and thereby, its capability to melt the solid was gradually decreased to the minimum at the bottom of the cavity.

The timewise variation of the molten volume fraction has been evaluated by integrating the melting front contours, and the results are depicted in Fig. 3. It can be seen that all the data collapse quite well into a single curve by employing the parameter $Ra^{1/4}$ Ste Fo as an abscissa, and a correlation by least squares fit has been obtained as

$$V/V_o = 0.523\,(\mathrm{Ra}^{1/4}\,\mathrm{Ste}\,\mathrm{Fo})^{0.68} \qquad (15)$$

This correlation is depicted in Fig. 3 by the solid line. The

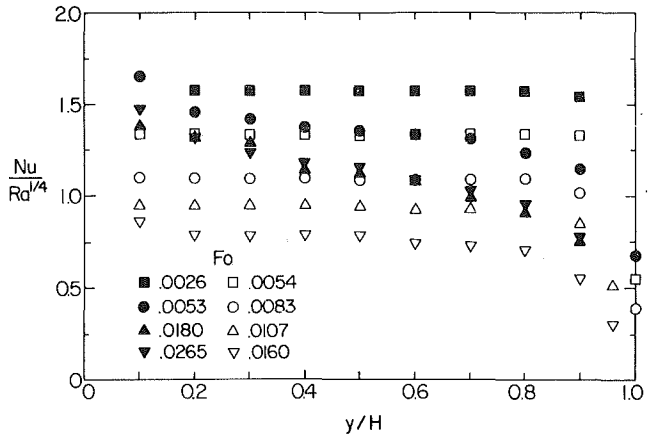

Fig. 4 Timewise variation of the local Nusselt number along the vertical wall, Ste = 0.063, S_c = 0.012, Ra = 6.3 x 10^7 (open points) and Ste = 0.132, S_c = 0.008, Ra = 1.4 x 10^8 (solid points)

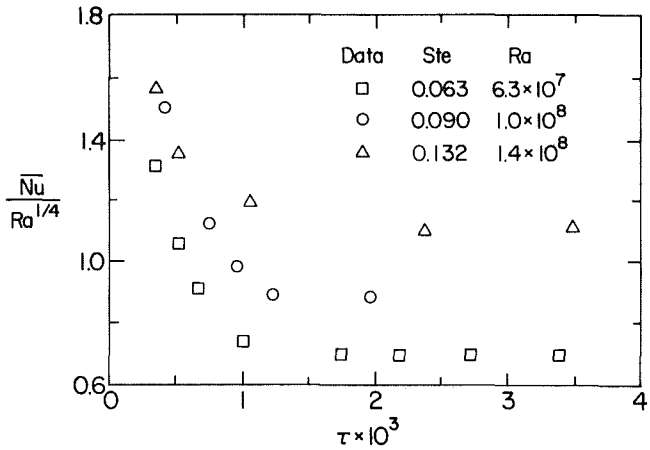

Fig. 5 Timewise variation of the average Nusselt number at the heated vertical wall for various Stefan numbers, $S_c \simeq 0$

height, H, of the initially present solid was chosen as the characteristic length for the Rayleigh number. A variable similar to $Ra^{1/4}$ Ste Fo was also used by others for correlating the molten fraction during an inward melting inside a vertical tube [20]. The initial subcooling was found to significantly impede the melting process. This is expected because of the following: first, only a portion of the energy transported to the solid-liquid interface contriubtes directly to the melting of the material as a result of heat conduction occurring across the interface toward the inner core of the solid. Second, the slowdown in the progression of the melt front resulting from conduction in the solid core causes a delay in the onset and development of the buoyancy driven recirculation in the melt.

Heat Transfer From the Heat Source Surface. The timewise variation of the aforementioned local heat transfer characteristics along the heated plate are depicted quantitatively in terms of the heat transfer parameter $Nu/Ra^{1/4}$ for different Stefan numbers as shown in Fig. 4. The height, H, of the initially present solid was chosen as the characteristic length for both Nusselt and Rayleigh numbers. It is realized that this length scale may not be appropriate for all times because the shape and the size of the melt region changes with time. The melt layer thickness may be the more appropriate characteristic length at early times, but unfortunately it is not constant and increases with time.

The results of Fig. 4 show that at early time the heat transfer coefficent is independent of position along the wall. This is indicative of conduction dominated heat transfer. The sharp decrease in the heat transfer coefficient in the vicinity of the free interface (y/H = 1.0) at Fo = 0.0054 is attributed to

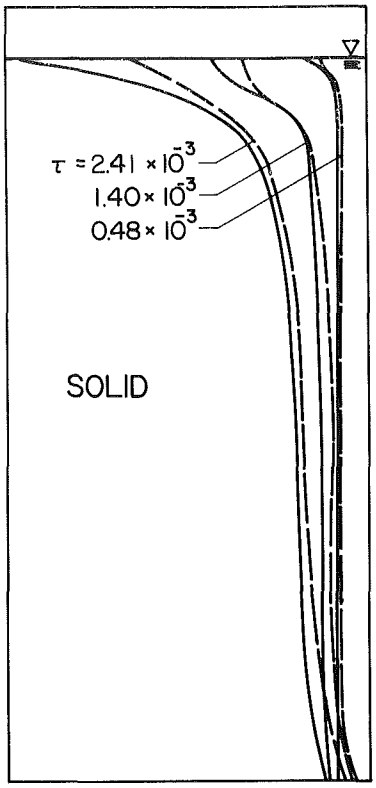

Fig. 6 Comparison of the predicted melting front profiles with experimental results, Ste = 0.090

the fluid motion induced by the difference in densities between the solid and the liquid. As the melting progresses and natural convection develops and intensifies, the heat transfer coefficients decrease. The results of the figure indicate that for higher Rayleigh number (Ra = 10^8) nearly quasi-steady heat transfer coefficient has been reached at late times (Fo > 0.026).

A quantitative comparison of the local heat transfer results at the heated wall with those reported earlier [10] could not be made because of the large difference in the Stefan numbers. Nevertheless, the qualitative trends of the spatial variation of the local heat transfer coefficients of this study are quite similar to those results. Local heat transfer coefficients show a maximum at the bottom edge and then decrease upward to the top of the wall.

The instantaneous average heat transfer coefficients at the heated wall, $\overline{Nu}_w$, are determined by spatial averaging of the local values and are presented in Fig. 5. During the initial stages of melting, the average heat transfer coefficent decreases rapidly, which is a characteristic of transient heat conduction. At later times, in the presence of density-induced motion and buoyancy-driven natural convection, the decrease of heat transfer slows down and eventually reaches a quasi-steady state.

Comparison Between Predictions and Experimental Data.

Melt Shape and Volume. A comparison between the experimentally determined and predicted melting front profiles at different times is illustrated in Fig. 6. The solid and dashed lines depict the measured and predicted melting fronts, respectively. At early time (τ = 0.00048), the agreement is excellent except at the very bottom and top regions of the cavity. The slightly greater measured melting rate at the bottom edge could be partly attributed to heat conduction along the bottom wall of the cavity due to the removal of initial singularity in the solution by a false-start. As for the

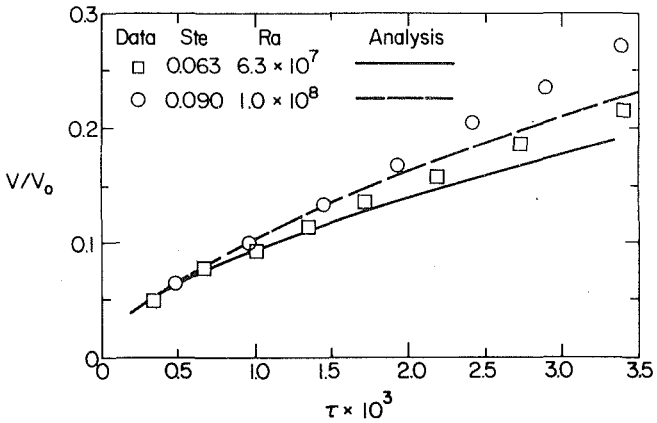

Fig. 7 Predicted and experimental molten volume fraction as function of dimensionless time

discrepancy at the top free surface, it is primarily attributed to the neglect in the mathematical model of the volume expansion due to the phase change from the solid to the liquid. As melting continues, the effect of this density-induced overflow motion appears to become more significant as indicated by the greater discrepancy between the measured and predicted melting front positions, particulary in the vicinity of the free surface.

The two main factors responsible for the discrepany between measured and predicted interface predictions are believed to be the volumetric expansion of the material and the buildup of the truncation errors with time due to a relatively coarse grid used. In order to assess the truncation errors, the grid was increased from 13 × 21 to 21 × 21, and good agreement was obtained between the two results; however, the calculations were not carried out for long simulation times. Other possible factors could be the inherent uncertainty in the physical and transport properties, which were assumed to be temperature- independent in the analysis, the non-Newtonian behavior of the liquid near the solid-liquid interface, and surface tension effects at the top of the melt. During melting, the solid-liquid interface is moving out of the liquid region, which is analogous to blowing fluid away from the boundary. This effect may have also contributed to the discrepancy between the data and predictions, because it has not been accounted for in the model.

The predicted instantaneous molten volume fraction, V/V_o, is evaluated from the solid-liquid interface position by a numerical integration of the instantaneous positions and is defined as

$$V/V_o = 1 - \frac{1}{V_o}\int_0^1 \Gamma(\xi,\mathrm{Fo})\, d\xi \qquad (16)$$

A comparison of the experimental data with the predicted molten volume fractions is shown in Fig. 7. It is apparent from the figure that the melting rate predicted by numerical simulation is lower than the measured one. Furthermore, the deviation increases not only with time but also with the Stefan number (or Rayleigh number). The possible reasons for the discrepancy between data and predictions have already been mentioned.

Heat Transfer. Typical predicted isopleths of streamlines and temperature in the melt during the numerical simulation of the melting process are illustrated in Fig. 8 through a sequence of contour plots. At early time (τ = 0.00076 not shown), a uniform temperature distribution with a weak and symmetrical flow field was predicted in the narrow melt layer. The maximum of the stream function was located at the midplane of the narrow melt gap. This is a characteristic of heat conduction dominated energy tranpsort. As melting

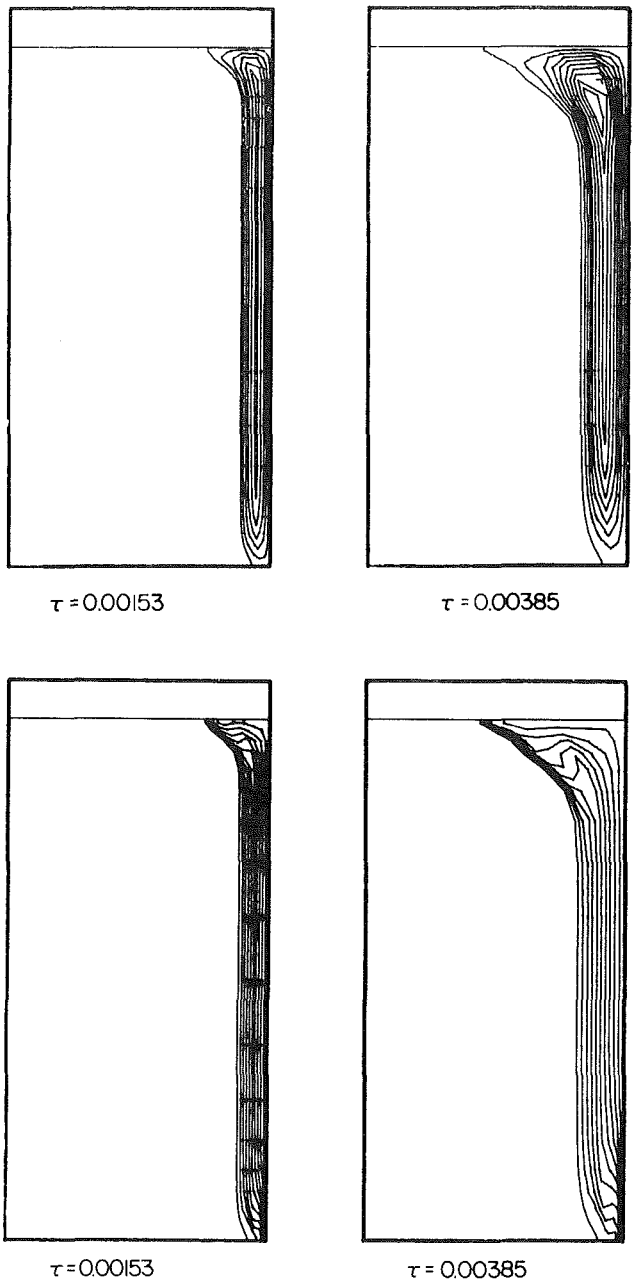

Fig. 8 Predicted distribution of streamlines (upper panels) and isotherms (lower panels) Ste = 0.063 and Ra = 6.3 × 10^7

continues (τ = 0.00153), the intensification of the convective recirculating flow is indicated by the upward shifting of the vortex center to the region in the vicinity of the free surface (Fig. 8). A rather linear temperature variation is displayed across the central portion of the melt region, whereas a uniform temperature zone appears in the upper part as well as in the very bottom edge of the melt cavity. The highest temperature gradients exist at the very bottom of the heated wall as well as at the upper part of the solid-liquid interface. As a result, heat transfer at the upper portion is enhanced and leads to greater interface velocity. Similary, slower melting is expected at bottom because the liquid has cooled as it flows along the interface. In view of the characteristics of temperature and flow fields in the melt as described above, it follows that at time τ = 0.00385 heat is transported by the buoyancy-driven recirculating flow as well as by conduction directly across the melt layer.

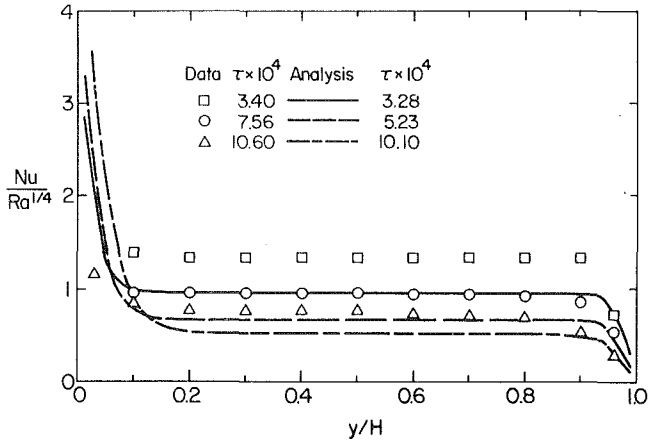

Fig. 9 Comparison of measured and predicted local Nusselt numbers along the heated vertical wall, Ste = 0.063 and Ra = 6.3×10^7

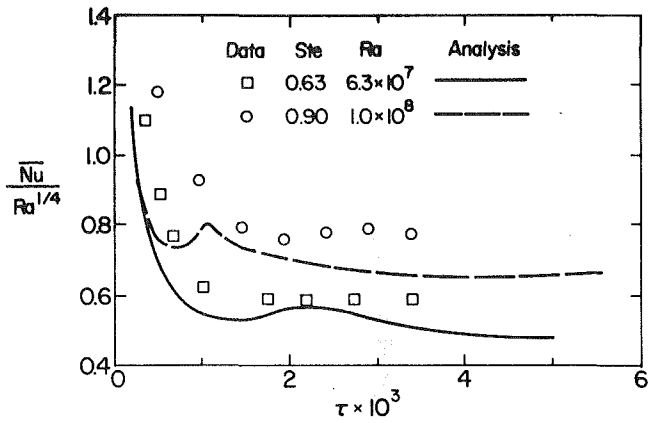

Fig. 10 Comparison of meaured and predicted average Nusselt numbers at the heated wall as a function of dimensionless time

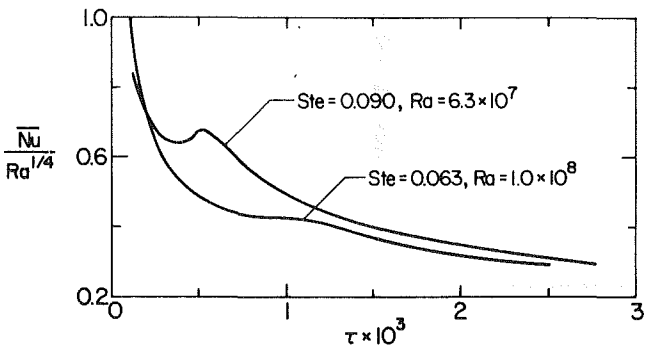

Fig. 11 Predicted average Nusselt numbers at the solid-liquid interface as a function of dimensionless time

Figure 9 shows a comparison of the predicted local heat transfer coefficients along the vertical wall with the experimental data for a given Stefan number. It is evident from the figure that the predicted local heat transfer coefficients are somewhat lower than the measured ones. Results could not be obtained for early times and/or close to the leading ($y/H - > 0$) and trailing ($y/H - > 1$) edges of the plate, because clear shadowgraph images could not be formed at these locations. The reasons already discussed may be responsible for the discrepancies. However, the predicted local heat transfer variation along the heated vertical wall displays a similar trend to those of the measurements. Additional comparisons can be found elsewhere [16].

The average heat transfer coefficients at the solid-liquid interface $\overline{Nu}_s$ and at the heat wall $\overline{Nu}_w$ have been evaluated from the temperature distribution in the melt as

$$\overline{Nu}_w = \int_0^1 -\left[\frac{\partial \eta}{\partial \zeta}\frac{\partial \theta}{\partial \eta}\right] d\xi \tag{17}$$

$$\overline{Nu}_s = -\frac{1}{\Gamma_l}\int_0^1 \frac{\partial \eta}{\partial \zeta}\frac{\partial \theta}{\partial \eta}\left[1+\left(\frac{\partial \Gamma}{\partial \xi}\right)^2\right]^{1/2} \Gamma\, d\xi \tag{18}$$

where the quantity Γ_l in equation (18) denotes the length of the solid-liquid interface contour. Figure 10 depicts the calculated average heat transfer coefficient at the heated wall for two different Stefan numbers. The results display a rapid decrease in heat transfer rate at the early stages of melting which is indicative of transient heat conduction. As the melting progresses, natural convection sets in and develops, the decrease in heat transfer slows down, and then is followed by an increase over some period of time. This period of time as well as the magnitude of the increase in heat transfer appears to depend on the Rayleigh number; for ($Ra = 6.3 \times 10^7$), only a slight increase exists while for higher Rayleigh number, $Ra = 1.0 \times 10^8$, a sharp increase occurs at early time ($\tau = 0.001$). Later as the melt region becomes wider, the heat transfer coefficient passes through a local maximum and starts to decline gradually until a quasi-steady value is reached. This trend of having a maximum heat transfer at some time during the melting has also been predicted [13] for an outward melting from a vertical cylinder. For purposes of comparison the experimental data are also included in Fig 10. The experimental results show that following the sharp decrease at the early times in the process, the heat transfer continues to decline gradually toward a quasi-steady value without the indication of a local maximum predicted by the numerical solution. It is also clear that the numerically predicted results are lower than the experimental data. There are several factors which could lead to these discrepancies in the trend of the timewise variation as well as the numerical magnitude of the average heat transfer coefficients. The neglect of the density-induced motion in the numerical model appears to be the main cause responsible for this discrepancy.

The variation of the average heat transfer coefficient with dimensionless time at the solid-liquid interface has been predicted (Fig. 11). In general, the timewise variation of the heat transfer at the interface exhibits a similar trend to that at the heated wall. However, at the very late time, the results show that a gradual decline in the heat transfer coefficient continues and gives no indication that a quasi-steady condition has been reached as that which was displayed at the heated wall. This is due to the increase in the heat transfer surface area at the solid-liquid interface as the melting progresses [16].

Conclusions

The experimental results have clearly established that the melting rate, the melting front profiles, and the heat transfer are significantly affected by the fluid motion in the melt induced by the buoyancy force (natural convection) and by the volumetric expansion which accompanies the phase change from the solid to the liquid. The latter process is particularly significant at the early times while the heat transfer is still dominated by conduction. The initial subcooling of the solid significantly impedes the melting process, because a portion of the energy transported to the soild-liquid interface. The resulting slowdown of the melt layer growth also causes a delay in the onset and development of the buoyancy-driven recirculation in the melt.

The instantaneous local heat transfer coefficients at the heated surface during melting from an isothermal vertical wall of a rectangular cavity were independent of the vertical

position at the early times. As time progressed, the local heat transfer coefficients became nonuniform and decreased from the bottom edge of the wall toward the top, as a result of the density-induced and the buoyancy-driven fluid motion in the melt. The spatially averaged heat transfer coefficients at the heated vertical wall displayed a rapid decrease at the early stages of melting and later reached a quasi-steady state value.

Based on the numerical simulation for the two-dimensional inward melting from a vertical wall of a rectangular cavity, it is concluded that the neglect of the volumetric expansion in the mathematical model associated with the melting and the truncation errors due to insufficiently fine grid are mainly responsible for the discrepany between the predictions and the experimental data. The numerical results obtained with a rather crude (13 $\times$ 21) grid should be considered as preliminary. Much more efficient algorithms are needed for solving numerically moving boundary problems of the type considered here.

Acknowledgments

This work was supported by the National Science Foundation Heat Transfer Program under Grant MEA-8014061.

References

1 Benard, C., Gobin, D., and Gutierrez, M., "Experimental Results of a Latent-Heat Solar-Roof Used for Breeding Chickens," *Solar Energy*, Vol. 26, No. 3, 1981, pp. 347-359.

2 Benard, C., Body, Y., Gobin, D., and Guerriez, B., "Use of a Variable Parameter Test-Cell for the Study of Latent-Heat Solar Walls," *Solar Energy*, Vol. 29, No. 2, 1982, pp. 101-109.

3 Carslaw, H. S. and Jaeger, J. C., *Conduction of Heat in Solids*, Claredon Press, Oxford, 1959.

4 Hsu, C. F., and Sparrow, E. M., "A Closed-Formed Analytical Solution for Freezing Adjacent to a Plane Wall Cooled by Forced Convection," ASME JOURNAL OF HEAT TRANSFER, Vol. 103, No. 3, 1981, pp. 596-598.

5 Lunardini, V. J., *Heat Transfer in Cold Climates*, Van Nostrand Reinhold Co., New York, 1981.

6 Saitoh, T., "Numerical Method for Multidimensional Freezing Problems in Arbitrary Domains," ASME JOURNAL OF HEAT TRANSFER, Vol. 100, No. 2, 1978, pp. 294-299.

7 Hsu, C. F., Sparrow, E. M., and Patankar, S. V., "Numerical Solution of Moving Boundary Problems by Boundary Immobilization and a Control-Volume-Based, Finite Difference Scheme," *International Journal of Heat and Mass Transfer*, Vol. 24, 1981, pp. 1335-1343.

8 Sparrow, E. M., and Hsu, C. F., "Analysis of Two-Dimensional Freezing on the Outside of a Coolant-Carrying Tube," *International Journal of Heat and Mass Transfer*, Vol. 24, 1981, pp. 1345-1357.

9 Hale, N. W., Jr., and Viskanta, R., "Photographic Observation of the Solid-Liquid Interface Motion During Melting of a Solid Heated from an Isothermal Vertical Wall," *Letters in Heat and Mass Transfer*, Vol. 5, No. 6, 1978, pp. 329-337.

10 Van Buren, P. D., and Viskanta, R., "Interferometric Measurement of Heat Transfer During Melting From a Vertical Surface," *International Journal of Heat and Mass Transfer*, Vol. 23, No. 4, 1980, pp. 568-571.

11 Viskanta, R., "Phase-Change Heat Transfer," *Solar Heat Storage: Latent Heat Materials*, Vol. 1, edited by G. A. Lane, Uniscience Edition, CRC Press, Boca Raton, (1983).

12 Bathelt, A. G., and Viskanta, R., "Heat Transfer and Interface Motion During Melting and Solidification From a Finned Heat Source/Sink," ASME JOURNAL OF HEAT TRANSFER, Vol. 103, No. 4, 1981, pp. 720-726.

13 Sparrow, E. M., Patankar, S. V., and Ramadhyani, S., "Analysis of Melting in the Presence of Natural Convection in the Melt Region," ASME JOURNAL OF HEAT TRANSFER, Vol. 99, No. 4, 1977, pp. 520-526.

14 Rieger, H., Projahn, U., Bereiss, M., and Beer, H., "Heat Transfer During Melting Inside Horizontal Tube," ASME JOURNAL OF HEAT TRANSFER, Vol. 105, No. 2, 1983, pp. 226-234.

15 Kublbeck, K., Merker, G. P., and Straub, J., "Advanced Numerical Computation of Two Dimensional Time-Dependent Free Convection in Cavities," *International Journal of Heat and Mass Transfer*, Vol. 23, No. 2, 1980, pp. 203-217.

16 Ho, C.-J., "Solid-Liquid Phase Change Heat Transfer in Enclosures," Ph.D. thesis, Purdue University, Dec. 1982.

17 Peaceman, D. W., and Rachford, H. H., Jr., "The Numerical Solution of Parabolic and Elliptic Differential Equations," *Journal of the Society of Industrial Applied Mathematics*, Vol. 23, No. 1, 1955, pp. 28-41.

18 Gerald, C. F., *Applied Numerical Analysis*, Addison-Wesley Publishing Co., Reading, Mass., 1978.

19 Duda, J. L., Malone, M. F., Notter, R. H., and Vrentas, J. S., "Analysis of Two-Dimensional Diffusion-Controlled Moving Boundary Problems," *International Journal of Heat and Mass Transfer*, Vol. 18, Nos. 7/8, 1975, pp. 901-910.

20 Sparrow, E. M., and Broadbent, J. A., "Inward Melting in a Vertical Tube Which Allows Free Expansion of the Phase-Change Medium," ASME JOURNAL OF HEAT TRANSFER, Vol. 104, No. 2, 1982, pp. 309-315.

Analysis of Two-Dimensional Melting in Rectangular Enclosures in Presence of Convection

A. Gadgil[1]

D. Gobin

Equipe TESS, ERA 1028. CNRS,
Campus Universitaire,
Bat. 502. 91405-Orsay,
France

Two-dimensional melting of a solid phase change material in a rectangular enclosure heated from one side is simulated numerically. The simulations are carried out by dividing the process in a large number of quasi-static steps. In each quasi-static step, steady-state natural convection in the liquid phase is calculated by directly solving the governing equations of motion with a finite difference technique. This is used to predict the shape and motion of the solid-liquid boundary at the beginning of the next step. The predictions are found to be in good agreement with experiment. Influence of some of the governing parameters on the time development of the melting process is studied using the numerical simulation procedure.

1 Introduction

An analysis of heat transfer and thermal storage in a phase-change material (PCM) generally must take into account natural convective heat transfer in the liquid phase. Such an analysis can be adequately based on conduction alone, only if either the liquid phase of the PCM is always homogeneous in temperature, or the temperature gradients in the liquid phase are either stable or below the critical value needed for natural convection. Many typical applications of heat transfer and thermal storage in PCMs involve convection in the liquid phase at Rayleigh numbers, (Ra based on height) in excess of 10^7. As will be shown below, the convective contribution to the heat transfer process in such a case may be as much as 50 times larger than the contribution of conduction, invalidating any analysis based on conduction alone.

The problem of melting in the presence of convection, in a two-dimensional rectangular enclosure heated from one side and containing initially solid PCM at its fusion temperature is considered here. The convection in the liquid phase is usually significant, and in many cases desirable, since PCMs often have poor thermal conductivity. Careful investigation of convective effects is important to any study aiming to optimize PCM elements for specific thermal storage applications.

There is clear and overwhelming experimental evidence [1-7] that, except in very early times, convective heat transfer dominates over conductive heat transfer in the liquid phase during the melting process. Several studies [1, 5, 8, 9] have treated this problem in one dimension, using either analytic or empirical expressions for convective heat transfer in the liquid phase. However, studies which take account of the two- (or three-) dimensional convective heat transfer process are very rare in the literature, probably due to the formidable difficulty of analyzing convection in an irregular-shaped cavity with a moving boundary. Numerical solutions for a two-dimensional melting problem in a cylindrical geometry, with recirculating flow in the liquid phase, were presented by Sparrow, Patankar, and Ramadhyani [10]. Their predictions were limited to moderate Rayleigh numbers ($Ra < 10^6$). Though Hale and Viskanta [3] have reported experimental results in qualitative agreement with these predictions, the authors are unaware of any explicit experimental verification of the predictions of [10].

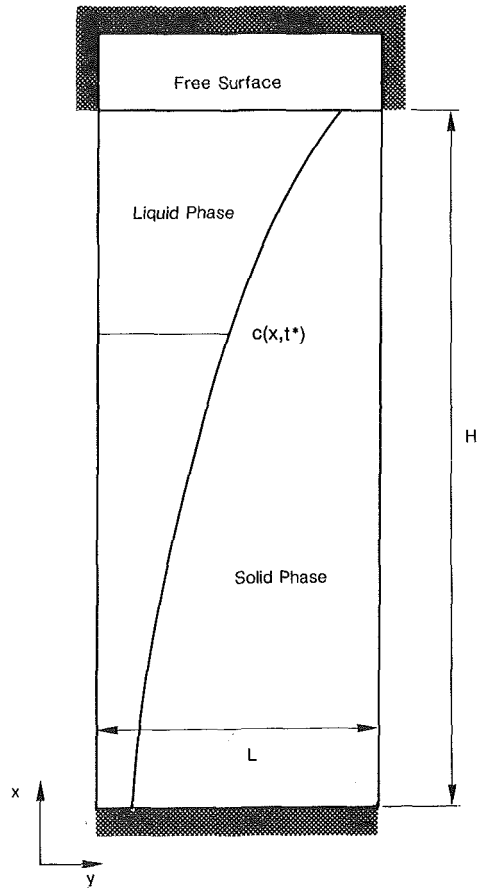

Fig. 1 System geometry

In most thermal storage applications, and consequently in most experimental investigations [1-7, 11, 12], the Rayleigh number in the liquid region is very high, typically in the range $10^6 < Ra < 10^9$. The fluid flow in enclosures driven with such high Ra numbers is characterized by fast moving thin boundary layers through which most of the heat transfer takes place, while the region away from the walls, often called the "core region," is mostly inactive. Experimental evidence (e.g., [13]) indicates that the flow remains entirely laminar in this range of Ra numbers, transition to turbulence occurring only beyond Ra numbers of 10^{10}.

[1] Present address: Lawrence Berkeley Laboratory, University of California, Berkeley, Calif., 94720.

Contributed by the Heat Transfer Division for publication in the JOURNAL OF HEAT TRANSFER. Manuscript received by the Heat Transfer Divison May 7, 1982.

2 Problem Definition and Governing Equations

A two-dimensional rectangular enclosure (height H, width L), contains the PCM initially at its fusion temperature, T_F. The top and bottom surface of the enclosure are adiabatic; the bottom surface is no-slip, while the top surface is full slip due to an air gap which is customarily present at the top. At time $t^* = 0$, one vertical wall is raised to a temperature $T_H = T_F + \Delta T$; the other vertical wall is maintained isothermal at temperature T_F. Heat propagates into the PCM by conduction and convection, and at a later time, $t^* > 0$, the liquid-solid interface (henceforth called the melting front) has a shape similar to that shown in Fig. 1. The melting front is defined in this paper by a function, $c(x,t^*)$ such that at height, x, and at time, t^*, it equals the horizontal distance between the hot wall and the melting front. The shape and average position of the melting front at any given time $t^* > 0$ are of both theoretical and practical interest. The shape of the melting front is an extremely sensitive indicator of the variation in the local heat transfer rate to the solid and is used as a test of the numerical simulation procedure. The average position of the melting front yields, to a close approximation, the total amount of heat stored in the PCM element since the onset of melting.

The Navier Stokes equations (with Boussinesq approximation), are nondimensional with scales ν, ΔT, H, and Ste for kinematic viscosity, temperature difference, enclosure height, and the Stefan number, respectively. The four dimensionless groups characterizing the problem are: A (enclosure aspect ratio), Pr (Prandtl number of the liquid phase), Ra (Rayleigh number based on enclosure height), and Ste (Stefan number). Time is nondimensionalized using the relation

$$t = t^* \nu / H^2$$

To obtain a rectangular enclosure with orthogonal rectilinear coordinates system in the computational space ($\hat{X}$, $\hat{Y}$), whose boundaries match with the (nonrectangular) enclosure boundaries in the physical space (x, y), the coordinates are nondimensionalized and transformed according to the following equations

$$\hat{X} = x/H \tag{1}$$

$$\hat{Y} = y/(C(\hat{X},t)H) \tag{2}$$

where $C(\hat{X},t)$ is the dimensionless shape function for the melting front defined as

$$C(\hat{X},t) = c(x,t^*)/L$$

The dimensionless coordinates ($\hat{X}$, $\hat{Y}$) extend from 0 to 1, and from 0 to $1/A$, respectively in the computational space. The grid lines of constant $\hat{X}$ and constant $\hat{Y}$ are rectilinear and orthogonal in the computational space, and in general, curvilinear and nonorthogonal in the physical space. Since most of the fluid flow is in the boundary layers which flow along lines of constant $\hat{X}$ and $\hat{Y}$, problems of false diffusion arising from flow crossing the grid lines at large angles [14] are minimized.

For representative values of the governing dimensionless parameters considered in this paper (Pr = 50, Ra = 10^8, Ste = 0.2, A = 2.5), it was observed in the experiments described in [15] that the velocity of propagation of the melting front was $0(3 \times 10^{-6})$ m/s, which is several orders of magnitude smaller than the fluid velocities in the boundary layers on the vertical walls estimated to be $0(3 \times 10^{-3})$ m/s. This suggests that the calculations of the melting front motion can be decoupled from the calculations of the natural convective flow in the melt region by dividing the process in a number of quasi-static steps. Within each quasi-static step, the melting front position, $C(\hat{X},t)$ will be held fixed for calculation of the steady-state natural convection flow in the liquid phase. At the end of this calculation, the shape and motion of the melting front are recalculated before beginning the calculations of natural convection flow in the newly defined melted region for the next quasi static step.

Arguing from experimental observations [3, 15] of typical melting front shapes, first and higher space derivatives of $C(\hat{X},t)$ will be dropped from the equations governing natural convection in the melt region. It is estimated from experimentally observed melting front shapes that this simplification will cause underprediction of the heat transfer to the melting front by less than 8 percent. Though $C(\hat{X},t)$ is a function of time, its use in the steady state governing equations is legitimate due to the quasi-static nature of the solution procedure.

We define $\hat{\nabla}$ and $\hat{\nabla}^2$, the Gradient and Laplacian operators in dimensionless computational space, as

Nomenclature

A = aspect ratio of the enclosure, equal to H/L
$c(x,t^*)$ = dimensional distance of the melting front from the hot wall
C_p = heat capacity of the liquid PCM
f = percentage of the volume of the enclosure in the liquid phase
g = acceleration due to gravity
Gr = Grashof number, based on the height of the enclosure, equal to $g \cdot \beta \cdot \Delta T \cdot H^3/\nu^2$
H = height of the enclosure
L = width of the enclosure
Nu = Nusselt number at the hot wall (average), equal to $\int_0^A \nabla\theta \cdot \mathbf{n} \cdot dX$
Nu* = Nusselt number at the liquid-solid interface (average), equal to $\int_{\text{melting front}} \nabla\theta \cdot \mathbf{n} \cdot dX$
p = pressure
Pr = Prandtl number of the liquid PCM, equal to ν/α
Q_F = latent heat of fusion of the PCM
Ra = Rayleigh number, based on the height of the enclosure, equal to Gr•Pr
Ste = Stefan number, equal to $C_p \cdot \Delta T/Q_F$
T_F = fusion temperature of the PCM
T_H = temperature of the hot wall
t^* = dimensional time
t = dimensionless time, equal to $t^* \cdot \nu/H^2$
$U(V)$ = vertical (horizontal) component of the velocity
x,y = dimensional coordinates
$\hat{X},\hat{Y}$ = computational dimensionless coordinates
X,Y = physical dimensionless coordinates
α = thermal diffusivity of the liquid PCM
β = expansion coefficient
θ = dimensionless temperature
ν = viscosity of the liquid PCM
∇ = gradient operator

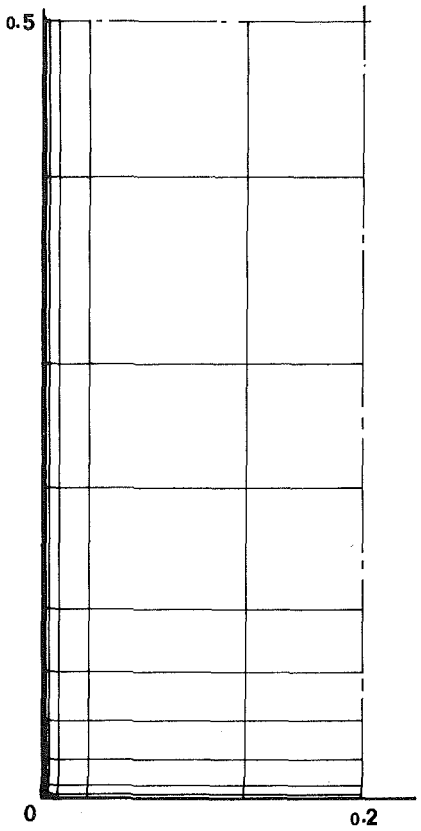

Fig. 2(a) Computational grid

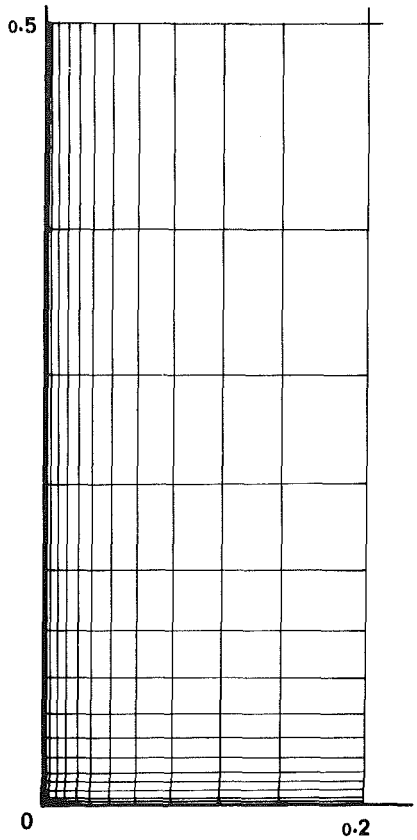

Fig. 2(b) Reference grid

$$\hat{\nabla} = \left(\frac{\partial}{\partial \hat{X}}\mathbf{i} + (1/C(\hat{X},t))\frac{\partial}{\partial \hat{Y}}\mathbf{j}\right) \tag{3}$$

$$\hat{\nabla}^2 = \left(\frac{\partial^2}{\partial \hat{X}^2} + (1/C(\hat{X},t))^2\frac{\partial^2}{\partial \hat{Y}^2}\right) \tag{4}$$

where $\mathbf{i}$ and $\mathbf{j}$ are the unit vectors along $\hat{X}$ and $\hat{Y}$, respectively. The nondimensionalized, steady-state equations in these coordinates are

$$\text{continuity:} \quad \hat{\nabla} \cdot \mathbf{V} = 0 \tag{5}$$

$$\text{momentum:} \quad (\mathbf{V} \cdot \hat{\nabla})\mathbf{V} = \hat{\nabla}^2\mathbf{V} - \hat{\nabla} p + \mathrm{Gr}\,\Theta\mathbf{z} \tag{6}$$

$$\text{energy:} \quad (\mathbf{V} \cdot \hat{\nabla})\Theta = (1/\mathrm{Pr})\hat{\nabla}^2\Theta \tag{7}$$

where Gr is the Grashof number based on height, and $\mathbf{z}$ is the unit vector in the direction of gravity. The boundary conditions are:

Top horizontal wall: $\hat{X}=1;\ d\Theta/d\hat{X}=0,\ U=0,\ dV/d\hat{X}=0$ (8*a*)

Bottom horizontal wall: $\hat{X}=0;\ d\Theta/d\hat{X}=0,\ U=0,\ V=0$ (8*b*)

Left vertical wall: $\hat{Y}=0,\ \Theta=0.5,\ U=0,\ V=0$ (8*c*)

Right wall (melting front): $\hat{Y}=1/A;\ \Theta=-0.5,\ U=0,\ V=0$ (8*d*)

In the experiments with paraffin described in [15] at the representative values of the governing parameters, the melting front velocity was $0(3 \times 10^{-6})$ m/s, causing the normal velocity imparted to the newly melted liquid layer, due to the 10 percent decrease in PCM density on melting, to be $0(3 \times 10^{-7})$ m/s. This normal velocity is several orders of magnitude smaller than the velocities in the boundary layers on the vertical walls estimated at $0(3 \times 10^{-3})$ m/s. Calculations carried out using the methodology of Kast [16] show that this small normal velocity can be safety neglected.

The equation of motion of the melting front is solved in the following different dimensionless coordinate system (X, Y) defined as

$$X = \hat{X} = x/H \tag{9}$$

$$Y = y/H \tag{10}$$

In the foregoing orthogonal coordinate (equations (9-10)), the equation of motion of the melting front is

$$dn/dt = (\nabla\Theta \cdot \mathbf{n})\,\mathrm{Ste}/\mathrm{Pr} \tag{11}$$

where $\hat{n}$ is the local normal to the melting front, and dn/dt is the local velocity of the melting front along $\hat{n}$.

The thermal conductivity of the liquid phase does not vary appreciably with temperature for paraffins [17] in the temperature range of interest (T_F to about $T_F + 25°C$). The kinematic viscosity is temperature dependent, and its value at the mean temperature has been used.

3 Numerical Solution Procedure

The computations are begun by applying the classical Stefan solution (melting with pure conduction) so as to melt a small amount of PCM adjacent to the hot wall. This volume is small enough (< 5 percent of PCM volume with $A = 2.5$, and $\mathrm{Ra} = 10^7$) that Ra_L is much less than 10^4, the conduction limit. It has been computationaly ascertained that the further time-development of the melting simulation is not sensitive to the initially melted volume of this order.

The rest of the simulation is carried out by dividing the melting process into a large number of quasi-static steps as explained earlier. In each quasi-static step, the heat transfer rate to the melting front obtained from the previous step is first used to obtain the new position of the melting front according to equation (11). Steady-state natural convection

flow in the newly defined cavity is then obtained numerically. The resulting temperature field in the melt region is used to obtain the new value of the heat transfer rate to the melting front for use in the next step. The simulation is terminated when 95 percent of the PCM has passed into the liquid phase.

3.1 Simulating the Motion of the Melting Front. Each quasi-static step calculation begins with converting the convective heat flux at the cold vertical wall ($\hat{Y}=1/A$ wall in $(\hat{X},\hat{Y})$ coordinates, equation (8*d*)) produced in the previous step, into the (X,Y) coordinates used for melting front propagation. The (X,Y) coordinates are preferred for calculating the melting front propagation, since they are rectilinear and orthogonal in the physical space, and thus the effects of melting front curvature on the melting front propagation are easier to analyze and approximate in these coordinates. The local Nusselt numbers obtained in the (X,Y) coordinates are interpolated at 60 equidistant points using a cubic spline fit to obtain a smooth and continuous estimate of the variation of Nu with distance along the melting front. The new position of the melting front at these 60 points is calculated using equation (11). Local convexity of the melting front, which if neglected would lead to an underestimation of the locally melted volume, is carefully taken into account in the calculation of the new position of the melting front.

The Nu decreases very rapidly at early times when the melt region is small (see Fig. 6, also Fig. 2 of [10]). The simulation

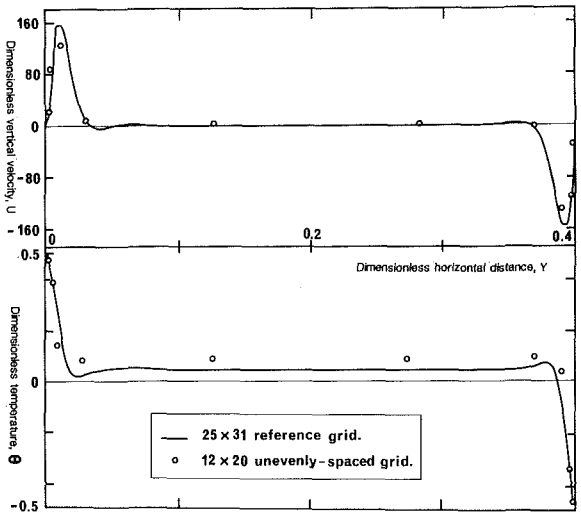

Fig.3 Comparison of computed temperature and velocity fields near midheight ($x = 0.6$)

of melting front propagation requires special care in this period, since use of a large time step in the period of steeply declining Nusselt number can lead to an overprediction of the rate of melting front propagation. The problem is conveniently solved by scaling the time step with the inverse of the average Nusselt number; when the Nu numbers are large (and rapidly decreasing), the time step is small, and when the Nu numbers are smaller (and more or less steady), the time steps are larger. It is found sufficient to so scale the time step (with the average Nu) as to melt 5 percent of the PCM volume in each quasi-static step. A smaller subdivision of the time step leads to substantially the same results, while a larger scaling produces quite different, large predictions for the melting rate.

The finite enclosure size is taken into account by imposing a maximum limit on the value of $C(\hat{X},t)$

$$\text{Max}(C(\hat{X},t)) \leq 1.0$$

The melting front propagation thus ends when it reaches the right, cold vertical wall of the enclosure. Since this wall is assumed isothermal at the fusion temperature, T_F, this has no effect on the computation of the flow fields in the liquid phase except in so far as to affect the shape of the cavity defining the liquid region. The heat transfer to the melting front is recorded at every quasi static step; this amount, proportional to Nu*, decreases to 0 as the solid PCM disappears from the enclosure.

After the new position of the melting front is obtained from equation (11), the melting shape function is again calculated using interpolation with cubic spline fits at the main grid locations, for use in the simulation of fluid flow in the liquid phase.

3.2 Simulating the Fluid Flow in the Liquid Phase. For each quasi-static step, the coordinate transformation (1–2) is used to map the newly defined (nonrectangular) cavity onto the rectangular computational space. Equations (5–7) have been cast into a finite difference form, using the Patankar-Spalding differencing scheme [18], and solved with an alternating direction implicit (ADI) iteration procedure. The computational method is described in detail in [19]. Numerical predictions of natural convection flows in enclosures at high Ra numbers ($10^6 < \text{Ra} < 10^{10}$), based on this method, have shown very good agreement [19–21] with published analytic, numerical, and experimental data. Staggered grids (displaced from the main grid by half a grid spacing in $\hat{X}$ and $\hat{Y}$ directions) are used to define the U and V components of fluid velocity, while the temperature and pressure fields are evaluated on the main grid. Since the $\hat{Y}-$coordinate has been

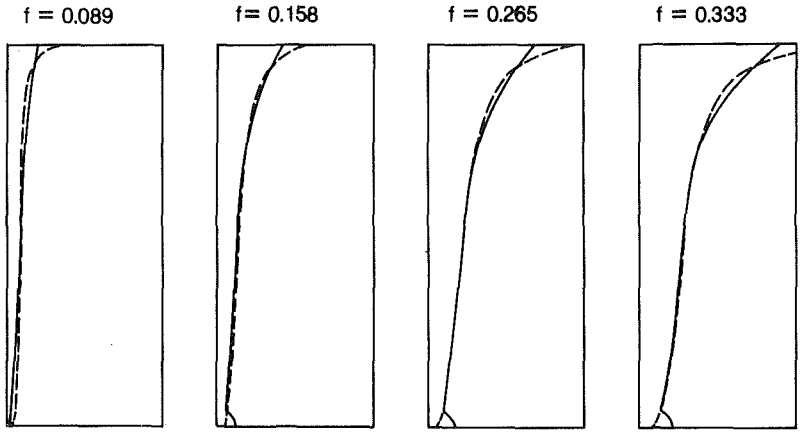

Fig. 4 Comparison of numerical simulation with experimental observations of Hale and Viskanta [3]: ———— present work; _____ [3]

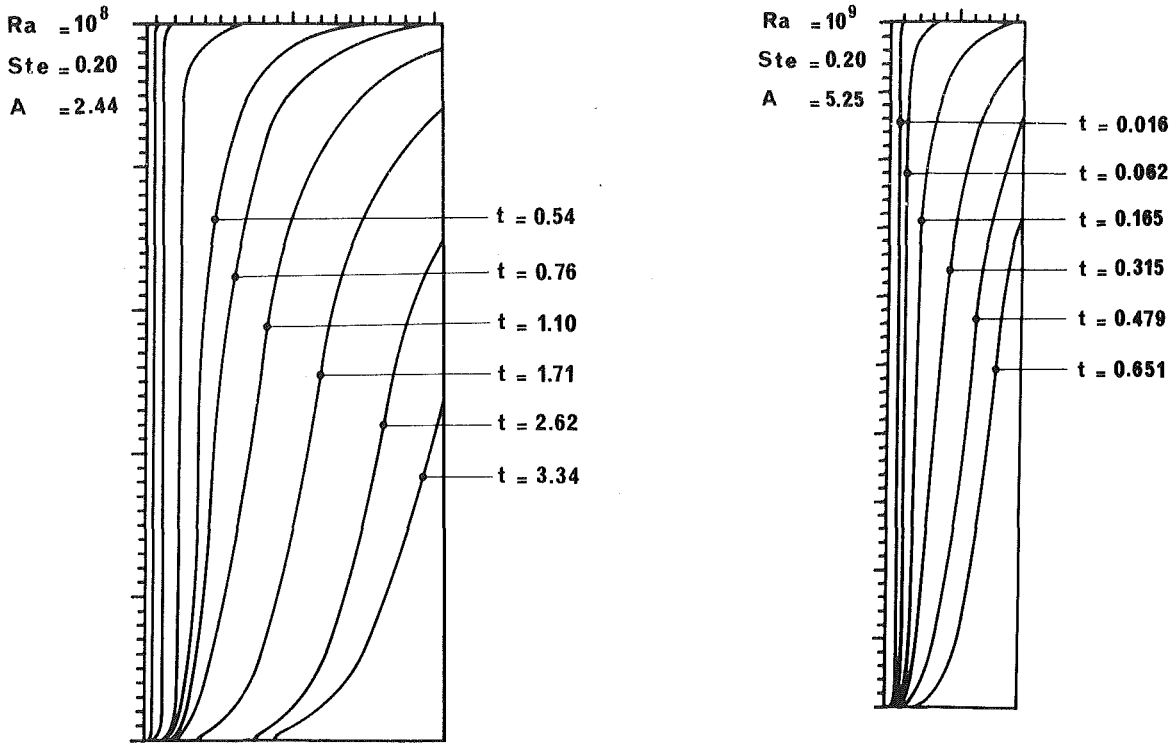

Fig. 5 Time evolution of the melting front position

unevenly scaled (with $C(\hat{X},t)$ equation (2)), each vertically staggered grid line is scaled using the harmonic mean of the scaling used for its neighboring main grid lines.

An unevenly spaced 20 × 12 grid (Fig. 2(*a*)) has been selected for use after solving a test problem of high Ra convection in a rectangular enclosure (Ra = 10^9, A = 2.5, Pr = 50) and comparing the solution with that obtained with a specially constructed high resolution 31 × 25 grid, (Fig. 2(*b*)). The temperature and velocity profiles near midheight, predicted with the two grids, are compared in Fig. 3. The predictions show good agreement, particularly in the boundary layer regions, which are of main interest from the viewpoint of heat transfer at the vertical walls. The Nusselt number predictions for this problem were 58.5 and 58.0 with the two grids in Fig. 2(*a*), and 2(*b*). This agreement, and also the agreement between the local Nusselt number profiles, were considered sufficiently good to justify the use of the grid in Fig. 2(*a*) in the rest of the calculations in the interest of computational efficiency.

Since the computational grid is curvilinear and nonorthogonal in the physical space, computations were performed to confirm that the predicted solutions conserve mass and energy. Calculations of flow in a steeply diverging channel (inlet: outlet: length = 1:2:5) conserve mass to within 1 percent; energy is conserved to the same order in solutions for conduction in a trapezoidal wedge of this shape.

For each quasi-static step, convective flow fields in the liquid phase are computed by iteratively solving equations (5–8) in the newly defined cavity. The velocity, pressure, and temperature fields and their fractional residues are printed out for each grid mode every 100 iterations. At convergence, typical residues are $0(10^{-4})$. On a UNIVAC 1100 machine, 0(250) s of execution time, (0(1000) iterations), are needed to reach convergence for each convection calculation. At the end of every quasi-static step, the melting front shape function, $C(\hat{X},t)$, the converged flow fields, and the resulting convective heat flux at the $\hat{Y} = 1/A$ boundary are recorded. Since every quasi-static step melts 5 percent of the PCM volume, to melt all the PCM needs about 5000 s of CPU time for UNIVAC 1100.

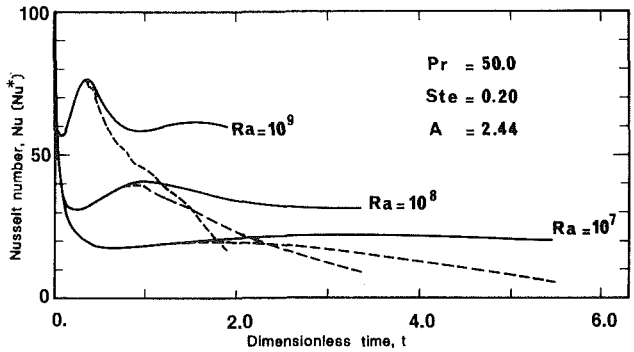

Fig. 6 Heat transfer from the hot wall as a function of time: ____ heat transfer from the hot wall, Nu; – – – – – – heat transfer to the melting front, Nu*

4 Results and Discussion

4.1 Comparison With Experiment. The foregoing numerical scheme has been used for simulating the experiments with n-octadecane performed by Hale and Viskanta [3] with the same geometry and initial conditions as described in section 2 (Problem Definition). The authors of [3] have presented detailed information on the development of the melting front profile as a function of time. Strict agreement between the results of [3] and the predictions of the numerical simulations is not expected since the experiments involved significant heat losses from the side walls, and also deviations from adiabatic conditions on the top and bottom horizontal walls of the test cell, which is described below.

The inside dimensions of the test cell of [3] were 14.6 cms high, 8.9 cms wide and only 2.2 cms deep. Thus, the hot and cold walls of the test cell were each 32.1 sq. cms, but additional uncontrolled losses could take place through the part of the four side walls (total area = 299 sq. cms) exposed to the melt, decreasing the heat deposited at the melting front. This

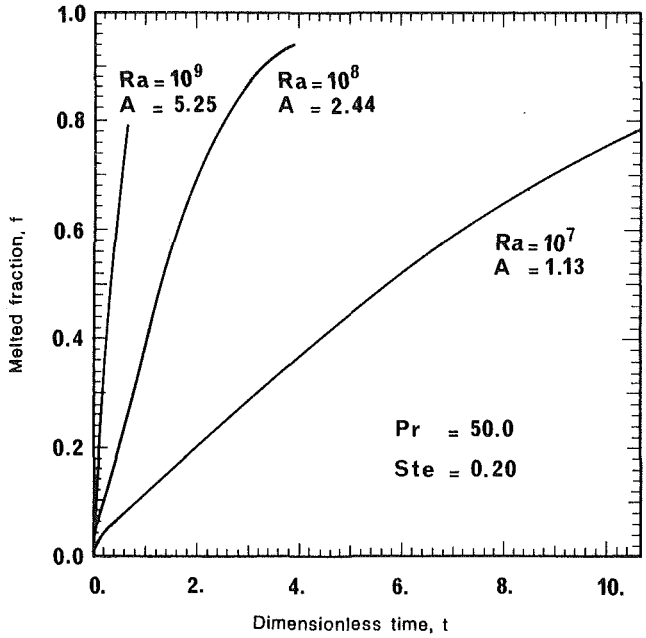

Fig. 7 Melting rates for enclosures of different aspect ratios having same ΔT

cell was enclosed in a plexiglass air chamber that was initially set at T_F, and maintained more or less at this temperature by the effect of the thermal mass of two additional water-filled heat exchangers located in it. The numerically predicted speed of propagation of the melting front is 37 percent larger than that observed experimentally; this difference appears to be acceptable in the light to the significant side wall heat losses reported in the experiment.

Due to the limitations described above, melting front profiles have been compared when the same fraction of the solid had passed into the liquid phase, rather than comparing them at the same elapsed time. This comparison is a very sensitive test of the variation of Nu over height. The comparisons, presented in Fig. 4, show excellent agreement over the central 85 percent of the melting front, where the effects from nonadiabatic horizontal walls are less important. To compare the simulation results with experiment at same elapsed time, a well controlled and carefully performed experimental study needs to be undertaken.

4.2 Predictions From Numerical Simulations. Predictions from the numerical simulations for two different enclosure aspect ratios (A = 2.44 and 5.25) are shown for two values of Ra (Ra = 10^8 and 10^9) in Fig. 5. The positions of the melting front at different dimensionless times have been indicated. The interpolation technique (described in section 3.1) gives remarkably smooth melting front profiles except near the top and bottom 5 percent of the enclosure height. It is found that changing the velocity boundary condition on the top horizontal surface from full slip (equation 8(*a*)) to a no slip does not significantly alter the predictions of the simulation regarding the melting front propagation, though the horizontal velocity profile near the top wall does change as expected.

Variation with time of the Nusselt numbers on the hot wall (Nu), and on the melting front (Nu*), is shown in Fig. 6 for three different Ra numbers. Nu gives the heat transfer from the hot wall to the liquid PCM, while Nu* gives the heat transfer from the liquid PCM to the melting front. The difference between Nu and Nu* gives the heat deposited into the cold vertical wall (also at temperature T_F) by the liquid PCM. As the melting front touches the cold vertical wall, the curves for Nu and Nu* begin to depart. Nu* begins to decrease rapidly as more and more heat is directly deposited into the cold vertical wall and less and less heat is deposited into the shrinking melting front. Finally, Nu* tends to 0 as the solid PCM surface exposed to the liquid vanishes.

Each curve in Fig. 6 starts with a very large value of Nu and Nu* (= 0(200)) corresponding to an extremely narrow vertical cavity. As the cavity widens, the Nusselt numbers rapidly decrease till the cavity is wide enough to allow onset of convection. This slows down the decrease in the Nusselt numbers, and as convection is fully developed, the Nusselt numbers increase slightly again. At still later times, due to the increasing width of the melted region, the Nusselt numbers show a slight decline. In the Nu curve corresponding to the highest Ra number (10^9) in Fig. 6, one more oscillation is seen. The cause of this oscillation is not clearly understood at present.

A thermal storage wall of a specified depth may be made up from several identical PCM-filled enclosures stacked on top of one another [15, 22]. A range of possible aspect ratios for the enclosures is possible. It is of practical interest to investigate the influence of the aspect ratio, A, on the melting curve for such a case, since this has bearing on optimizing the dimensions of latent heat storage elements. Results from one such investigation are displayed in Fig. 7, where the fraction of PCM in the liquid phase is plotted against dimensionless elapsed time for three different values of A and Ra (with Ra/A^3 being the same in all three cases). The results show that A has a strong influence on the melting curve, an increase in A from 1.13 to 5.25 causing a more than sixteenfold decrease in the time required to melt 80 percent of the PCM.

4.3 Sensitivity of Numerical Results. Some variation in the Nu profile predicted with different grids was observed in spite of the care taken to resolve the boundary layers. This variation was the largest (10 percent) for low A enclosures (A = 1.15) at lower Ra values (10^7). This is probably due to the highly uneven stretching of the Y-coordinate needed to simulate the melt cavity in low A enclosures. At higher A values and higher Ra numbers, the Nu variation was very small (< 1 percent). The numerical procedure described herein thus begins to break down for value of A close to 1, and some other approach (such as orthogonal curvilinear coordinate generators) will have to be employed for that range of A.

5 Conclusions

In many applications of PCM thermal storage the Ra numbers in the melt region are very high (10^6 < Ra < 10^9), and almost all the heat transfer through the liquid phase is by laminar natural convection in the melt. A two-dimensional numerical simulation model has been described that gives predictions in good agreement with the experimentally observed shape of the melting front for this range of Ra and for A < 1. The numerical model has been used to investigate the influence of Ra and A on the melting behavior of PCM in a two-dimensional rectangular enclosure with adiabatic horizontal walls and with one vertical wall at fusion temperature, and the other vertical wall at a higher temperature

6 Acknowledgments

Most of the work for this study, which was led by Dr. Christine Benard, was done when the first author was a visiting scientist at TESS. Dr. Benard's support and encouragement is gratefully acknowledged. The second author would like to thank the Passive Research and Development Group of the Lawrence Berkeley Laboratory for its hospitality during his stay in Berkeley.

References

1 Bareiss, M., and Beer, H., "Influence of Natural Convection on the

Melting Process in a Vertical Cylindrical Enclosure," *Letters in Heat and Mass Transfer*, Vol. 7, 1980, p. 329.

2 Sparrow, E. M., Schmidt, R. R., and Ramsey, J. W., "Experiments on the Role of Natural Convection in the Melting of Solids," ASME JOURNAL OF HEAT TRANSFER, Vol. 100, 1978, p. 11.

3 Hale, N. W., and Viskanta, R., "Photographic Observations of the Liquid-Solid Interface Motion During Melting of a Solid Heated from an Isothermal Vertical Wall," *Letters in Heat and Mass Transfer*, Vol. 5, 1978, p. 329.

4 Bathelt, A. G., and Viskanta, R., "Heat Transfer at the Solid-Liquid Interface During Melting From a Horizontal Cylinder," *International Journal of Heat and Mass Transfer*, Vol. 23, 1980, p. 1493.

5 Bardon, J. P., Vrignaud, R., and Delaunay, D., "Etude Experimentale de la Fusion et de la Solidification Periodique d'une Plaque de Paraffine," Revue Generale de Thermique, 1979, pp. 212–213.

6 Ramsey, J. W., and Sparrow, E. M., "Melting and Natural Convection due to a Vertical Embedded Heater," ASME, JOURNAL OF HEAT TRANSFER, Vol. 100, 1978, p. 368.

7 Goldstein, R. J., and Ramsey, J. W., "Heat Transfer to a Melting Solid With Application to Thermal Energy Storage Systems," *Heat Transfer Studies: A Festschrift for E. R. G. Eckert*, Hemisphere, 1979, p. 199.

8 Ramachandran, N., Jaluria, Y., and Gupta, J. P., "Thermal and Fluid Flow in One Dimensional Solidification," *Letters in Heat and Mass Transfer*, Vol. 8, 1981, p. 69.

9 Lapudula, C. A., and Mueller, W. K., "The Effect of Buoyancy on the Formation of a Solid Deposit Freezing on a Vertical Surface," *International Journal of Heat and Mass Transfer*, Vol. 13, 1970, p. 13.

10 Sparrow, E. M., Patankar, S. V., and Ramadhyani, S., "Analysis of Melting in the Presence of Natural Convection in the Melt Region," ASME, JOURNAL OF HEAT TRANSFER, Vol. 99, 1977, p. 520.

11 Sparrow, E. M., Larson, E. D., and Ramsey, J. W., "Freezing on a Finned Tube for Either Conduction-Controlled or Natural Convection-Controlled Heat Transfer," *International Journal of Heat and Mass Transfer*, Vol. 24, 1981, p. 273.

12 Sparrow, E. M., Ramsey, J. W., and Kemink, R. G., "Freezing Controlled by Natural Convection," ASME JOURNAL OF HEAT TRANSFER, Vol. 101, 1979, p. 578.

13 Nansteel, M. W., and Greif, R., "Natural Convection Heat Transfer in Undivided and Partially Divided Rectangular Enclosures," ASME, JOURNAL OF HEAT TRANSFER, Vol. 103, 1981, pp. 623–629.

14 Raithby, G. D., and Torrance, K. E., "Upstream-Weighted Differencing Schemes and Their Application to Elliptic Problems Involving Fluid Flow," *Computers and Fluids*, Vol. 2, 1974, p. 191.

15 Sanson Ortega, A., Benard, C., and Gobin, D., "Paraffin Trombe Wall for Space Heating," *Proceedings, International Conference on Building Energy Management*, Porto, 1980.

16 Kast, W., "Coefficients for the Combined Heat and Momentum Transfer in Laminar and Turbulent Boundary Layers," *Proceedings, Seventh International Heat Transfer Conference*, Vol. 3, Munich, 1982, pp. 263–268.

17 American Petroleum Institute, Research Project 44, Texas University; and Humphries, W. R., and Griggs, E. I., "A Design Handbook for Phase Change Thermal Control and Energy Storage Devices," NASA Technical Paper 1074, 1977.

18 Patankar, S. V., and Spalding, D. B., "Numerical Prediction of Three Dimensional Flows," Imperial College, Mechanical Engineering Department Report EF/TN/A/46, June 1972.

19 Gadgil, A. J., On Convective Heat Transfer in Building Energy Analysis," Ph.D thesis, Physics Department, University of California, Berkeley, 1979.

20 Bauman, F., Gadgil, A., Kammerud, R., and Greif, R., "Buoyancy driven Convection in a Rectangular Enclosure: Experimental Results and Numerical Calculations," ASME Paper No. 80-HT-66, presented at the ASME/AIChE 19th National Heat Transfer Conference, Orlando, Fla, July,

19 Gadgil, A. J., "On Convective Heat Transfer in Building Energy Analysis," Ph.D. thesis, Physics Department, University of California, Berkeley, 1979.

20 Bauman, F., Gadgil, A., Kammerud, R., and Greif, R., "Buoyancy driven Convection in a Rectangular Enclosure: Experimental Results and Numerical Calculations," ASME Paper No. 80-HT-66, presented at the ASME/AIChE 19th National Heat Transfer Conference, Orlando, Fla., July 1980, pp. 27–30.

21 Shiralkar, G., Gadgil, A., and Tien, C.-L., "High Rayleigh Number Convection in Shallow Enclosures With Different End Temperatures," INTERNATIONAL JOURNAL OF HEAT AND MASS TRANSFER, Vol. 24, 1981, p. 1621.

22 Farouk, B., and Guceri, S. I., "Trombe-Michel Wall With Phase Change Materials," *Proceedings, 2nd Miami International Conference on Alternative Energy Sources*, Hemisphere 1979.

The Effect of Entrainment Temperature on Jet Impingement Heat Transfer

S. A. Striegl
Westinghouse Electric Corporation,
Idaho Falls, Idaho 83401
Assoc. Mem. ASME

T. E. Diller
Mechanical Engineering Department,
Virginia Polytechnic Institute
and State University,
Blacksburg, Va. 24061
Mem. ASME

An experimental study was done to determine the effect of entrainment temperature on the local heat transfer rates to single and multiple, plane, turbulent impinging air jets. To determine the effect of entrainment of the surrounding fluid, the single jet issued into an environment at a temperature which was varied between the initial temperature of the jet and the temperature of the heated impingement plate. An analytical model was used to correlate the measured heat transfer rate to a single jet. The effect of the entrainment temperature in a single jet was then used to analyze the effect of entrainment from the recirculation region between the jets of a jet array. Using the measured temperature in the recirculation region to include the effect of entrainment, the single jet correlations were successfully applied to multiple jets.

Introduction

When a jet issues into an environment which is at a temperature different from that of the jet, the entrainment of the fluid in the environment surrounding the jet will affect the temperature distribution of the jet. This thermal entrainment affects the heat transfer from a surface to an impinging jet whenever the initial temperature of the jet differs from the temperature of the surrounding environment. The effect of thermal entrainment on the heat transfer to a single, plane, turbulent impinging jet was investigated analytically in [1]. Because of the entrainment of spent fluid in the recirculation region between the jets, thermal entrainment is an inherent component of jet arrays. It was demonstrated that if the effect of thermal entrainment was considered, the heat transfer to jet arrays in many cases could be accurately modeled with a single jet model.

Most of the experimental studies on the heat transfer to a single, plane, turbulent impinging jet are for the case when the environment is at the same temperature as the jet [2–4]. Schuh and Petterson [5], Saad et al. [6], Gardon [2], and Martin [4] have presented heat transfer results for plane multiple jets, but they did not consider the effect of thermal entrainment. Martin [4] did mention the possible effect of entrainment for multiple jets but assumed that it was negligible in his measurements. Gardon and Akfirat [2] and Martin [4] found that the average heat transfer coefficient for a jet array was lower than the corresponding average heat transfer for a single jet.

Two investigations have considered the effect of thermal entrainment on the heat transfer to a single impingment jet. Vlachopoulos et al. [7] obtained empirical expressions for the heat transfer from a single, hot axisymmetric impinging jet issuing into a cool environment. Schauer and Eustis [8] investigated the heat transfer to a single plane impinging jet issuing into (*i*) an environment at the same temperature as the jet and (*ii*) an environment at the same temperature as the surface. To develop expressions for environment temperatures between these two extremes, the two cases were superposed. Schauer and Eustis did not experimentally investigate the heat transfer for the intermediate environment temperatures, nor did they compare the results for case 1 and case 2. Only results for very large impingement heights, $h/b_o = 40$, were presented. At these large impingement heights, most of the entrainment occurs in the free jet. For the smaller impingement heights considered here, $6 < h/b_o < 25$, entrainment in the wall jet is also significant.

The present paper gives the details of an experimental investigation of thermal entrainment effects. The results are compared with an analytical model developed by the authors and described in an earlier publication [1]. In addition, the effect of entrainment on multiple jet heat transfer is considered in more detail.

Analytical Model

The analytical model developed in the earlier paper [1] used a dimensionless entrainment factor, $\bar{F}$, to specify the boundary conditions.

$$\bar{F} = \frac{T_i - T_\infty}{T_i - T_w} \tag{1}$$

When the temperature of the environment, T_∞, equals the initial temperature of the jet, T_i, $\bar{F} = 0$ and thermal entrainment does not affect the heat transfer. When the temperature of the environment equals the temperature of the surface, T_w, $\bar{F} = 1$ and thermal entrainment has the maximum effect on the heat transfer.

Analytical models for the heat transfer in the impingement and wall jet regions were developed for boundary conditions corresponding to $\bar{F} = 0$ and $\bar{F} = 1$. To obtain solutions for intermediate values of $\bar{F}$, the $\bar{F} = 0$ and $\bar{F} = 1$ solutions were linearly superposed. Series solutions to the laminar momentum equation were used in the impingement region. A one-constant algebraic turbulence model was used to obtain similarity solutions to the momentum and energy equation in the inner and outer regions of the wall jet (two-layer model). The heat transfer coefficient is referenced to the difference between the initial temperature of the jet, T_i, and the wall temperature, T_w.

In the impingement region the model gives

$$\mathrm{Nu}_s = \frac{q_{\mathrm{act}}\, b_o}{(T_w - T_i)k} = 1.64\, C_7 \sqrt{\mathrm{Re}} \left(\frac{b_o}{h}\right)^{3/4} \left\{\left[1 - 2.89\left(\frac{X}{h}\right)^2\right](1 - \bar{F}) + C_1 \sqrt{\frac{b_o}{h}}\left[1 - 3.86\left(\frac{X}{h}\right)^2\right]\bar{F}\right\} \tag{2}$$

prescribed for $X/h < 0.34$. C_7 is a parameter which accounts

Contributed by the Heat Transfer Division for publication in the JOURNAL OF HEAT TRANSFER. Manuscript received by the Heat Transfer Division June 20, 1982.

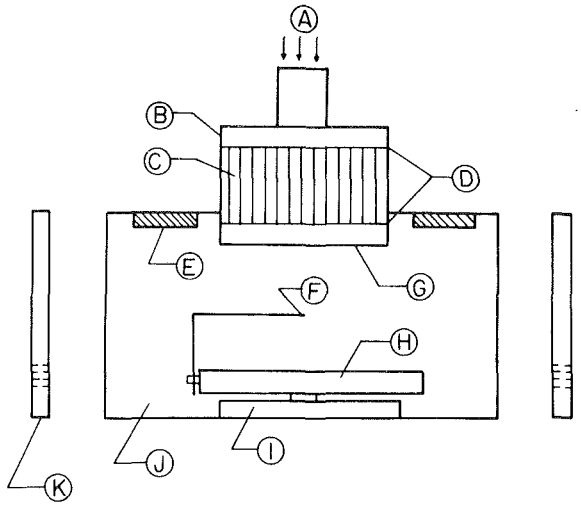

Fig. 1 Experimental apparatus: (A) air flow from blower (B) plenum (C) flow straighteners (D) screens (E) side heater (F) thermocouple probe (G) orifice plate (H) plate assembly (I) slider mechanism (J) four-sided enclosure (K) removable end

for the effect of turbulence on the heat transfer in the impingement region. Values of C_7 are presented in the earlier paper [1] as a function of Re and h/b_o. The values range from 1.2 at Re = 5000 and $h/b_o = 6$ up to 2.6 at Re = 40,000 and $h/b_o = 13$. C_1 is the free jet temperature decay, and a value of $C_1 = 2.13$ was used.

In the wall jet region the model gives

$$\mathrm{Nu}_{wj} = \frac{q_{\mathrm{act}}\, b_o}{(T_w - T_i)k}$$

$$= 0.00174\, C_3\, \mathrm{Re}\sqrt{\frac{b_o}{X}}\left[(1-\bar{F}) + 4.85\, C_5\sqrt{\frac{b_o}{X}}\,\bar{F}\right] \qquad (3)$$

prescribed for $X/h > 0.34$. As used in equation 3, C_3 and C_5 are the maximum velocity and temperature decays, respectively. Values of C_3 and C_5 are given in the earlier paper [1] as a function of slot width. For the 15-mm slot, $C_3 = 2.78$ and $C_5 = 0.236$. For the 3-mm slot, $C_3 = 4.03$ and $C_5 = 0.581$. The turbulence constants C_1, C_3, and C_5 result from the eddy diffusivity modeling and can be related directly to the macroscopic flow parameters.

Experimental Apparatus and Procedure

Figure 1 shows the apparatus used to determine the Nusselt number distributions. Air flow from the blower (A) was controlled by a blocking plate upstream of the plenum. The flow entered the plenum (B), passed through screens (D) and flow straighteners (C) (0.6-cm-dia by 19-cm-long plastic drinking straws), and left the plenum through the orifice in the orifice plate (G). The exit velocity of the jet was determined from the pressure drop across the orifice, which was measured with a water manometer. No measureable velocity fluctuations were observed during a test. The initial temperature of the jet was measured with a thermocouple just upstream of the orifice. The jet flow from the orifice then impinged on a heated plate assembly (H), which was mounted in a four-sided enclosure (J). The side walls of the enclosure helped to ensure the two-dimensionality of the flow.

The four-sided enclosure was fitted with removable ends (K). The ends were perforated to allow the flow to escape with a negligible pressure drop across the ends. When the entrainment factor for a single jet was to be zero, the ends were left off. When the entrainment factor for a single jet was to be greater than zero, the ends were attached and the side heaters (E) were turned on to increase the temperature in the enclosure above the initial temperature of the jet. For multiple jet tests, the ends were attached and the side heaters were used only to maintain the air in the enclosure outside the end jets at the same temperature as the air in the recirculation region between the jets. This was done to eliminate end effects and better approximate the situation which would be encountered in a large jet array. The temperature of the environment surrounding the jets was measured with a thermocouple probe (F). The temperature of the environment surrounding a single jet was uniform to within 1°C. An example of the temperature distribution in the recirculation region between the jets of the jet array is given in the results. To experimentally determine $\bar{F}$ for multiple jets, the temperature in the recirculation region was measured midway between the orifice plate and the impingement surface, where the temperature was uniform to within 1°C.

Nomenclature

b = actual slot width
b_o = effective slot width, equation (4)
C_3 = wall jet velocity decay rate, equation (3)
C_5 = wall jet temperature decay rate, equation (3)
C_7 = parameter used to account for the effect of turbulence on the heat transfer in the impingement region, equation (2)
C_d = discharge coefficient
C_P = specific heat of air
E = output voltage of heat flux gage, equation (A3)
f = gage calibration factor, equation (A4)
$\bar{F}$ = entrainment factor, equation (1)
h = impingement height
h_c = corrected heat transfer coefficent from the gage, equation (A2)
h_m = heat transfer coefficient from manufacturer's calibration, equation (A5)
I_o = Bessel function, equation (A1)
K = thermal conductivity of air
K_C = thermal conductivity of constantan
K_2 = thermoelectric constant for copper-constantan
L = half length between jets of the jet array
Nu = Nusselt number
$\mathrm{Nu}_{\mathrm{av}}$ = average Nusselt number, equation (B5)
Nu_s = impingement region Nusselt number, equation (2)
Nu_{so} = stagnation point Nusselt number
Nu_{wj} = wall jet region Nusselt number, equation (3)
Pr = Prandtl number
Re = Reynolds number, $\frac{V_o b_o}{\nu}$
q_{act} = plate heat flux
q_{cal} = calibration heat flux, equation (A4)
r = radial distance from gage center
R = gage radius
t = gage disk thickness
T_c = temperature at gage center
T_i = initial temperature of jet
T_w = temperature of isothermal plate
T_∞ = temperature of environment surrounding the jet
V_o = initial velocity of jet
X = coordinate parallel to plate with origin at the stagnation point
λ = parameter defined by equation (A2), dimensionless
ν = kinematic viscosity
ρ = density

Table 1 Discharge coefficients for slot orifices

Orifice	C_d Mean	b_o (mm)	Standard deviation of C_d	Number of tests	Re $\times 10^{-4}$
15-mm slot	0.736	11.0	0.010	5	1.5–1.7
10-mm slot	0.693	6.93	0.017	8	1.3–1.5
5-mm slot	0.709	3.55	0.026	9	0.7–1.2
3-mm slot	0.703	2.11	0.014	12	0.6–1.0

The orifice plates were constructed from 1.6-mm aluminum sheet. The slots were milled to produce a clean edge. Four single-slot orifice plates were machined with slots 3-, 5-, 10-, and 15-mm wide by 170-mm long. The discharge coefficient of each slot was measured by using a measured flow of carbon dioxide as a tracer gas and measuring the concentration of carbon dioxide in the fully mixed stream with an infrared gas analyzer. One jet array was constructed by adding an idential slot spaced 99-mm from the 3-mm center slot on both sides of the 3-mm single slot. The discharge coefficients of the outside slots were not measured since all heat transfer measurements were taken for the center slot only. The distance between the orifice plate and the impingement plate was adjusted by using spacers of various heights.

The impingement plate was constructed from a 15- by 36-cm piece of 12.7-mm-thick aluminum. The heat flux from the plate was measured with a Gardon type [9, 10] heat flux gage mounted in the center of the plate flush with the plate surface. The gage was 3-mm in diameter and was manufactured by Medtherm Corp., Huntsville, Alabama. The manufacturer's calibration was corrected for use in a convective heat transfer situation by the method given in Appendix A. The gage's view of the side heaters was obstructed by the orifice plate so the gage was shielded from radiative heat transfer with the side heaters.

Lateral variations in the plate temperature were measured with thermocouples embedded in the plate 7.6 and 15.7 cm from the center along the length and 2.5 cm from the center along the width of the plate. The surface temperature was measured with a thermocouple mounted on the heat flux gage 0.13 mm from the surface. During the course of a test, the surface temperature at the gage varied less than 1°C. The maximum lateral temperature variation was less than 3°C. The plate temperature was typically 20°C above the initial temperature of the jet. All temperature measurements were made with a digital thermocouple readout calibrated to ± 0.05°C.

The plate was heated from the bottom with a resistance mat heater coated with silicone rubber. The plate and heater assembly was insulated on the sides and bottom with 1.3 cm of foam insulation. The energy input to both the plate heater and the side heaters was adjusted with Variacs.

The plate assembly and thermocouple probe were mounted on a slider (I) so that they could be traversed across the flow by a screw drive. The slider was equipped with a resistance strip so that the plate position could be converted to an electrical signal. A d-c voltage was applied across the strip and the output voltage was applied to one axis of an $X-Y$ recorder. The output from the heat flux gage or the thermocouple probe was amplified and applied to the other axis of the $X-Y$ recorder. Thus, as the plate was traversed across the flow, a profile of the heat flux or environment temperature was obtained. Discrete measurements were taken from the heat flux profiles and used to determine the heat transfer coefficients at discrete locations. These values were then used for the comparison of the analytical model with the experiments.

Results

The measured discharge coefficients are given in Table 1 along with the Reynolds numbers. Variation of the Reynolds number by ± 50 percent produced no significant changes in the measured discharge coefficients. Thus, a mean value of

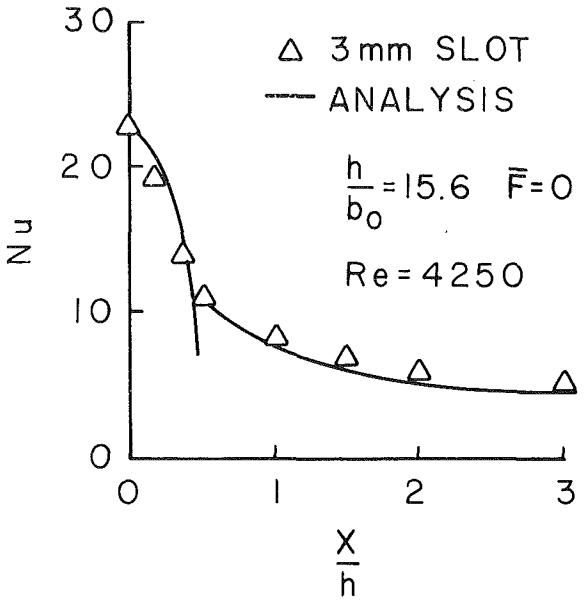

Fig. 2 Nusselt number distribution for a single-jet when $\bar{F} = 0$

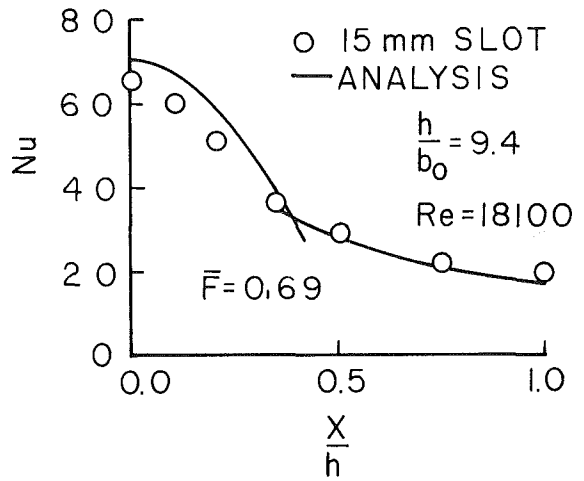

Fig. 3 Nusselt number distribution for a single-jet when $0 < \bar{F} < 1$

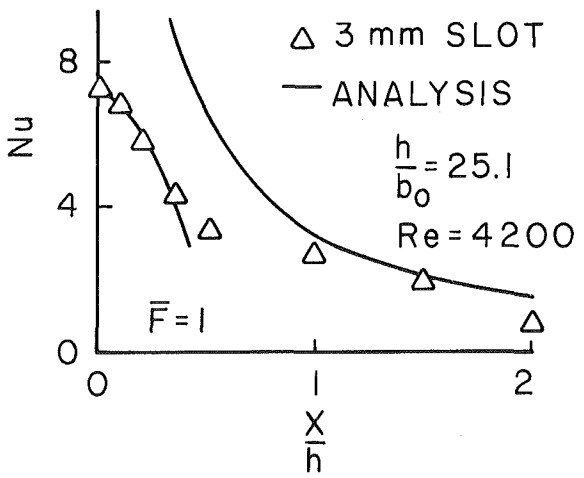

Fig. 4 Nusselt number distribution for a single-jet when $\bar{F} = 1$

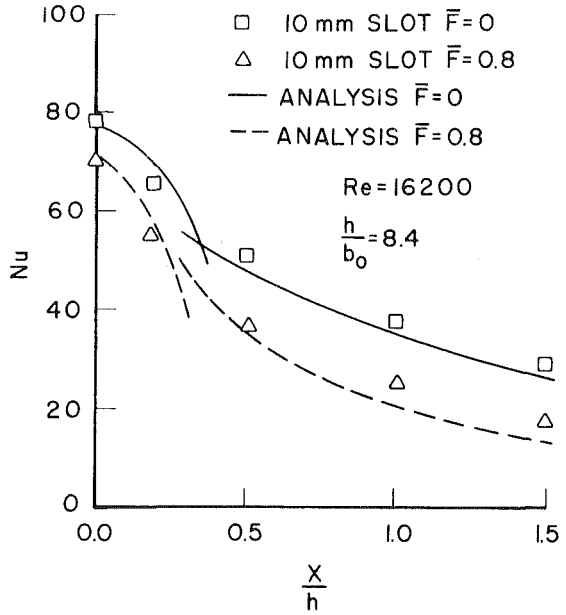

Fig. 5 The significance of thermal entrainment on jet impingement heat transfer for a single jet

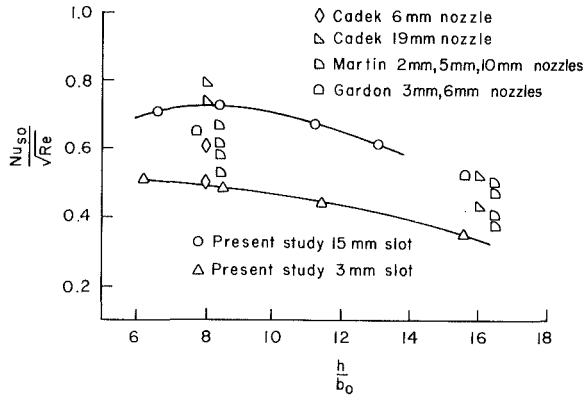

Fig. 6 Comparison of stagnation point Nusselt numbers for single jets when $\bar{F} = 0$

the discharge coefficient was used to define the effective slot width, b_o, for each slot

$$b_o = C_d\, b \tag{4}$$

where b is the actual slot width.

The values of the parameters in the analytical correlations for the Nusselt number are presented and discussed in [1]. Using these values of the parameters, the analytical correlations are compared to the measured Nusselt number distributions. A total of 100 single jet Nusselt number distributions were measured for $0 \le \bar{F} \le 1$, $3000 \le \mathrm{Re} \le 40{,}000$, and $6 \le h/b_o \le 25$. Figure 2 shows one example of the measured and analytical Nusselt number distributions for a single jet when $\bar{F} = 0$. Figure 3 shows a comparison between the measured and analytical Nusselt number distributions for a single jet at intermediate values of $\bar{F}$. Figure 4 compares the measured and analytical Nusselt number distributions when $\bar{F} = 1$. Because the value of h/b_o was always greater than 6.0, no secondary peaks were recorded or predicted in the impingement region.

To show the significance of thermal entrainment on jet impingement heat transfer, data were taken for a single jet at the same Reynolds number and impingement height for two

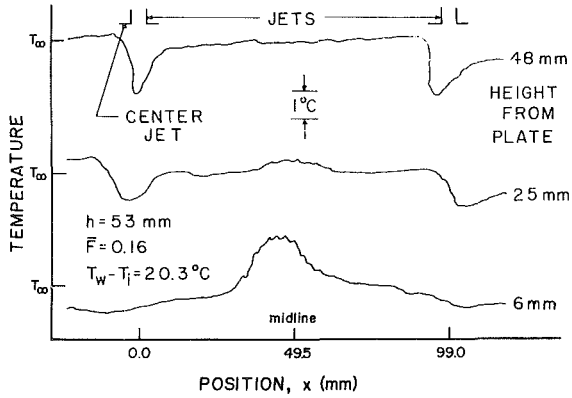

Fig. 7 Temperature distributions in the recirculation region

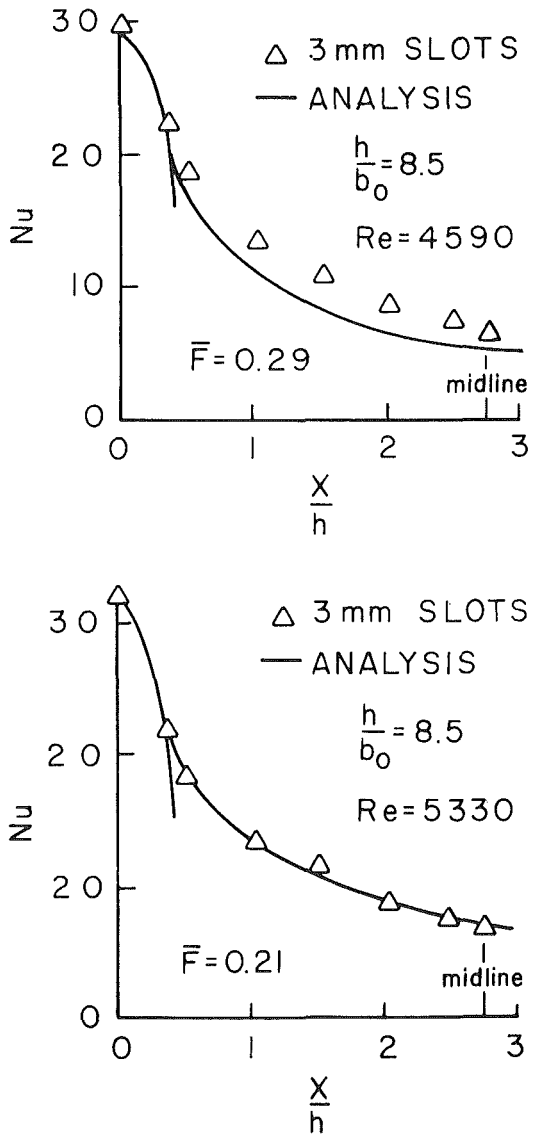

Fig. 8 Nusselt number distributions for multiple jets

different values of the entrainment factor. Figure 5 shows an example of the significance of thermal entrainment.

As a check on the validity of the measured Nusselt numbers for single jets, the stagnation point Nusselt numbers for $\bar{F} = 0$ determined in the present study are compared with those of other investigators. Figure 6 shows the stagnation point

Nusselt number data for the 3- and 15-mm slots along with similar measurements from [2, 3, 4]. Differences in the initial turbulence levels of the jets, due to differences in slot width, supposedly cause the Nusselt number to be dependent on slot width [2]. The data did show this dependence with the data from the 3- and 15-mm slots representing the low and high Nusselt number at a given impingement height and Reynolds number. The data of Cadek and Zerkle [3] also shows a similar dependence on slot width.

In applying the single-jet model to multiple jets, the assumption of a constant environment temperature surrounding the jets was employed. To test this assumption, temperature distributions in the recirculation region were recorded at several heights above the plate surface. Figure 7 shows an example of the temperature distribution around the jet. Near the plate surface, a temperature peak occurs when the two adjacent wall jets collide and the boundary layer separates from the plate. However, apparently due to the high degree of mixing in the recirculation region, the temperature becomes uniform a short distance above the plate.

A total of 15 Nusselt number distributions were measured for the multiple jet array with three 3-mm slots (b_o = 2.11 mm) and b_o/L = 0.0426 (2.1 percent open area) for $2700 < \mathrm{Re} < 6000$ and $6 < h/b_o < 25$. Figure 8 shows two examples of the comparison between the measured Nusselt number distributions for multiple jets and the analytical corrrelations developed for single jets. The significance of entrainment on the multiple jet heat transfer is examined in the discussion.

Discussion

As can be seen in Figs. 2, 3, and 4, the agreement between the data and the correlations for the heat transfer to a single jet is the best at smaller values of $\bar{F}$. Two factors account for the poorer agreement when $\bar{F}$ is near one. As $\bar{F}$ increases, the magnitudes of the terms in equations (2) and (3) which are multiplied by $\bar{F}$ increase. Since these terms contain some experimentally determined parameters (C_1 and C_5), the significance of the uncertainties in these terms on the value of the Nusselt number increases as $\bar{F}$ increases. The second factor affecting the agreement between the data and the correlations at high values of $\bar{F}$ arises because of the manner in which $\bar{F}$ was controlled. To obtain high values of $\bar{F}$ for single jets, the temperature of the environment must approach the plate temperature. To avoid large heat losses through the enclosure which would decrease $\bar{F}$, the difference between the plate temperature and the initial temperature of the jet had to be kept small (typically 5°C for $\bar{F}$ = 1). The lower temperature difference between the jet and the surface and the high values of $\bar{F}$ combined to give lower heat flux rates which increased the uncertainties in the heat flux measurements.

At values of $\bar{F}$ near 1, the correlations for the impingement and wall jet regions do not merge. This lack of continuity between the correlations points out the difficulty of modeling the region where the flow undergoes a transition from the laminar type flow in the impingement region to the turbulent flow in the wall jet region. Cadek and Zerkle [3] also mention the difficulty of modeling the flow in this transition region.

Figure 6 shows a comparison of the measured transfer at the stagnation point with that of three other investigations for $\bar{F}$ = 0. Although there is some scatter in all of the results due to differences in slot width and Reynolds number, there appears to be good agreement between the present results and these values from the literature. The results in the wall jet region (as illustrated in Figs. 2 and 5) also were in good agreement with the literature values [2–4].

Comparison with literature values was much more difficult in the $\bar{F} > 0$ cases. The only results found in the literature with a recorded value of $\bar{F} > 0$ were a few measurements by Schauer and Eustis [8] at $\bar{F}$ = 1. Although their values of h/b_o were much larger than those used here, extrapolation of the present results are consistent with their findings.

For large arrays of multiple jets, the value of $\bar{F}$ will be determined by the air flow rate, the jet to jet spacing, and the heat transferred from the plate. Values of $\bar{F}$ for a large array of multiple jets can be determined using a simple energy balance, which is presented in Appendix B. The result for this energy balance gives

$$\bar{F} = \frac{\mathrm{Nu}_{\mathrm{av}}}{\mathrm{RePr}} \left(\frac{2L}{b_o} \right) \tag{5}$$

where $\mathrm{Nu}_{\mathrm{av}}$ is the average Nusselt number over the length, L, and is obtained by integrating the analytical correlations. Equation (5) and the expression for $\mathrm{Nu}_{\mathrm{av}}$ (equation (B5)) form a linear set of two equations which can then be solved for $\bar{F}$.

As the spacing between the jets increases (less open area), the entrainment factor will increase. Moreover, for larger spacing between jets, the wall jets are longer and thus entrain more fluid. Large impingement heights will also increase the effect of thermal entrainment because of increased entrainment in the free jet. Figure 5 illustrates these two main points that (*i*) thermal entrainment can have a significant effect on the heat transfer at the stagnation point because of entrainment in the free jet and that (*ii*) the significance of thermal entrainment increases as the jet spreads out into the wall jet region and continues to entrain fluid. At the end of the wall jet region shown in Fig. 5 (X/h = 1.5), thermal entrainment has decreased the heat transfer for the $\bar{F}$ = 0.8 case to nearly half of that for the corresponding $\bar{F}$ = 0 case.

Comparison of the multiple jet results in Fig. 8 with the single jet results shows that the agreement between the analysis and measurements for multiple jets is as good as that for single jets. Moreover, this was true for all of the fifteen multiple jet tests measured. The difference in fit between the two cases shown in Fig. 8 was indicative of the variation between theory and experiment for both the single and multiple jet tests. This was attributed to the experimental uncertainties described earlier. Therefore, by including the effect of $\bar{F}$, the heat transfer coefficients from multiple jets were found to be equal to those from single jets at the same conditions.

Consequently, the single-jet analysis can be applied with equal accuracy to multiple jet heat transfer for these conditions. For the values of $\bar{F} < 0.3$ normally encountered in multiple-jet heat transfer, the correlations for the local heat transfer can be expected to be within 30 percent at a confidence level of 90 percent at all values of X. Values for the average Nusselt number, although not measured in this study, would be expected to be much closer.

The midline between jets is marked on the plots in Fig. 8. The model does not include any effects of jet interaction at this point. Consequently, the analytical curves simply intersect at the midline. Indeed, no pronounced changes in transfer were measured around the midline. Apparently, the velocity in the wall jet has decreased enough by this point so that any interaction effects are negligible. Other investigators [2, 11] have reported significant increases in the transfer at the midline, but these occurred only when using much smaller jet spacings.

One of the ramifications of the entrainment temperature effect is the importance of controlling the temperature boundary conditions in both single and multiple jet tests. Laboratory experiments with multiple jets usually are of small size, consisting only of a few jets. Therefore, entrainment of room air, if not controlled, can lead to significant alteration of the entrainment temperature and consequently the measured heat transfer. In addition, because entrainment temperatures have not been previously reported, comparison of average measurements with equation (B5) are difficult.

For multiple jets, the additional effect of crossflow may also need to be considered. Crossflow was minimized in this study because the flow exits the flow field symmetrically from the center jet for which the measurements were taken. In addition, the exhaust velocities are low relative to the jet velocities.

The initial jet velocities were less than 50 m/s ($M < 0.15$), so compressibility effects were negligible. At these low Mach numbers the temperature drop across the orifice is also negligible.

Conclusion

Local heat transfer rates were measured for single and multiple, plane, turbulent impinging air jets. To determine the effect of thermal entrainment on single jets, results were obtained for jets issuing into an environment which was varied between the initial temperature of the jet and the temperature of the heated impingement plate. The single jet results were correlated with an analytical model. Results were then obtained for multiple jets, where thermal entrainment is important because of entrainment of the spent air in the recirculation region. Using the measured temperature in the recirculation region, the single jet model was successfully applied to multiple jets. For the impingement heights tested (less than 25 slot widths) entrainment effects were most pronounced in the wall jet region.

References

1 Striegl, S. A., and Diller, T. E., "An Analysis of the Thermal Entrainment Effect on Jet Impingement Heat Transfer," ASME Paper No. 82-WA/HT-54, 1982.

2 Gardon, R., and Akfirat, J. C., "Heat Transfer Characteristics of Impinging Two-Dimensional Air Jets," ASME JOURNAL OF HEAT TRANSFER, Vol. 88, 1966, pp. 101–108.

3 Cadek, F. F., and Zerkle, R. D., "Local Heat Transfer Characteristics of Two-Dimensional Impinging Air Jets—Theory and Experiment," *Heat Transfer 1974*, Vol. II, Japan Society of Mech. Engrs., 1974, pp. 15–19.

4 Martin, H., "Heat and Mass Transfer Between Impinging Gas Jets and Solid Surfaces," *Advances in Heat Transfer*, Vol. 13, 1977, pp. 1–60.

5 Schuh, H., and Petterson, R., "Heat Transfer by Arrays of Two-Dimensional Jets Directed Normal to Surfaces Including the Effects of a Superposed Wall-Parallel Flow," *Proceedings Third International Heat Transfer Conference*, Vol. 2, 1966, pp. 280–291.

6 Saad, N. R., Mujumdar, A. S., and Douglas, W. J. M., "Heat Transfer Under Multiple Turbulent Slot Jets Impinging on a Flat Plate," *Drying '80*, Vol. 1: *Developments in Drying*, edited by A. S. Mujumdar, Hemisphere Pub. Co., Washington, D. C., 1980, pp. 422–430.

7 Vlachopoulos, J., and Tomich, J. F., "Heat Transfer from a Turbulent Hot Air Jet Impinging Normally on a Flat Plate," *Canadian Journal of Chemical Engineering*, Vol. 49, 1971, pp. 462–466.

8 Schauer, J. J., and Eustis, R. H., "The Flow Development and Heat Transfer Characteristics of Plane Turbulent Impinging Jets," Stanford University Department of Mechanical Engineering, Technical Report No. 3, 1963.

9 Gardon, R., "A Transducer for the Measurement of Heat Flow Rate," ASME JOURNAL OF HEAT TRANSFER, Vol. 82, 1960, pp. 396–398.

10 Gardon, R., "An Instrument for the Direct Measurement of Intense Thermal Radiation," *The Review of Scientific Instruments*, Vol. 24, No. 5, 1953, pp. 366–370.

11 Korger, M., and Krizek, F., "Mass-Transfer Coefficient in Impingement Flow from Slotted Nozzles," *International Journal of Heat and Mass Transfer*, Vol. 9, 1966, pp. 337–344.

12 Woodruff, L. W., Hearne, L. F., and Keliher, T. J., Interpretation of Asymptotic Calorimeter Measurements," *AIAA Journal*, Vol. 5, No. 4, 1967, pp. 795–797.

APPENDIX A

Heat Flux Gage Correction

Two factors must be considered when using a Gardon gage for measuring convective heat transfer.

1 Nonuniform heat flux across the gage

2 Disturbance of the thermal boundary layer growth due to the nonisothermal gage surface

The effect of nonuniform heat flux arises because the gage is calibrated by radiation with a uniform heat flux condition which is not affected by the gage temperature distribution. In a convective heat transfer situation, the assumption of a constant heat transfer coefficient is more reasonable.

With the assumption of radial heat flow in the gage surface and a constant heat transfer coefficient, the gage surface temperature is given by a Bessel series solution

$$\frac{T-T_\infty}{T_w-T_\infty}=\frac{I_o\left(\lambda\frac{r}{R}\right)}{I_o(\lambda)} \tag{A1}$$

where

$$\lambda^2=\frac{R^2h_c}{K_c t} \tag{A2}$$

K_c is the thermal conductivity of constantan, t is the gage disk thickness, h_c is the heat transfer coefficient, and R is the gage disk radius. The effect of this temperature distribution on the measured heat flux is approximated as follows.

The gage output voltage is linearly proportional to the difference between the center and edge temperature of the disk as

$$E=K_2(T_w-T_c) \tag{A3}$$

where K_2 is the thermoelectric constant for copper-constantan. The calibration heat flux is linearly related to the output voltage of the gage as

$$q_{\text{cal}}=E\frac{4K_c\,t}{K_2\,R^2}=\frac{E}{f} \tag{A4}$$

where the parameter f is the manufacturer's calibration factor. The heat transfer coefficient based on the manufacturer's calibration is

$$h_m=\frac{q_{\text{cal}}}{T_w-T_\infty} \tag{A5}$$

The gage heat flux is found by integrating the gage surface temperature distribution across the gage surface using the first two terms of the Bessel series

$$q_g=h_c(T_w-T_\infty)\frac{1+\lambda^2/8}{1+\lambda^2/4} \tag{A6}$$

The ratio of the two heat transfer coefficients is then expressed as

$$\frac{h_c}{h_m}=\frac{1}{1-\frac{f h_m}{K_2}} \tag{A7}$$

For the manufacturer's calibration of $f = 2.38 \times 10^{-5}$ mV/W/m^2 and $K_2 = 0.042$ mV/°C for copper-constantan, equation (A7) is rewritten as

$$\frac{h_c}{h_m}=\frac{1}{1-\frac{h_m}{\text{W/m}^2\,^\circ\text{C}}} \tag{A8}$$

where h_c and h_m have units of W/m^2°C. Thus, the actual heat transfer coefficient is greater than that which would be determined from the manufacturer's calibration. The measured heat transfer coefficients obtained in this investigation were as large as 350 W/m^2°C and consequently h_c/h_m was as large as 1.25.

The effect of the nonisothermal gage on the development of the thermal boundary layer has been investigated analytically by Woodruff [12]. In the region where the wall jet boundary

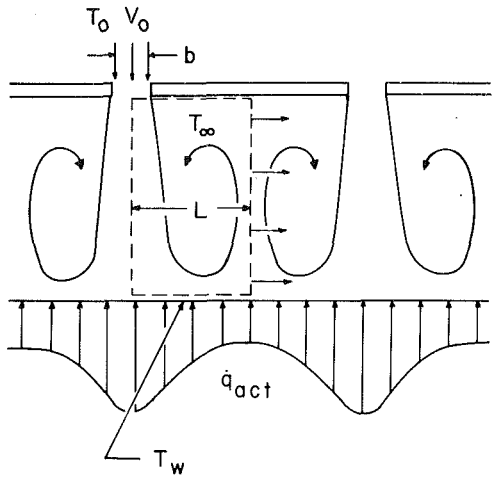

Fig. 9 Control volume for the determination of $\bar{F}$ for multiple jets

layer is fully developed, the effect of the nonisothermal gage on the heat transfer coefficient is less than 3 percent for the heat transfer coefficients obtained in this investigation. Thus, the effect of the nonisothermal gage on the development of the thermal boundary layer is neglected.

APPENDIX B

Determination of $\bar{F}$ for Jet Arrays

The entrainment factor for a jet array can be determined with a simple energy balance on the control volume shown in Fig. 9. The assumptions are:

1 The air in the recirculation region is at a uniform temperature.

2 All the air exits from the right side of the control volume as shown.

3 The air leaving the control volume is at a uniform temperature equal to that of the air in the recirculation region.

4 All surfaces except the surface of the impingement plate are adiabatic.

The energy balance states that the increase in the enthalpy of the air as its passes through the control volume must be equal to the heat transferred from the plate

$$\frac{\rho C_p V_o b_o}{2} (T_\infty - T_i) = q_{act} L \tag{B1}$$

Combining this with the average heat transfer coefficient for the plate surface

$$q_{act} = \frac{K \mathrm{Nu}_{av}}{b_o} (T_w - T_i) \tag{B2}$$

yields

$$\frac{\rho C_p V_o b_o}{2} (T_\infty - T_i) = \frac{K \mathrm{Nu}_{av}}{b_o} (T_w - T_i) L \tag{B3}$$

Consequently, the entrainment factor can be expressed as

$$\bar{F} = \frac{T_i - T_\infty}{T_i - T_w} = \frac{\mathrm{Nu}_{av}}{\mathrm{RePr}} \left(\frac{2L}{b_o}\right) \tag{B4}$$

The average Nusselt number is obtained by integrating the analytical correlations (equations (2) and (3)) over L.

$$\mathrm{Nu}_{av} = 1.64 C_7 \sqrt{\mathrm{Re}} \left(\frac{b_o}{h}\right)^{3/4} \left[0.302 \frac{h}{L} (1 - \bar{F}) + 0.289 C_1 \frac{h}{L} \sqrt{\frac{b_o}{h}} \bar{F}\right] + 0.00174 C_3 \mathrm{Re} \left[2 \sqrt{\frac{b_o}{L}} \left(1 - \sqrt{\frac{0.34 h}{L}}\right) (1 - \bar{F}) + 4.85 C_5 \left(\frac{b_o}{L}\right) \ln\left(\frac{L}{0.34h}\right) \bar{F}\right] \tag{B5}$$

Equations (B4) and (B5) form a set of two linear coupled equations which can be solved directly for $\bar{F}$.

Because of the additional heat gain from the side heaters, the use of this procedure for the jet arrays used in this study produced values of $\bar{F}$ that were 20 to 40 percent lower than the measured values of $\bar{F}$. For large jet arrays, this calculation would be expected to give accurate values of $\bar{F}$ because of the minimal end and side effects.

Heat Transfer Characteristics for Jet Array Impingement With Initial Crossflow

L. W. Florschuetz
Mem. ASME

D. E. Metzger
Mem. ASME

C. C. Su
Student Mem. ASME

Department of Mechanical and Aerospace Engineering, Arizona State University, Tempe, Ariz. 85287

Two-dimensional arrays of circular air jets impinging on a heat transfer surface parallel to the jet orifice plate are considered. The jet flow, after impingement, is constrained to exit in a single direction along the channel formed by the jet orifice plate and the heat transfer surface. In addition to the crossflow that originates from the jets following impingement, an initial crossflow is present that approaches the array through an upstream extension of the channel. The configurations considered are intended to model the impingement cooled midchord region of gas turbine airfoils in cases where an initial crossflow is also present. A major objective is determination of the effect of initial crossflow air temperature relative to jet array air temperature on impingement surface heat fluxes. Dimensionless adiabatic wall temperatures and Nusselt numbers resolved to one streamwise jet hole spacing were experimentally determined for ratios of initial crossflow rate to total jet flow rate ranging from zero to unity. These results are presented and discussed relative to the flow and geometric parameters.

Introduction

The most critical areas in modern high-performance gas turbine engines from the viewpoint of thermal exposure are the first-stage airfoils, both stator vanes and turbine blades. For an internal cooling scheme the large external heat loads require high heat transfer coefficients between the cooling air and inner surface of the airfoil. An impingement-cooled arrangement is often the choice because of the high heat transfer coefficients possible and the capability of placing jets in patterns dictated by the external thermal loading. A typical midspan arrangement of circular jets is shown in cross section in Fig. 1. The drop-off in external load behind the leading edge eliminates the need for new cooling jets in this region and the leading edge coolant flows around to become a separate, or initial, crossflow to the midchord jet array. Alternate types of arrangements do not include the presence of an initial crossflow approaching the midchord jet array. It should be recognized, however, that crossflow is always present downstream of the first row of the midchord array, whether or not a separate initial crossflow is imposed. The geometry of the airfoil application dictates that all of the jet flow will exit in the chordwise direction toward the trailing edge. This fact has stimulated much of the prior work on the effects of crossflow on confined jets, as typified by [1-9].

Earlier work by the authors was directed at modeling uniform arrays in cases where an initial crossflow is not present [6, 7, 8]. More recently, the study was expanded to consider the effects of initial crossflow, including the effect of an initial crossflow temperature which is elevated above the jet temperature. The latter condition is of considerable importance. The designer is often faced with an initial crossflow temperature that is substantially above the midchord jet temperature because of heat pickup in the leading edge region. Confident design can be achieved only if the designer knows the proper effective coolant temperatures and heat transfer coefficients to use in the region where the initial crossflow penetrates into the midchord array. To date, there appears to be little or no information in the literature on the effect of initial crossflow rate and temperature relative to jet flow rate and temperature on heat transfer characteristics of two-dimensional jet arrays.

This paper reports some results of the present study intended to respond to this need. Heat transfer coefficients and adiabatic wall temperatures resolved to one streamwise hole spacing were experimentally determined for uniform rectangular arrays of circular jet orifices with an initial crossflow. The arrays are intended to model the types of midchord cooling arrangements illustrated schematically in Fig. 1. Streamwise and spanwise hole spacings, expressed in jet hole diameters (x_n/d, y_n/d) were (5, 4), (5, 8), (10, 4), and (10, 8). Each array had 10 spanwise rows of holes. The jet plate-to-impingement surface spacings (z/d) were 1, 2, and 3 hole diameters. The configuration with (x_n/d, y_n/d, z/d) = (5, 4, 3) was also tested in a staggered hole pattern. Most tests were conducted with a nominal mean jet Reynolds number $\overline{\mathrm{Re}}_j$ of 10^4. The ratio of initial crossflow rate to total jet flow rate (m_c/m_j) was set at nominal values of 0.2, 0.5, and 1.0 for each geometry with a reference test at zero initial crossflow also included. Both Nusselt numbers and dimensionless adiabatic wall temperatures are presented and discussed in relation to the flow and geometric parameters. Flow distribution effects associated with the presence of an initial crossflow were previously reported in detail in [11].

Initial Crossflow Experimental Facility

The basic test model geometry and nomenclature are shown schematically in Fig. 2. The flow region of primary interest is that bounded by the jet exit plane and the impingement surface. The length (L) of this region is considered to extend

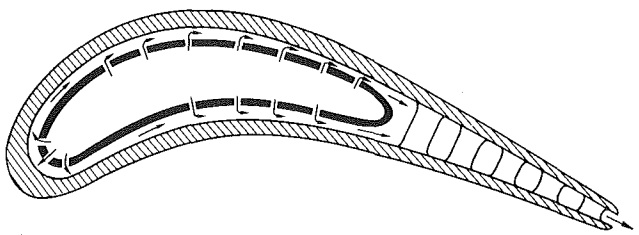

Fig. 1 Impingement cooled airfoil—midchord jet arrays subject to initial crossflow

Contributed by the Heat Transfer Division and presented at the 28th International Gas Turbine Conference and Exhibit, Phoenix, Arizona, March 27-31, 1983. Manuscript received by the Heat Transfer Division January 3, 1983. Paper No. 83-GT-28.

from one-half a streamwise hole spacing ($x_n/2$) upstream of the first spanwise row of holes to the same distance downstream of the last row. The total crossflow rate approaching a given row is equivalent to the initial crossflow rate (m_c) combined with the total jet flow introduced upstream of that row.

The basic experimental facility was that originally used for a comprehensive series of noninitial crossflow tests [6, 7, 8], but set up in a modified form it is suitable for conducting tests with initial crossflow. A complete description of the original facility may be found in [10]. Here a description of the facility in the initial crossflow configuration will be given. For the convenience of the reader certain basic features previously described in detail [10], will also be noted.

A cross-sectional view of the arrangement is shown in Fig. 3. There are two plenum chambers, each with two sections of porous plenum packing supported by screens, supplied individually with dried and filtered laboratory compressed air, one for introducing air to the main jet plate and one for introducing the initial crossflow air to the channel. An electric resistance heater (not shown) in the line immediately upstream of the initial crossflow plenum permits independent control of the initial crossflow air temperature at levels above the jet plenum air temperatures. The initial crossflow was introduced to the channel through two spanwise rows of jet holes. The main jet plates, each with 10 spanwise rows of holes, are interchangeable. The plenum/jet plate assembly was mounted over the test plate unit (impingement plate) through interchangeable spacers which fixed the channel height (i.e., the jet exit plane-to-impingement surface spacing). The spacers also formed the upstream end-surface and side walls of the channel, thus constraining the initial crossflow and the jet flow to discharge in a single direction to the laboratory environment at atmospheric pressure. The test plate unit consists of a segmented copper heat transfer test plate with individual segment heaters, the necessary thermal insulation, and the test plate support structure. The segmented design provides for control of the streamwise thermal boundary

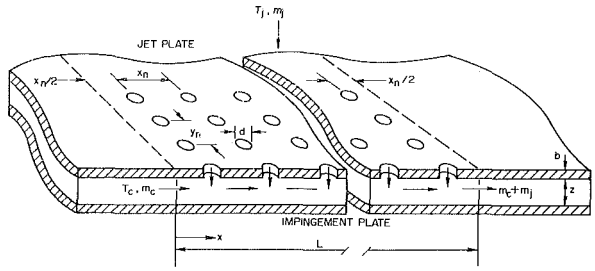

Fig. 2 Initial crossflow basic test model geometry and nomenclature

condition at the heat transfer surface, as well as for determination of spatially resolved heat transfer coefficients in the streamwise direction. Note that in the configuration shown the spanwise rows of jet holes are centered over the test plate segments, one row per segment. This results in a streamwise resolution of measured heat transfer coefficients equivalent to one streamwise jet hole spacing. There are a total of 31 segments in the test plate, 19 upstream of the jet array, 10 immediately opposite the array, and 2 downstream of the array.

Significant geometric characteristics of the configurations tested are summarized in Table 1. The array of length L = 12.7 cm with matching jet plenum (Fig. 3) was designated as size B. The jet plates are identified by the notation $B(x_n/d, y_n/d)I$, where the I designates an inline hole pattern, replaced by S to designate a staggered pattern. Throughout the text specific test configurations, including the channel height, are identified by notations in the form $B(x_n/d, y_n/d, z/d)I$. A staggered pattern was identical to its inline counterpart, except that alternating spanwise rows of holes were offset by one-half the spanwise spacing. Note that the overall channel width exceeded the width of the heat transfer test plate and that the number of holes across the channel (N_s') exceeded the number across the test plate (N_s). Jet holes were always symmetrically aligned with both the edges of the channel and the edges of the heat transfer test plate. Reckoned from the

Nomenclature

A_o = total jet hole area
A_o^* = ratio of jet hole area to opposing impingement surface area (open area ratio), $\pi/[4(x_n/d)(y_n/d)]$
b = local thickness of jet plate at jet hole location
C_D = jet plate discharge coefficient
c_p = constant pressure specific heat
d = jet hole diameter
D_h = hydraulic diameter
f = friction coefficient defined as $2\tau_w\rho/G_c^2$
G_c = crossflow mass velocity based on channel cross-sectional area
G_j = jet mass velocity based on jet hole area
h = heat transfer coefficient at impingement surface defined by equation (1)
L = streamwise length of jet plate and impingement surface (Fig. 2)
L_e = initial crossflow development (entrance) length upstream of jet array
m_c = initial crossflow rate
m_j = total jet flow rate
N_c = number of spanwise rows of holes in streamwise direction
N_s = number of jet holes across span of heat transfer test surface
N_s' = number of jet holes across span of channel
Nu = Nusselt number, hd/k
q = heat flux at impingement surface
Q_n = heat rate at surface of test plate segment n in initial crossflow channel
Re_c = crossflow (channel) Reynolds number, $G_c(2z)/\mu$
Re_j = jet Reynolds number, $G_j d/\mu$
T_{aw} = adiabatic wall temperature
T_c = characteristic temperature of initial crossflow
T_j = characteristic temperature of jet flow
T_f = characteristic injection temperature for film cooling
T_m = characteristic mainstream temperature for film cooling
T_o^c = initial crossflow plenum air temperature
T_s = heat transfer surface temperature
w = width (span) of channel
x = streamwise location along jet plate or impingement surface (Fig. 2)
x_n = streamwise jet hole spacing
y_n = spanwise jet hole spacing
z = channel height (jet exit plane-to-impingement surface spacing)

Greek

η = dimensionless adiabatic wall temperature defined by equation (3) for jet array impingement with initial crossflow and by equation (2) for film cooling.
μ = dynamic viscosity
ρ = fluid density
τ_w = channel wall shear stress

Superscript

$(\bar{\ })$ = overbar refers to mean value over jet plate

Table 1 Geometric parameters and mean discharge coefficients for jet plates tested

Jet plate $B(x_n/d, y_n/d)I$	A_o^*	d and b (cm)	N_s	N_s'	C_D
$B(5,4)I$(and S)	0.0393	0.254	12	18	0.85
$B(5,8)I$	0.0196	0.254	6	9	0.80
$B(10,4)I$	0.0196	0.127	24	36	0.76
$B(10,8)I$	0.0098	0.127	12	18	0.76

Channel heights, $(z/d) = 1$, 2, and 3; in the text specific configurations are referred to by notations in the form $B(x_n/d, y_n/d, z/d)I$ where I = Inline and S = staggered hole pattern.

Fixed Parameters:

Channel width (span), $w = 18.3$ cm
Heat transfer test plate width, 12.2 cm
Heat transfer test plate length, 39.4 cm
Overall channel length, 43.2 cm
Initial crossflow channel length, 26.0 cm
B-size jet array and plenum length, $L = 12.7$ cm
Downstream exit length, 4.5 cm
Initial crossflow development length, $L_e = 24.1$ cm
Number of spanwise rows of jet holes, $N_c = 10$

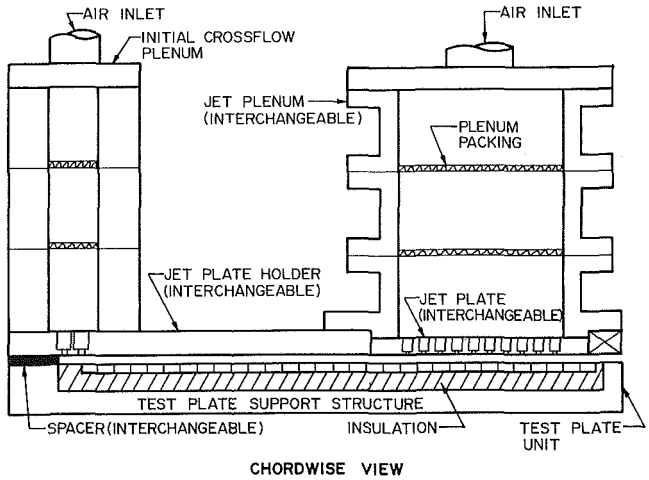

Fig. 3 Initial crossflow test facility schematic

centerline of the second (i.e., downstream) spanwise jet row of the initial crossflow plenum, the channel length available for flow development upstream of the jet array (initial crossflow development length, 24.1 cm) ranged from 16 to 95 hydraulic diameters, depending on the channel height. It may also be noted that this length was 19 times the streamwise hole spacing in the main jet array ($x_n = 1.27$ cm). Average jet plate discharge coefficients are also included in Table 1.

Impingement With Crossflow as a Three-Temperature Problem

The simplest and most frequently encountered convection heat transfer conditions can usually be treated in terms of two characteristic temperatures—a surface temperature and a fluid temperature (a two-temperature problem). Jet array impingement cooling with initial crossflow (Fig. 2) in which the initial crossflow temperature differs from that of the jets can be viewed as a three-temperature problem. This is a convection heat transfer situation where the surface heat transfer is to a fluid in the process of mixing from two different sources at two different temperatures. The best known example of a three-temperature situation is film cooling. In film cooling it is well known that the interaction of a secondary fluid stream with a primary stream affects not only the heat transfer coefficient, but also the value of the reference fluid temperature which drives the heat flux. In the simplest terms

$$q = h(T_s - T_{aw}) \tag{1}$$

where T_{aw} is the adiabatic wall temperature and is embodied in a nondimensional effectiveness

$$\eta = (T_{aw} - T_m)/(T_f - T_m) \tag{2}$$

The heat fluxes for jet array impingement with an initial crossflow can also be written as in (1), but T_{aw} is now expressed as the nondimensional adiabatic wall temperature in terms of T_j and T_c (Fig. 2)

$$\eta = (T_{aw} - T_j)/(T_c - T_j) \tag{3}$$

For jet impingement cooling it is appropriate to identify the jet flow as the primary flow and the crossflow as the secondary flow. With this in mind, the form of the definition of η given in (3) for impingement cooling is analogous to the established form utilized for film cooling. However, in the case of impingement it may not be appropriate to refer to this η as an "effectiveness," since in cases of practical interest in turbine impingement cooling it is desirable to have the jet flow dominating. This condition is reflected by η approaching zero.

It is useful to emphasize that (1) and (3) may be combined to give

$$q = h[(1-\eta)(T_s - T_j) + \eta(T_s - T_c)] \tag{4}$$

This form points up the fact that η is merely a "temperature-difference weighting factor," and for jet impingement with crossflow is perhaps best viewed in this manner.

In order to define the heat transfer characteristics (h, η) of a two-dimensional array of discrete impinging jets with an initial crossflow, it is necessary to characterize T_c and T_j. For low-speed flow, T_c may be characterized by the mixed-mean temperature of the initial crossflow at the entrance to the array ($x = 0$, Fig. 2), while T_j may be taken as the mixed-mean fluid temperature at the jet exit plane. However, for high-speed flow, a somewhat generalized definition is necessary, just as in the case of film cooling [12]. T_c may be characterized as the adiabatic wall temperature at the array entrance, and T_j as the adiabatic wall temperature opposite the given jet row in the absence of an initial crossflow. In the case of low-speed flow, these values reduce to the mixed-mean temperatures previously indicated.

In cases of practical interest in turbine cooling, the distinction previously indicated in establishing T_c and T_j will not be particularly significant since differences between T_s and both T_c and T_j are quite large. However, for the experimental results to be reported herein these temperature differences were small (5 to 35 K). Also with the relatively low laboratory air pressures utilized, jet and crossflow velocity magnitudes in some cases may be rather high. Hence it was appropriate to utilize the more general definition in reducing the heat transfer data obtained from the test runs.

Experimental Procedures and Data Reduction

Many details of the experimental procedures and data reduction techniques utilized for the initial crossflow tests were similar to or identical with those previously reported in [10]. Those details will be included here only as necessary with emphasis placed primarily on those additional features which were unique to the initial crossflow tests.

Standard Test Runs. A standard test run was initially defined by setting up a selected initial crossflow geometry with x_n/d, y_n/d, and z/d the primary geometric parameters as previously summarized in Table 1. The number of spanwise jet rows was always 10. The centerlines of these rows were always aligned directly opposite the spanwise centerlines of segment numbers 20 through 29 of the test plate, counting from upstream (Fig. 3). Segments 1 through 19 formed the

heat transfer surface of the initial crossflow channel, and segments 30 and 31 formed an extension of the heat transfer surface in the exit channel downstream of the array. Values of η and h, as defined by equations (1) and (3) (or by (4)) were determined for each segment opposite the array (20 through 29) as well as for segment 30 immediately downstream. Segment 31 was used as a guard element. Values of h could also be determined upstream of the array where $\eta = 1$ by definition.

Two separate sets of tests were required to determine these streamwise profiles of η and h for a given geometry, $\overline{\mathrm{Re}}_j$, and flow ratio, m_c/m_j. First, with the initial crossflow geometry, but with zero initial crossflow ($m_c = 0$), a set of tests was conducted to determine T_j, the characteristic temperature for jet flow alone, for each segment. These tests were conducted at three different steady-state conditions corresponding to three different power input levels to the segment heaters. A linear least-squares fit to the three resulting data sets (q, T_s) for each of the segments under the jet rows (plus Segment 30) was used to determine the appropriate T_j for each segment from $q = h(T_s - T_j)$. In addition, the fits result in streamwise resolved values of h for the array in the absence of initial crossflow.

Second, a similar set of tests at three different power levels was conducted with the heated initial crossflow present. For the conditions of these tests, the adiabatic wall temperature of the initial crossflow at the entrance to the array, used to characterize T_c, was essentially identical to the mixed-mean stagnation (i.e., total) temperature of the initial crossflow. This stagnation temperature was determined for each steady-state condition from the measured initial crossflow plenum temperature, combined with an energy balance over the initial crossflow channel

$$T_c = T_o^c + \frac{1}{m_c c_p} \sum_{n=1}^{19} Q_n \tag{5}$$

With T_j and T_c determined, a linear least-squares fit to the three data sets (q, T_s) was used to determine the two unknowns h and η from equation (4) for each of the segments 20 through 30. Values of h in the initial crossflow channel were also determined using the adiabatic wall temperature at the given segment as the reference temperature approximated by the local mixed-mean stagnation temperature again determined from an energy balance.

It was shown experimentally by McAdams et al. [13] that for duct flows at subsonic velocities the heat transfer coefficient defined on the difference between the temperature of the heated wall and adiabatic wall temperature is independent of this difference. They also showed that for such flows preferred values of the recovery factor lie in the range 0.875–0.905. Using a recovery factor of 0.89, it was determined that for the present tests the difference between the stagnation temperature and the adiabatic wall temperature for the initial crossflow channel was normally less than 0.1 K and always less than 0.2 K. Hence the use of the stagnation temperature as satisfactorily representing the adiabatic wall temperature is justified for the conditions of these tests.

Additional details relating to the test procedure will now be discussed. For each standard test run the jet flow rate (m_j) was set at the appropriate value to give a nominal $\overline{\mathrm{Re}}_j$ of 10^4. The jet plenum air temperature was normally at an ambient level of about 300 K. For each geometry, the initial crossflow rate (m_c) was set, in turn, at the appropriate levels to give nominal values of m_c/m_j of 0.2, 0.5, and 1.0. The initial crossflow plenum air temperature was brought to a value approximately midway between the jet plenum temperature and the maximum value of the heat transfer surface temperature to be utilized (about 330 K).

The first steady-state condition was achieved with zero power input to the test plate segment heaters, and the segment temperatures were recorded. The entire test plate was then brought to a uniform temperature at the maximum value of about 330 K by individually adjusting the power input to each of the 31 test plate segment heaters. When this second steady-state condition was achieved, both the segment temperatures and the individual segment heater power inputs were recorded. The third and final condition was set with the heater power inputs cut to about half of their maximum values. Segment (surface) heat fluxes were determined from the measured power inputs suitably corrected for heat leaks [10]. Heat fluxes for the zero power input condition were not precisely zero because of these small but unavoidable heat leaks.

Test run procedures for the determination of T_j were similar, except for the absence of the initial crossflow. Segments 1 through 18 were inactive, with Segment 19 used as a guard element.

Experimental Uncertainties. The linear least-squares fit based on equation (4) was actually carried out in the form

$$\frac{q}{T_s - T_c} = h(1-\eta)\frac{T_s - T_j}{T_s - T_c} + h\eta \tag{6}$$

with the coefficients $h(1-\eta)$ and $h\eta$ determined directly from the fit. It is clear from either equation (4) or (6) that only two independent test conditions are required to determine η and h. The use of three independent conditions provided additional confidence to the fit. As a measure of this confidence, three values of η and of h were also computed using each of the three possible combinations of two members of each data set (zero/maximum, zero/half, and half/maximum power input conditions). These values were then compared with the original values of η and h based on the linear least squares fit to all three members of each data set.

Considering all standard test runs with initial crossflow present, 95 percent of the values of h computed from two members of each set deviated from the values based on the fit by less than ± 3 percent. For η, the result was ± 7 percent, with most of the larger deviations coming at downstream rows where the η values were smaller. For the zero initial crossflow tests, 95 percent of the h values were within ± 2 percent.

The percentage deviations noted above provide some indication of the uncertainty associated with the η and h results. Experimental uncertainties must be at least as large as these values. Composite uncertainties for η and Nu were also calculated by the method of [14]. Input uncertainties were estimated at ± 1 percent to ± 2 percent for the heat fluxes, ± 0.25 K for ($T_s - T_c$), ± 0.1 K for ($T_s - T_j$), and ± 1 percent for d as it enters the Nusselt number calculated from h. ($T_s - T_j$) values depended only on differences between measurements made with the same thermocouple, whereas ($T_s - T_c$) values depended on the difference between measurements from two different thermocouples plus an energy balance. The calculated η and Nu composite uncertainties varied depending on the particular conditions but for Nu within the array most conditions resulted in values of ± 6 percent or less. For η the composite uncertainties, expressed on a percentage basis, vary more widely depending on conditions, from about ± 2 to ± 4 percent for η values near unity to as much as ± 20 percent for a downstream value as low as 0.1. Overall, the calculated composite uncertainty ranges appear consistent with the percentage deviations from

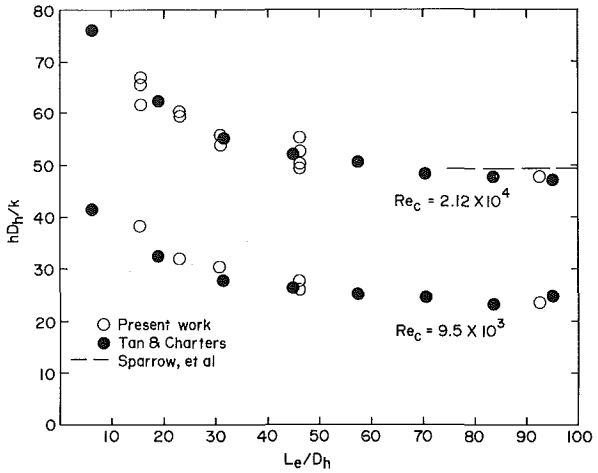

Fig. 4 Nusselt numbers in initial crossflow channel immediately upstream of jet array compared with prior data from literature

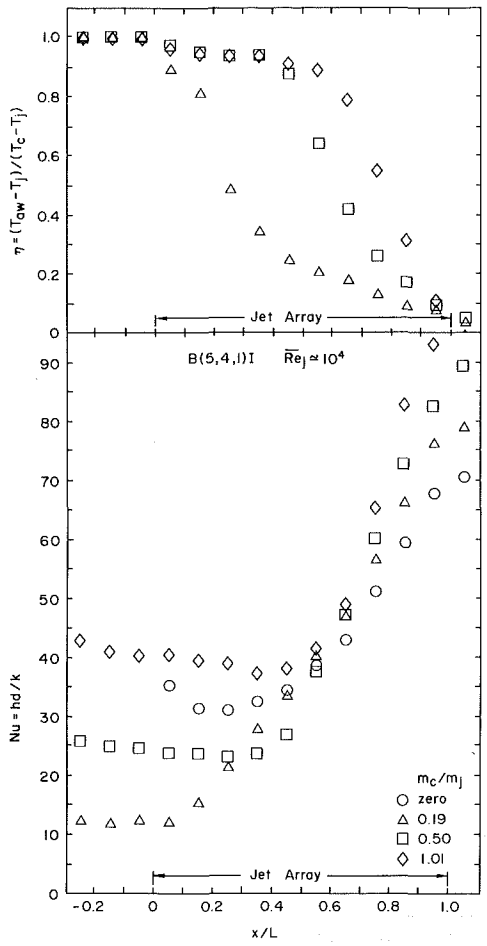

Fig. 5 Effect of initial crossflow rate on η and Nu profiles for *B*(5, 4, 1)*I* geometry

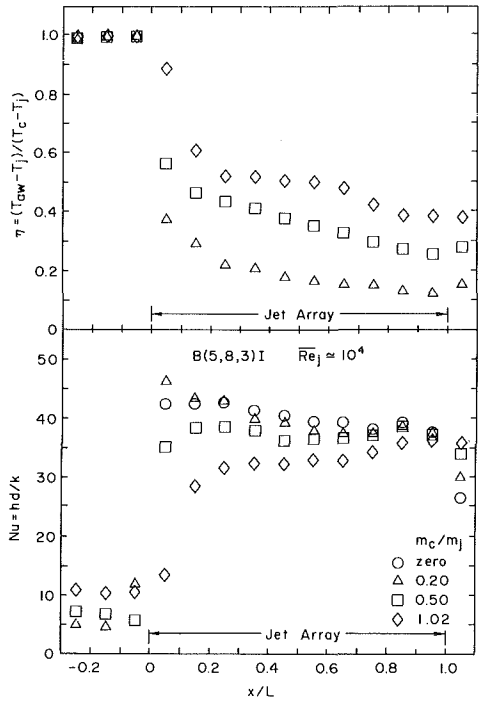

Fig. 6 Effect of initial crossflow rate on η and Nu profiles for *B*(5, 8, 3)*I* geometry

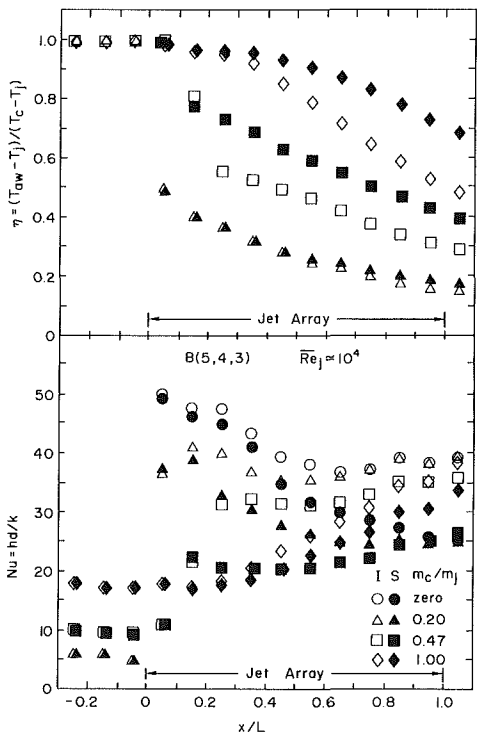

Fig. 7 Effect of initial crossflow rate on η and Nu profiles for *B*(5, 4, 3) geometry: *I* = in-line pattern, *S* = staggered pattern

the linear least-squares fits as summarized in the preceding paragraph.

Results and Discussion

Results from the standard test runs for streamwise profiles of η and Nu within the jet array will be presented and discussed shortly. First, however, heat transfer coefficients in the initial crossflow channel immediately upstream of the jet array section will be compared with prior data from the literature for asymmetrically heated ducts of rectangular cross section with one of the two widest sides heated and the opposite side adiabatic. Since for all standard test runs the initial crossflow development length (L_e) was fixed (Table 1), L_e measured in terms of hydraulic diameters ($D_h = 2z$) varied with the channel height z set for the particular test. Channel Nusselt numbers (hD_h/k) at Segment 19 from the present tests

are compared in Fig. 4 with the data of Tan and Charters [15] for the entrance region and with a fully developed Nusselt number based on the data of Sparrow et al. [16]. The three sets of results are seen to be quite consistent.

We turn now to the main results for heat transfer characteristics in the jet array impingement region with the presence of the initial crossflow at a temperature different from the jet temperature. Sample results drawn from the standard test series are presented for four different geometric configurations in Figs. 5–7. Each figure shows streamwise profiles of η and Nu resolved to one streamwise hole spacing. η and Nu are paired in each figure to emphasize that, in general, in order to appropriately relate the heat flux to the surface and characteristic fluid temperatures both parameter values are needed. For each geometry, profiles are shown for m_c/m_j at nominal values of 0.2, 0.5, and 1.0. Nusselt number profiles for the initial crossflow configuration, but with $m_c = 0$, are also shown as a reference or baseline case for comparison. Since each array had 10 spanwise rows of holes, each profile includes 10 points within the array proper, with three additional points included for the initial crossflow channel immediatedly upstream of the array and 1 point immediately downstream.

Consider first the results for η. In general, η decreases with increasing x/L and decreasing m_c/m_j. These trends simply reflect the increasing influence of the jet flow. Of particular note is the fact that overall, η covers the range from unity to nearly zero, and for the $B(5, 4, 1)I$ geometry represented by Fig. 5, covers this range for a single configuration. This geometry also has the most highly nonuniform flow distribution (Fig. 8). Here the effect of initial crossflow not only penetrates into the array, but essentially dominates ($\eta \simeq 1$) at the first row for all m_c/m_j; and for $m_c/m_j = 0.5$ and 1.0, dominates over halfway through the array. This dominance can also be seen by examining the Nu profiles for this case which remain essentially at their upstream initial crossflow channel levels well into the array. This behavior is quite consistent with the very large cross-to-jet mass velocity ratios which persist well into this array (Fig. 8).

Turning to Fig. 6, a contrasting behavior is observed for the geometry with the most nearly uniform flow distribution (Fig. 9). Here η has already dropped to about 0.5 at the first row, except for $m_c/m_j = 1.0$, where this level of decrease requires two rows. Similarly, the strong immediate influence of the jets is reflected in the very large increase in Nu from upstream of the array to the first or second row of jets. It is interesting to note that at the first row an increase of G_c/G_j (Fig. 9) from 0.2 to 0.4 causes a reduction in Nu (Fig. 6) by a factor of more than two-and-one-half, while the increase from 0 to 0.2 causes essentially no change. It is possible that at the larger value of G_c/G_j the impingement points of the jets are displaced downstream by $x_n/2$ or more and thus provide little cooling of the area $0 \le x \le x_n$ associated with the first row. This explanation is reinforced by examining the Nu values immediately downstream of the array. For $m_c/m_j = 1.0$, this Nu value is 3.5 times the value upstream of the array though the downstream crossflow Reynolds number would be just twice that upstream of the array. This indicates that the jets in the last row of the array must be displaced enough to be impinging on the surface segment immediately downstream of the array.

The final sample results for η and Nu presented here (Fig. 7) are for the $B(5, 4, 3)$ geometry, for both inline and staggered hole patterns. The flow distributions for this geometry (not shown here) fall between those for the two inline geometries of Figs. 5 and 6. Considering the relative flow distributions the results for the inline pattern in Fig. 7 are consistent with the trends exhibited for η and Nu in Figs. 5 and 6 as discussed in the preceding paragraphs. The results for the staggered hole pattern included in Fig. 7 will be discussed shortly. Complete graphical and tabular results for both heat transfer characteristics and flow distributions for all geometries tested (Table 1) may be found in [17].

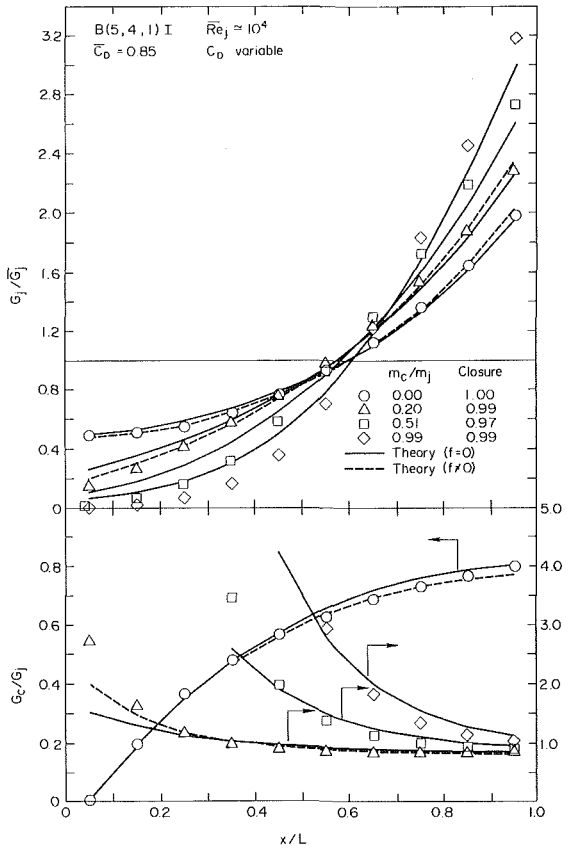

Fig. 8 Effect of initial crossflow on jet array flow distribution for $B(5, 4, 1)I$ geometry—experimental data compared with predictive model [11]

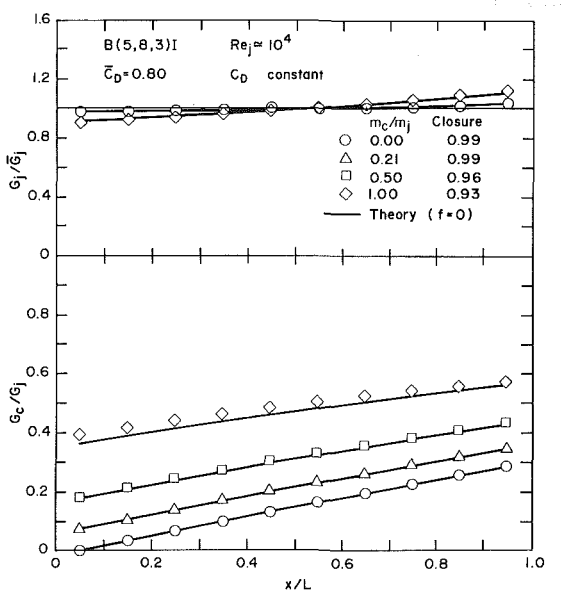

Fig. 9 Effect of initial crossflow on jet array flow distribution for $B(5, 8, 3)I$ geometry—experimental data compared with predictive model [11]

Considering the entire set of results, the Nu profiles, unlike the η profiles, do not all vary monotonically with streamwise location. Rather, Nu variations inlcude monotone decreasing,

monotone increasing, and cases with one or two local minima and/or maxima. An important observation to emphasize is that in most cases the addition of the initial crossflow (which means an increase in the total coolant flow, since m_j was kept essentially constant for each geometry), resulted in reduced mean values of Nusselt number over the jet array region. Of all the arrays tested only those with $z/d = 1$ showed higher mean values of Nu at one or more of the initial crossflow values, as compared with the zero initial crossflow case. Even these cases resulted in a degradation in mean Nusselt number due to the presence of an initial crossflow, when considered per unit of total coolant flow rate ($m_c + m_j$).

Now consider the results for the staggered array, $B(5, 4, 3)S$, as compared with the results for its inline counterpart in Fig. 7. This geometry was selected for testing with a staggered hole pattern, since in prior noninitial crossflow tests it showed the largest effect of hole pattern on the spanwise averaged heat transfer coefficients [7, 10]; it has the closest hole spacings and largest z/d of all the arrays tested. Streamwise flow distributions for this staggered pattern were found to be essentially the same as those for the inline case. The η profiles for the staggered array fall above those for the inline array, insignificantly for the smallest initial crossflow ratio, $m_c/m_j = 0.2$, but noticeably for $m_c/m_j = 0.5$ and 1.0, especially downstream.

For all flow ratios from zero to unity, the staggered array Nusselt numbers are the same as the inline values at the first upstream row in the array, with inline values becoming larger than the staggered values as one proceeds downstream. An explanation for this type of behavior was originally presented in some detail in connection with noninitial crossflow test results [8, 10]. Basically it may be speculated that there is less mixing of the jet and crossflow at downstream rows for the inline pattern than for the staggered pattern. Hence the inline impinging jets more nearly retain their identity and provide more effective cooling than those in the staggered pattern. Though the phenomena involved is extremely complex, so that conclusive explanations are premature, the η behavior also fits the above interpretation in that the jets are less dominant in the staggered case, since they mix somewhat more with the crossflow.

With the $B(5, 8, 3)I$ geometry at $m_c/m_j = 0.51$, a test was conducted with the mean jet Reynolds number nearly double the nominal standard test run value of 10^4. The resulting streamwise η profile agreed with the standard test run result to within experimental uncertainty. The heat transfer coefficient profiles were compared in the form of Nusselt numbers normalized by $\overline{\mathrm{Re}}_j^{0.73}$. The exponent on $\overline{\mathrm{Re}}_j$ is from the noninitial crossflow jet array impingement correlation previously reported [6]. This exponent value accounted quite satisfactorily for the Nusselt number dependence on Reynolds number observed in these tests.

Prior heat transfer measurements for one geometric configuration for a two-dimensional array of circular impinging jets with an initial crossflow were made by Saad et al. [9]. Only Nusselt number results were presented. No indication of adiabatic wall temperatures or the relation of the initial crossflow temperatures to the jet temperatures was given. The Nusselt numbers could not be directly compared with results of the present measurements, because the hole spacings of the array studied in [9] were below the range covered in the present study. However, on a relative basis, the Nusselt number magnitudes were consistent with the present results.

Concluding Remarks

Experimentally determined, spanwise-averaged, streamwise-resolved dimensionless adiabatic wall temperatures (η values) and Nusselt numbers for jet arrays with 10 spanwise rows of holes in the presence of an initial crossflow have been presented. Nusselt numbers at the upstream rows of the array are in many cases significantly reduced, even by small initial crossflow rates relative to the total jet flow rate. The η values within the array, under some conditions, span the range from unity to nearly zero. The practical implication of these results is of considerable importance. For example, in a highly cooled first stage vane like that shown in Fig. 1, T_c is often several hundred degrees above T_j. Typical values are $T_s = 1260$ K, $T_j = 760$ K, and $T_c = 870$ K. Given the heat flux, values for T_c and T_j, and presupposing the availability of reliable results for h, predictions for T_s will differ by an amount equivalent to $T_c - T_j$ (110 K for the above example) as η is varied from unity to zero. The effect of uncertainties in predicting η (or an appropriate alternative parameter) would be compounded by lack of reliable results for h; a deficiency which would certainly exist for two-dimensional jet arrays in cases where, because of the presence of an initial crossflow, relevant values of G_c/G_j would fall outside the range of available results.

It should be emphasized that the η values presented, though resolved in the streamwise direction, are defined in terms of the initial crossflow temperature at the entrance to the array. In applications of these coefficients, the designer should also use this characteristic temperature. As a very close approximation the stagnation temperature (mixed-mean value) at the entrance to the array may be used. Or, for better accuracy, the corresponding adiabatic wall temperature may be used, computed on the basis of a recovery factor. Unless more specific information is available for the the particular conditions being considered, a recovery factor of 0.9 is recommended [13].

Most of the measurements were carried out for nominal mean jet Reynolds number values of 10^4. The Nusselt number data tabulated in Appendix D, Table D.2 of [17] may be applied at other $\overline{\mathrm{Re}}_j$ (or Re_j) by assuming the Nusselt numbers to be proportional to $\mathrm{Re}_j^{0.73}$ [6], unless upstream rows are being considered in a case where the initial crossflow dominates ($\eta \sim 1$). Then the use of the exponent 0.80 on the Reynolds number is recommended since a duct or channellike flow is not only penetrating within the array but dominating the flow field.

Acknowledgment

The support of the National Aeronautics and Space Administration, Lewis Research Center, is hereby gratefully acknowledged.

References

1 Kercher, D. M., and Tabakoff, W., "Heat Transfer by a Square Array of Round Air Jets Impinging Perpendicular to a Flat Surface Including the Effect of Spent Air," ASME *Journal of Engineering for Power*, Vol. 92, No. 1, Jan. 1970, pp. 73–82.

2 Gauntner, J. W., Gladden, H. J., Gaunter, D. J., and Yeh, F. C., "Crossflow Effects on Impingement Cooling of a Turbine Vane," NASA TM X-3029, Mar. 1974.

3 Bouchez, J. P., and Goldstein, R. J., "Impingement Cooling From a Circular Jet in a Crossflow," *International Journal of Heat and Mass Transfer*, Vol. 18, 1975, pp. 719–730.

4 Sparrow, E. M., Goldstein, R. J., and Rouf, M. A., "Effect of Nozzle-Surface Separation Distance on Impingement Heat Transfer for a Jet in a Crossflow," ASME JOURNAL OF HEAT TRANSFER, Vol. 97, 1975, pp. 528–533.

5 Hollworth, B. R., and Berry, R. D., "Heat Transfer From Arrays of Impinging Jets with Large Jet-to-Jet Spacing," ASME JOURNAL OF HEAT TRANSFER, Vol. 100, 1978, pp. 352–357.

6 Florschuetz, L. W., Truman, C. R., and Metzger, D. E., "Streamwise Flow and Heat Transfer Distributions for Jet Array Impingement with Crossflow," ASME JOURNAL OF HEAT TRANSFER, Vol. 103, 1981, pp. 337–342.

7 Metzger, D. E., Florschuetz, L. W., Takeuchi, D. I., Behee, R. D., and Berry, R. A., "Heat Transfer Characteristics for Inline and Staggered Arrays of Circular Jets with Crossflow of Spent Air," ASME JOURNAL OF HEAT TRANSFER, Vol. 101, 1979, pp. 526–531.

8 Florschuetz, L. W., Berry, R. A., and Metzger, D. E., "Periodic Streamwise Variations of Heat Transfer Coefficients for Inline and Staggered Arrays of Circular Jets with Crossflow of Spent Air," ASME JOURNAL OF HEAT TRANSFER, Vol. 102, 1980, pp. 132–137.

9 Saad, N. R., Mujumdar, A. S., Abdel Messeh, W., and Douglas, W. J. M., "Local Heat Transfer Characteristics for Staggered Arrays of Circular Impinging Jets with Crossflow of Spent Air," ASME Paper 80-HT-23, 1980.

10 Florschuetz, L. W., Metzger, D. E., Takeuchi, D. I., and Berry, R. A., "Multiple Jet Impingement Heat Transfer Characteristics—Experimental Investigation of Inline and Staggered Arrays with Crossflow," NASA Contractor Report 3217, Department of Mechanical Engineering, Arizona State University, Tempe, Ariz., Jan. 1980.

11 Florschuetz, L. W., and Isoda, Y., "Flow Distributions and Discharge Coefficient Effects for Jet Array Impingement with Initial Crossflow," ASME *Journal of Engineering for Power*, Vol. 105, 1983, pp. 296–304.

12 Goldstein, R. J., "Film Cooling," *Advances in Heat Transfer*, Vol. 7, 1971, pp. 321–379.

13 McAdams, W. H., Nocolai, A. L., and Keenan, J. H., "Measurements of Recovery Factors and Coefficients of Heat Transfer in a Tube for Subsonic Flow of Air," *Transactions AIChE*, Vol. 42, 1946, pp. 907–925.

14 Kline, S. J., and McClintock, F., "Describing Uncertainties in Single Sample Experiments," *Mechanical Engineering*, Vol. 75, Jan. 1953, pp. 3–8.

15 Tan, H. M., and Charters, W. W. S., "An Experimental Investigation of Forced-Convective Heat Transfer for Fully Developed Turbulent Flow in a Rectangular Duct with Asymmetric Heating," *Solar Energy*, Vol. 13, 1970. pp. 121–125.

16 Sparrow, E. M., Lloyd, J. R., and Hixon, C. W., "Experiments on Turbulent Heat Transfer in an Asymmetrically Heated Rectangular Duct," ASME JOURNAL OF HEAT TRANSFER, Vol. 88, 1966, pp. 170–174.

17 Florschuetz, L. W., Metzger, D. E., Su, C. C., Isoda, Y., and Tseng, H. H., "Jet Array Impingement Flow Distributions and Heat Transfer Characteristics—Effects of Initial Crossflow and Nonuniform Array Geometry," NASA Contractor Report 3630, Department of Mechanical and Aerospace Engineering, Arizona State University, Tempe, Ariz., Nov. 1982.

Effect of Location in an Array on Heat Transfer to a Short Cylinder in Crossflow

R. J. Simoneau
Head, Heat Transfer Fundamentals Section. Mem. ASME

G. J. VanFossen, Jr.
Aerospace Engineer.

Turbine Branch, Aerothermodynamics and Fuels Division, NASA Lewis Research Center, Cleveland, Ohio 44135

An experiment was conducted to measure the heat transfer from a heated cylinder, three diameters in length, in crossflow in an array of identical circular cylinders. Both in-line and staggered array patterns were studied. The cylinders were spaced on a 2.67 × 2.67 pitch. The Reynolds number range, based on cylinder diameter and average unobstructed channel velocity, was from 5000 to 125,000. Turbulence intensity profiles were measured for each case at a point one-half space upstream of the row containing the heated cylinder. The basis of comparison for all the heat transfer data was the single row with the heated cylinder. For the in-line cases, the addition of a single row of cylinders upstream of the row containing the heated cylinder increased the heat transfer by an average of 50 percent above the base case. Adding up to five more rows caused no increase or decrease in heat transfer. On the other hand, adding rows in the staggered array cases resulted in average increases in heat transfer of 21, 64, 58, 46, and 46 percent for one to five upstream rows, respectively.

Introduction

The desire for increased gas turbine reliability and efficiency has stimulated research in all areas of turbine blade cooling. One widely used method of increasing the heat transfer to the coolant is to cast pin fins into the blade coolant flow passages. These pins must be relatively short because of passage size and manufacturing limitations. The large body of heat transfer data available for tube banks that is reviewed in [1] is not applicable to the turbine cooling case, because the influence of the endwalls is not included. (Endwalls are defined as the plane surfaces perpendicular to the pins that form the top and bottom of the flow channel.) Also, in turbines the pins are usually quite short, less than four diameters. Recently, several experiments have been directed at this problem.

In [2], heat transfer and pressure drop results are presented for several geometries that model a turbine blade trailing edge. For these results, a converging channel was used to simulate a turbine blade trailing edge cooling passage with pin length decreasing in the streamwise direction. However, high experimental uncertainty limits the usefulness of this work.

VanFossen [3] measured the average heat transfer coefficients for two four-row staggered arrays of short pin fins. The length-to-diameter ratios of the pins in the two arrays were 1/2 and 2. It was found that short pin fins increase the heat transfer significantly over that of the plain passage, even though the 1/2-dia-long pins cover up as much endwall area as they add in pin surface area. It was also shown in [3] that the limited data available for pins as short as four diameters, from [4] and [5], are significantly different from the case of short fin pins.

In [6, 7] the spanwise averaged heat transfer was measured for each row of pins for several staggered arrays of ten rows each. Heat transfer for short pins was found to be considerably lower than for long pins, and the heat transfer increased in the streamwise direction for the first several rows until a peak was reached at about the third to fifth row. Heat transfer then decreased slightly in the streamwise direction. Reference [7] also showed that turbulence level, measured at a single point directly upstream of a given pin, was highest in the forward portion of the array and decreased to a lower level downstream.

The present work was performed concurrently with the work of [6] and [7] to gain some understanding of how array geometry and position within the pin array affects heat transfer to an individual pin. A single, heated pin was used to measure heat transfer in both staggered and in-line arrays. Length-to-diameter-ratio for all arrays was 3.01. Up to five rows of pins for both the staggered and in-line arrays were placed upstream of a row containing the heat transfer element. Turbulence intensity profiles across the channel, upstream of the heated pin, were measured for each configuration. Endwall heat transfer was not considered in this work.

This paper compares the various geometric configurations in terms of average Nusselt number over a Reynolds number range from 5000 to 125,000. The results are discussed in terms of turbulence intensity profiles associated with each configuration.

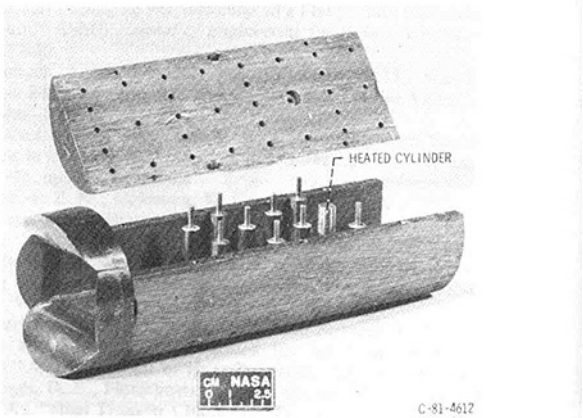

Fig. 1 Photograph of test section channel with four row staggered array in place

Contributed by the Heat Transfer Division for publication in the JOURNAL OF HEAT TRANSFER. Manuscript received by the Heat Transfer Division July 18, 1982. Presented at the AIAA/ASME Fluids Plasma Thermophysics and Heat Transfer Conference, St. Louis, Missouri, June 7-11, 1982.

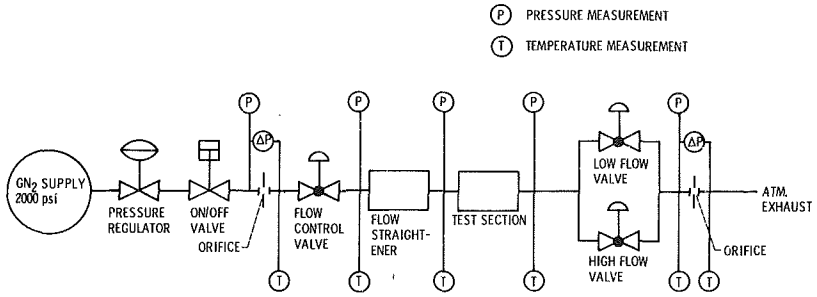

Fig. 2 Flow schematic for pin wake heat transfer experiment

Description of Experiment

Apparatus. All of the tests were conducted using a rectangular flow channel 5.87 cm wide by 2.87 cm high. Pins, which were 0.953 cm in diameter (length-to-diameter ratio of 3.01) were installed in various array patterns. A typical pattern, four rows staggered, is shown in Fig. 1. The axial and transverse spacing were both 2.54 cm (spacing-to-diameter ratio of 2.67). Both staggered and in-line array patterns were used in configurations of one to six rows. The cover shown in Fig. 1 indicates the range of possible patterns. Only one cylinder was heated and that cylinder remained in a fixed position in the channel, as shown in Fig. 1. The various array patterns were achieved by adding or removing nonheated pins. For most of the tests the heated cylinder was in the last row in the array as shown. For a few tests two rows of pins were placed downstream of the heater. The pins touching the sidewalls of the channel had a small 0.083-cm flat machined on the side in order to fit the channel. The entrance to the channel was contoured as shown in Fig. 1.

The assembled channel with a given array pattern in place was subsequently installed in a cylindrical pressure chamber as part of a flow system which is shown schematically in Fig. 2. The flow system was a once-through system of pressurized nitrogen gas. The gas was lowered in pressure with a regulator and then passed through a calibrated metering orifice to a flow control valve, which further lowered the pressure and controlled the flow rate. The gas was then passed through a flow straightener, as shown in Fig. 2. The straightener, which was also used to reduce the inlet turbulence, had three elements. The first element was a wire screen with 0.23-mm-dia wire on a 16 mesh. The second was a honeycomb of plastic soda straws, approximately 0.64-cm-dia and 30-dia long, while the third element was another screen which was the same as the first. This produced a turbulence intensity immediately ahead of the heated cylinder of about 2 percent. The test section pressure was controlled with two valves downstream in parallel for fine and course control. A range of pressures from 100 to 600 kPa were normally used; however, at the higher flow rates pressures below about 500 kPa were not possible. Finally, the flow was passed through a second calibrated metering orifice before being vented to the atmosphere. Because of the large pressure drop the gas temperature in the test section was low, ranging from 260 to 290 K.

Instrumentation. The heated cylinder was a commercial heater made of high resistance wire wound up and buried in a 0.953-cm-dia stainless steel tube. The tube wall thickness was approximately 0.080 cm. The heater was 3.81 cm long; thus, approximately 25 percent of it extended into the channel walls. The heater was instrumented with eight chromel-constantan (type E) sheathed thermocouples buried in slots equispaced on the circumference. The thermocouple junctions were at the longitudinal midpoint of the cylinder with the orientation such that one was on the stagnation point. The power dissipated in the heater was measured using voltage taps on the power leads and a current shunt. The power source was a commercial SCR type D-C power supply.

The flow system instrumentation is indicated on Fig. 2. Pressures were measured with strain gage transducers and temperatures were measured primarily with chromel-constantan thermocouples. The downstream orifice temperatures were measured with platinum resistance thermometers. The upstream orifice meter was used to measure the flow rate and the downstream orifice was used for redundancy. The upstream orifice static pressure could be varied from 300 to 6700 kPa. This allowed accurate metering over a 25 to 1 flow range with a single orifice plate and differential transducer.

The turbulence intensity measurements were made with a conventional temperature compensated hot-film anemometer probe. The same probe was used for the entire experiment. The probe was a single-element sensor traversed across the channel in front of the heated cylinder midway between it and the position of the first upstream row and at midchannel height. The wire was aligned parallel to the cylinder axis. Position was measured with a linear potentiometer attached to the actuator.

All data except the turbulence measurements were recorded on the laboratory central data acquisition/minicomputer system, known as ESCORT [8] which provided real time updates at approximately 2-s intervals on a CRT. The mean and rms turbulence signals were recorded versus position on a two-pen x-y recorder.

Nomenclature

A = channel cross-section area, m^2
D = cylinder diameter, m
e_{rms} = root mean square of hot wire voltage fluctuation, V
E = mean hot wire voltage, V
I = heater current, A
k = thermal conductivity, W/m K
L = cylinder length, m
n = exponent in hot wire heat transfer law
Nu = Nusselt number (equation (2))
q = heat flux, W/m^2
Re = Reynolds number (equation (1))
T = temperature, K
Tu = turbulence intensity (equation (3)), percent
U = velocity, m/s
V = heater voltage, V
w = mass flow rate, kg/s
y = distance across channel, m
μ = viscosity, N/s m^2

Subscripts

avg = average
b = bulk fluid conditions
o = no flow condition
w = wall

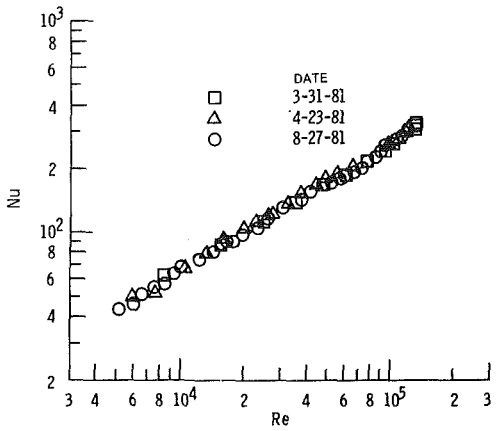

Fig. 3 Heat transfer with heater only (no unheated pins) in channel

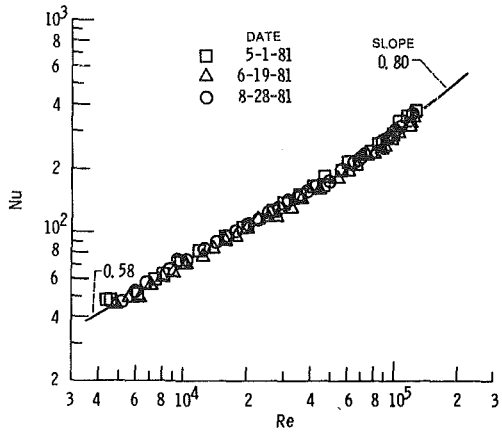

Fig. 4 Heat transfer with one row in channel – base case

Data Reduction and Accuracy. The heat transfer data are presented in terms of standard Nusselt number versus Reynolds number plots. As will be discussed in the Results section, the data taken in this experiment do not support the use of the maximum velocity, based on minimum flow area, in computing the Reynolds number. The Reynolds numbers used herein are based on the mass flow rate and the channel cross-sectional area.

$$\mathrm{Re} = \frac{wD}{\mu A} \tag{1}$$

The Nusselt number was computed on the basis of the total power dissipated divided by the exposed surface area of the heated cylinder.

$$\mathrm{Nu} = \frac{qD}{(\Delta T)k} = \frac{(VI)}{\pi(T_{w,\mathrm{avg}} - T_b)kL} \tag{2}$$

The wall temperature was the average of the eight surface thermocouples, and the fluid temperature was measured at the inlet to the channel. A heat loss calibration was conducted with no flow and power to the heater. Over temperature differences from 6 to 40 K, the calibration data normalized by equation (2) was constant at Nu = 11. To check on the effect of flow on the heat loss to the endwalls, a finite difference heat conduction analysis was performed. The result showed the loss calibration number of 11 to be affected by less than 10 percent, a negligible effect on the overall calibration. Thus, all data presented herein have a loss correction of Nu = 11 subtracted from the raw data.

The thermophysical properties used in equations (1) and (2) were all calculated at the inlet temperature. The density was calculated on the basis of ideal gas. The viscosity and thermal conductivity were simple curve fits to the data of [9].

The turbulence data were all acquired using an uncalibrated temperature compensated probe, since the operating conditions were well below room temperature. The temperature compensated probe was used merely to minimize drift. Since the primary interest was to make relative comparisons, this was considered adequate. For uncalibrated probes, it is possible to derive an approximate linearized expression for turbulence intensity (10-11).

$$\mathrm{Tu} = \frac{2nE\, e_{\mathrm{rms}}}{(E^2 - E_o^2)} \times 100 \tag{3}$$

Where $1/n$ is the exponent in the heat transfer law governing the performance of the hot wire. For the present work, $n = 2$ was assumed. Equation (3) was used for all turbulence data.

The parameters in equations (1-3) were analyzed for uncertainty by the methods of Kline and McClintock [12]. Both the Nusselt and Reynolds numbers had uncertainties 1.5 percent of full scale. This means that for the majority of the data the uncertainty was 3-5 percent. At the very low end, where the instruments were being used at only a few percent of full scale, the uncertainty could be as high as 15 percent. It should be noted that this method only deals with random errors and not with bias errors, such as produced by heat losses. This was corrected by the calibration described above. Because the hot wire was not calibrated, the uncertainty in the turbulence intensity is on the order of 10 percent. This is due primarily to uncertainty in n, the slope of the hot wire heat transfer equation. Experience with calibrating hot wires suggests n could vary 10 percent. Also, because the derivation of equation (3) assumed small levels of fluctuation in the velocity, while in some cases the experiment showed very high levels, the absolute level of turbulence intensity could be significantly in error. This contribution to the uncertainty cannot really be estimated. However, the important thing is not the absolute level but the comparison of turbulence intensity between various cases. These comparisons should be valid even at high levels of turbulence intensity. The probe was lined up with the heated cylinder axis by eye, and the probe position is estimated to be accurate within ±0.3 mm.

Results

Heat Transfer. The experiment was conducted over a Reynolds number range from 5000 to 125,000. The fluid temperature ranged from 260 to 290 K, and the surface to fluid temperature difference from about 20 to 40 K. The system pressure ranged from 100 to 600 kPa. In general, the higher flow rates resulted in higher pressures and vice versa; however, the back pressure was frequently and randomly varied to insure that there was no systematic pressure effect. This was important because changing pressure at a given Re really meant changing velocity.

Two reference cases are presented in Figs. 3 and 4. The data of Fig. 3 were taken with only the heated cylinder in the channel, while Fig. 4 is for data with a single row containing the heated cylinder. The latter case is referred to as a one-row array. In both cases the data plotted were taken on three separate days, spanning time from the beginning of the total experiment to the end. The results show good repeatability.

The first observation is that the two cases are not much different, especially at the lower Reynolds numbers. The one-row case is above the heater-only case by 7 percent at Re = 10^4 and 15 percent at Re = 10^5. The ratio of the two maximum velocities based on flow blockage for these cases is 1.55. It is clear that the small difference is not a direct result of flow blockage, and for this data the maximum velocity is not the correct choice for computing Reynolds number. The data of Fig. 4 will be the base reference for all the rest of the data.

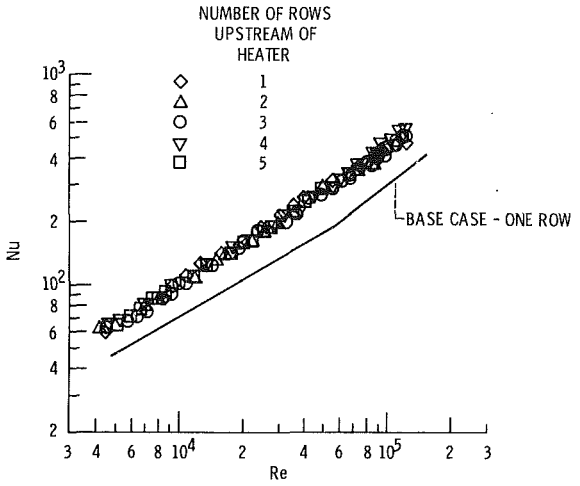

Fig. 5 Heat transfer in two to six row arrays with in-line pattern

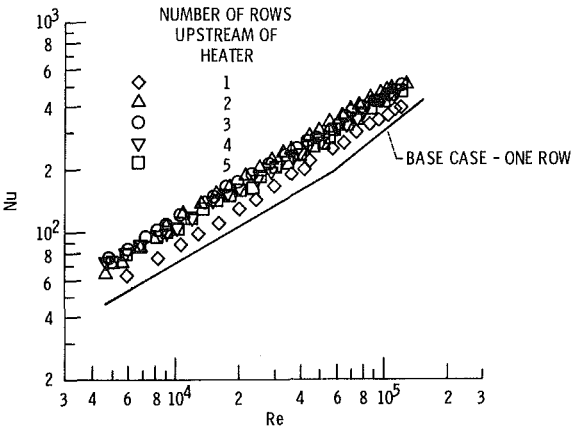

Fig. 6 Heat transfer in two to six row arrays with staggered pattern

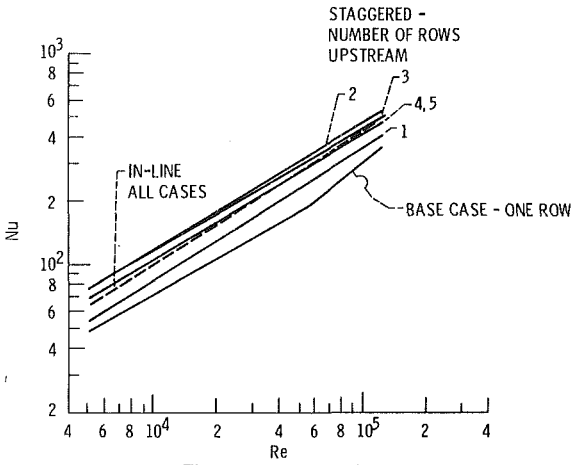

Fig. 7 Summary of data

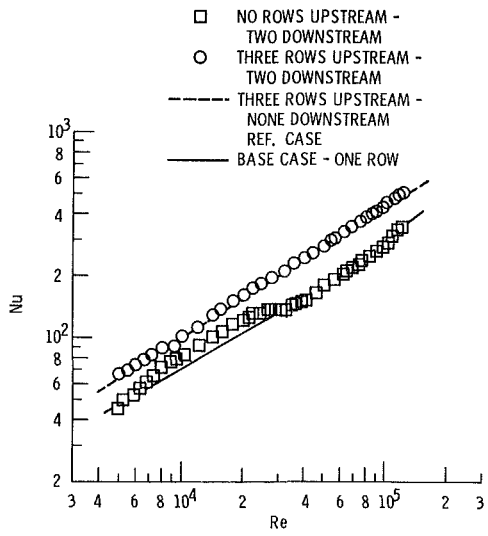

Fig. 8 Effect of adding two rows downstream-in-line pattern

Although the heavy cylinder wall yielded an approximately isothermal surface, there was a small circumferential temperature gradient (2 to 4 K). This pattern varied over the Reynolds number range. At high Re the temperature increased from its lowest value at the stagnation point to about the 90 deg point, then decreased to a value at 180 deg, which was near the stagnation value. At low Re the increase in temperature continued well past the 90 deg point with highest value frequently being at the rear of the cylinder. Usually slope changes in the data were accompanied by changes in the circumferential temperature pattern.

Heat transfer data obtained from two- to six-row arrays are presented in Fig. 5 for the in-line pattern and in Fig. 6 for the staggered pattern. The row containing the heater pin is always the last row. A mean line from the one-row data of Fig. 4 is included for reference and is labeled base case. Three results stand out distinctly in these data. First, the addition of cylinders upstream of the heated cylinder in either pattern significantly increases heat transfer. Second, for the in-line arrays the number of upstream rows has little or no effect on the heat transfer level, whereas for the staggered arrays the heat transfer level is definitely affected by the number of upstream rows. Finally, the rather strong knee that exists in the one-row base case does not appear in the multiple row data. Slight slope changes do occur but nothing as strong or consistent as the reference case.

In order to facilitate comparison, mean lines of all the data, without symbols, are plotted together on Fig. 7. In producing Fig. 7, each array case was plotted separately and a best fit straight line was drawn through the data. The in-line data actually showed slight (3 percent) level differences but no pattern was exhibited. A single line is shown, since these differences were within experimental error. The staggered array data exhibit level differences from row to row. Relative to the one row case, the average increase in heat transfer for two to six-row arrays was 21, 64, 58, 46, and 46 percent, respectively. The in-line results had an average heat transfer increase of 50 percent over the one-row base case. The maximum that occurs for a three-row array in the staggered pattern was seen also by Metzger and coworkers [6, 7]. Level comparisons with Metzger et al., are not appropriate since their data included heat transfer from the endwalls. In addition to level, the staggered arrays show variations in slope of 0.63, 0.62, 0.59, 0.60, and 0.65 for two to six rows, respectively. The in-line data had a fairly constant slope of 0.66.

Since in the present experiment the instrumented row was fixed in the channel and the array pattern was changed for each run, a few tests were performed where two rows of pins were added downstream of the row containing the heater. Two cases were run for each pattern. One was the no upstream row case, making the heater row the first in a three row array. The other was the three rows upstream case, making the heater row fourth in a six row array. The results are shown in Fig. 8 for the in-line pattern and in Fig. 9 for the staggered pattern. On each figure the one-row base case is drawn as a solid line and the three-row upstream / no-rows downstream case is drawn as a dashed line. The first result to observe is that for either pattern, if the row of interest is embedded in an array (i.e., three rows upstream), the addition of rows downstream had no effect on the heat transfer. If, however,

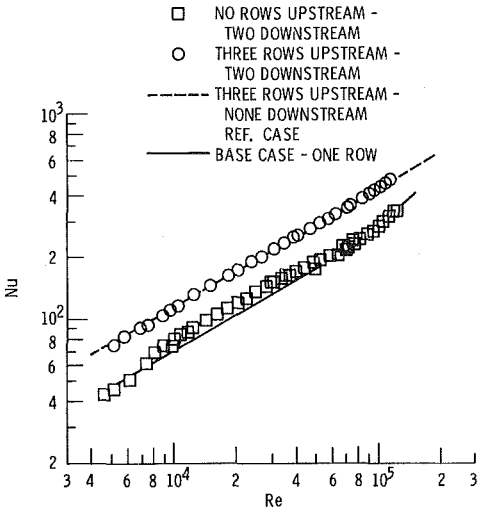

Fig. 9 Effect of adding two rows downstream – staggered pattern

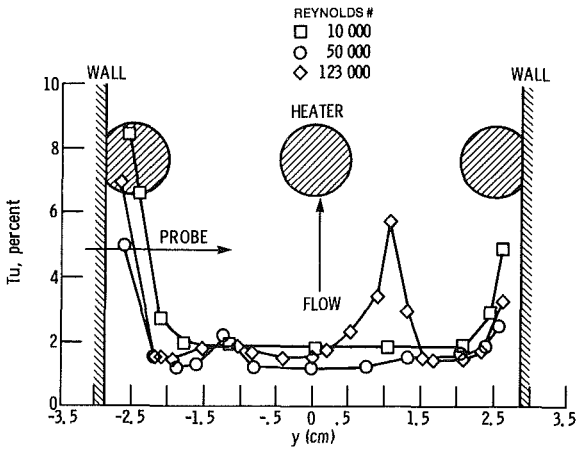

Fig. 10 Turbulence intensity for one row array (no upstream disturbance) at several Reynolds numbers

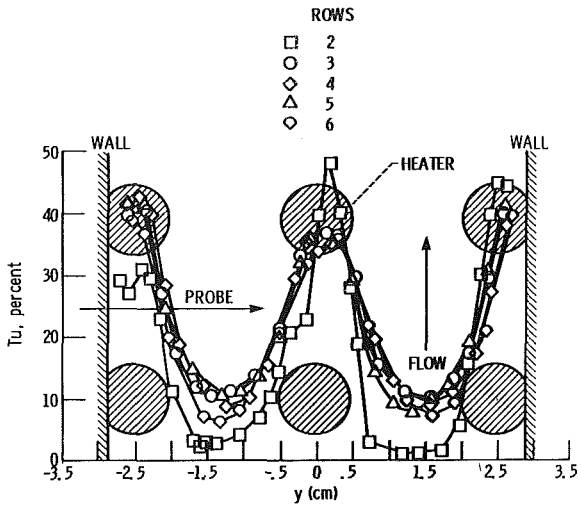

Fig. 11 Turbulence intensity profiles for two to six row arrays with in-line pattern at nominal Re = 50,000

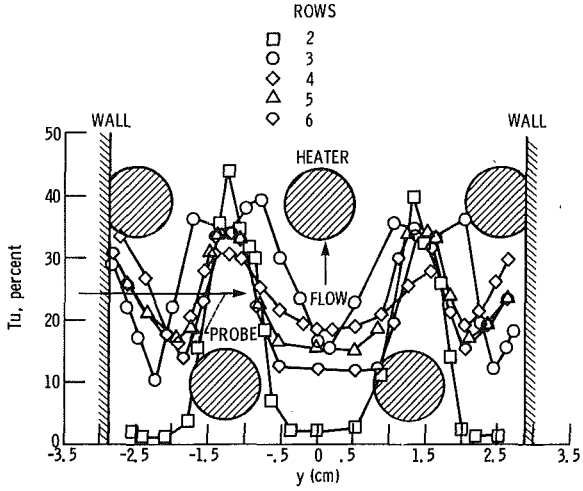

Fig. 12 Turbulence intensity profiles for two to six row arrays with staggered pattern at nominal Re = 50,000

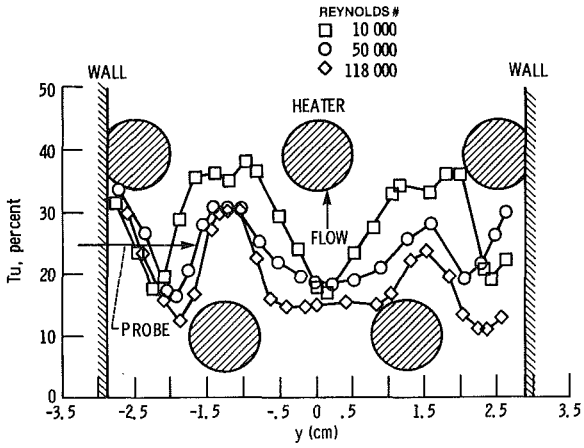

Fig. 13 Turbulence intensity profiles for four row arrays in staggered pattern at several Reynolds numbers

the row of interest is the first row, then as can be seen, there is a difference whether or not there are downstream rows. Additional data points were taken in the regions where deviations form the base occurred. The results appears both real and stable. Variations appeared in the circumferential temperature patterns. Some type of transition seemed to be occurring. It seems reasonable that the downstream pins are affecting the flow around the heated cylinder, possibly affecting separation. What seems strange is that the results are fairly similar for both the in-line and staggered arrays.

Although it is not the focus of the present paper, the tube bank literature was examined to see if the current experiment followed the general trends found in tube arrays. In addition to Zukauskas [1], books by McAdams [13] and Kreith [14] were consulted. Detailed comparisons were sometimes difficult, because it was not always clear how Reynolds numbers were computed or how averages were taken. Nevertheless, the following general statements can be made.

The exponent in the Nusselt number versus Reynolds number plots of about 0.60–0.65 is consistent with tube bank data. The present Nusselt numbers appear to be about 12 percent below those reported by McAdams [13] and about 15 to 20 percent above those reported by Zukaukas [1]. In both the present experiment and the literature, the heat transfer increases more rapidly from row to row with in-line arrays than with staggered arrays. In all cases asymptotic values are reached in about five or six rows. In general, the literature indicates that the first row heat transfer is about 2/3 of the asymptotic value, which is the case herein. Neither McAdams [13] nor Zukauskas [1] report any peaking axially in the heat transfer, as seen herein; however, Kays et. al. [15] do report one such case in a staggered array.

The present single cylinder results are from 15 to 25 percent higher than those reported in Zukauskas [1], McAdams [13], and Kreith [14], particularly at the lower Reynolds numbers. It is believed that this is due to higher free-stream turbulence (2 percent herein versus less than 1 percent in the aforementioned literature) and also because the endwall

boundary layer affected a larger fraction of the heated surface on the short cylinders used herein.

It should be noted that McAdams [13] reports data based on both the entire array being heated and on single tubes being heated. No differences were noted. Also, many correlations in the literature use a film temperature reference. In the present experiment the difference between the use of film or bulk temperature is only 2.3 percent in the worst case.

Turbulence. Turbulence intensity profiles were measured for each configuration discussed in the heat transfer results. They were measured at nominal Reynolds numbers of 10,000, 50,000 and 120,000 for each configuration. The heater was not powered during these runs. Since it would be impossible to show all the data, representative samples are shown in Figs. 10 to 13. The array pattern is sketched on the figures as a visual reference. In all cases the probe traverses from left to right across the figure.

The first case, Fig. 10, is the one-row base case at the three Reynolds numbers. In general, the turbulence intensity over two-thirds of the channel approaching the first row is about 2 percent. The data of Fig. 10 was repeated several times. The spike in the Re = 120,000 case repeats and appears to occur as the thickest part of the hot-wire probe passes in front of the center cylinder, as it moves from left to right. This is probably the probe body wake interacting with the heated cylinder. The small turbulence increases on the left are also repeatable and are probably not a probe influence, but this cannot be said for sure, since the thick part of the probe is already in the channel at this point.

Figure 11 are intensity profiles at Re = 50,000 for the two to six-row arrays in the in-line pattern. The heat transfer result, which showed no influence of adding rows upstream, is very consistent with the turbulence intensity profiles. Only the two-row array (one row upstream) shows any difference. It shows a higher peak in the cylinder wake and lower intensity between the cylinders. Apparently, a fully developed flow condition has not yet been reached. The average intensity may well be equivalent to the fully developed (three rows and greater) value. The fact that the one row upstream, in-line heat transfer values are the same as the rest could be fortuitous. Obviously, though, by two rows upstream for the in-line case the flow is fully developed and a channel between the cylinders is formed.

Figure 12 displays the intensity profiles at Re = 50,000 for the two to six-row arrays in the staggered array. Again, the turbulence intensity profiles, which exhibit a maximum in intensity in the range of two to three rows upstream of the heated cylinder, are consistent with the heat transfer results. Since the staggered array is an alternating pattern, the profiles are more complex, but in general the row immediately upstream of the heated row has a major influence. Since the profile shape is changing, the row causing maximum average intensity is not clear, but it is either the second or third upstream. After three rows, the intensity clearly decreased as did the heat transfer. The heat transfer appears to level off but the intensity is still decreasing, with five rows upstream. Metzger's results [6–7] suggest a leveling off by five rows.

An overlay of Figs. 11 and 12 shows that, although the profile shapes are quite different, the average turbulence intensity for both cases is similar at about 25 percent. Similarly, the average increase in heat transfer for either pattern is about 50 percent. One would suspect that these numbers would change as the spacing is changed.

Finally, to examine the effect of Reynolds number the intensity profiles for three Reynolds numbers are shown in Fig. 13 for the four row staggered array. The average turbulence intensity decreases with increasing Reynolds number. The profiles also tend to flatten out more in front of the heated cylinder as the Reynolds number increases. Thus, for the four row array there is less turbulence at high Re than at low Re. This may explain the tendency of the heat transfer to increase more slowly with Re in the four row array than in the one row base case, where there is little effect of Re on turbulence level.

In general, it would appear that the heat transfer results are very consistent with and explainable in terms of the turbulence intensity profiles.

At the very end of the experiment a few turbulence surveys were made with the probe parallel to the heated cylinder at the same axial location as all the other surveys. Unfortunately, at this point the probe which had survived the entire experiment broke and a new probe had to be used. Three configurations were tested: the one-row base case, four rows staggered, and four rows in-line. The same Reynolds numbers as above were run. In all cases, the turbulence profiles were flat over the center 80 percent of the channel, with turbulence increasing at the wall boundary layers. In all cases, the intensities were about 25 percent higher than at the same flow conditions with the probe normal to the heater axis. This is outside the measurement uncertainty. In the parallel orientation the probe pin wakes were in the plane of the measurement and in our opinion were interacting with the heater cylinder, which was less than one-cylinder dia away. This could explain the higher turbulence levels.

Summary and Conclusions

1 There was very little difference in the heat transfer levels for the case with only the heater in the channel and the case with the heater and two dummy pins across the channel, despite a 55 percent difference in open area. This suggests that average channel velocity is a more appropriate reference than maximum velocity.

2 The base reference case for all configurations was one row that contained the heater and two dummy pins. This base case followed the general trend of the data in the literature for heat transfer to a cylinder in crossflow at about a 25 percent higher level.

3 Addition of cylinders upstream in an in-line array pattern, one to five rows, produced an average of about 50 percent increase in heat transfer level above the base case. The number of upstream rows had little or no influence.

4 The turbulence intensity profiles for the in-line arrays were virtually identical for the cases of two to five upstream rows. The intensity varied from a peak of about 46 percent in the wake (i.e., channel centerline) to an average of about 10 percent between the cylinders. The one row upstream case was somewhat different, exhibiting a higher peak and lower midchannel value.

5 Addition of cylinders upstream in a staggered array pattern produced average increases in heat transfer of 21, 64, 58, 46, and 46 percent above the base case for one to five rows, respectively.

6 The turbulence intensity profiles for the staggered arrays were different for each case, one to five rows. In general, the average intensity first increased then decreased with the addition of upstream rows of cylinders. This behavior of the turbulence intensity is reflected in the heat transfer results.

7 The addition of cylinders downstream of the heater row in either array pattern had no affect on the heat transfer results due to upstream rows. It had some influence on the base case.

8 While the specific heat transfer results are only applicable to the short pin cases commonly found in turbine blades, the observations on the turbulent wake profiles and their influence on heat transfer should be applicable to broader cases of tube banks.

References

1 Zukauskas, A., "Heat Transfer From Tubes in Crossflow," *Advances in Heat Transfer*, Vol. 8, edited by J. P. Hartnett and T. F. Irvine, Jr., Academic Press, 1972, pp. 93–160.

2 Brown, A., Mandjikas, B., and Mudyiwa, J. M., "Blade Trailing Edge Heat Transfer," ASME Paper No. 80-GT-45, Mar. 1980.

3 VanFossen, G. J., "Heat Transfer Coefficients for Staggered Arrays of Short Pin Fins," ASME Paper NO. 81-GT-75, Mar. 1981.

4 Kays, W. M., and London, A. L., *Compact Heat Exchangers*, National Press, Palo Alto, Calif., 1955.

5 Theoclitus, G., "Heat Transfer and Flow Friction Characteristics of Nine Pin-Fin Surfaces," ASME JOURNAL OF HEAT TRANSFER, Vol. 88, No. 4, Nov. 1966, pp. 385–390.

6 Metzger, D. E., Berry, R. A., and Bronson, J. P., "Developing Heat Transfer in Rectangular Ducts With Arrays of Short Pin Fins," ASME Paper No. 81-WA/HT-6.

7 Metzger, D. E., and Haley, S. W., "Heat Transfer and Flow Visualization for Arrays of Short Pin Fins," ASME Paper No. 82-GT-138, presented at the 1982 ASME Gas Turbine Conference, London.

8 Miller, R. L., "ESCORT: A Data Acquisition and Display System to Support Research Testing," NASA TM-78909, May 1978.

9 Hilsenrath, J., et al., "Tables of Thermal Properties of Gases," NBS Circular 564, Nov. 1955.

10 "Hot Wire and Hot Film Measurements and Applications," Thermal Systems, Inc., Technical Bulletin No. 4, p. 35.

11 Bearman, P. W., "Corrections for the Effects of Ambient Temperature Drift on Hot Wire Measurements in Incompressible Flow," *DISA Information Bulletin* No. 11, May 1971, p. 26.

12 Kline, S. J., and McClintock, F. A., "Describing Uncertainties in Single-Sample Experiments," *Mechanical Engineering*, Jan. 1953.

13 McAdams, W. H., *Heat Transmission*, McGraw-Hill Book Company, Inc., New York, 1954.

14 Kreith, F., *Principles of Heat Transfer*, 2nd ed., International Textbook Company, Scranton, Pa., 1966.

15 Kays, W. M., London, A. L., and Lo, R. K., "Heat Transfer and Friction Characteristics for Gas Flow Normal to Tube Banks—Use of a Transient-Test Technique," *ASME Transactions*, Vol. 76, 1954, pp. 387–396.

Finite Difference Analysis of Laminar Separated Forced Convection in Cavities

A. Bhatti
Research Assistant,
Mechanical Engineering Department,
Howard University,
Washington, D.C.

W. Aung
Director,
Heat Transfer Program,
National Science Foundation
and Adjunct Professor,
Mechanical Engineering Department,
Howard University,
Washington, D.C. 20059
Fellow ASME

Results are presented for a comprehensive numerical analysis of the two-dimensional heat transfer in cavities of rectangular profiles. The walls of the cavity are held at a uniform temperature and calculations are carried out at various aspect ratios and Reynolds numbers in laminar flow. The numerical technique is based on a hybrid upwind/central differencing of the governing differential equations that are first integrated over control volumes surrounding the node points in a rectilineal, nonuniform grid system. Results indicate that while the average Nusselt number in the cavity is related to the Reynolds number raised to a power, the latter depends on the aspect ratio and varies between the cavity floor and the side walls. The influence of the upstream boundary layer thickness is found to be negligible. The numerical results are found to be well represented by the following equation:

$$\overline{\mathrm{Nu}}_t = 0.0345\,(\mathrm{Re}_s)^{0.46}(w/s)^{-0.142}$$

Introduction

The fluid flow and heat transfer in cavities is an important topic in contemporary heat transfer research. In addition to its common occurrence in engineering applications, this flow configuration has relatively well defined end points for the separated shear layer. Hence, many of the inherent characteristics of separated forced convection can be investigated conveniently. In a recent paper, Aung [1] has presented experimental data on the temperature distributions and heat transfer coefficients for laminar flow past two-dimensional rectangular cavities where the walls are kept at a constant temperature. A schematic diagram of the convective heat transfer situation is shown in Fig. 1. The experimental data show that the thermal conditions of the flow outside the cavity are little affected by the presence of the cavity. This may signify the insensitivity of the flow inside the cavity to the detail of the flow outside though, obviously, the magnitude of the velocity is an influencing parameter. In this circumstance, the heat transfer in the cavity becomes a function only of the geometry and the velocity of the approaching flow, but is independent of the approaching flow boundary layer thickness. Indeed, the data in [1] suggests a 1/2-power dependency of the average cavity floor Nusselt number on the Reynolds number, with the aspect ratio having a strong influence. However, the available data are insufficient to allow firm conclusions to be drawn. It is the purpose of the present paper to report on the results of a follow-up, theoretical examination of the class of problems, represented in Fig. 1, that is sometimes known as open cavity flow where the shear layer reattaches on the downstream wall of the cavity. It is known from the work of Nicoll [2], Sinha et al. [3], and Yamamoto et al. [4] that this flow situation prevails up to $w/s \approx 7$ or 8. Beyond this value, shear layer reattachment occurs on the cavity floor. The latter situation is not investigated in the present study.

Numerical calculation techniques, developed by Gosman et al. [5] and widely applied to a number of problems in turbulent flow, are adapted in the present study. These methods are systematically applied to the problem depicted in Fig. 1 with an upstream plate (not shown completely) of fixed length such that by specifying different free-stream velocities, the approach flow boundary layer thickness can be altered. The heat transfer inside the cavity can then be studied as a function of the free-stream velocity and boundary layer thickness. Though numerical methods capable of dealing with separated forced convection problems have been available for many years, only in a few previous instances have these numerical techniques been subjected to rigorous validation by comparing with experimental data. Recent computations by Gooray [6] and Gooray et al. [7, 8] have shown that these methods can be applied to give reasonably accurate quantitative heat transfer results for separated forced convection in the turbulent flow past a backstep. The problem examined by Gooray et al. involves the need to properly account for the turbulent motion and for streamline curvature. In addition, a two-pass procedure, the second pass instituted after the reattachment location is identified, is found necessary to yield acceptable results. These complications are avoided in the cavity problem.

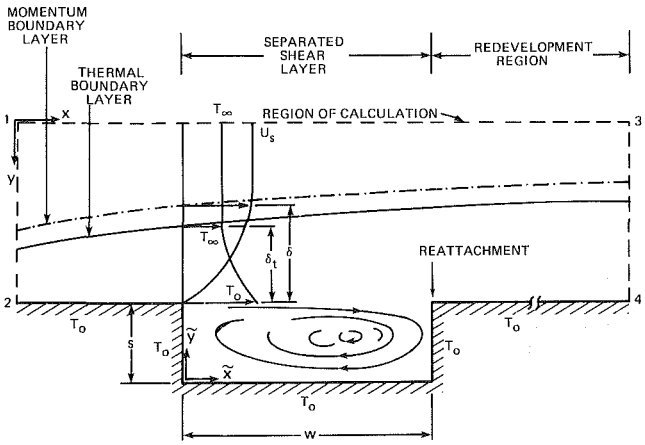

Fig. 1 Schematic diagram of the two-dimensional cavity

Theoretical Method

Governing Equations. The differential equations describing the velocity and temperature fields in the constant-property, two-dimensional flow past a heated cavity, as shown in Fig. 1, are

Contributed by the Heat Transfer Division for publication in the JOURNAL OF HEAT TRANSFER, Manuscript received by the Heat Transfer Division February 3, 1983.

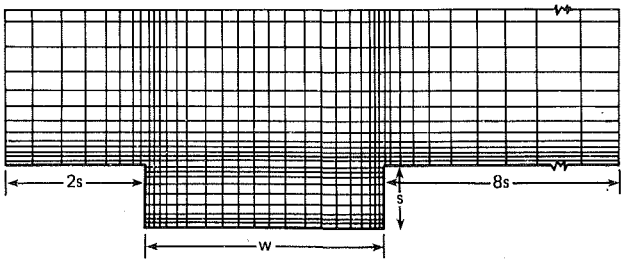

Fig. 2 Typical grid distribution for finite difference solution

$$\frac{\partial u}{\partial x}+\frac{\partial u}{\partial y}=0 \qquad \text{(continuity)} \qquad (1)$$

$$\rho\left(u\frac{\partial u}{\partial x}+v\frac{\partial u}{\partial y}\right)=\mu\left(\frac{\partial^2 u}{\partial x^2}+\frac{\partial^2 u}{\partial y^2}\right)-\frac{\partial p}{\partial x}$$
(x-momentum) (2)

$$\rho\left(u\frac{\partial v}{\partial x}+v\frac{\partial v}{\partial y}\right)=\mu\left(\frac{\partial^2 v}{\partial x^2}+\frac{\partial^2 v}{\partial y^2}\right)-\frac{\partial p}{\partial y}$$
(y-momentum) (3)

$$\rho c_p\left(u\frac{\partial T}{\partial x}+v\frac{\partial T}{\partial y}\right)=k\left(\frac{\partial^2 T}{\partial x^2}+\frac{\partial^2 T}{\partial y^2}\right)$$
(energy) (4)

In each of equations (2–4), the terms on the left side are the convection terms, while the first group of terms on the right side constitute the diffusion terms. The pressure gradient terms in equations (2) and (3) are the so-called "source" terms.

Boundary Conditions. In the present study, the solution to equations (1–4) is sought within the region bounded by the solid walls and the broken lines indicated in Fig. 1. The following boundary conditions are specified.

(*i*) On all solid boundaries

$$u=0;\ v=0;\ T=T_w \qquad (5)$$

(*ii*) On plane 1–2

$$p_o=0;\ v=0$$
$$u=u(y) \text{ specified} \qquad (6)$$
$$T=T(y) \text{ specified}$$

The velocity distribution $u(y)$ and temperature distribution $T(y)$ are specified by choosing U_s, T_∞, and T_w and using results from laminar boundary theory for a flat plate at zero incidence. The upstream wall is assumed to have an unheated starting length of 15 cm, following a heated length of 30.5 cm that is maintained at the temperature T_w.

(*iii*) On plane 1–3

$$\frac{\partial u}{\partial y}=0;\ \frac{\partial v}{\partial y}=0;\ \frac{\partial T}{\partial y}=0 \qquad (7)$$

(*iv*) On plane 3–4

$$\frac{\partial u}{\partial x}=0;\ \frac{\partial v}{\partial x}=0;\ \frac{\partial T}{\partial x}=0 \qquad (8)$$

Finite Difference Method. To effect the solution of the foregoing system of equations, the region of interest is overlaid with a rectilineal grid system of unequal spacing. In this approach, nodes are more closely spaced in the vicinity of solid boundaries and in the shear layer where steeper gradients of the dependent variables are expected. A typical grid system is shown in Fig. 2.

The calculations are started at a distance of two cavity depths upstream of the cavity. Downstream of the cavity the grids are extended a distance of eight cavity depths. The calculation domain in the y-direction is extended to a distance sufficient to make sure that for the smallest value of the Reynolds number the plane 1–3 in Fig. 1 lies well outside of the boundary layer specified on plane 1–2. In the present study locating plane 1–3 at a distance of 2.5 times the cavity depth above the cavity has been found to be sufficient since having a larger distance does not materially affect the solutions.

The numerical procedure used is based on the iterative scheme outlined by Gosman [5]. This procedure used the

Nomenclature

c_p = specific heat
d = characteristic length
h = heat transfer coefficient: $-\frac{k}{(T_w-T_\infty)}\left(\frac{\partial T}{\partial n}\right)_0$
$\bar{h}$ = average heat transfer coefficient; see equation (12)
$\bar{h}_t$ = average heat transfer coefficient based on w
k = thermal conductivity
n = coordinate normal to wall
$\underline{\mathrm{Nu}}$ = Nusselt number; hs/k
$\overline{\mathrm{Nu}}$ = average Nusselt number; $\bar{h}s/k$
$\overline{\mathrm{Nu}}_t$ = average Nusselt number based on w; $\bar{h}_t s/k$
p = static pressure
p_o = reference pressure on plane 1-2, Fig. 1
Pr = Prandtl number
Q = total heat transfer from cavity
Re = Reynolds number; $U_s d/\nu$
s = depth of cavity
$\overline{\mathrm{St}}$ = average Stanton number; $\overline{\mathrm{Nu}}/\mathrm{Pr\ Re}$
T = temperature
T_∞ = free-stream temperature
u,v = velocity components in x- and y-direction, resp.
U_s = free-stream velocity
w = length of cavity
x,y / $\tilde{x},\tilde{y}$ = coordinates defined in Fig. 1
ν = kinematic viscosity
μ = dynamic viscosity
ξ = distance defined in Fig. 7

Subscripts

b = value on cavity base or floor
c = value averaged over all three walls of cavity
o = value at wall
s = parameter based on cavity depth
t = parameter defined with $\bar{h}_t$; see equation (14)
v = value on side wall
$v,1$ = value on upstream side wall
$v,2$ = value on downstream side wall
w = parameter based on length of cavity

Greek Letter

ρ = density
δ = boundary layer thickness just upstream of cavity

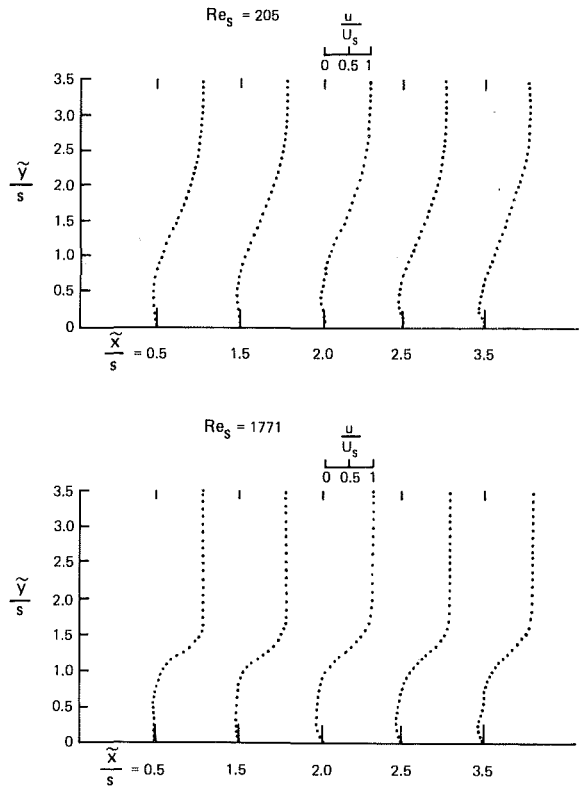

Fig. 3 Velocity distributions at various axial locations for $w/s = 4$

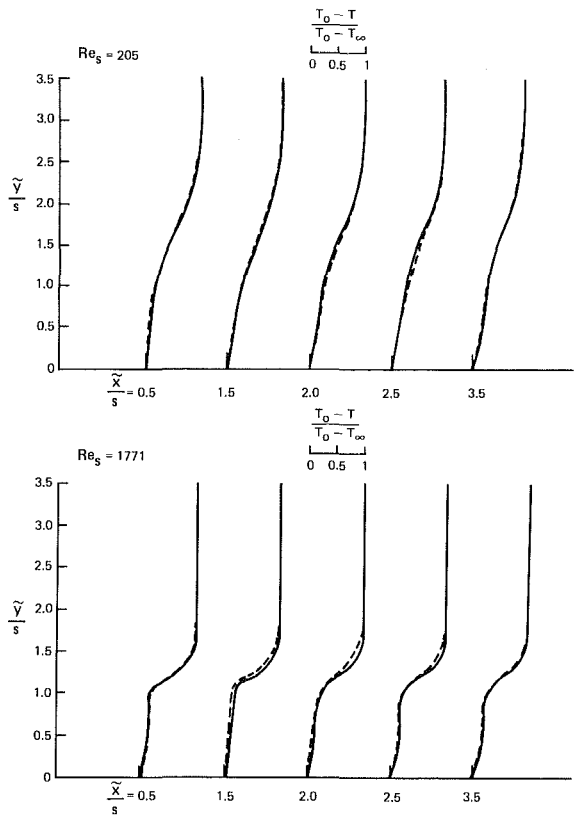

Fig. 4 Temperature distributions in the cavity ($w/s = 4$; solid line: present calculations; broken line: experiments from [1])

hybrid central/upwind difference scheme for the convective terms with central differences for the diffusion terms. For the convective terms, upwind differencing is used if the grid Peclet number in a given direction is greater than 2. When the grid Peclet number is less than 2 central differences are employed. Gosman's procedure incorporates the SIMPLE solution technique initiated by Patankar and Spalding [9]. This technique is based on the solution of difference equations obtained by integrating the differential equations for momentum and energy over control volumes enclosing the nodal points. The solution of the set of difference equations over the entire region of interest is obtained by evaluating new values for any desired variable by taking into account the latest known estimated value of the variable on neighboring nodes. One iteration of the solution is completed when, in a line-by-line technique, all the lines in a chosen direction have been accounted for.

In the present study calculations are performed for $w/s = 4$, 2, and 1. By first assuming a pressure distribution within the calculation domain, the set of difference equations for the x- and y-momentum and energy equations is solved by line iteration. After a sweep of the solution domain is completed, adjustments are then made to the pressure field so that the continuity equation is satisfied. The procedure is repeated until the continuity, momentum, and energy equations are simultaneously satisfied. The convergence criterion used is that the percentage change of a variable at any node should be less than 0.1 percent. The majority of the computation is performed using a 40 × 33 nonuniform grid system. (Nodes inside the upstream and downstream walls do not enter into the computation and are not shown in Fig. 2.) Convergence is typically achieved after about 200 iterations with a central processor time of 3 min on the IBM 3033 computer. To validate the numerical approach utilized in the present study, initial calculations are performed for the laminar heat transfer over a flat plate. The results are in good agreement with existing solutions. The present numerical approach has also been coupled with a turbulence model and applied to flow

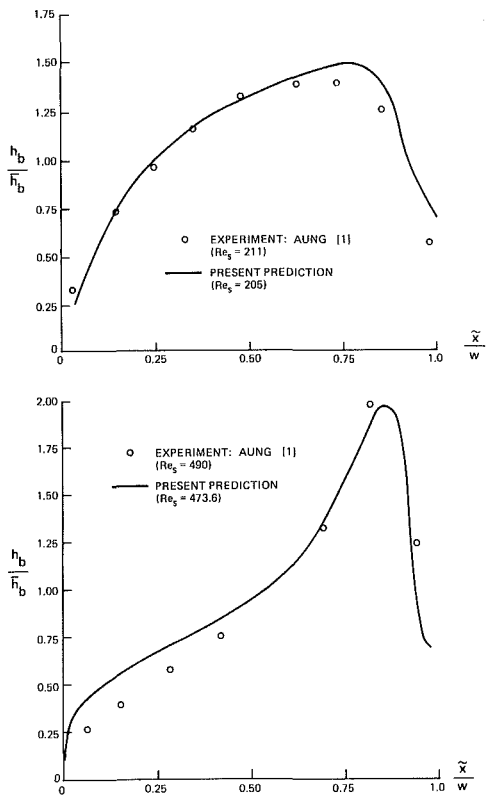

Fig. 5 Normalized local heat transfer coefficient on cavity floor

in a heated cavity, producing results that agree reasonably well with existing data [10].

Results

Representative computed results for the flow field are indicated using the case of $w/s = 4$ at two Reynolds numbers. Nondimensional velocity profiles at various axial locations along the cavity are shown in Fig. 3. For the two Reynolds numbers shown, the recirculating flow is seen to extend practically along the entire cavity, with the maximum reverse flow velocity equal to roughly 15 percent of the free-stream value. Near the downstream wall, fluid flow occurs essentially parallel to the vertical wall at the midheight of the cavity, giving rise to a region where the axial velocity component is nearly zero. Similar characteristics are observed in the velocity profiles near the upstream wall though the effect is not as pronounced owing to the differences in the nearby flows. Additional results relating to the flow problem may be found in [11]. It may be inferred from Fig. 3 (especially the lower figure) that below the horizontal line joining the two corners of the cavity (that is, the line $\tilde{y}/s = 1$), the velocity is completely negative when $\tilde{x}/s \approx 2$. This phenomenon arises because, in the relatively low Reynolds number flow dealt with here, the comparatively high vorticity in the cavity causes streamlines to bulge slightly out towards the main flow. Among others, Jacobs and Sutton [12] have observed this.

Typical temperature distributions are given in Fig. 4. The relevant experimental data from [1], obtained by the Mach-Zehnder interferometer, are also indicated for comparison. Good agreement is shown, in spite of the fact that in the theoretical study the transverse velocity component has been arbitrarily set equal to zero in specifying the boundary conditions on the plane 1-2. The self-similarity of the computed temperature profiles for $\tilde{y}/s \geq 1$, approximately, is evident. The same conclusion can be drawn for the velocity profiles of Fig. 3. The present study thus reaffirms the observation made in [1] that the external flow appears to skim past the cavity without a strong interaction with the flow inside, except near the reattachment zone. In such a case the details of the approaching flow, its boundary layer thickness in particular, are immaterial in describing the heat transfer inside the cavity.

Local heat transfer coefficients on the cavity floor are normalized by the respective average values and plotted against axial distance along the cavity in Fig. 5 for $w/s = 4$. The experimental data from [1] are also plotted for comparison. Again, the agreement is encouraging. Close to the upstream wall, the heat transfer is seen to be nearly zero while the heat transfer near the downstream wall is significantly higher. The maximum local heat transfer occurs near the downstream wall. The average Nusselt number on the cavity floor is plotted against the Reynolds number for all three values of w/s in Fig. 6. The influence of the parameter w/s can be noted distinctly with the larger aspect ratio giving the higher heat transfer. The experimental measurements reported in [1] are indicated by the broken line. Here, the discrepancy is relatively larger being on the average of the order ± 10 percent, which is roughly in the range of the experimental error band. The theoretical results are represented by the following equations

$$\overline{\mathrm{Nu}}_b = c(\mathrm{Re}_s)^{0.46} \tag{9}$$

where

$$c = 0.01428 \text{ for } w/s = 4$$

$$c = 0.01074 \text{ for } w/s = 2$$

and

$$c = 0.00522 \text{ for } w/s = 1$$

No comparison of the present calculations with the data in [4] is possible because of the large differences in the boundary condition. However, it is noted that the present theoretical

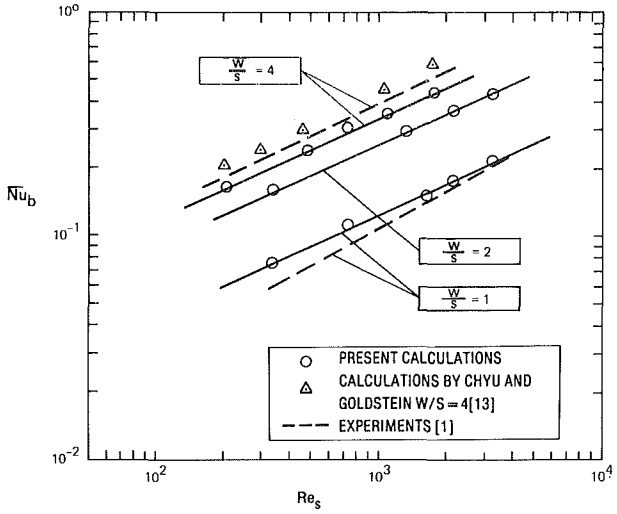

Fig. 6 Average Nusselt number on cavity floor

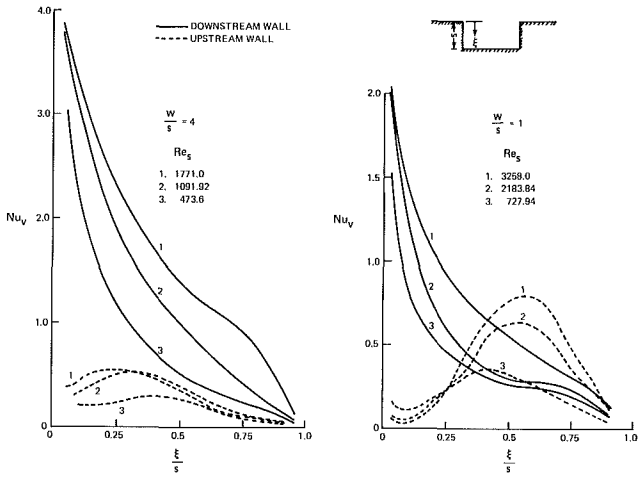

Fig. 7 Local Nusselt number on the side walls

results and the experimental data in [1] all show a decrease in the average heat transfer on the cavity floor as the aspect ratio w/s decreases. This is at variance with the experimental findings of Yamamoto et al. [4] who recommend a single correlation for cavities which is of the form: $\overline{\mathrm{Nu}}_w = 0.427\ \mathrm{Re}_w{}^{1/3}$, which when written in terms of $\overline{\mathrm{Nu}}_b$ and Re_s becomes

$$\overline{\mathrm{Nu}}_b = 0.427(\mathrm{Re}_s)^{1/3}(w/s)^{-2/3} \tag{10}$$

Equation (10) suggests that the average floor Nusselt number decreases as the aspect ratio increases. The cavities in [4] have heating on the floor, but the side walls are insulated and the upstream plate is unheated; in the present study and in [1], the walls are everywhere heated to the same temperature, and there is significant upstream heating. It is precisely this difference in the upstream thermal conditions in the two situations that lead to the opposing effects of w/s on the average heat transfer from the cavity floor. For, the correlation of equation (10) is equivalent to one for a heated, short flat plate; as the plate length increases, the average heat transfer is reduced, when other conditions remain unchanged. On the other hand, when a heated upstream plate is present, the cavity becomes more and more akin to an insulated gap as w decreases, and the heat transfer from the cavity floor diminishes.

The triangular points in Fig. 6 represent recent numerical computation by Chyu and Goldstein [13] on a similar problem. Their results exhibit both similarities and dif-

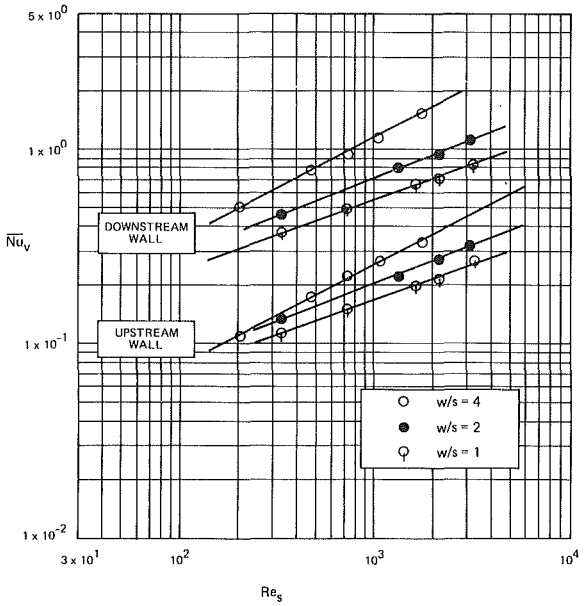

Fig. 8 Average Nusselt number on the side walls

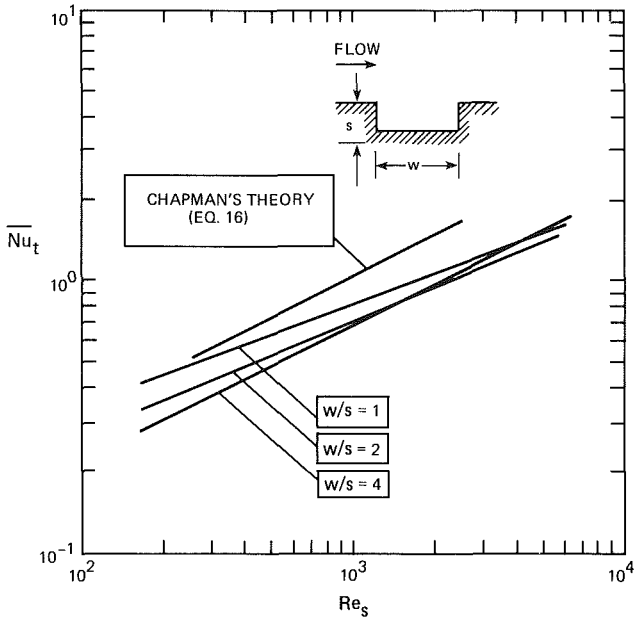

Fig. 9 Overall average Nusselt number and comparison with Chapman's theory

ferences with those reported herein. Based on the SIMPLER algorithm of Patankar ([9] p. 131-134), the Chyu and Goldstein results for $\overline{Nu}_b$ at $w/s = 4$ show approximately a 1/2-power dependency on Re_s, but their predictions lie above the experimental curve indicated in Fig. 6.

The local Nusselt number variations on the side walls for the present study are given in Fig. 7 for $w/s = 4$ and 1. The Nusselt number on the downstream wall is seen to be much larger than that on the upstream wall. Further, the peak value on the downstream wall is located at the upper corner, whereas on the upstream wall the maximum heat transfer occurs away from corner regions. The large heat transfer on the downstream wall is associated with the submerged jetlike heat transfer in the reattachment process, while on the upstream wall the heat transfer is governed by the cellular motion in the cavity. The present results are represented by the following equations and are graphically displayed in Fig. 8.

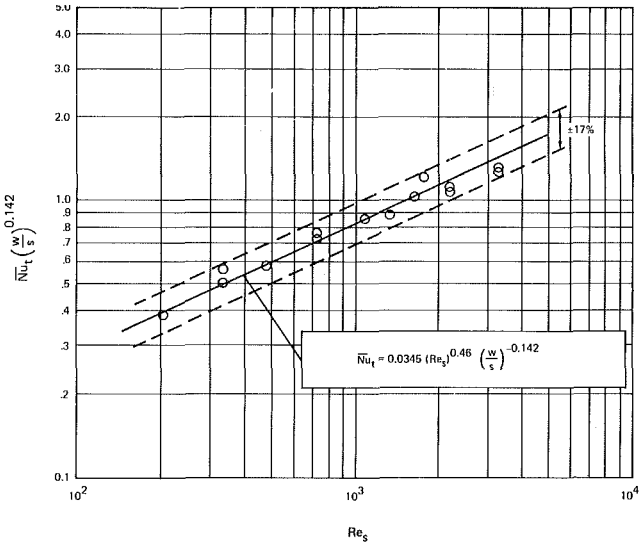

Fig. 10 Single correlation for the computed results

Downstream wall

$$\left.\begin{aligned}\overline{Nu}_{v,2} &= 0.03193\,(Re_s)^{0.52},\ w/s=4\\ \overline{Nu}_{v,2} &= 0.0486\,(Re_s)^{0.39},\ w/s=2\\ \overline{Nu}_{v,2} &= 0.0455\,(Re_s)^{0.36},\ w/s=1\end{aligned}\right\} \quad (11a)$$

Upstream wall

$$\left.\begin{aligned}\overline{Nu}_{v,1} &= 0.00693\,(Re_s)^{0.52},\ w/s=4\\ \overline{Nu}_{v,1} &= 0.01388\,(Re_s)^{0.39},\ w/s=2\\ \overline{Nu}_{v,1} &= 0.01414\,(Re_s)^{0.36},\ w/s=1\end{aligned}\right\} \quad (11b)$$

The average heat transfer coefficient considering all three walls of the cavity may be evaluated from the equation

$$\bar{h}_c(2s+w) = \int_0^s h_{v,1}\,d\xi + \int_0^s h_{v,2}\,d\xi + \int_0^w h_b\,d\tilde{x}$$

Hence,

$$\bar{h}_c = \frac{1}{2s+w}\left[\bar{h}_{v,1}s + \bar{h}_{v,2}s + \bar{h}_b w\right] \quad (12)$$

Using this relation, the average Nusselt number $\overline{Nu}_c$ is calculated. The results are

$$\left.\begin{aligned}\overline{Nu}_c &= 0.0152\,(Re_s)^{0.494},\ w/s=4\\ \overline{Nu}_c &= 0.0196\,(Re_s)^{0.42},\ w/s=2\\ \overline{Nu}_c &= 0.0215\,(Re_s)^{0.37},\ w/s=1\end{aligned}\right\} \quad (13)$$

It is more useful, however, to define an overall cavity heat transfer coefficient, $\bar{h}_t$, such that the total heat transfer from the cavity can be calculated as

$$\bar{h}_t w(T_w - T_\infty) = Q = \bar{h}_c(2s+w)(T_w - T_\infty)$$

Therefore

$$\bar{h}_t = \bar{h}_c\left(\frac{2s+w}{w}\right) \quad (14)$$

Combining equations (13) and (14) results in

$$\left.\begin{aligned}\overline{Nu}_t &= 0.0228\,(Re_s)^{0.494},\ w/s=4\\ \overline{Nu}_t &= 0.0392\,(Re_s)^{0.42},\ w/s=2\\ \overline{Nu}_t &= 0.0645\,(Re_s)^{0.372},\ w/s=1\end{aligned}\right\} \quad (15)$$

Comparisons of equations (9), (11), and (15) and of Figs. 6 and 8 lead to some interesting insight into transport phenomena in cavities. When $w/s = 1$, the heat transfer is dominated by the heat removal associated with the reattachment of the shear layer on the downstream wall. This is reflected in the nearly identical dependence of $\overline{Nu}_t$ on Re_s and $\overline{Nu}_{v,2}$ on Re_s. In this case, available flow visualization studies indicate that the recirculation in the cavity consists of a single laminar eddy. For $w/s = 2$ and $w/s = 4$, the heat transport due to shear layer reattachment and to the reverse flow on the cavity floor are equally important. Consequently, at these larger aspect ratios, the power in the $\overline{Nu}_t \sim Re_s$ relation is approximately the average of those for $\overline{Nu}_b \sim Re_s$ and $\overline{Nu}_{v,2} \sim Re_s$. In these instances, the eddy in the cavity is elongated with its center displaced towards the downstream wall. Note that the power (0.494) of the Reynolds number for the largest aspect ratio investigated here is very nearly equal to the predictions in a number of theoretical studies dealing with laminar separated forced convection. For cavities where $w/\delta \to \infty$ and $s \to \infty$, Chapman [14] has predicted that $\overline{Nu} \propto Re^{1/2}$. For flow past unconfined bluff bodies, the analyses of Virk [15] and Mitchell [16] also indicate that $\overline{Nu} \propto Re^{1/2}$.

The change in the powers of the Reynolds number as w/s varies from 1 to 4 illustrates the significance of the aspect ratio in the type of flow under investigation. As the ratio increases, the power approaches the 1/2-power relation predicted by Chapman's analysis [14]. However, Chapman's theory, which as shown in [1] is represented by the following equation for the cases under consideration

$$\overline{Nu}_t = 0.0332\,(Re_s)^{1/2} \tag{16}$$

overpredicts the Nusselt number at $w/s = 4$ by approximately 50 percent. A comparison of equation (16) with equations (15) is given in Fig. 9. The present results suggest that the overall heat transfer from cavities is not given by any unique analytical relation. Nevertheless, the power of the Reynolds number varies only about ± 14 percent from the average of values at $w/s = 4$ and $w/s = 1$, and it is therefore decided to obtain an approximate, single correlation for all the results of this study. Since the correlation is intended for the range $1 \le w/s \le 5$, the power of the Reynolds number at the midpoint of $w/s = 3$ is obtained by interpolation. This value turns out to be coincidentally 0.46, the same as for $\overline{Nu}_b$. Following the procedure used in [1] for each cavity, the ratio δ/s, which ranges from 0.66 to 1.95 in the present study, is plotted against the group $X \cdot Re_w^{0.54}$ where

$$X = \overline{St}_t[2(1 + w/s)]^{0.5}$$

This gives a relation of the form

$$X \cdot Re_w^{0.54} = c_2(\delta/s)^r$$

where c_2 and r are dependent on w/s. Again, the value of r at $w/s = 3$ is picked for the regime $1 \le w/s \le 5$, giving $r = 0.015$. The low value of r confirms the suggestion made previously that the heat transfer is rather insensitive to the approaching boundary layer thickness, and hence its influence is neglected in the remaining procedure for deriving the final correlation. Thus after setting $r = 0$, the group $X \cdot Re_w^{0.54}$ is plotted against w/s to obtain c_2. The result, after simplification, is the equation

$$\overline{Nu}_t = 0.0345\,(Re_s)^{0.46}(w/s)^{-0.142} \tag{17}$$

This equation is valid for

$$1 \le w/s \le 5$$

$$150 \le Re_s \le 4000$$

$$0.5 \le \delta/s \le 2$$

Equation (17) is plotted in Fig. 10, where it is compared with all the data obtained in the present numerical solution. It is seen that the equation represents the raw numerical data to within ± 17 percent. Note that the calculations by Chyu and Goldstein [13] lead to values for $\overline{Nu}_t$ that are approximately 15 percent larger than those given by equation (17).

Conclusion

The present study is aimed at providing an understanding of the heat transfer phenomena in a relatively simple class of separated forced convection problem, namely, the forced convection in open cavity flow. The detailed investigation conducted here shows that the downstream wall has the largest influence on the overall heat transfer. The overall heat transfer cannot be given by any simple relation derived from a similarity analysis of the shear layer. The observations made in the present study should not be extended to other separated forced convection situations, such as in the flow over backsteps and flow past bluff bodies where the separated regions is relatively unconfined.

The opinions expressed in this paper are not necessarily those of the National Science Foundation.

References

1 Aung, W., "An Inteferometric Investigation of Separated Forced Convection in Laminar Flow Past Cavities," accepted for publication in ASME JOURNAL OF HEAT TRANSFER, Vol. 105, Aug. 1983, pp. 505–512.

2 Nicoll, K. M., "A Study of Laminar Hypersonic Cavity Flows," *AIAA Journal*, Vol. 26, 1964, pp. 1535–1541.

3 Sinha, S. N., Gupta, A. K., and Oberai, M. M., "Laminar Separating Flow Over Backsteps and Cavities—Part II: Cavities," *AIAA Journal*, Vol. 20, No. 3, 1981, pp. 370–375.

4 Yamamoto, H., Seki, N., and Fukusako, S., "Forced Convection Heat Transfer on Heated Bottom Surface of a Cavity," ASME JOURNAL OF HEAT TRANSFER, Vol. 101, Aug. 1979, pp. 475–479.

5 Gosman, A. D., "The TEACH-T Computer Program Structure, Flow, Heat and Mass Transfer in Turbulent Recirculating Flows—Prediction and Measurement," Lecture Notes from McGill University, Canada, 1976.

6 Gooray, A. M., "Numerical Calculation of Turbulent Recirculating Heat Transfer Beyond Two-Dimensional Backsteps and Sudden Pipe Expansion," Ph.D. thesis, Mechanical Engineering Department, Howard University, May, 1982.

7 Gooray, A. M., Watkins, C. B., and Aung, W., "Numerical Calculations of Turbulent Heat Transfer Downstream of a Rearward-Facing Step," *Proceedings of the 2nd International Conference on Numerical Methods in Laminar and Turbulent Flow*, Venice, Italy, 1981, pp. 639–651.

8 Gooray, A. M., Watkins, C. B., and Aung, W., "k-ϵ Calculations of Heat Transfer in Redeveloping Turbulent Boundary Layers Downstream of Reattachment," presented at AIAA/ASME Thermophysics Conf., St. Louis, Mo., June 6–9, 1982, ASME Paper No. 82-HT-77.

9 Patankar, S. V., *Numerical Heat Transfer and Fluid Flow*, McGraw-Hill, 1980.

10 Gooray, A. M., Watkins, C. B., and Aung, W., "Numerical Calculations of Heat Transfer in Turbulent Recirculating Flow Over an Open Surface Cavity," *Proceedings of ASME/JSME Thermal Engineering Joint Conference*, March 20–24, 1983, Honolulu, Hawaii, Vol. 3, pp. 79–86.

11 Bhatti, A., "Heat Transfer from Open Surface Cavities in Laminar Flow," M.S. thesis, Department of Mechanical Engineering, Howard University, Washington, D.C., May 1982.

12 Jacobs, H. R., and Sutton, S. B., "A Numerical Study of Cavity Flows With and Without Mass Addition," *Heat Transfer 1974, Proceedings of 5th International Heat Transfer Conference*, Tokyo, Japan, 1974, Vol. II, pp. 40–44.

13 Goldstein, R. J., and Chyu, M. K., Department of Mechanical Engineering, University of Minnesota, Personal Communication, December, 1982.

14 Chapman, D. R., "A Theoretical Analysis of Heat Transfer in Regions of Separated Flow," NACA TN 3792, 1956.

15 Virk, P. S., "Heat Transfer from the Rear of a Cylinder in Transverse Flow," ASME JOURNAL OF HEAT TRANSFER, Vol. 92, 1970, pp. 206–207.

16 Mitchell, J. W., "Base Heat Transfer in Two-Dimensional Subsonic Fully Separated Flows," ASME JOURNAL OF HEAT TRANSFER, Vol. 93, 1971, pp. 342–348.

Periodically Converging-Diverging Tubes and Their Turbulent Heat Transfer, Pressure Drop, Fluid Flow, and Enhancement Characteristics

P. Souza Mendes

E. M. Sparrow
Fellow ASME

Department of Mechanical Engineering,
University of Minnesota,
Minneapolis, Minn. 55455

A comprehensive experimental study was performed to determine entrance region and fully developed heat transfer coefficients, pressure distributions and friction factors, and patterns of fluid flow in periodically converging and diverging tubes. The investigated tubes consisted of a succession of alternately converging and diverging conical sections (i.e., modules) placed end to end. Systematic variations were made in the Reynolds number, the taper angle of the converging and diverging modules, and the module aspect ratio. Flow visualizations were performed using the oil-lampblack technique. A performance analysis comparing periodic tubes and conventional straight tubes was made using the experimentally determined heat transfer coefficients and friction factors as input. For equal mass flow rate and equal transfer surface area, there are large enhancements of the heat transfer coefficient for periodic tubes, with accompanying large pressure drops. For equal pumping power and equal transfer surface area, enhancements in the 30–60 percent range were encountered. These findings indicate that periodic converging-diverging tubes possess favorable enhancement characteristics.

Introduction

Ways and means of enhancing turbulent heat transfer in tubes have been vigorously explored in the recent past with a view toward increasing the efficiency of heat exchangers (e.g., [1–3]). In particular, disturbance and mixing promoters constitute a very commonly employed group of enhancement techniques. Invariably, the improvement in heat transfer brought about by such techniques is accompanied by undesired increases in pressure drop. It is, therefore, necessary that performance comparisons between unenhanced and enhanced flow passages take account of both heat transfer and pressure-drop-related impacts [4–6]. The execution of such performance comparisons requires the availability of basic information in the form of Nusselt numbers and friction factors. In view of the highly complex fluid flows induced by enhancement techniques, it is usually necessary to rely on experiment for the determination of the aforementioned basic information.

In the research described in this paper, a many-faceted study of a family of enhanced turbulent tube flows is performed. The tubes to be considered here consist of a succession of converging and diverging sections—in effect, an array of conical sections placed end to end. The resulting periodic enlargement and contraction of the flow cross section can give rise to appreciable transverse motions, and the related fluid mixing should lead to increases in the heat transfer coefficients. In addition, at larger angles of convergence and divergence, the fluid flow is unable to follow the contour of the tube wall at the junctions of the converging and diverging sections. As a consequence, there are zones of flow separation and recirculation, the presence of which further increases the mixing.

The research encompassed four distinct but interrelated parts. In the first part, experiments were carried out to determine both entrance region and fully developed heat transfer coefficients. Then, using a modified test section, pressure distributions were measured, from which friction factors were evaluated. Next, with the same test section as for the pressure drop work, flow visualizations were carried out using the oil-lampblack technique in order to identify the regions of separation, recirculation, and reattachment. Finally, by employing the basic heat transfer and pressure drop data, a performance analysis was made which yielded comparisons between periodically converging-diverging tubes and the classical straight circular tube.

The geometry of the periodically converging-diverging tubes investigated here can be characterized by two parameters. One is the taper angle of the respective conical sections, while the other is the aspect ratio (length/maximum diameter) of the individual sections. Tubes having half taper angles ranging from 0 (straight tube) to about 15 deg were utilized during the course of the experiments (five taper angles > 0), while two aspect ratios were employed. For each tube configuration, the Reynolds number was varied systematically, with an overall range for the experiments extending from 6000 to 70,000 (to 100,000 for the straight tube).

The performance comparisons between the periodically converging-diverging tubes and the straight tube were carried out for two sets of constraints, namely, for equal mass flow and equal surface area, and for equal pumping power and equal surface area. These comparisons enable definitive conclusions to be drawn about the effectiveness of the periodic convergences and divergences as an enhancement technique.

With regard to the aforementioned fully developed heat transfer coefficients, it should be noted that a periodic geometry such as that investigated here does not admit the same type of fully developed regime as that for a conventional pipe flow. Rather, in a periodic configuration, the fully

Contributed by the Heat Transfer Division for publication in the JOURNAL OF HEAT TRANSFER. Manuscript received by the Heat Transfer Division March 10, 1983.

developed velocity field repeats itself at corresponding axial stations in successive cycles, with a similar repetition pattern for a properly defined dimensionless temperature. Another important feature of the periodic fully developed regime is that the cycle-average heat transfer coefficient is the same for all cycles. Also, the pressures at axial stations separated by the length of one cycle fall on a straight line. These attributes will be revisited during the presentation of the results.

The work described here is believed to be the first fundamentals-level study of periodically converging-diverging tubes, at least with regard to the open literature. Such tubes resemble the periodically crimped tubes that are often encountered in commercially available heat exchange devices, but basic heat transfer and pressure drop information for crimped tubes could not be found in the open literature.

The Experiments

For the determination of the heat transfer coefficients, it was found highly advantageous to employ the naphthalene sublimation technique in conjunction with the analogy between heat and mass transfer. Not only does the naphthalene technique offer general advantages, such as higher accuracy, minimal extraneous losses, and better control of boundary conditions, it also facilitates simplicity and flexibility in the fabrication of the test section. Of particular advantage is the capability (to be described shortly) that it affords for easy variation of the taper angle of the converging and diverging conical sections.

Test Section. The test section is made up of interlocking modules as illustrated in Fig. 1. Two such modules, one diverging and one converging, comprise one cycle in the periodically varying tube geometry. The figure shows a typical cycle as well as portions of the adjacent upstream and downstream cycles. Also identified in the figure are the half taper angle, θ, the module length, L_{mod}, and the maximum and minimum diameters, $D_{\max}$ and $D_{\min}$. All modules in a given test section had common values of θ, L_{mod}, $D_{\max}$, and $D_{\min}$. Each test section tube used for naphthalene sublimation experiments included as many as 10 cycles (i.e., 20 modules).

As can further be seen in Fig. 1, each module consists of a cylindrical metallic (aluminum) shell whose inner surface is coated with a layer of solid naphthalene. The coating is applied by a casting procedure which will be outlined in the next paragraph. Precise mating of the successive modules is ensured by interlocking recesses that are provided at the respective ends of each module. After the modules had been assembled prior to the start of a data run, the joints at the module interfaces were sealed by pressure-sensitive tape applied at the outer surface of the metallic wall.

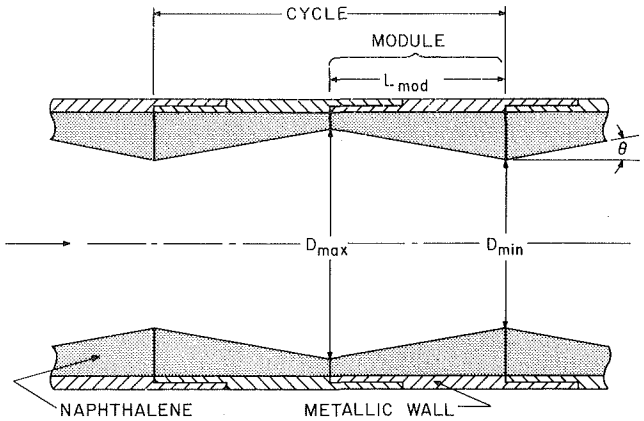

Fig. 1 Typical cycle and adjoining portions of periodically converging-diverging tube

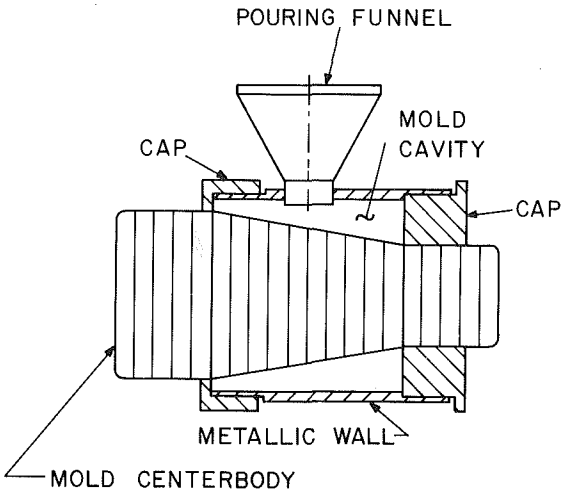

Fig. 2 Mold setup for naphthalene coating procedure

With regard to the naphthalene coating procedure, the first step was to remove from all modules the coating remaining from the preceding data run. This was accomplished by melting and evaporation. Then, a mold was assembled as shown in Fig. 2. The components of the mold included the

Nomenclature

A_w = per-module transfer surface
$\mathfrak{D}$ = diffusion coefficient
$D_{\max}$ = diameter at maximum cross section
$D_{\min}$ = diameter at minimum cross section
D^* = equivalent diameter, equation (7)
f_{fd} = fully developed friction factor, equation (12)
K_{fd} = fully developed mass transfer coefficient
$K_{fd,\text{cyc}}$ = per-cycle fully developed mass transfer coefficient
K_i = per-module mass transfer coefficient (module i)
L_{cyc} = axial length of cycle, $2L_{\text{mod}}$
L_{mod} = axial length of module
$\dot{M}_{\text{cyc}}$ = per-cycle mass transfer rate
$\dot{M}_i$ = per-module mass transfer rate (module i)
PP = pumping power, $(\dot{w}/\rho)\,\Delta p$
p = pressure
p_{atm} = ambient pressure
$\dot{Q}$ = volumetric flow rate
Re = Reynolds number, $4\dot{w}/\mu\pi D^*$
Sc = Schmidt number
Sh = per-module Sherwood number
Sh_{fd} = per-module fully developed Sherwood number
Sh_i = per-module Sherwood number (module i)
V = velocity, $\dot{w}/(\rho\pi D^{*2}/4)$
$\dot{w}$ = rate of mass flow
X = axial coordinate
θ = half taper angle (Fig. 1)
μ = viscosity
ν = kinematic viscosity
ρ = mean density of air
ρ_n = naphthalene vapor density
ρ_{nb} = bulk density of naphthalene vapor
ρ_{nw} = density of naphthalene vapor at wall
$\Delta\rho_{n,\text{cyc}}$ = wall-to-bulk density difference for cycle
$\Delta\rho_{n,i}$ = wall-to-bulk density difference for module (module i)

metallic wall of the module, end caps which mated with the recesses at the respective ends of the metallic wall, and a tapered shaft which passed through apertures in the end caps. The shaft served as the centerbody of the mold. Its surface had been polished to a mirrorlike finish with a succession of lapping compounds.

Molten naphthalene was poured into the annular cavity between the metallic wall and the centerbody through an aperture in the wall. Once the naphthalene had solidified, the shaft and the end caps were removed, as was the pouring funnel. The resulting finish of the sloping naphthalene surface was comparable to that of the polished shaft against which it had been cast. As a final step, the pouring aperture in the metallic wall was sealed with tape to prevent extraneous sublimation. In one of the modules, a thermocouple was cast into the naphthalene layer, flush with the surface which bounds the airflow.

The just-described casting procedure facilitated the parametric variation of the taper angle. For each preselected taper angle, a shaft with a corresponding taper was fabricated along with end caps having apertures appropriately sized to permit passage of the shaft. For each of the two module lengths that were employed during the course of the experiments, five tapered shafts were fabricated, yielding half taper angles, θ, of 2, 3.4, 6.3, 10, and 14.8 deg (the θ-value illustrated in Fig. 1 is 10 deg). The shafts and end caps were made so that D_{max} (Fig. 1) was maintained the same for all the investigated geometries, whereas D_{min} varied in accordance with the taper angle and module length.

The aforementioned common value of D_{max} was 4.450 cm, in terms of which the two module lengths may be expressed as $L_{mod}/D_{max} = 0.762$ and 1.143. Thus, taking account of the five taper angles and two module lengths, a total of 10 converging-diverging test section geometries were employed. An eleventh test section was used for the straight tube case in order to obtain baseline values of the heat (mass) transfer coefficient and the friction factor. For this case, an untapered cylindrical shaft was utilized in the casting process for the naphthalene-coated modules.

For the pressure drop experiments, additional modules, each equipped with a pressure tap at its axial midpoint, were incorporated into the array of naphthalene-coated modules. These additional modules were fabricated from either aluminum or plexiglass and did not, therefore, participate in the mass transfer process. They were geometrically identical to the naphthalene-coated modules.

For each one of the test sections, six of the tap-equipped modules were fabricated. During the course of the pressure drop runs, the six modules were installed at various positions along the test section in order to yield information in both the hydrodynamic development and fully developed regions.

Of the six tap-equipped modules for each test section, two modules (one converging, one diverging) were made of plexiglass in order to enable visual observations of the flow pattern to be made. The fluid motions were made visible by the oil-lampblack technique, which will be described shortly.

Flow Circuit. The test section was oriented horizontally and was situated at the upstream end of an open-loop flow circuit that was operated in the suction mode. Air was drawn into the inlet of the test section from the temperature-controlled laboratory room. From the test section exit, the air was ducted to a flow metering section (one of two calibrated orifices), to a control valve, and then to a blower. The blower was situated in a service corridor adjacent to the laboratory room, and its compression-heated, naphthalene-laden discharge was vented away from the laboratory.

The upstream end of the test section was built into a large baffle plate. The presence of the baffle created a plenumlike space upstream of the tube inlet from which the test section drew its air. Axial alignment of the test section was facilitated by fixtures which provided support from below and also compressed the array of modules from either end. The alignment was checked at the beginning of each data run.

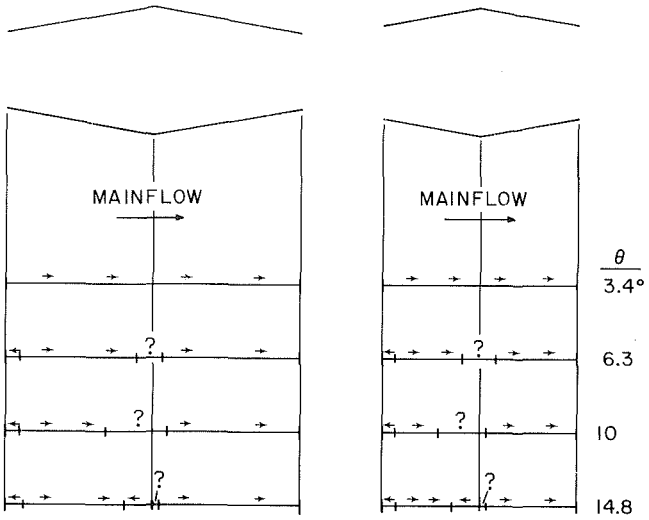

Fig. 3 Directions of fluid flow adjacent to the tube wall

Instrumentation. For the mass transfer experiments, the key quantity is the change of mass of each module during the course of a data run. To this end, mass measurements were made immediately before and after the run using a Sartorius ultraprecision, electronic analytical balance with a resolving power of 10^{-5} g and a capacity of 166 g (typical changes in mass during a data run were in the range of 0.1 g).

The thermocouples used in the experiments, one embedded in the test section and one in the airflow approaching the tube inlet, were made from specially calibrated copper-constantan wire. Periodic readings of the thermocouple emfs were made during the course of a data run by a programmable datalogger having a 1 μV resolution.

For the axial pressure distributions, the pressures from the individual taps were conveyed by plastic tubing to a pressure selector switch, the selected output of which was conveyed to a Baratron solid-state, capacitance-type pressure meter. Two sensing heads were employed—a 100 Torr head for the higher Reynolds numbers and a 10 Torr head for the lower Reynolds numbers. Both sensors afford an accuracy of 0.05 percent of the reading.

Experimental Procedure. Various aspects of the experimental procedure have already been mentioned, and additional features will be discussed. It was standard practice to leave the naphthalene-coated modules in the temperature-controlled laboratory overnight in order to attain thermal equilibrium with the room air. During this period, the modules were kept in a sealed plastic bag in order to avoid sublimation and also to ensure that the air in the room was free of naphthalene vapor.

Immediately prior to a data run, the modules were individually weighed and then assembled to form the test section. The blower had been warmed up in preparation for the run, so that it provided a steady flow from the moment of its activation. After the preselected duration of the run, the test section was disassembled and the modules reweighed. During all of these operations, the modules were never directly touched by the hand; rather, either insulated gloves or padded tongs were used.

To obtain a correction for possible extraneous sublimation which might have occurred between the two weighings (e.g.,

during the setup and disassembly of the test section), a so-called after-run was made. During the after-run, all aspects of the actual data run were repeated, but without the airflow period. The mass measurement following the after-run provided the sought-for correction ($\sim$ 1 percent).

Flow Visualization. As was noted earlier, the flow visualization was carried out using the oil-lampblack technique. According to this technique, a suitable mixture of oil and lampblack powder is applied to a surface, which is then exposed to the airflow whose characteristics are to be studied. Ideally, under the action of the forces exerted by the flow, the mixture will move along the surface, following the paths of the adjacent fluid particles. However, in regions of very low velocity, the mixture remains stationary, and the flow pattern cannot be resolved.

In the flow visualization runs, attention was focused on the plexiglass modules. Before the test section was assembled for such a run, white, plasticized, self-adhering contact paper was affixed to the plexiglass walls which bounded the airflow, but with a portion left uncovered to enable visual observations to be made. Then, drops of oil-lampblack mixture were applied to the contact paper surface in the form of dots. The contact paper gave a contrasting background for the black dots and, being removable at the end of the run, provided a record of the flow pattern.

After the assembly of the test section, the airflow was initiated and maintained until there was no further movement of the oil-lampblack mixture. At this point, the flow was terminated, the test section disassembled, and the contact paper removed.

By far the best resolution of the flow field was obtained at the highest attainable Reynolds numbers, which ranged from 40,000 to 70,000 for the various periodically converging-diverging test sections. All of the final visualization runs were made at these Reynolds numbers.

Flow Visualization Results

The direction of fluid flow adjacent to the converging and diverging walls, as obtained from the oil-lampblack flow visualization, is presented in Fig. 3. The figure is subdivided into left- and right-hand parts, which pertain respectively to the $L_{\text{mod}}/D_{\text{max}} = 0.762$ and 1.143 test sections. At the top of each part is a sketch depicting one cycle of the periodic tube geometry, showing a diverging module followed by a converging module. Below the sketch are four horizontal straight lines. Each line represents the axial length of a cycle and, furthermore, each such line corresponds to one of the investigated taper angles, as listed at the right of the figure. The arrows deployed along the lines indicate the direction of the wall-adjacent fluid flow. For those regions where the forces exerted by the fluid were too weak to move the oil-lampblack mixture, question marks are shown.

For the half taper angle of 3.4 deg (as well as 2 deg (not shown)), the flow adjacent to the wall is in the mainflow direction at all axial stations along the cycle. Thus, for these angles, the flow is able to follow the contour of the wall and does not separate.

The case of the 6.3-deg half taper does, however, show a small backflow region just downstream of the beginning of the diverging section, indicating the occurrence of flow separation and the presence of a recirculation zone. In addition, there is a region situated to either side of the interface of the diverging and converging sections where the velocities were too low to enable the resolution of their direction. This region is believed to be a recirculation zone caused by the inability of the mainflow to penetrate into the "valley" at the midpoint of the cycle. The flow pattern for the 10-deg half taper differs from the 6.3-deg case only in that the low velocity region has broadened and is shifted forward.

The most complete resolution of the flow pattern was attained for the 14.8-deg case. The backflow region adjacent to the cycle inlet is seen to be somewhat enlarged compared with those for the 6.3- and 10-deg cases. Furthermore, a second, clearly defined backflow region is in evidence upstream of the interface of the converging and diverging sections. Thus there are two pockets of separated, recirculating flow adjacent to the surface of the diverging module. For the converging module, the wall-adjacent flow is in the mainstream direction, except possibly for the small region of uncertainty at its upstream end.

The occurrence of flow separation adjacent to axial stations where there is a sharp change in the slope of the wall is not unexpected. On the other hand, the fact that a significant portion of the wall of the diverging module is washed by a forward (i.e., unseparated) flow is noteworthy, especially so at the largest taper. The flow which enters a diverging module resembles a converging jet, with the extent of the convergence increasing with the taper angle. At a fairly large half taper angle such as 14.8 deg, it might be expected that the jet would arch over the wall of the diverging module and reattach downstream of it, at the adjacent converging module. From this viewpoint, the observed early reattachment of the flow at the wall of the diverging module is somewhat surprising.

Mass (Heat) Transfer Results

The mass transfer coefficients and Sherwood numbers obtained here can be converted to heat transfer coefficients by employing the analogy between the two processes. Because of this, the phrases *heat transfer* and *mass transfer* will be used interchangeably in the presentation of results. The thermal boundary condition for the heat transfer situation which is analogous to the present mass transfer situation is uniform wall temperature.

Data Reduction. The per-module mass transfer coefficient, K_i, for a typical module, i, was evaluated from the defining equation

$$K_i = (\dot{M}_i/A_w)/\Delta\rho_{n,i} \tag{1}$$

In this equation, $\dot{M}_i$, the rate of mass transfer at module i, was obtained from the ratio $\Delta M_i/\tau$, where ΔM_i is the measured (and corrected) change in the module mass and τ is the duration of the data run. The quantity A_w is the per-module surface area which bounds the flow

$$A_w = \pi(D_{\text{max}}^2 - D_{\text{min}}^2)/4\sin\theta \tag{2}$$

For a given test section, A_w is the same for all modules.

The denominator $\Delta\rho_{n,i}$ of equation (1) is the wall-to-bulk difference in naphthalene vapor density for module i. Its evaluation requires that the axial variation of the bulk vapor density, ρ_{nb}, first be determined. For this purpose, let j denote any module in the test section, with ρ_{nb}^{j-1} representating the bulk vapor density at the inlet of the module and ρ_{nb}^{j} representing the bulk vapor density at the module exit. Then, from a mass balance

$$\rho_{nb}^{j} = \rho_{nb}^{j-1} + \dot{M}_j/\dot{Q} \tag{3}$$

where $\dot{Q}$ is the volumetric flow rate. Then, since $\rho_{nb} = 0$ at the test section inlet

$$\rho_{nb}^{i} = \sum_{j=1}^{i} \dot{M}_j/\dot{Q} \tag{4}$$

The volumetric flow rate appearing in equation (4) was evaluated as $\dot{w}/\rho$, where $\dot{w}$ is the test section mass flow rate and ρ is the mean density of the air in the test section.

The other ingredient needed for the evaluation of the wall-to-bulk density difference is the naphthalene vapor density, ρ_{nw}, at the tube wall. This quantity was obtained by a two-step

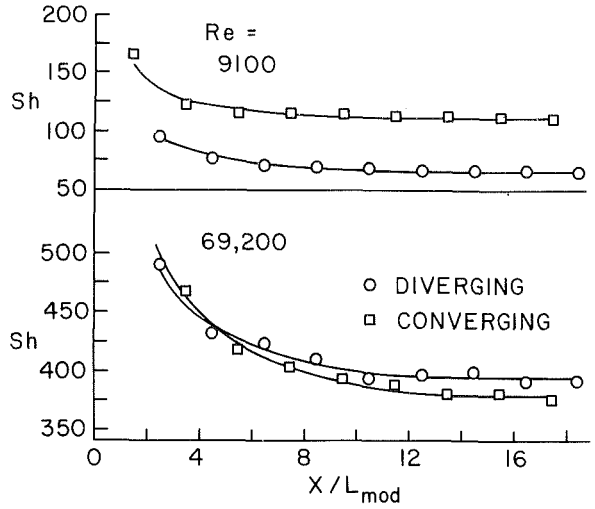

Fig. 4 Effect of Reynolds number on the axial distribution of the per-module Sherwood number (θ = 6.3 deg, L_{mod}/D_{max} = 0.762)

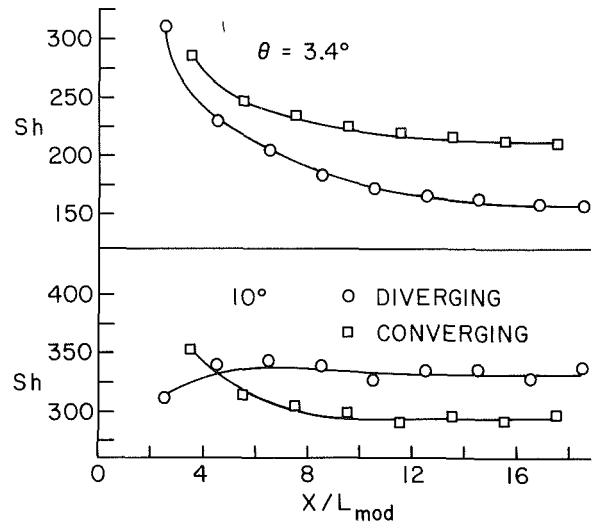

Fig. 5 Effect of taper angle on the axial distribution of the per-module Sherwood number (Re ≃ 34,000, L_{mod}/D_{max} = 0.762)

process. First, by using the measured wall temperature, the naphthalene vapor pressure at the wall was calculated by the Sogin vapor pressure/temperature equation [7]. Then, ρ_{nw} was evaluated from the perfect gas law.

Two definitions of the wall-to-bulk difference in vapor density were considered—the arithmetic-mean difference and the log-mean difference, respectively

$$\Delta\rho_{n,i} = \rho_{nw} - \tfrac{1}{2}(\rho^i_{nb} + \rho^{i-1}_{nb}) \tag{5}$$

$$\Delta\rho_{n,i} = \{ (\rho_{nw} - \rho^{i-1}_{nb}) - (\rho_{nw} - \rho^i_{nb}) \} / ln\{ (\rho_{nw} - \rho^{i-1}_{nb})/(\rho_{nw} - \rho^i_{nb}) \} \tag{6}$$

For all the experiments, the per-module rise in bulk density was small compared with the wall-to-bulk density difference $\Delta\rho_{n,i}$. As a consequence, equations (5) and (6) yielded indistinguishable results. The log-mean difference was used in the data reduction because it is conventional practice in the heat transfer literature.

The dimensionless counterpart of the mass transfer coefficient is the Sherwood number which, in common with the Nusselt number, contains a characteristic length. Since it is natural to compare the results for periodically converging-diverging tubes with those for the straight tube, it is convenient to employ a characteristic length which facilitates such comparisons. To this end, an equivalent diameter, D^*, for a

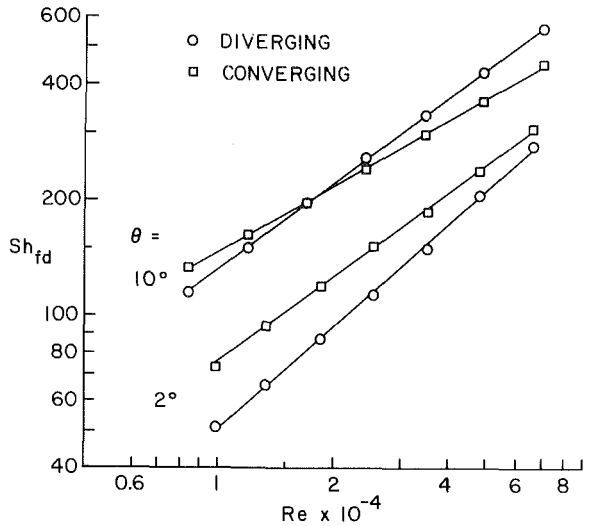

Fig. 6 Illustrative results for the per-module fully developed Sherwood number (L_{mod}/D_{max} = 0.762)

periodic tube is defined so that its mass transfer surface area (for a given axial length) is equal to that for a straight tube of diameter, D^*. If, as before, A_w denotes the per-module mass transfer area, and L_{mod} is the axial length of the module, then the aforementioned definition of D^* yields

$$\pi D^* L_{mod} = A_w \tag{7}$$

where A_w is given by equation (2) and from which D^* can be expressed in terms of the geometric parameters of the periodically converging-diverging tube.

Thus, in terms of D^* and of the Schmidt number Sc = $\nu/\mathfrak{D}$, the per-module Sherwood number can be expressed as

$$Sh_i = K_i D^*/\mathfrak{D} = (K_i D^*/\nu)Sc \tag{8}$$

where Sc = 2.5 for naphthalene diffusion in air. The kinematic viscosity ν was evaluated as that for pure air. Consistent with the foregoing, the Reynolds number was defined as that for a straight circular tube of diameter, D^*

$$Re = 4\dot{w}/\mu\pi D^* \tag{9}$$

in which $\dot{w}$ is the rate of mass flow through the test section.

Entrance Region Results. Owing to space limitations, only a representative sample of the entrance region results will be presented here. These results will serve to illustrate the main trends. A more complete presentation is available in [8].

The effect of Reynolds number on the axial distribution of the Sherwood number is illustrated in Fig. 4 for fixed geometrical parameters (θ = 6.3 deg, L_{mod}/D_{max} = 0.762). In the figure, the per-module Sherwood number is plotted as a function of the dimensionless axial coordinate X/L_{mod}. In particular, the Sherwood number for each module is plotted at the axial midpoint of the module, and the data for the converging and diverging modules are identified by different symbols. The figure contains two graphs, respectively, for Re = 9100 and 69,200.

From this figure, it is seen that the Sherwood numbers for the converging and diverging modules fall naturally along separate lines. At lower Reynolds numbers, the Sherwood numbers for the converging modules exceed those for the diverging modules, while an opposite relationship exists at the higher Reynolds numbers. This finding can be rationalized by recalling the flow visualization results and the fact that more of a diverging module is washed by a separated recirculating flow than is a converging module. Furthermore, it is well known (e.g., from the results for a transverse blockage element in a duct [9]) that the Nusselt (Sherwood) number for

a separated region increases more rapidly with Reynolds number than does that for a related unseparated flow. These facts fit well with the aforementioned finding evidenced in Fig. 4.

The effect of the taper angle on the axial distribution of the per-module Sherwood number is illustrated in Fig. 5 for a fixed Reynolds number ($\simeq$34,000) and a fixed $L_{\text{mod}}/D_{\text{max}}$ ($=0.762$). The upper graph is for a half taper angle $\theta = 3.4$ deg, while the lower graph is for $\theta = 10$ deg. As before, different symbols are used to identify the results for the converging and diverging modules.

There are three main effects of the taper angle on the Sherwood number distributions. First, at all axial stations except those near the tube inlet, the level of the Sherwood number increases significantly as the taper angle increases. Furthermore, since the angle-related enhancement is much more marked for the diverging modules than for the converging modules, the ordering of the Sherwood numbers for the two types of modules reverses with an increase in angle. Finally, there is a change in the shape of the axial distributions. At small angles, the distributions decrease with downstream distance as in a conventional entrance region. On the other hand, at larger angles, the distribution for the diverging modules is nearly flat while that for the converging modules displays a much smaller variation than at small angles.

The transverse fluid motions and the flow separation which occur at larger taper angles give rise to vigorous mixing and enhanced heat transfer. Since the major zones of separation occur at the diverging modules, these modules experience greater angle-related enhancement than do the converging modules. The aformentioned enhancing tendencies build up with increasing distance from the inlet (in a manner similar to what occurs in a tube bank in crossflow) and, thereby, neutralize the otherwise-standard entrance region decrease in the mass (heat) transfer coefficient.

Fully Developed Results. Fully developed Sherwood numbers were deduced for each case from axial distributions of the type illustrated in Figs. 4 and 5. A representative sample of these fully developed results is presented in Fig. 6, with the full complement of results available in [8].

In Fig. 6, per-module fully developed Sherwood numbers are plotted as a function of the Reynolds number for two cases respectively characterized by a small and a large half taper angle (for both cases, $L_{\text{mod}}/D_{\text{max}} = 0.762$). At the lower Reynolds numbers, the Sherwood numbers for the converging modules tend to be higher than those for the diverging modules. However, as the Reynolds number increases, the latter Sherwood numbers increase more rapidly than do the former. Thus, with an increase in Reynolds number, the difference between the two sets of Sherwood numbers decreases and, at larger taper angles, there is a crossover point beyond which the diverging modules display higher Sherwood numbers which differ more and more from those for the converging modules.

Figure 6 also affirms the enhancing effect of an increase in the taper angle. Both larger taper angles and higher Reynolds numbers promote vigorous recirculation adjacent to the walls of the diverging modules, with a corresponding increase in the Sherwood number. Another noteworthy feature of the figure is the excellence of the least-squares, straight-line representations of the data.

Up to now, attention has been focused on the per-module Sherwood number. For applications, however, it may be more useful to provide *per-cycle* Sherwood numbers or mass transfer coefficients, where a cycle consists of a converging module and a diverging module. Such per-cycle information will be presented here for the fully developed regime.

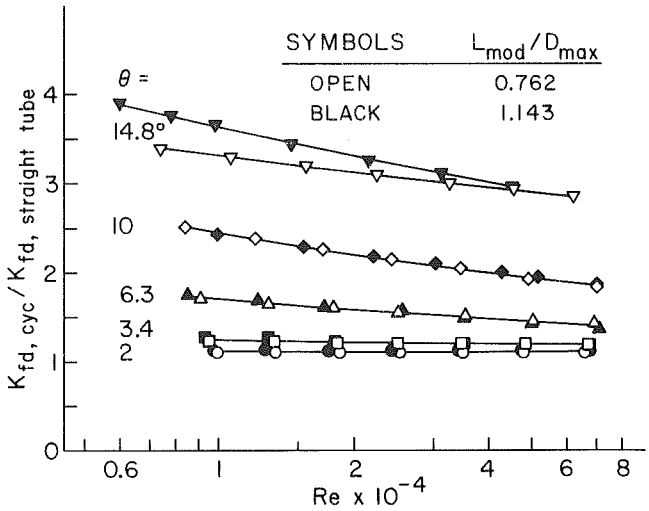

Fig. 7 Per-cycle fully developed mass transfer coefficients

Let $K_{fd,\text{cyc}}$ denote the per-cycle, fully developed mass transfer coefficient, which was evaluated from

$$K_{fd,\text{cyc}} = (\dot{M}_{\text{cyc}}/2A_w)/\Delta\rho_{n,\text{cyc}} \tag{10}$$

where $\dot{M}_{\text{cyc}}$ and $2A_w$ are the mass transfer rate and mass transfer surface area per cycle, while $\Delta\rho_{n,\text{cyc}}$ is the log-mean, wall-to-bulk difference in naphthalene vapor density evaluated between the inlet and exit of the cycle.

To achieve a very compact yet particularly insightful presentation of the results for all the investigated θ, $L_{\text{mod}}/D_{\text{max}}$, and Re, the ratio

$$K_{fd,\text{cyc}}/K_{fd,\text{straight tube}} \tag{11}$$

will be employed. This ratio compares the value of $K_{fd,\text{cyc}}$ for a periodically converging-diverging tube with the fully developed K value for a corresponding straight tube. For the comparison, the diameter of the straight tube is equal to the D^* value for the periodic tube, and both tubes carry the same mass flow $\dot{w}$. Since $\text{Re} = 4\dot{w}/\mu\pi D^*$, the Reynolds numbers of the two tubes being compared are the same.

The results for the K_{fd} ratio expressed by equation (11) are plotted in Fig. 7 as a function of the Reynolds number. These results encompass all of the parameter values employed during the experiments. As seen from the figure, the K_{fd} ratio increases steadily with the half taper angle, starting with a value of about 1.1 for $\theta = 2$ deg and attaining values in the range of 3–4 for $\theta = 14.8$ deg. Since the ratio is a direct measure of the enhancement corresponding to common values of Re and of the transfer surface area (i.e., common value of D^*) for the periodic tube and the straight tube, it is evident that larger taper angles are highly enhancing.

Another remarkable feature of Fig. 7 is the success of the presentation format in bringing together the results for the two investigated values of $L_{\text{mod}}/D_{\text{max}}$. Indeed, for all half taper angles up to and including 10 deg, the two sets of results are virtually coincident. Only for $\theta = 14.8$ deg do substantial deviations occur. It may be noted that other presentation formats were explored, but only that of Fig. 7 succeeded in bringing together the results for the two $L_{\text{mod}}/D_{\text{max}}$ values. Another virtue of this presentation format is that it yields a very much weaker Reynolds number dependence than would exist had the Sherwood number itself been plotted.

To assist in its application, the procedure by which Fig. 7 is used for determining mass (or heat) transfer coefficients will now be outlined. For a specified periodic tube geometry (θ, L_{mod}, D_{max}), the equivalent diameter, D^*, is calculated from equations (7) and (2). With this and with the selected airflow rate, $\dot{w}$, the Reynolds number is obtained from equation (9).

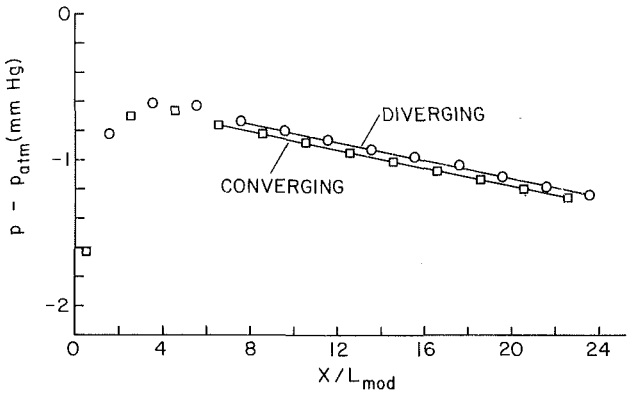

Fig. 8 Representative measured axial pressure distribution (θ = 6.3 deg, L_{mod}/D_{max} = 0.762, Re ≈ 25,000)

The Reynolds number is used both as an input to Fig. 7 (yielding the K_{fd} ratio) and to a Nusselt (Sherwood) number correlation for turbulent heat transfer in a straight tube. The latter, taken together with D^*, yields $K_{fd,\text{straight tube}}$. Then, $K_{fd,cyc}$ for the periodic tube follows from the K_{fd} ratio.

In view of the foregoing discussion, it is relevant to comment on the straight-tube mass (heat) transfer coefficient. Measurements made here (and reported in [8]) over the Reynolds number range from 10,000 to 100,000 yielded fully developed Sherwood numbers that are in excellent agreement with the well-established Petukhov-Popov equation (equations (8–23) and (8–24) of [10]). The *maximum* deviation of the data from the correlation is 4.2 percent, which is well within the 6 percent confidence limit specified by Petukhov-Popov. It is, therefore, appropriate to evaluate $K_{fd,\text{straight tube}}$ from the Petukhov-Popov equation when using Fig. 7 to determine $K_{fd,cyc}$ for periodic tubes.

Pressure Drop and Friction Factor Results

In a periodic duct such as that considered here, the flow pattern repeats itself cyclically in the fully developed regime. Similarly, the pressure has certain periodic characteristics. In particular, if L_{cyc} ($=2L_{mod}$) denotes the axial length of a cycle and X_1 is any station in the fully developed regime, then the pressures at points X_1, $(X_1 + L_{cyc})$, $(X_1 + 2L_{cyc})$, $(X_1 + 3L_{cyc})$, . . . lie on a straight line. Different straight lines correspond to different choices of X_1 within a cycle, but all such straight lines will have the same slope. Within any given cycle, the pressure distribution along the cycle will not be linear.

In the present experiments, all points of pressure measurement were situated at the axial midpoint of their respective module. Therefore, the measurement points for the diverging modules were spaced apart by the cycle length, L_{cyc}, and similarly for the measurement points for the converging modules. In view of this, it is expected that in the fully developed regime, the measured pressures for the diverging modules will lie on one straight line and those for the converging modules will lie on another straight line, with the two lines being parallel.

With these expectations in mind, attention may be turned to a typical measured pressure distribution as shown in Fig. 8. In this figure, the difference between the local pressure, p, at X and the ambient pressure, p_{atm}, is plotted as a function of X/L_{mod}. The data correspond to θ = 6.3 deg, L_{mod}/D_{max} = 0.762, and Re ≈ 25,000. The figure shows that downstream of a hydrodynamic development length, the pressure distribution becomes linear, with separate, parallel lines for the converging and diverging modules.

The pressure gradients dp/dX determined from the measured pressure distributions enabled evaluation of the fully developed friction factor

$$f_{fd} = (-dp/dX)D^*/\tfrac{1}{2}\rho V^2 \tag{12}$$

where $V = \dot{w}/(\rho\pi D^{*2}/4)$, and ρ is the mean density in the fully developed region of the tube. The thus-determined friction factors are plotted in Fig. 9 as a function of the Reynolds number for all of the investigated cases. Also included for reference purposes is the Blasius f,Re relation for a straight tube.

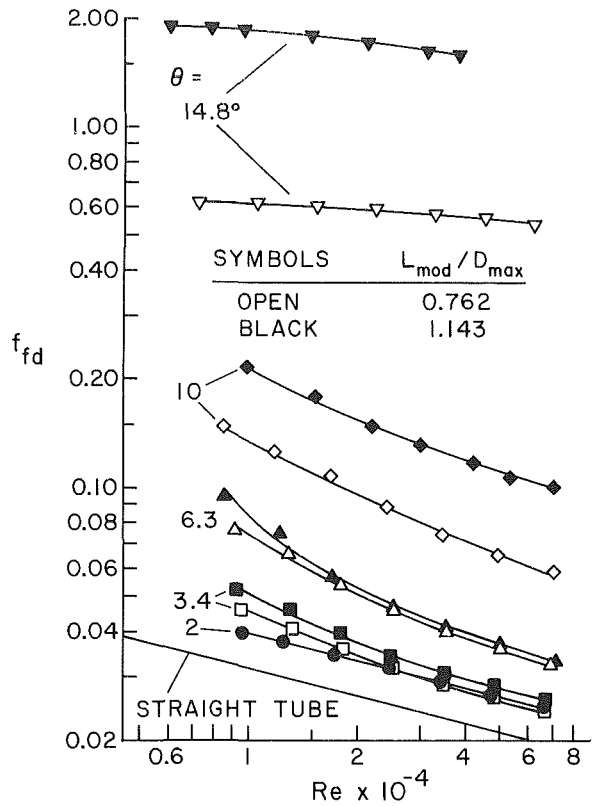

Fig. 9 Fully developed friction factors

The figure shows that the friction factor increases with the half taper angle, with the extent of the increase escalating markedly at the larger taper angles. Thus, for example, the friction factors for the 6.3 deg case are 1.7–3.9 times those for the straight tube, while the corresponding range for the 14.8 deg case is 18–70. It may also be noted that the f-values for the longer modules are greater than those for the shorter modules, a result attributable to the larger changes of cross section for the former (i.e., larger D_{max}/D_{min}).

Figure 9 documents the pressure drop penalty that is associated with the increase in the mass (heat) transfer coefficients evidenced in Fig. 7. To assess the *net* benefit of using a periodically converging-diverging tube instead of a straight tube, performance analyses are appropriate, as will now be illustrated.

Performance Evaluations

In comparing the performance of enhanced and unenhanced heat transfer passages, it is necessary to specify the constraints under which the comparison is made. There is a broad variety of constraints that may be employed [3–6]. In this paper, the basic heat transfer and pressure drop data have been provided so that performance evaluations can be made for any set of constraints that is appropriate to a specific application. However, because of journal space limitations, only representative performance evaluations can be carried out here. Specifically, performance comparisons between

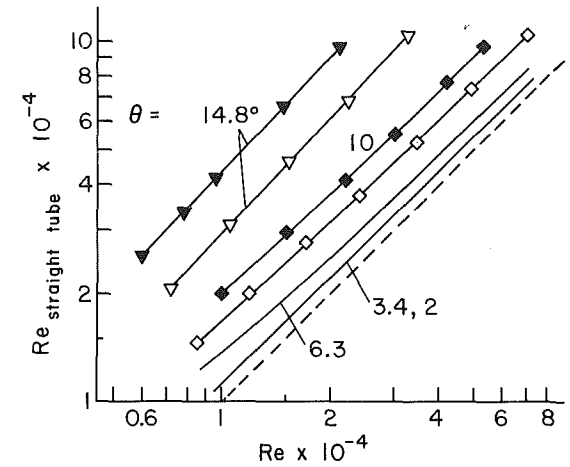

Fig. 10 Relationship between the constant-pumping-power Reynolds numbers for the periodic and straight tubes

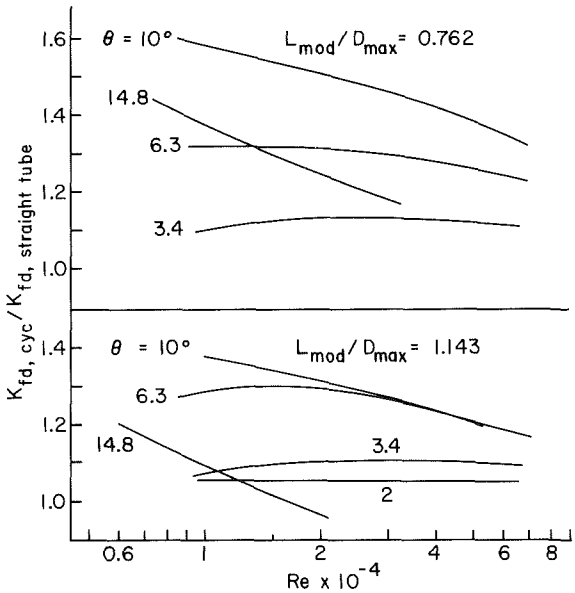

Fig. 11 Comparison of constant-pumping-power, fully developed mass transfer coefficients for the periodic and straight tubes

periodically converging and diverging tubes and the straight tube will be made for two sets of constraints, as follows:

1 Equal airflow rate and equal transfer surface area
2 Equal pumping power and equal transfer surface area

For each of these two cases, the fully developed mass (heat) transfer coefficients for periodic and straight tubes will be compared in order to find which is higher. The condition of equal heat transfer surface area will be fulfilled by comparing a periodic tube of equivalent diameter, D^*, with a straight tube having the same diameter, D^*.

The comparison of mass (heat) transfer coefficients for Case 1 has already been made in Fig. 7. As seen there, the periodic tube affords very significant enhancements which increase as the taper angle increases. The constraints of Case 1 imply that the pressure drop and pumping power penalties which accompany the heat transfer enhancement can be accommodated. This would surely be so if the pressure drop associated with the heat exchanger is a small portion of the overall pressure drop of the system.

Attention is next turned to Case 2. To implement this case, it may be noted that the pumping power, PP, required to drive a flow rate, $\dot{w}$, through a pressure drop, Δp, is

$$PP = (\dot{w}/\rho)\,\Delta p \tag{13}$$

For a periodic tube and a straight tube which have equal diameters, D^*, and equal lengths (any multiple of L_{cyc}), it is readily shown that the constraint of equal pumping power reduces to

$$f\mathrm{Re}^3 = (f\mathrm{Re}^3)_{\text{straight tube}} \tag{14}$$

where the unsubscripted quantities pertain to the periodic tube. For the straight tube, the fully developed friction factor can be evaluated from the Blasius equation $f = 0.3164/\mathrm{Re}^{1/4}$, so that equation (14) becomes

$$\mathrm{Re}_{\text{straight tube}} = (3.161 f\mathrm{Re}^3)^{4/11} \tag{15}$$

The dependence of f on Re for the periodic tube is given by Fig. 9.

Equation (15) provides a relationship between the Reynolds numbers for periodic and straight tubes which have equal pumping power. For a selected value of Re for the periodic tube, f is read from Fig. 9, and the Re and f values are introduced into the right side of equation (15), yielding the Reynolds number for the straight tube. Results obtained in this way are presented in Fig. 10, where the straight-tube Reynolds number is plotted as a function of the periodic-tube Reynolds number. Also shown in the figure is a dashed reference line which corresponds to equal values of the two Reynolds numbers.

The figure shows that, as expected, a periodic tube must be operated at a lower Reynolds number than a straight tube in order to achieve equal pumping power. The differences between the two Reynolds numbers grow larger as the half taper angle of the periodic tube increases. For example, for a half taper angle of 6.3 deg, the ratio of the Reynolds numbers for the two tubes is about 1.25, while for $\theta = 14.8$ deg, the ratio is in the range from 3–4.5.

With the just-determined Reynolds number information, the fully developed mass (heat) transfer coefficients for periodic and straight tubes having equal diameters, D^*, have been determined. These coefficients, which correspond to equal pumping power, have been ratioed and are plotted in Fig. 11 as a function of Re (the Reynolds number for the periodic tube). The figure consists of two graphs, the upper one for the $L_{\text{mod}}/D_{\text{max}} = 0.762$ modules and the lower one for the $L_{\text{mod}}/D_{\text{max}} = 1.143$ modules.

Inspection of the figure shows that for the most part, the periodic-tube transfer coefficient exceeds that for the straight tube. In fact, only for the 14.8 deg half taper and the longer modules ($L_{\text{mod}}/D_{\text{max}} = 1.143$) is the plotted ratio less than unity, an outcome which might have been expected because of the high pressure drop for this case (see Fig. 9). Thus, on a constant pumping power basis, the periodic converging-diverging geometry is enhancing. Further inspection of the figure shows that greater enhancement occurs for the shorter modules. For both of the investigated module lengths, the 10-deg half taper angle appears to yield the greatest enhancement. For this angle and for the shorter modules, the enhancement ranges from 60 to 30 percent over the Reynolds number range from 8500 to 70,000. These enhancements compare favorably with those given in Bergles' survey of enhancement techniques [3].

Concluding Remarks

The research described here constitutes a comprehensive study of the turbulent heat transfer and fluid flow characteristics of periodically converging and diverging tubes. During the course of the work, three parameters were systematically varied, including the Reynolds number, the taper angle of the converging and diverging modules, and the module aspect ratio. The investigation encompassed four distinct but closely related parts. These included experiments which yielded entrance region and fully developed mass

(heat) transfer coefficients, pressure distributions and friction factors, and patterns of fluid flow. The fourth part was a performance analysis which used the experimentally determined mass (heat) transfer coefficients and friction factors as input.

In the performance analysis, periodically converging and diverging tubes were compared with the conventional straight tube for two sets of constraints. In Case 1, the comparison was made for equal mass flow and for equal transfer surface area, while for Case 2 the imposed constraints were equal pumping power and equal transfer surface area.

The Case 1 comparison yielded large enhancements in the mass (heat) transfer coefficient for the periodic tube, which increases as the taper angle increased. These enhancements are accompanied by large pressure drop and pumping power penalties. For the Case 2 comparison, enhancements in the 30–60 percent range were encountered, and these occurred at a half taper angle of 10 deg.

References

1 Webb, R. L., Bergles, A. E., and Junkhan, G. H., "Bibliography of U.S. Patent Literature on Heat Transfer Augmentation Techniques," Report No. HTL-25, Engineering Research Institute, Iowa State University, Ames, Iowa, 1980.

2 Bergles, A. E., Webb, R. L., Junkhan, G. H., and Jensen, M. K., "Bibliography of Augmentation of Convective Heat and Mass Transfer," Report No. HTL-19, Engineering Research Institute, Iowa State University, Ames, Iowa, 1979.

3 Bergles, A. E., "Survey and Evaluation of Techniques to Augment Convective Heat and Mass Transfer," *Progress in Heat and Mass Transfer*, Vol. 1, Pergamon Press, Oxford, 1969, pp. 331–424.

4 Webb, R. L., "Performance Evaluation Criteria for Use of Enhanced Heat Transfer Surfaces in Heat Exchanger Design," *International Journal of Heat and Mass Transfer*, Vol. 24, 1981, pp. 715–726.

5 Bergles, A. E., Bunn, R. L., and Junkhan, G. H., "Extended Performance Evaluation Criteria for Enhanced Heat Transfer Surfaces," *Letters in Heat and Mass Transfer*, Vol. 1, 1974, pp. 113–120.

6 Bergles, A. E., Blumenkrantz, A. R., and Taborek, J., "Performance Evaluation Criteria for Enhanced Heat Transfer Surfaces," Paper FC6.3, *Proceedings Fifth International Heat Transfer Conference*, Vol. II, 1974, pp. 239–243.

7 Sogin, H. H., "Sublimation from Disks to Air Streams Flowing Normal to their Surfaces," ASME *Trans.*, Vol. 80, 1958, pp. 61–71.

8 Souza Mendes, P., "Effect of Periodic, Tapered Enlargements and Contractions on Turbulent Heat Transfer and Fluid Flow in a Circular Duct," Ph.D. thesis, Department of Mechanical Engineering, University of Minnesota, Minneapolis, Minnesota, 1982.

9 Sparrow, E. M., Molki, M., and Chastain, S. R., "Turbulent Heat Transfer Coefficients and Fluid Flow Patterns on the Faces of a Centrally Positioned Blockage in a Duct," *International Journal of Heat and Mass Transfer*, Vol. 23, 1981, pp. 507–520.

10 Karlekar, B. V., and Desmond, R. M., Heat Transfer, 2d ed., West Publishing Company, St. Paul, Minnesota, 1982.

J. W. Baughn
Professor.
Mem. ASME

M. A. Hoffman
Professor.

University of California,
Davis, Calif. 95616

B. E. Launder
Professor,
University of Manchester Institute
of Science and Technology,
Manchester, England

R. K. Takahashi
Postgraduate Research Engineer,
University of California,
Davis, Calif. 95616

Turbulent Heat Transport in Circular Ducts With Circumferentially Varying Heat Flux

Experiments have been performed with turbulent air flow in a tube with uniform and with top-half heating; the flow was hydrodynamically fully developed at the start of the heated section, and there were negligible buoyancy effects. Numerical solutions of the mean momentum and energy equations which use the suggestion [1] that the ratio of radial-to-circumferential turbulent diffusivities is equal to the corresponding ratio of mean square velocity fluctuations in these directions agree well with the experimental results.

1 Introduction

The problem of heat transfer to turbulent flow in a circular pipe is very widely encountered in engineering applications. Over the last fifty years, numerous fundamental studies have been carried out to establish the thermal characteristics of such flows. Although these studies have largely adopted circumferentially uniform boundary conditions, many practical problems (e.g., heat exchanger tubes) involve significant departures from axial symmetry due to either flow nonuniformity, to circumferential variations in wall heating or both. The effect of these nonuniformities is of considerable interest, since local overheating could cause equipment failure.

From the available experimental studies, it is clear that the effective thermal or mass diffusivity in a circular pipe is significantly nonisotropic, being markedly higher in the circumferential than in the radial direction. From the practical standpoint, this directional variation is helpful because it will tend to reduce the circumferential temperature gradients in the tube that are the primary cause of failure. There are few sets of data, however, that are sufficiently well documented to allow this anisotropy to be quantified with any certainty. For example, the heat and mass transfer data of Quarmby and Quirk [2] indicate circumferential diffusivities near the wall between 2 and 50 times that in the radial direction. This wide variation is due at least in part to the fact that the radial fluxes and gradients both approach zero at the wall, so there is great uncertainty in their ratio (which is proportional to the radial diffusivity).

Heat transfer experiments with nonuniform circumferential heat flux have been reported by Black and Sparrow [3], Knowles and Sparrow [4], and Baughn et al. [5] using air (Pr $\simeq$ 0.7) and by Chan, Baughn, and Hoffman [6] and Schmidt and Sparrow [7] using water (Pr $\simeq$ 3.5–11.5). The processing of these data to extract definitive diffusivity ratios is hampered by the fact that the thermal field requires a much greater downstream distance to reach full development than in the axisymmetric case, so estimates made on the assumption of fully developed flow can be very seriously in error [8]. Moreover, in several cases there is a relatively large circumferential heat conduction in the tube wall, and while corrections are applied, there is inevitably some associated uncertainty in the circumferential heat flux boundary conditions for the fluid.

Most computational studies of nonaxisymmetric heat diffusion in pipes have been based on intuitive notions about turbulent mixing. In the scheme of Gartner et al. [9], for example, effective radial and circumferential mixing lengths are evaluated geometrically from the particular cross-sectional shape in question. Although the scheme has been successfully applied in a number of geometries, the ad hoc empirical inputs suggest that the model is unlikely to achieve great breadth of applicability.

In the last few years a more fundamental and potentially more general approach to modeling turbulent heat transport processes, the second-moment closure model, has begun to be used. These schemes are based on the solution of transport equations for each of the nonzero turbulent heat fluxes, $u_i t$, and Reynolds stresses $u_i u_j$. A review of alternative closure forms is given in [1].

For flow in tubes of uniform cross section, the transport terms in these equations are small compared with source and sink terms; the transport terms can then be discarded without significantly altering the characteristics of the predicted velocity and flow fields. A much simpler model then emerges. For the case of an axisymmetric velocity field, it turns out that the ratio of circumferential to radial diffusivities can be approximated by (see [1])

$$\frac{\Gamma_{t,\theta}}{\Gamma_{t,r}} = \frac{\overline{u_\theta^2}}{\overline{u_r^2}} \tag{1}$$

where Γ_t denotes the turbulent diffusivity and the subscripts indicate the direction. Reference [1] compares the variation across a pipe of the diffusivity ratio given by equation (1) (using Laufer's measurements [10] for $\overline{u_\theta^2}$ and $\overline{u_r^2}$) with values from measurements of temperature profiles and heat fluxes. The latter data, as noted above, exhibit great scatter, though, on the average, give rather larger anisotropies in the diffusion coefficients than indicated by equation (1). However, recent computations of Sparrow and Black's [3] experiments by Chieng and Launder [8] using equation (1) and Laufer's data

Contributed by the Heat Transfer Division for publication in the JOURNAL OF HEAT TRANSFER. Manuscript received by the Heat Transfer Division March 4, 1983.

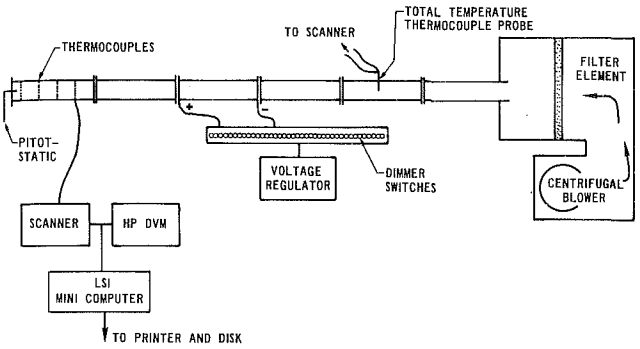

Fig. 1 Diagram of the experimental apparatus

result in excellent agreement with the limited experimental temperature distributions. This result underlines the difficulty of processing out reliable values of turbulent diffusivities from measured temperature or concentration fields.

In order to provide more evidence for assessing the usefulness of equation (1), it was felt necessary to obtain further experimental data on nonuniform heating in which a much stronger circumferential variation in surface heat flux was provided than in [3]. This paper describes the experiments performed with this goal in mind and provides a detailed comparison with numerical computations based on equation (1).

2 Description of the Experimental Apparatus

A diagram of the experimental apparatus is shown in Fig. 1. Air is blown through a filter element and then through an acrylic tube. The tube sections have an i.d. of 9.5 cm with a 0.32-cm wall thickness, and are each 1.83 m long. Three to five tubes were used upstream of the heated section to obtain hydrodynamically fully developed flow. The hydrodynamic conditions in this unheated section and at the entrance to the heated region were investigated in detail by Friesen [11] to ensure that the flow was indeed hydrodynamically fully developed. In that study, measurements were made of the velocity profiles (pitot tube and single hot wire), the turbulence intensity distribution and turbulence spectra (single hot wire), the turbulent shear stress distribution (x-wire), and pressure gradients for different types of duct entrances and entry lengths. It was concluded that, for a range of Reynolds numbers (13,000–80,000) the flow was fully developed and thoroughly characterized for an L/D equal to or greater than about 56 (three unheated entry tubes).

The heated sections used acrylic tubes identical to the entry length tubes, except that a transparent, gold-coated polyester sheet (*Intrex*)[1] was glued on the inside using a plexiglass cement[2] (see Fig. 2). The gold coating served as the electrical resistance heating element, with a resistance of about 6 ohms/sq (ohms/sq is used as a measure of the electrical resistivity of a film since the resistance across a square is the same if it is 1 cm, or 1 m). These sheets had scribed electrical isolation lines at 30 deg (circumferential) intervals and individual electrodes at the flanges, which made it possible to individually heat the strips in any programmed fashion. The electrodes consisted of 0.09-mm aluminum foil glued to the gold surface of the *Intrex* with silver-loaded epoxy.

The a-c electrical power to each strip was individually controlled with a dimmer switch. Copper-constantan (40 gauge) thermocouples were mounted with epoxy cement on the outside of the polyester sheet through holes in the tube wall at various axial and circumferential positions (see Fig. 3), and 5 cm of urethane foam insulation was mounted on the outside of the tubes. The entire apparatus was wrapped with an aluminized mylar jacket to minimize radiation heat losses. This design allowed us to program in precise heat flux boundary conditions since there was very little heat loss and very little conduction in the thin walls of the acrylic tubes. A two-dimensional conduction analysis of the acrylic tube and urethane foam demonstrated that the thermocouples were at the inside wall temperature and that essentially all the local electrical heating in the gold film was transferred directly to the air flow in the tube. A small (usually much less than 4 percent) correction for the wall conduction was made to the data.

Referring back to Fig. 1, the thermocouple EMF's were fed via an HP-scanner directly to an on-line LSI-11 computer, which calculated the local Nusselt number for the prescribed heat flux distribution. This data acquisition system was programmed with individual thermocouple calibrations and performed the complete data reduction.

3 Mathematical Model for Nonuniform Circumferential Heating

The development of the thermal field in an asymmetrically heated turbulent pipe flow is described by the three-dimensional mean energy equation

$$U_z \frac{\partial T}{\partial z} = \frac{1}{r}\frac{\partial}{\partial r}\left[(\Gamma+\Gamma_{t,r})r\frac{\partial T}{\partial r}\right] + \frac{1}{r}\frac{\partial}{\partial \theta}\left[\frac{1}{r}(\Gamma+\Gamma_{t,\theta})\frac{\partial T}{\partial \theta}\right] \tag{2}$$

[1] *Intrex* is a trade name for a gold-coated polyester film manufactured by Sierracin/Sylmar Co., Sylmar, Calif.

[2] Weld-On-3 Solvent for Cementing Plexiglas, Industrial Polychemical Service, Gardena, Calif.

Nomenclature

c_p = specific heat
D = inner diameter
f_1 = factor defined by equation (A2)
f_2 = factor defined by equation (A5)
h = heat transfer coefficient
L = length of tube
$\dot{m}$ = mass flow rate
Nu = Nusselt number, hD/k
Pe = Peclet number, Re Pr
Pr = Prandtl number, $\mu c_p/k$
q'' = heat flux
R = electrical resistance
r = radial distance from center of tube
r_o = tube inner radius
Re = Reynolds number, $U_z D/\nu$
T = mean temperature
t = fluctuating temperature component
U = mean velocity component
u = fluctuating velocity component
V = voltage
w = width of a gold heating strip
y = distance from tube wall, $r_o - r$
y^+ = dimensionless distance, $(y/\nu)\sqrt{\tau_w/\rho}$
z = axial flow direction
β = temperature coefficient of resistivity
δ_G = local thickness of the gold film
Γ = thermal diffusivity
ν = kinematic viscosity
θ = circumferential direction
ρ_e = electrical resistivity

Subscripts

b = bulk mean
e = electrical power
L = heat loss
r = radial direction
t = turbulent
U = uniform circumferential heating
w = wall
θ = circumferential direction
∞ = fully developed

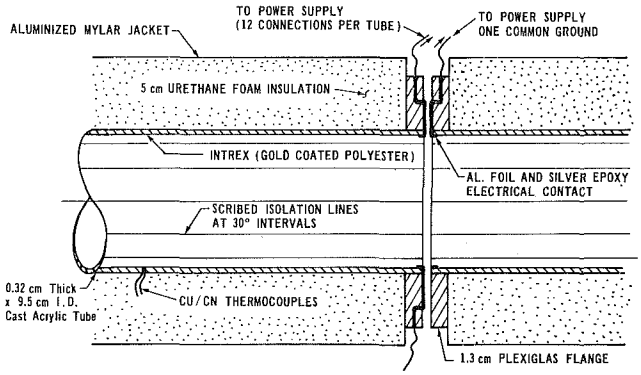

Fig. 2 Cross-section of a portion of the heated tube showing the electrical connections at the flange between two tube sections

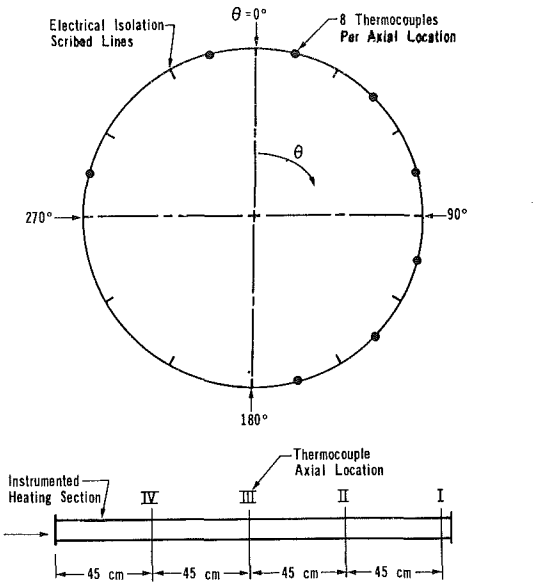

Fig. 3 Thermocouple positions on the heated tube and locations of the electrical isolation lines

The turbulent diffusivities have been introduced to replace the velocity-temperature correlations

$$-\overline{u_r t} = \Gamma_{t,r} \frac{\partial T}{\partial r} \quad ; \quad -\overline{u_\theta t} = \Gamma_{t,\theta} \frac{1}{r} \frac{\partial T}{\partial \theta} \tag{3}$$

The velocity field is assumed to be axisymmetric and fully developed at entry to the heated section and to be entirely unmodified by the wall heating. The mean velocity distribution $U_z(r)$ was obtained by solving the axial mean momentum equation using the following two-part, algebraic prescription of the (radial) turbulent viscosity across the pipe to express the turbulent shear stress $-\overline{u_r u_z}$ in terms of the mean velocity gradient

$$\nu_t = (0.41)^2 y^2 (1 - \exp(-y^+/26))^2 \left| \frac{dU}{dr} \right| \tag{4}$$

$$\nu_t = \nu \left(\frac{0.41\, y^+}{6} \right) \left(1 + \frac{r}{r_0} \right) \left[1 + 2 \left(\frac{r}{r_0} \right)^2 \right] \tag{5}$$

Here y denotes distance from the pipe wall ($y = r_o - r$). Equation (4) is used in the viscous sublayer and buffer zones; switchover to (5) is made as soon as equation (5) gives a smaller value of ν_t than (4). The radial thermal diffusivity is then obtained from

$$\Gamma_{t,r} = \nu_t / \mathrm{Pr}_t \tag{6}$$

where the turbulent Prandtl number is given by the following function of Peclet number

$$\mathrm{Pr}_t(r) = \frac{1}{\frac{1}{2\,\mathrm{Pr}_{t\infty}} + C\,\mathrm{Pe}_t \sqrt{\frac{1}{\mathrm{Pr}_{t\infty}}} - (C\,\mathrm{Pe}_t)^2 \left[1 - \exp\left(- \frac{1}{C\,\mathrm{Pe}_t \sqrt{\mathrm{Pr}_{t\infty}}} \right) \right]} \tag{7}$$

where

$$\mathrm{Pe}_t = (\nu_t/\nu)\mathrm{Pr} \ , \quad \mathrm{Pr}_{t\infty} = 0.86 \ , \quad C = 0.2$$

The model specification of equations (4–7) is that suggested by Kays and Crawford [12]. It may be regarded as a correlation of the experimental data for ν_t and $\Gamma_{t,r}$ in hydrodynamically fully developed pipe flow. This prescription of ν_t is superior to the ramp mixing-length profile used in the earlier study of [8], since that gave $\nu_t = 0$ at the pipe axis and (in order to provide a global compensation for that weakness) an excessively large level of turbulent viscosity in the range $0.2 \lesssim r/r_0 \lesssim 0.8$. We felt the changeover to the present specification was desirable to remove any possible effect of the prescribed radial profile of diffusivity on conclusions reached about the validity of equation (1). The adoption of a radius- and Peclet-number- dependent Pr_t (equation (7)) gives an improved description of the thermal boundary layer growth near the start of heating where the thermal layer is thin. Finally, the circumferential turbulent diffusivity is obtained from equation (1) where, following the practice in [8], the distribution of $\overline{u_r^2}/\overline{u_\theta^2}$ across the pipe is taken from a curve fit to Laufer's [10] measurements given in [8].

Numerical solutions to equation (2) have been obtained by adapting the finite-volume heat conduction code TEACH-C, [13]. The principal changes have been documented in a user's guide [14]. The additional modifications introduced in the present study are the incorporation of the newly prescribed $\nu_t(r)$ and $\mathrm{Pr}_t(r)$ and the generalization of the alternating sweep capability to include arbitrary circumferential spacing of nodes. The latter modification was necessary because of the abrupt variation in wall heat-flux distribution in the present top-half heating experiments (the computations of [8] had considered only the Black and Sparrow experiment, which was admirably resolved with a uniform θ spacing). In the calculations reported, Γ in equation (2) was assumed constant. However, one check run at Re = 47,400 using a temperature-dependent Γ in equation (2) showed only a 0.6 percent difference in the Nusselt number.

The mesh comprised 26 unequally spaced nodes in the radial direction and 26 circumferential nodes mapping the half circle $0 \le \theta \le \pi$, the greatest concentration being in the region of rapidly varying circumferential heat flux (see Fig. 7). The circumferential grid spacing was about 16 deg at $\theta = 0$ deg and decreased geometrically to 0.4 deg at $\theta = 90$ deg. The value of y^+ at the wall-adjacent cell was less than 1.0. Previous grid-dependency studies in the work reported in [8] showed this grid density to be adequate. The forward step size was initially $0.02 \times r_0$ gradually expanding to $1.0 \times r_0$ as the thermal layer approached full development. The computations have been performed on a PDP 11/34 with a typical CPU time of 10 min for a development length of 50 dia (compared to about 106 min before the modification to permit alternating sweep).

The above modified model is referred to as the nonisotropic turbulence model 3m in this paper. The original version of this nonisotropic turbulence model in [8], is referred to as model 3. Model 1m is the isotropic diffusivity model ($\Gamma_{t,\theta} =$

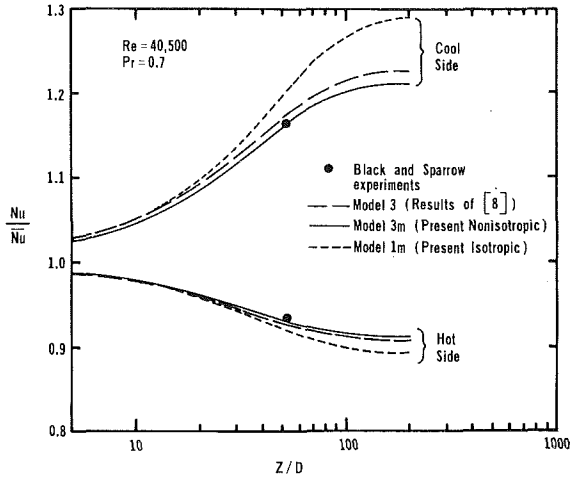

Fig. 4 Axial distribution of normalized Nusselt number at positions of maximum and minimum heating for the heat flux distribution used by Chieng and Launder [8]

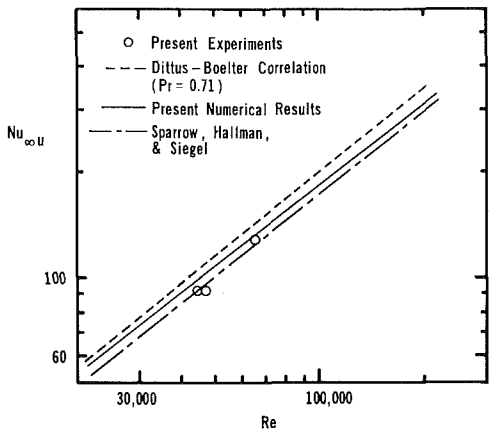

Fig. 5 Variation of fully developed Nusselt number with Reynolds number for uniform heating

$\Gamma_{t,r}$), and model 2m is the highly nonisotropic diffusivity model ($\Gamma_{t,\theta} = 10 \times \Gamma_{t,r}$).

It is of interest to compare the predictions of the original nonisotropic turbulence model 3 with those of the modified model 3m just described. The predictions for the Black and Sparrow near-cosinusoidal heating case presented in [8] are compared to the modified model on Fig. 4. It can be seen that the modifications introduced here do not change the basic conclusion of [8]; namely, that equation (1) model predicts the Black and Sparrow results better than does an assumption of isotropic diffusivities (model 1m).

4 Data Reduction and Error Analysis

The primary measurement in our experiment was the wall temperature distribution about the circumference at specific locations along the length of the asymmetrically heated tube. Before local heat transfer coefficients can be calculated, the local electrical heat input and local heat losses must be determined. The local heat transfer coefficient is calculated from

$$h(\theta,z) = \frac{q_e''(\theta,z) - q_L''(\theta,z)}{T_w(\theta,z) - T_b(z)} \tag{8}$$

where $q_e''(\theta,z)$ is the local electrical power input, $q_L''(\theta,z)$ is the local heat loss, and $T_w(\theta,z)$ and $T_b(z)$ are the local wall and bulk temperatures, respectively.

Calculation of $q_e''(\theta,z)$. In the Appendix, we define a

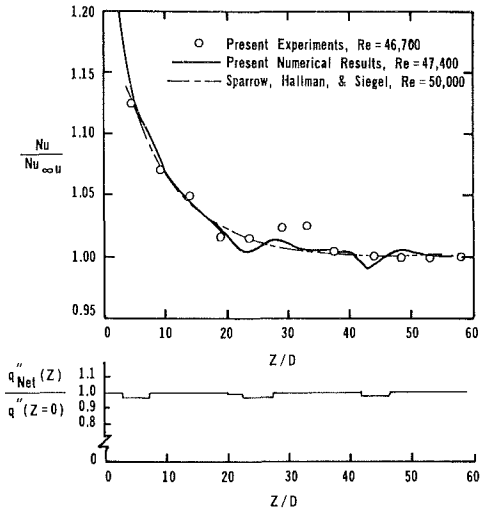

Fig. 6 Axial variation of normalized Nusselt number for the uniform heating case (upper graph), and axial variation of circumferentially averaged heat flux input to the computer code for uniform heating case, nominal Re = 46,700, $q_o'' = 245$ W/m^2 (lower graph)

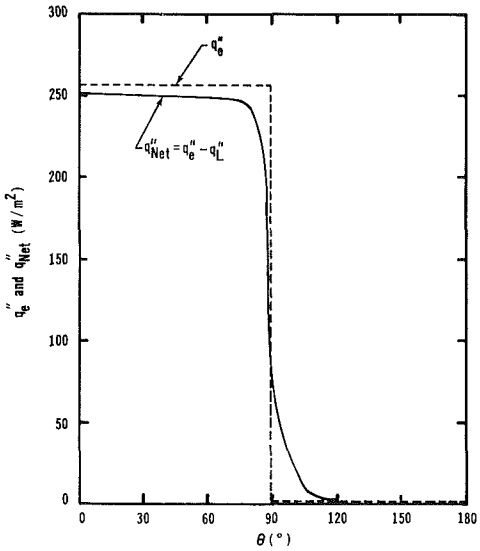

Fig. 7 Effects of two-dimensional conduction analysis on a 0.318-cm-thick by 9.525-i.d. cast acrylic tube with the heating film on the inside wall for the case of top-half heating

correction factor $f_2(\theta,z)$ which accounts for the effect of the small local variations in the thickness of the gold coating and the width of the strip on the local electrical heat flux input, $q_e''(\theta,z)$. The local heat transfer coefficient then becomes

$$h(\theta,z) = \frac{\overline{q_e''} f_2(\theta,z) - q_L''(\theta,z)}{T_w(\theta,z) - T_b(z)} \tag{9}$$

Now $f_2(\theta,z)$ was still an unknown because the local variations in gold coating width and thickness were not measured quantities. Instead, $f_2(\theta,z)$ was determined from experimental data by using our runs for the uniform heating boundary condition. By assuming that $h(\theta,z) = h_\infty$ = a constant for fully developed flow beyond z/D of 40, $f_2(\theta,z)$ could be determined from the equation (9).

The first estimate for h_∞ was made assuming $f_2(\theta,z) = 1.0$ and calculating $h(\theta,z)$ at each thermocouple location for the fully developed flow region

$$h(\theta,z) = \frac{\overline{q_e''} - q_L''(\theta,z)}{T_w(\theta,z) - T_b(z)} \tag{10}$$

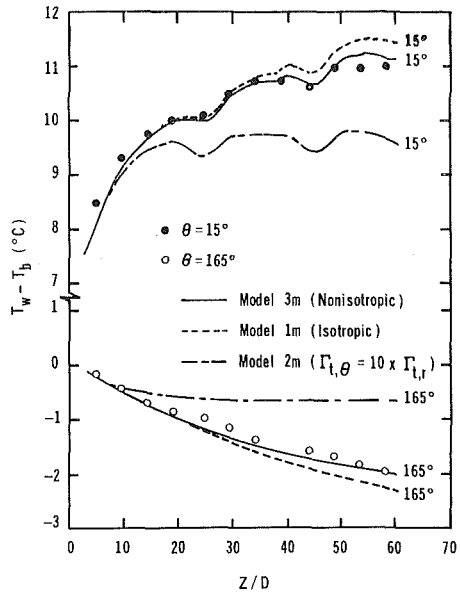

Fig. 8(*a*) Comparisons of the present experiments with predictions for the top-half heating conditions, nominal Re = 47,400

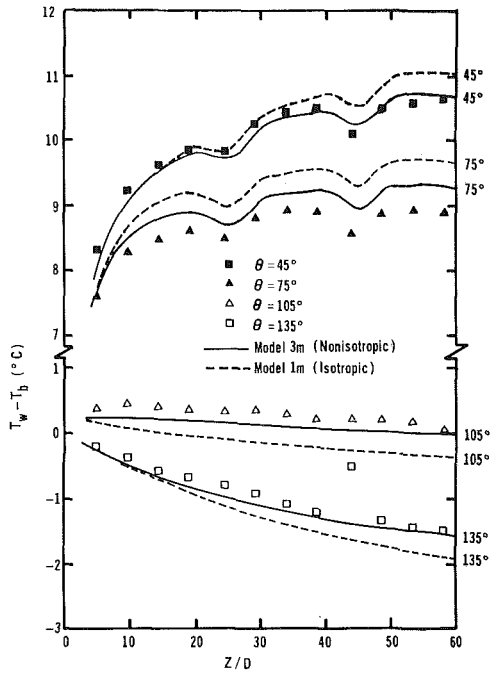

Fig. 8(*b*) Comparisons of present experiments and predictions for the top-half heating conditions, nominal Re = 47,400

Then

$$h_{\infty}^{(1)} = \frac{\sum^{n} h(\theta,z)}{n} \tag{11}$$

where n is the number of thermocouples around the circumference. Using this first estimate of h_{∞}, the first estimates of $f_2(\theta,z)$ could be obtained from equation (9). A second iteration could then be performed, if necessary. This "in-situ" calibration technique of the gold film using the fully developed region of the uniformly heated pipe permitted us to obtain very high-accuracy results even with the slight nonuniformities present in the commercially available Intrex

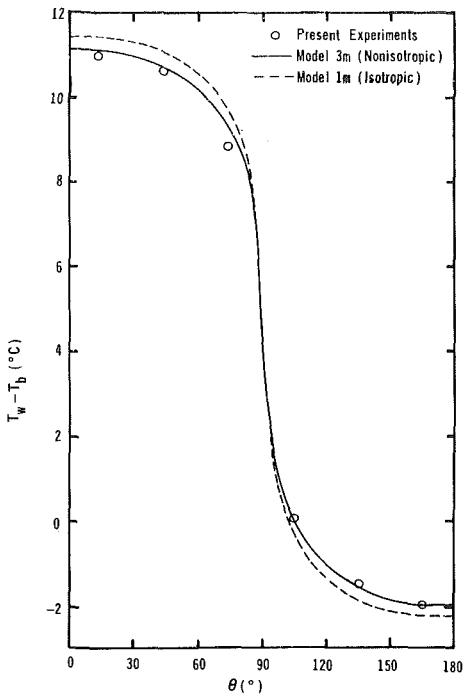

Fig. 9 Circumferential distribution of wall minus bulk temperatures for top-half heating Z/D = 58.2, nominal Re = 47,400

film. The full range of $f_2(\theta,z)$ was 0.93 to 1.04, but typically the values were in the range of 0.98 to 1.02. Using these f_2 values, q_e'' was then calculated from equation (A6).

Calculation of $q_L''(\theta,z)$. The local heat loss due to radial and circumferential conduction was calculated using a two-dimensional, finite-element heat conduction code. The conduction code utilized 210 elements—2 rows of 42 elements in the cast acrylic tube wall and 3 rows of 42 elements in the urethane foam insulation. The inner-wall boundary conditions were the measured wall temperatures and the outer-wall boundary condition was the sum of a circumferentially varying, free-convection heat transfer coefficient and an effective heat transfer coefficient for radiation.

Also contained in q_L were local heat losses due to radiant exchange between the heated and unheated surfaces of the inner wall. A radiation analysis using the emissivity value $\epsilon = 0.15$ (the manufacturer recommended 0.10-0.20), showed that the maximum local internal radiation heat loss was about 0.014 q_e'' for the case of top-half heating. The value for q_L'' (considering all mechanisms for local heat losses) varied up to about 0.04 q_e''. The calculation of q_L'' was not very sensitive to the outside wall free-convection boundary condition since the heated tube was well insulated.

Calculation of $T_b(z)$. The local bulk temperature was calculated from

$$T_b(z) = \frac{1}{\dot{m}c_p}(\dot{q}_e - \dot{q}_L)\left(\frac{z}{L}\right) + T_{b(\text{in})}$$

where $\dot{m}$ is the mass flow rate, $T_{b(\text{in})}$ is the bulk temperature at the inlet of the heated tube, and $\dot{q}_e$ and $\dot{q}_L$ are the heat flows for the entire tube length; $\dot{q}_L$ in this case contains only the heat loss from the outer surface of the tube insulation.

It may be appropriate to note here that as $T_b(z)$ increases along the length of the tube, the viscosity increases and the Reynolds number decreases proportionally. For our experiments where the exit bulk temperature was typically 3-6°C above the inlet bulk temperature, the Reynolds number decreased by only about 1 percent, and its effect is thus negligible. In our data reduction, we nevertheless calculate $h(\theta,z)$ (and $\text{Nu}(\theta,z) \equiv h(\theta,z)D/k$) using properties based on

the local bulk temperature, and present the data as a ratio $Nu/Nu_{\infty U}$, where $Nu_{\infty U}$ for uniform heating is based on the local Reynolds number. The value of $Nu_{\infty U}$ is assumed to vary as $Re^{.8}$. By presenting the data in this normalized manner, most of the effects due to varying Reynolds number are eliminated. In our data reduction, we also correct $(T_w - T_b)$ by the local $Re^{.8}$ factor when this temperature difference is plotted.

It should be noted that the nominal Re quoted for a given run is based on the properties at the entrance to the heated section.

Uncertainties in the Results. The uncertainties in our experimental results were determined following the procedures recommended in [15]. The measurements which were responsible for the largest uncertainties (all considered "accidental, single-sample errors") were the velocity measurements with the pitot tube (± 1.5 percent), the heating-strip resistance measurements at T_{Ref} (± 1 percent), the thermocouple measurements of the wall temperatures (± 0.15°C), and the air bulk temperature measurements (± 0.30°C).

The final estimates of the uncertainties in the parameters used in the plots (quoted for 20:1 odds) are:

Reynolds number	± 1.5 percent
$[T_w(\theta,z) - T_b(z)]$	± 0.34°C
Nusselt number	± 4.5 percent
$Nu/Nu_{\infty U}$	± 5.0 percent

5 Results and Discussion

Uniform Heating Results. An experiment was first run with a uniform heat flux boundary condition (with a fully developed velocity field at the entrance of the heated section), and the results were compared with generally accepted experimental and theoretical results of previous workers. These results are shown in Figs. 5 and 6. Note that from Fig. 5 the present numerical results for the fully developed Nu, obtained using equations (4–7), are in generally close agreement with the theoretical result of Sparrow et al. [16] and with our data. (Our experimetnal result at Re = 46,700 does, however, lie 8 percent below the numerical computation, a discrepancy which did not, for some unknown reason appear in the test with asymmetric heating.) The data and theory of [16] lie 15–20 percent below the Dittus-Boelter correlation, indicating that the Dittus-Boelter correlation is probably too high for air, as is widely acknowledged.

Results for the thermal development are shown in Fig. 6(*a*). These normalized Nusselt numbers can be seen to show satisfactory agreement between the present experiments and our computations as well as with the theory of Sparrow et al. [16]. On Fig. 6(*a*), our numerical results were obtained using circumferentially uniform heating but using the nonuniform axial heating condition shown in Fig. 6(*b*). This latter heat flux boundary condition is directly proportional to the $f_2(\theta,z)$ factor (previously discussed) and provides the best approximation to our actual experimental conditions. Note that the four data points for $43 < z/D < 60$ for the present experiments were forced to lie exactly on $Nu/Nu_{\infty U} = 1.0$. These data were all assumed to be fully developed and were used in the data reduction scheme to correct the other data points. As a result, the normalization of the Nu using $Nu_{\infty U}$ "suppresses" the 8 percent difference between our data and the computational results referred to above.

Top-Half Heating Results. Heating the top half of the tube (-90 deg $\le \theta \le 90$ deg) was achieved by applying electrical current through the six upper Intrex strips shown in Fig. 3. The resultant step profile of q_e'' is shown in Fig. 7. After taking into account radial and circumferential conduction in the tube wall and insulation, and also considering radiation transfer between surfaces on the inner wall, the *net* heat flux into the flow, q''_{net}, was calculated and is also shown in Fig. 7. As expected, the net heating profile gives a good approximation to a step heating profile. This heat flux profile is used in calculating Nusselt numbers from the experimental data, as previously discussed, and also serves as the heat flux boundary condition for the numerical computations.

Figures 8(*a*) and 8(*b*) show the full set of experimental data obtained for the top-half heating run. One can see that the temperature field is not yet fully developed at a $z/D = 60$, as expected for nonuniform heating [8]. The $(T_w - T_b)$ data for $\theta = 15$ deg (the thermocouple position closest to the top of the tube) and $\theta = 165$ deg (closest to the bottom) are compared to the three theoretical models in Fig. 8(*a*). The data at these positions are probably the most reliable, because they are least affected by tube-wall conduction. As a result, they offer the most sensitive test of the physical models of diffusion. The basic $(T_w - T_b)$ data can be seen to agree more closely with the nonisotropic diffusivity model 3m using equation (1) than with the isotropic modle 1m, particularly at large z/D.

For interest, computational results are also shown for a 10:1 ratio of diffusion coefficients (model 2m), a situation that had been considered in [8], following a suggestion by Black and Sparrow that such a ratio seemed to be indicated by their data close to the wall. As in [8], this model gives completely erroneous trends with fully developed flow being reached at z/D of only about 20.

In Fig. 8(*b*), the data for the thermocouples at 45, 75, 105, and 135 deg are compared in the numerical results for the isotropic model 1m and nonisotropic model 3m. Once again the data agree better with the nonisotropic model 3m. Crossplots of the data and theoretical curves are shown on Fig. 9 for $z/D = 58.2$. The better agreement of the data with the nonisotropic model 3m is again apparent.

It is interesting to note that the predictions of the wall temperature in Fig. 8(*b*) at 75 deg are slightly above, while the predictions at 105 deg are slightly below the experimental data. This suggests that the circumferential diffusion of turbulent heat flux in the turbulent transport equation, a process implicitly neglected in arriving at equation (1), may be significant in this region of rapidly varying heat flux (see Fig. 7). However, no definitive conclusion is possible, because this is also a region where the experimental uncertainties due to wall conduction are largest.

6 Conclusions

A set of experiments has been run to try to assess the adequacy of the nonisotropic diffusion model (equation (1)) for representing heat diffusion processes in pipe flow with strongly nonuniform circumferential heating. The use of a gold-coated polyester sheet to provide the electrically heated boundary has proved to be particularly suitable for the study of convective heat transfer in tubes with a circumferentially varying heat input. It has allowed the establishment of an essential step change in heat input with only minor corrections needed to account for conduction effects in the tube walls and heat losses through the polyurethane insulation.

Numerical simulations were made of the present experiments and of the earlier less severely asymmetric heating data of Black and Sparrow [3] employing equation (1) in conjunction with radial profiles of turbulent viscosity and Prandtl number obtained from axisymmetric data. The computations show clearly that equation (1) gives a more satisfactory prediction of the wall temperatures than is obtained by assuming isotropic diffusivities.

Further experiments would be useful in which the asymmetric heating extended far enough downstream for the fully developed state to be reached i.e., $z/D \sim 200$. Our computations indicate (in conformity with those of [8]) that the fully developed levels of Nu are more sensitive to the

nonisotropy of the diffusion coefficient than those in the developing region.

Acknowledgments

The authors gratefully acknowledge the support of the National Science Foundation for this research under Grant CME-77-27613.

References

1 Launder, B. E., "Heat and Mass Transport," *Topics in Applied Physics: Vol. 12 Turbulence*, Chapter 6, edited by P. Bradshaw, Springer, 1976.

2 Quarmby, A., and Quirk, R., "Measurements of the Radial and Tangential Eddy Diffusitivites of Mass in Turbulent Flow in a Plain Tube," *International Journal of Heat and Mass Transfer*, Vol. 15, 1972, p. 2309.

3 Black, A. W., and Sparrow, E. M., "Experiments on Turbulent Heat Transfer in a Tube with Circumferentially Varying Thermal Boundary Conditions," ASME JOURNAL OF HEAT TRANSFER, Vol. 89, 1967, pp. 258-268.

4 Knowles, G. R., and Sparrow, E. M., "Local and Average Heat Transfer Characteristics for Turbulent Airflow in an Asymmetrically Heated Tube," ASME JOURNAL OF HEAT TRANSFER, Vol. 101, 1979, pp. 635-641.

5 Baughn, J. W., Hoffman, M. A., Launder, B. E., and Samaraweera, D. S. A., "Three-Dimensional Turbulent Heat Transport in Pipe Flow: Experiment and Model Validation," ASME Paper 78-WA/HT-15, Dec. 1978.

6 Chan, A. L., Baughn, J. W., and Hoffman, M. A., "Nonuniform Circumferential Heat Flux Experiments in a Circular Tube," ASME Paper 75-WA/HT-52, Nov.-Dec. 1975.

7 Schmidt, R. R., and Sparrow, E. M., "Turbulent Flow of Water in a Tube with Circumferentially Nonuniform Heating, With and Without Buoyancy," ASME JOURNAL OF HEAT TRANSFER, Vol. 100, 1978, pp. 403-409.

8 Chieng, C. C., and Launder, B. E., "On the Calculation of Turbulent Transport in Flow Through an Asymmetrically Heated Pipe," *Numerical Heat Transfer*, Vol. 2, 1979, pp. 359-371.

9 Gartner, D., Johanssen, K., and Ramm, H., "Turbulent Heat Transfer in a Circular Tube with Circumferentially Varying Thermal Boundary Conditions," *International Journal of Heat and Mass Transfer*, Vol. 17, 1974, pp. 1003-1013.

10 Laufer, J., "The Structure of Turbulence in Fully Developed Pipe Flow," NACA Rep. 1174, 1954.

11 Friesen, T., "Design and Testing of an Apparatus which Provides *Hydrodynamically Fully Developed Flow in a Circular Duct*," *Project Report*, Department of Mechanical Engineering, University of California, Davis, Mar. 1981.

12 Kays, W. M., and Crawford, M. E., *Convective Heat and Mass Transfer*, 2nd ed., McGraw-Hill, 1980.

13 Gosman, A. D., Launder, B. E., Newton, P. A., and Reece, G. J., "A User's Guide to the TEACH-C Computer Program," Rep. CAL-CO-77, Mechanical Engineering Department, Imperial College, Feb. 1977.

14 Chieng, C. C., and Launder, B. E., "A Summary Guide to TEACH-C 3DCONV," Department of Mechanical Engineering, University of California, Davis, Aug. 1979.

15 Kline, S. J., and McKlintock, F. A., "Describing Uncertainties in Single-Sample Experiments," *Mechanical Engineering*, Vol. 75, No. 1, Jan. 1953, pp. 3-8.

16 Sparrow, E. M., Hallman, T. M., and Siegel, R., "Turbulent Heat Transfer in the Thermal Entrance Region of a Pipe with Uniform Heat Flux," *Applied Science Research*, Sec. A, 7, 1957, pp. 37-52.

APPENDIX

Correction Technique for Slight Nonuniformities in the Gold Coating

The gold coating on the *Intrex* film had slight variations in thickness and hence in local resistance. In addition, when the longitudinal lines were scribed on the gold coating to subdivide it into strips, there were inevitably some small variations in the widths of the strips. The following technique was used to correct the local electrical heat flux inputs, $q_e''(\theta,z)$, for use in the calculation of the local $h(\theta,z)$ as described in the text.

The measurements available to calculate $q_e''(\theta,z)$ were the voltage, $V(\theta)$, across the length of the gold coated strip (at position θ); the local wall temperatures, $T_w(\theta,z)$; the temperature coefficient of resistivity, β; and the total resistance, $R(T_{\text{ref}})$, in ohms, measured across the length of the strip. The measurement of $R(T_{\text{ref}})$ was made when the strips were not being heated and at uniform temperature T_{ref}. Thus

$$q_e''(\theta,z) = \frac{V(\theta)^2}{R^2(T_{\text{ref}})[1+\beta(\bar{T}-T_{\text{ref}})]^2} \frac{\rho_e(T(\theta,z))}{w^2(\theta,z)\,\delta_G(z)} \tag{A1}$$

where $\bar{T}$ is the average temperature of the heated strip, $\rho_e(T(\theta,z))$ is the local resistivity of the gold coating, $\delta_G(z)$ is the local thickness of the gold coating, and $w(\theta,z)$ is the local width of the gold coating strip. By introducing a factor $f_1(\theta,z)$, representing the relative local thickness of the gold coating for a given strip at an angle, θ, such that

$$\frac{1}{L}\int_0^L f_1(\theta,z)\,dz = 1.0 \tag{A2}$$

where L is the length of the strip, we can then write

$$\frac{\rho_e(T)}{\delta_G(z)} = \frac{\bar{w}}{L} R(T_{\text{ref}})\,[1+\beta(T_w(\theta,z)-T_{\text{ref}})]\,f_1(\theta,z) \tag{A3}$$

Thus,

$$q_e''(\theta,z) = \frac{V(\theta)^2}{R(T_{\text{ref}})} \frac{(\bar{w}/L)[1+\beta(T_w(\theta,z)-T_{\text{ref}})]}{w^2(\theta,z)[1+\beta(\bar{T}_w-T_{\text{ref}})]^2} f_1(\theta,z) \tag{A4}$$

If we let the factor $f_2(\theta,z)$ include both relative variations in local thickness and width of the gold coating such that

$$\frac{1}{L}\int_0^L f_2(\theta,z)\,dz = 1.0\,;\, f_2(\theta,z) = \frac{f_1(\theta,z)\,\bar{w}^2}{w^2(\theta,z)} \tag{A5}$$

then

$$q_e''(\theta,z) = \frac{V(\theta)^2 f_2(\theta,z)}{R(T_{\text{ref}})L\bar{w}} \frac{[1+\beta(T_w(\theta,z)-T_{\text{ref}})]}{[1+\beta(\bar{T}_w-T_{\text{ref}})]^2} \tag{A6}$$

where $\bar{w}$ is the average width of the strip.

Heat Convection in a Horizontal Curved Pipe

L. S. Yao
Department of Mechanical and Aerospace Engineering, Arizona State University, Tempe, Ariz. 85287
Mem. ASME

Thermally and hydrodynamically developing flow in heated horizontal curved pipes is analyzed. The perturbation solution is quantitatively valid only in a small region near the pipe inlet. The solution, however, provides information about the physical importance of centrifugal force and buoyancy on the developing flow. It also reveals the length and the velocity scales for the downstream regions where the secondary flow can not be treated as a small perturbation. The relative importance of centrifugal force and buoyancy is determined by the ratio of the Dean number and the Grashof number.

1 Introduction

Heat convection in curved tubes is of considerable interest in many applications. The induced secondary flow in curved tubes causes a significant azimuthal variation in the heat flux and delays transition to turbulent flow. It appears that there is no available criterion to judge the relative importance of free convection to that of centrifugal forces for a developing flow. Also, the appropriate parameters to correlate data are not known at present. This paper will address these points. A comprehensive review of curved-pipe flows can be found in [1, 2] and will not be repeated here.

It is well known that the secondary flow induced by centrifugal force in a curved pipe behaves like a local stagnation-point flow near the outer bend where the local maximum heat flux occurs. Near the inner bend, the secondary flow looks like a "reverse" stagnation-point flow, and the result is a local minimum heat flux. On the other hand, centrifugal force is not the only important body force in heated curved pipes. It has been demonstrated that, for a fully developed, curved-pipe flow heated with nearly constant wall-heat flux, the buoyancy force can be the dominant body force [3, 4]. The centrifugal force and the buoyancy force are characterized by a Dean number, D, and by the product of Grashof number, Gr, and Reynolds number, Re, respectively. Relatively few studies [5] have been reported which identify the importance of buoyancy in the entry region of curved pipes. A perturbation solution is presented in this paper which describes the flow development and the variation of heat flux in the entry region of a heated curved pipe. The pipe is assumed to be connected to a large chamber. A sharp reduction of the flow passage between the chamber and the curved pipe induces a nearly uniform velocity profile at the entrance of the pipe. The fluid temperature at the inlet of the pipe, T_{in}, is also nearly uniform. The pipe wall is held at a constant temperature, T_w, which is warmer than T_{in}.

The perturbation solution is only valid within a small region near the pipe inlet. Its asymptotic form, however, reveals the essential physics of the developing flow, the relative importance of centrifugal force and buoyancy, and the axial azimuthal variation of the local heat flux. Furthermore, it provides information about the axial length scales, and the associated velocity scales of several downstream regions where neither centrifugal force nor buoyancy can be treated as a perturbed quantity.

One of the interesting findings from the perturbation solutions is that the local maximum wall heat flux occurs at the inner bend near the inlet. This is due to the effect of the local accelerating flow over the convex surface (inner bend) before the secondary flow becomes influential. Downstream, the local maximum heat flux point gradually moves to the region between the outer bend and the bottom of the pipe. The asymptotic position depends on the ratio, D/Gr. The asymptotic form of the perturbation solution also shows that an almost uniform flow is induced in the core region of the pipe by the displacement effect of the boundary layer. The phenomenon is similar to that near the top of a heated cylinder [6]. The momentum of the flow is low close to the "reverse" stagnation point which, in turn, is near the location where the local minimum wall heat flux occurs. The fluid is sucked into the almost uniform crossflow from the area of low local wall heat flux to the region of high local heat flux. This flow is analagous to the thermal plume above a heated cylinder [6]. The model of two colliding secondary boundary layers near the reverse stagnation point, suggested by some investigators, is not physically sound.

2 Governing Equations

Near the inlet, the appropriate characteristic length is the radius of the pipe, a, and the velocities are scaled by the uniform inlet velocity, W_{in} (Fig. 1). The pressure is nondimensionalized by ρW_{in}^2 where ρ is the density. The dimensionless temperature is defined as

$$H=\frac{T-T_{in}}{T_w-T_{in}} \tag{1}$$

The dimensionless equations of motion and energy with the Boussinesq approximation in toroidal coordinates become

$$\frac{1}{r}\frac{\partial(rU)}{\partial r}+\frac{1}{r}\frac{\partial V}{\partial\psi}\frac{1}{1+\alpha\cdot r\cdot\sin\psi}\frac{\partial W}{\partial\theta_1}+\alpha\cdot\frac{U\cdot\sin\psi+V\cdot\cos\psi}{1+\alpha\cdot r\cdot\sin\psi}=0, \tag{2a}$$

$$U\frac{\partial U}{\partial r}+\frac{V}{r}\frac{\partial U}{\partial\psi}+\frac{W}{1+\alpha\cdot r\cdot\sin\psi}\frac{\partial U}{\partial\theta_1}-\frac{V^2}{r}-\alpha\cdot\frac{W^2\cdot\sin\psi}{1+\alpha\cdot r\cdot\sin\psi}-\epsilon\cdot(H-H_c)\cdot\cos\psi$$
$$=-\frac{\partial P}{\partial r}-\frac{1}{\mathrm{Re}}\left\{\left(\frac{1}{r}\frac{\partial}{\partial\psi}+\frac{\alpha\cdot\cos\psi}{1+\alpha\cdot r\cdot\sin\psi}\right)\left(\frac{\partial V}{\partial r}+\frac{V}{r}-\frac{1}{r}\frac{\partial U}{\partial\psi}\right)+\frac{1}{(1+\alpha\cdot r\cdot\sin\psi)^2}\frac{\partial U}{\partial\theta_1}\left[\frac{\partial U}{\partial\theta_1}-\alpha\cdot\sin\psi\cdot W-(1+\alpha\cdot r\cdot\sin\psi)\frac{\partial W}{\partial r}\right]\right\}, \tag{2b}$$

Contributed by the Heat Transfer Division for publication in the JOURNAL OF HEAT TRANSFER. Manuscript received by the Heat Transfer Division April 20, 1983.

Table 1 Coefficients for wall heat flux and shear stress

A.

$f_0''(0) = 0.4696$

$f_{10}''(0) = -0.7044$, $f_{11}''(0) = 0.0641$, $f_2''(0) = -0.7679$

$\beta_0 = 1.2167$, $\beta_1 = -0.6084$, $\beta_3 = -1.2231$

B.

Pr	$h_0'(0)$	$h_{10}'(0)$	$h_{11}'(0)$	$h_{20}'(0)$
0.1	−0.1980	0.09895	−0.0168	−0.0171
1.0	−0.4696	0.2348	−0.0641	−0.0468
10.0	−1.0295	0.5149	−0.1782	−0.0677

C.

Pr	$f_3''(0)$	$f_4''(0)$	β_3
0.1	0.0916	0.4350	3.9454
1.0	0.0468	0.2907	0.8534
10.0	0.0209	0.1867	0.0996

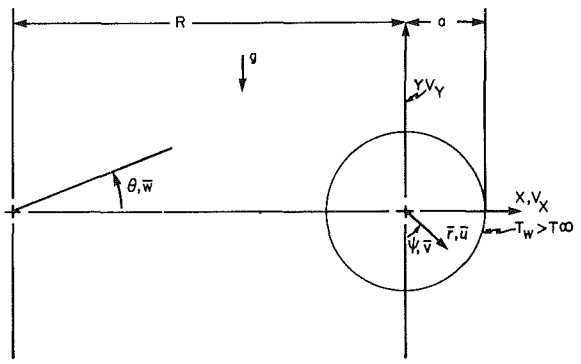

Fig. 1 Physical model and coordinates

$$U\frac{\partial V}{\partial r}+\frac{V}{r}\frac{\partial V}{\partial \psi}+\frac{W}{1+\alpha\cdot r\cdot\sin\psi}\frac{\partial V}{\partial \theta_1}+\frac{UV}{r}-\alpha\cdot\frac{W^2\cdot\cos\psi}{1+\alpha\cdot r\cdot\sin\psi}+\epsilon\cdot(H-H_c)\cdot\sin\psi$$
$$=-\frac{1}{r}\frac{\partial P}{\partial \psi}+\frac{1}{\mathrm{Re}}\left\{\left(\frac{\partial}{\partial r}+\frac{\alpha\cdot\sin\psi}{1+\alpha\cdot r\cdot\sin\psi}\right)\left(\frac{\partial V}{\partial r}+\frac{V}{r}-\frac{1}{r}\frac{\partial U}{\partial \psi}\right)+\frac{1}{(1+\alpha\cdot r\cdot\sin\psi)^2}\cdot\frac{\partial V}{\partial \theta_1}\left[\frac{\partial V}{\partial \theta_1}-\alpha\cdot\sin\psi\cdot W-\frac{1+\alpha\cdot r\cdot\sin\psi}{r}\frac{\partial W}{\partial \psi}\right]\right\},\quad (2c)$$

$$U\frac{\partial W}{\partial r}+\frac{V}{r}\frac{\partial W}{\partial \psi}+\frac{W}{1+\alpha\cdot r\cdot\sin\psi}\frac{\partial W}{\partial \theta_1}+\alpha\cdot\frac{W(U\sin\psi+V\cos\psi)}{1+\alpha\cdot r\cdot\sin\psi}$$
$$=-\frac{1}{1+\alpha\cdot r\cdot\sin\psi}\frac{\partial P}{\partial \theta_1}+\frac{1}{\mathrm{Re}}\left\{\left(\frac{\partial}{\partial r}+\frac{1}{r}\right)\left[\frac{\partial W}{\partial r}+\frac{1}{1+\alpha\cdot r\cdot\sin\psi}\left(\alpha\cdot\sin\psi\cdot W-\frac{\partial U}{\partial \theta_1}\right)\right]+\frac{1}{r}\frac{\partial}{\partial \psi}\left[\frac{1}{r}\frac{\partial W}{\partial \psi}+\frac{1}{1+\alpha\cdot r\cdot\sin\psi}\left(\alpha\cdot\cos\psi\cdot W-\frac{\partial V}{\partial \theta_1}\right)\right]\right\},\quad (2d)$$

$$U\frac{\partial H}{\partial r}+\frac{V}{r}\frac{\partial H}{\partial \psi}+\frac{W}{1+\alpha\cdot r\cdot\sin\psi}\frac{\partial H}{\partial \theta_1}=\frac{1}{\mathrm{Pr}\cdot\mathrm{Re}}\cdot\frac{1}{r\cdot(1+\alpha\cdot r\cdot\sin\psi)}.$$

Nomenclature

a = radius of the pipe, Fig. 1
D = $\alpha\cdot\mathrm{Re}^2$, Dean number
f = stream functions, equation (9)
g = gravitational acceleration
Gr = Grashof number, equation (3)
h,H = temperature functions, equations (1, 9)
H_c = dimensionless temperature at $\bar{r}=0$
Nu = Nusselt number, equation (13)
P,p = pressure
r = radial coordinate, Fig. 1
R = Radius of curvature of curved pipes
Re = Reynolds number, equation (3)
S = distance measured from the inlet along $\bar{r}=0$
T = temperature
U,V,W,u,v,w = velocity components, Fig. 1
X,Y = coordinates, Fig. 1
y = coordinates, equation (6)
α = a/R, curvature ratio
β = constants, equations (24), (26) and Table 1
γ = thermal expansion coefficient, equation (2)
δ = $\mathrm{Re}^{1/2}$
ϵ = $\mathrm{Gr}/\mathrm{Re}^2$, equation (3)
η = Blasius variable, equation (9)
θ = coordinate, Fig. 1
ν = kinematic viscosity, equation (3)
τ = wall shear, equations (15, 17)
ψ = coordinate, Fig. 1

Superscripts

prime = derivative with respect to η

Subscripts

numbers = indicate the expansion order
in = inlet condition
w = wall condition

$$\left\{\frac{\partial}{\partial r}\left[r\cdot(1+\alpha\cdot r\cdot\sin\psi)\cdot\frac{\partial H}{\partial r}\right]+\frac{\partial}{\partial\psi}\right.$$

$$\left.\left[\frac{1+\alpha\cdot r\cdot\sin\psi}{r}\frac{\partial H}{\partial\psi}\right]+\frac{\partial}{\partial\theta_1}\left[\frac{r}{1+\alpha\cdot r\cdot\sin\psi}\frac{\partial H}{\partial\theta_1}\right]\right\}, \quad (2e)$$

where

$$\theta_1 = \frac{R\cdot\theta}{a},$$

$$\alpha = \frac{a}{R},$$

$$\epsilon = \frac{\mathrm{Gr}}{\mathrm{Re}^2}, \quad (3)$$

$$\mathrm{Gr} = \frac{\beta g\cdot(T_w - T_{\mathrm{in}})\cdot a^3}{\nu^2},$$

$$\mathrm{Re} = \frac{W_{\mathrm{in}}\cdot a}{\nu}$$

and H_c is the temperature along $r=0$.

The entry conditions impose a uniform inlet axial velocity and temperature; the reference pressure at the inlet is set equal to zero. It may be noted that, in the absence of viscosity and thermal conductivity, the exact solution of (2) satisfying the inlet condition and a slip wall condition is

$$W=1, U=V=H=0, P=\ln(1+\alpha\cdot r\cdot\sin\psi) \quad (4)$$

where ln denotes the natural logarithm.

3 Solution

As the fluid flows into the pipe, viscous forces are confined to the thin boundary layer near the pipe wall. The temperature gradient is established inside the thermal boundary layer and induces buoyancy forces. The ratio of the thickness of the thermal boundary layer to that of the momentum boundary layer depends on the Prandtl number. Viscous forces and heat conduction can be ignored outside the boundary layer: the flow is inviscid and isothermal in the central region of the pipe. The inviscid flow is accelerated in the central region of the pipe due to the displacement effect of the boundary layer, and fluid particles are pushed away from the wall toward the center of the pipe. Simultaneously, the buoyancy force tends to accelerate the boundary-layer flow so that the fluid is drawn into the boundary layer along the lower half of the pipe wall and is pushed away from the upper half of the pipe wall. This induces a uniform downward flow in the core of the pipe. Similarly, the pressure gradient induced by the centrifugal forces on the cross section of the pipe generates a uniform horizontal flow from the inner bend to the outer bend. The effects of forced convection, natural convection, and the centrifugal forces compete among themselves as the flow develops in the entry region of heated curved pipes.

The effects of buoyancy and centrifugal forces are accumulative. Therefore, the magnitude of the induced secondary flow is small near the pipe inlet, but grows downstream. The analysis shows that the development of the boundary layer and its displacement effect on the inviscid flow near the entrance can be obtained by perturbing the solution for developing flow in an unheated straight pipe. The perturbation solution is only valid within a small region that is a few radii from the pipe inlet; however, it clearly demonstrates the interaction of buoyancy and centrifugal forces. It also provides the length scales and velocity scales further downstream where neither buoyancy nor centrifugal forces are small.

Zeroth-Order Inviscid Flow. The solution of the inviscid core flow can be obtained by expanding the dependent variables in an asymptotic series, such as

$$W = W_0 + \delta\cdot[W_{10} + \alpha W_{11} + \epsilon W_{12} + \ldots] + \ldots, \text{ etc.} \quad (5)$$

where W_{10} is due to the displacement effect of the forced-convection boundary layer, W_{11} is due to the secondary boundary layer induced by the centrifugal forces, and W_{12} is due to the natural convection. The governing equations of the zeroth-order inviscid core flow can be obtained by taking limit as $\mathrm{Re}\to\infty$ in equations (2). The zeroth-order solutions which satisfy the uniform inlet velocity and temperature conditions and the slip condition at the pipe wall are just the undisturbed flow given in equation (4).

Zeroth-Order Boundary Layer. Near the wall, viscous forces and heat conduction normal to the wall are important. The normal coordinate y is stretched to reflect this physical fact. Accordingly, we introduce inner variables, as in the classical boundary-layer theory

$$y = 1 - \delta r, U = -\delta u, W = w(y,\psi,\theta_1), \text{etc.} \quad (6)$$

A combination of equations (2) and (6), after neglecting the smaller order terms, yields

$$\frac{\partial u}{\partial y} + \frac{\partial v}{\partial\psi} + \frac{1}{1+\alpha\cdot\sin\psi}\frac{\partial w}{\partial\theta_1} + \alpha\cdot\frac{v\cdot\sin\psi}{1+\alpha\cdot\sin\psi} = 0, \quad (7a)$$

$$u\frac{\partial v}{\partial y} + v\frac{\partial v}{\partial\psi} + \frac{w}{1+\alpha\cdot\sin\psi}\frac{\partial v}{\partial\theta_1}$$

$$-\alpha\cdot\frac{w^2\cdot\cos\psi}{1+\alpha\cdot\sin\psi} + \epsilon\cdot h\cdot\sin\psi = -\frac{\alpha\cdot\cos\psi}{1+\alpha\cdot\sin\psi} + \frac{\partial^2 v}{\partial y^2} \quad (7b)$$

$$u\frac{\partial w}{\partial y} + v\frac{\partial w}{\partial\psi} + \frac{w}{1+\alpha\cdot\sin\psi}\frac{\partial w}{\partial\theta_1}$$

$$+\alpha\cdot\frac{w\cdot v\cdot\cos\psi}{1+\alpha\cdot\sin\psi} = \frac{\partial^2 w}{\partial y^2} \quad (7c)$$

$$u\frac{\partial h}{\partial y} + \frac{\partial h}{\partial\psi} + \frac{w}{1+\alpha\cdot\sin\psi}\frac{\partial h}{\partial\theta_1} = \frac{1}{\mathrm{Pr}}\cdot\frac{\partial^2 h}{\partial y^2} \quad (7d)$$

where the pressure gradients are evaluated from the zeroth-order invisid core flow, since the pressure gradient normal to the wall is small order. The boundary conditions associated with equations (7) are

at $\theta_1 - 0$,	$w=1$,	$u=v=h=0$	(entrance condition)
at $y=0$,	$w=u=v=0$,	$h=1$	(wall condition)
at $y\to\infty$,	$w\to 1$,	$u,v,h\to 0$	(matching condition with the zeroth-order inviscid flow)

The solution of equations (7) for small α can be expressed as

$$w = f_0' + \alpha\cdot\sin\psi\cdot[f_0' + f_{10}' + (2\theta_1)^2\cdot f_{11}']$$
$$+ \epsilon\cdot\cos\psi\cdot(2\theta_1)^2\cdot f_3' + \ldots,$$

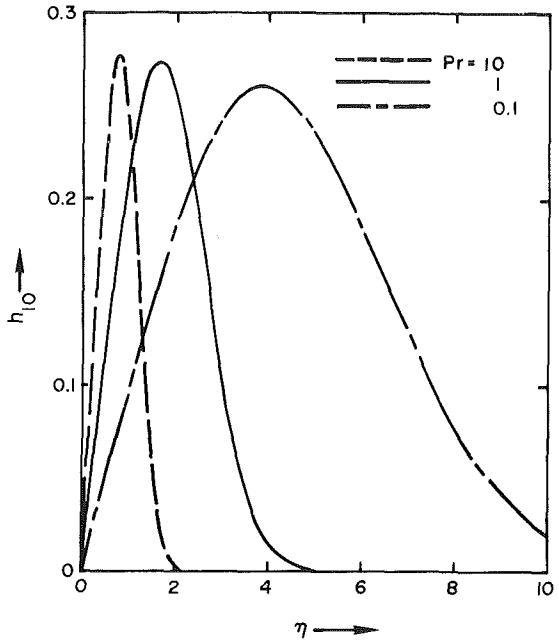

Fig. 2 Temperature function h_{10}

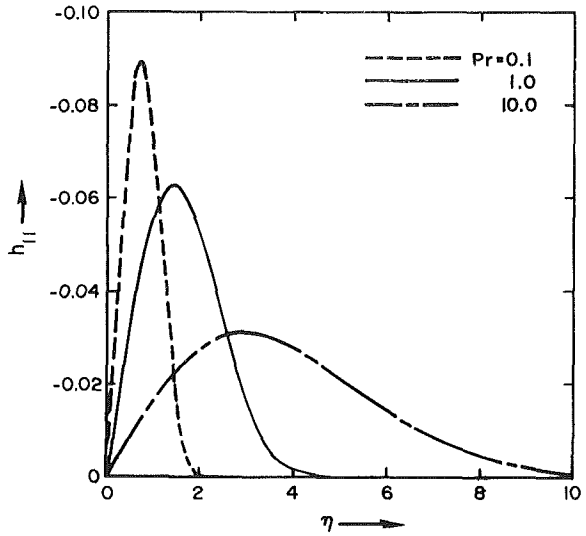

Fig. 3 Temperature function h_{11}

The required boundary conditions can be easily obtained by substituting equations (9) into equations (8). Equations (10) represent the classical forced convection in a straight pipe while equations (11) are due to centrifugal force and

$$
\left.
\begin{aligned}
u &= \frac{1}{\sqrt{2\theta_1}}\Big\{(\eta f_0' - f_0) + \alpha\cdot\sin\psi\cdot[(\eta f_{10}' - f_{10}) + (2\theta_1)^2 \\
&\cdot(\eta f_{11}' - 5f_{11} + f_2)^* \quad + \epsilon\cdot\cos\psi\cdot(2\theta_1)^2\cdot(\eta f_3' - 5f_3 - f_2) + \ldots\Big\}, \\
v &= (2\theta_1)\cdot[\alpha\cdot\cos\psi\cdot f_2' + \epsilon\cdot\sin\psi\cdot f_4'] + \ldots, \\
h &= h_0 + \alpha\cdot\sin\psi\cdot[h_{10} + (2\theta_1)^2\cdot h_{11}] \\
&\quad + \epsilon\cdot\cos\psi\cdot(2\theta_1)^2\cdot h_{20} + \ldots,
\end{aligned}
\right\} \quad (9)
$$

where the prime denotes the derivative with respect to η, and $\eta = y/(2\theta_1)^{1/2}$ is the Blasius variable. The various functions in the expansion of (9) are functions of η only. The governing equations for these functions are listed below.

$$
\left.
\begin{aligned}
f_0''' + f_0 f_0'' &= 0, \\
h_0'' + \mathrm{Pr}\cdot f_0\cdot h_0' &= 0
\end{aligned}
\right\} \quad (10)
$$

$$f_{10}''' + f_0\cdot f_{10}'' + f_0''\cdot f_{10} = 0 \quad (11a)$$

$$f_2''' + f_0 f_2'' - 2\cdot f_0'\cdot f_2' = 1 - f_0'^2 \quad (11b)$$

$$f_{11}''' + f_0 f_{11}''' - 4\cdot f_0' f_{11}' + 5\cdot f_0''\cdot f_{11} = f_0''\cdot f_2 \quad (11c)$$

$$\frac{1}{\mathrm{Pr}}\cdot h_{10}'' + f_0\cdot h_{10}' = -f_{10}\cdot h_0' \quad (11d)$$

$$\frac{1}{\mathrm{Pr}}\cdot h_{11}'' + f_0\cdot h_{11}' - 4\cdot f_0'\cdot h_{11} = (f_2 - 5\cdot f_1)\cdot h_0' \quad (11e)$$

and

$$
\left.
\begin{aligned}
f_3''' + f_0\cdot f_3'' - 4\cdot f_0'\cdot f_3' - 5\cdot f_0''\cdot f_3 + f_0''\cdot f_4 &= 0 \\
f_4''' + f_0\cdot f_4 - 2 f_0'\cdot f_4' &= -h_0 \\
\frac{1}{\mathrm{Pr}}\cdot h_{20}'' + f_0\cdot h_{20}' - 4\cdot f_0'\cdot h_{20} &= -h_0'\cdot(5\cdot f_3 + f_4)
\end{aligned}
\right\} \quad (12)
$$

equations (12) reflect the influence of buoyancy. Solutions of equation (10) and (12) can be found in [7, 8], and those of equations (11) can be found in [9, 10], except for equations (11*d*) and (11*e*). Therefore, the solutions of equations (11*d*) and (11*e*) are plotted in Figs. 2 and 3 for Pr = 0.1, 1.0, and 10, which show the forced convective heat transfer induced by centrifugal force.

Heat Transfer Rate. The local Nusselt number can be expressed in terms of a, k, and $T_w - T_{\mathrm{in}}$ as

$$\mathrm{Nu}\cdot\left[\frac{2\theta_1}{\mathrm{Re}}\right]^{1/2} = h_0' + \alpha\cdot\sin\psi\cdot[h_{10}' + (2\theta_1)^2 h_{11}'] + \epsilon\cdot\cos\psi\cdot(\partial\theta_1)^2\cdot h_{20}' \quad (13)$$

The values of $h_0'(0)$, $h_{10}'(0)$, $h_{11}'(0)$, and $h_{20}'(0)$ are listed in Table 1. The terms proportional to $\alpha\cdot\sin\psi$ represent the curvature effect and, thus, the centrifugal force effect. Initially, the maximum local heat transfer rate occurs along the inner bend due to the positive values of $h_{10}'(0)$. This is a purely geometric effect. As the fluid flows downstream, the maximum local Nusselt number shifts toward the outer bend since the values of $h_{11}'(0)$ are negative. This is the often cited result, of course not quite correct, that the maximum local heat transfer rate in a curved pipe occurs at the outer bend. The actual distribution of the local Nusselt number is further complicated by the effect of natural convection which is represented by the terms proportional to $\epsilon\cdot\cos\psi$ in equation (13). It shows that the natural convection induces a local

maximum Nusselt number at the bottom of the pipe and a local minimum at the top of the pipe. By combining the effects of centrifugal force and buoyancy, the location of the local maximum Nusselt number can be determined from equation (13)

$$\psi = \tan^{-1}\left[\frac{D}{Gr} \cdot \frac{h'_{10}(0) + (2\theta_1)^2 h'_{11}(0)}{(2\theta_1)^2 h'_{20}(0)}\right] \tag{14}$$

where $D = \alpha \cdot Re^2$ is the Dean number. This result shows that the maximum local Nusselt number initially occurs at the inner bend ($\psi = 270$ deg) gradually moves toward the bottom of the pipe ($\psi = 0$ deg) at $\theta_1 = 1/2[h'_{10}(0)/h'_{11}(0)]^{1/2}$ and finally settles between $0 < \psi < 90$ deg. Its actual location depends on the ratio of the Dean number to the Grashof number. If this ratio is large, the location of the maximum local Nusselt number is closer to the outer bend ($\psi = 90$ deg) than the bottom of the pipe. The actual location can be estimated from equation (14) by using the results provided in Table 2.

It is interesting to compare equation (14) with the formula for a *fully developed* flow in a curve pipe with constant wall heat flux [3, 4]. For a fully developed flow, the location of the maximum local heat flux depends on the parameter of $D/(Re \cdot Gr)$. This suggests that even the buoyancy effect could be small compared with that of the centrifugal force near the inlet where equation (14) is valid; the buoyancy can become as important, or even more important, than the centrifugal-force effect further downstream.

Before we discuss the distribution of local shear stresses, it is worthwhile to point out that the perturbation expansions of equations (9) are valid rigorously only when $\theta_1 < 0.1/\epsilon^{1/2}$, or $< 0.1/\sqrt{\alpha}$ for $\alpha < 0.1$. They, however, explicity reveal the relevant length scales and velocity scales for the downstream regions where the effects of buoyancy and the centrifugal forces are no longer small. We will discuss those scales in the last section.

Local Shear Stresses. The local axial shear can be estimated from equation (9) as

$$-\frac{[2\theta_1 \cdot Re]^{1/2}}{1/2\rho W_{in}^2} \cdot \tau_r \theta_1 = f_0''(0) + \alpha \cdot \sin\psi \cdot [f_0''(0) + f_{10}''(0) + (2\theta_1)^2 \cdot f_{11}''(0)] + \epsilon \cdot \cos\psi \cdot (2\theta_1)^2 \cdot f_3''(0) \tag{15}$$

The values of f's are given in Table 1. An interpretation of equation (15) similar to that for equation (13) can be provided and is not repeated here. It is important to note that the maximum local shear due to the curvature effects initially occurring at the inner bend and shifting to the outer bend has been approved experimentally [11]. Similarly, the actual location of the maximum local axial shear can be determined from equation (15)

$$\psi = \tan^{-1}\left[\frac{D}{Gr} \cdot \frac{f_0''(0) + f_{10}''(0) + (2\theta_1)^2 \cdot f_{11}''}{(2\theta_1)^2 \cdot f_3''}\right] \tag{16}$$

The aximuthal shear stress is

$$-\frac{[2\theta_1 \cdot Re]^{1/2}}{1/2\rho W_{in}^2} \cdot \tau_{r\psi} = (2\theta_1) \cdot [-\alpha \cdot \sin\psi \cdot f_2'(0) + \epsilon \cdot \sin \cdot f_4''(0)] \tag{17}$$

and its maximum locations are at

$$\psi = \tan^{-1}\left[\frac{D}{Gr} \cdot \frac{f_4''(0)}{f_2''(0)}\right] \tag{18}$$

which does not vary, to the first order, as a function of θ_1.

First-Order Inviscid Core Flow. The equations of the first-order inviscid core flow due to the boundary layer displacement effects can be obtained by substituting equation (5) into equations (2) and collecting the terms of $0(\delta)$, $0(\delta\alpha)$, and $0(\delta\epsilon)$, respectively. The equations that accounted for the displacement effects of the forced-convection boundary layer are, $0(\delta)$

$$\begin{aligned}
&\frac{1}{r}\frac{\partial(rU_{10})}{\partial r} + \frac{1}{r}\frac{\partial V_{10}}{\partial \psi} + \frac{\partial W_{10}}{\partial \theta_1},\\
&\frac{\partial U_{10}}{\partial \theta_1} = -\frac{\partial P_{10}}{\partial r},\\
&\frac{\partial V_{10}}{\partial \theta_1} = -\frac{1}{r}\frac{\partial P_{10}}{\partial \psi},\\
&\frac{\partial W_{10}}{\partial \theta_1} = -\frac{\partial P_{10}}{\partial \theta_1},\\
&\frac{\partial H_{10}}{\partial \theta_1} = 0
\end{aligned} \tag{19}$$

Those induced by the displacement effect of the centrifugal boundary layer are, $0(\delta\alpha)$

$$\begin{aligned}
&\frac{1}{r}\frac{\partial(rU_{11})}{\partial r} + \frac{1}{r}\frac{\partial V_{11}}{\partial \psi} + \frac{\partial W_{11}}{\partial \theta_1} - r \cdot \sin\psi \cdot \frac{\partial W_{10}}{\partial \theta_1} + U_{10} \cdot \sin\psi = 0,\\
&\frac{\partial U_{11}}{\partial \theta_1} - \left(r \cdot \frac{\partial U_{10}}{\partial \theta_1} + \alpha \cdot W_{10} \cdot \cos\psi\right) = -\frac{1}{r}\frac{\partial P_{11}}{\partial \psi},\\
&\frac{\partial V_{11}}{\partial \theta_1} - \alpha \cdot W \cdot \cos\psi = -\frac{1}{r}\frac{\partial P_{11}}{\partial \psi},\\
&\frac{\partial W_{11}}{\partial \theta_1} + U_{10} \cdot \sin\psi = -\frac{\partial P_{11}}{\partial \theta_1},\\
&\frac{\partial H_{11}}{\partial \theta_1} = 0
\end{aligned} \tag{20}$$

The equations of $0(\delta\epsilon)$ for the displacement of the natural-convection boundary layer are

$$\begin{aligned}
&\frac{1}{r}\frac{\partial(rU_{12})}{\partial r} + \frac{1}{r}\frac{\partial V_{12}}{\partial \psi} + \frac{\partial W_{12}}{\partial \theta_1} = 0,\\
&\frac{\partial U_{12}}{\partial \theta_1} = -\frac{\partial P_{12}}{\partial r},\\
&\frac{\partial V_{12}}{\partial \theta_1} = -\frac{1}{r}\frac{\partial P_{12}}{\partial \psi},\\
&\frac{\partial W_{12}}{\partial \theta_1} = -\frac{\partial P_{12}}{\partial \theta_1},\\
&\frac{\partial H_{12}}{\partial \theta_1} = 0
\end{aligned} \tag{21}$$

The solutions of equations (19–21) are available from [7, 8] and are listed below for convenience in the following discussion.

The solution of equations (19) are

$$\begin{aligned}
P_{10} &= -\frac{\beta_0}{\sqrt{\pi}}\int_0^\infty q^{-1/2} \cdot \frac{I_0(qr)}{I_1(q)} \cdot \sin q\theta_1 \cdot dq\\
W_{10} &= -P_{10},\\
U_{10} &= -\int_0^{\theta_1} \frac{\partial P_{10}}{\partial r} \cdot d\theta_1,\\
V_{10} &= 0,\\
H_{10} &= 0
\end{aligned} \tag{22}$$

where $\beta_0 = \lim_{\eta\to\infty} (\eta f_0' - f_0)$ is the consequence of matching the solution of equation (19) with the zeroth-order boundary layer. In equation (22), I_i are modified Bessel functions.

The solutions of $0(\delta\alpha)$ are

$$P_{11} = \frac{\sin\psi}{\sqrt{\pi}} \cdot \left\{ \int_0^\infty \frac{I_1(qr)}{I_1'(q)} \left[\left\{ \left(\frac{1}{\sqrt{2}} - 2 \right) \beta_0 - \frac{\beta_1}{2} \right\} \cdot q^{-1/2} + 3 \cdot \beta_2 \cdot q^{-5/2} + \frac{\beta_0}{2} \cdot (q^{-3/2} - q^{1/2}) \cdot \frac{I_0(q)}{I_1(q)} \right] \cdot \sin q\theta_1 \cdot dq \right. \quad (23)$$

$$\left. + \frac{\beta_0}{2} \int_0^\infty \frac{q^{-3/2}}{I_1(q)} \cdot [q^2 \cdot r^2 \cdot I_1(qr) + 3 \cdot q \cdot r \cdot I_0(qr)] \cdot \sin q\theta_1 \cdot dq \right\},$$

$$H_{11} = 0$$

and W_{11}, U_{11}, and V_{11} can be expressed in terms of P_{11} by simple integration from equations (20). The values of

$$\beta_1 = \lim_{\eta\to\infty} (-\eta - f_{10}),$$
$$\beta_2 = \lim_{\eta\to\infty} (f_2 - 5f_{11}) \quad (24)$$

are given in Table 1.

The solution of $0(\delta\epsilon)$ are

$$P_{12} = -\frac{6\beta_3}{\sqrt{\pi}} \cdot \cos \cdot \int_0^\infty q^{-5/2} \cdot \frac{I_1(qr)}{I_0(q) + I_1(q)} \cdot \sin q\theta_1 \cdot dq$$
$$W_{12} = -P_{12},$$
$$U_{12} = -\int_0^{\theta_1} \frac{\partial P_{12}}{\partial r} \cdot d\theta_1, \quad (25)$$
$$V_{12} = --\int_0^{\theta_1} \frac{\partial Pr}{\partial \psi} \cdot d\theta_1,$$
$$H_{12} = 0$$

where the values of

$$\beta_3 = \lim_{\eta\to\infty} (5f_3 + f_4) \quad (26)$$

are given in Table 1.

The complete solution of the inviscid core flow can be obtained by combining equations (5), (22), (23) and (25). For convenience in the discussion of physical phenomena, the asymptotic form for large θ_1 is listed below

$$W = 1 + \delta \cdot [2\beta_0 \cdot (2\theta_1)^{1/2} + \ldots] + \delta\alpha \cdot [(5\beta_0 + 3\beta_2) \cdot r \cdot (2\theta_1)^{1/2} \cdot \sin\psi + \ldots] + \delta\epsilon \cdot [3\beta_3 \cdot (2\theta_1)^{1/2} \cdot \cos\psi + \ldots] + \ldots, \quad (27a)$$

$$U = \delta \cdot [-\beta_0 \cdot r \cdot (2\theta_1)^{-1/2} + \ldots], + \delta\alpha \cdot [1/3(8\beta_0 + 3\beta_1) \cdot (2\theta_1)^{3/2} \cdot \sin\psi + \ldots] + \delta\epsilon \cdot [\beta_3 \cdot (2\theta_1)^{3/2} \cdot \cos\psi + \ldots] + \ldots, \quad (27b)$$

$$V = \delta\alpha \cdot [1/3(8\beta_0 + 3\beta_1) \cdot (2\theta_1)^{3/2} \cdot \cos\psi + \ldots] + \delta\epsilon[-\beta_3 \cdot (2\theta_1)^{3/2} \cdot \sin\psi + \ldots] + \ldots, \quad (27c)$$

$$P = 1 - W \quad (27d)$$

$$H = 0 \quad (27e)$$

Equations (27*b*) show that the displacement effect of the axial momentum boundary layer, terms of $0(\delta)$, decays as the fluid flows downstream. In contrast, the displacement effects of the secondary boundary layers due to buoyancy and natural convection grow as $\theta_1^{3/2}$. The secondary inviscid core flow can be interpreted clearly in (X, Y) coordinates, Fig. 1. The horizontal velocity, V_x, and the vertical velocity, V_y, can be estimated as

$$V_x = U \cdot \sin\psi + V \cdot \cos\psi = (2\theta_1)^{3/2} \cdot \{ -\beta_0 \cdot \delta \cdot r \cdot \sin\psi \cdot (2\theta_1)^{-2} + \delta\alpha \cdot [1/3(8\beta_0 + 3\beta_2)] \} \quad (28a)$$

and

$$V_y = -U \cdot \cos\psi + V \cdot \sin\psi = (2\theta_1)^{3/2} \cdot \{ \beta_0 \cdot \delta \cdot r \cdot \cos\psi \cdot (2\theta_1)^{-2} + \delta\epsilon \cdot \beta_3 \} \quad (28b)$$

Equation (28*b*) shows that the displacement effects of the secondary boundary layer due to natural convection induce the uniform downward flow in the core, if the displacement effect of the axial boundary layer is negligible, which is indeed true for large θ_1. Similarly, equation (28*a*) indicates that the displacement effect of the secondary boundary layer generated by the centrifugal forces induces a horizontal flow from the inner bend to the outer bend. Consequently, for large θ_1, a uniform secondary flow is induced in the core and its direction is given by

$$\psi = \tan^{-1} \left| \frac{V_y}{V_x} \right| = \frac{D}{Gr} \cdot \frac{8\beta_0 + 3\beta_2}{3\beta_2} \quad (29)$$

This is consistent with the fact that the maximum local wall heat flux and the maximum axial wall shear occur in $0 \text{ deg} < \psi < 90 \text{ deg}$.

4 Downstream Flow Development

The boundary-layer solution, equations (9), and the core flow, equations (27), both show that the effects of buoyancy and centrifugal force grow downstream. The relevant length scales and the velocity scales can be deduced from equations (9) and (27). Since the length scales are more important and more representative, we will discuss only the different length scales.

Equations (9) indicate that the buoyancy becomes 0(1) when $\epsilon\theta_1^2 \sim 1$, or $S \sim a/\sqrt{\epsilon}$, where S measures the distance along the center of the pipe from the inlet of the pipe. Physically, this means at the distance $a/\sqrt{\epsilon}$ from the inlet, the secondary boundary layer induced by buoyancy becomes as strong as the axial forced-convection boundary layer. On the other hand, equations (27) show that its effect on the inviscid core flow is still small. Similarly, the effects of the centrifugal force becomes 0(1) when $S \sim a/\sqrt{\alpha}$. Therefore, a substantial secondary boundary layer is developed at $S > a/\sqrt{\alpha}$ and/or $a/\sqrt{\epsilon}$, but its effect on the inviscid core flow is still weak.

The magnitude of the secondary core flow becomes 0(1) downstream from the region at a distance $a/\sqrt{\alpha}$ and/or $a/\sqrt{\epsilon}$ from the inlet. In the following discussion we assume that the values of D and Gr are about the same order of magnitude to rule out the possibility that either the buoyant effect or the centrifugal effect is still negligible before the other effect becomes dominant on the core flow.

In the third region, the displacement effect of the secondary boundary layer is 0(1). The relevant length scales can be derived from equations (27) by setting the terms, due to the displacement effect of the secondary boundary layer, to 0(1). The process shows that $a \cdot \mathrm{Re}/\mathrm{D}^{4/5}$ and $a \cdot \mathrm{Re}/\mathrm{Gr}^{2/5}$ are the proper length scales for the third region.

A recent study of the fully developed flows, which will be reported separately, indicates that the flow structure can be described in the following way. In the core of the pipe, an induced pressure gradient balances with the body forces. For an isothermal flow in a curved pipe, the secondary flow drifts slowly from the inner bend toward the outer bend; for a heated, straight pipe flow, the secondary flow moves downward. Near the pipe wall, a boundary layer, with much faster velocity than the core flow, flows in the opposite

direction of the core flow. This type of flow structure is well known and has been previously used by several authors to model curved-pipe flows or heated, straight-pipe flows for large Dean numbers or large Grashof numbers. The work to be reported also shows that there is a middle layer between these two well-known regions. This middle layer is driven by the difference between the pressure gradient and the body forces, and is an inviscid boundary layer which flows in the same direction as the core flow. This type of flow structure is probably shared by flows that are driven by forces near boundaries such as natural convection in enclosures. The phenomenon of thermal inversion that occurs in natural convection in enclosures is a consequence of the middle layer.

The wall layer is almost fully developed in the third region and can be described as quasi-fully developed. The major development of the core flow and the middle layer occurs in the third region, and they eventually become 0(1) as the flow asymptotically reaches the fully developed stage.

We can conclude that the developing flow under the influence of body forces passes through three different regions. Near the inlet, the effect of body forces is small. Within the secondary region, the effect of body forces on the boundary layer becomes important; its influence on the core flow is still weak. In the third region, before it reaches a fully developed state, the effect of body forces becomes dominant even on the core flows. The actual order of regions is more complicated when two kinds of body forces are active such as discussed in this paper. Various combinations are possible and depend on the relative values of D and Gr.

For a curved-pipe flow heated under a constant wall temperature condition, the effects of buoyancy eventually decays when the fluid becomes isothermal. The associated length scale is $a \cdot \mathrm{Re}$; on the other hand, the centrifugal-force effect stays. Therefore, the decay of buoyancy should be considered as a different problem, and $a \cdot \mathrm{Re}$ should not be taken as a relevant length scale to correlate data. This rule is also applicable to flow in a straight pipe at constant wall temperature.

5 A Brief Discussion of the Developing Flow in Heated Vertical Curved Pipes

For a heated vertical curved pipe, whose axis around which the pipe is coiled is horizontal, the direction of buoyancy is parallel to the centrifugal forces and goes through periodic variation [3]. The effects of buoyancy grow downstream similarly to those in a horizontally placed curved pipe irrespective of its periodic variation. Therefore, the relative importance of buoyancy to the centrifugal forces on the flow development will depend on the ratio of Gr/D.

Acknowledgment

The author wishes to express appreciation to Dr. M. K. Ellingsworth of the Office of Naval Research for generous research support under award number N00014-81-K-0428.

References

1 Berger, S. A., et al., "Flow in Curved Pipes," *Annual Review for Fluid Mechanics*, Vol. 15, 1983, pp. 461-512.

2 Kalb, C. E., and Seader, J. D., "Entrance Region Heat Transfer in a Uniform Wall-Temperature Helical Coil With Transition From Turbulent to Laminar Flow," *International Journal of Heat and Mass Transfer*, Vol. 26, 1983, pp. 23-32.

3 Yao, L. S., and Berger, S. A., "Flow in Heated Curved Pipes," *Journal of Fluid Mechanics*, Vol. 88, 1978, pp. 339-354.

4 Prusa, J., and Yao, L. S., "Numerical Solution of Fully-Developed Flow in Heated Curved Tubes," *Journal of Fluid Mechanics*, Vol. 123, 1982, pp. 503-522.

5 Akiyama, M., Kikuchi, K., Susuki, M., Nishiwaki, I., and Cheng, K. C., "Mixed Laminar Convection of the Thermal Entry Region in Curved Rectangular Channels," ASME-JSME Thermal Engineering Conference, Honolulu, Mar. 20-24, 1983.

6 Kuehn, T. H., and Goldstein, R. J., "Numerical Solution to the Navier-Stokes Equations for Laminar Natural Convection About a Horizontal Isothermal Circular Cylinder," *International Journal of Heat and Mass Transfer*, Vol. 23, 1980, pp. 971-979.

7 Yao, L. S., "Free-Forced Convection in the Entry Region of a Heated Straight Pipe," ASME JOURNAL OF HEAT TRANSFER, Vol. 100, 1978, pp. 212-219.

8 Yao, L. S., "Entry Flow in a Heated Tube," *Journal of Fluid Mechanics*, Vol. 88, 1978, pp. 465-483.

9 Singh, M. P., "Entry Flow in a Curved Pipe," *Journal of Fluid Mechanics*, Vol. 65, 1974, pp. 517-539.

10 Yao, L. S., and Berger, S. A., "Three-Dimensional Boundary Layer in the Entry Region of Curved Pipes," in preparation.

11 Choi, U. S., Talbot, L., and Cornet, "Experimental Study of Wall Shear Rates in the Entry Region of a Curved Tube," *Journal of Fluid Mechanics*, Vol. 93, 1979, pp. 465-489.

A Finite Element Model for Temperature Induced Electrohydrodynamic Pumping in Horizontal Pipes

B. S. Kuo
Bechtel Power Corporation,
San Francisco, Calif. 94101

J. C. Chato
Fellow ASME

J. M. Crowley
University of Illinois
at Urbana-Champaign,
Urbana, Ill. 61801

The electrohydrodynamic (EHD) pumping created by an axially traveling electric wave superimposed on a dielectric fluid with a transverse temperature field has been investigated using a finite element technique. Both forward wave (cooled wall) and backward wave (heated wall) modes of operation have been considered. The secondary flow generated by buoyancy effects in the cross section were included in the calculations. The driving effects of the traveling wave were calculated by assuming that only the average electric shear stress produced movement while the sinusoidally varying transient effects cancelled out. The results show that effective pumping can be achieved without the use of a grounding electrode along the axis of the tube but the design parameters have to be carefully selected. Increasing the diameter-to-wavelength ratios increases the velocities. The flow rate is maximum at an optimum frequency, about 0.8 Hz in our typical cases, but it drops off rather quickly as the frequency is either decreased or increased. The velocities were much less sensitive to heating/cooling rates (i.e., Rayleigh numbers) or changes in the magnitude of the electrical conductivity values. Although the pumping effect increases approximately as the square of the maximum applied electric potential, in practice, the electric gradients are limited by the dielectric strength of the fluid. The results indicate the EHD heat exchanger/pumps can be feasible alternatives to mechanical pumps in certain circumstances when dielectric liquids require both heat tranfer and circulation.

Introduction

Electrohydrodynamic (EHD) pumping is produced by the interaction of electric fields and free charges in an insulating fluid medium. Pumping is achieved when traveling electric fields are generated which drag charges in a given direction.

Free charges may be established in the fluid medium in two different ways. The first is the direct injection of free charges by means of a corona source. An electric field is established between this source, called an emitter, and another electrode, called the collector. This electric field drags the free charges through the fluid, thus setting the fluid in motion. EHD pumps of this nature are known as ion drag pumps, several of which were built and studied by O. M. Stuetzer [1].

The disadvantage of ion drag pumps is that the corona source used to inject free charges tends to degrade the insulating properties of the fluid medium. For this reason, a second method of producing the free charges, known as induction charging, is used when the insulating properties of the fluid must be maintained.

Induction charging is based upon the establishment of a conductivity or permittivity gradient perpendicular to the desired direction of fluid motion. One obvious means to produce this gradient is the use of a gas-liquid interface. This method was utilized by J. R. Melcher and his students to build several different EHD pumps in the mid-1960s [2–4].

Another way to establish the conductivity gradient is based on the fact that in insulating fluids conductivity is a function of temperature. Thus, if a temperature gradient is present, a conductivity gradient will also exist. Induction pumps of this nature, in both rectangular and cylindrical geometries, have been the subject of experimentation by several different researchers [5–11].

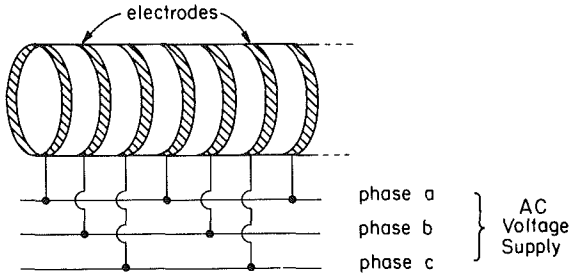

Fig. 1 Electrodes surrounding the fluid to be pumped

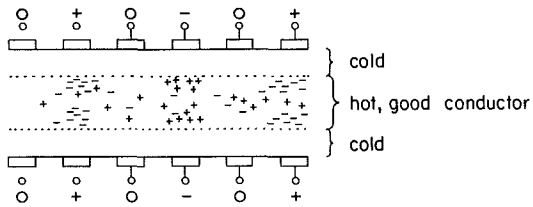

Fig. 2 Cross section of EHD pump

The basic induction mechanism can be explained by considering the electrode structure of a practical EHD pump as shown in Fig. 1. Each electrode surrounds the flow channel, generating an electric field inside. Every third electrode in this realization of the pump is connected to the same phase of a three-phase alternating voltage supply. This produces a voltage wave which travels down the pipe at a velocity determined by the frequency of the voltage, f, and the wavelength of the electrode structure, λ. For the fundamental components of frequency and wavelength, the wave velocity is $\Omega\lambda/2\pi = f\lambda$.

Contributed by the Heat Transfer Division and presented at the ASME Winter Annual Meeting, Phoenix, Arizona, November 14–19, 1982. Manuscript received by the Heat Transfer Division September 9, 1982. Paper No. 82-WA/HT-23.

Inside the pipe, the fluid responds to the voltage wave with current flows and charge buildups which depend primarily on the electrical conductivity gradients. One possibility is an attraction pump shown in Fig. 2 in which the better conductor, usually the hotter liquid, lies along the centerline away from the electrode. Application of a voltage will cause separation of the ions as shown. The positive ions will be attracted toward the negative potential, but they cannot reach it because the colder, more insulating liquid blocks them. As a result, they pile up at the interface, giving a positive space charge there. The opposite situation occurs with the negative ions and the positive potential.

While this is happening, however, the voltage wave is moving along the pipe. By the time the space charge arrives at the interface, it finds itself upstream of the potential that is attracting it, and it responds by moving in the wave direction along the pipe. This ion motion drags the liquid along with it, giving rise to a flow in the wave direction. It is this flow which forms the basis of an EHD induction pump.

Actually, charge can also be induced at places where the dielectric constant of the fluid changes and these charges also lead to fluid pumping [12], which may enhance or oppose the conductivity induced pumping. The relative magnitudes of the electric pumping pressure arising from conductivity and permittivity effects are $\Delta\sigma/\sigma$ and $\Delta\epsilon/\epsilon$, respectively. In gases, the electrical conductivity is too small to allow the conductivity mechanism to work at all, so the only possibility for EHD induction pumping rests with the gradient of the dielectric constant. In an insulating liquid, which we studied, on the other hand, $\Delta\sigma/\sigma$ exceeds $\Delta\epsilon/\epsilon$ by orders of magnitude over the temperature range of interest so the change in dielectric constant can be completely neglected.

The ability to move insulating fluids through the use of EHD pumps has a number of possible applications. The earlier research carried out by Melcher and his coworkers primarily viewed EHD pumping as a means to study fluid properties [2, 5]. It was also recognized that the EHD concept might be applied in the plastics industry as a means to move liquid plastics without the use of mechanical pumps [4].

In many types of high-voltage electrical equipment, such as transformers and underground cables, the Joule heat generated must be removed by, or through, a dielectric fluid whose primary purpose is electrical insulation. Dielectric fluids, in general, are also good thermal insulators; consequently, their heat transfer effectiveness must be enhanced in most cases by forced circulation between the heat generating electrical device and an external heat exchanger or heat sink to provide adequate cooling.

Conventional mechanical pumping systems require moving parts which tend to wear in time, contaminating the system. Mechanical pumps also produce pressure differentials in the flow system which can be a limiting factor, such as in long underground cable systems, if both maximum and minimum pressures are determined by other considerations. In contrast, EHD pumping generates a distributed body force inside the fluid. Thus the system neither has moving mechanical parts nor does it need pressure differential for operation.

In our work with cable systems at the University of Illinois at Urbana-Champaign since 1976, we have demonstrated the feasibility of pumping dielectric oils with maximum speeds of around 10 cm/s [9, 10]. This limit was governed in part by the following circumstances:

1 Less than 60 percent of the flow circuit was pumped, i.e., had electrodes in it, and the rest of the circuit produced unfavorable pressure drops due to friction.

2 Because of the simple, two-dimensional geometry

Nomenclature

a = characteristic cross-sectional dimension such as pipe radius, m
E_x, E_y = X- and Y-components of electric field intensity, V/m
E_0 = reference electric field intensity, $\phi_{e,p}/a$
f = frequency, $\Omega/2\pi$, s^{-1}
j = $\sqrt{-1}$
k = thermal conductivity, W/m-C
K_n = $2\pi n/\lambda$, m^{-1}
L_q = heated perimeter, m
P_Z = axial component of pressure, Pa
Pr = Prandtl number
$\bar{q}$ = average heat flux at the wall, positive for heating and negative for cooling, W/m^2
Ra^* = modifed Rayleigh number[1]
Re = Reynolds number, $\bar{W}a/\nu$, also real part of a complex variable
T = temperature, °C
T_K = absolute temperature, K
T^* = characteristic temperature difference,[1] °C
u,v,w,w' = dimensionless velocities[1]
$U,V,W,$ = velocities in the X-, Y-, Z-directions, m/s
$\bar{W}$ = bulk mean axial velocity, m/s
x,y,z = dimensionless coordinates[1]
X,Y = Cartesian coordinates in the horizontal and vertical directions in the cross section, m
Z = axial coordinate, m
Z_c = characteristics axial length[1]
$< >$ = time-averaged value

Greek Letters

α = thermal diffusivity, m^2/s
β = isobaric expansion coefficient, C^{-1}
Δ = change of the following variable
ϵ = electric permittivity, F/m
λ = wavelength, m
μ = dynamic viscosity, kg/m-s
ν = kinematic viscosity, μ/ρ, m^2/s
ξ = vorticity[1]
ρ = density, kg/m^3
σ = electrical conductivity, mho/m or S/m
$\bar{\sigma} \equiv \sigma + j\epsilon\,(\Omega - K_n w)$
τ = shear stress, N/m^2
τ_e = electric shear stress, N/m^2
ϕ = dimensionless temperature[1]
ϕ_e = electric field potential, V
ϕ_{xy} = x- and y-dependent component of ϕ_e
ψ = stream function[1]
Ω = angular velocity, rad/s

Subscripts

b = bulk mean value
e = electric quantity
o = entrance condition (generally uniform in cross section)
p = peak or maximum value
w = value at the wall
x,y,z = components in three directions

Superscripts

$*$ = nondimensional[1]
$'$ = complex conjugate in equations (19) and (20)

[1] Defined in equations (2), (5), (6), (9), (11), and (16).

studied, only one side of the channel had electrodes in it. The other three walls generated local viscous drag without significant electrical forces acting in their vicinity.

Theoretical as well as experimental considerations indicate that the optimum induction type EHD pumping configuration consists of (*i*) electrodes embedded on all walls around the flow and (*ii*) the presence of strong temperature gradients, which produce the required electrical charges in the fluid, right next to the walls containing the electrodes. Thus, the concept of the EHD heat exchanger/pump was developed which ideally combines these requirements. As a result of this earlier work, many of the general design criteria are already known. For example, the maximum pressure which can be developed by such a single-stage pump will be on the order of $\epsilon\bar{E}\cdot\bar{E}$, regardless of the geometry or materials used. The pump is therefore limited by the dielectric strength of the fluid and not by the magnitude of the applied voltage. Although, the magnitude of $\epsilon\bar{E}\cdot\bar{E}$ is usually smaller than required in most applications, the pressure contributions of many stages or wavelengths can be summed with proper design to give practical pump capabilites. The efficiency of the pump has also been analyzed with the aid of simpler models which predict efficiencies comparable to conventional combinations of electric motors and mechanical pumps [13].

The purpose of the present work was to adapt our finite element technique to the electric field driven flows and explore the characteristics of such flows in a horizontal circular tube acting as an EHD heat exchanger/pump where heat transfer, i.e., temperature gradients, plays an essential role.

Analysis of Multiple-Coupled Heat Transfer

The analysis is an extension of the work by Chern and Chato [14, 15] who used a finite element technique to calculate combined natural and forced convective flows in horizontal channels with irregular cross sections. This extension consists of two substantial additions: first, the temperature dependent variations of the viscosity and electrical conductivity are included; and, second, the electrical forces created within the fluid, due to an axially traveling electrical field, are considered as the main cause of axial motion. Thus, the overall flow pattern is driven axially by combined electrical and pressure forces and in the cross-sectional plane by gravitational effects alone.

It is assumed that the traveling electric field is generated by stationary electrodes imbedded into the walls of the channel as described above. More than three phases can be added to give a better approximation to a pure sinusoidal traveling wave. It is assumed that, for the purpose of calculating the force effects on the fluid, the sinusoidally varying components of the electric shear cancel out and only the time-averaged, nonzero, axial components need to be considered. Other simplifying assumptions are:

1 The heat transferred to (or from) the fluid per unit length, $\bar{q}$, is constant.

2 The externally imposed axial pressure gradient, dP_z/dZ, is constant along the axial direction, Z.

3 All partial derivatives with respect to the axial direction, Z, except for $\partial T/\partial Z$, can be neglected in comparison to the partial derivatives with respect to X and Y.

4 The effects of inertia are negligible when compared to those of viscosity, pressure, or electric forces.

With these assumptions, the steady-state, axial momentum equation can be expressed in dimensionless form as follows

$$\frac{\partial^2 w}{\partial x^2}+\frac{\partial^2 w}{\partial y^2}+\frac{1}{\mu^*}\left(\frac{\partial w}{\partial x}\frac{\partial \mu^*}{\partial x}+\frac{\partial w}{\partial y}\frac{\partial \mu^*}{\partial y}\right) = \frac{2a}{\mu^*\epsilon E_o^2}\frac{dP_z}{dZ}-\frac{1}{\mu^*}\left(\frac{\partial <\tau_{xz}>^*}{\partial x}+\frac{\partial <\tau_{yz}>^*}{\partial y}\right) \quad (1)$$

where the following variables are used

$$x\equiv X/a;\ y\equiv Y/a;\ w\equiv 2\mu_o\ W/a\,\epsilon E_o^2;\ \mu^*\equiv \mu/\mu_o;\ E_o\equiv \phi_{e,p}/a$$

$$<\tau_{xz}>^*\equiv <\tau_{e,xz}>/(\epsilon E_o^2/2);$$

$$<\tau_{yz}>^*\equiv <\tau_{e,yz}>/(\epsilon E_o^2/2) \quad (2)$$

Expressions for the electrical shear forces will be derived later.

For the buoyancy driven secondary flow in the cross section, the steady-state, dimensionless momentum equations in the horizontal, x, and vertical, y, directions become

$$\frac{\partial^2 u}{\partial x^2}+\frac{\partial^2 u}{\partial y^2}=-\frac{2}{\mu^*}\frac{\partial u}{\partial x}\frac{\partial \mu^*}{\partial x}-\frac{1}{\mu^*}\left(\frac{\partial u}{\partial y}+\frac{\partial v}{\partial x}\right)\frac{\partial \mu^*}{\partial y} \quad (3)$$

$$\frac{\partial^2 v}{\partial x^2}+\frac{\partial^2 v}{\partial y^2}=-\phi\,\mathrm{Ra}^*-\frac{2}{\mu^*}\frac{\partial v}{\partial y}\frac{\partial \mu^*}{\partial y}-\frac{1}{\mu^*}\left(\frac{\partial u}{\partial y}+\frac{\partial v}{\partial x}\right)\frac{\partial \mu^*}{\partial x} \quad (4)$$

where the following additional variables are introduced

$$u\equiv Ua/\alpha;\ v\equiv Va/\alpha;\ \phi\equiv (T-T_b)/\Delta T^*;\ \mathrm{Ra}^*\equiv g\beta\,\Delta T^*\,a^3/\nu\alpha$$

$$\beta\simeq -\frac{1}{\rho}\left(\frac{\rho-\rho_b}{T-T_b}\right);\ \Delta T^*\equiv \bar{q}a/k \quad (5)$$

where ΔT^* was chosen as the constant, reference temperature differential, positive for heating and negative for cooling.

Equations (3) and (4) can be combined into a single vorticity equation by taking the partial derivative of equation (3) with respect to y and that of equation (4) with respect to x, then introducing the concepts of stream function, ψ, and vorticity, ξ

$$\partial\psi/\partial y\equiv u;\ \partial\psi/\partial x\equiv -v;\ \xi\equiv\nabla^2\psi \quad (6)$$

The resulting equation for secondary flow is

$$\nabla^2\xi=\mathrm{Ra}^*\frac{\partial\phi}{\partial x}+\phi\frac{\partial \mathrm{Ra}^*}{\partial x}+\frac{1}{\mu^*}\left\{\left(\frac{\partial u}{\partial y}+\frac{\partial v}{\partial x}\right)\cdot\left[\frac{\partial^2\mu^*}{\partial x^2}-\frac{\partial^2\mu^*}{\partial y^2}+\frac{1}{\mu^*}\left\{\left(\frac{\partial\mu^*}{\partial y}\right)^2-\left(\frac{\partial\mu^*}{\partial x}\right)^2\right\}\right]+2\left(\frac{\partial u}{\partial x}-\frac{\partial v}{\partial y}\right)\left[\frac{1}{\mu^*}\frac{\partial\mu^*}{\partial x}\frac{\partial\mu^*}{\partial y}-\frac{\partial^2\mu^*}{\partial x\partial y}\right]+\frac{\partial\mu^*}{\partial x}\left(\frac{\partial^2 v}{\partial x^2}-\frac{\partial^2 u}{\partial x\partial y}\right)-\frac{\partial\mu^*}{\partial y}\left(\frac{\partial^2 u}{\partial y^2}-\frac{\partial^2 v}{\partial x\partial y}\right)\right\} \quad (7)$$

The liquids under consideration are electrical insulators, so that heat generation due to ohmic heating is negligible, and the energy equation can be written as

$$\frac{\partial^2\phi}{\partial x^2}+\frac{\partial^2\phi}{\partial y^2}=u\frac{\partial\phi}{\partial x}+v\frac{\partial\phi}{\partial y}+\left(\frac{a^2\bar{W}}{\alpha Z_c}\right)w'\frac{\partial\phi}{\partial z}+\left(\frac{a^2\bar{W}}{\alpha\Delta T^*}\right)w'\frac{dT_b}{sZ} \quad (8a)$$

where $z\equiv Z/Z_c$ and

$$w'\equiv W/\bar{W}=w(a\,\epsilon E_o^2/2\,\mu_o\,\bar{W}) \quad (9)$$

The overall energy balance for a section of the channel is

$$A\,\bar{W}\rho\,c_p\frac{dT_b}{dZ}=\bar{q}\,L_q \quad (10a)$$

Rearranging yields

$$\left(\frac{a^2\,\bar{W}}{\alpha\Delta T^*}\right)\frac{dT_b}{dZ}=\frac{a\,L_q}{a} \quad (10b)$$

If we define

$$Z_c \equiv \frac{a^2 \bar{W}}{\alpha} = a \,\mathrm{Re}\,\mathrm{Pr} \tag{11}$$

then equation (8*a*) becomes

$$\frac{\partial^2 \phi}{\partial x^2} + \frac{\partial^2 \phi}{\partial y^2} = u \frac{\partial \phi}{\partial x} + v \frac{\partial \phi}{\partial y} + w' \left(\frac{\partial \phi}{\partial z} + \frac{a L_q}{A} \right) \tag{8b}$$

Finally, the electric shear forces in equation (1) have to be determined in terms of the electric potential, ϕ_e. By combining the basic laws of electrostatics and assuming constant permittivity, ϵ, an equation for the electric potential can be derived.

$$\nabla \cdot (\sigma \nabla \phi_e) + \nabla \cdot (\epsilon \bar{V} \nabla^2 \phi_e) + \frac{\partial}{\partial t} (\epsilon \nabla^2 \phi_e) = 0 \tag{12}$$

We assumed that the electrodes embedded in the walls created a sinusoidally varying potential distribution with a wavelength, λ, determined by the spacing of the electrodes. (With three-phase excitation, for example, λ is equal to three electrode spaces.) Thus

$$\phi_e = \phi_{xy} \exp[j(\Omega t - K_n Z)]$$
$$= \phi_{xy} \exp[j(\Omega - K_n W) t] \tag{13}$$

where $K_n = 2\pi n/\mu$ and $n = 1$ for a single wave. The minus sign is valid for a forward wave and should be changed to a plus sign for a backward wave. Substituting equation (13) into equation (12), assuming incompressibility, and neglecting $\partial\sigma/\partial z$ yields

$$\bar{\sigma} \nabla^2 \phi_{xy} + \nabla \sigma \cdot \nabla \phi_{xy} - \bar{\sigma} K_n^2 \phi_{xy} = 0 \tag{14}$$

where $\bar{\sigma} \equiv \sigma + j\epsilon(\Omega - K_n W)$. if $K_n W << \Omega$, then the electrical potential (i.e. equation (14)) is decoupled from the velocity and can be solved independently. Equation (14) can be written in nondimensional form as

$$\frac{\partial^2 \phi^*_{xy}}{\partial x^2} + \frac{\partial^2 \phi^*_{xy}}{\partial y^2} + \frac{1}{\bar{\sigma}^*} \left(\frac{\partial \sigma^*}{\partial x} \frac{\partial \phi^*_{xy}}{\partial x} + \frac{\partial \sigma^*}{\partial y} \frac{\partial \phi^*_{xy}}{\partial y} \right)$$
$$- K_n^{*2} \phi^*_{xy} = 0 \tag{15}$$

where

$$\phi^*_{xy} \equiv \phi_{xy}/\phi_{e,p};\ \bar{\sigma}^* \equiv \bar{\sigma}/\sigma_o;$$
$$\sigma^* \equiv \sigma/\sigma_o;\ K_n^* \equiv K_n a \tag{16}$$

The boundary condition is that ϕ_{xy} at the electrode walls is equal to $\phi_{e,p}$, i.e., $\phi^*_{xy} = 1$.

Now we can obtain expressions for the average axial shear stresses in equation (1) in terms of the electric field. For the ohmic conduction model used here with essentially constant permittivity, we can assume that the electro-mechanical coupling occurs at the charges. Then the relevant electric shear stresses acting in the axial direction are

$$\tau_{e,xz} = \epsilon E_x E_z \tag{17a}$$

$$\tau_{e,yz} = \epsilon E_y E_z \tag{17b}$$

The components of the electric field are given by

$$E_x = -\frac{\partial \phi_e}{\partial X} \tag{18a}$$

$$E_z = -\frac{\partial \phi_e}{\partial Z} \tag{18b}$$

With sinusoidal excitation, the electrical force has two Fourier components, one constant and the other varying at twice the frequency of the imposed traveling wave. We assume that only the time-averaged shear stresses need to be considered, which are

$$<\tau_{e,xz}> = (\epsilon/2) <E_z E_x>$$
$$= (\epsilon/2)\,\mathrm{Re}\left[-j K_n \phi_{xy} \frac{\partial \phi'_{xy}}{\partial X} \right]$$
$$= (\epsilon E_o^2/2)\,\mathrm{Re}\left[-j K_n^* \phi^*_{xy} \frac{\partial \phi^{*\prime}_{xy}}{\partial x} \right] \tag{19a}$$

$$<\tau_{e,yz}> = (\epsilon/2) <E_z E_y>$$
$$= (\epsilon/2)\,\mathrm{Re}\left[-j K_n \phi_{xy} \frac{\partial \phi'_{xy}}{\partial Y} \right]$$
$$= (\epsilon E_o^2/2)\,\mathrm{Re}\left[-j K_n^* \phi^*_{xy} \frac{\partial \phi^{*\prime}_{xy}}{\partial y} \right] \tag{19b}$$

where primed quantities, $'$, are complex conjugates. Therefore

$$<\tau_{xz}>^* = \mathrm{Re}\left[-j K_n^* \phi^*_{xy} \frac{\partial \phi^{*\prime}_{xy}}{\partial x} \right] \tag{20a}$$

$$<\tau_{yz}>^* = \mathrm{Re}\left[-j K_n^* \phi^*_{xy} \frac{\partial \phi^{*\prime}_{xy}}{\partial y} \right] \tag{20b}$$

It is to be noted again that for backward wave pumping, K_n or K_n^* is negative.

Solution Method and Results

As discussed before, the equations presented in the previous section were solved by a finite element technique which is an extension of our previous work [14, 15]. Since we now included variations of the properties (in particular the viscosity and electrical conductivity), the numerical solution had to include an additional iteration at each step in which the velocity and temperature distribution in a cross section were calculated by adjusting the local properties at each iteration based on the previous temperature distribution. In addition, of course, the electric force terms have also been included into the axial momentum equation, equation (1). The following additional boundary conditions were assumed:

1 No slip at the boundaries, $u = v = w = \psi = 0$

2 No crossflow at the vertical line of symmetry, $u = \psi = \xi = 0$

3 Uniform flow at the entrance $z = 0$, $u = v = \phi = 0$

The computations started at the entrance plane where uniform temperature field was specified and marched downstream by steps. At each step, i.e., cross section, first the electric shear stresses were calculated using the temperature distributions calculated in the previous iteration, then the axial velocity distribution was determined using the finite element formulation of equation (1). Now the secondary flow pattern was calculated iteratively from equation (7) (using again the previously obtained temperature distribution for the derivatives of the properties). Finally, a new temperature distribution was found from equation (8*b*), which was compared with the previous temperatures to determine convergence. If the differenes were significant, the new temperatures were used for another iteration. When convergence was obtained, the next axial step was taken. For details of the method, [11, 14–16] can be consulted.

Typical results of the calculations are shown in Figs. 3–11. The characteristics of the fluid were that of a typical insulating oil (see the Appendix). Most of the calculations

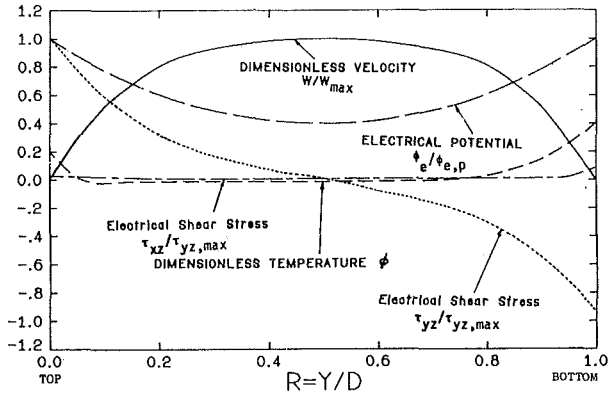

Fig. 3 Relationship between electrical potential, temperature, electrical shear stresses, axial velocity along the vertical centerline in dimensionless form for ω = 1 Hz, λ = 0.06 m, Ra* = 5 x 10^4, forward pumping, cooled wall

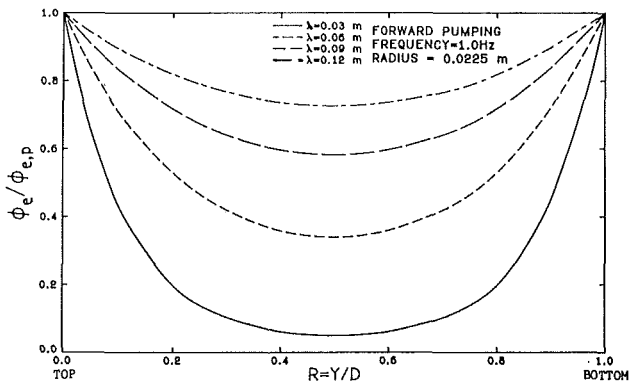

Fig. 4 Dimensionless electrical potential distributions along the vertical centerline for various wavelengths

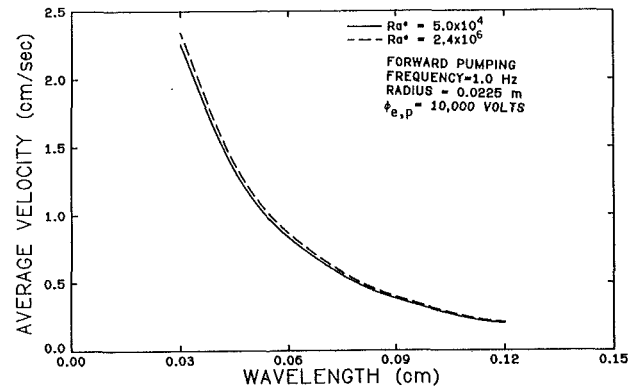

Fig. 5 The effects of wavelength and Rayleigh number on average pumping velocity

assume a voltage of 10 kV which produced good puming in our experimental work. Although 10 kV may appear to be a high voltage, it would actually be considered very small in the electric power applications we are studying. Electric power is normally transmitted at voltage levels of 300 kV and higher so a cooling device which requires 10 kV would not require any additional protective designs. In fact, voltages of this level are routinely present in many commercial and consumer devices such as televisions, copy machines, and air cleaners. Figure 3 shows the distributions of velocity, temperature, electric potential, and the two axial components of the electrical shear stress in dimensionless forms. Note that the dimensionless temperature increases towards the cooled wall because the heat input, $\tilde{q}$, and, consequently ΔT^* is negative. Figure 4

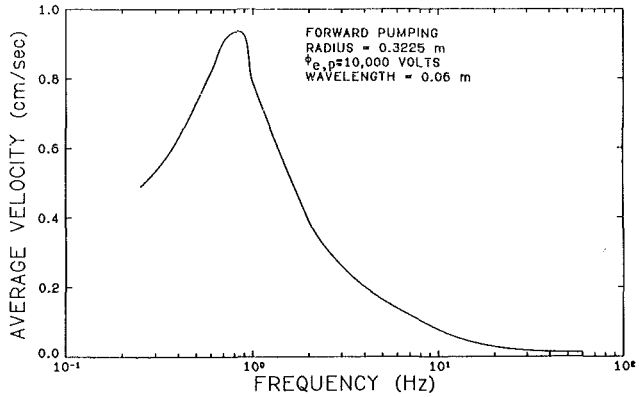

Fig. 6 The effect of frequency on the average pumping velocity

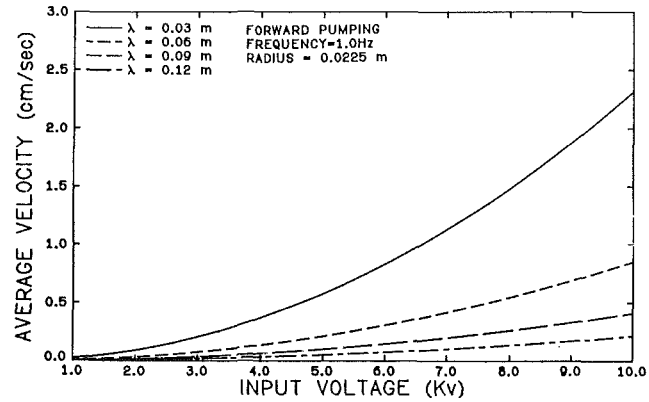

Fig. 7 Average velocity as a function of input voltage and wavelength

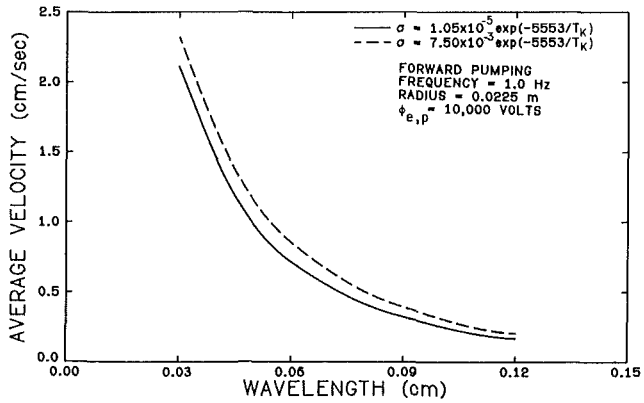

Fig. 8 The effect of electrical conductivity on the average pumping velocity

demonstrates that with proper selection of the parameters, the electrical potential can be reduced in the center without the presence of a grounding electrode which would reduce the flow rate. Figure 5 indicates that the pumping rate increases with increasing diameter-to-wavelength (i.e., electrode spacing) ratio. The effect of natural convection is relatively small as shown in the same figure. Figure 6 displays the influence of the frequency on the average velocity. It shows that the maximum velocities occur in a narrow range around 0.8 Hz. The average pumping velocity increases approximately as the square of the input voltage and decreses with increasing wavelength as shown in Fig. 7. The average velocity also increases with increasing electrical conductivity (Fig. 8). Figure 9 shows the effects of an externally imposed pressure gradient, CPZ. The bottom curve corresponds to the adverse pressure gradient, which creates a zero net mass flow with the

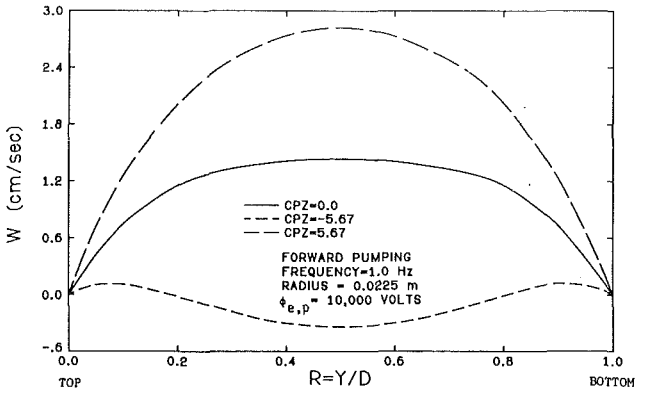

Fig. 9 Axial velocity distributions along the vertical centerline for various forcing functions – CPZ = $[a(dP/dZ)/(\epsilon E_0^2/2)]$

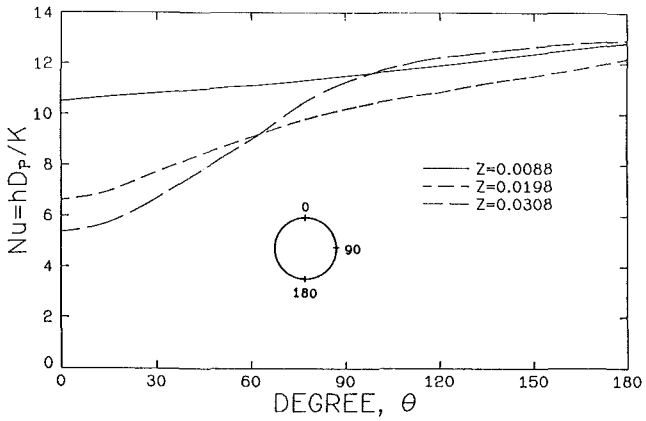

Fig. 10 Local Nusselt numbers at various axial positions with Ra* = 5 × 10^4

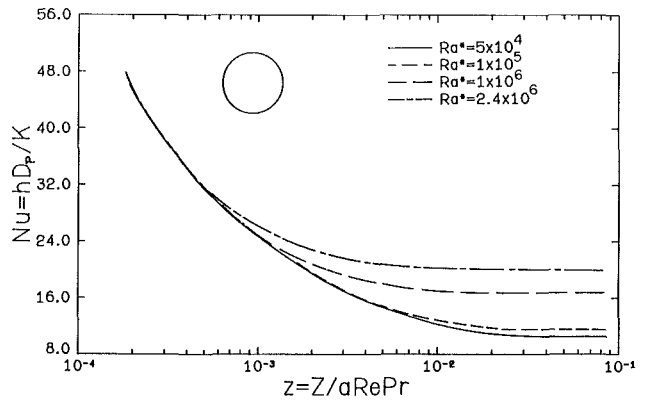

Fig. 11 Axial variation of the Nusselt number for circular pipe with various Rayleigh numbers

fluid moving forward near the wall due to electrical forces and moving backward in the center due to the pressure gradient. These results suggests that the design of heat exchanger/pumps must account for the pressure gradients created by the rest of the flow circuit. Qualitatively the results are quite similar for backward-wave pumps.

The velocities calculated were kept low in order to avoid numerical instabilities. Even at these low velocities the Peclet number is of the order of 1200 which justifies the basically parabolic model. The ultimate application of such an analysis is for velocities over an order of magnitude bigger, i.e., > 10 cm/s.

Figures 10 and 11 demonstrate typical thermal behavior under the constant heat flux condition in a heated pipe. Due to the secondary flow, the Nusselt number is lowest at the top where the temperature is maximum. The thermal entrance length becomes shorter with increasing Rayleigh numbers and the magnitude of the Nusslet number at fully developed flow varies approximately as

$$Nu = 1.7\,(Ra^*)^{1/6} \tag{21}$$

Conclusion and Recommendations

The governing equations have been developed for quasi-steady-state flows driven in horizontal channels by the interaction of axially traveling electric fields with the transverse temperature gradients. A finite element technique has been successfully adapted to the solution of these equations. Numerical results were obtained for a specific set of horizontal, circular tubes to illustrate the behavior of such EHD heat exchanger/pumps.

Perhaps the most significant result is that effective pumping can be obtained without a grounded electrode inside the tube; i.e., near zero electric potential can be created around the centerline by proper adjustment of the parameters without external ground connections. Even a very thin wire along the centerline would significantly reduce the EHD pumping because the velocities next to wire would always be zero. Without such a wire the velocities are maximum near the center.

For effective pumping, the electric fields should be high and the electrode spacing short. However, in practice, the electric gradients are limited by the dielectric strength of the fluid. The optimum frequencies are of the order of 1 Hz and are goverened by the electrical properties of the fluid, i.e., the synchronus speed. It seems that increasing the optimum frequency (e.g., to 60 Hz) is not very promising because this would require increasing the electrical conductivity of the fluid; thus, the electrical losses would increase. The axial velocities are relatively insensitive to heating/cooling rates (i.e., Rayleigh numbers) or changes in the magnitude of electrical conductivity. These effects, however, need further studies, particularly at higher heat flux levels.

Externally imposed pressure gradients have significant effects on the flow. Consequently, the design of EHD heat exchanger/pumps will require careful consideration of the entire flow circuit. For example, natural convection in the circuit should assist the EHD flow.

Although experimental results in an essentially two-dimensional channel qualitatively confirmed our results, we expect to build an experimental apparatus to obtain experimental, quantitative comparisons, as well as to study the limits of this type of EHD pumping.

Acknowledgments

Special thanks are due to Professor P. Krein for his very significant contributions to the analysis and to Mr. J. Seyed-Yagoobi for assistance in various aspects of work. The project was supported in part by Contract NO. EPRI-RP7871-1 from the Electric Power Research Institute with Messrs. T. Rodenbaugh and B. Bernstein as able project monitors.

References

1 Stuetzer, O. M., "Ion Drag Pumps," *J. Appl. Physics*, Vol. 31, 1960, pp. 136–146.

2 Melcher, J. R., "Travelling-Wave Induced Electroconvection," *Phys. Fluids*, Vol. 9, 1966, pp. 1548–1555.

3 Firebaugh, M. S., "Electrohydrodynamic Induction Pumping in a Closed Conduit," M.S. thesis, Department of Electrical Engineering, Massachusetts Institute of Technology, 1966.

4 Ochs, H. T., "Traveling-Wave Electrohydrodynamic Pumping," M.S. thesis, Department of Electrical Engineering, Massachusetts Institute of Technology, 1967.

5 Melcher, J. R., and Firebaugh, M. S., "Traveling-Wave Bulk Electroconvection Induced across a Temperature Gradient," *Phys. Fluids*, Vol. 10, 1967, pp. 1178–1185.

6 Gerdt, R. E., "Electrohydrodynamic Pumping of Cable Oil in Coaxial Geometry with Segmented Electrodes," M.S. thesis, Department of Mechanical and Industry Engineering, University of Illinois at Urbana-Champaign, 1977.

7 Okapal, M. F., "Traveling Wave Generation and Electrohydrodynamic Pumping with a Single Phase Voltage Supply," M.S. thesis, Department of Mechancial and Industry Engineering, University of Illinois at Urbana-Champaign, 1978.

8 Krein, P. T., "Analysis and Operation of an Electrohydrodynamic Pump Using a Single-Phase Voltage Supply," M.S. thesis, Department of Electrical Engineering, University of Illinois at Urbana-Champaign, 1980.

9 Kervin, D., "Variable Parameter Three-Phase Electrohydrodynamic Pumping in Rectangular Geometry," M.S. thesis, Department of Electrical Engineering, University of Illinois at Urbana-Champaign, 1980.

10 Kervin, D., Crowley, J. M., Krein, P., and Chato, J. C., "Parametric Studies of a Large Thermal EHD Induction Pump," Conference Record," IEEE-IAS Annual Meeting, Oct. 1981; also submitted to IEEE *Transactions on Industry Applications*.

11 Kuo, B.-S., "Flow Characteristics and Heat Transfer for Pressure and Electric Field Driven Laminar Flow with Temperature-Dependent Properties in a Pipe with Irregular Cross Section," Ph.D. thesis, Department of Mechanical and Industry Engineering, University of Illinois at Urbana-Champaign, 1981.

12 Melcher, J. R., *Continuum Electomechanics*, MIT Press, Cambridge, Mass., 1982.

13 Crowley, J. M., "The Efficiency of Electrohydrodynamic Pumps in the Attraction Mode," *J. of Electrostatics*, Vol. 8, 1980, pp. 171–181.

14 Chern, S.-Y., "Numerical Analysis of Convective Cooling of Pipe-Type Electric Cables," Ph.D. thesis, Department of Mechanical and Industry Engineering, University of Illinois at Urbana-Champaign, 1977.

15 Chern, S.-Y., and Chato, J. C., "A Finite Element Technique to Determine the Friction Factor and Heat Transfer for Laminar Flow in a Pipe With Irregular Cross Section," *Numerical Heat Transfer*, Vol. 1, 1978, pp. 453–470.

16 Crowley, J. M., Chato, J. C., et al., *Electrohydrodynamic Pumping in Cable Pipes*, Final Report, EPRI EL-2834, University of Illinois at Urbana-Champaign, 1983.

APPENDIX

Properties of Sun No. 4 oil used in the calculations:

Thermal conductivity: $k = 0.126$, W/m-C

Density: $\rho = 906.70\text{-}0.63571\ T$, kg/m^3

Dynamic viscosity: $\mu = 0.0430975\text{-}0.16751 \times 10^{-2}\ T + 0.248312 \times 10^{-4}\ T^2 - 0.127225 \times 10^{-6}\ T^3$, kg/m-s

Specific heat: $C_p = 1587.3 + 3.3186\ T$, J/kg-C

Electrical conductivity: $\sigma = C \exp(-5553/T_K)$, S/m

which C is a constant, e.g., 1.05×10^{-5}, depending on the purity of the oil, and T_K is absolute temperature in K whereas T is temperature in °C

Permittivity: $\epsilon = 2.2135 \times 10^{-11}$ F/m

Heat Transfer in Large Particle Bubbling Fluidized Beds

R. L. Adams
Associate Professor,
Department of Mechanical Engineering,
Oregon State University,
Corvallis, Ore. 97331
Mem. ASME

The potential use of fluidized bed combustion of coal as a means of meeting air quality standards with high-sulfur fuels has motivated the development of theoretical models of heat transfer in large particle gas fluidized beds. Models of the separate contributions of emulsion and bubble phase heat transfer have been developed by Adams and Welty [1] and Adams [2, 3, 4] and have been substantiated by experimental data for a horizontal tube immersed in a two-dimensional cold bed obtained by Catipovic [5, 6]. The consolidation of these models to predict local and overall time-average heat transfer to immersed surfaces requires information regarding emulsion phase residence time and bubble phase contact fraction for the particular geometry of interest. The analytical procedure to consolidate these models is outlined in the present work, then applied to the case of a horizontal tube immersed in a two-dimensional atmospheric pressure cold bed. Measurements of emulsion phase residence time and bubble phase contact fraction obtained by Catipovic [5] are used in the calculations for particle diameters ranging from 1.3 to 6 mm. The results agree favorably with experimental data and further substantiate the fundamental assumptions of the model.

Introduction

The potential use of fluidized bed combustion of coal as a means of meeting air quality standards has motivated a number of investigations of heat transfer in large particle or high-pressure fluidized beds (e.g., Chandron, Chen, and Staub [7], Glicksman and Decker [8], Zabrodsky et al. [9], Botterill and Denloye [10], Catipovic et al. [6], and Adams and Welty [1]). The baseline geometry for most investigations have been a tube immersed horizontally in the bed, though some investigators have considered vertical geometries as well (e.g., Botterill and Denloye [10]). Much of the experimental work has been in cold two- and three-dimensional beds, except the recent high-temperature, three-dimensional bed results obtained by George and Welty [11]. The purpose of this paper is to present an approximate analytical model of heat transfer to a horizontal tube immersed in a large particle bed, which has evolved from the gas convection model originally proposed by Adams and Welty [1].

Model Description. The baseline geometry for this analysis consists of a single tube immersed horizontally in a gas fluidized bed with a single bubble contacting the tube as shown in Fig. 1. The model is restricted to the bubbly flow regime of fluidization and therefore not applicable to the higher velocity turbulent regime. The bubble pushes the emulsion phase aside as it passes the tube so that the time-averaged local Nusselt number at a given location on the tube is given, according to Botterill [12]

$$\mathrm{Nu}_p = f_B \mathrm{Nu}_{p_B} + (1 - f_B)\,\mathrm{Nu}_{p_e} \tag{1}$$

where Nu_{p_B} and Nu_{p_e} are the bubble and emulsion phase Nusselt numbers, respectively, and f_B is the bubble contact fraction.

The bubble phase contribution to the heat transfer consists of the combined effects of gas convection due to flow through the bubble and thermal radiation from the particle surfaces defining the bubble boundary. A detailed investigation of the radiative contribution is presently underway so this contribution will not be addressed here. The gas convection contribution of the bubble phase heat transfer is dependent upon the flow field within the bubble, which is produced as the gas flows into the bottom and out the top of the bubble. Thus the bubble-phase heat transfer is highly dependent upon the hydrodynamic characteristics of the tube/bubble geometry.

A detailed analysis of the hydrodynamic interaction between two-dimensional bubbles and a horizontal tube is presented in Adams and Welty [18]. The results of this analysis show that bubble convective heat transfer is relatively insensitive to bubble velocity. This result is further supported by instantaneous heat transfer measurements performed by Catipovic [5] in which minimum instantaneous heat transfer coefficients were found to be relatively insensitive to superficial gas velocity. Accordingly, the bubble convective heat transfer will be estimated based on a hydrodynamic model for stationary ("slow") contacting bubbles.

For a single two-dimensional slow bubble of circular geometry contacting a horizontal tube, Adams [13] has shown that the boundary layer edge velocity for the portion of the tube within the bubble is given by

$$u/u_{mf} = 4 \sin\theta \tag{2}$$

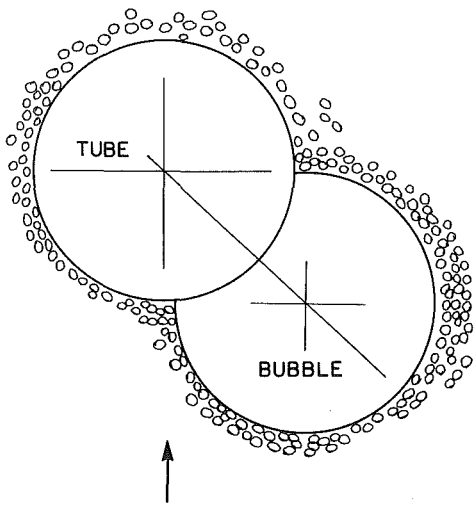

Fig. 1 Immersed tube with contacting bubble

Contributed by the Heat Transfer Division for publication in the JOURNAL OF HEAT TRANSFER. Manuscript received by the Heat Transfer Division February 3, 1983.

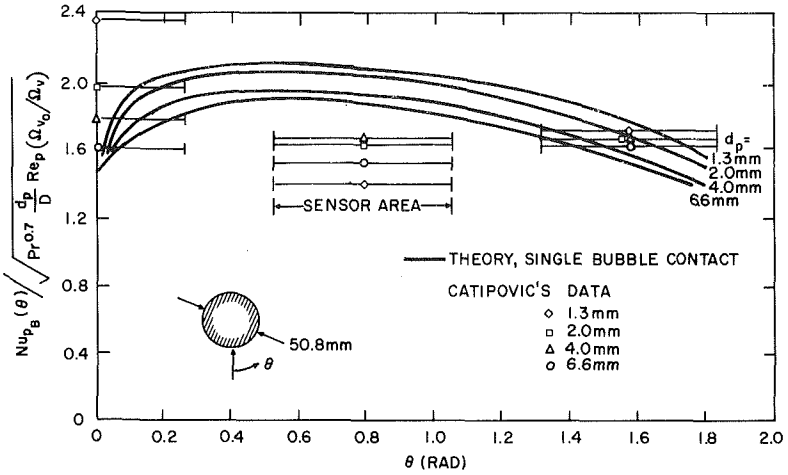

Fig. 2 Time-averaged local Nusselt number parameter for a contacting bubble with $u' = 0$, Pr = 0.72, and $\epsilon_\infty = 0.5$

with angle θ measured from the lower stagnation point on the tube. The result given by equation (2) is independent of bubble position as long as the boundary layer along the tube surface within the bubble does not separate from the surface. The simple velocity distribution given by equation (2) is used with the method of Smith and Spalding [14], modified to account for interstitial turbulence, to calculate local instantaneous heat transfer to the tube surface within the contacting bubble. Then the average bubble phase heat transfer is determined by integrating this result over possible bubble boundary positions. This analysis is given in [3] and produces the following bubble Nusselt number

$$\frac{\mathrm{Nu}_{p_B}(\theta)}{\sqrt{\mathrm{Pr}^{0.7}\frac{d_p}{D}\mathrm{Re}_p(\Omega_v/\Omega_{v_o})^{-1}}} = \frac{\sin^{b/2}\theta}{\theta} \Bigg/ \int_0^\theta \sqrt{1.13\int_{\theta_o}^\theta \sin^{b-1}\theta_1 d\theta_1 + \frac{0.297\epsilon_\infty}{\sqrt{1-\epsilon_\infty}}\frac{d_p}{D}\sin^{b-1}\theta_o}\, d\theta_o \tag{3}$$

$$\text{with}\ \Omega_v/\Omega_{v_o} = \left(02. + 0.8\ \exp\ (-0.849u'\sqrt{\frac{\mathrm{Re}_p}{\epsilon_\infty}}\right) \tag{4}$$

where d_p and D are particle and tube diameter, respectively, u' is the intensity of interstitial turbulence, ϵ_∞ is the bed voidage, Pr is the gas Prandtl number, Re_p is Reynolds number based upon average gas properties, u_{mf}, and particle diameter, and $b \simeq 2.95\ \mathrm{Pr}^{0.07}$. (Note that taking $b = 3$ is a reasonable approximation for gases.) The results of testing this model for average bubble heat transfer against two-dimensional cold bed data obtained by Catipovic are shown in Fig. 2. The extension of the model to the case of a three-dimensional spherical bubble can be accomplished by increasing the bubble through flow velocity by a factor of 1.5 in accordance wtih the isolated bubble fluid mechanical theory of Davidson [15]. This procedure results in an increase of about 22 percent in the bubble-phase Nusselt number. The analysis [3] also indicated that boundary layer separation always occurs within bubbles near $\theta = 1.8$ radians from the lower stagnation point. This suggests that contacting bubbles should be limited to the lower portion of the tube because the resulting reverse flow would cause the bubble to collapse. However, Catipovic's [5] hydrodynamic data indicate the present of bubbles on the upper portion of the tube at $u_o/u_{mf} \gtrsim 1.1$. These bubbles probably surround the tube completely

Nomenclature

b = parameter appearing in Smith and Spalding Nusselt number formula, $2.95\ \mathrm{Pr}^{0.07}$
C_{p_s} = particle specific heat
D = tube diameter
d_p = particle diameter
f_B = bubble contact fraction
Fo_m = Fourier number based upon average emulsion phase residence time, $k_s\bar{\tau}_e(\rho_e/C_{p_s}r_p^2)$
k_g = gas thermal conductivity based upon average temperature
k_s = particle thermal conductivity
k_β = pressure gradient parameter
k_1, k_2 = parameters appearing in formula for Stokes region edge location
L_c = interstitial channel dimension
Nu_p = time-averaged local Nusselt number, $\dot{q}''d_p/k_g(T_B - T_W)$
$\mathrm{Nu}_{p_{\mathrm{ave}}}$ = average Nusselt number for tube, $(\dot{q}'')_{\mathrm{ave}}d_p/k_g(T_B - T_W)$
Nu_{p_B} = time-averaged local Nusselt number for bubble contact, $\dot{q}''_B d_p/k_g(T_B - T_W)$
Nu_{p_e} = time-averaged local Nusselt number for emulsion phase contact, $\dot{q}''_e d_p/k_g(T_B - T_W)$
$\mathrm{Nu}_{p_{gc}}, \mathrm{Nu}_{p_{pc}}$ = gas convective and particle convective Nusselt numbers
Nu_{p_m} = parameter appearing in formula for Stokes region edge location
Nu_{p_s} = Nusselt number for Stokes region, $\dot{q}''_s d_p/k_g(T_B - T_W)$
$\mathrm{Nu}_{p_{sm}}$ = time-averaged Stokes region Nusselt number, $\dot{q}''_{sm}d_p/k_g(T_B - T_W)$
$\mathrm{Nu}_{p_{2D}}$ = two-dimensional Nusselt number for interstitial channel, $\dot{q}''_{2D}d_p/k_g(T_B - T_W)$
Pr = gas Prandtl number
Q_g = average interstitial gas velocity
$\dot{q}''$ = time-averaged local heat transfer rate per unit area
$(\dot{q}'')_{\mathrm{ave}}$ = heat transfer per unit area for tube
$\dot{q}''_B$ = heat transfer rate per unit area for bubble phase contact

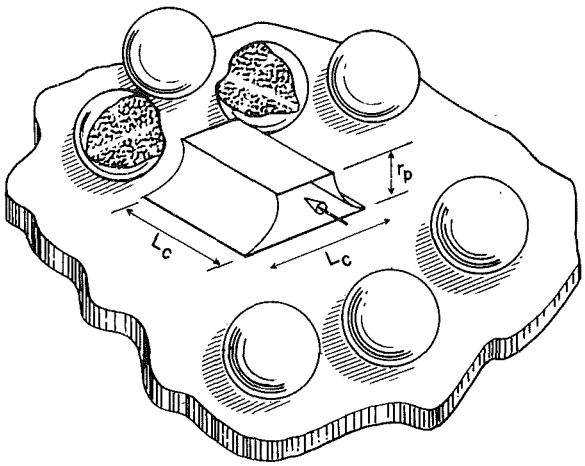

Fig. 3 Interstitial flow model

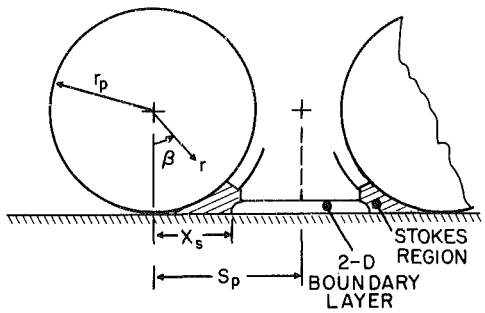

Fig. 4 Stokes region geometry

and the heat transfer in this case is approximated by using the lower stagnation value given by equation (3).

The emulsion phase heat transfer is based upon the model of Adams and Welty [1] with additional refinements and approximations [2, 4, 16]. The fundamental element of the model is the interstitial channel illustrated in Fig. 3, and the model is based upon a detailed analysis of the flow within this channel coupled with transient conduction within spherical particles that define the channel boundaries. The interstitial flow is partitioned into an inviscid core and surrounding boundary layers and the boundary layers are further divided into a two-dimensional region near the channel center, and three-dimensional, but Stokes-like regions, near the contact points as shown in Fig. 4. Furthermore, the inviscid core flow is assumed to be stagnationlike as a result of particle encounters. Then the emulsion phase Nusselt number (again not including thermal radiation) is expressed

$$\mathrm{Nu}_{p_e} = \mathrm{Nu}_{p_{2D}} \left(1 - \frac{x_s}{s_p}\right) + \mathrm{Nu}_{p_s} x_s / s_p \tag{5}$$

where x_s defines the edge of the Stokes region (here from the particle contact point rather than channel center as in previous publications), and s_p is half of the distance between particle centers. The particle spacing, s_p, is related to voidage according to

$$s_p \simeq 0.75 r_p / \sqrt{1-\epsilon} \tag{6}$$

where ϵ is the local emulsion phase voidage.

Most phenomenological models of fluid bed heat transfer [9, 17] assume

$$\mathrm{Nu}_{p_e} = \mathrm{Nu}_{p_{gc}} + \mathrm{Nu}_{p_{pc}} \tag{7}$$

where $\mathrm{Nu}_{p_{gc}}$ and $\mathrm{Nu}_{p_{pc}}$ are gas and particle convective contributions, respectively. A portion of the heat transfer to the surface beneath the Stokes region is independent of particle surface temperature so that the two terms in equation (4) do not exactly partition gas and particle convective contributions. In fact, the packed bed model previously proposed [16] includes the Stokes region contribution

$$\left[\mathrm{Nu}_{p_s}\right]_{\substack{\text{packed}\\ \text{bed}}} = -2S_o / (s_p / r_p) \tag{8}$$

Based upon the approximations given previously [2, 4], the two-dimensional Nusselt number for the stagnationlike interstitial flow, including the effect of interstitial turbulence, is

$$\mathrm{Nu}_{p_{2D}} = 0.798\,\mathrm{Pr}^{0.4} [\mathrm{Re}_c / [(s_p/r_p)\,(\Omega_v/\Omega_{v_o})]]^{1/2} \tag{9}$$

where Re_c is the Reynolds number based upon local average interstitial velocity, and the velocity profile parameter ratio, Ω_v/Ω_{v_o}, is given in equation (4) with Re_c in place of $\mathrm{Re}_p/\epsilon_\infty$. Also, the Stokes region edge location, obtained by requiring

Nomenclature (cont.)

$\dot{q}''_e$ = heat transfer rate per unit area for emulsion phase contact
$\dot{q}''_s, \dot{q}''_{sm}$ = heat transfer rate per unit area for Stokes region and average value
$\dot{q}''_{2D}$ = heat transfer rate per unit area for two-dimensional portion of interstitial channel
Re_c = channel Reynolds number, $Q_g d_p / \upsilon_g$
Re_p = Reynolds number, $u_{\mathrm{ref}} d_p / \upsilon_g$
r_p = particle radius
s_p = half of distance between particle centers
S_o = temperature-conductivity parameter
T = temperature
T_B = bed temperature
T_W = wall temperature
u = boundary layer edge velocity within contacting bubble
u' = interstitial turbulence intensity
u_{mf} = minimum fluidizing velocity
u_{ref} = reference velocity for interstitial gas velocity calculations ($\leq u_{mf}$)
u_o = superficial velocity
x_s = Stokes region edge location from particle contact point

Greek Symbols

α = exponent for gas thermal conductivity variation with temperature
ϵ = local voidage
ϵ_∞ = bed voidage
θ = angle coordinate from lower stagnation point
θ_0 = bubble trailing edge coordinate
θ_1 = integration variable
υ_g = gas kinematic viscosity at average temperature
ρ_s = particle density
ϕ_s = particle sphericity
$\bar{\tau}_e$ = average emulsion phase residence time
Ω_v, Ω_{v_o} = velocity profile parameter with and without interstitial turbulence

the Nusselt number to be continuous across the channel, is [16]

$$\left(1-\frac{x_s}{s_p}\right) \simeq \begin{cases} 0.76 + S_o k_1 / \mathrm{Nu}_{p_{2D}} \geq \mathrm{Nu}_{p_m} & \mathrm{Nu}_{p_{2D}} \geq \mathrm{Nu}_{p_m} \\ -k_2 \mathrm{Nu}_{p_{2D}} / S_o & \mathrm{Nu}_{p_{2D}} < \mathrm{Nu}_{p_m} \end{cases} \tag{10}$$

with

$$S_o = \frac{-2^\alpha}{(\alpha+1)} \frac{\left[1-\left(\frac{T_W}{T_B}\right)^{\alpha+1}\right]}{(1-T_W/T_B)\left(1+\frac{T_W}{T_B}\right)^\alpha} \tag{11}$$

where T_W and T_B are wall and bed temperatures, respectively, and the gas thermal conductivity is of the form $k_g \sim T^\alpha$. Also

$$k_1 \simeq 5.26 - 7.72[(s_p/r_p) - 1] \tag{12}$$

$$k_2 \simeq 0.0217 + .0222[(s_p/r_p) - 1] \tag{13}$$

$$\mathrm{Nu}_{p_m} \simeq -2k_1 S_0 / [0.76 - (0.578 - 4k_1 k_2)^{1/2}] \tag{14}$$

Thus the gas convective contribution to the emulsion phase heat transfer is determined once the interstitial gas velocity and hence Re_c is specified.

The heat transfer to the portion of the surface beneath the Stokes region is established from analysis of the steady conduction within the gas layer between the wall and particle surface. The amount of heat transfer depends on the particle surface temperature distribution, as well as on other details involving contact between rough surfaces. Thus it is necessary to couple the Stokes region conduction analysis with an analysis of transient conduction within the solid particles. In this analysis, the thermal mass of the gas is neglected, and the gas is assumed to respond instantaneously to changes in particle surface temperature. Then an alternating direction implicit finite difference scheme is used to carry out the transient conduction analysis for a spherical particle with symmetry about an axis perpendicular to the surface and passing through the contact point. The Stokes region analysis provides the necessary boundary conditions in the vicinity of the contact point, while the convective boundary conditions for the upper portion of the sphere are determined from the two-dimensional Nusselt number (e.g., equation (9)). The details of this analysis are presented in [4], and typical results for an air-sand system at low temperatures are shown in Fig. 5. Note from this figure that x_s/s_p Nu_{p_s} depends primarily upon particle Fourier number and is relatively insensitive to

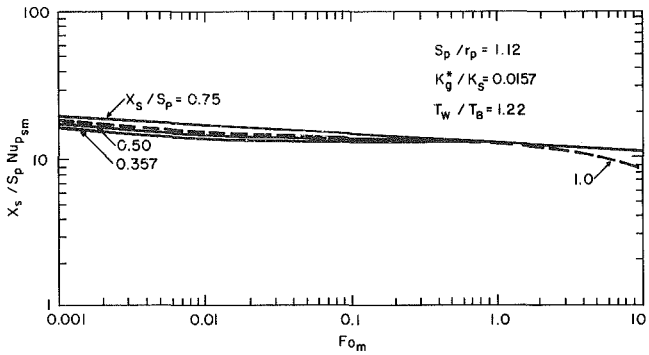

Fig. 5 Effect of Stokes region size upon particle convective heat transfer for an air-sand system at low temperature

Stokes region size (x_s/s_p). This result is consistent with previous empirical observations regarding the separation of particle and gas convective contributions [9, 10, 17].

The calculation of the average heat transfer according to equation (1) requires information regarding the hydrodynamic characteristics of the bed. Among the parameters required are the emulsion phase voidage, the emulsion phase mean residence time (i.e., Fourier number), the bubble contact fraction, and the average interstitial gas velocity. The bubble contact fraction and emulsion phase residence time are necessary ingredients for virtually all models of fluid bed heat transfer. Generally, these parameters must be obtained experimentally, though some correlations for small particles exist (see e.g. Baskakov et. al [21]). For the present study, the data obtained by Catipovic [5] based on the capacitance method were used. Note that Catipovic's data were obtained in a two-dimensional bed and will differ from those for a three-dimensional bed. The interstitial gas velocity can be estimated analytically when pressure gradient and gas velocity are linearly related. A detailed model of the interstitial flow around a horizontal tube immersed in a bubbling two-dimensional bed was reported by Adams and Welty [18]. This model provides the instantaneous velocity distribution at the tube surface from which the instantaneous heat transfer rates can be determined. The results obtained from the detailed model indicate that adjacent bubbles cause local instantaneous heat transfer coefficient to either increase or decrease relative to bubble-free levels depending upon bubble position. In order to simplify the calculation, the time-averaged heat transfer is assumed to be unaffected by adjacent bubbles (i.e., the effect is self compensating). Thus the interstitial velocity for the emulsion phase is taken to be equivalent to the bubble-free case, which Adams and Welty [1] have shown to reduce to

$$Q_g/u_{\mathrm{ref}} = 2(k_\beta(\epsilon_\infty)/k_\beta(\epsilon))\sin\theta/\epsilon \tag{15}$$

with $u_{\mathrm{ref}} \leq u_{mf}$ and where

$$k_\beta(\epsilon) \simeq \frac{150}{\mathrm{Re}_p}\left(\frac{1-\epsilon}{\epsilon\phi_s}\right)^2 + \frac{1.75}{\epsilon_\infty}\left(\frac{1-\epsilon}{\epsilon\phi_s}\right) \tag{16}$$

from a linearized form of the Ergun equation [1] for pressure gradient in packed beds. Also, the finite difference solution of George et al. [19] for the interstitial flow field is used for the high voidage lower stagnation region, yielding the approximation

$$\mathrm{Nu}_{p_{2D}} \underset{\epsilon \geq 0.8}{\simeq} 1.10\left\{\frac{k_\beta(\epsilon_\infty)\, d_p/D \mathrm{Re}_p \mathrm{Pr}^{.7} (\Omega_v/\Omega_{v_o})^{-1}}{\epsilon_\infty k_\beta(\epsilon)\left(1+(\epsilon/\epsilon_\infty - 1)^2\left(.065 + d_p/D\left(12.13 + \frac{991}{\mathrm{Re}_p}\right)\right)\right)}\right\}^{1/2} \tag{17}$$

The Stokes region contribution for the high-voidage regions is estimated by taking $x_s = r_p$ so that

$$\mathrm{Nu}_{p_e} \underset{\epsilon \geq 0.8}{\simeq} (1 - r_p/s_p)^2)\mathrm{Nu}_{p_{2D}} + \left(\frac{r_p}{s_p}\right)^2 \left\{\frac{x_s}{s_p}\mathrm{Nu}_{p_s}(\mathrm{Fo}_m)\right\} \tag{18}$$

with x_s/s_p $\mathrm{Nu}_{p_s}(\mathrm{Fo}_m)$ estimated from the transient conduction analysis for a particular gas/solid system, e.g., Fig. 5.

The model contains a few parameters, such as interstitial turbulence intensity and voidage at the heat transfer surface, which are difficult to specify in general. Measurements by Galloway and Sage [20] indicate a turbulence intensity (u') of about 0.2 for the interstitial voids of packed and fluidized beds. Varying u' between 0.1 and 0.3 will produce a change in

Table 1 Calculation parameters

Bed voidage (ϵ_∞)	0.4	(packed)
	0.5	(fluidized)
Surface voidage (ϵ)	0.44	(packed)
	0.55	(fluidized)
	0.90	($\theta = 0$)
Temperature ratio (T_W/T_B)	1.22	
Interstitial turbulence intensity (u')	0.2	(Galloway and Sage [20])
Prandtl number (Pr)	0.72	(air)
Reynolds numbers at u_{mf} (Re_p)	46.2	(1.3-mm Sand)
	116	(2-mm Dolomite)
	208	(2.85-mm Dolomite)
	371	(4-mm Dolomite)
	817	(6.6-mm Dolomite)
Fourier number range (Fo_m)	.0148 to 7.92	Catipovic[a] [5]
Bubble contact fraction (f_B)		Catipovic[a] [5]

[a]Interpolated from data for 1.3-mm sand and 4.0 dolomite

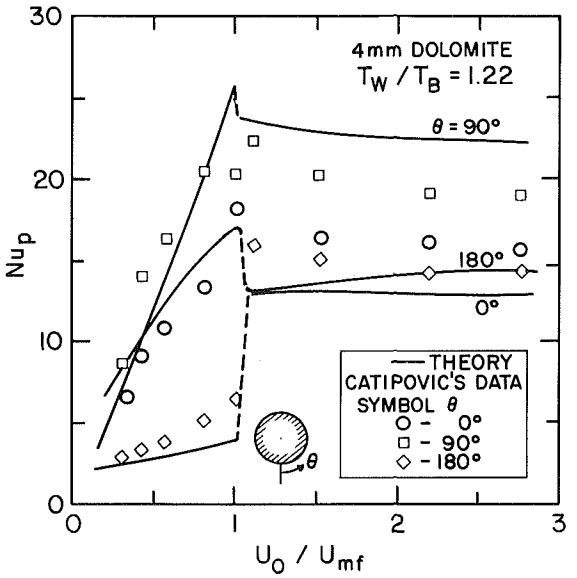

Fig. 6 Comparison of overall time-averaged Nusselt numbers for 4-mm dolomite particles with Catipovic's data

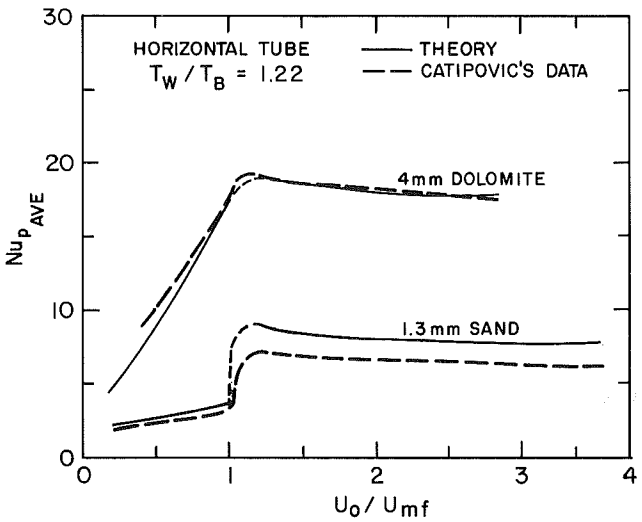

Fig. 7 Comparison of overall time-averaged Nusselt numbers for 4-mm dolomite and 1.3-mm sand with Catipovic's data

gas convective Nusselt number of about 5 to 14 percent for Reynolds numbers of 100 to 1000, respectively. The gas convective heat transfer is more sensitive to surface voidage, (ϵ) variations in ϵ of 30 percent produces a 19 percent variation in convective heat transfer at a Reynolds number of 100 and a 15 percent variation at a Reynolds number of 1000. The values of surface voidage used in the calculations shown below were selected on the basis of a combination of qualitative experimental observation and reasonable agreement between data and theory.

Application of the Model

The detailed heat transfer and hydrodynamic parameters measured by Catipovic [5] provide sufficient information to test the model. Catipovic's experiments were conducted in low-temperature, two-dimensional beds of sand and dolomite fluidized with air. Heat transfer, bubble contact fraction and emulsion phase residence times were determined locally for a horizontal tube of 50.8-mm dia and with sand particles of 1.3-mm mean dia and dolomite particles with mean dia of 2.0, 2.8, 4.0, and 6.6 mm. A summary of parameters used in the calculations is provided in Table 1.

Local time-averaged Nusselt numbers are compared with data for 4 mm dolomite particles in Fig. 6. Shown are results

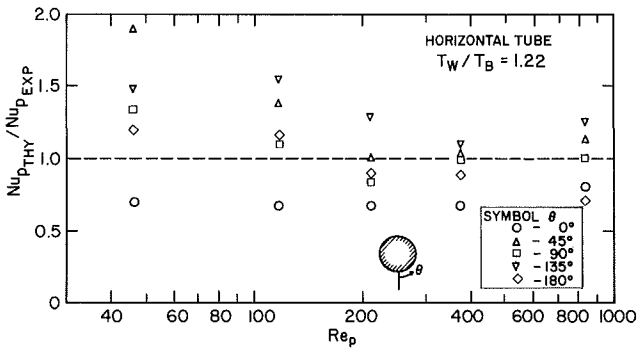

Fig. 8 Local Nusselt number comparison at $u_o \simeq 1.1\, u_{mf}$

for a packed bed ($u_o/u_{mf} < 1$) as well as the fluidized state up to $u_o/u_{mf} = 2.75$. The agreement with the packed-bed data was noted previously [16], while the values at $u_p/u_{mf} > 1$ were not previously reported. Generally, the trend of the theory is correct, but predicted values are at best reasonable when compared to data. The overall time-averaged Nusselt number for the tube is shown with Catipovic's data for 4-mm- and 1.3-mm-dia particles in Fig. 7. In this figure, note that compensating errors in local values (particularly at $\theta = 45$ and 135 deg and not shown in Fig. 6) result in excellent

agreement between theory and experiment for the 4-mm dolomite case while the 1.3-mm sand case is overpredicted for $u_o/u_{mf} > 1$.

The overall success of the model in predicting local time-averaged Nusselt numbers at $u_o/u_{mf} \simeq 1.1$ (so that significant bubbling occurs) is illustrated in Fig. 8. Shown in this figure is the ratio of predicted and measured values over a range of particle Reynolds number from 46.2 to 817 (particle sizes of 1.3, 2.0, 2.85, 4.0, and 6.6 mm).

These results show a trend toward overprediction at the lower Reynolds number (smaller particles) that is most likely due to the single particle feature of model. Though local values are not accurately predicted with the model, the errors are self-compensating so that reasonable agreement is obtained for the total time-averaged heat transfer, as Fig. 9 shows. Also shown are data obtained by Zabrodsky et al. [9] and Chandron, Chen, and Staub [7] that further supports the general validity of the model.

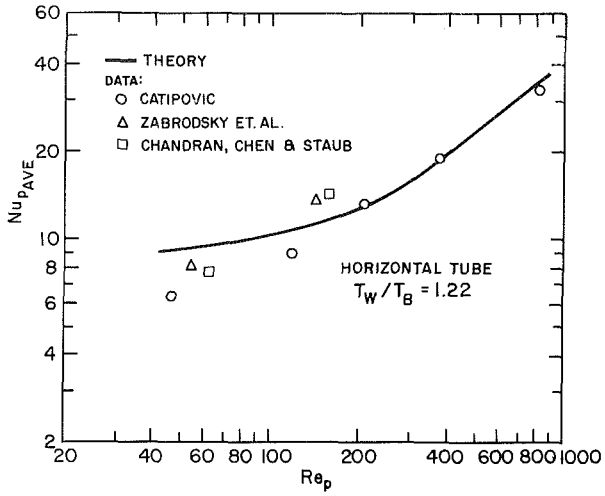

Fig. 9 Theoretical and experimental overall Nusselt numbers at $u_o \simeq 1.1\, u_{mf}$

Summary

A consistent model of the time-averaged heat transfer to a horizontal tube immersed in a gas fluidized bed has been presented. The model is based upon a consolidation of approximations and refinements of the gas convective model of Adams and Welty [1]. Calculations for overall Nusselt number agree reasonably well with cold two-dimensional bed measurements by Catipovic [5] when appropriate hydrodynamic parameters are used. However, local values of Nusselt number differ considerably with experimental results, particularly for the small particle cases. However, the overall agreement seems reasonable in view of the extreme complication of the phenomena and the purely theoretical nature of the model.

Acknowledgment

This work was funded by the National Science Foundation under Grant MEA80-20781 and the content of this paper does not necessarily reflect the views or policies of the sponsor.

References

1 Adams, R. L., and Welty, J. R., "A Gas Convection Model of Heat Transfer in Large Particle Fluidized Beds," *AIChE Journal*, Vol. 25, No. 3, 1979, pp. 395-405.

2 Adams, R. L., "An Approximate Formula for Gas Convection Dominant Heat Transfer in Large-Particle Fluidized Beds," ASME JOURNAL OF HEAT TRANSFER, Vol. 103, 1981, pp. 395-397.

3 Adams, R. L., "An Approximate Model of Bubble Phase Heat Transfer to a Horizontal Tube in a Large Particle Fluid Bed," ASME JOURNAL OF HEAT TRANSFER, Vol. 104, 1982, pp. 565-567.

4 Adams, R. L., "Coupled Gas Convection and Unsteady Conduction Effects in Fluid Bed Heat Transfer Based on a Single Particle Model," *International Journal of Heat and Mass Transfer*, Vol. 25, No. 12, 1982, pp. 1819-1828.

5 Catipovic, N. M., "Heat Transfer to Horizontal Tubes in Fluidized Beds: Experiment and Theory," Ph.D. thesis, Oregon State University, Corvallis, Ore., 1979.

6 Catipovic, N. M., Fitzgerald, T. J., George, A. H., and Welty, J. R., "Experimental Validation of the Adams-Welty Model for Heat Transfer in Large-Particle Fluidized Beds," *AIChE Journal*, Vol. 28, No. 5, 1982, pp. 714-720.

7 Chandron, R., Chen, J. C., and Staub, F. W., "Local Heat Transfer Coefficients Around Horizontal Tubes in Fluidized Beds," ASME JOURNAL OF HEAT TRANSFER, Vol. 102, No. 1, 1980, pp. 152-157.

8 Glicksman, L. R., and Decker, N., "Heat Transfer in Fluidized Beds with Large Particles," private communication.

9 Zabrodsky, S. S., Epanov, Y. G., Galershtein, D. M., Saxena, S. C., and Kolar, A. K., "Heat Transfer in a Large-Particle Fluidized Bed with Immersed In-Line and Staggered Bundles of Horizontal Smooth Tubes," *International Journal of Heat and Mass Transfer*, Vol. 24, 1981, pp. 571-579.

10 Botterill, J. S. M., and Denloye, A. O. O., "Gas Convective Heat Transfer in Packed and Fluidized Beds—1. A Theoretical Model," AIChE Symp., Ser. 74, No. 176, 1978, p. 194.

11 George, A. H., and Welty, J. R., "Local Heat Transfer Coefficients for a Horizontal Tube in a Large Particle Fluidized Bed at Elevated Temperature," *AIChE Journal*, to appear in 1983.

12 Botterill, J. S. M., *Fluid-Bed Heat Transfer*, Academic Press, New York, 1975.

13 Adams, R. L., "An Exact Solution for the Inviscid Flow Field Within a Two-Dimensional Bubble Contacting a Horizontal Tube in a Gas Fluidized Bed," *Chem. Engrg. Sci.*, Vol. 37, No. 9, 1982, pp. 1438-1440.

14 White, R. M., *Viscous Fluid Flow*, McGraw-Hill, New York, 1974.

15 Davidson, J. F., and Harrison, D., *Fluidized Particles*, Cambridge University Press, 1963.

16 Adams, R. L., "Extension of the Adams-Welty Fluid Bed Heat Transfer Model to the Packed Bed Case," ASME JOURNAL OF HEAT TRANSFER, Vol. 103, 1981, pp. 602-604.

17 Catipovic, N. M., Jovanovic, G. N., Fitzgerald, T. J., and Levenspiel, O., "A Model of Heat Transfer to Horizontal Tubes Immersed in a Fluidized Bed of Large Particles," *Fluidization—Proceedings of the 1980 Int. Fluidization Cont.*, edited by J. R. Grace and J. M. Matsen, Plenum Press, New York, 1980, pp. 225-234.

18 Adams, R. L., and Welty, J. R., "An Analytical Study of Bubble and Adjacent Tube Influence on Heat Transfer to a Horizontal Tube in a Gas Fluidized Bed," ASME JOURNAL OF HEAT TRANSFER, Vol. 104, 1982, pp. 206-209.

19 George, A. H., Catipovic, N. M., and Welty, J R., "An Analytical Study of Heat Transfer to a Horizontal Cylinder in a Large Particle Fluidized Bed," ASME Paper No. 79-HT-78, 1979.

20 Galloway, T. R., and Sage, H., "A Model of the Mechanism of Transport in Packed, Distended and Fluidized Beds," *Chem. Engrg. Sci.*, Vol. 25, 1970, pp. 495-516.

21 Baskakov, A. P., Berg, B. V., Vitt, O. K., Filippovsky, N. F., Kirakosyan, R. A., Goldobin, J. M., and Maskauv, V. K., "Heat Transfer to Objects Immersed in Fluidized Beds," *Power Technology*, Vol. 8, 1973, pp. 273-282.

Heat Transfer From Rough and Finned Horizontal Tubes in a Gas Fluidized Bed

I. Goel

S. C. Saxena

A. F. Dolidovich[1]

Department of Chemical Engineering,
University of Illinois at Chicago,
Chicago, Ill. 60680

Experimental results of the heat transfer coefficient for smooth, rough, and finned tubes of o.d. 12.7 and 50.8 mm immersed in fluidized beds of silica sand particles of average diameters ($\bar{d}_p$) 145, 167, 488, and 788 μm are reported as a function of fluidizing velocity. The surface roughness is of V-shaped fins with the values of pitch (P_f) as 5.08, 3.18, 1.58, 0.79, 0.40, and 0.24 mm. The qualitative trends of these heat transfer coefficients in regard to their dependence on various systems and operating parameters are discussed on the concept of particle mode of heat transfer, contact geometry of the heat transfer surface, particle residence time, particle size and size range, tube diameter, etc. Results are also analyzed in terms of the fin effectiveness factor (ϕ) and heat transfer function (β). It is shown that ϕ and β are only weakly dependent on tube diameter, particle size range, and fluidizing velocity and therefore have been correlated in terms of the dimensionless ratio ($P_f/\bar{d}_p$). It is also shown that particle residence time on the heat transfer surface controls the value of the heat transfer coefficient rather sensitively.

Introduction

In the design of fluidized-bed coal combustors the knowledge of heat transfer coefficient, h_w, between a bed and an immersed surface is crucial. The reliable calculation of h_w from basic mechanistic heat transfer models is not possible at the present time because a number of mechanisms for energy exchange between a surface and a bed have been proposed and these are reviewed by Botterill [1] and Saxena and Gabor [2]. The mechanistic process is quite complicated due to the involvement of a large number of geometrical and operating parameters. Further, adequate characterization of the bubble dynamics and solids movement in the bed is seldom achieved. As a result, a number of correlations have been proposed with verification against experimental data. For smooth horizontal single tubes recent investigations of Grewal and Saxena [3], and Goel and Saxena [4] from this laboratory may be quoted, and these papers also include all the major earlier studies. It is well known that heat transfer from finned and rough surfaces is greater generally, in comparison to that from smooth surfaces under otherwise identical conditions.

Work on heat transfer coefficient of a surface with artificial roughness in a gas fluidized bed is somewhat limited [1, 5], but many types of rough surfaces have been employed. These are transverse (serrated, continuous, or helical) and longitudinal (continuous) fins of different profiles such as rectangular, parabolic, triangular, and trapizoidal. For better understanding of the heat transfer process, it is essential to know the orientation, height, thickness, and separation of fins. The orientation of fins with respect to gas flow is also important. Due to the large number of these variable factors, intercomparison of data of different workers have been difficult as also the development of a correlation involving all the parameters. In recent years, the papers of Grewal and Saxena [6], Krause and Peters [7], and Goel [8], have reviewed the major works on heat transfer from finned tubes.

Here, we report our experimental data on smooth and finned horizontal tubes of o.d. 12.7 and 50.8 mm immersed in gas fluidized beds of silica sands. The finned tubes consist of V-threads having pitches, P_f, of 5.08, 3.18, 1.58, 0.79, 0.40, and 0.24 mm. Four silica sands are used as bed materials and their average diameters and ranges are: 145 (106–250)μm, 167 (106–300)μm, 488 (300–850)μm, and 788 (500–1000)μm. In each case the measurements are taken as a function of fluidizing velocity at ambient temperatures and pressures in a 0.305 m square fluidized bed which is described briefly in the next section.

Experimental Facility and Procedure

The entire fluidized-bed facility, consisting of a fluidization

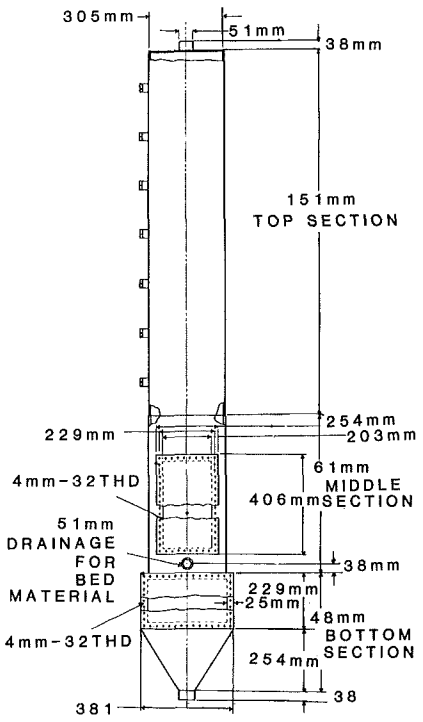

Fig. 1 Front view of the 0.305 m (12.0 in.) square fluidized bed (all dimensions are in inches)

[1]Permanent address: Luikov Institute of Heat and Mass Transfer, BSSR Academy of Sciences, Minsk, BSSR, USSR.

Contributed by the Heat Transfer Division for publication in the JOURNAL OF HEAT TRANSFER. Manuscript received by the Heat Transfer Division February 7, 1983.

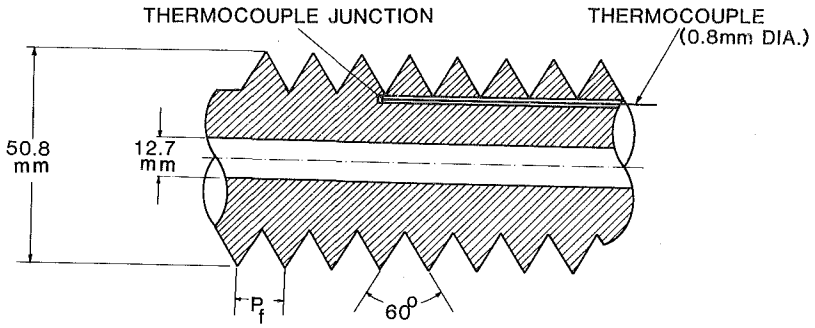

Fig. 2 A typical view of the middle section of a finned heat transfer tube

column, air supply system, electrical heating system for heat transfer tubes, and an off-gas system comprising of a cyclone and a fabric filter, is quite similar to that used in earlier works reported from this laboratory by Grewal and Saxena [3, 6]. However, the fluidization column is rebuilt from 9-mm-thick steel sheets and its schematic, emphasizing the front view is shown in Fig. 1, where some of the pertinent dimensions are also indicated. The use of thick sheet metal enabled fastening the side plates to the test section by tapping blind holes in the steel plates. This modification eliminated the possibility of any air leakage through the mounting bolts. Most of the bed joints are also welded to avoid air leakage.

The fluidization column consists of the bottom, middle, and top sections. The top section or freeboard, is 1.51 m in height and has seven solids sampling and seven pressure probes. The middle test section is 0.61 m tall and is provided with three temperature and nine pressure probes. A front plexiglass window permits the visual observations. The bottom section or wind box, is about 0.48 m in height and here the fluidization air rearranges itself for a uniform flow through the bed. The air first flows through an air jet breaker plate in the wind box and then through the fluidized bed distributor plate. Both these plates employ flat top bubble caps screwed into a 0.318-cm-thick steel plate with 0.635-cm-dia holes on 2.8 cm center-to-center spacing. Each bubble cap is constructed from a 1.59-cm-long hexagonal cap steel screw, and three equally spaced 0.8-mm-dia holes are drilled into the base of the cap at a 45 deg angle. The free area of the distributor plate is 0.2 percent.

The fluidizing air, supplied by a 25 HP compressor, is dried and filtered before entering the fluidization column. A d-c power supply with a voltage regulation of ±0.01 percent is used to energize the calrod cartridge heaters employed in heat transfer tubes. Iron-constantan thermocouples measure the heat transfer tube surface, bed and supply air temperatures. The thermocouple wires are connected to an Omega digital temperature indicator, model 400A, with a resolution of 0.1 K. The pressure probes are 6.4-mm o.d. copper tubes with porous metal plugs to prevent the flow of solid particles. The design details are given by Goel and Saxena [4].

A typical finned heat transfer tube is shown in Fig. 2. The tube is heated by a calrod heater, and its ends are provided

Nomenclature

A_w = surface area of smooth heat transfer tube, m^2
C_{pf} = specific heat of fluidizing air at a constant pressure, kJ/kg.K
C_{ps} = specific heat of solid particles, kJ/kg K
$\bar{d}_p$ = average particle diameter defined by equation (1), m
d_{pi} = arithmetic average diameter of the successive screens, m
D_T = outside diameter of a smooth heat transfer tube or diameter of imaginary cylindrical surface passing through the tips of fins, m
g = acceleration due to gravity, m/s^2
G = superficial mass fluidizing velocity of air, kg/m^2s
G_{mf} = mass fluidizing velocity of air at minimum fluidizing conditions, kg/m^2s
G_{opt} = gas velocity at which maximum value of h_w occurs, kg/m^2s
h_w = total heat transfer coefficient for a surface W/m^2K
h_{ws} = total heat transfer coefficient for a smooth tube, W/m^2K
h_{wfb} = total heat transfer coefficient for a finned tube based on the surface area of a smooth tube with outside diameter equal to finned tube tip diameter, W/m^2K
h_{wft} = total heat transfer coefficient based on actual surface area, W/m^2K
k_f = thermal conductivity of air, W/m.K
Nu_{wt} = Nusselt number based on tube diameter = $h_w D_T/k_f$, dimensionless
P_f = pitch for V-threaded tubes, it is the distance between two identical points of the consecutive threads, m
Q = electrical power supplied to the heater, W
T_b = average bed temperature, K
T_w = average surface temperature of heat transfer tube, K
w_i = weight fraction consecutive sieves, kg

Greek Letters

β = heat transfer capacity function defined as the ratio of the effective heat transfer coefficient for a finned tube, h_{wfb}, to the heat transfer coefficient for a smooth tube having the same outside diameter as the tip diameter of the finned tube, h_{ws}, at the same fluidizing velocity, h_{wfb}/h_{ws}, dimensionless
ϵ = void fraction of the fluidized bed, dimensionless
μ = viscosity of the fluidizing gas, Ns/m^2 or kg/m.s
ρ_f = density of fluidizing air density, kg/m^3
ρ_s = solid particle density, kg/m^3
ϕ = fin effectiveness factor defined as the ratio of the total heat transfer coefficient based on actual surface area for a finned tube, h_{wft}, to the heat transfer coefficient for a smooth tube having the same outside diameter as the tip diameter of the finned tube, h_{ws}, at the same fluidizing velocity, h_{wft}/h_{ws}, dimensionless

Table 1 Particle size, size range, and minimum fluidization velocity of the various silica sands used in the present work

Average particle diameter, μm	145	167	488	788
RMS dev.	60	69	212	464
Size range, μm	106–250	106–300	300–850	500–1000
Minimum fluidization velocity, m/s	0.029	0.027	0.150	0.400

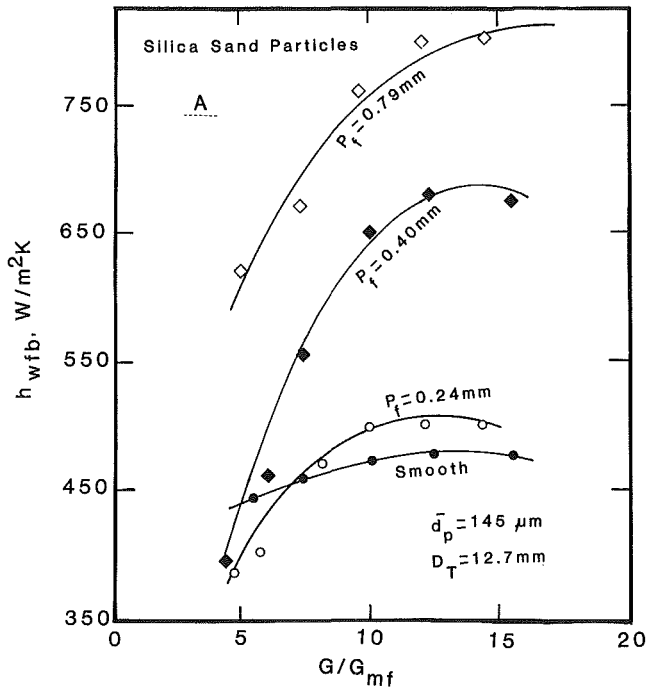

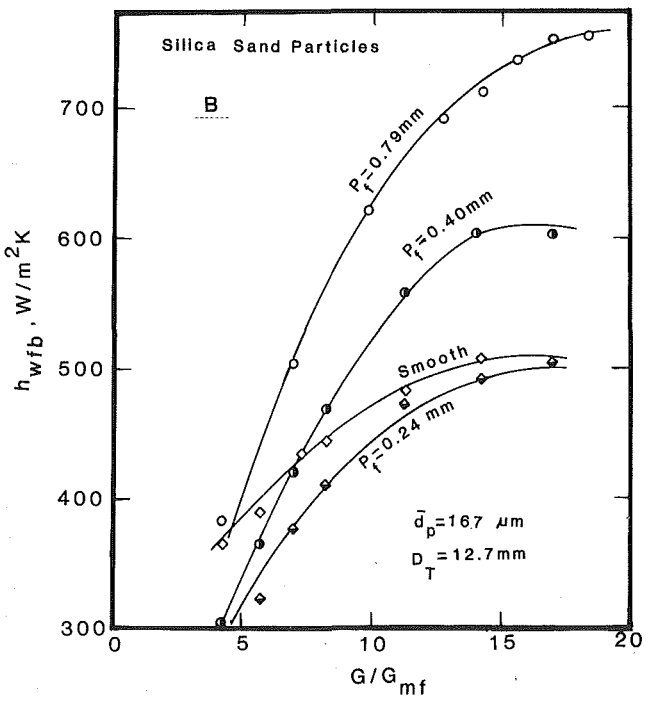

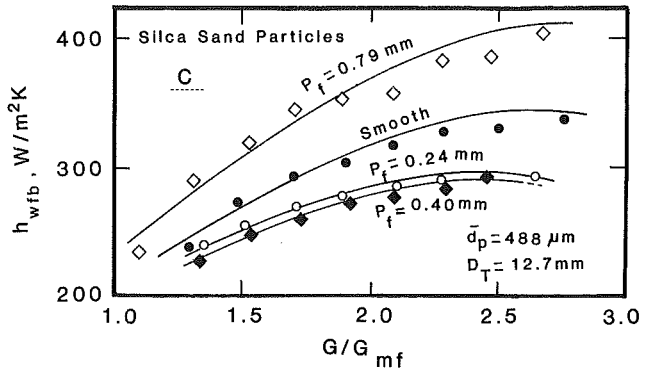

Fig. 3 Variation of h_{wfb} with G/G_{mf} for 12.7-mm-dia smooth and finned tubes immersed in fluidized beds of sand particles

with teflon support to reduce axial heat loss which is estimated to be less than 1 percent of the total heat supplied to the tube. These iron-constantan thermocouples are bonded to the tube surface in milled grooves with technical quality copper cement. A calibrated voltmeter and ammeter, having an accuracy of 1 percent, are used to determine the power supplied to the heaters.

The equipment for particle size analysis consists of a Riffle Sampler, analytical balance and a sonic sifter with a complete set of sieves. The details about this equipment are given by Goel [8], and the cumulative particle size distribution of the four silica sand particles are given elsewhere [4, 9]. The average particle diameters, $\bar{d}_p$, are computed from the following relation

$$\bar{d}_p = \frac{1}{\sum_1 (w_i/d_{pi})} \tag{1}$$

where w_i the weight fraction between consecutive sieving screens, and d_{pi} is the arithmetic average diameter of the successive screens. These values are reported in Table 1.

The heat transfer tubes are mounted 35 cm above the distributor plate and the unfluidized bed height varies between 37 to 40 cm. The bed temperature is established as the mean of temperatures registered by the three thermocouples located 19.5, 34.5, and 49.5 cm above the distributor plate. The mean surface temperature of the tube is always smaller than 384 K so that thermal radiation loss is certainly negligible. The testing procedure is similar to that of Grewal and Saxena [6], and the steady state is assumed to have established when the changes in the temperatures of the thermocouples registering the bed temperature are less than 0.1 K in 10 min. The total heat transfer coefficient for a smooth tube, h_{ws}, is determined from the following relation

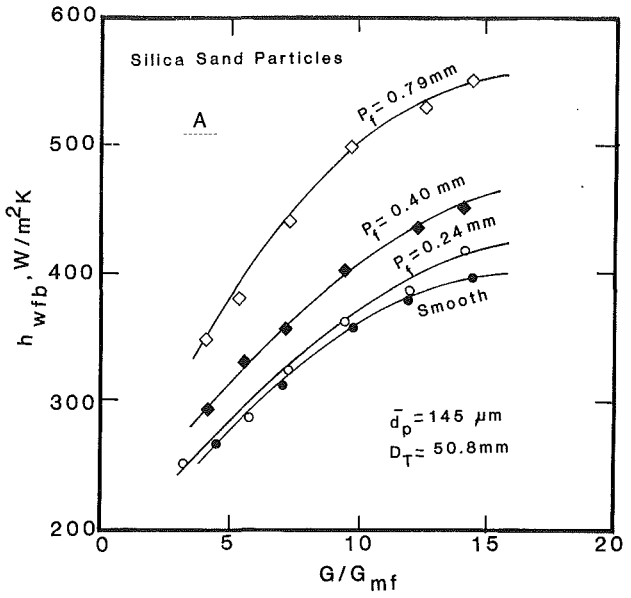

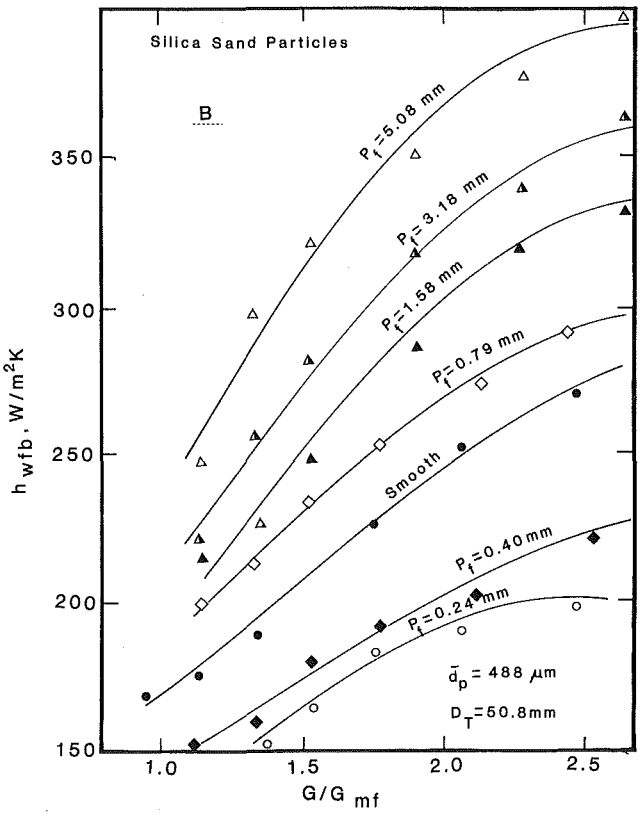

$$h_{ws} = \frac{Q}{A_w (T_w - T_b)} \tag{2}$$

The total heat transfer coefficient for rough or finned tubes, h_{wft}, is also given by equation (2), except that A_w now represents the total surface area of the rough or finned tube. Another practice for finned tubes is to base the total heat transfer coefficient on the surface area of a smooth tube whose o.d. is equal to the tip diameter of the finned tube and is represented by h_{wfb}. In our discussion of results of heat transfer data, we employ two more parameters, ϕ and β. ϕ is called the fin effectiveness factor and for a given system is defined as the ratio of h_{wft} to h_{ws}, both referring to the same fluidizing velocity. In an analogous manner, β, for a system at a given fluidizing velocity, is defined as the ratio of h_{wfb} to

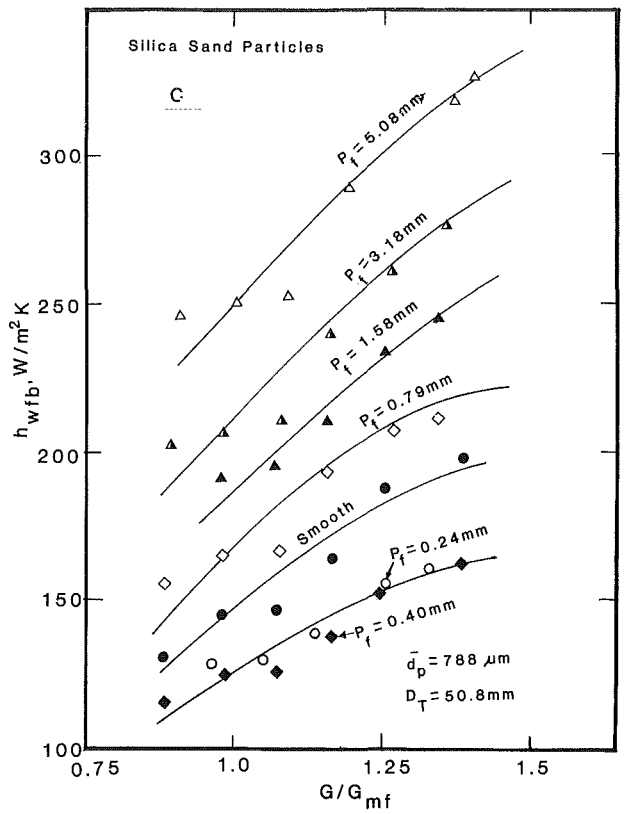

Fig. 4 Variation of h_{wfb} with G/G_{mf} for 50.8-mm-dia smooth and finned tubes immersed in fluidized beds of sand particles

h_{ws}, β is also referred to as the heat transfer capacity function [7, 10]. To the extent h_{wfb} is an effective heat transfer coefficient for a finned tube, β is a very important practical parameter, because it is a direct measure of the increase in heat transfer due to the rough nature of the surface. Specific results for tubes of different sizes and pitches for beds of different sizes of silica sands are reported and discussed in the next section.

Results and Discussion

Experimental values of heat transfer coefficient for smooth tubes, h_{ws}, effective heat transfer coefficient, h_{wfb}, and total heat transfer coefficient, h_{wft}, for finned tubes are shown plotted against fluidization number, G/G_{mf}, in Figs. 3 and 4 for tubes of diameter 12.7 and 50.8 mm, respectively. The computed probable and maximum errors in h_w are 4 and 7.5 percent, respectively [8]. It is shown by many investigators [1, 5–7, 10–12] that surface roughness of the heat transfer tube submerged in a fluidized bed affects its heat transfer coefficient significantly. The magnitude, however, in general depends on many factors, such as parameters characterizing the roughness, the diameter, and shape of the particles, tube diameter, fluidizing velocity, etc. Workers on tubes with V-shaped fins have found that h_{wfb} is greater than h_{ws} when P_f is greater than $\bar{d}_p$, but the trend reverses for P_f smaller than $\bar{d}_p$ when h_{wfb} is smaller than h_{ws}. Grewal and Saxena [6], in particular, have found from their experimental results that $\beta = (h_{wfb}/h_{ws})$ decreases from its value of unity as $(P_f/\bar{d}_p)$ is increased from zero to about 0.8, and thereafter β increases with further increase in $P_f/\bar{d}_p$ and becomes greater than unity. As pointed out by Chen and Withers [10], on conceptual grounds that β will approach the value of unity again as $(P_f/\bar{d}_p)$ is continuously increased to infinity by letting P_f approach infinity as then the finned surface approaches the smooth surface. This qualitative variation of β with $(P_f/\bar{d}_p)$

Table 2 Values of ϕ and β for tubes of different diameters and particle sizes averaged over the experimental velocity range

$P_f/\bar{d}_p$	$\bar{d}_p$, μm	ϕ		β	
		$D_T = 12.7$ mm	$D_T = 50.8$ mm	$D_T = 12.7$ mm	$D_T = 50.8$ mm
0.305	788	-	0.42 ± 0.01	-	0.83 ± 0.01
0.495	488	0.48 ± 0.01	0.39 ± 0.02	0.90 ± 0.03	0.77 ± 0.02
0.508	788	-	0.42 ± 0.01	-	0.83 ± 0.01
0.820	488	0.47 ± 0.01	0.43 ± 0.02	0.88 ± 0.02	0.83 ± 0.01
1.004	788	-	0.56 ± 0.01	-	1.11 ± 0.02
1.437	167	0.48 ± 0.05	-	0.93 ± 0.07	1.10 ± 0.02
1.619	488	0.66 ± 0.00	0.57 ± 0.01	1.19 ± 0.01	-
1.655	145	0.52 ± 0.05	0.49 ± 0.03	1.01 ± 0.06	1.03 ± 0.04
2.001	788	-	0.65 ± 0.02	-	1.27 ± 0.02
2.395	167	0.57 ± 0.07	-	1.10 ± 0.13	-
2.759	145	0.65 ± 0.10	0.57 ± 0.01	1.27 ± 0.18	1.14 ± 0.01
3.228	488	-	0.62 ± 0.00	-	1.22 ± 0.01
4.034	788	-	0.75 ± 0.03	-	1.42 ± 0.02
4.731	167	0.71 ± 0.10	-	1.32 ± 0.17	-
5.448	145	0.79 ± 0.12	0.68 ± 0.02	1.57 ± 0.12	1.37 ± 0.04
6.455	788	-	0.92 ± 0.02	-	1.67 ± 0.04
6.506	488	-	0.71 ± 0.01	-	1.32 ± 0.01
10.416	488	-	0.80 ± 0.00	-	1.47 ± 0.03

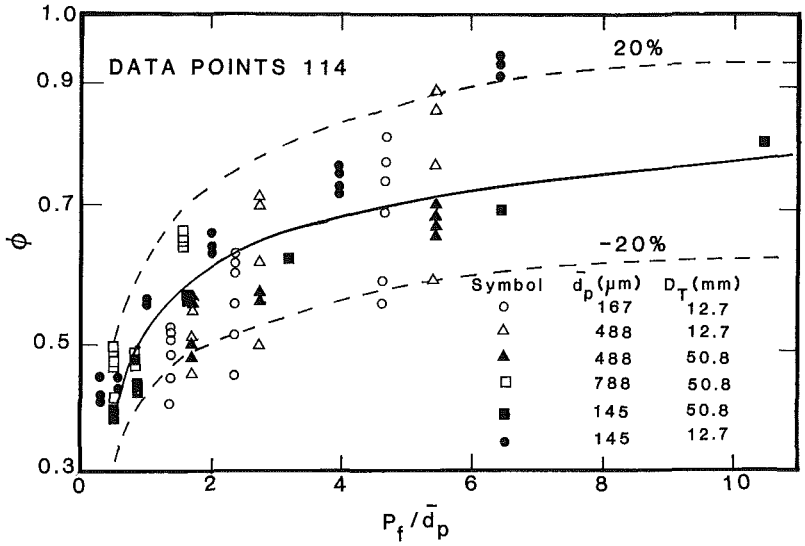

Fig. 5 Variation of ϕ with $P_f/\bar{d}_p$. The continuous curve is based on equation (3).

has been explained by many workers [6, 11, 12] by invoking such ideas as the bed porosity near the heat transfer surface, particle residence time on the surface, particle and surface contact geometry, particle clogging, etc.

Figures 3 and 4 reveal that h_{wfb} values depend on the fluidizing velocity, surface roughness (i.e., P_f for these V-shaped fins), particle size, and tube diameter. The qualitative variation of h_{ws} and h_{wfb} with G/G_{mf} is in complete accord with the reported trends in the literature. The heat transfer coefficient both for smooth and rough tubes increases with the increase in the value of G greater than G_{mf} till an optimum value of G is reached beyond which h_w decreases as G is further increased. This characteristic dependence of h_{ws} on G is explained on the basis of "particle mode" heat transfer [3]. From our data shown in Figs. 3 and 4, it appears that generally, but not always, h_{wfb} is larger than h_{ws} when P_f is greater than $\bar{d}_p$, and h_{wfb} is smaller than h_{ws} when P_f is less than $\bar{d}_p$. This trend, which also has been reported earlier in the literature, is not well substantiated by our results in Fig. 3(*b*) and to some extent in Fig. 4(*c*). Qualitatively, these results can be explained on the basis of particle size distribution, and therefore we would like to infer that the dependence of β on $P_f/\bar{d}_p$ is not simple and particle size range in addition to mean particle diameter must be included in a precise interpretation of results.

Grewal and Saxena [6] concluded from their work that the fluidizing velocity at which the heat transfer coefficient attains its maximum value, G_{opt}, is greater for finned tubes than for smooth tubes. It appears that most of our data are also in accord with this earlier conclusion, except in a few cases a clear trend is not obvious. Particle sphericity or its shape controls the heat transfer coefficient because its residence time on the surface is dependent on its sphericity. In our earlier work [6], we employed glass beads of average diameter 427 μm, which were almost spherical in shape. One of the silica sands used in the present work has a value of $\bar{d}_p$ = 488 μm, and its particles are nonspherical. On comparison with the results of spherical glass beads of about the same mean diameter, we found [8] that h_w for silica sand is almost 50 percent smaller than glass beads. We attribute this to the shape of glass beads which exhibit a much higher mobility on the heat transfer surface, and hence a relatively smaller residence time. It may be recalled that both the particles have about the same value of heat capacity.

The total heat transfer coefficient for finned tubes, h_{wft}, is also computed for all the cases shown in Figs. 3 and 4, and

these plots for the sake of brevity will not be reported here but are available elsewhere [8]. One important qualitative result that is evident from these graphs is that h_{wft} is always smaller than h_{ws} (smooth tubes). This inequality applies over the entire fluidization velocity range and for all the six values of the pitches and for the two values of the tube diameter. As a result the value of the fin effectiveness factor, ϕ, computed from these h_{wft} and h_{ws} values for a given bed particle size, finned tube, and fluidizing velocity is always less than unity. The calculations revealed that the dependence of ϕ on G/G_{mf} is relatively weak, and the variation is less for large particles in comparison to small particles. The standard deviation in ϕ for particles of mean sizes, 488 and 788 μm, is always less than ± 0.025, while for particles of $\bar{d}_p = 145$ and 167 μm, it is always between ± 0.025 and ± 0.125. The ϕ values are shown plotted in Fig. 5 as a function of $P_f/\bar{d}_p$ and Table 2 lists the various ϕ values averaged over the velocity range of our present experiments. The standard deviations in the ϕ values are also given in this table.

From Table 2 and Fig. 5, it is evident that ϕ is not a unique function of $P_f/\bar{d}_p$ and for a precise functional representation of ϕ, the dependence on such parameters as G, D_T, particle size range, etc., must also be included. We could not find any simple function capable of meeting these requirements, and in view of the weak dependence of ϕ on these factors we have ignored it. This led us to regard ϕ as a function of $(P_f/\bar{d}_p)$ only. The qualitative trend of Fig. 5 suggests a simple function and the following correlation is found adequate

$$\phi = 1 - 0.49(P_f/\bar{d}_p)^{-0.33} \tag{3}$$

As P_f approaches infinity, the finned tube will behave more and more like a smooth tube so that ϕ will approach unity. The above correlation meets this requirement. As long as $(P_f/\bar{d}_p)$ is greater than 0.5, we find that 92 percent of our data points show a scatter of ± 20 percent. This is also ascribed as the probable uncertainty of the values generated from this correlation. Knowing the fin effectiveness factor, the total heat transfer coefficient for a finned tube can be generated from the following relation

$$h_{wft} = \phi . h_{ws} = \phi \mathrm{Nu}_{wt} (k_f/D_T) \tag{4}$$

For tubes of D_T smaller than 50.8 mm, the correlation for Nu_{wt} of Grewal and Saxena [3] is recommended

$$\mathrm{Nu}_{wt} = 47(1-\epsilon)\left[\frac{GD_T\rho_s}{\mu_f\rho_f}\left(\frac{\mu_f^2}{\bar{d}_p^3\rho_s^2 g}\right)\right]^{0.325} \left[\frac{\rho_s C_{ps} D_T^{3/2} g^{1/2}}{k_f}\right]^{0.23} \left[\frac{\mu_f C_{pf}}{k_f}\right]^{0.3} \tag{5}$$

While for tubes of D_T greater than or equal to 50.8 mm, the correlation of Goel and Saxena [4] may be employed,

$$\mathrm{Nu}_{wt} = 17.9(1-\epsilon) \left[\left(\frac{GD_T\rho_s}{\mu_f\rho_f}\right)\left(\frac{\mu_f^2}{\bar{d}_p^3\rho_s^2 g}\right)\right]^{0.325} \left[\frac{\rho_s C_{ps} D_T^{3/2} g^{1/2}}{k_f}\right]^{0.23} \left[\frac{\mu_f C_{pf}}{k_f}\right]^{0.3} \left[\frac{D_T G^2}{g\bar{d}_p^2\rho_f^2}\right]^{0.147} \tag{6}$$

Comparison of the calculated and experimental values of heat transfer coefficient is shown in Fig. 6. The experimental h_{wft} values refer to four particles (Table 1), two D_T values (12.7 and 50.8 mm) and for several fluidizing velocities in each case. The total data points are 150, and the points shown at the upper end of the figure pertain to particles of 145 and 167 μm average diameter. The calculated values are according to equation (4) in which ϕ is obtained from equation (3). Nu_{wt} is obtained from equation (5) for $D_T < 50.8$ mm and from equation (6) for $D_T \geq 50.8$ mm. The agreement between the

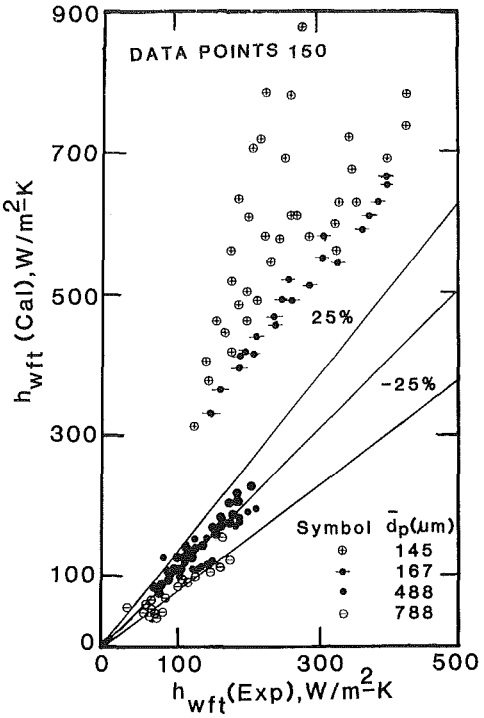

Fig. 6 Comparison of experimental and computed h_{wft} values

calculated and experimental values is quite good, the deviations are well within ± 25 percent, except for small particles ($\bar{d}_p = 145$ and 167 μm). It has been observed by us as well as by others that the experimental heat transfer values are smaller than the calculated values for small particles due to particle agglomeration.

So far we have used the rough and finned tubes without making any distinction between the two. Grewal and Saxena [6] distinguished between them on the basis of the heat transfer mechanism involved depending on the value of $P_f/\bar{d}_p$. Certainly, other factors are involved, and as mentioned earlier in this section, particle size range also is very important. However, when the pitch is large compared to the mean particle diameter, $P_f/\bar{d}_p > 2$, the bulk of the increase in heat transfer is attributed to the increase in the effective area of the heat transfer surface, and it appears appropriate to refer to them as finned surfaces. The majority of our data lie in the range of: $2 \leq P_f/\bar{d}_p \leq 10$ and the foregoing correlations can be applied to finned surfaces in general, particularly if the operating and system geometry is close to what has been employed in the present investigations.

From a practical standpoint, the knowledge of the heat transfer capacity function, β, is very significant for design calculations. If the geometry of the finned tube is precisely known, β is related to ϕ and this relationship can be derived. For V-shaped fins

$$\beta = \phi R^{-1} \tag{7}$$

where

$$R = \frac{2}{\pi D_T}\sqrt{P_f^2 + \pi^2(D_T - 0.866P_f)^2}$$

Our experimental β values are shown in Fig. 7 as a function of $P_f/\bar{d}_p$. This simple functional dependence, which ignores the dependence of β on such factors as D_T, particle size range, fluidizing velocity, etc., is valid only as long as an uncertainty of ± 20 percent can be tolerated in β. A regression analysis of 114 data points for $0.5 < (P_f/\bar{d}_p) < 10.5$ leads to the following correlation for β

$$\beta = 0.977 + (P_f/\bar{d}_p)^{0.21} \tag{8}$$

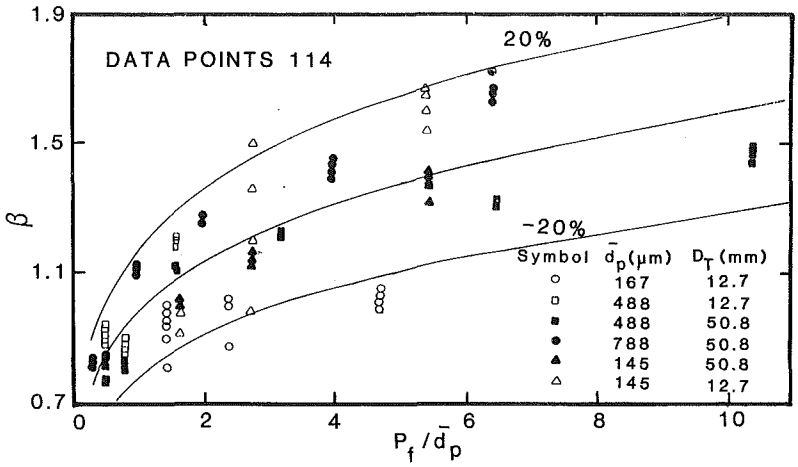

Fig. 7 Variation of β with $P_f/\bar{d}_p$. The continuous curve is based on equation (8).

Table 2 lists the mean values of β averaged over the entire range of fluidizing velocity. The dependence of β on D_T is evident from this table which suggests that β decreases as the tube diameter increases. As expected, it is noted that the qualitative variation of ϕ and β on various factors are similar. Figure 7 indicates that the use of finned tubes would increase the heat transfer rate from the surface to the bed by a significant amount, a good 50 percent, and therefore the use of such tubes is advocated. However, economic and material problems will complicate adoption and assessment of total potential for a specific application.

Acknowledgments

The authors are thankful to National Science Foundation for partly supporting this work under Grant No. MEA-8022097 with Dr. Win Aung as the program director.

References

1 Botterill, J. S. M., *Fluid-Bed Heat Transfer*, Academic Press, 1975.

2 Saxena, S. C., and Gabor, J. D., "Mechanisms of Heat Transfer between a Surface and a Gas-Fluidized Bed for Combustor Application," *Prog. Energy Comb. Sci.*, Vol. 7, 1981, pp. 73–102.

3 Grewal, N. S., and Saxena, S. C., "Heat Transfer Between a Horizontal Tube and a Gas-Solid Fluidized Bed," *International Journal of Heat and Mass Transfer*, Vol. 23, 1980, pp. 1505–1519.

4 Goel, I., and Saxena, S. C., "Dependence of Heat Transfer Coefficient for an Immersed Smooth Horizontal Tube in a Fluidized Bed on Operating and System Variables," *Proceedings of the Seventh International Fluidized Bed Combustion Conference*, Vol. 2, 1982, pp. 804–818.

5 Saxena, S. C., Grewal, N. S., Gabor, J. D., Zabrodsky, S. S., and Galershtein, D. M., "Heat Transfer Between a Gas Fluidized Bed and Immersed Tubes," *Advances in Heat Transfer*, Vol. 14, 1978, pp. 149–247.

6 Grewal, N. S., and Saxena, S. C., "Effect of Surface Roughness on Heat Transfer From Horizontal Immersed Tubes in a Fluidized Bed," ASME JOURNAL OF HEAT TRANSFER, Vol. 101, No. 3, 1979, pp. 397–403.

7 Krause, W. B., and Peters, A. R., "Heat Transfer From Horizontal Serrated Fluid Tubes in an Air-Fluidized Bed of Uniformly Sized Particles," Paper No. 80-HT-48, ASME-AIChE Heat Transfer Conference, Orlando, Fla., July 27–30, 1980.

8 Goel, I., "Heat Transfer From Immersed Smooth and Finned Horizontal Tubes in a Gas Fluidized Bed," M.S. thesis, University of Illinois at Chicago, Dec. 1982.

9 Shah, P. J., Upadhyay, S. N., and Saxena, S. C., "Heat Transfer From Smooth Horizontal Tubes Immersed in Gas Fluidized Beds," Paper No. HMT-21-81, Sixth National Heat and Mass Transfer Conference, Indian Institute of Technology, Madras, India, 1981.

10 Chen, J. C., and Withers, J. G., "An Experimental Study of Heat Transfer From Plain and Finned Tubes in Fluidized Beds," AIChE Paper No. 34, The 15th National Heat Transfer Conference, San Francisco, Aug. 1975.

11 Vijayaraghavan, M. R., and Sastri, V. M. K., "Effect of Surface Roughness on Heat Transfer in Fluidized Beds," Conference on Future Energy Production, Int. Center Heat and Mass Transfer, Dubrovnic, 1975, pp. 571–578.

12 Korolev, V. N., and Syromyatnikov, N. I., "Heat Transfer From a Surface With Artificial Roughness to a Fluidized Bed," *Journal of Engineering Physics*, Vol. 28, No. 6, 1975, pp. 698–700.

The Boundary Layer Natural Convection Regime in a Rectangular Cavity With Uniform Heat Flux From the Side

S. Kimura

A. Bejan
Assoc. Mem. ASME

Department of Mechanical Engineering,
University of Colorado,
Boulder, Colo. 80309

This paper summarizes an analytical and numerical study of buoyancy-driven convection in a rectangular cavity filled with fluid. The new feature of this study, suggested by architectural applications of the convection phenomenon, is the presence of constant heat flux heating and cooling along the vertical side walls. It is shown analytically that in the boundary layer regime the boundary layer thickness must be constant (independent of altitude), that the core must be motionless and linearly stratified, and that the vertical walls temperature must vary linearly with the same gradient as the core temperature. The Nusselt number $(q''/\Delta T)H/k$ *was found to be equal to 0.34* $(H/L)^{1/9}\,Ra^{2/9}$, *where* H/L *is the height/length ratio and* $Ra = g\beta q'' H^4/(k\alpha\nu)$. *The second part of the paper presents a numerical study of the same phenomenon: the numerical results agree very well with the analytical predictions made in the first part of the paper.*

1 Introduction

Numerous engineering applications have made the topic of "natural convection in enclosures" one of the most active subfields in heat transfer research today. Much of this activity has been summarized in reviews and reference books, most recently by Catton [1], Jaluria [2], and the NSF Natural Convection Workshop [3]. Based on these reviews, it is fair to conclude that the fundamental research on natural convection in enclosures is focused almost exclusively on the two-dimensional model of a rectangular enclosure with vertical isothermal walls at different temperatures. This model may offer certain advantages if the research is conducted analytically or numerically; however, it poses serious problems in the laboratory where isothermal wall conditions are notoriously difficult to simulate (constant heat flux conditions are much easier to establish).

In addition, if the study of natural convection in enclosures is to enhance our understanding of how the air and energy carried by air circulates through buildings, the "isothermal walls" model is clearly inadequate: the temperature of the great majority of walls encountered in architectural and solar applications is not maintained uniform, rather, it is the "consequence" of the heat flux administered to the wall. The temperature of a wall separating two fluid chambers at different temperatures "floats" such that the wall becomes increasingly warmer with altitude and the heat flux through the wall is essentially uniform [4-6].

It seems that a more appropriate model for the study of convection in enclosures is the rectangular cavity with uniform heat flux along the two vertical sides (Fig. 1). This fact was pointed out earlier by Balvanz and Kuehn [7] in their study of convection in a vertical slot with one isothermal wall facing a conducting wall with internal heat generation. The object of this paper is to document the flow and heat transfer characteristics in a vertical enclosure where both walls are subjected to the uniform heat flux condition. The following presentation has two parts. In the first part, an analytical solution for the boundary layer regime is developed along the lines of the solution constructed by Gill [8] for the same regime in a box with isothermal side walls. In the second part, the phenomenon is simulated numerically, and the numerical results are shown to agree well with the analytical solution.

2 Boundary Layer Analysis

Consider the two-dimensional rectangular slot shown in Fig. 1. The uniform heat flux is specified along both side walls,

$$q'' = k\left(\frac{\partial T}{\partial x}\right)_{x=0,L} = \text{constant} \tag{1}$$

and the top and bottom walls are assumed insulated. The boundary layer equations governing the conservation of mass, momentum, and energy are

$$\frac{\partial u}{\partial x} + \frac{\partial v}{\partial y} = 0 \tag{2}$$

$$u\frac{\partial v}{\partial x} + v\frac{\partial v}{\partial y} = -\frac{1}{\rho}\frac{dP}{dy} + \nu\frac{\partial^2 v}{\partial x^2} + \beta g(T - T_o) \tag{3}$$

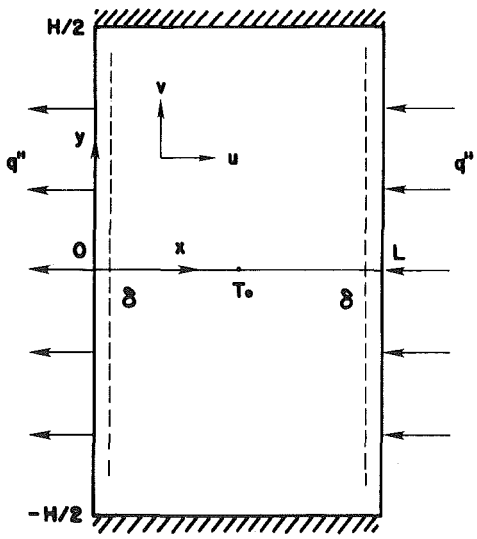

Fig. 1 The coordinate system (the broken lines indicate the extent of the boundary layer)

Contributed by the Heat Transfer Division for publication in the JOURNAL OF HEAT TRANSFER. Manuscript received by the Heat Transfer Division August 23, 1982.

$$u\frac{\partial T}{\partial x}+v\frac{\partial T}{\partial y}=\alpha\frac{\partial^2 T}{\partial x^2} \tag{4}$$

where the fluid has been modeled as Boussinesq–incompressible. T_o is the temperature in the geometric center of the slot and is taken as the reference temperature of the sytem. The other symbols appearing in equations (2–4) and on Fig. 1 are defined in the Nomenclature.

On scaling grounds, Gill [8] showed that for Pr >> 1 fluids the inertia terms are negligible in equation (3), in the *thermal* boundary layer region [9]. This simplification and the observation that in the boundary layer the pressure is a function of y only yields the momentum equation

$$\frac{\partial^3 v}{\partial x^3}+\frac{g\beta}{\nu}\frac{\partial T}{\partial x}=0 \tag{5}$$

Now in the thermal boundary layer of thickness δ, equations (1–5) guarantee the equivalence of the following scales

$$q''\sim k\frac{\Delta T}{\delta} \tag{6}$$

$$\frac{u}{\delta}\sim\frac{v}{H} \tag{7}$$

$$\frac{v}{\delta^3}\sim\frac{g\beta}{\nu}\frac{\Delta T}{\delta} \tag{8}$$

$$\left(\frac{u\Delta T}{\delta}\text{ or }\frac{v\Delta T}{H}\right)\sim\alpha\left(\frac{\Delta T}{\delta^2}\right) \tag{9}$$

These four statements define the unknown scales of the flow and temperature field

$$\begin{aligned}\delta &= H\mathrm{Ra}^{-1/5}\\ \Delta T &\sim \frac{\alpha\nu}{g\beta H^3}\mathrm{Ra}^{4/5}\\ u &\sim \frac{\alpha}{H}\mathrm{Ra}^{1/5}\\ v &\sim \frac{\alpha}{H}\mathrm{Ra}^{2/5}\end{aligned} \tag{10}$$

where Ra is the Rayleigh number based on prescribed heat flux and height

$$\mathrm{Ra}=\frac{g\beta q'' H^4}{\alpha\nu k} \tag{11}$$

The scales of the boundary layer, equations (9), suggest the following nondimensional set of governing equations

$$\frac{\partial u^*}{\partial x^*}+\frac{\partial v^*}{\partial y^*}=0 \tag{12}$$

$$\frac{\partial^3 v^*}{\partial x^{*3}}+\frac{\partial T^*}{\partial x^*}=0 \tag{13}$$

$$u^*\frac{\partial T^*}{\partial x^*}+v^*\frac{\partial T^*}{\partial y^*}=\frac{\partial^2 T^*}{\partial x^{*2}} \tag{14}$$

where the dimensionless variables are

$$\begin{aligned}x^* &= \frac{x}{H\mathrm{Ra}^{-1/5}}, y^*=\frac{y}{H}, v^*=\frac{v}{\frac{\alpha}{H}\mathrm{Ra}^{2/5}}\\ u^* &= \frac{u}{\frac{\alpha}{H}\mathrm{Ra}^{1/5}}, T^*=\frac{T-T_o}{\frac{\alpha\nu}{g\beta H^3}\mathrm{Ra}^{4/5}}\end{aligned} \tag{15}$$

The corresponding dimensionless boundary conditions for the left boundary layer are

$$\begin{aligned}&(i)\ u^*=v^*=0\ ,\ \frac{\partial T^*}{\partial x^*}=1 \text{ at } x^*=0\\ &(ii)\ \left.\begin{array}{l}u^*\to u^*_\infty(y^*)\\ v^*\to 0\\ T^*\to T^*_\infty(y^*)\end{array}\right\}\ \text{as } x^*\to\infty\end{aligned} \tag{16}$$

where u^*_∞ and T^*_∞ are the flow and temperature in the "core" (at $x^* >> 1$).

Equations (12–14) are the same equations that Gill [8] solved for the boundary layer regime in a slot with isothermal walls. Indeed, the governing equations (2), (4), (5) were nondimensionalized as equations (12–14) so that Gill's linearized solution can be adopted unchanged

$$v^*=\sum_{n=1}^{2}a_n(y^*)\exp[-\lambda_n(y^*)x^*] \tag{17}$$

where λ_1, λ_2 are complex numbers with positive real parts [8]. Subjecting this solution to the *present* conditions, equations (16), yields

$$v^*=\frac{1}{\lambda_1^3-\lambda_2^3}(e^{-\lambda_1 x^*}-e^{-\lambda_2 x^*}) \tag{18}$$

$$T^*=\frac{-1}{\lambda_1^3-\lambda_2^3}(\lambda_1^2 e^{-\lambda_1 x^*}-\lambda_2^2 e^{-\lambda_2 x^*})+T^*_\infty(y^*) \tag{19}$$

The unknown functions $\lambda_1(y^*)$, $\lambda_2(y^*)$ and $T^*_\infty(y^*)$ are determined based on three additional statements

Nomenclature

a_n = coefficient in equation (17)
c_p = specific heat at constant pressure
g = gravitational acceleration
Gr = Grashof number, $g\beta q'' L^4/(\nu^2 k)$
H = vertical dimension of the slot (height)
k = thermal conductivity
L = horizontal dimension of the slot (width)
Nu = Nusselt number, $(q''/\Delta T)H/k$
P = pressure
p = odd function of y
Pr = Prandtl number
q = even function of y
q'' = heat flux
Ra = Rayleigh number, $g\beta q'' H^4/(\alpha\nu k)$
Ra_L = Rayleigh number, $g\beta\Delta T L^3/(\alpha\nu)$
T = temperature
T_o = reference temperature
ΔT = temperature difference between the side walls
u = horizontal velocity
v = vertical velocity
x = horizontal coordinate
y = vertical coordinate
α = thermal diffusivity
β = coefficient of thermal expansion
δ = thickness of the boundary layer
ν = kinematic viscosity
ρ = density
λ_n = function of y
ψ = stream function
ω = vorticity

Subscript

∞ = indicating conditions in the core

Superscript

$*$ = nondimensional quantities

(*a*) Mass conservation integral

$$\psi^*_\infty = -\int_0^\infty v^* dx^* \tag{20}$$

where $\psi^*_\infty(y^*)$ is the dimensionless core stream function.

(*b*) Energy conservation integral

$$\left| u^* T^* \right|_0^\infty + \frac{d}{dy}\int_0^\infty v^* T^* dx^* = \left| \frac{\partial T^*}{\partial x^*} \right|_0^\infty \tag{21}$$

(*c*) Core centrosymmetry about $x = L/2$, $y = 0$ in Fig. 1, which means that

$$\begin{aligned} T^*_\infty(y^*) &= -T^*_\infty(-y^*) \\ T^{*\prime}_\infty(y^*) &= T^{*\prime}_\infty(-y) \\ \psi^*_\infty(y^*) &= \psi^*_\infty(-y^*) \end{aligned} \tag{22}$$

The two integral conditions (*a*, *b*) yield in the present case

$$\psi^*_\infty = \frac{1}{\lambda_1\lambda_2(\lambda_1^2 + \lambda_1\lambda_2 + \lambda_2^2)} \tag{23}$$

$$\frac{d}{dy^*}\left[\frac{\psi^{*2}_\infty}{2}\frac{(\lambda_1\lambda_2)^2}{\lambda_1+\lambda_2}\right] - \psi^*_\infty T^{*\prime}_\infty(y^*) = -1 \tag{24}$$

In order to take full advantage of the centrosymmetry conditions (*c*), it is convenient to express equations (23, 14) in terms of Gill's functions [8]

$$\begin{aligned} p(y^*) &= \text{odd function} \\ q(y^*) &= \text{even function} \end{aligned}$$

where

$$\lambda_{1,2} = \frac{q}{4}(1-p)[1 \pm i\sqrt{1+2p}] \tag{25}$$

Thus, equations (23, 24) become

$$\psi^*_\infty = \frac{64}{q^4(1-p)^4(1-p^2)} \tag{26}$$

$$\frac{d}{dy^*}\left[\frac{1}{2}\left(\frac{64}{q^4(1-p)^4(1-p^2)}\right)\frac{q^3}{32}\right] - \frac{64}{q^4(1-p)^4(1-p^2)} T^{*\prime}_\infty(y^*) = -1 \tag{27}$$

The essence of the entire analysis is hidden in these two equations: it is clear that in order for both ψ^*_∞ and the left-hand-side of equation (27) to be even functions of y^*, we must have at the same time

$$\begin{aligned} p &= 0 \\ q &= \text{constant} \\ T^{*\prime}_\infty &= \text{constant} \end{aligned} \tag{28}$$

In conclusion, in the boundary layer regime of a vertical slot with uniform heat flux, the core must be motionless (u^*, $v^* \to 0$) and linearly stratified. Furthermore, since the λ's are constant, equation (25), the actual boundary layer thickness is independent of y^*. In summary, the solution is

$$\begin{aligned} \lambda_{1,2} &= \frac{1}{4}q(1 \pm i) \\ v^* &= -\frac{32}{q^3} e^{-\frac{q}{4}x^*} \sin\left(\frac{q}{4}x^*\right) \\ T^* &= -\frac{4}{q} e^{-\frac{q}{4}x^*} \cos\left(\frac{q}{4}x^*\right) \\ \psi^*_\infty &= 64/q^4, T^*_\infty = y^*/\psi^*_\infty \end{aligned} \tag{29}$$

where q is an unknown constant.

The solution is completed by determining q from the observation that in the arbitrary control volume of Fig. 2 the vertical enthalpy flow through the flow must be balanced *exactly* by the downward heat conduction

$$\int_0^L \rho c_p v T dx = \int_0^L k\frac{\partial T}{\partial y} dx, \text{ at any } y = \text{constant} \tag{30}$$

This property stems from the fact that the top of the control volume is insulated, and the heat entering through the right wall exists undiminished through the left wall (q'' = constant is specified along both vertical walls). Thus equation (30) is the first law of thermodynamics for the control volume of arbitrary height in Fig. 2. Writing expressions similar to equations (29) for the boundary layer ascending along the right wall ($x = L$, Fig. 1), and substituting these along with equations (29) into equation (30) yields

$$q^9 = 8192\frac{H}{L}\mathrm{Ra}^{1/5} \tag{31}$$

For brevity, the algebra associated with the path from equation (30) to equation (31) is not shown.

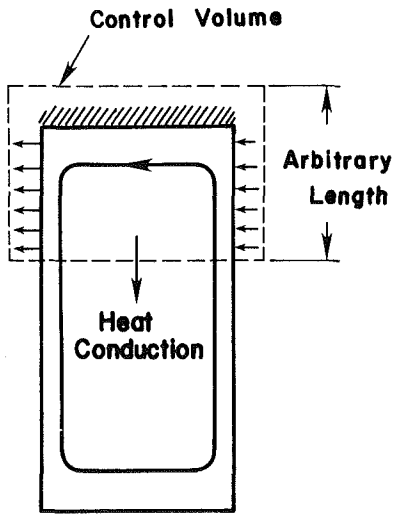

Fig. 2 Control volume argument, showing that the net upflow of enthalpy must be balanced by conduction downward

Table 1 Nusselt numbers for natural convection in a vertical slot with uniform heat flux from the side (Pr = 7)

			Nu, equation (33)		
		Grid	Numerical		
H/L	Ra	points	overall	at $y=0$	Theoretical
1	3.5×10^5	21×21	4.61	5.66	5.80
1	3.5×10^6	31×31	7.94	9.19	9.68
2	5.6×10^6	21×41	9.86	10.83	11.60
2	5.6×10^7	31×61	16.50	18.90	19.35
3	2.835×10^7	21×61	14.80	15.30	17.40
3	2.835×10^8	31×91	23.7	24.3	29.04

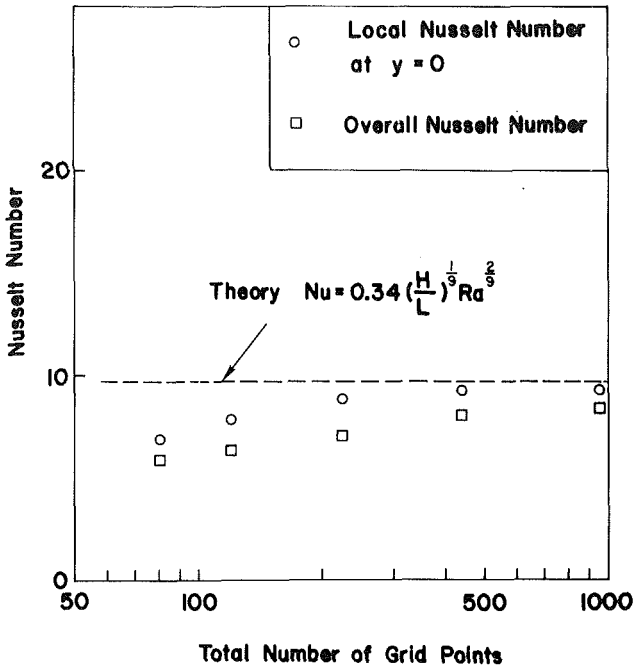

Fig. 3 The dependence of Nu on the total grid points employed ($Gr = 5 \times 10^5$, $Pr = 7$, $H/L = 1$)

The analytical solution for the boundary layer regime is now complete and represented by equations (29) with q given by equation (31). The Nusselt number predicted by this analysis can be derived by first evaluating the wall-to-wall dimensionless temperature difference

$$\Delta T^* = T^*_{x=L} - T^*_{x=0} = 2(-T^*_{x=0}) = 8\left(8192\frac{H}{L}\mathrm{Ra}^{1/5}\right)^{-1/9} \tag{32}$$

The Nusselt number follows

$$\mathrm{Nu} = \frac{(q''/\Delta T)H}{k} = \frac{8192^{1/9}}{8}\left(\frac{H}{L}\right)^{1/9}\mathrm{Ra}^{2/9} = 0.340\left(\frac{H}{L}\right)^{1/9}\mathrm{Ra}^{2/9} \tag{33}$$

where ΔT is the actual wall-to-wall temperature difference (note that the temperature of both walls increases linearly with y, at the same rate, so that ΔT is independent of y). It is worth noting that the corresponding analysis for a cavity with isothermal boundaries yields, in the present notation, $\mathrm{Nu} = 0.364\,\mathrm{Ra}^{1/4}$, where Ra is based on the horizontal temperature difference and the cavity height [11].

To demonstrate the validity of these analytical results, the next section reports a set of numerical solutions obtained by solving the complete Navier Stokes equations in the cavity of Fig. 1. The numerical simulations show that the above analysis for the boundary layer regime is indeed correct.

3 Numerical Solutions

The vorticity-streamfunction formulation of the complete governing equations is

$$\frac{\partial\omega^*}{\partial t^*} + u^*\frac{\partial\omega^*}{\partial x^*} + v^*\frac{\partial\omega^*}{\partial y^*} = \nabla^2\omega^* + \mathrm{Gr}\frac{\partial T^*}{\partial x^*} \tag{34}$$

$$\frac{\partial T^*}{\partial t^*} + u^*\frac{\partial T^*}{\partial x^*} + v^*\frac{\partial T^*}{\partial y^*} = \frac{1}{\mathrm{Pr}}\nabla^2 T^* \tag{35}$$

$$\nabla^2\psi^* = -\omega^* \tag{36}$$

where ψ^* is the dimensionless stream function

$$u^* = \frac{\partial\psi^*}{\partial y^*}, v^* = -\frac{\partial\psi^*}{\partial x^*} \tag{37}$$

and

$$t^* = \frac{t}{L^2/\nu}, (x^*,y^*) = \frac{(x,y)}{L}, (u^*,v^*) = \frac{(u,v)}{(\nu/L)}$$

$$\mathrm{Gr} = \frac{g\beta L^4 q''}{\nu^2 k}, T^* = \frac{T - T_o}{Lq''/k} \tag{38}$$

The boundary conditions for the present formulation are

$$\psi^* = \frac{\partial\psi^*}{\partial y^*} = 0, \frac{\partial T^*}{\partial y^*} = 0, \text{ at } y^* = \pm\frac{1}{2}$$

$$\psi^* = \frac{\partial\psi^*}{\partial x^*} = 0, \frac{\partial T^*}{\partial x^*} = 1, \text{ at } x^* = 0,1 \tag{39}$$

To solve these equations numerically, we chose a reliable scheme, namely the alternating direction implicit method (ADI) described by Wilkes and Churchill [10]. Since the overall algorithm closely follows the method described in detail in [10], it will only be outlined here. The entire $x-y$-domain was divided into either 20 or 30 equal segments in the x-direction, and from 20 to 90 equal segments in the y-direction, depending on the aspect ratio H/L and Gr. The "adequate" number of grid points was determined based on tests of the type shown in Fig. 3; for example, when $\mathrm{Gr} = 5 \times 10^5$, $H/L = 1$ a total of 31×31 grid points. Figure 3 shows already how nicely the numerical solution tends toward agreement with the analytical solution as the number of grid points increases. The steady state was defined based on the following convergence criteria

$$\frac{\sum_i\sum_j |\omega_{ij}^{k+1} - \omega_{ij}^k|}{\sum_i\sum_j |\omega_{ij}^{k+1}|} \le \epsilon$$

$$\frac{|\mathrm{Nu}^{k+1} - \mathrm{Nu}^k|}{\mathrm{Nu}^{k+1}} \le \epsilon \tag{40}$$

where ϵ is typically 3×10^{-5} and the superscript k represents the iteration order. Further decrease of ϵ does not cause any significant change in the final results. For example, in our test case ($\mathrm{Gr} = 5 \times 10^5$, $A = 1$), the Nu value obtained when $\epsilon = 1.2 \times 10^{-6}$ agrees within 2 percent with that obtained based on criteria (40).

Numerical values for both the overall and the local Nusselt numbers are shown in Table 1. The local Nu at midheight ($y = 0$) agrees very well with the theoretical prediction; this makes sense, because the "end" effects are minimized at $y = 0$. The overall Nusselt numbers fall by 15-20 percent below the theoretical predictions, however, the agreement between the two sets of data improves steadily as the slot aspect ratio increases.

It is worth pointing out that, relative to [10] where the temperature was specified along the side walls, in the present study the imposition of temperature derivative (q'') had a numerically stabilizing effect. For example, Wilkes and Churchill [10] found that their method becomes numerically unstable above $\mathrm{Ra}_L = 1.4 \times 10^5$ where $\mathrm{Ra}_L = g\beta\Delta TL^3/(\alpha\nu)$. In the present study, the scheme worked stably up to corresponding values of Ra_L as high as 3.5×10^6 and,

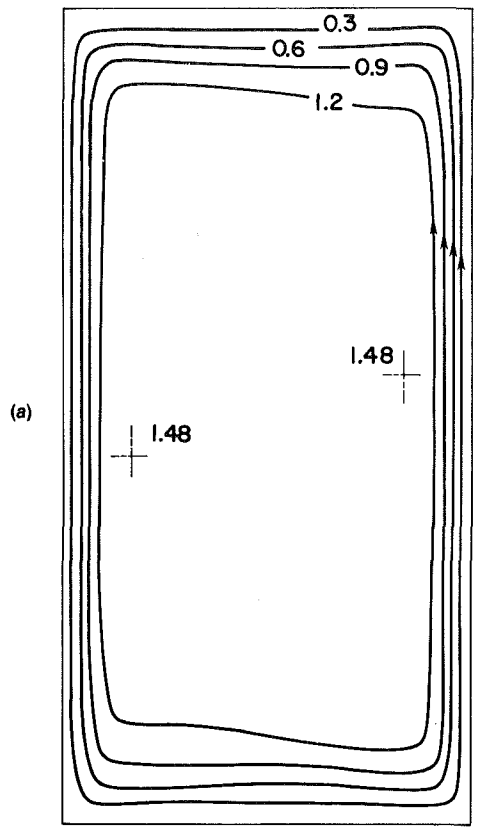

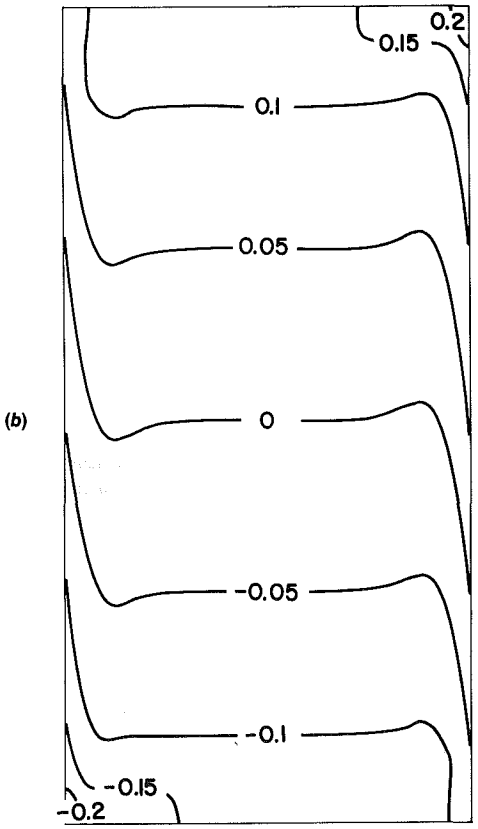

Fig. 4 Numerical solutions for the flow and the temperature field $Gr = 5 \times 10^5$, $Pr = 7$, $H/L = 2$: (*a*) streamlines, ψ^*; (*b*) isotherms, T^*

perhaps, higher (the upper Ra_L limit for stability was not the objective of the present numerical simulations).

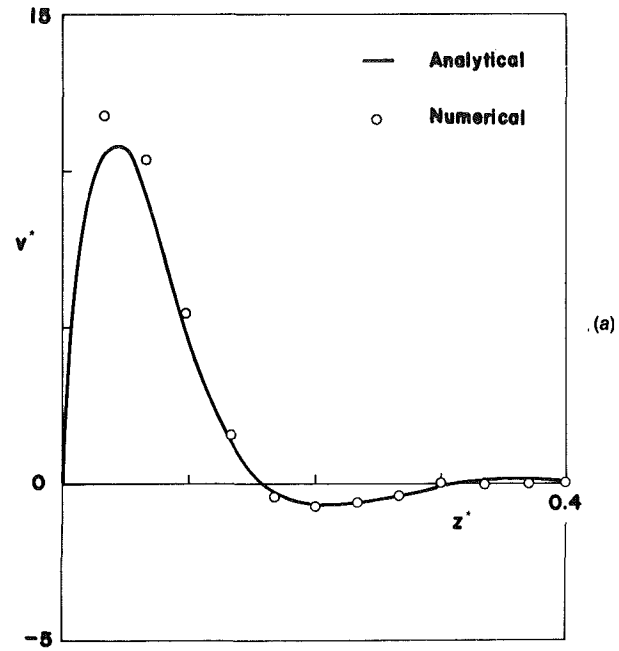

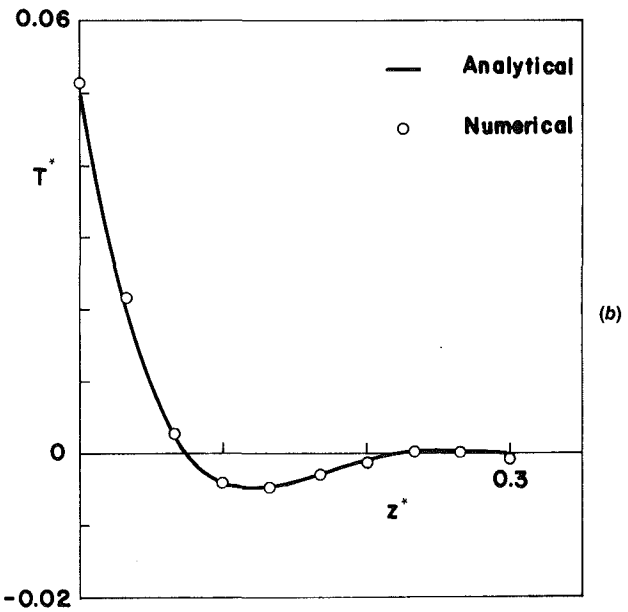

Fig. 5 Velocity and temperature profiles in the boundary layer at $y^* = 0$, $Gr = 5 \times 10^5$, $Pr = 7$, $H/L = 1$: (*a*) the velocity profile; (*b*) the temperature profile

Figures 4(*a*) and (*b*) show a representative case of flow and temperature patterns obtained numerically. These patterns confirm the features predicted analytically in the preceding section, namely

- Constant boundary layer thickness along the side walls (note the streamline parallelism, in Fig. 4(*a*))
- Linear thermal stratification both in the core and in the vertical boundary layers

Figures 5(*a*) and (*b*) show the boundary layer velocity and temperature profiles obtained numerically in the $y = 0$ plane. The numerical profiles agree very well with the analytical expressions (29, 31). It is also appropriate to compare the numerical and analytical solutions in *global* terms, for example, by examining the thermal stratification along both walls and in the core. Figures 6(*a*) and (*b*) show that the numerical solution agrees very well with the theory: the wall

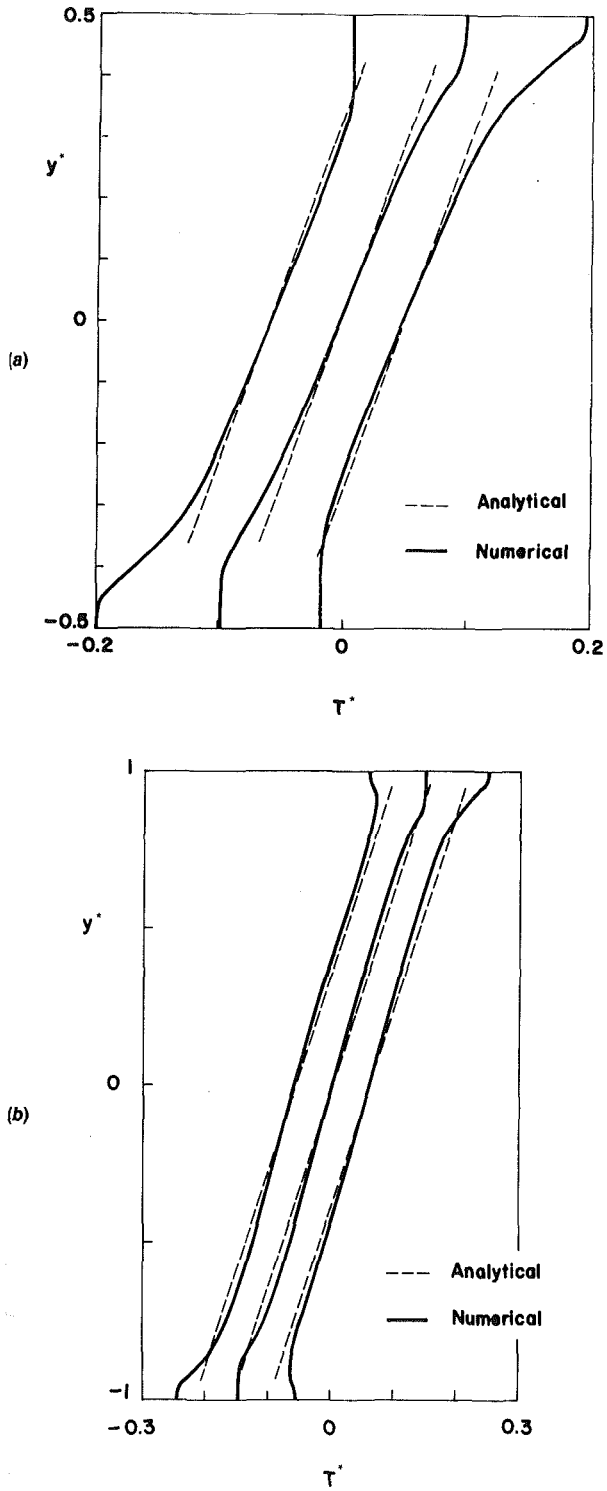

Fig. 6 The temperature distribution in three vertical planes, at $x^* = 0$, 0.5, 1.0: (a) $Gr = 5 \times 10^5$, $Pr = 7$, $H/L = 1.0$; (b) $Gr = 5 \times 10^5$, $Pr = 7$, $H/L = 2.0$

and core temperatures vary linearly over most of the cavity height and, in addition, the temperature gradient is nearly the same as the value predicted analytically. As expected, the boundary layer theory breaks down near the top and bottom walls where the fluid *must* flow horizontally, and the vertical temperature gradient *must* vanish. Finally, the numerical and analytical Nusselt number results are compared in Table 1, where the numerical Nu is defined as in equation (33) with $(\Delta T)_{y=0}$ instead of ΔT; the agreement between numerical results and equation (33) is good.

4 Conclusions

This paper reported an analytical and numerical study of natural convection in a rectangular enclosure with uniform heat flux cooling and heating along the vertical walls. Analytically, it was shown that in the boundary layer regime the flow and temperature fields differ from the corresponding patterns in a slot with isothermal walls [8]. The features of the constant-heat-flux enclosure model are

1 Constant (y-independent) boundary layer thickness of order $\delta \sim H\mathrm{Ra}^{-1/5}/q$, where q is given by equation (31)

2 The core fluid sandwiched between the boundary layers is motionless

3 The core temperature varies linearly in y, the vertical temperature gradient being

$$\left(\frac{dT}{dy}\right)_{\text{core}} = \frac{(8192)^{1/9}}{64}\frac{\alpha\nu}{g\beta H^4}\left(\frac{H}{L}\right)^{4/9}\mathrm{Ra}^{8/9}$$

4 The temperature of the two vertical walls increases linearly at exactly the same rate as the core temperature.

5 In the high Ra limit, an exact balance exists between upward enthalpy flow and downward heat conduction through any y = constant plane (Fig. 2).

The above features were strongly confirmed by numerical simulations of the same natural convection phenomenon (Figs. 4–6). Since the assumption $Pr > 0(1)$ is built into the analysis, all the numerical simulations were carried out for the case $Pr = 7$. However, as discussed in Gill's paper [8] and in more recent studies (e.g., [9], [11]), the Prandtl number does not have a significant influence on the Nu(Ra) function as long as Pr is 0(1) or greater. The Prandtl number influences the relative thickness of the outer (thermally-inert) fluid layer entrained viscously by the buoyant thermal boundary layer and, in this way, does not figure in the Nu scaling [9]. In conclusion, the analytical and numerical results presented here for $Pr = 7$ provide a reasonable approximation for the heat transfer in the entire range $Pr > 0(1)$, which marginally includes air ($Pr = 0.72$).

Acknowledgment

This work was supported in part by NSF Grant No. MEA-82-07779.

References

1 Catton, I., "Natural Convection in Enclosures," *Proceedings of the 6th International Heat Transfer Conference*, Toronto 1978, Vol. 6, 1979, pp. 13–43.

2 Jaluria, Y., *Natural Convection Heat and Mass Transfer*, Pergamon, Oxford, 1980, pp. 209–235.

3 Yang, K. T., and Lloyd, J. R., *Proceedings Workshop Natural Convection*, Breakenridge, Colo., July 18–21, 1982.

4 Sparrow, E. M., and Prakash, C., "Interaction Between Internal Natural Convection in an Enclosure and an External Natural Convection Boundary Layer Flow," *International Journal of Heat and Mass Transfer*, Vol. 24, 1981, pp. 895–907.

5 Viskanta, R., and Lankford, D. W., "Coupling of Heat Transfer Between Two Natural Convection Systems Separated by a Wall," *International Journal of Heat and Mass Transfer*, Vol. 24, 1981, pp. 1171–1177.

6 Anderson, R., and Bejan, A., "Natural Convection on Both Sides of a Vertical Wall Separating Fluids at Different Temperatures," ASME JOURNAL OF HEAT TRANSFER, Vol. 102, 1980, pp. 630–635.

7 Balvanz, J. L., and Kuehn, T. H., "Effect of Wall Conduction and Radiation on Natural Convection in a Vertical Slot With Uniform Heat Generation on the Heated Wall," *Natural Convection in Enclosures*, ASME HTD Vol. 8, 1980, pp. 55–62.

8 Gill, A. E., "The Boundary-Layer Regime for Convection in a Rectangular Cavity," *Journal of Fluid Mechanics*, Vol. 26, 1966, pp. 515–536.

9 Patterson, J., and Imberger, J., Unsteady Natural Convection in a Rectangular Cavity," *Journal of Fluid Mechanics*, Vol. 100, 1980, pp. 65–86.

10 Wilkes, J. O., and Churchill, S. W., "The Finite-Difference Computation of Natural Convection in a Rectangular Enclosure," *AIChE Journal*, Vol. 12, No. 1, 1966, pp. 161–166.

11 Bejan, A., "Note on Gill's solution for free convection in a vertical enclosure," *Journal of Fluid Mechanics*, Vol. 90, 1979, pp. 561–568.

On the Existence of an Oscillatory Approach to Steady Natural Convection in Cavities

J. C. Patterson[1]
National Water Research Institute,
Burlington, Ontario L7R 4A6
Canada

The recent paper by Patterson and Imberger [1], which analysed the transient phase of natural convection in low aspect ratio cavities, gave a criterion for the presence of an oscillatory approach to steady state in such flows. However, the experiments of Yewell et al. [3] displayed no evidence of this oscillatory approach, even though the criterion was apparently satisfied. In this paper, it is shown that since the flow regimes are described by a series of critical Rayleigh numbers, the ordering of which changes with changing aspect ratio, a criterion for the existence of transient internal waves, valid for all orderings, may be established. Further, the results of [1] are extended by means of flow descriptions valid for two additional orderings. Consequently, it is shown that the experiments addressed a transient flow regime in which internal wave activity would not be expected and that the experimental results are in support of the scaling analysis of [1].

Introduction

In a recent paper, Patterson and Imberger [1] reported a theoretical and numerical analysis of the natural convection flows in cavities of small aspect ratios, started by instantaneously raising and lowering the opposite end wall temperatures with respect to the fluid temperature. The evaluation of time and length scales for some aspects of the transient and steady flows in [1] led to the derivation of a series of critical Rayleigh number criteria; the value of the actual Rayleigh number relative to these critical values led to a flow and heat transfer of a specific character, and the critical values thus determined the boundaries of a number of transient flow regimes characterized by different approaches to steady state. In particular, some regimes were characterized by an oscillatory approach to steady state, the result of decaying internal wave activity.

The mechanism for the generation of internal waves was clearly demonstrated numerically in [1], and the predicted (from the scaling analysis) and simulated wave periods were in close agreement. The occurrence, amplitude, and period of the oscillatory behavior (as evidenced by the variation of the Nusselt number at the centre line of the cavity) were independent of the mesh size and time step chosen for the algorithm, suggesting that the oscillatory behavior was other than a numerical artifact. This view is supported by the results of Gresho et al. [2], who, using a completely different numerical method, found a similar decaying oscillatory approach to steady state, with a period in close agreement with the value predicted by [1]. A similar mechanism for generation was also qualitatively described in [2].

Despite the unsteady nature of many naturally occurring convection flows, evidently the first experiments to address the transient phase were those of Yewell et al. [3]. These experiments were, at least in part, motivated by [1] and were designed to test certain of the results contained therein. The results of the two experiments indicated substantial agreement with the scales proposed in [1]; however, the approach to steady state was smooth, contrary to the expected result as interpreted by Yewell et al. [3].

This apparently contradictory result is in fact not due to an error in [1], but as will be shown below, is due to a misinterpretation of the meaning of the regime boundaries. As a result, the experiments of [3] actually fall into regimes where no internal wave activity is expected. This occurred because the change in ordering of the critical Rayleigh number criteria as the aspect ratio alters was not taken into account.

In [1], only one of the possible orderings of the critical Ra values was considered in detail. In this paper, the interpretation of the critical values is briefly discussed and all possible orderings are given. The mechanism for the generation of internal wave activity is reviewed and a criterion for the presence of transient internal wave activity, valid for all orderings, is established. Descriptions of the transient flow regimes resulting from two further critical Ra orderings are given, extending the scope of the scaling analysis contained in [1]. Consequently, it is shown that the experiments of [3] do not meet the criterion for internal wave activity and that a smooth approach to steady state should be expected. Finally, the experimental results are shown to support the flow descriptions given, and to be substantially in agreement with the scales proposed in [1].

The Critical Ra Values and Orderings

The various transient flow regimes discussed in [1] were defined in terms of seven critical values of Ra: 1, $A^{-4/3}$, A^{-12}, Pr^2, Pr^4A^{-4}, Pr^{10}, and $Pr^{16}\ A^{-12}$. The value of Ra relative to each of these critical values gives a description of some aspect of the transient or steady flow and thus a qualitative picture of the evolution of the flow may be constructed for a particular Ra, depending on its value relative to the critical values. The derivation of the critical values and their interpretation is fully discussed in [1] and will not be repeated here, where a brief summary will suffice.

It was shown in [1] that if $Ra < 1$, the vertical thermal boundary layer on the heated (or cooled) endwall advances to encompass the entire cavity before convection acts, yielding a pure conduction mode of heat transfer. If, on the other hand, $1 < Ra < Pr^2$, although the vertical thermal layer is potentially distinct, diffusion of vorticity occurs over a length scale $0(h)$, the cavity depth. Further if $1 < Ra < A^{-4/3}$, the heated horizontal intrusion layers ejected by a distinct vertical thermal layer are of thickness $0(h)$, again implying a diffusion of vorticity over a length scale $0(h)$. In both cases, the mixing of fluid over the scale of the cavity depth suggests that vertical thermal gradients cannot exist, the vertical heat transport increasing the region of horizontal conduction at the expense

[1]Present address: Department of Civil Engineering, The University of Western Australia, Nedlands, W.A., 6009, Australia

Contributed by the Heat Transfer Division for publication in the JOURNAL OF HEAT TRANSFER. Manuscript received by the Heat Transfer Division December 22, 1982.

of convection. Finally, a balance between the heat convected across the cavity by a distinct intrusion layer and the loss of heat from the intrusion layer to the core by vertical conduction yielded the criterion A^{-12}; for $Ra < A^{-12}$, the intrusion loses a significant component of its heat content to the core, again reducing the effects of convection.

Since $A^{-4/3} < A^{-12}$ for $A < 1$, these results led to a broad classification of the possible flow types into conductive ($Ra < 1$), transitional ($1 < Ra < Max(Pr^2, A^{-12})$), and convective ($Ra > Max(Pr^2, A^{-12})$). The nature of the subsequent layering in the core was determined by the value of Ra relative to Pr^{10} and $Pr^{-16}\,A^{-12}$ and it was shown that in the convective mode, the value of Ra relative to $Pr^4\,A^{-4}$ determined the approach to steady state; for $Ra < Pr^4\,A^{-4}$ the approach was smooth, whereas if $Ra > Pr^4\,A^{-4}$, the approach was by a decaying oscillation.

Each of these seven critical values then describes a different aspect of the transient flow, and consequently, the order in which they occur is significant in determining the actual regime boundaries and the evolution of the flow for a given value of Ra. As noted in [1], which presented one possible ordering, there are actually six orderings of the seven critical values possible for $Pr > 1$, $A < 1$, depending on the relative values of Pr and A. These are:

$A^{-6} < Pr$: $\quad 1 < A^{-4/3} < A^{-12} < Pr^2 < Pr^4 A^{-4} < Pr^{10} < Pr^{16} A^{-12}$

$A^{-2} < Pr < A^{-6}$: $\quad 1 < A^{-4/3} < Pr^2 < A^{-12} < Pr^4 A^{-4} < Pr^{10} < Pr^{16} A^{-12}$

$A^{-6/5} < Pr < A^{-2}$: $\quad 1 < A^{-4/3} < Pr^2 < Pr^4 A^{-4} < A^{-12} < Pr^{10} < Pr^{16} A^{-12}$

$A^{-2/3} < Pr < A^{-6/5}$: $\quad 1 < A^{-4/3} < Pr^2 < Pr^4 A^{-4} < Pr^{10} < A^{-12} < Pr^{16} A^{-12}$

$A^{-2/15} < Pr < A^{-2/3}$: $\quad 1 < Pr^2 < A^{-4/3} < Pr^{10} < Pr^4 A^{-4} < A^{-12} < Pr^{16} A^{-12}$

$Pr < A^{-2/15}$: $\quad 1 < Pr^2 < Pr^{10} < A^{-4/3} < Pr^4 A^{-4} < A^{-12} < Pr^{16} A^{-12}$

The first of these orderings only was considered in [1]; for this ordering, the upper boundary of the transitional regime was Pr^2 and no generality was lost by taking the case $A = 1$. This led to the formation of six possible flow regimes, each of which was characterized by a different approach to steady state. Each flow regime was goverened by a different hierarchy of time scales and, in particular, all regimes with $Ra > Pr^4 A^{-4}$ were characterized by an oscillatory approach to steady state for this particular ordering.

Each of the remaining orderings results in a potentially different set of flow regimes with different approaches to steady state. In particular, as will be shown below, the criterion for the presence of transient internal waves is not the same for all orderings; a general criterion may, however, be established, valid for all orderings.

Criteria for Internal Wave Activity

At first sight, the criterion derived in [1] for the presence of transient internal waves, $Ra > Pr^4 A^{-4}$, appears valid for all orderings. Consider, however, the mechanism for the generation of internal wave activity. The initial heated intrusion layer travelling across the top of the cavity is, by symmetry, carrying exactly the amount of fluid required for entrainment in the cold wall layer, which has ejected an identical cold intrusion along the bottom of the cavity. Considering only the cold wall layer, this ejection occurs over a length scale much less than $0(h)$, provided $Ra > A^{-4/3}$, and entrainment must occur over the remainder of its length. The heated intrusion layer, which is also of thickness much less than $0(h)$, must therefore spread vertically towards the cold end of the cavity to meet this entrainment requirement. Put another way, the heated intrusion layer brings fluid to the cold wall on a scale much less than $0(h)$ to be entrained on a scale $0(h)$. Consequently, the heated fluid "piles up," and the resulting horizontal gradient generates an adverse pressure gradient opposing the intrusion. The result is the generation of internal wave activity.

Implicit in this qualitative description of the mechanism, which is supported by the numerical results of both [1] and [2], is the assumption that the intrusion layer is convecting the required heat across in a thin layer. This is the case if $Ra > A^{-12}$, however, if $Ra < A^{-12}$, a significant quantity of heat is lost to the core by vertical conduction and subsequently carried to the far boundary by the secondary core motion, over a scale $0(h)$, for entrainment. Thus if $Ra < A^{-12}$, the vertical distribution of heat is spread over the length of the cavity, and the "piling up" of heated fluid does not occur. In this case, there is no mechanism for the generation of internal waves and the $Pr^4 A^{-4}$ parameter is not relevant.

The same argument is true for the case $Ra < A^{-4/3}$; in this case, the heated fluid is ejected over a length scale $0(h)$ and the "piling up" of heated fluid again does not occur. However, since $Pr^4 A^{-4} > A^{-4/3}$ for $Pr > 1$, $A < 1$, this secondary criterion is of no importance. Thus, the criterion for the presence of internal wave activity may be expressed simply as

$$Ra > Max(Pr^4 A^{-4}, A^{-12}) \tag{1}$$

valid for all orderings.

Description of the Flow Regimes

It is possible to describe, using the scales derived in [1], the characteristics of each of the flow regimes resulting from the orderings of critical Ra values not treated in [1]. Such a general discussion would however be unsupported by experimental or numerical evidence and would be well beyond the scope of this paper. Consequently, in the following, two orderings only, which will later be seen to be applicable to the experiments of [3], are discussed.

(i) $A^{-2/15} < Pr < A^{-2/3}$. For this ordering of critical Ra

Nomenclature

A = aspect ratio of the cavity h/L
g = gravitational acceleration
h = vertical dimension of the cavity
L = horizontal dimension of the cavity
Pr = Prandtl number ν/κ
Q = volume flux passing through the thermal boundary layer, equation (4)
Ra = Rayleigh number $g\alpha\Delta T h^3/\nu\kappa$
T_f = filling time, equation (5)
v = vertical velocity scale, equation (3)
α = coefficient of thermal expansion
ΔT = end to end temperature difference
Δ_{vf} = intrusion layer thickness scale, equation (6)
δ_T = thermal boundary layer thickness scale, equation (2)
κ = thermal diffusivity
τ = thermal boundary layer growth time scale, equation (2)
ν = kinematic viscosity
$\sim$ = of the same order of magnitude as

values, it is again possible, following [1], to broadly classify the flow as conductive, transitional, or convective, depending on the relative values of Ra and the values 1 and A^{-12}.

The conductive regime is defined by Ra < 1. In this case, the thermal boundary layers on the endwalls simply advance across the cavity, yielding essentially a pure conduction result. The resulting horizontal temperature gradient drives a weak circulation which has no convective effect. Steady state is achieved in a time $0(L^2/\kappa)$, the pure conduction time scale, and no other time scales are relevant.

The upper boundary of the transitional regime is A^{-12}; for Ra > A^{-12}, the flow is convective with horizontal conduction playing a role only in thin vertical boundary layers on the endwalls. Internal wave activity will be present in this regime, since the criterion Ra > A^{-12} is satisfied, and the flow will be characterized by thin horizontal intrusion layers, since Ra > $A^{-4/3}$. The nature of the layers is determined by the value of Ra relative to $\mathrm{Pr}^{16}A^{-12}$; for A^{-12} < Ra < $\mathrm{Pr}^{16}A^{-12}$ the layers are initially inertial becoming viscous, for Ra > $\mathrm{Pr}^{16}A^{-12}$, the flow is inertially dominated. Since steady state is achieved by the decay of the internal wave activity, the estimated steady state time is the viscous decay time $0(h^2/\nu)$.

The transitional regime 1 < Ra < A^{-12} contains a number of subregimes. Firstly, for 1 < Ra < $A^{-4/3}$, which includes the Pr^2 criterion, the diffusion of vorticity over a scale $0(h)$ expands the potentially distinct vertical and horizontal layers into the core region, and the flow and heat transport behave essentially as in the conductive regime. The overall heat transport is augmented by the additional (over conduction) heat carried out from the boundary and transported vertically with the fluid as it mixes over the cavity depth. Secondly, for $A^{-4/3}$ < Ra < A^{-12}, distinct vertical thermal layers form on the endwalls and eject distinct horizontal intrusion layers into the core, convecting heat across the cavity. Since Ra < A^{-12}, however, these layers lose a significant quantity of heat to the core, losing their thermal identity and generating a linear vertical temperature gradient in the core. The velocity layers, however, remain distinct. The nature of the layers changes with increasing Ra from viscous for Ra < Pr^{10}, to inertial becoming viscous for Pr^{10} < Ra < A^{-12}. Steady state in this transition regime is achieved in a time scale lying between the conduction time scale $0(L^2/\kappa)$ and the viscous time scale $0(h^2/\nu)$ (see Table 1).

The evolution of the flow in each of the various flow regimes may again be described in terms of the transient time scales given in [1]. The development and interpretation of these scales was fully discussed in [1] and will not be repeated here. There is, however, one subregime (1 < Ra < $A^{-4/3}$) of the transitional regime not treated in [1], but relevant to the present case.

It was shown in [1] that, for the case 1 < Ra < $A^{-4/3}$, the viscous-buoyancy balance in the thermal boundary layers on the vertical walls should be replaced by a pressure-buoyancy balance. This yielded a growth time scale, τ, and layer thickness scale, δ_T, given by

$$\tau \sim \frac{L^2}{\kappa \mathrm{Ra}^2}, \quad \delta_T \sim \frac{L}{\mathrm{Ra}} \tag{2}$$

The resultant vertical velocity scale became

$$v \sim \frac{\kappa \mathrm{Ra}^2 A}{L} \tag{3}$$

and the flux through the boundary layer, Q, was given by

$$Q \sim v\delta_T \sim \kappa \mathrm{Ra}\, A \tag{3}$$

The filling time, T_f, is the time taken for all of the fluid in the cavity to pass through the boundary layer to be heated, and is given by $T_f \sim hL/Q$. Thus, incorporating the result from [1]

$$T_f \sim \begin{cases} \dfrac{L^2}{\kappa \mathrm{Ra}} & 1 < \mathrm{Ra} < A^{-4/3} \\ \dfrac{hL}{\kappa \mathrm{Ra}^{1/4}} & A^{-4/3} < \mathrm{Ra} \end{cases} \tag{5}$$

These two estimates for T_f coincide at Ra ~ $A^{-4/3}$, and the first collapses to the pure conduction time scale L^2/κ for Ra ~ 1. Thus, as in [1], T_f provides an estimate for the steady-state time scale for that range of Ra values where T_f exceeds the viscous time scale h^2/ν.

The evolution of the flow in each regime is summarized in Table 1, which briefly describes the hierarchy of time scales as each flow progresses to steady state. The time scales in Table 1 are taken directly from [1].

(ii) $A^{-2/3}$ < **Pr** < $A^{-6/5}$. The only difference between this ordering and the previous one are the relative values of $A^{-4/3}$ and Pr^2 and of Pr^{10} and Pr^4A^{-4}. Since all of these values are contained in the transitional flow regime 1 < Ra < A^{-12}, the convective and conductive flow descriptions given above will also apply here.

Within the transitional regime, both the Pr^2 and $A^{-4/3}$ criteria are related to diffusion of vorticity over a length scale $0(h)$. Thus, unless both are satisfied, that is Ra > Max(Pr^2, $A^{-4/3}$), distinct intrusions cannot be expected. Thus, in this case, where $A^{-4/3}$ < Pr^2, the assumption that the intrusion layer is distinct (Ra > $A^{-4/3}$) is not valid if Ra < Pr^2, since the analysis on which the $A^{-4/3}$ criteria is based assumes a distinct vertical boundary layer, which is not true unless Ra > Pr^2. Consequently, if the subregime boundary for distinct intrusions is defined as Ra ~ Max(Pr^2, $A^{-4/3}$), the flow description in the flow regime 1 < Ra < Max(Pr^2, $A^{-4/3}$) is the same in this ordering as in the previous one.

The Pr^4A^{-4} criterion arises from a comparison of the filling time scale, T_f, with the viscous time scale, h^2/ν, and the Pr^{10} criterion from the nature of the layering as the flow evolves to steady state. An interchange of these criteria then implies that a particular layering flow will reach steady state in a different time scale in this ordering if Pr^4A^{-4} < Ra < Pr^{10} than in the previous ordering with Pr^{10} < Ra < Pr^4A^{-4}. Outside of these subregimes, Ra > Max(Pr^{10}, Pr^4A^{-4}) and Ra < Min(Pr^{10}, Pr^4A^{-4}), the flow descriptions within the transitional regimes in both orderings are identical

The description of the flow regimes relevant to this ordering are then only marginally different from those relevant to the previous ordering. These differences are confined to small subregimes of the transitional flow regimes and are of only minor importance. Consequently, a full discussion of the flow regimes of this ordering is not necessary.

Interpretation of the Experimental Results of [3]

As noted above, the experiments of [3] failed to show evidence of transient internal wave activity. Since in both cases Ra > Pr^4A^{-4}, the internal wave criterion cited in [1], the authors concluded that this oscillatory behavior was not a feature of the intended flow regime.

The experiments however did not fall into the regime intended. In the first case (Pr = 6, A = 0.0625), the ordering valid for $A^{-2/15}$ < Pr < $A^{-2/3}$ is relevant, and in the second, the ordering valid for $A^{-2/3}$ < Pr < $A^{-6/5}$ is required; in both cases, the internal wave criterion is Ra > A^{-12}. This critical Ra value takes the value 2.8×10^{14} and 2.6×10^{11}, respectively, for the first and second experiments and in neither case is the criterion satisfied. Consequently, internal wave activity cannot be expected.

Other of the scales given in [1] may however be verified. In terms of the flow descriptions, the two orderings relevant to the experiments have been shown above to the similar, and only the first experiment will be discussed.

Table 1

Regime	Time scale	Comments
Conductive		
$Ra < 1$	$L^2\kappa^{-1}$	Steady state by the thermal boundary layer encompassing the entire cavity before convection acts
Transitional		
$1 < Ra < A^{-4/3}$	$L^2\kappa^{-1}Ra^{-2}$	Thermal boundary layer formed. Horizontal intrusion layers ejected over cavity depth.
	$L^2\kappa^{-1}Ra^{-1}$	Steady state achieved by a combination of an advance of the thermal boundary layer and convective effects being dissipated by vertical diffusion of heat. No distinct velocity or thermal structure evident
$A^{-4/3} < Ra < Pr^{10}$	$h^2\kappa^{-1}Ra^{-1/2}$	Thermal boundary layer formed. Viscous horizontal intrusion layers ejected
	$L^{5/4}h^{3/4}\kappa^{-1}Ra^{-7/16}$	Intrusion layers reach the far end wall. Layering commences.
	$hL\kappa^{-1}Ra^{-1/4}$	Steady state by horizontal layering. Distinct velocity structure is evident but the thermal structure is diffusive.
$Pr^{10} < Ra < Pr^4A^{-4}$	$h^2\kappa^{-1}Ra^{-1/2}$	Thermal boundary layer formed. Inertial horizontal intrusion layers ejected.
	$h^2\kappa^{-1}Pr^{-5/3}Ra^{-1/3}$	Inertial intrusions become viscous
	$L^{5/4}h^{3/4}\kappa^{-1}Ra^{-7/16}$	Intrusions reach far end wall. Layering commences.
	$hL\kappa^{-1}Ra^{-1/4}$	Steady state by horizontal layering. Distinct velocity structure and increasingly distinct thermal structure. Convection becoming increasingly important.
$Pr^4A^{-4} < Ra < A^{-12}$	$h^2\kappa^{-1}Ra^{-1/2}$	Thermal boundary layer and inertial intrusions formed.
	$h^2\kappa^{-1}Pr^{-5/3}Ra^{-1/3}$	Inertial intrusions become viscous
	$L^{5/4}h^{3/4}\kappa^{-1}Ra^{-7/16}$	Intrusions reach the far end wall. Layering commences.
	$hL\kappa^{-1}Ra^{-1/4}$	Cavity filled by horizontal layering but the core acceleration is not yet complete
	$h^2\nu^{-1}$	Steady state as diffusion of vorticity finalises the core motion. Distinct layering in the velocity profile, weak thermal structure.
Convective		
$A^{-12} < Ra < Pr^{16}A^{-12}$	$h^2\kappa^{-1}Ra^{-1/4}$	Thermal boundary layer and inertial intrusions formed
	$h^2\kappa^{-1}Pr^{-5/3}Ra^{-1/3}$	Inertial intrusions become viscous
	$L^{5/4}h^{3/4}\kappa^{-1}Ra^{-7/16}$	Intrusions reach the far end wall. Internal wave activity and layering commence.
	$hL\kappa^{-1}Ra^{-1/4}$	Cavity filled by layering but internal wave activity present
	$h^2\nu^{-1}$	Steady state by decay of the wave motion. Distinct thermal and velocity layers present. Convection dominates the heat transfer.

Table 1 (cont.)

Regime	Time scale	Comments
$Pr^{16}A^{-12} < Ra$	$h^2\kappa^{-1}Ra^{-1/4}$	Thermal boundary layer and inertial intrusions formed
	$hL\kappa^{-1}Pr^{-1/3}Ra^{-5/12}$	Inertial intrusions reach the far end wall. Internal wave activity and layering commence.
	$hL\kappa^{-1}Ra^{-1/4}$	Cavity filled by horizontal layering but internal wave activity present
	$h^2\nu^{-1}$	Steady state by decay of wave motion. Distinct velocity and thermal layers present. The flow in dominated by inertia and the heat transfer by convection.

In this case, $Ra = 1.28 \times 10^9$ and the experiment belongs to the transitional regime $1 < Ra < A^{-12}$. The expected approach to steady state will not be oscillatory but smooth, as reported. Further, since $Ra > A^{-4/3}$ $(=40.3)$, distinct horizontal intrusion layers will be present and, according to [1], are of thickness $0(\Delta_{vf})$, where

$$\Delta_{vf} \sim \frac{h^{3/4}L^{1/4}}{\kappa Ra^{3/16}} \tag{6}$$

For the given parameter values $\Delta_{vf}/h \sim 0.04$; measuring from the actual velocity profile at the cavity centre line given in [3] yields a thickness of 0.17, within an order of magnitude of the scaling analysis result. The unsteady temperature profiles at the center line reported in [3] also suggest the vertical heat leakage described for $Ra < A^{-12}$. Thin conducting boundaries will also be present, since $Ra > Pr^2$, and the filling time estimate for steady state, T_f, will still therefore apply. As noted in [3], this proves to be an excellent estimate.

Conclusions

In the foregoing sections, the possible orderings of the critical Ra values described in [1] are given, and from the interpretation of these critical values, a general criterion for the presence of an oscillatory approach to steady state, valid for all orderings, is determined. The detailed analysis of one ordering contained in [1] is extended into two further orderings. The result is that the two orderings yield almost idential flow regimes which may again be broadly classified into conductive, transitional, and convective regimes. Both transitional and convective regimes contain subregimes with different approaches to steady state. The evolution of the flow in each regime is summarized in Table 1.

It would of course be possible to further extend the description of the transient flow to cover the remaining three orderings; indeed, in some cases particular flow regimes arising from these orderings are evidently identical to the corresponding regimes previously described. However, no experimental or numerical results exist to verify the flow descriptions.

The experimental results reported in [3] however may be used, in a limited way, to test the the scales described above. As a result it is shown that, while the experiments are of considerable value in their own right, they are not a valid test of the scaling analysis pertaining to the oscillatory approach to steady state apparent in some transient flow regimes. In fact, the flow regime addressed by the experiments of [3] is not one of those characterized by internal wave activity as intended, but rather a different, transitional regime characterized by a smooth approach to steady state, and the experimental results are substantially in agreement with the qualitative description of the evolution of the flow. The experiments therefore go some way towards confirming the scaling analysis relevant to the particular regime accessed, rather than demonstrating a disparity.

Two other points should also be noted in connection with the Yewell et al. [3] experiments. Even if the experiments had fallen into an oscillatory regime, the location (in the first experiment) of the thermistor probe at the cavity centerline (the node of the classical first mode internal wave) may mean that any wave activity present would be difficult to detect. Further, the analysis of [1] is based on an instantaneous initialization; in both experiments, although the boundary set up times are small when compared with the steady-state times, they are not small when compared with some of the transient time scales, which determine the nature of the following behavior. This effect is difficult to analyze and has not been pursued.

Naturally, these conclusions do not confirm the presence of internal wave activity for $Ra > A^{-12}$; in the Yewell et al. experiments this would require $Ra \sim 0(10^{15})$. Such a high Ra may be difficult to achieve experimentally, and an alternate approach involving an increase in A and a reduction in Pr may prove less difficult. Either way, such an experiment would provide considerable insight into the nature of transient natural convection.

This research was completed while the author was on sabbatical leave at the National Water Research Institute. The support provided during this period by Environment Canada and by the Gledden Foundation of the University of Western Australia in the form of a Gledden Overseas Fellowship is acknowledged. Initial support was provided by the Australian Research Grants Committee grant number F7915301.

References

1 Patterson, J., and Imberger, J., "Unsteady Natural Convection in a Rectangular Cavity," *Journal of Fluid Mechanics*, Vol. 100, 1980, pp. 65–86.

2 Gresho, P. M., Lee, R. L., Chan, S. T., and Sani, R. L., "Solution of the Time-Dependent Incompressible Navier-Stokes and Boussinesq Equations Using the Galerkin Finite Element Method," *Approximation Methods for Navier-Stokes Problems*, Springer-Verlag Lecture Notes in Mathematics, No. 771, 1980, pp. 203–222.

3 Yewell, R., Poulikakos, D., and Bejan, A., "Transient Natural Convection Experiments in Shallow Enclosures," ASME JOURNAL OF HEAT TRANSFER, Vol. 104, 1982, pp. 533–538.

An Experimental Study of Natural Convection in an Inclined Rectangular Cavity Filled With Water at Its Density Extremum

H. Inaba
Associate Professor.

T. Fukuda
Research Assistant.

Department of Mechanical Engineering,
Kitami Institute of Technology,
Kitami, Hokkaido 090, Japan

An experimental investigation pertaining to the effect of the density inversion of water on steady natural convective flow patterns and heat transfer in an inclined rectangular cavity whose two opposing walls are kept at different temperatures is carried out. Water as a testing fluid has its maximum density at about 4 °C. The temperature of one wall is maintained at 0 °C, while that of the opposing hot wall is varied from 2 to 20 °C. Photographs of the flow patterns, temperature distribution in the water layer, and average Nusselt number are presented under various hot wall temperatures and inclination angles of the cavity. The present results could indicate that the density inversion of water has an influential effect on the natural convective heat transfer in the prescribed water layer. Moreover, the average Nusselt number is a peculiar function of the temperature difference between the cold and hot walls and inclination angle, unlike the previous results for common fluids without density inversion.

Introduction

Numerous experimental and analytical studies on natural convective heat transfer in an inclined rectangular cavity with a common fluid (a monotonic relationship between density and temperature) have been performed, concerning the heat loss from the hot solar absorber to the cooler environment, heat transmission between window glazings or in wall cavities. Previous results obtained have clarified that as the inclination angle is increased from the horizontal fluid layer heated from below to the vertical fluid layer heated from vertical side wall, natural convective flow pattern was shifted from the three-dimensional Benard cellular flow to the two-dimensional boundary layer flow through the transient convoluted flows (coil or screw flows with axes directed up slope). It had been understood that those flow patterns influenced strongly on the convective heat transfer in an inclined rectangular cavity.

Recently the natural convection heat transfer with density inversion of water related to the melting of ice in a confined rectangular cavity has been carried out by some researchers. The effect of maximum density of water at about 4 °C and 1 atm. has been known to be considerably important on natural convective heat transfer in cold water layer related to the formation and decay of an ice layer in a confined vessel. Studies of natural convective heat transfer on the horizontal ice layer melted from below or from above have been seen in the literature [1-5]. On the other hand, Watson [6] and Seki et al. [7] investigated analytically and experimentally the natural convective heat transfer of water under the influence of density inversion in a confined rectangular cavity, whose one vertical wall was kept at the freezing point of water and whose opposing vertical wall was maintained at various temperatures above the freezing point. Most previous studies of natural convection in a rectangular cavity related to the density inversion of water have been done in the horizontal orientation (freezing front is horizontal) and the vertical orientation (freezing front is vertical). However, the occurrence of an inclined natural convective movement related to the confined water cavity is rather common, since it occurs in the earth's surfaces which are aligned with geopotential lines. Little attention has been paid to date to obtaining information about natural convection in the inclined rectangular cavity with density inversion, which is important to predict the formation or decay of an inclined ice layer.

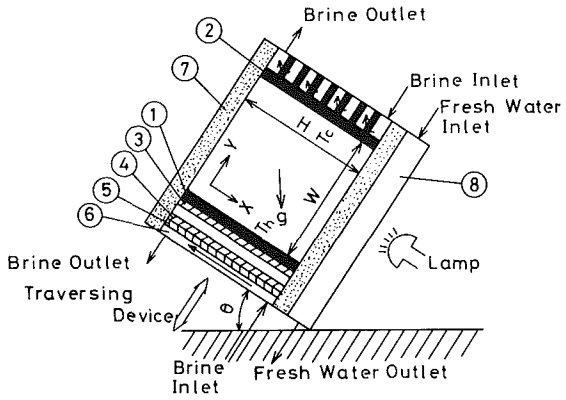

Fig. 1 A schematic diagram of experimental apparatus

The primary objective of this experimental study is to obtain the fundamental information about the effect of density inversion of water on natural convective flow pattern and heat transfer of melted water contained in an inclined rectangular cavity, whose two opposing surface temperatures are kept isothermally. The temperature of one cold wall, T_c, is uniformly maintained at 0 °C, while that of the opposing hot wall, T_h, can be varied from about 2 to 20 °C. The inclination angle, θ, of the rectangular cavity can be changed from $\theta = 0$ deg (heated from below) to $\theta = 180$ deg (heated from above) by 30 deg. The present results obtained refer to visual flow patterns, temperature profiles in the water layer, and average Nusselt number Nu.

Contributed by the Heat Transfer Division for publication in the JOURNAL OF HEAT TRANSFER. Manuscript received by the Heat Transfer Division October 21, 1982.

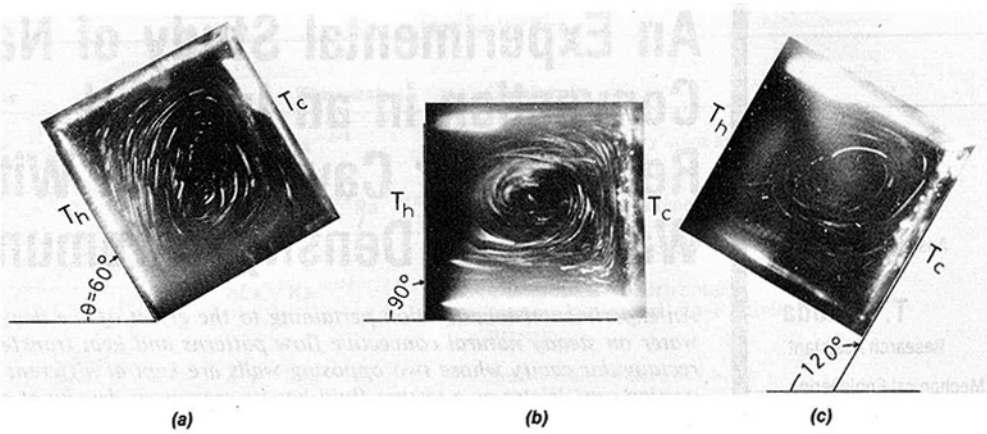

Fig. 2 Photographs of flow pattern for T_h = 4 °C: (a) θ = 60 deg, (b) θ = 90 deg, (c) θ = 120 deg

Experimental Apparatus and Procedure

The present experiments were carried out using an inclined water-filled rectangular cavity whose one wall was kept at 0 °C, and the opposing wall was maintained at various temperatures above 0 °C, while the other walls were thermally insulated. The main parts of the experimental apparatus consisted of the heating part, a water-filled test section, and the cooling part, as depicted in Fig. 1. The test section was constructed by inserting the lucite frame (10 mm in thickness) of 15 mm (height H) × 15 mm (width W) section area and 100 mm (depth D) between the heating and cooling parts. Inside surfaces of the test section were painted with a black color in order to avoid the reflection of the light beam on them, except the slit for the light beam and the front wall made of lucite plate for the convenience of the visual observation of flow patterns.

The surface temperature of the cold wall (copper plate of 5 mm in thickness) was uniformly kept at 0 °C by inducing a temperature-controlled coolant into the cooling chamber attached to the outside of the cold wall. The surface temperature of the hot wall (copper plate of 5 mm in thickness) was uniformly maintained at a constant temperature using controllable main mica electrical heater (maximum output power of 100 W). The guard mica electrical heater was mounted on the rear side of the main heater across a bakelite plate (5 mm in thickness) to minimize the heated loss from the main heater to the environment. The other cooling chamber was equipped on the rear side of the guard heater to absorb the heat from the guard heater. It was possible to control the surface temperature gradients of the hot wall and cold wall in the X-direction within ± 0.1 °C/cm. The temperature gradients of hot and cold walls were evaluated from the temperature measurements with the Cu-Co thermocouples (0.1 mm in diameter) embedded into the copper plates of the hot and cold walls at the positions of X^* = 0.1, 0.5, and 0.9 and at the half position (Z = 50 mm) in the depth direction (D = 100 mm).

One small probe (stainless steel pipe of 0.8 mm in diameter) having Cu-Co thermocouple of 0.1 mm in diameter was arranged at the position of $X = H/2$ (X^* = 0.5) in order to measure the temperature distribution in the water layer in the Y-direction. The probe was traversed from the hot wall to the cold wall by a traversing device which was composed of a micrometer mechanism, a guide pipe (1-mm i.d.) setting into the heating part and moving stainless steel pipe (0.8 mm in diameter) with the thermocouple. The temperature measurements on the test section after the visual observation of flow patterns and measurements of heat flow were carried out by moving very slowly the traversing device and standing still over 3–5 min at the given measuring position. From the results of visual observations of flow behaviors, it would be understood that the probe in the test section did not disturb almost the flow field due to very slow circulation rate of the convective flows in the present study in spite of small test section (15 mm × 15 mm).

In order to minimize heat loss, the experimental apparatus was covered with styrofoam insulating material of 100-mm thickness, except during the usual observation, and was placed into the temperature-controllable cold room which was

Nomenclature

A = nondimensional temperature, $(T_h - T_m)/(T_h - T_c)$
g = gravitational acceleration
H = height of rectangular cavity
Nu = Nusselt number, $qW/\lambda\Delta T$
q = heat flux
Ra = Rayleigh number, $g|\beta|\Delta T W^3/\nu\alpha$
Ra* = modified Rayleigh number,

$$\frac{2g\gamma_1 A(\Delta T)^2 W^3}{\nu\alpha}\left(1+\frac{3\gamma_2}{2\gamma_1}A\Delta T\right)$$

T = temperature
T^* = nondimensional temperature, $(T - T_c)/(T_h - T_c)$
ΔT = temperature difference, $T_h - T_c$ ($= T_h$)
W = width of rectangular cavity
X, Y = coordinates
X^*, Y^* = nondimensional coordinates, X/W, Y/W
α = thermal diffusivity
β = coefficient of thermal expansion
ν = kinematic viscosity
λ = thermal conductivity
θ = inclination angle
γ_1, γ_2 = coefficients of density of water in equation (1)

Subscript

c, h = refers to cold wall (0 °C) or hot wall
m = value at 4 °C of water

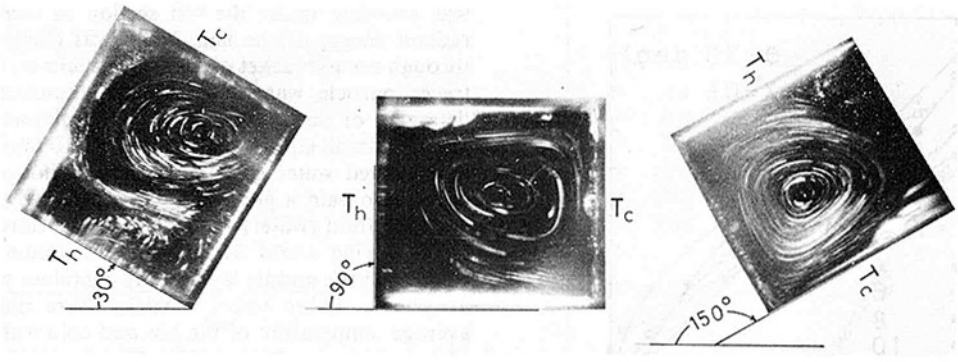

(a) (b) (c)

Fig. 3 Photographs of flow pattern for T_h = 10 °C: (a) θ = 30 deg, (b) θ = 90 deg, (c) θ = 150 deg

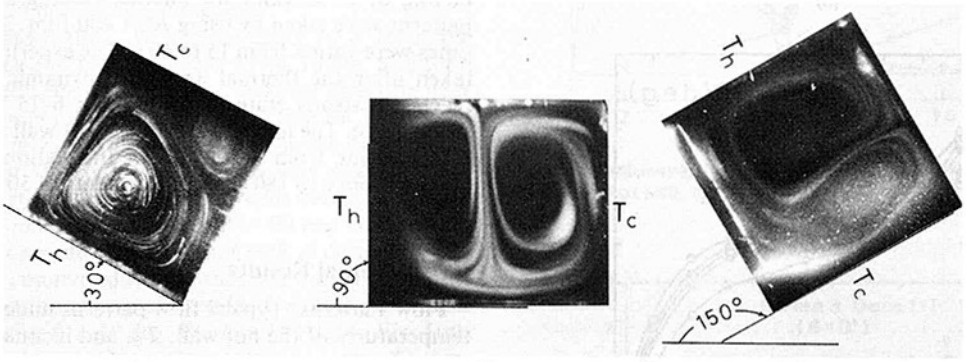

(a) (b) (c)

Fig. 4 Photographs of flow pattern for T_h = 14 °C: (a) θ = 30 deg, (b) θ = 90 deg, (c) θ = 150 deg

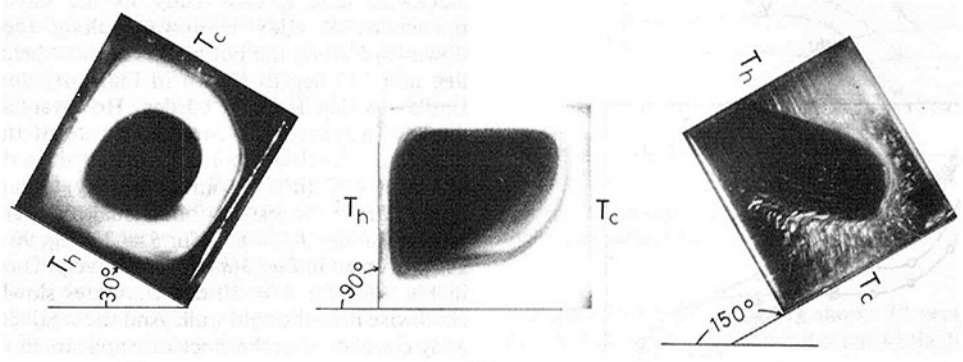

(a) (b) (f)

Fig. 5 Photographs of flow pattern for T_h = 8 °C: (a) θ = 30 deg, (b) θ = 90 deg, (c) θ = 150 deg

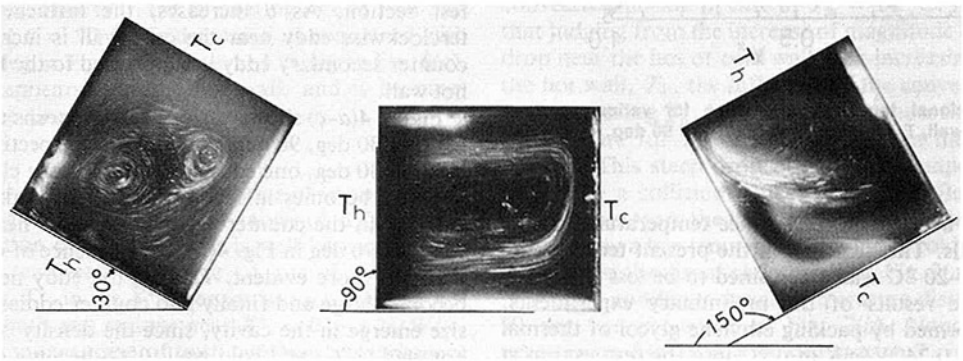

(a) (b) (c)

Fig. 6 Photographs of flow pattern for T_h = 6 °C: (a) θ = 30 deg, (b) θ = 90 deg, (c) θ = 150 deg

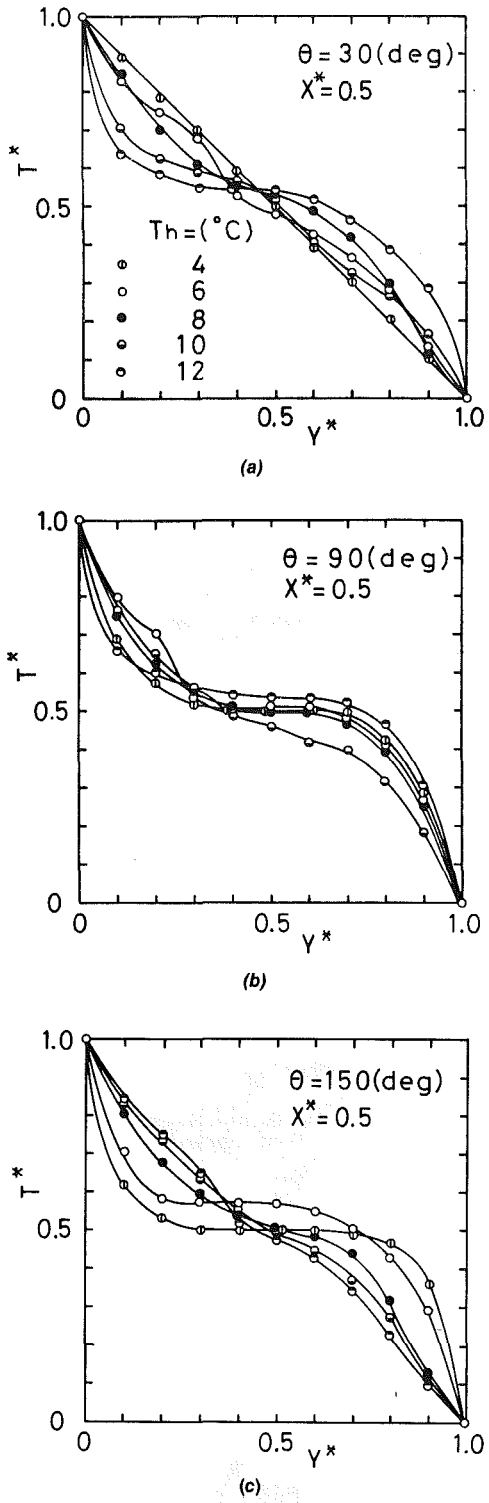

Fig. 7 Nondimensional temperature profiles for various surface temperature of hot wall, T_h: (a) θ = 30 deg, (b) θ = 90 deg, (c) θ = 150 deg

controlled at the average of the surface temperatures of the hot and cold walls. The heat loss in the present temperature range of T_h = 2–20 °C was ascertained to be less than ± 6 percent from the results of the preliminary experiments, which were performed by packing ethylene glycol of thermal conductivity λ = 0.24 W/mK at 0 °C into the test section at the inclination angle θ = 180 deg (heated from above) without an existence of natural convection.

To visualize the flow patterns, a 100-W projection lamp was arranged under the test section as seen in Fig. 1. The radiant energy of the light beam was eliminated by passing through a water jacket of 20 mm in thickness beforehand. The tracer particle was a mixture of aluminium powder and detergent or detergent only. The aluminium tracer particles having a small equivalent diameter (5–10 μm) were mingled in the distilled water containing the alcohol and detergent in order to obtain a good affinity between the tracer particles and test fluid (water). After they were clarified in the container during about 24 hrs, the aluminium tracer particles floating in the middle layer in the container were decanted by a syringe. Those tracer particles were maintained at the average temperature of the hot and cold walls for 5–10 min. They were injected slowly into the test section by the syringe. Therefore, it would be said that the tracer particles used in the present study were neutrally buoyant to the test fluid.

Distilled water was used as a testing fluid to avoid the mixing of undesirable air bubble. Photographs of the flow patterns were taken by using ASA 400 film. Typical exposure times were varied from 15 to 60 s. The experimental data were taken after the thermal and fluid dynamic conditions had reached a steady state. It took about 6–15 hrs to reach the steady state. The temperature of the hot wall was varied every 2 °C ranging from 2–20 °C. The inclination angle θ was increased from 0 to 180 deg by increments of 30 deg.

Experimental Results

Flow Patterns. Typical flow patterns under several surface temperatures of the hot wall, T_h, and inclination angles θ are shown in Figs. 2–6. Figure 2(*a–c*) for θ = 60 deg, 90 deg, and 120 deg show the flow patterns observed under T_h = 4 °C. These flows seem to be very stable and two dimensional. One eddy in Fig. 2(*a*) for θ = 60 deg circulates in the counter clockwise and spreads fully in the cavity, that is, the movement of eddy is upward along the cold wall but downward along the hot wall. The flow behavior for θ = 90 deg and 120 deg as shown in Fig. 2(*b*) and (*c*) is basically similar to that for θ = 60 deg. However, as the inclination angle θ increases, the circulating rate of the eddy becomes larger and the flow vigor is increased since the layer of water at about 4°C (it's maximum density) occupies vertical and upper part in the test section. Visual photographs of the flow patterns under T_h = 6°C for θ = 30 deg, 90 deg, and 150 deg are presented in Fig. 3(*a–c*), respectively. One influential eddy in Fig. 3(*a*) for θ = 30 deg circulates slowly in the counter clockwise near the cold wall. And the weak counter secondary eddy circulating in the clockwise appears in the vicinity of the hot wall because the layer of water at 0°C with smaller density than that at 6 °C occupies the upper part in the test section. This appearance of the counter secondary eddy is due to the existence of the density extremum of water at about 4°C in the test section. As θ increases, the influence of the counterclockwise eddy near the cold wall is increased, while the counter secondary eddy is suppressed to the lower part of the hot wall.

Figure 4(*a–c*) shows various flow patterns under T_h = 8 °C for θ = 30 deg, 90 deg, and 150 deg, respectively. In Fig. 4(*a*) for θ = 30 deg, one eddy circulating in the clockwise near the hot wall becomes influential while the weak other eddy circulating in the counterclockwise appears near the cold wall. For θ = 90 deg in Fig. 4(*b*), the influence of density inversion becomes more evident. That is, the eddy near the cold wall becomes large and finally two counter eddies of almost equal size emerge in the cavity, since the density of water near the hot wall (8°C) and cold wall (0°C) become almost the same, which means the almost same flow vigors of two eddies developed near both walls. For θ = 150 deg in Fig. 4(*c*), one eddy near the cold wall becomes influential and the other

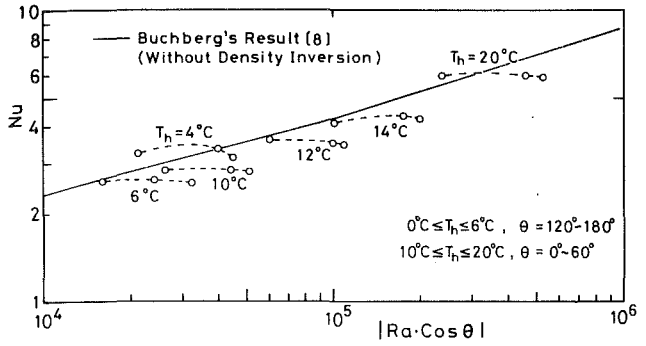

Fig. 8 Comparison between the present data and previous data without density inversion

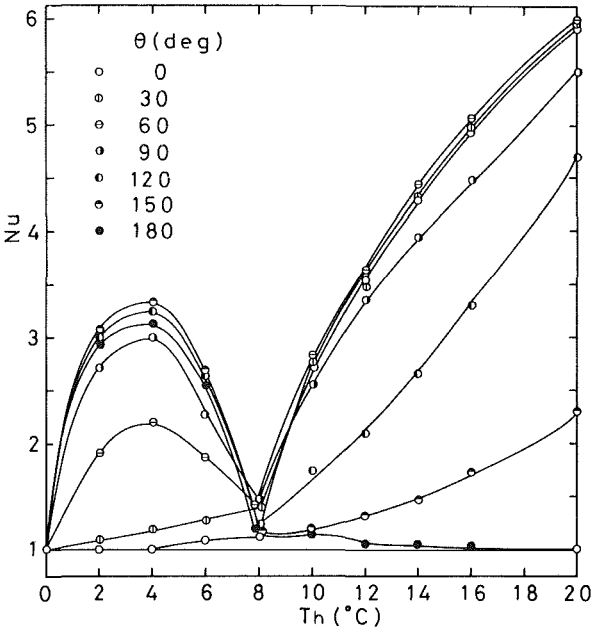

Fig. 9 Relationship between Nusselt number, Nu, and surface temperature of hot wall, T_h, for various θ

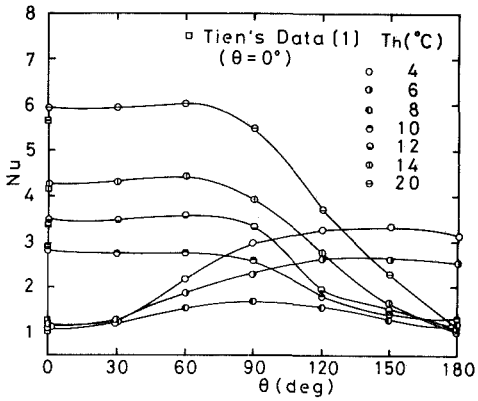

Fig. 10 Relationship between Nusselt number, Nu, and inclination angle, θ, for various T_h

counter eddy is suppressed to the hot wall in contrast to the eddies observed for $\theta = 30$ deg in Fig. 4(*a*).

Figure 5(*a-c*) shows the flow patterns under $T_h = 10$ °C for $\theta = 30$ deg, 90 deg and 150 deg, respectively. In Fig. 5(*a*) for $\theta = 30$ deg, one eddy circulating in the clockwise direction near the hot wall becomes more influential than that for $T_h = 8$ °C as could be seen in Fig. 4(*a*), while the influence of the other counter eddy near the cold wall becomes very weak because the density of water at 10°C near hot wall becomes smaller than that at 0°C near cold wall. For $\theta = 90$ deg in Fig. 5(*b*), the influence of one eddy near the hot wall is decreased and that of the other counter eddy near the cold wall is increased. However, the circulating rate of flow for $\theta = 90$ deg becomes smaller than that for $\theta = 30$ deg. For $\theta = 150$ deg in Fig. 5(*c*), the flow seems to be unstable and three dimensional. That is, one eddy circulating in the clockwise with very slow speed appears in the part of the cavity. This anomolous unsteadiness of the flow pattern could be explained because the instability of the transient flow behavior at $\theta = 150$ deg from two-dimensional boundary layer flows that developed near the hot and cold walls observed at $\theta = 90$ deg for three-dimensional Benard cellular type flow (reported by Hart [9] and Krishnamurti [10]) appears in the flow field. Figure 6(*a-c*) shows the flow patterns under $T_h = 14$ °C for $\theta = 30$ deg, 90 deg, and 150 deg, respectively. For $\theta = 30$ deg in Fig. 6(*a*), one basic main boundary layer flow circulating in the clockwise direction appears at the inside of the surface wall, and two secondary eddies emerge in the center core region due to a viscous shearing force induced by the outside main boundary layer flows developed near the hot and cold walls, as mentioned in the previous results using a Boussinesq fluid. Therefore, it can be explained that the appearance of these secondary eddies is independent of the effect of density inversion of water since the density of water at 14 °C near the hot wall is smaller by 99.94 percent of that at 0°C near cold wall. For $\theta = 90$ deg in Fig. 6(*b*), the flow pattern is similar to that for $\theta = 30$ deg. However, the circulating rate of flow and the flow vigor for $\theta = 90$ deg is decreased as compared with that for $\theta = 30$ deg in Fig. 6(*a*). For $\theta = 150$ deg in Fig. 6(*c*), one weak eddy appears near the hot wall, and it becomes unstable and three dimensional.

Temperature Distributions. Distributions of temperature T in the Y-direction are obtained for all values of $\Delta T(=T_h)$ at the selected position of $X = H/2$. It is well known that the nondimensional temperature profile of the fluid without density inversion, T^*, in the Y^*-direction at each selected X^*-position, except both end regions near $X^* = 0$ and $H/W(=1)$, is similar and independent of both temperature difference ΔT and a Boussinesq fluid.

The typical nondimensional temperature distributions T^* in the Y^*-direction at the position of $X^* = 0.5$ are shown in Fig. 7. Figure 7(*a*) for $\theta = 30$ deg shows T^* versus Y^* for various T_h. In this figure, one can note that as the temperature of the hot wall, T_h, increases, the temperature profile is changed gradually from the almost linear relationship between T^* and Y^*, indicating the conduction in case of $T_h = 4$ °C, to the curved temperatrue profile ("S" type), indicating the natural convective motion in case of $T_h = 14$ °C. It can be expected that judging from the increase of magnitude of the precipitous drop near the hot or cold wall with increasing temperature of the hot wall, T_h, the influence of the convection is increased with increasing T_h. It is interesting to note that a steep drop of temperature for $T_h = 6$ °C appears in the range of $Y^* = 0.4$-0.5. This steep drop of the fluid temperature would be caused by a collision between one fluid flow having a high temperature from the hot wall ($T_h = 6$ °C) and the other fluid flow having a low temperature from the cold wall ($T_c = 0$°C), as shown in the visual photograph of Fig. 3(*a*).

Typical nondimensional temperature distributions for $\theta = 90$ deg are presented in Fig. 7(*b*). Nondimensional temperature profile for $\theta = 90$ deg at each T_h is basically similar to that for $\theta = 30$ deg as could be seen in Fig. 7(*a*). However, one can note that a precipitous drop of temperature for $T_h = 6$ °C mentioned for $\theta = 30$ deg moves to the hot wall in the

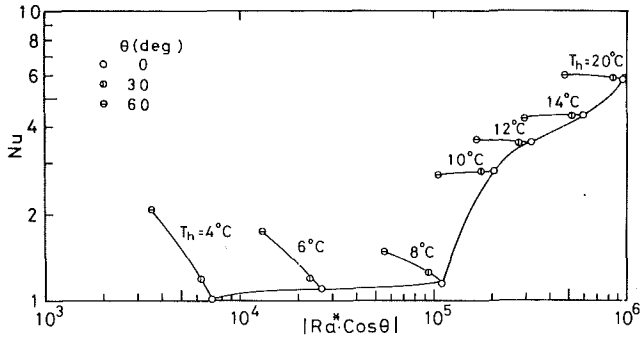

Fig. 11 Correlation of Nusselt number, Nu, and modified Rayleigh number, Ra* cos θ

range of $Y^* = 0.2$–0.3, corresponding to the flow pattern for $\theta = 90$ deg as could be seen in Fig. 3(*b*).

Figure 7(*c*) shows the results for $\theta = 150$ deg. The results of temperature profile for various T_h in case of $\theta = 150$ deg are inversion of those in case of $\theta = 30$ deg as shown in Fig. 7(*a*). That is, from the temperature distributions in Fig. 7(*c*), it can be presumed that the mode of heat transmission through water layer is shifted gradually from the convection to the conduction as T_h increases from $T_h = 4$ °C.

Average Nusselt Number. A comparison between the present data and those obtained by previous investigators (i.e., Buchberg et al. [8]) is shown in Fig. 8. They summarized their experimental results for common fluids without density inversion in the range of $\theta \leqq 60$ deg, and presented their correlations in terms of Nusselt number $\mathrm{Nu} = qW/\lambda\Delta T$ and Rayleigh number $\mathrm{Ra}\cos\theta = g|\beta|\Delta TW^3\cos\theta/\nu\alpha$, where the physical properties of fluid used were evaluated at the average temperature of the hot and cold walls. However, the effect of density inversion on the convective heat transfer was not discussed in their studies. In Fig. 8, the present data for $\theta =$ 120–180 deg in the range of $T_h \leqq 6$ °C and for $\theta = 0$–60 deg in the range of $T_h \geqq 10$ °C are plotted according to the aforementioned previous method in consideration of the flow patterns and the temperature distributions. The present data agree well with those of previous investigators in the temperature ranges without the effect of density inversion, that is, $T_h \leqq 4$ °C and $T_h \geqq 14$ °C. However, it can be seen that the present data resulted from the strong effect of density inversion in the range of $T_h = 6$–12 °C lie below the previous results. These differences would be explained from the fact that the convective heat transfer through the water layer is prevented by two counter eddies existing due to the density inversion in the water layer, as shown in visual photographs of the flow patterns in Figs. 3–5.

The Effect of Temperature of the Hot Wall T_h on the Average Nusselt number Nu

Figure 9 shows the relationship between Nu and T_h ($= \Delta T$) for various θ. In this figure, it is evident that Nu does not increase monotonously with increasing ΔT as reported in the case of using a Boussinesq fluid without density inversion. Namely, for $T_h \leqq 4$°C, when a single eddy occupies the entire part of the fluid layer, as T_h becomes higher, Nu increases monotonously till it reaches a peak point at about 4°C, because the flow vigor is increased with increasing density difference of water in the test section. But the minimum value of Nu appers at about 8 °C. The appearance of such a minimum value of Nu at about 8 °C may be caused by the existence of two counter eddies as shown in Fig. 4. The heat exchange by convection from the hot wall to the cold wall is performed by a collision between two counter eddies and the decrease of the flow vigor of two counter eddies due to a collision between them. That is, it takes a longer distance for two counter eddies to transfer the heat from the hot wall to the cold wall, and the circulating rate of their eddies are decreased as compared with that of a single eddies without density inversion. And Nu increases monotonously again with increasing T_h in the range of $T_h > 8$ °C. This increase of Nu could be explained from the fact that the flow vigor near the hot wall is increased with increasing T_h, since the density of water at $T_h > 8$°C becomes smaller than that at 0 °C and is decreased almost linearly with increasing T_h. This peculiar behavior between Nu and T_h appears in the range of $\theta =$ 60–150 deg. However, the tendencies of Nu to T_h for $\theta =$ 0–30 deg and 180 deg are different from those for $\theta = 60$–150 deg. In case of $\theta = 0$–30 deg, Nu increases gradually with increasing T_h for $T_h \leqq 8$ °C, and it increases steeply against T_h in the range of $T_h > 8$ °C. That is, the influence of the convection becomes remarkable for $T_h > 8$ °C. On the other hand, in case of $\theta = 180$ deg the change of Nu to T_h for $T_h \leqq$ 8 °C is similar to that for $\theta = 60$–150 deg, but for $T_h > 8$°C Nu decreases gradually with increasing T_h and also the absolute value of Nu becomes small.

The Influence of Inclination Angle θ on the Average Nusselt Number Nu

Figure 10 presents the relationship between Nu and θ for various T_h, together with Tien's data [1] for $\theta = 0$ deg. In this figure, it would be understood that the value of Nu changes complicatedly with increasing θ, according to T_h. For $T_h < 8$ °C, Nu increases gradually with increasing θ, and it becomes a maximum value between $\theta = 120$ and 150 deg. Moreover, in the range of $\theta < 90$ deg Nu becomes smaller, since the influence of the convection is reduced by the existence of lighter water layer of 0 °C at the upper part in the water layer. Meanwhile, in the range of $\theta > 90$ deg the value of Nu becomes large, since the convection is to be influential due to the condition of top heavy fluid layer, as shown in Figs. 2(*c*) and 3(*c*). In case of $T_h = 8$ °C, it can be noticed that Nu increases gradually with increasing θ from 0 to 90 deg, and it takes a maximum value of about $\theta = 90$ deg, while Nu decreases gradually with increasing from 90 deg. On the other hand, for $T_h > 8$ °C, the change of Nu against θ indicates the reverse tendency as compared with that for $T_h < 8$ °C. That is, Nu increases slightly with increasing θ for $\theta < 60$ deg, and its becomes a maximum value at about 60 deg. For $\theta > 60$ deg, Nu decreases steeply with increasing θ. This behavior of Nu against θ is similar to previous results obtained by using a Boussinesq fluid without density inversion.

Nondimensional Arrangement of the Heat Transfer Data

In general, it is difficult to nondimensionalize the data of heat transfer with density inversion of water by the previous correlation in terms of Nusselt number and common Rayleigh number, where the physical properties of water are estimated by the average temperature between the hot and cold walls. That is, in the present study the value of Ra at $T_h = 8$ °C becomes almost zero since the thermal expansion coefficient β is zero at about 4 °C. In the present study, the modified Rayleigh number Ra* used by Sun et al. [3] is adopted to correlate the present data as follows

$$\mathrm{Ra}^* = \frac{2g\gamma_1 A(\Delta T)^2 W^3}{\nu\alpha}\left(1 + \frac{3\gamma_2}{2\gamma_1}A\Delta T\right) \qquad (1)$$

Figure 11 shows the relationsip between Nu and Ra* cos θ in the range of $\theta \leqq 60$ deg. In this figure, it would be un-

derstood that for $\theta = 0$ deg, that is, the horizontal water layer heated from below, the value of Nu increases slightly with increasing $Ra^* \cos\theta$ in the range of $Ra^* \cos\theta = 7 \times 10^3$–$10^5$, and for $Ra^* \cos\theta > 10^5$, Nu increases precipitously with increasing $Ra^* \cos\theta$. It is intriguing that the value of Nu for $T_h \leq 8$ °C is strongly dependent on $Ra^* \cos\theta$ in the range of $\theta = 0$–60 deg, while for $T_h > 8$ °C, it is little dependent on $Ra^* \cos\theta$.

Conclusions

The behavior of natural convection flows with the effect of density inversion of water in an inclined rectangular cavity is clarified by experiments. From the aforementioned results, it can be concluded that the flow patterns of water in the cavity are changed by the effect of density inversion and inclination angle of the cavity, and consequently, the density inversion and inclination angle have an important effect on the convective heated transfer in the cavity. It is clear that two counter eddies due to the density inversion disturbed the convective heat transfer from the hot wall to the cold wall, and the influence of two counter eddies is strongly dependent on the inclination angle.

References

1 Tien, C., "Thermal Instability of a Horizontal Layer of Water Near 4 °C," AIChE Journal, Vol. 14, 1968, pp. 652–655.

2 Yen, Y. C., and Galea, F., "Onset of Convection in a Water Layer Formed Continuously by Melting Ice," *The Physics of Fluids*, Vol. 12, 1969, pp. 509–516.

3 Sun, Z. S., Tien, C., and Yen, Y. C., "Thermal Instability of a Horizontal Layer of Liquid with Maximum Density," *AIChE Journal*, Vol. 15, 1969, pp. 910–915.

4 Sugawara, M., Fukusako, S., and Seki, N., "Experimental Studies on the Melting of a Horizontal Ice Layers," *Transactions JSME*, Vol. 40, 1974, pp. 3155–3165.

5 Merker, G. P., and Straub, J., "Rayleigh-Benard Konvektion in Wasser im Bereich der Richteanomalie," Wärme-und Stoffübertragung, Vol. 16, 1982, pp. 63–68.

6 Watson, A., "The Effect of the Inversion Temperature on the Convection of Water in an Enclosed Rectangular Cavity," *Quarterly Journal of Mechanics and Applied Mathematics*, Vol. 15, 1972, pp. 423–446.

7 Seki, N., Fukusako, S., and Inaba, H., "Free Convective Heat Transfer With Density Inversion in a Confined Rectangular Vessel," Wärme-und Stoffübertragung, Vol. 11, 1978, pp. 145–156.

8 Buchberg, H., Catton, I., and Edwards, D. K., "Natural Convection in Enclosed Spaces- A Review of Application to Solar Energy Collection," ASME JOURNAL OF HEAT TRANSFER, Vol. 98, 1976, pp. 182–188.

9 Hart, J. E., "Stability of the Flow in a Differentially Heated Inclined Box," *Journal of Fluid Mechanics*, Vol. 47, 1971, pp. 547–576.

10 Krishnamurti, R., "On the Transition to Turbulent Convection, Part 1, The Transition from Two- to Three-Dimensional Flow," *Journal of Fluid Mechanics*, Vol. 42, 1970, pp. 295–307.

Thermally Optimum Spacing of Vertical, Natural Convection Cooled, Parallel Plates

A. Bar-Cohen
Department of Mechanical Engineering,
Ben-Gurion University of the Negev,
Beer-Sheva, Israel
Fellow ASME

W. M. Rohsenow
Department of Mechanical Engineering,
Massachusetts Institute of Technology,
Cambridge, Mass. 02139
Fellow ASME

While component dissipation patterns and system operating modes vary widely, many electronic packaging configurations can be modeled by symmetrically or asymmetrically isothermal or isoflux plates. The idealized configurations are amenable to analytic optimization based on maximizing total heat transfer per unit volume or unit primary area. To achieve this anlaytic optimization, however, it is necessary to develop composite relations for the variation of the heat transfer coefficient along the plate surfaces. The mathematical development and verification of such composite relations as well as the formulation and solution of the optimizing equations for the various boundary conditions of interest constitute the core of this presentation.

Introduction

Vertical two-dimensional channels formed by parallel plates or fins are a frequently encountered configuration in natural convection cooling in air of electronic equipment, ranging from transformers to main-frame computers and from transistors to power supplies [1, 2, 3]. Packaging constraints and electronic considerations, as well as device or system operating modes, lead to a wide variety of complex heat dissipation profiles along the channel walls. In many cases of interest, however, a symmetric isothermal or isoflux boundary representation, or use of an isothermal/isoflux boundary together with an insulated boundary condition along the adjoining plate, can yield acceptable accuracy in the prediction of the thermal performance of such configurations.

Elenbaas [4] was the first to document a detailed study of the thermal characteristics of one such configuration, and his experimental results for isothermal plates in air were later confirmed numerically [5] and shown to apply as well to the constant heat flux conditions [6]. More recently, Aung and coworkers [7, 8] and Miyatake and coworkers [9, 10] extended the available results to include both asymmetric wall temperature and heat flux boundary conditions, including the single insulated wall.

From these and complementary studies emerges a unified picture of thermal transport in such a vertical channel. In the inlet region and in relatively short channels, individual momentum and thermal boundary layers are in evidence along each surface and heat transfer rates approach those associated with laminar flow along isolated plates in infinite media. Alternately, for long channels, the boundary layers merge near the entrance and fully developed flow prevails along much of the channel.

In this fully developed regime, the local heat transfer coefficient is constant (neglecting the temperature dependence of fluid properties) and equal to the well-documented forced convection values [11]. However, since the local fluid temperature is not explicitly known, it is customary to reexpress the fully developed heat transfer coefficient in terms of the ambient or inlet temperature. The Nu for isothermal plates appropriate to this definition can be derived from the "incompressible natural convection" form of the Navier-Stokes equations. This was done semianalytically by Elenbaas [4], confirmed by the laborious numerical calculations of Bodia and Osterle [5], and extended to asymmetric heating by Aung [7] and Miyatake et al. [9, 10]. In a subsequent section of this discussion, the limiting relations for fully developed laminar flow, in a symmetric isothermal or isoflux channel, as well as in a channel with an insulated wall, will be rederived by use of a straightforward integral formulation.

The analytic relations for the isolated plate (or inlet region) limit and the fully developed (or exit region) limit can be expected to bound the Nu values over the complete range of flow development. Intermediate values of Nu can be obtained from detailed experimental and/or numerical studies or by use of the correlating expression suggested by Churchill and Usagi [12] for smoothly varying transfer processes. This correlation technique relies on the analytic expressions at the two boundaries and a limited number of data points to derive a highly accurate composite correlation and its use will be demonstrated in later sections.

Fully Developed Limit

Momentum Considerations. In laminar, fully developed, two-dimensional flow between parallel plates—as shown in Fig. 1—the pressure drop is given by [11]

$$\left.\frac{dP}{dx}\right|_{\text{loss}} = -12\ \mu w/\rho b^3 \tag{1}$$

For free-convection flow, this flow resistance is balanced by the buoyant potential expressible as [11]

$$\left.\frac{dP}{dx}\right|_{\text{buoy}} = (\bar{\rho}_f - \rho_o)g = -\bar{\rho}\beta g(\bar{T}_f - T_o) \tag{2}$$

Equating equations (1) and (2), the flow rate per unit width, w, in the channel, is found equal

$$w = \bar{\rho}^2 g\beta b^3(\bar{T}_f - T_o)/12\ \mu \tag{3}$$

Nusselt Number—Symmetric, Isothermal Plates. An energy balance on the differential volume, shown in Fig. 1, equating heat transferred from two isothermal walls with that absorbed in the flow, yields

$$wc_p dT = 2h(T_w - T_f)dx \tag{4}$$

From continuity considerations the flow rate, w, is constant, and in fully developed flow with temperature-independent properties, the local heat transfer coefficent, h, as well as c_p, is constant. Consequently, $wc_p/2h$ can be considered

Contributed by the Heat Transfer Division for publication in the JOURNAL OF HEAT TRANSFER. Manuscript received by the Heat Transfer Division November 1, 1982.

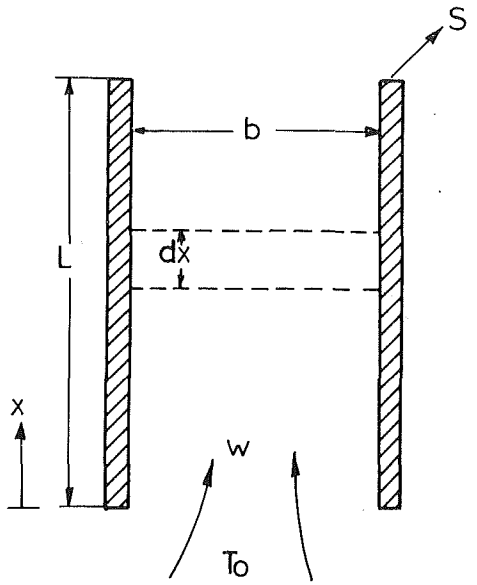

Fig. 1 Schematic of flow in a vertical channel

constant along the channel, and equation (4) can be simply integrated to yield the local fluid or bulk temperature

$$T_f = T_w - (T_w - T_o)e^{-\Gamma x} \tag{5}$$

where Γ has replaced $2h/wc_p$.

To accommodate the desire to obtain a Nusselt number based on the temperature difference between the wall and the ambient fluid, Nu_o can be defined as

$$\mathrm{Nu}_o \equiv \left[\frac{q/A}{T_w - T_o}\right]\frac{b}{k} \tag{6}$$

The transfer rate, q, can be determined from the flow rate and the temperature rise in the channel by the use of equations (3) and (5), with the latter evaluated at $x = L$ to find the exit temperature. The average fluid temperature in the channel can be found by integrating equation (5) from $x = 0$ to $x = L$ and dividing by the length of the channel, L. Following these operations

$$q = \left[\frac{c_p\bar{\rho}^2 g\beta b^3 S}{12\,\mu}(T_w - T_o)\left(1 - \frac{1-e^{-\Gamma L}}{\Gamma L}\right)\right]\left[(T_w - T_o)(1-e^{-\Gamma L})\right] \tag{7}$$

Inserting equation (7) into (6) with the surface area, A, equal to $2LS$, the desired Nusselt number is found as

$$\mathrm{Nu}_o = \frac{1}{24}\left[\frac{c_p\bar{\rho}^2 g\beta b^4(T_w - T_o)}{\mu k L}\right]\left[\left(1 - \frac{1-e^{-\Gamma L}}{\Gamma L}\right)(1-e^{-\Gamma L})\right] \tag{8}$$

The combination of parameters appearing in the first bracketted term of equation (8) is recognizable as the channel Rayleigh number, i.e., $\mathrm{Ra}\ b/L \equiv \mathrm{Ra}'$. Consequently, at the fully developed limit, where $L \to \infty$ and the second term in equation (8) approaches unity, Nu_o is seen to approach $\mathrm{Ra}'/24$. This result agrees exactly with the previously cited analytical and numerical results [4, 5, 7].

Nusselt Number—Asymmetric, Isotherm Plates. For fully developed flow in a channel formed by a single isothermal plate and an insulated plate, only the isothermal surface is involved in heat transfer, and Nu_o must be based on that surface alone. Modifying equations (4, 5) and (6) in this vein, the derivation of Nu_o is found to exactly parallel the development of equation (8) and yield $\mathrm{Nu}_o = \mathrm{Ra}'/12$ at the limit of $L \to \infty$ in agreement with [10]. Comparison with the results obtained by Aung [7] reveals this value to be approximately 7 percent lower then the Nu_o associated with the second surface being at ambient temperature (rather than adiabatic).

Nusselt Number—Symmetric, Isoflux Plates. In a channel formed by two constant heat flux plates, the fluid temperature increases lineary along the channel and equation (5) can be replaced by

$$T_f = T_o + 2\,q''x/wc_p \tag{9}$$

Nomenclature

A = area, m^2; coefficient
b = plate spacing, m
B = coefficient
c_p = specific heat at constant pressure, J/kg°C
C = coefficient
d = fin thickness, m
g = gravitational acceleration, m/s^2
h = heat transfer coefficient, W/m^2°C
k = thermal conductivity, W/m°C
L = channel or plate length, m
m = number of fins
n = exponent
Nu_o = channel Nusselt number, $\equiv q''b/k(T_w - T_o)$ dimensionless
p = exponent
p = pressure, N/m^2
q = exponent in equation (17); heat flow rate, W
q'' = heat flux, W/m^2
Q_T = total heat flow rate, W
Ra = Rayleigh number, $\equiv \rho^2 g\beta c_p L^3 \Delta T/\mu k$, dimensionless
Ra* = modified Rayleigh number, $\equiv \rho^2 g\beta c_p L^4 q''/\mu k^2$, dimensionless
Ra′ = channel Rayleigh number, $\equiv \rho^2 g\beta c_p b^4 \Delta T/\mu L$, dimensionless
Ra″ = modified Channel Rayleigh number, $\equiv \rho^2 g\beta c_p b^5 q''/\mu L k^2$
S = plate width, m
T = temperature, °C
w = mass flow rate per unit width, kg/m-s
W = width of prime area, m
x = length coordinate, m
y = generalized parameter in equation (19)
Y = modified generalized parameter in equation (19), $\equiv y/Az^p$
z = generalized parameter in equation (19)
Z = modified generalized parameter in equation (19), $\equiv Bz^{p-q}/A$

Greek Letters

β = volumetric coefficient of thermal expansion, $°K^{-1}$
Γ = thermal parameter, $2h/wc_p$, m^{-1}
ρ = density, kg/m^3
μ = dynamic viscosity, kg/m-s
Δ = difference

Subscripts

buoyant = natural convection driving force
f = fluid
loss = pressure drop
o = entrance or ambient value
opt = optimum
w = wall
x = local value
L = at the $x \equiv L$ location

Since, in many electronic applications, it is the maximum channel wall temperature that is of critical importance, it is desirable to define the Nusselt number in the isoflux configuration according to

$$\mathrm{Nu}_o \equiv \left[\frac{q''}{T_{w,L}-T_o}\right]\frac{b}{k} \tag{10}$$

From basic heat transfer considerations and equation (9), the defining temperature difference in Nu_o is found as

$$T_{w,L}-T_o=(T_{w,L}-T_f)+(T_f-T_o)=q''\left(\frac{1}{h}+\frac{2L}{wc_p}\right) \tag{11}$$

Using equation (9) to find the height-averaged fluid temperature in the channel and combining equations (3, 10) and (11), yields for the two-dimensional flow assumption

$$\mathrm{Nu}_o=\left[\frac{1}{h}+\frac{2L}{c_p\sqrt{\bar{\rho}^2 g\beta b^3 q'' L/12\mu c_p}}\right]^{-1}\frac{b}{k} \tag{12}$$

and following algebraic manipulation

$$\mathrm{Nu}_o=\left[\frac{k}{bh}+6.93\sqrt{\frac{\mu L k^2}{\bar{\rho}^2 g\, b^5 q'' c_p}}\right]^{-1} \tag{13}$$

The combination of parameters under the square-root in equation (13) is recognizable as the inverse of the modified channel Rayleigh number, i.e., $\mathrm{Ra}^* \cdot b/L \equiv \mathrm{Ra}''$. For the large values of L and small values of b appropriate to the fully developed limit, the first term in equation (13) is negligible relative to the square-root and the sought after limiting expression is thus found to equal

$$\mathrm{Nu}_o=\sqrt{\mathrm{Ra}''/48}=0.144\sqrt{\mathrm{Ra}''} \tag{14}$$

This result is identical to that obtained in previously cited studies and was found in [7] to apply as well to various ratios of surface heat flux, i.e., q_1''/q_2'', when Ra'' is based on the average value of q''.

When, as often is the case in experimental studies, the Nu_o is defined in terms of the midheight (or approximately average) wall temperature, the above development yields

$$\mathrm{Nu}_o \equiv \left[\frac{q''}{T_{w,L/2}-T_o}\right]\frac{b}{k}=\sqrt{\mathrm{Ra}''/12}=0.289\sqrt{\mathrm{Ra}''} \tag{15}$$

Nusselt Number—Asymmetric, Isoflux Plates. When the vertical channel under consideration is formed by an insulated plate on one side, the vertical temperature gradient in the fluid is half that indicated in equation (9). Modifying the above development to reflect this change, and proceeding as before, the limiting channel Nusselt number based on the maximum wall temperature is found to equal

$$\mathrm{Nu}_o=\sqrt{\mathrm{Ra}''/24}=0.204\sqrt{\mathrm{Ra}''} \tag{16}$$

in agreement with [9]. Alternately, the nu_o based on the midheight temperature is expressible as

$$\mathrm{Nu}_o=\sqrt{\mathrm{Ra}''/6}=0.41\sqrt{\mathrm{Ra}''} \tag{17}$$

Composite Relations for Air Cooling

Introduction. When a function is known to vary smoothly between two limiting expressions which are themselves well defined and when solutions for intermediate values of the function are either difficult to obtain or involve other tabulated functions, an approximate composite relation can be obtained by appropriately summing the two limiting expressions. Churchill and Usagi [12] have suggested that the frequently employed linear superposition be viewed as a special case of a more general summation of the form

$$y=[(Az^p)^n+(Bz^q)^n]^{1/n} \tag{18}$$

where

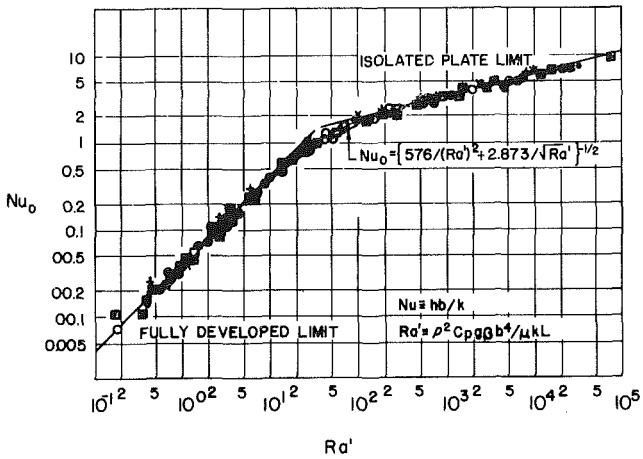

Fig. 2 Nu variation for symmetric isothermal plates

$$\begin{aligned} y &\to Az^p \quad \text{as } z\to 0\\ y &\to Bz^q \quad \text{as } z\to\infty\\ n &> 0 \quad \text{if } p<q\\ n &< 0 \quad \text{if } p>q \end{aligned}$$

For the natural convection problem under consideration, the Nu_o variation takes the form of $C_1\mathrm{Ra}'$ or $C_2\sqrt{\mathrm{Ra}''}$ for small values of the gap Rayleigh number and for the large Rayleigh number increases towards the isolated plate limit where, in laminar flow

$$\mathrm{Nu}_L=C_3(\mathrm{Ra})^{1/4}$$

for an isothermal surface, and

$$=C_4(\mathrm{Ra}^*)^{1/5} \tag{19}$$

for an isoflux surface. Multiplying both sides of equation (19) by b/L, this isolated plate relation can be converted to a relation between the channel Nusselt number, hb/k, and the channel Rayleigh number, Ra' and Ra'', for isothermal and isoflux plates, respectively.

Applying equation (18) to natural convection in channels, it might thus be anticipated that the Nu_o would vary according to

$$\mathrm{Nu}_o=[(C_1\mathrm{Ra}')^{-n}+(C_3\sqrt[4]{\mathrm{Ra}'})^{-n}]^{-1/n}$$

for isothermal plates, and

$$\mathrm{Nu}_o=[(C_2\sqrt{\mathrm{Ra}''})^{-n}+(C_4\sqrt[5]{\mathrm{Ra}''})^{-n}]^{-1/n} \tag{20}$$

for isoflux plates.

The correct, or most nearly correct, value of the correlating exponent, n, can be evaluated by comparing equation (20) with experimental data or computed values of Nu_o.

Symmetric, Isothermal Plates. As noted previously, Nu for laminar free convection on isothermal surfaces is dependent on $(\mathrm{Ra}')^{1/4}$ and configurational variations are generally reflected in different values of the coefficient, C_3. For moderately short vertical plates in air and $10^4 < \mathrm{Ra} < 10^9$, McAdams [13] reports C_3 to equal 0.59. This expression, together with the fully developed Nu_o relation (equation (8)), can be inserted into equation (20) to yield

$$\mathrm{Nu}_o=\left[\left(\frac{1}{24}\mathrm{Ra}'\right)^{-n}+\left(0.59\sqrt[4]{\mathrm{Ra}'}\right)^{-n}\right]^{-1/n} \tag{21}$$

The Elenbaas [4] correlation for this same thermal configuration takes the form

$$\mathrm{Nu}_o=\frac{1}{24}\mathrm{Ra}'[1-e^{-35/\mathrm{Ra}'}]^{3/4} \tag{22}$$

Following the correlating procedure described by Churchill

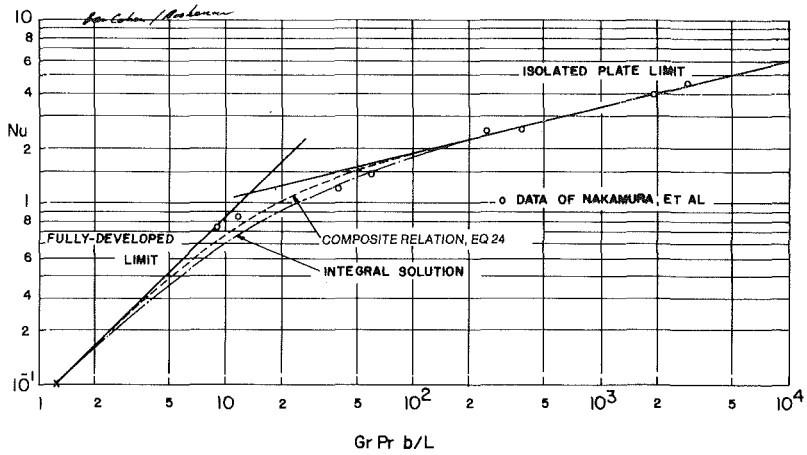

Fig. 3 Nu variation for parallel plates—one isothermal, one insulated

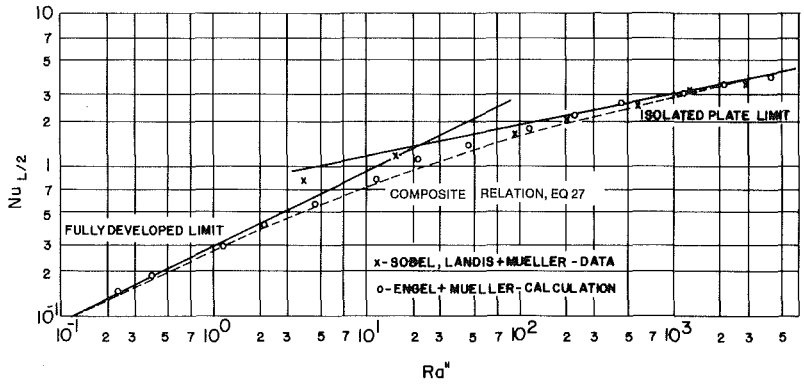

Fig. 4 $Nu_{o,L/2}$ variation for symmetric isoflux plates—data of [6]

and Usagi [12], the correlating exponent, n, is found to equal approximately 2, yielding a composite relation for two isothermal surfaces as

$$Nu_o = (576/(Ra')^2 + 2.873/\sqrt{Ra'})^{-1/2} \quad (23)$$

The close proximity of the Elenbaas data points to the composite relation, and the asymptotic equations at both limits, indicated in Fig. 2, serves to validate this approach.

Asymmetric, Isothermal Plates. For vertical channels formed by an isothermal plate and an insulated plate, the asymptotic limits were previously shown to be $Nu_o = Ra'/12$ for $Ra' \to 0$ and $Nu_o = 0.59\ Ra^{1/4}$ for $Ra' \to \infty$. Inserting these limiting expressions into equation (20) and assuming that despite channel asymmetry the symmetric correlating exponent $n = 2$ applies to this configuration as well, the composite relation for asymmetric isothermal plates is found to be

$$Nu_o = [144/(Ra')^2 + 2.873/\sqrt{Ra'}]^{-1/2} \quad (24)$$

Comparison of equation (24) with the limited data of Nakamura et al. [14] reported in [10] and the numerical solution of Miyatake and Fujii [10], as in Fig. 3, shows equation (24) to offer near-excellent agreement with the data and to improve somewhat on the predictive accuracy of the numerical solution in the region where Nu_o displays the effects of both fully developed and developing flow. Figure 3 and equation (24) also reveal the Nu_o from the thermally active surface in an asymmetric channel to be higher than from a comparable surface in a symmetric configuration, for a fixed channel width or Rayleigh number, at low values of Ra'.

Symmetric, Isoflux Plates. Natural convection heat transfer from an isolated, uniform heat flux, vertical plate is generally correlatable in the form

$$Nu_x = C_4(Ra^*)^{1/5} \quad (25)$$

While theoretically C_4 for air has been shown to equal 0.519 [15], the empirical large-spacing asymptote for channel heat transfer is generally higher [6, 8, 9], yielding

$$Nu_o = 0.73(Ra'')^{1/5} \quad (26)$$

for Nu_o based on the midheight temperature difference or $Nu_o = 0.63(Ra'')^{1/5}$ when the maximum channel wall to inlet air temperature difference is used.

Much of the available Nu data for channels formed by isoflux plates is presented in terms of the temperature difference between the wall, at the channel midheight, and the inlet air, e.g., [6, 8]. Superposing the two relevant asymptotes, equations (15) and (26), the composite Nu relation appropriate to this definition is found as

$$Nu_{o,L/2} = \{(12/Ra'') + 1.88/(Ra'')^{0.4}\}^{-0.5} \quad (27)$$

Comparison in Fig. 4 of equation (27) with typical data of Sobel et al. [6] and the results of the Engel and Mueller numerical calculation presented in [8] reveals the composite isoflux relation to have a high predictive accuracy and no further adjustment of the correlating exponent appears to be necessary. The larger than anticipated Nu values at the low Ra'' data points of Sobel et al. [6] may be explained by unaccounted-for radiation and conduction losses at the channel exit, as noted by the authors.

In a recent study [17], both direct temperature measurements and analysis of interferograms were used to

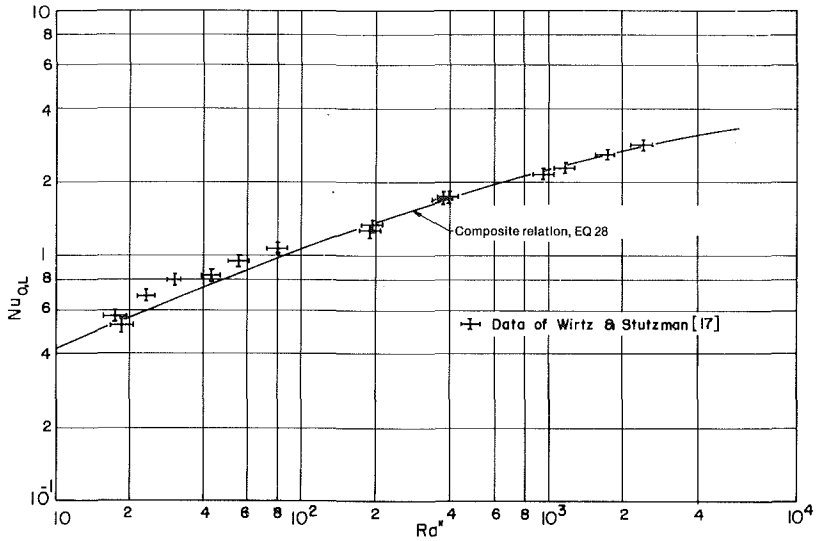

Fig. 5 $Nu_{o,L}$ variation for symmetric isoflux plates—data of [17]

determine the empirical variation of the heat transfer rate for the symmetric, isoflux, air-cooled channel. The results were reported in terms of Nu based on the temperature difference at $x=L$ and are compared in Fig. 5 with the composite Nu relation, equation (28), based on the same definition. Examination of Fig. 5 reveals the predicted values to lie within the experimental error band (Nu ± 5 percent, Ra ± 16 percent) of the data for all but the lowest values of Ra″.

$$\mathrm{Nu}_{o,L} = \{(48/\mathrm{Ra}'') + 2.51/(\mathrm{Ra}'')^{0.4}\}^{-0.5} \tag{28}$$

Asymmetric, Isoflux Plates. When a vertical channel is formed by a single isoflux plate and an insulated plate, the desired composite relation for Nu, based on the midheight temperature difference, can be found by appropriately combining equations (17) and (27) (with $n = 2$) to yield

$$\mathrm{Nu}_{o,L/2} = \{6/\mathrm{Ra}'' + 1.88/(\mathrm{Ra}'')^{0.4}\}^{-1/2} \tag{29}$$

Optimum Plate Spacing

The composite relations derived in the previous section can be used to predict the value of the heat transfer coefficient for each of the four thermal configurations examined. No less important, however, is their potential use in optimizing the spacing between vertical, heat-dissipating plates when two-dimensional flow can be assumed to prevail.

Symmetric, Isothermal Plates. The total heat transfer rate from an array of vertical plates, Q_T, is given by

$$Q_T = (2LS\Delta T_o)\,(m)\,(\mathrm{Nu}_o k/b) \tag{30}$$

where m, the number of plates, equals $W/(b+d)$, b equals the spacing between adjacent plates, and d is the thickness of each plate.

Examination of Fig. 2 shows that the rate of heat transfer from each plate decreases as plate spacing is reduced. Since the total number of plates or total plate surface area increases with reduced spacing, Q_T may be maximized by finding the plate spacing at which the product of total plate surface area and local heat transfer coefficient is maximum. Based on his experimental results, Elenbaas determined that this optimum spacing for negligibly thick plates could be obtained by setting $\mathrm{Ra}'_{\mathrm{opt}} = 46$ yielding a Nu_o of 1.2 [4].

Using equation (23) to determine Nu_o and dividing both sides of equation (30) by the product of total fin area, temperature difference, thermal conductivity, and width of the base area, yields

$$(Q_T/2LSW\Delta T_o k) = (b+d)^{-1}b^{-1}(576/P^2b^8 + 2.873/P^{0.5}b^2)^{-0.5} \tag{31}$$

where

$$P \equiv C_p(\bar{\rho})^2 g\beta\Delta T_o/\mu kL$$

Differentiating equation (31) with respect to b, setting the derivative to zero and cancelling common terms leads to

$$-(b+d)^{-1} - b^{-1} + \frac{1}{2}(576/P^2b^8 + 2.873/P^{0.5}b^2)^{-1}(8\cdot 576/P^2b^9 + 2\cdot 2.873/P^{0.5}b^3) = 0 \tag{32}$$

Following additional algebraic operations, equation (32) is found to reduce to

$$(2b + 3d - 0.005\,P^{1.5}b^7)_{\mathrm{opt}} = 0 \tag{33}$$

Solution of equation (33) should now yield the value of b which maximizes Q_T, i.e., the b_{opt} value.

In general, b_{opt} is seen to be a function of both the plate/air parameter, P, and the plate thickness, d, but for negligibly thick plates

$$b_{\mathrm{opt}} = 2.714/P^{1/4} \tag{34}$$

This result exceeds the Elenbaas optimum spacing by only 4 percent and yields optimum values of channel Rayleigh and Nusselt numbers of 54.3 and 1.31, respectively.

In electronic cooling applications, it is often of interest to maximize the rate of heat transfer from individual plates or component carrying, printed circuit boards. This can be achieved by spacing the plates in such a manner that the isolated plate Nu prevails along the surface. To achieve this aim precisely requires an infinite plate spacing, but setting Nu (via equation (23)) equal to 0.99 of the isolated plate value yields $\mathrm{Ra}' = 463$ and $b_{\max}$ equal to $4.64/P^{1/4}$. This result is in general agreement with [18] where the identically defined maximum plate spacing was determined to occur at Ra′ approximately greater than 600. It is perhaps of interest to note that at $\mathrm{Ra}' = 600$, the composite Nu is found to reach 0.993 of the isolated plate value.

As might have been anticipated, the $b_{\max}$ spacing can be shown to correspond to approximately twice the boundary layer thickness along each surface at the channel exit, i.e, $x = L$. By comparison b_{opt} corresponds to nearly 1.2 boundary layer thicknesses at $x = L$.

Asymmetric, Isothermal Plates. In analyzing the asymmetric, isothermal configuration, equation (31) can

Table 1 Summary of heat transfer relations for vertical natural convection arrays

Condition	Heat transfer rate	Optimum spacing[a]	Optimum Nu_o[a]
Isothermal plates Symmetric	$Nu_o = \left[\frac{576}{(Ra')^2} + \frac{2.873}{\sqrt{Ra'}}\right]^{-0.5}$	$b_{opt} = 2.714\, P^{-0.25}$	$(Nu_o)_{opt} = 1.31$
Asymmetric	$Nu_o = \left[\frac{144}{(Ra')^2} + \frac{2.873}{\sqrt{Ra'}}\right]^{-0.5}$	$b_{opt} = 2.154\, P^{-0.25}$	$(Nu_o)_{opt} = 1.04$
Isoflux plates[b] Symmetric	$Nu_{o,L/2} = \left[\frac{12}{Ra''} + \frac{1.88}{(Ra'')^{0.4}}\right]^{-0.5}$	$b_{opt} = 1.472\, R^{-0.2}$	$(Nu_{o,L/2})_{opt} = 0.62$
Asymmetric	$Nu_{o,L/2} = \left[\frac{6}{Ra''} + \frac{1.88}{(Ra'')^{0.4}}\right]^{-0.5}$	$b_{opt} = 1.169\, R^{-0.2}$	$(Nu_{o,L/2})_{opt} = 0.49$

[a]For negligibly thick plates
[b]Based on the plate temperature at $x = L/2$

again be used to calculate the total heat transfer from a given base area and to determine the optimum spacing between plates when m, the number of thermally active plates, is now set equal to $W/2(b+d)$. Proceeding as before, the governing relation for the optimum spacing is found to be

$$(2b + 3d - 0.02P^{1.5}b^7)_{opt} = 0 \tag{35}$$

For negligibly thick plates, b_{opt} is then given by

$$b_{opt} = 2.154/P^{1/4} \tag{36}$$

At this optimum spacing, $Ra'_{opt} = 21.5$ and $Nu_{opt} = 1.04$.

To maximize the heat transfer rate from each individual, thermally active plate, it is again desirable to set the plate spacing such that fully developed flow does not develop in the channel and that, as a consequence, the isolated plate Nu limit is attained along the entire surface. Calculating via equation (24), Ra'_{max} at the 0.99 limit is found to equal approximately 184 and $b_{max} = 3.68/P^{1/4}$.

Symmetric, Isoflux Plates. When the boundary conditions along the surfaces of the parallel plates are identically or approximately equal to uniform heat flux, total heat transfer from the array can be maximized simply by allowing the number of plates to increase without limit. In most electric cooling applications, however, the plate, printed circuit board, or component surface must be maintained below a critical temperature and, as a consequence, plate spacing and Nu_o values cannot be allowed to deteriorate to very small values.

Recalling the Nu_o definition of equation (15) and rewriting equation (29), the relationship between the midheight temperature difference and the other parameters is found to be expressible as

$$\Delta T_{L/2} = \frac{q''b}{k}\left[\frac{12}{Ra''} + \frac{1.88}{Ra''^{2/5}}\right]^{1/2} \tag{37}$$

Thus, when both the surface heat flux and the allowable temperature difference are specified, equation (37) can be used to solve for the requisite interplate spacing.

Alternately, when only the heat flux is specified, it is of interest to determine the plate spacing yielding the lowest possible surface temperature. This condition corresponds to a spacing which is sufficiently large to avoid boundary layer interference and, by the method previously described, is found to occur at Ra'' equal approximately to 17000 and $b_{max} = 7.02R^{-0.2}$.

In distinction to the b_{max} value and the plate spacing obtained via equation (37), the optimum b value for an array of isoflux plates an be defined to yield the maximum volumetric (or prime area) heat dissipation rate per unit temperature

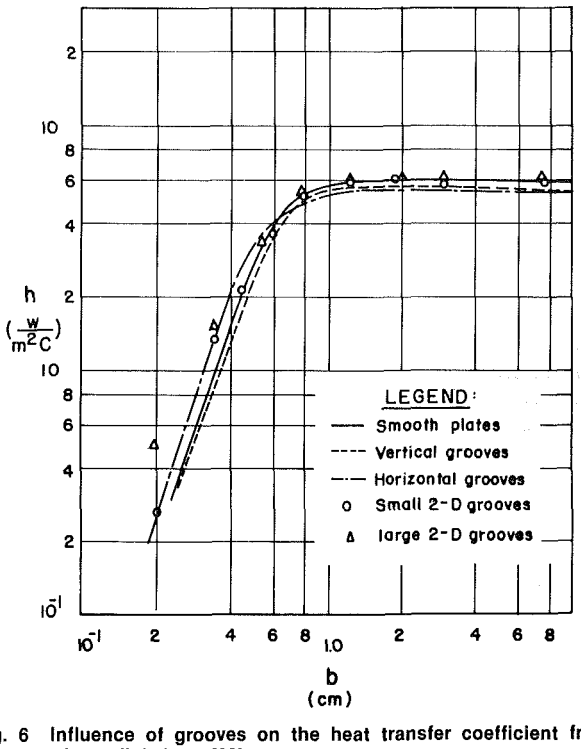

Fig. 6 Influence of grooves on the heat transfer coefficient from isothermal, parallel plates [20]

difference. Thus, when equation (29) is used to evaluate Nu_o in the equation (30) formulation of total array heat transfer, the optimizing equation for the symmetric, isoflux configuration takes the form

$$\frac{d}{db}\left(\frac{Q_T}{2LSW\Delta T_{L/2}k}\right.$$

$$\left. = \frac{d}{db}\left\{(b^2 + db)^{-1}\left(\frac{12}{R}b^{-5} + + \frac{1.88}{R^{0.4}}b^{-2}\right)^{-1/2}\right\} = 0 \right. \tag{38}$$

where

$$R \equiv c_p\rho^2 g\beta q''/\mu\, Lk^2$$

Following differentiation, the governing relation for b_{opt} is found as

$$\left(\frac{12}{R}b - \frac{3.76b^4}{R^{0.4}} + \frac{36}{R}d\right)_{opt} = 0 \tag{39}$$

For negligibly thick plates, i.e., $d = 0$, the optimum isoflux

plate spacing is then found to equal

$$b_{\text{opt}} = 1.472\ R^{-0.2} \tag{40}$$

The value of Ra''_{opt} is thus 6.9 and $\text{Nu}_{o,L/2}$ at the optimum spacing is found to equal 0.62.

Asymmetric, Isoflux Plates. By analogy to the symmetric, isoflux configuration, the requisite plate spacing for specified values of q'' and $\Delta T_{L/2}$ on the thermally active surface can be obtained by appropriate solution of equation (29).

Similarly, equation (29) can be used to determine the lowest Ra'' at which the prevailing Nu_o is indistinguishable from the isolated plate limit. This condition is found to occur at Ra'' equal approximately to 5400 and to yield the plate spacing required to obtain the lowest surface temperature, $b_{\max}$, equal to $5.58R^{-0.2}$.

Finally, when the relation governing the total heat dissipation of an array of alternating isoflux and insulated plates is differentiated relative to the plate spacing and the derivative set equal to zero, the optimum value of b for this configuration can be found by solving

$$\left(\frac{6}{R}b - \frac{3.76\ b^4}{R^{0.4}} + \frac{18}{R}d\right)_{\text{opt}} = 0 \tag{41}$$

For negligibly thick plates

$$b_{\text{opt}} = 1.169\ R^{-0.2} \tag{42}$$

The optimum modified channel Rayleigh Number is thus 2.2, yielding a $\text{Nu}_{o,L/2}$ of 0.49.

Discussion

The preceding has established an analytical, albeit approximate, structure for determining the channel width, or spacing between surfaces forming a two-dimensional channel, appropriate to various thermal constraints for symmetric and asymmetric, isothermal, and isoflux boundary conditions. With the developed relations summarized in Table 1 and subject to the stated assumptions, it is thus possible to select the interplate spacing which will maximize heat transfer from the individual, thermally active surfaces or, alternately, choose the spacing which yields the maximum heat dissipation from the entire array. In the absence of a large body of verified experimental results, the agreement found between both the composite and optimum spacing relations for symmetric, isothermal plates, and the classic Elenbaas [4] data, serves to verify the credibility and engineering accuracy of the approach described herein. Several noteworthy features of the composite and optimizing relations are discussed below.

Asymmetric Versus Symmetric Fully Developed Limit. Comparison of the derived relations for the fully developed Nu_o reveals the asymmetric value to exceed the symmetric value by a factor of two for isothermal surfaces and a factor of $\sqrt{2}$ for the isoflux condition. At first glance this experimentally verified result [9, 10] appears counterintuitive since the thicker thermal boundary layer in the asymmetrically heated channel (equal to the interplate spacing) could be expected to yield *lower* heat transfer coefficients than encountered with the thinner boundary layers of the symmetrically heated configuration. While this assertion is correct for Nusselt numbers based on the local wall-to-fluid temperature difference, it must be recalled that the Nu_o is defined in such a way as to include the temperature rise in the convecting air. As a result, Nu_o can be expected to reflect the "helpful" influence of reduced heat addition in the asymmetric case and to yield the observed higher values.

Asymmetric Versus Symmetric Optimum Arrays. The higher Nu_o to be expected in asymmetric configurations has led some thermal designers to suggest that whenever possible this configuration be preferred over a symmetric distribution of the heat dissipation on the array of parallel plates. Examination of the results for both maximum and optimum plate spacing reveals the error inherent in such an approach.

For isothermal plates $b_{\max}$ was found to equal $4.64\ P^{-0.25}$ in the symmetric configuration and $3.68\ P^{-0.25}$ in the asymmetric configuration. Similarly, $b_{\max}$ equals $7.02\ R^{-0.2}$ for symmetric, isoflux plates and $5.58\ R^{-0.2}$ when the channel is formed by an isoflux plate and an adiabatic plate. Since the plate spacing required for maximum heat transfer from each surface in the asymmetric configuration is thus substantially greater than 50 percent of the symmetric value, the total dissipation of an asymmetric array subject to the same constraints must fall below the heat dissipation capability of a symmetric array.

It can be shown that, for a given array base area or volume, an optimum array of negligibly thick isothermal plates alternating with insulated plates cannot dissipate more than 63 percent of the heat dissipated by an optimum array of isothermal plates. This finding is reenforced by the results obtained by Aung [16], which indicate that thermal asymmetry reduces total heat dissipation to approximately 65 percent of the comparable symmetric configuration when every second plate is at the ambient temperaure.

Use of the derived optimum spacing and optimum Nu_o values for symmetric and asymmetric isoflux channels yields a nearly identical reduction in total heat dissipation for the asymmetric configuration as encountered in isothermal plates.

Three-Dimensional Flow and Geometric Effects. In the present development of design equations for the spacing between isothermal and isoflux plates no attempt has been made to address the influence of three-dimensional flow, i.e., side in-flow or lateral edge effects, on the anticipated Nu_o values nor on the recommended optimum spacings. Clearly such effects can be anticipated to become progressively greater as the ratio of interplate spacings to channel height is reduced. In [19] the lateral edge effects for 7.6 cm square plates were found to be of no consequence for Ra' values greater than 10 but to produce deviations of up to 30 percent or more in the equivalent Nu_o when Ra' was below 4. Furthermore, for larger square plates (15.2 × 15.2 cm) the two-dimensional theory has been found to apply for all Ra' values greater than 2 [20]. Consequently, while the asymptotic approach of the Elenbaas data [4] to the analytical, two-dimensional, fully developed flow limit—as shown in Fig. 2—may be fortuitous there is little likelihood of three-dimensional flow effects in the Ra' region corresponding to the optimum and maximum interplate spacings derived.

While smooth plates may serve as a convenient idealization for component-carrying, Printed Circuit Boards (PCB's), in reality such PCB's are better represented by plates with both horizontal and vertical grooves. This configuration was studied in [20] where heat transfer coefficients from two dimensional, grooved, parallel plates were found to exceed the smooth plate values at small interplate spacings and to equal the smooth plate values for spacings appropriate to the isolated plate limit. As shown in Fig. 6, the enhancement of the heat transfer rate for small spacings appears to be dependent on the groove geometry.

Summation

The complexity of heat dissipation in vertical parallel plate arrays encountered in electronic cooling applications frequently dissuade thermal analysts and designers from attempting an even first-order analysis of anticipated temperature profiles and little theoretical effort is devoted to thermal optimization of the relevant packaging con-

figurations. The foregoing has aimed at establishing an analytical structure for such analyses while presenting and verifying useful relations for heat distribution patterns identical to or approaching isothermal or isoflux boundary conditions.

References

1 Bar-Cohen, A., "Fin Thickness for an Optimized Natural Convection Array of Rectangular Fins," ASME JOURNAL OF HEAT TRANSFER, Vol. 101, 1979, pp. 564-566.

2 Kraus, A. D., *Cooling Electronic Equipment*, McGraw Hill, New York, 1962.

3 Aung, W., Kessler, T. J., and Beitin, K. L., "Free-Convection Cooling of Electronic Systems," *IEEE Transaction on Parts, Hybrids and Packaging*, Vol. PHP-9, No. 2, 1973, pp. 75-86.

4 Elenbaas, W., "Heat Dissipation of Parallel Plates by Free Convection," *Physica*, Vol. 9, No. 1, Holland, 1942.

5 Bodoia, J. R., and Osterle, J. F., "The Development of Free Convection between Heated Vertical Plates," ASME JOURNAL OF HEAT TRANSFER, Vol. 84, 1964, pp. 40-44.

6 Sobel, N., Landis, F., and Mueller, W. K., "Natural Convection Heat Transfer in Short Vertical Channels Including the Effect of Stagger," *Proceedings - Third International Heat Transfer Conference*, Vol. 2, 1966, pp. 121-125.

7 Aung, W., "Fully Developed Laminar Free Convection between Vertical Plates Heated Asymmetrically," *International Journal of Heat and Mass Transfer*, Vol. 15, 1972, pp. 1577-1580.

8 Aung, W., Fletcher, L. S., and Sernas, V., "Developing Laminar Free Convection Between Vertical Flat Plates with Asymmetric Heating," *International Journal of Heat and Mass Transfer*, Vol. 15, 1972, pp. 2293-2308.

9 Miyatake, O., Fujii, T., Fujii, M., and Tanaka, H., "Natural Convective Heat Transfer Between Vertical Parallel Plates—One Plate with a Uniform Heat Flux and the other Thermally Insulated," *Heat Transfer—Japanese Research*, Vol. 4, 1973, pp. 25-33.

10 Miyatake, O., and Fujii, T., "Free Convective Heat Transfer Between Vertical Plates—One Plate Isothermally Heated and the Other Thermally Insulated," *Heat Transfer—Japanese Research*, Vol. 3, 1972, pp. 30-38.

11 Rohsenow, W. M., and Choi, H., *Heat, Mass and Momentum Transfer*, Prentice Hall, New Jersey, 1961.

12 Churchill, S. W., and Usagi, R., "A General Expression for the Correlation of Rates of Transfer and Other Phenomena," *AIChE Journal*, Vol. 18, No. 6, 1972, pp. 1121-1128.

13 McAdams, W. H., *Heat Transmission*, McGraw Hill, New York, 1954.

14 Nakamura, H., et al., Paper No. 126, *Proceedings of the 42nd National Meeting of the Japan Society of Mechanical Engineering*, Vol. 5, 1964.

15 Sparrow, E. M., and Gregg, J. L., "Laminar Free Flow Convection from a Vertical Plate with Uniform Surface Heat Flux," ASME Transaction C, 1956, pp. 435-440.

16 Aung, W., "Heat Transfer in Electronic Systems with Emphasis on Asymmetric Heating," *Bell System Technical Journal*, Vol. 52, 1973, pp. 907-925.

17 Wirtz, R. A., and Stutzman, R. J., "Experiments on Free Convection Between Vertical Plates with Symmetric Heating," ASME JOURNAL OF HEAT TRANSFER, Vol. 104, 1982, pp. 501-507.

18 Levy, E. K., "Optimum Plate Spacings for Laminar Natural Convection Heat Transfer from Parallel Vertical Isothermal Flat Plates," ASME JOURNAL OF HEAT TRANSFER, Vol. 93, 1971, pp. 463-465.

19 Sparrow, E. M., and Bahrami, P. A., "Experiments on Natural Convection from Vertical Parallel Plates with Either Open or Closed Edges," ASME JOURNAL OF HEAT TRANSFER, Vol. 102, 1980, pp. 221-227.

20 Horton, S. F., "Natural Convection from Parallel Plates With Grooved Surfaces," MSc thesis, Department of Mechanical Engineering, Massachusetts Institute of Technology, Aug. 1981.

Enhancement of Natural Convection Heat Transfer From A Horizontal Cylinder Due to Vertical Shrouding Surfaces

E. M. Sparrow
Fellow ASME

D. R. Pfeil

Department of Mechanical Engineering,
University of Minnesota,
Minneapolis, Minn. 55455

A comprehensive experimental study has been performed to determine the natural convection heat transfer characteristics of a heated horizontal cylinder situated in a vertical channel in air. Fifteen different channel configurations were employed, encompassing a wide range of channel heights and of spacings between the channel walls. Shroud walls having various thermal characteristics (highly conducting, highly conducting/rear insulated, and insulating) were used to form the channel. For each configuration, the cylinder Rayleigh number ranged from 1.5 × 10^4 to 2 × 10^5. It was found that a cylinder situated in a channel experiences enhanced natural convection heat transfer compared with a cylinder situated in unbounded space. Enhancements of up to 40 percent were encountered for the parameter ranges of the experiments. The enhancement is accentuated as the interwall spacing is decreased and as the channel height is increased. There is no enhancement for interwall spacings of 10 diameters or more. It was also found that the Nusselt number was quite insensitive to the various types of shroud walls employed. Measured temperature distributions along the shroud walls displayed different degrees of uniformity depending on whether the wall was conducting or insulating.

Introduction

The natural convection heat transfer characteristics of a single horizontal cylinder situated in an essentially unbounded domain have been extensively investigated, as witnessed by the lengthy compilation of experimental work set forth in [1]. However, very little information is available for natural convection heat transfer at a horizontal cylinder positioned between walls which form a vertical channel. The paucity of information is surprising considering the many applications of shrouded horizontal cylinders in natural convection. For example, in a commonly encountered radiator used for space heating, a horizontal tube (or tubes) is situated between a wall and a protective vertical shroud, with openings at the top and bottom to permit the passage of air through the vertical channel. Furthermore, cylindrical components which are cooled by natural convection (e.g., computer components) are often located between vertical walls.

The work described here is a results-oriented study of natural convection from a horizontal cylinder symmetrically situated between a pair of unheated vertical walls, hereafter referred to as the shrouds. The two shrouds, plus a pair of passive endwalls, formed a flow channel with an open top and bottom, as can be seen in Fig. 1, which is a schematic diagram of the physical situation being investigated. The shroud height, H, and the spacing, S, between the shrouds were varied systematically throughout the experiments, with the results that 15 different flow channel geometries were investigated. In all the experiments, the cylinder was positioned at the channel midheight. The experiments were performed in air.

Another special feature of the research was the various types of shroud walls that were employed, representing different thermal boundary conditions. In one case, the shrouds were highly conducting metal plates backed by insulation, whereas in the second case the metal plates were uninsulated. In the third investigated case, the shrouds consisted entirely of insulation. For all cases, the shroud surfaces which bounded the flow channel had radiation properties close to those of a blackbody. Thermocouples were installed in the various shroud walls to measure the temperature at the surface of the channel.

For each of the flow channel geometries and shroud-wall thermal boundary conditions, experiments were performed over the Rayleigh number range between 1.5 × 10^4 and 2 × 10^5. An additional set of experiments was carried out over the same range for the case of the classical unshrouded horizontal

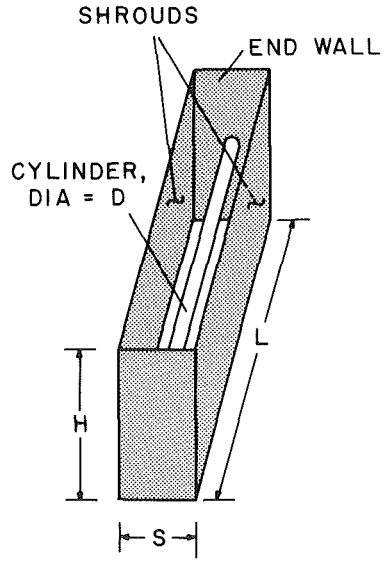

Fig. 1 Schematic diagram of a horizontal cylinder situated in a vertical channel

Contributed by the Heat Transfer Division for publication in the JOURNAL OF HEAT TRANSFER. Manuscript received by the Heat Transfer Division February 14, 1983.

cylinder in order to enable comparisons with the literature and to provide baseline results for the shrouded-cylinder results.

The nature of the natural convection flow in the shrouded case differs fundamentally from that for the classical horizontal cylinder in an unbounded domain. In the latter, the driving force for the flow is the difference between the ambient fluid density and the density of the fluid in the boundary layer at a given horizontal plane. A heated cylinder creates a density deficit relative to the ambient. The less dense fluid rises and is replaced by fluid which flows from the ambient into the boundary layer, with the replacement fluid being drawn both from the sides and from below the cylinder.

For the shrouded cylinder case, the fluid flow is induced by a mismatch between the hydrostatic pressure variations which occur inside and outside the flow channel. Outside the channel, there exists a hydrostatic pressure drop between the bottom and the top. Inside the channel, the heated cylinder causes the fluid density to be lower than that of the fluid outside the channel. Consequently, the integrated bottom to top hydrostatic pressure drop inside the channel is less than the external hydrostatic drop. Thus, if there were no flow in the channel, the static pressure at the exit would exceed that of the adjacent ambient. Such a pressure imbalance would induce an outflow from the channel exit, and continuity demands a corresponding inflow at the bottom. The magnitude of the velocity is such that the sum of the motion-related pressure drops and the internal hydrostatic drop equals the external hydrostatic drop.

The fluid passing upward through the channel and approaching the cylinder from below appears, from the standpoint of the cylinder, similar to a forced convection flow. The resulting boundary layer on the cylinder surface is therefore expected to be somewhat thinner than that for the unshrouded cylinder, with a consequent increase in the natural convection heat transfer.

The only prior experimental work on the shrouded horizontal cylinder appears to be that of [2]. However, since the data reported there for air were confined to $Ra < 4 \times 10^3$, which is well below the present range $Ra > 1.5 \times 10^4$, no direct comparisons can be made. Furthermore, the apparatus of [2] appears to have been underinstrumented (one thermocouple on the cylinder and no shroud thermocouples). No mention was made of an accounting of thermal radiation, nor was the effect of the shroud-wall thermal properties investigated. A numerical solution for the shrouded cylinder was recently published in [3], but the boundary conditions at the exit of the channel were chosen from the standpoint of computational feasibility and do not necessarily reflect reality. In view of this, the results have to be regarded as possessing some degree of uncertainty. References [2] and [3] will be revisited for comparison purposes later in the paper.

Experimental Apparatus and Procedure

The main components of the experimental apparatus include the electrically heated horizontal cylinder, three sets of channel walls, structural elements which serve to support and position the cylinder and the shrouds, and instrumentation. Also of significance to the attainment of results of high accuracy is the fully isolated laboratory room which provided an ideal ambient for natural convection studies.

Horizontal Cylinder. The cylinder was of aluminum, with an outside surface that had been polished to a mirror finish (i.e., *highly polished* from the standpoint of radiative properties). The finished outer diameter, D, was 3.787 cm, and its length, L, was equal to $20D$. With the precautions taken to avoid end effects (to be discussed later), the 20:1 L/D ratio is believed to be a close approximation to the infinite cylinder situation. The relatively thick wall of the cylinder (0.635 cm) aided the attainment of the desired uniform surface temperature boundary condition. Heating was accomplished by a specially fabricated, uniformly wound brass heater core situated in the bore of the cylinder.

Temperatures were measured at seven points on the surface of the cylinder by fine gage (0.0127-cm dia), specially calibrated iron-constantan thermocouples. The thermocouple junctions were situated 0.05 cm beneath the surface, and the lead wires were led radially inward through the walls of the cylinder and the heater core, emerging in the hollow bore of the core and being drawn out to one end.

The cylinder was supported at each end by a horizontal, fingerlike plexiglass rod which was inserted into the bore of the cylinder. Point contact between the rod and the surface of the bore was achieved by shaping the end of the rod to leave an up-pointing pyramidal protrusion on which the cylinder rested. This type of support, particularly the point contact, and the use of a nonmetallic structural member provided a significant defense against extraneous heat conduction. An additional defense at each end was provided by a layer of fiberglass insulation which shrouded the end face of the cylinder wall. Each of the aforementioned plexiglass rods was attached to a support structure which was situated outside the flow channel and which enabled the elevation of the cylinder above the floor of the laboratory to be varied in a controlled, continuous manner.

Flow Channel. As noted earlier, three different types of wall systems were employed for the flow channel. Since the endwalls (Fig. 1) merely served as closures, they were made the same for all the wall systems. Each endwall consisted of a facing of wrinkle-free, smoothly stretched brown kraft paper backed by fiberglass insulation. A leak-free seal between the endwalls and the shrouds was achieved by tape.

The three types of shrouds employed in the experiments will be designated as I, II, and III and have the following general characteristics:

I Highly conducting metallic wall heavily insulated at the rear
II Highly conducting metallic wall without insulation
III Insulating wall

For the Type I shroud, the metallic wall was a 0.635-cm thick aluminum plate whose flatness was ensured by sections of angle iron bolted to its rear face. The insulation that backed the metal plate consisted of two layers—5.08 cm of

Nomenclature

A = cylinder surface area
D = cylinder diameter
g = acceleration of gravity
H = shroud height
h = convective heat transfer coefficient
k = thermal conductivity
L = length of cylinder and shroud
Nu = Nusselt number, hD/k
P = electric power
Pr = Prandtl number
Q_c = convective heat transfer at cylinder
Q_{cond} = conduction heat loss
Q_{rad} = radiation heat loss
Ra = Rayleigh number, $\{g\beta(T_w - T_\infty)D^3/\nu^2\}$Pr
T_s = shroud surface temperature
T_w = cylinder surface temperature
T_∞ = ambient air temperature
β = thermal expansion coefficient
ϵ = emissivity of cylinder surface
ν = kinematic viscosity
σ = Stefan-Boltzmann constant

extruded, closed-pore polystyrene (notched to accommodate the angle iron sections) and an 8.9-cm batt of fiberglass.

The Type II shroud is simply the Type I shroud without the backing insulation, so that the backside of the aluminum plate was exposed to the ambient air. Out of concern about the possible role of the angle iron sections as fins, experiments were performed both with and without the sections.

The Type III shroud was an assembly of two layers of insulation. In designing this shroud, it was necessary to employ a structurally rigid flat-faced material to serve as the bounding surface of the flow channel. A slab of extruded, closed-pore polystyrene, especially selected for flatness and reinforced at the rear with sections of aluminum C-channel, fulfilled these criteria. The 5.08-cm thickness of the available polystyrene did not provide the desired thermal resistance and it was, therefore, backed by 8.9 cm of fiberglass. It may be noted that the thermal resistance for heat flow between the bounding surface of the channel and ambient was identical for the Type I and III shrouds.

To provide identical radiation properties and hydrodynamic smoothness for all of the shroud surfaces which bounded the flow channel, these surfaces were covered with white, self-adhering, plasticized, contact paper (thickness equal to 0.006 cm). In auxiliary experiments, the emissivity of the contact paper was measured to be 0.855. This emissivity value is representative of a broad class of surfaces including painted surfaces and those of nonmetallic structural materials in general.

The shrouds, while not directly heated, receive heat from the cylinder via two paths. One of these is by radiation and the other is by convection from the air which had been heated as it passed over the cylinder. Neither the Type I nor Type III shrouds permit the thus-received heat to be lost to the ambient because of their thick insulation layers. In the case of the Type I shroud, the highly conducting surface plate tends to spread the heat along the surface, thereby smoothing possible temperature nonuniformities associated with the spatially nonuniform heating of the shroud. On the other hand, for the Type III shroud, there will be little spreading of the heat along the surface, and localized temperature nonuniformities may well occur. For the Type II shroud, the tendency toward surface temperature uniformity will be coupled with a tendency toward a lower temperature level due to possible heat losses to the ambient at the rear of the shroud.

For each type of shroud and for each shroud height, H (Fig. 1), two identical shroud walls were fabricated to serve as the principal bounding surfaces of the flow channel. Three shroud heights were employed during the course of the research: respectively, H/D = 5, 10, and 20. Also, to provide information about the shroud temperature distribution, each shroud wall was equipped with six thermocouples, the locations of which will be evident from the plotted results.

The shrouds were suspended from a frame by braided nylon line, and similar nylon line attached tc the lower ends of the shroud was used in fixing the vertical alignment of the shroud surface which bounded the flow channel. The use of the nylon line, in contrast to rigid structural materials, was a precaution taken to avoid extraneous heat losses. Five interwall spacings, S/D = 1.5, 2, 3, 6, and 10, were employed for each shroud height. The settings were established with the aid of feeler gages for the small spacings and a machinists scale for the larger spacings.

For all of the experiments, the cylinder was positioned midway between the shroud walls and at the midheight of the shroud. The minimum clearance between the channel inlet and the laboratory floor was about 75 cm.

Instrumentation, Ambient, and Procedure. In addition to the aforementioned thermocouples used for the heated cylinder and the shroud, the ambient temperature was measured by three shielded thermocouples affixed to the support frame and deployed vertically over a height equal to that of the shroud. Power was supplied to the heater core by a regulated a-c source. The current flow through the core was measured in terms of the voltage drop across a calibrated shunt, while the core voltage drop measurement was made between fine-gage tap wires attached to the respective ends of the heater wire.

All instrumentation was situated in a service area adjacent to the laboratory in which the experiments were performed. The laboratory possessed various features which made it ideal for natural convection experiments. It is situated in a basement, away from any exterior walls, and is literally a room within a room. The walls, ceiling, and floor are insulated with a 46-cm-thick layer of cork, while the door is a 15-cm-thick composite polystyrene slab. Neither vents, grilles, nor heating/cooling conduits pass through the walls. The volume of the room is approximately 70 m^3, and it contains various objects whose total heat capacity is large. The combination of thermal isolation and large heat capacity makes for excellent thermal stability and minimal stratification.

In executing the experiments, it was found convenient to fix the channel height, H/D, and to systematically vary the interwall spacing, S/D. At each interwall spacing, data were collected at five Rayleigh numbers in the range from 1.5 - 2 $\times$ 10^4 to 2 $\times$ 10^5, the variation being accomplished by varying the power input to the cylinder. For each data run, 6–8 hrs were allowed for the attainment of equilibrium prior to the collection of the data.

Data Reduction

The objectives of the data reduction were to evaluate the cylinder Nusselt and Rayleigh numbers from the experimental data. For the Nusselt number

$$\mathrm{Nu} = hD/k, \quad h = Q_c/A\,(T_w - T_\infty) \tag{1}$$

where Q_c is the rate of convective heat transfer at the cylinder, T_∞ and T_w are, respectively, the ambient temperature and the cylinder wall temperature, and A is the surface area of the cylinder. For T_∞, the readings of the three ambient thermocouples were averaged, the typical variation among them being on the order of 0.2 percent of $(T_w - T_\infty)$. With regard to T_w, the typical variations among the seven cylinder surface thermocouples were about 2½ percent (maximum to minimum) relative to $(T_w - T_\infty)$. The measured temperatures were fit with a quadratic polynomial in the axial coordinate along the cylinder, and the polynomial was integrated to yield the average value of T_w which was used as input to equation (1). The overall range of $(T_w - T_\infty)$ extended from 3.5 to 55°C.

The cylinder convection, Q_c, was evaluated from the electric power, P, with account being taken of radiation and conduction, Q_{rad} and Q_{cond}, respectively

$$Q_c = P - Q_{\mathrm{rad}} - Q_{\mathrm{cond}} \tag{2}$$

The conduction loss from the ends of the cylinder through the fiberglass insulation barrier was estimated and found to be negligible, so that $Q_{\mathrm{cond}} \simeq 0$ in equation (2).

For the evaluation of Q_{rad}, first suppose that the bounding walls of the flow channel are at a temperature equal to the ambient temperature, T_∞. For that case

$$Q_{\mathrm{rad}} = \epsilon\sigma A\,(T_w^4 - T_\infty^4) \tag{3}$$

With ϵ = 0.05 (highly polished aluminum), the values of Q_{rad} from equation (3) ranged from about 5½ to 7½ percent of the power input. The measured shroud surface temperatures were, indeed, very close to T_∞. Only in the case of the smallest interwall spacing (S/D = 1.5) for the Type III shrouds (insulating wall) was there a local hot spot where the shroud

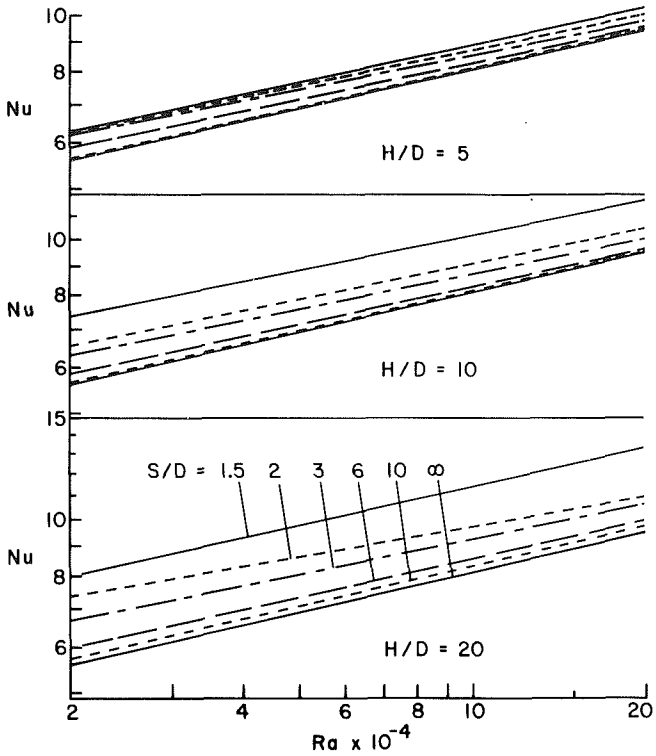

Fig. 2 Effect of interwall spacing on the cylinder Nusselt number for various fixed channel heights

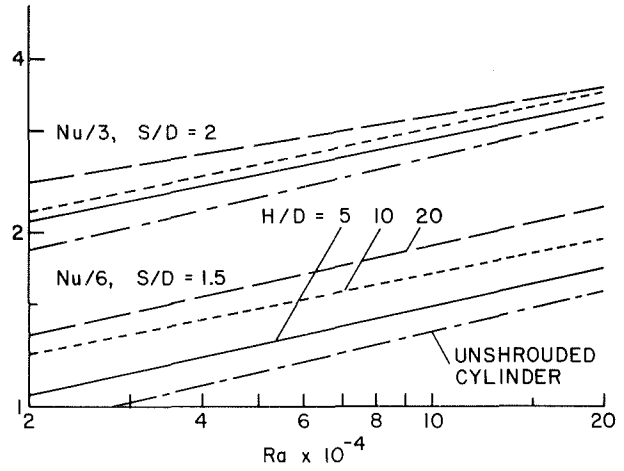

Fig. 3 Effect of channel height on the cylinder Nusselt number for fixed interwall spacings, S/D = 1.5 and 2

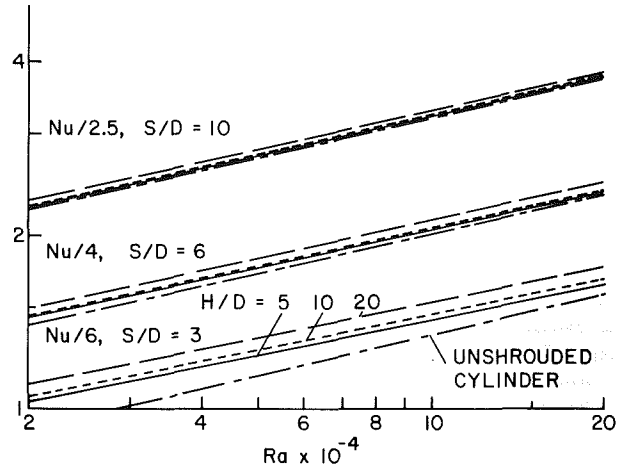

Fig. 4 Effect of channel height on the cylinder Nusselt number for fixed interwall spacings, S/D = 3, 6, and 10

temperature rise above ambient was about 15 percent of $(T_w - T_\infty)$. If an upper-bound estimate of the effect of this temperature rise is made, it is found that the aforementioned percentages for Q_{rad} are reduced by about 1 percent. Since this slight change in Q_{rad} is an overestimation and since there is virtually no change for almost all of the investigated cases, equation (3) was employed for the evaluation of Q_{rad}.

With h and Nu thus obtained, the Rayleigh number is next determined from

$$\mathrm{Ra} = [g\beta(T_w - T_\infty)D^3/\nu^2]\mathrm{Pr} \quad (4)$$

The thermophysical properties appearing in the Rayleigh and Nusselt numbers were evaluated at the film temperature $\frac{1}{2}(T_w + T_\infty)$, except for β which was evaluated as $1/T_\infty$.

Results and Discussion

As a prelude to the results for the shrouded cylinder, the case of the unshrouded cylinder will first be considered. The present data for the unshrouded cylinder spanned the range of Rayleigh number from 2×10^4 to 2×10^5 and are very well correlated by

$$\mathrm{Nu} = 0.605\mathrm{Ra}^{0.225} \quad (5)$$

with a data scatter of less than 1½ percent. With regard to literature comparisons, the finite difference solutions of [4] yielded a Nusselt number value at $\mathrm{Ra} = 10^5$ which agrees remarkably well with equation (5)—to better than 1 percent.

The most recent and encompassing literature correlations of experimental data for unshrouded horizontal cylinders are those of [1] and [5]. In the latter, a single algebraic equation is used to correlate Nusselt number data which span a Rayleigh number range of 10^{15}. Such a single-equation representation affords convenience but tends to sacrifice accuracy and, in particular, in the present Rayleigh number range falls below the data on which it is based. In contrast, [1] offers several correlation equations, each specific to a given Rayleigh number range. For the present range, [1] gives

$$\mathrm{Nu} = 0.480\mathrm{Ra}^{1/4} \quad (6)$$

from which equation (5) deviates by 2 to 7 percent—a level of agreement that is quite satisfactory.

Shrouded-Cylinder Nusselt Numbers. Attention is next turned to the Nusselt number results for the shrouded cylinder. As will be documented later, for a given channel configuration (i.e., given H/D and S/D), the various investigated thermal boundary conditions at the shroud walls had only a very slight effect on the Nusselt number. In view of this, the presentation will begin by highlighting those parameters which markedly affect the results—namely, H/D, S/D, and Ra, and Figs. 2–4 have been prepared for this purpose. To avoid crowding and overlap, the actual data points will be omitted from these figures. Rather, the data will be represented by least-squares lines of the form $\mathrm{Nu} = C\mathrm{Ra}^n$. All of the data will be presented in later figures where there is less crowding, and there the excellence of the least-squares representations and the absence of scatter will be evident.

In Fig. 2, the effect of variations of the interwall spacing, S/D, on the Nusselt number is shown for fixed channel heights, H/D, equal to 5, 10, and 20. The figure is subdivided into three graphs, with each graph corresponding to a fixed H/D. In each graph, the Nusselt number is plotted as a function of the Rayleigh number for parametric values of S/D ranging from a smallest value of 1.5 to a largest value (infinity) which corresponds to the unshrouded cylinder.

The most significant message of Fig. 2 is that the placement of a cylinder in a channel leads to enhanced heat transfer

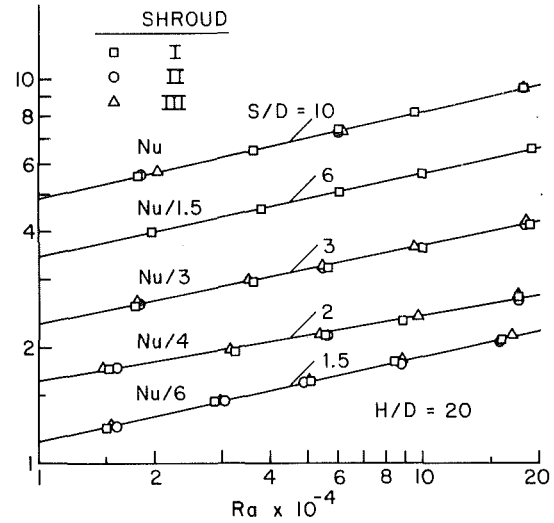

Fig. 5 Effect of shroud thermal characteristics on the cylinder Nusselt number, $H/D = 20$

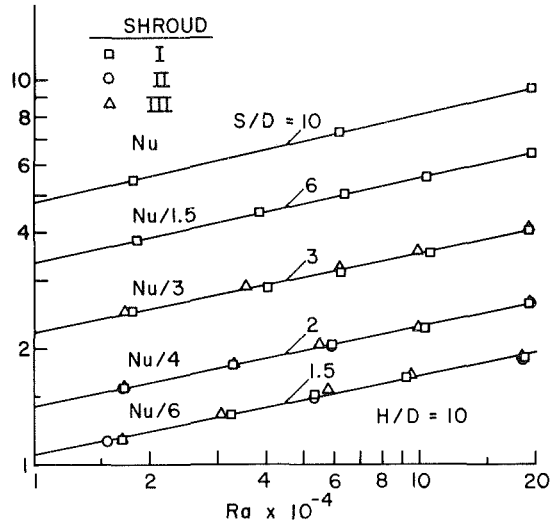

Fig. 6 Effect of shroud thermal characteristics on the cylinder Nusselt number, $H/D = 10$

compared with the unshrouded cylinder. Furthermore, the enhancement can be appreciable—as large as 40 percent for the conditions investigated here.

It is also evident from the figure that the enhancement is markedly affected by the interwall spacing, S/D. For the closest spacing, $S/D = 1.5$, the enhancement is about 40 percent when $H/D = 20$, while for this same H/D but with $S/D = 10$, the enhancement is only about 2 percent. This trend whereby the enhancement increases with decreasing S/D remains in force for all the investigated channel heights, but the extent of the enhancement diminishes markedly as the height decreases. Thus, for a height $H/D = 5$, the maximum measured enhancement is only 11 percent.

The aforementioned trend with S/D suggests that even greater enhancements might be attained at closer spacings, although the state of affairs corresponding to the blockage of the channel at $S/D = 1$ is uncertain. Experiments at spacings smaller than $S/D = 1.5$ were not attempted because departures of the shroud surfaces from perfect flatness would have begun to introduce uncertainties in the size of the shroud-cylinder gap.

Further examination of the figure provides information about the largest value of S/D at which enhancement occurs relative to the unshrouded cylinder. For all the shroud heights investigated, it appears that there is no significant enhancement for $S/D \geq 10$.

Figures 3 and 4 display the Nusselt number results from an alternative perspective, namely, the effect of varying the channel height at a given interwall spacing. The results for $S/D = 1.5$ and 2 are presented in Fig. 3, while those for $S/D = 3$, 6, and 10 are in Fig. 4. To accomplish the presentation of results for several S/D values in each figure, the Nusselt numbers for each S/D have been divided by a factor indicated in the respective figures.

It is seen from Figs. 3 and 4 that, at a fixed S/D, an increase of channel height increases the cylinder Nusselt number. The extent of the increase is highly sensitive to S/D. Thus, at $S/D = 1.5$, the enhancement ranges from 11 to 40 percent as H/D varies from 5 to 20. In contrast, at $S/D = 10$, the enhancement varies from 0 to 2 percent over the same range of H/D. Indeed, at large S/D, the effect of a shroud height increase is of little significance.

Figures 2–4, taken together, document the marked heat transfer enhancement attainable at small interwall spacings and with tall channel walls. This finding has immediate application to practice. For example, for a single unfinned baseboard heater, the required heat duty can be accomplished

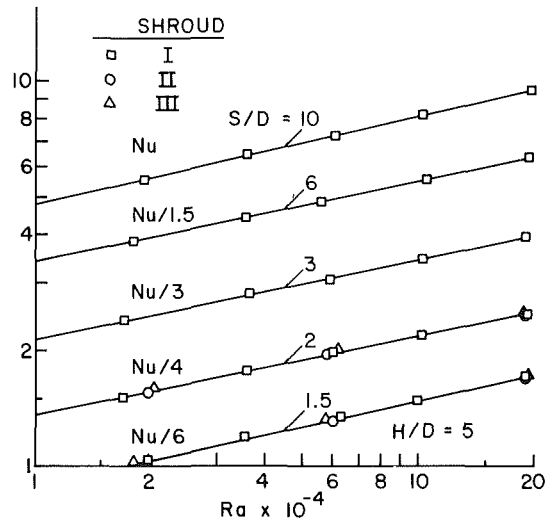

Fig. 7 Effect of shroud thermal characteristics on the cylinder Nusselt number, $H/D = 5$

with a cylinder wall temperature that is lower when vertical shrouds are employed. The advantage of the lower operating temperature is that transmission line losses are diminished. Alternatively, enhancement attained as a result of shrouding a cylinder would yield higher heat transfer rates for the same cylinder temperature.

The influence of the thermal characteristics of the different shroud types will now be examined, and Figs. 5–7 have been prepared for this purpose. Each figure corresponds to a fixed shroud height, respectively, $H/D = 20$, 10, and 5, and in each figure S/D appears as the curve parameter. To separate the results for the various S/D and thereby to avoid data point overlap, the Nusselt numbers for each S/D have been divided by a factor indicated in the respective figures.

The data for the various shroud types are identified by the symbols listed at the upper left of each figure. In addition, the least-squares curve fits (i.e., the straight lines) already shown in Figs. 2–4 are included here to enable the assessment of the fidelity with which they represent the data.

From an overview of Figs. 5–7, it is seen that the Nusselt numbers are remarkably insensitive to the thermal characteristics of the various shrouds. In general, the effect of the shroud type is in the 2 percent range. Even within this range,

Table 1 Values for C and n for the correlating equation, $Nu = CRa^n$

H/D	S/D	C	n
5	1.5	0.722	0.218
	2	0.836	0.204
	3	0.801	0.206
	6	0.734	0.211
	10	0.587	0.228
10	1.5	0.999	0.202
	2	0.853	0.206
	3	0.850	0.202
	6	0.668	0.219
	10	0.581	0.229
20	1.5	0.892	0.221
	2	1.348	0.171
	3	0.890	0.203
	6	0.682	0.219
	10	0.603	0.227

trends with respect to S/D and H/D can be identified. Specifically, the effect of shroud type diminishes with increasing interwall spacing and with decreasing channel height. In view of these characteristics, it was unnecessary to collect data for all three shroud types for all S/D. Thus, for a given channel height, starting with the smallest S/D and proceeding towards greater interwall spacings, note was taken of when the influence of the different shrouds became insignificant. Thereafter, at larger S/D, data were collected for only one of the shroud types.

The least-squares straight lines appearing in Figs. 5–7 are seen to be excellent representations of the data. Table 1 lists the coefficient, C, and exponent, n, of the correlation equation $Nu = CRa^n$ for each of the investigated geometries. With the correlation equation and with the tabulation, crossplots can be prepared to obtain Nusselt numbers at S/D and H/D values intermediate to those employed in the present experiments.

Comparisons of the present results with [2] and [3] will now be considered. As noted earlier, the Nusselt number results of [2] for air were confined to Rayleigh numbers that are much lower than those employed here. Higher Rayleigh number data were obtained in [2] for liquid Freon in a closed container, specifically at $Ra = 5 \times 10^4$ and 6×10^5, with the former falling in the present range. At that Rayleigh number, data were reported for a single shroud height $H/D = 64$, which is larger than the largest H/D investigated here. Furthermore, at that H/D, the data for the three employed S/D values displayed "considerable scatter," so that trends cannot be identified with certainty.

In [3], the Nusselt number is plotted as a function of S/D for parametric values of Ra, but H/D does not appear in the graph. At $Ra = 10^5$, the values of Nu from [3] are 8.6, 8.6, and 8.4, respectively for $S/D = 2$, 3, and 6. The insensitivity of these results to S/D is noteworthy but cannot be interpreted since no information is given about H/D. For comparison, the present Nu values corresponding to the aforementioned conditions and to $H/D = 20$ are 9.54, 9.20, and 8.55.

Shroud Surface Temperature Distributions. Measurements of the shroud surface temperature distribution were made for all of the cases for which heat transfer results have been presented in Figs. 2–7. However, owing to space limitations, only a representative sample of the temperature distributions can be included here, and Figs. 8–10 have been prepared for this purpose. All of these figures correspond to the intermediate height channel, $H/D = 10$, and the successive figures convey results for the Types I, II, and III shrouds. The reported temperature measurements were made with thermocouples in contact with the face of the shroud which bounded the airflow.

Each figure consists of two graphs, with that at the left being for low Rayleigh numbers (17,500–18,000) and that at the right for high Rayleigh numbers (~188,000). In each graph, the dimensionless shroud temperature distribution $(T_s - T_\infty)/(T_w - T_\infty)$ is plotted against the dimensionless vertical coordinate, Z/H, where Z measures distances upward from the bottom of the shroud wall. The quantity, T_s, denotes the local shroud temperature, while T_w and T_∞ are, respectively, the cylinder and ambient temperatures.

From an overview of the figures, it is seen that while the shapes of the temperature distributions are affected by the thermal characteristics of the specific shroud type, the shroud temperature rise (relative to ambient) is small compared with $(T_w - T_\infty)$. Indeed, aside from the closest interwall spacing $S/D = 1.5$, $(T_s - T_\infty)/(T_w - T_\infty) < 0.05$. For the $S/D = 1.5$ case, the largest value of $(T_s - T_\infty)/(T_w - T_\infty)$ is 0.151, and this occurs for the Type III shroud; appreciably lower values prevail for the other shroud types.

The temperature distributions for the Type III shroud (i.e., insulation wall) are the most nonuniform among those investigated, which is to be expected since this shroud type is not very effective as a diffuser of heat. Another interesting feature of these temperature distributions is the occurrence of a maximum at a location in the upper portion of the shroud surface. The fact that the maximum does not occur abreast of the cylinder (i.e., at $Z/H = 0.5$) indicates that it is not the result of radiation from the cylinder to the shroud surface. Rather, the maximum is believed due to the convective heating of the shroud by air which had previously passed over the cylinder. The dropoff of the temperature beyond the maximum may be attributed to a wall-adjacent *downflow* of fluid drawn from the ambient into the top of the channel. This downflow was encountered in the numerical solutions of [3].

Both the Types I and II shrouds are faced with an aluminum plate, and as a consequence, their surface temperature distributions are quite uniform. It is also evident that the level of the temperature is somewhat lower for the Type II shroud than for the Type I shroud. The lower temperatures are due to the heat losses from the uninsulated rear surface of the Type II shrouds.

The temperature distributions of Figs. 8–10 help to explain certain features of the Nusselt number results of Figs. 5–7. Very careful inspection of the latter figures indicates that within the very slight spread of the data for the three shrouds, the Nusselt numbers are arranged in the order III, I, II (highest to lowest). The temperature distributions of Figs. 8–10 are also arranged in the same order. The higher shroud temperatures induce additional buoyancy over and above that induced by the heated cylinder, giving rise to a greater throughflow and a higher Nusselt number.

The temperature distributions also show why the Nusselt numbers for the larger interwall spacings are uninfluenced by the thermal characteristics of the shrouds. For those spacings, the shroud temperatures are so close to ambient that the aforementioned supplementary buoyancy is virtually nonexistent, as are the backside heat losses.

Concluding Remarks

The research described here constitutes a results-oriented study of the effect of vertical shrouding surfaces on the heat transfer characteristics of a heated horizontal cylinder in air. Fifteen different channel configurations were investigated, encompassing heights ranging from 5 to 15 times the cylinder diameter and interwall spacings which ranged from 1.5 to 10 diameters. For each channel configuration, the cylinder Rayleigh number extended over the order of magnitude range from 1.5×10^4 to 2×10^5.

Three types of shroud walls having different thermal characteristics were employed during the course of the experiments. In one case, the wall consisted of an aluminum plate heavily insulated at the rear, while in the second case the

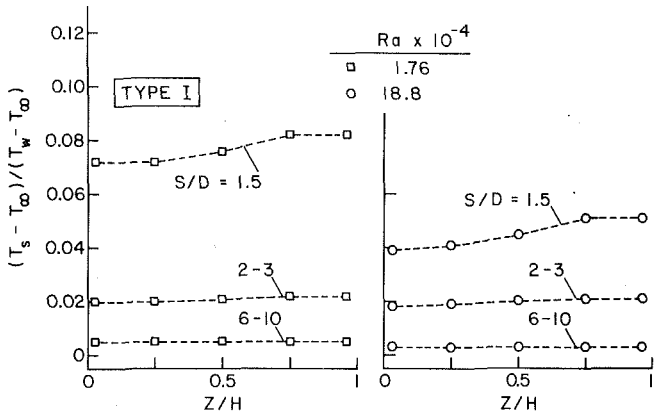

Fig. 8 Shroud surface temperature distributions, Type I shroud (conducting plate backed by thick insulation layer), $H/D = 10$

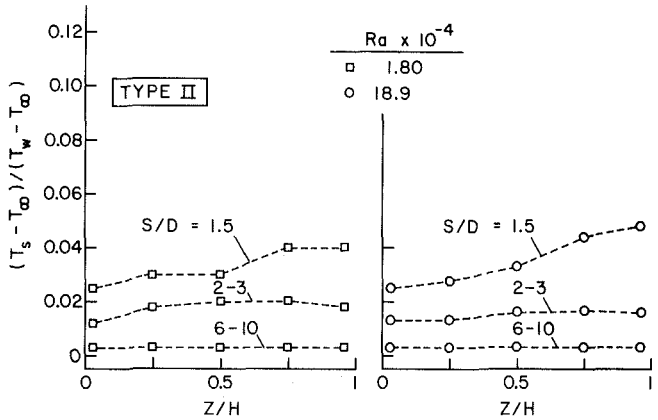

Fig. 9 Shroud surface temperature distributions, Type II shroud (conducting plate without backing insulation), $H/D = 10$

plate was uninsulated. The third type of shroud was a thick layer of insulation. All three types of shrouds were faced with a thin, high emissivity film. Experiments were also carried out for an unshrouded cylinder. The main finding of this investigation is that a cylinder situated in a vertical channel experiences enhanced heat transfer compared with an unshrouded cylinder. Enhancements of up to 40 percent were encountered for the investigated conditions. At a fixed channel height, the enhancement is increased as the interwall spacing decreases. Similarly, at a given interwall spacing, greater enhancements occur for taller channels. For interwall spacings of 10 diameters or more, there is no enhancement.

The Nusselt number results were found to be insensitive to

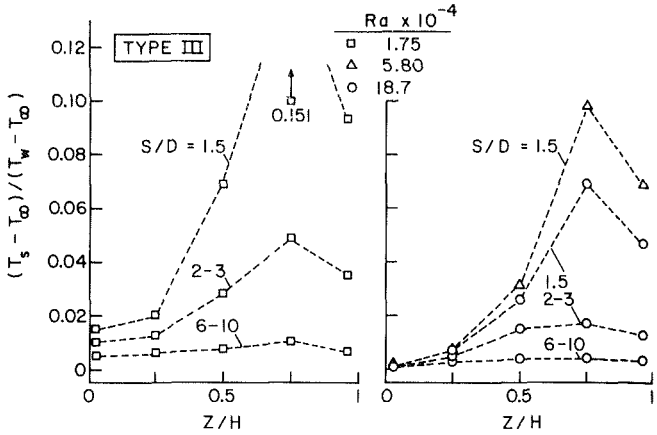

Fig. 10 Shroud surface temperature distributions, Type III shroud (thick insulating layer), $H/D = 10$

the investigated shroud thermal characteristics. The greatest effect of the different shrouds on the cylinder Nusselt number was about ±2 percent, and this occurred at the smallest interwall spacing and the largest channel height.

Temperature distributions along the height of the shroud wall were also measured. In general, the temperature rise of the shroud wall relative to ambient was very small compared to the temperature rise of the heated cylinder. The highest temperatures were attained for the insulating wall, which also exhibited the greatest spatial temperature nonuniformities. The other two shroud types displayed relatively uniform temperatures, in keeping with the high conductivity of the aluminum face plate.

The research would have been enhanced by interferometric visualizations and by velocity field measurements. These complementary experiments could not be performed because the requisite equipment was not available.

References

1 Morgan, V. T., "The Overall Convective Heat Transfer From Smooth Circular Cylinders," *Advances in Heat Transfer*, Vol. 11, Academic Press, New York, 1975, pp. 199–264.

2 Marsters, G. F., "Natural Convective Heat Transfer From a Horizontal Cylinder in the Presence of Nearby Walls," *Canadian Journal of Chemical Engineering*, Vol. 53, 1975, pp. 144–149.

3 Farouk, B., and Guceri, S. I., "Natural and Mixed Convection Heat Transfer Around a Horizontal Cylinder Within Confining Walls," *Numerical Heat Transfer*, Vol. 5, 1982, pp. 329–341.

4 Kuehn, T. H., and Goldstein, R. J., "Numerical Solution to the Navier-Stokes Equations for Laminar Convection About a Horizontal Isothermal Circular Cylinder," *International Journal of Heat and Mass Transfer*, Vol. 23, 1980, pp. 971–980.

5 Churchill, S. W., and Chu, H. H. S., "Correlating Equations for Laminar and Turbulent Free Convection From a Horizontal Cylinder," *International Journal of Heat and Mass Transfer*, Vol. 18, 1975, pp. 1049–1053.

Conductivity Models of Electrothermal Convection in a Plane Layer of Dielectric Liquid

P. J. Martin[1]

A. T. Richardson

Department of Engineering Mathematics, University of Bristol, BS8 1TR, England

Experiments have demonstrated that a d-c voltage applied across a thermally stabilized plane layer of dielectric liquid can induce both stationary and oscillatory instabilities and thereby significantly augment heat transfer. While a unipolar charge injection model can explain both types of instability, the predictions of a conductivity model depend crucially upon the way the electrical conductivity varies with temperature. Here a conductivity model is derived from a dissociation and recombination model in an Ohmic limit, and its linear instabilities for linear, quadratic, and Arrhenius-type conductivity variations are investigated numerically. Oscillatory instability is usually predicted and an energy argument rules out stationary instability for the type of conductivity variation observed experimentally. This casts doubts on the experimental relevance of earlier quadratic conductivity models predicting stationary instability. The relative merits of conductivity and charge injection models are discussed in the light of empirical evidence.

Introduction

Heat transfer across a dielectric liquid can be increased at least tenfold by the application of an electric field [1, 2]. The simplest configuration showing such electrohydrodynamic destabilization of a liquid heated from above consists of a horizontal layer of liquid between plane parallel electrodes at different but fixed temperatures and electric potentials. Using this geometry, Gross and Porter [3] applied a stabilizing temperature difference of 12°C to a 1-mm layer of transformer oil and observed convective (time-independent) liquid motion at a critical voltage of 180 V. On the other hand Turnbull [4] applied stabilizing temperature differences of 5, 10, 15, and 20°C to 0.0254-m (1-in) and 0.0508-m (2-in.) layers of corn and castor oil and observed oscillatory (time-periodic) motions with periods of about 14 to 40 s at critical voltages ranging from 5 to 17 kV.

The dominant destabilizing force in these d-c experiments is Coulombic, resulting from the interaction of the electric field with free space-charge originating either from injection at one or both electrodes or from the dissociation of impurities in the interior of the liquid. Theoretical models of this instability thus fall into two categories. The simplest *mobility models* consider autonomous unipolar injection of charge into a perfectly insulating liquid and, for suitable choices of the space-charge density on the injecting electrode and its mobility as a linear function of temperature, can predict both convective and oscillatory instabilities [5–7]. On the other hand, *conductivity models* ignore charge injection and implicity assume that the dissociation and recombination of impurities in the liquid result in an Ohmic but temperature-dependent electrical conductivity. The distribution of net space-charge is then regarded as resulting from the thermally induced gradients in conductivity. In addition, it is usual practice, in order to simplify the governing equations, to consider a weak linear or quadratic conductivity variation and make a pseudo-Boussinesq approximation. Roberts [8] considered a linear variation and found no convective instability when the liquid was heated from above. On the other hand, Takashima and Aldridge [9] extended this investigation to include quadratic terms and demonstrated that convective instability was possible if the conductivity variation was sufficiently nonlinear. They claimed an order of magnitude agreement with the Gross and Porter experiment. Bradley [10] looked for oscillatory instability with a linear conductivity variation and his results, if extended, are order of magnitude compatible with Turnbull's observations [4]. However, he assumed a zero charge relaxation time and used a simple trial function satisfying boundary conditions appropriate to free surfaces with no tangential force acting. Turnbull [11], using a quadratic variation, also obtained an order of magnitude agreement with his own experimental results but assumed an infinite Prandtl number and sought a plane-wave solution satisfying none of the boundary conditions.

In this paper, we show that a conductivity model does not predict convective instability for the type of conductivity variation observed experimentally, and thus does not explain Gross and Porter's observations. In the case of oscillatory instability, we solve the linear instability equations numerically without making the pseudo-Boussinesq, zero-charge relaxation time and infinite Prandtl number approximations and investigate the consequences of assuming linear, quadratic, and Arrhenius-type conductivity variations with temperature. We begin by deriving the temperature-dependent conductivity model as an Ohmic limit of a dissociation and recombination model.

Derivation of the Ohmic Conductivity Model

If conduction results from the dissociation of a single uncharged impurity in an incompressible liquid, the equations for conservation of positive and negative charge, on neglecting diffusion, are

$$\frac{\partial P}{\partial t} + \mathbf{u} \cdot \text{grad } P = -\text{div}(PK_+ \mathbf{E}) + K_D c - K_R NP \quad (1)$$

and

$$\frac{\partial N}{\partial t} + \mathbf{u} \cdot \text{grad } N = \text{div}(NK_- \mathbf{E}) + K_D c - K_R NP \quad (2)$$

where P and N are the number densities of positive and negative ions of mobility K_+ and K_-, respectively, $\mathbf{u}$ is liquid velocity, $\mathbf{E}$ is the electric field, K_D and K_R are the dissociation

[1] Now at Logica, Cobham, Surrey, England

Contributed by the Heat Transfer Division and presented at the ASME Winter Annual Meeting, Phoenix, Arizona, November 14–19, 1982. Manuscript received by the Heat Transfer Division December 9, 1982. Paper No. 82-WA/HT-21.

and recombination coefficients, and c is the density of the uncharged dissociable species.

Introducing a net space-charge density $Q=e(P-N)$, where e is the charge on a single ion, and an effective conductivity $\sigma=e(PK_+ + NK_-)$, equations (1) and (2) imply a net space-charge conservation law

$$\frac{\partial Q}{\partial t} + \mathbf{u}\cdot \text{grad } Q = -\text{div}(\sigma \mathbf{E}) \tag{3}$$

The conductivity is usually assumed to be a known function of temperature alone. However using the fact that

$$P = \frac{\sigma + K_- Q}{e(K_+ + K_-)} \tag{4}$$

it is possible from equation (1) to obtain an equation governing, σ, to complement equation (3). Since $Q \simeq \epsilon \Phi_0 / d^2$, where ϵ is the electrical permittivity of the liquid, d the electrode spacing, and Φ_0 the electrical potential on the cooler electrode (the warmer one being earthed), the nondimensional ratio of the two terms in the numerator of equation (4) gives

$$\frac{\sigma}{K_- Q} \simeq \frac{\sigma_0 d^2}{\epsilon K_0 \Phi_0} = C_0 \tag{5}$$

with σ_0 and K_0 being reference values on the cooler-electrode. The parameter, C_0, is the ratio of the ion transit time to charge relaxation time and in a more general context is the ratio of a typical conduction current to one arising from a charge injection mechanism. Thus it plays a crucial role in characterizing the nature of the dominant mechanism of charge transfer in any given physical configuration. A large value of C_0 would therefore suggest that an Ohmic conduction current $\simeq(\sigma_0 \Phi_0)$ resulting from a dissociation and recombination mechanism was more likely to be in evidence than one ($\simeq \epsilon K_0 \Phi_0^2 / d^3$) arising from injection at the electrode-liquid interfaces. It is not difficult to show that, in the Ohmic limit $C_0 \to \infty$, equation (1) reduces to

$$\left(\frac{\partial}{\partial t} + \mathbf{u}\cdot\text{grad}\right)\left[\frac{\sigma}{e(K_+ + K_-)}\right]$$

$$= K_D c - K_R \left[\frac{\sigma}{e(K_+ + K_-)}\right]^2 \tag{6}$$

Equation (3) and (6) for Q and σ then effectively replace equation (1) and (2) for P and N. Now a solution of equation (6) requires a detailed knowledge of the variations of K_+, K_-, K_D, and K_R with temperature and furthermore depends on the liquid velocity so that in general thermofluiddynamic field and constitutive equations must be included in the analysis. However, there is a steady hydrostatic solution to (6) for which

$$\sigma = \sigma(T) = e(K_+ + K_-)\sqrt{\frac{K_D c}{K_R}} \tag{7}$$

This is just the conductivity dependence on temperature, T, that would be determined in a series of hydrostatic isothermal conductivity measurements at different temperatures. In the absence of an electric field the fluid is neutrally charged and the density of both positive and negative ions is $\sqrt{K_D c / K_R}$. If we suppose that this quantity is independent of temperature then expression (7) for σ satisfies equation (6) exactly even in the time-dependent hydrodynamic case. The conductivity then depends on temperature only through the mobility of the positive and negative ions, a conjecture that is supported by the conductivity and mobility measurements in transformer oil, with various artificial impurities, made by Yasufuku et al. [12]. Provided then that C_0 is sufficiently large and $K_D c / K_R$ is constant, an Ohmic conductivity depending solely upon temperature can be assumed in the derivation of the linear instability equations of a dissociation and recombination model.

The Linear Instability Problem

Electrohydrodynamically induced motion in a thermally stabilized plane layer of dielectric liquid is governed by a reduced set of Maxwell's electrical equations and those expressing mass conservation and the linear momentum and energy balances. Assuming that the dissociation of a single

Nomenclature

A = dimensionless quadratic conductivity parameter
B = dimensionless quadratic conductivity parameter
c = concentration of dissociable impurity
C_0 = ratio of ion transit time to charge relaxation time
d = electrode spacing
D = dimensionless derivative with respect to z
e = charge on one positive ion
$\mathbf{E}$ = electric field
F = z-dependence of dimensionless electrical potential perturbation
$\mathbf{g}$ = gravitational acceleration
k = dimensionless horizontal wavenumber
$\tilde{K}$ = ratio of charge relaxation time to thermal decay time
K_+ = mobility of positive ions
K_- = mobility of negative ions
K_D = ion dissociation coefficient
K_R = ion recombination coefficient
M = dimensionless voltage parameter
M_t = dimensionless voltage parameter for $A << 1$
N = number density of negative ions
p = pressure
P = number density of positive ions
Pr = Prandtl number
Q = net space-charge density
R = Rayleigh number
s = dimensionless complex growth rate
t = time
T = temperature
$\mathbf{u}$ = liquid velocity
V = z-dependence of z-component of dimensionless liquid velocity
x,y,z = rectangular Cartesian coordinates
α = liquid thermal expansion coefficient
γ = dimensionless absolute temperature of cooler electrode
ϵ = liquid electrical permittivity
ϵ_f = free-space electrical permittivity
θ = z-dependence of dimensionless temperature perturbation
κ = thermal diffusivity
λ = dimensionless activation energy for Arrhenius-type conductivity
ν = kinematic viscosity
ρ = liquid density
σ = liquid electrical conductivity
Φ = electrical potential
ω = dimensionless angular oscillation frequency

Subscripts

0 = value of cooler electrode
1 = value on warmer electrode
c = critical value for linear instability
e = hydrostatic equilibrium solution
p = perturbation to hydrostatic equilibrium solution
x,y,z = vector component in the (x,y,z)-direction

uncharged impurity and associated recombination results in a weak Ohmic temperature-dependent conductivity the resulting currents are small and consequently the magnetic effects may be neglected. The liquid may be assumed to be an incompressible linear isotropic dielectric with constant permittivity, viscosity, and thermal conductivity. On making the Boussinesq approximation so that liquid density ρ is constant except in the buoyancy term, the governing equations reduce to

$$\mathbf{E} = -\text{grad}\Phi; \left(\frac{\partial}{\partial t} + \mathbf{u}\cdot\text{grad}\right) Q = -\text{div}(\sigma\mathbf{E});$$
$$\epsilon \text{ div } \mathbf{E} = Q; \text{ div } \mathbf{u} = 0;$$
$$\rho_0 \left(\frac{\partial}{\partial t} + \mathbf{u}\cdot\text{grad}\right)\mathbf{u} = -\text{grad}p + \rho_0 \nu \nabla^2 \mathbf{u} + \rho_0[1 - \alpha(T - T_0)]\mathbf{g} + Q\mathbf{E};$$
$$\left(\frac{\partial}{\partial t} + \mathbf{u}\cdot\text{grad}\right) T = \kappa \nabla^2 T \tag{8}$$

and are subject to boundary conditions

$$\left.\begin{array}{l} \mathbf{u} = 0; T = T_0; \Phi = \Phi_0 \text{ on the cooler boundary} \\ \text{and} \\ \mathbf{u} = 0; T = T_1; \Phi = 0 \text{ on the warmer boundary} \end{array}\right\} \tag{9}$$

Here Φ is the electrical potential, p the pressure, ν the kinematic viscosity, and $\mathbf{g}$ the gravitational acceleration. Subscripts '0' and '1' indicate values on the cooler and warmer electrodes, respectively.

After scaling length, time, liquid velocity, temperature, electric field and space-charge by factors d, d^2/ν, κ/d, $T_1 - T_0$, Φ_0/d and $\epsilon\Phi_0/d^2$, respectively, and remaining temperature-dependent variables with respect to their values on the cooler electrode corresponding to the plane $z = 0$, the one-dimensional steady electrodynamic hydrostatic equilibrium may be written, referred to rectangular Cartesian axes, as

$$T_e = \frac{T_0}{T_1 - T_0} + z; \mathbf{E}_e = \left(0, 0, \frac{E_0}{\sigma_e}\right); Q_e = \frac{d}{dz}\left(\frac{E_0}{\sigma_e}\right) \tag{10}$$

Since the equilibrium conductivity, σ_e, usually increases with temperature (and here therefore with z) and since the dimensionless constant E_0 is without loss of generality positive, the nondimensional net space-charge density, Q_e, is negative. Of course equations (10) embody two distinct physical cases depending upon the sign of Φ_0, i.e., the net space-charge is negative (positive) if the potential of the cooler electrode is positive (negative).

On linearly perturbing the equilibrium (10) and Fourier decomposing the z-component of velocity, temperature, and potential perturbations so that

$$[u_z(x,y,z,t), T_p(x,y,z,t), \Phi_p(x,y,z,t)] = [V(z), \theta(z), F(z)] \exp[i(k_x x + k_y y) + st] \tag{11}$$

it is straightforward to show that the dimensionless linear instability equations become, on writing the square of the modulus of the two-dimensional wave number (k_x, k_y) as $k^2 = k_x^2 + k_y^2$ and $D = d/dz$

$$(D^2 - k^2 - \text{Pr}s)\theta = V,$$
$$(D^2 - k^2)(D^2 - k^2 - s)V + k^2 R\theta = k^2 M[(D^2 E_e)F - E_e(D^2 - k^2)F]$$

and

$$\bar{K}(D^2 E_e)V = (\text{Pr}\bar{K}s + \sigma_e)(D^2 - k^2)F + (D\sigma_e)DF - D[E_e(D\sigma_e)\theta] \tag{12}$$

where

$$\text{Pr} = \frac{\nu}{\kappa}, \quad \bar{K} = \frac{\epsilon\kappa}{d^2\sigma_0},$$
$$M = \frac{\epsilon\Phi_0^2}{\rho_0\nu\kappa}, \quad R = \frac{\alpha(T_1 - T_0)gd^3}{\nu\kappa} \tag{13}$$

These are subject to the no-slip, fixed temperature and fixed potential boundary conditions which together with mass conservation imply that

$$V = DV = \theta = F = 0 \text{ at } z = 0,1 \tag{14}$$

The Prandtl number, Pr, is the ratio of a thermal decay time to a viscous decay time, $\bar{K}$ is the ratio of a charge relaxation time to a thermal decay time, and Rayleigh number, R, and voltage parameter, M, are the ratios of a buoyancy and Coulombic driving pressure, respectively, to a viscous pressure drop for a liquid speed κ/d. On fixing five of the six dimensionless parameters k, s, Pr, R, M and $\bar{K}$, equations (12) together with boundary conditions (14) then constitute an eighth-order eigenvalue problem for the remaining one. Before solving this numerically, we must consider how best to model the variation of electrical conductivity with temperature.

The Temperature Dependence of Electrical Conductivity

Previous theoretical studies of conductivity models have assumed a variation with temperature of the form

$$\sigma_e(z) = 1 + Az(1 + Bz) \tag{15}$$

where constant parameters A ($\simeq$0.1-2) and B($\simeq$0-1) are suitably chosen to make a physically reasonable approximation. In particular, most analyses assume that $A << 1$. This permits a pseudo-Boussinesq approximation to the linear instability equations which, on taking σ_e, E_e and their derivatives to leading order in A, reduce to

$$(1 + \text{Pr}\bar{K}s)(D^2 - k^2)(D^2 - k^2 - s)(D^2 - k^2 - \text{Pr}s)\theta - 2\bar{K}M_t B K^2 (D^2 - k^2 - \text{Pr}s)\theta + M_t(1 + 2Bz)k^2 D\theta + [R(1 + \text{Pr}\bar{K}s) + 2M_t B]k^2\theta = 0 \tag{16}$$

subject to the boundary conditions

$$\theta = D^2\theta = D(D^2 - k^2 - \text{Pr}s)\theta = 0 \tag{17}$$

where $M_t = ME_0^2 A$. This is the eigenvalue problem studied by Roberts ($s = B = 0$) [8], Takashima and Aldridge ($s = 0$, $B \neq 0$) [9] and Bradley ($s \neq 0$, $B = 0$) [10]. However, numerical solution of the exact problem (12) and (14) with conductivity given by equation (15) with a value of $A = 0.1$ (cf [9]), shows sufficient deviation from that of the problem (16) and (17) to cast doubt on the applicability of the pseudo-Boussinesq approximation to the reported experiments.

A quadratic variation of conductivity has the disadvantage of requiring the choice of two parameters, A and B, whilst a linear variation requires only a single choice for A but adequately models conductivity only over a small temperature range. On the other hand, experimental measurements of conductivity as a function of temperature [4, 12] suggest an Arrhenius-type behavior

$$\sigma_e(z) = \exp\left(\frac{\lambda}{\gamma} - \frac{\lambda}{z + \gamma}\right) \tag{18}$$

where λ ($\simeq$ 100-1000) is a dimensionless activation energy and $\gamma = (T_0 + 273)/(T_1 - T_0)$ ($\simeq$ 15-60) is fixed by the temperature boundary conditions. Such a dependence can also be inferred from equation (7) if the charge carrier mobilities have the same Arrhenius-type temperature variation.

An inviscid energy argument that assumes a small space-charge density and considers the exchange of two liquid

Table 1 Experimental data

	Transformer oil	Corn oil	Castor oil
ρ_0 (kg/m^3)	865.6	917	960.3
α (°C^{-1})	7.29×10^{-4}	6.6×10^{-4}	7.2×10^{-4}
ν (m^2/s)	4.224×10^{-5}	5.45×10^{-5}	10^{-3}
κ (m^2/s)	8.42×10^{-8}	1.2×10^{-7}	9×10^{-8}
ϵ/ϵ_f	2.2	3.1	4.67
T_0 (°C)	20	25	20
$\sigma(T_0)$ (S/m)	1.1×10^{-9}	1.4×10^{-10}	9×10^{-11}

Table 2 Comparison of experimental and theoretical critical values for the preferred mode of linear instability in transformer oil ($d = 0.001$m, Pr = 460, $\bar{K} = 0.001$). B denotes predictions by Bradley's method, and L, Q, and A predictions using Chebyshev collocation for linear, quadratic, and Arrhenius-type conductivities, respectively. E denotes experimental results.

$T_1 - T_0$ (°C)	$\sigma(T_1)$ (S/m)	R		M_c	k_c	ω_c
12	1.338×10^{-9}	−20	B	9.26×10^4	3.019	1.422
			L	5.63×10^4	4.994	0.582
			Q	5.33×10^4	4.918	0.549
			A	5.48×10^4	4.921	0.550
			E	205	-	0

Table 3 Critical values for the preferred mode of linear instability in corn oil ($d = 0.0254$m, Pr = 460, $\bar{K} = 4 \times 10^{-5}$)

$T_1 - T_0$ (°C)	$\sigma(T_1)$ (S/m)	R		M_c	k_c	ω_c
5	1.85×10^{-10}	-8.1×10^4	B	3.47×10^5	3.403	9.01
			L	4.10×10^5	6.925	6.86
			Q	3.78×10^5	6.694	6.36
			A	3.80×10^5	6.691	6.37
			E	1.14×10^5	-	2.98
10	2.40×10^{-10}	-1.6×10^5	A	2.58×10^5	7.652	8.22
			E	1.38×10^5	-	3.72
15	3.15×10^{-10}	-2.4×10^5	A	1.89×10^5	9.442	9.04
			E	1.14×10^5	-	4.09
20	4.80×10^{-10}	-3.2×10^5	A	1.21×10^5	11.25	9.02
			E	9.27×10^4	-	5.21

parcels provides a necessary condition $\mathbf{E}_e$ grad $Q_e < 0$ for convective instability. For linear, Arrhenius-type and reported experimental conductivity variations [4, 12], it is found that $\mathbf{E}_e \cdot \text{grad } Q_e \propto D^2(1/\sigma_e) > 0$ so that convective instability is ruled out. For a quadratic variation with $B > A$, on the other hand, $D^2(1/\sigma_e) < 0$ near the cooler electrode and convective instability is possible although it may still not be the preferred mode.

The conjecture that a realistic conductivity variation will not induce convective instability and the possibility of preferred oscillatory instability were investigated numerically using the full equations (12) and boundary conditions (14) for linear, quadratic, and Arrhenius-type variations with parameters (13) chosen to represent the Gross and Porter [3] and Turnbull [4] experiments.

Numerical Analysis

For a convective instability in the marginal state $s = 0$, Pr does not appear, and on fixing k, $\bar{K}$, and R, equations (12) and boundary conditions (14) constitute an eigenvalue problem for M. This was solved numerically using a Chebyshev collocation method expanding each unknown function in terms of Chebyshev polynomials of degree at most 25 in order to convert the problem to one of a matrix eigenvalue type. The smallest positive voltage parameter, M, was then minimized with respect to variations of wave number, k, using a quadratic fit to find the critical value $M_c = M(k_c)$. More generally, in order to seek oscillatory instability, parameters k, M, Pr, $\bar{K}$, and R were fixed, leaving an eigenvalue problem for the complex growth rate, s. By fitting a surface to the real part of the growth rate of the fastest growing mode as a function of k and M, the critical point (k_c, M_c) was found at which M had a minimum value with respect to k-variations subject to $\text{Re}(s) = 0$. If it was found that $\text{Im}(s) = \omega = 0$, then the most unstable mode was convective and coincided with the predictions of the convective instability method described above.

These numerical methods were applied to each of the eigenvalue problems, corresponding to the Gross and Porter [3] and Turnbull [4] experiments, using linear, quadratic, and Arrhenius-type conductivities fitted through the values of conductivity on the bounding electrodes using the data presented in Tables 1-6. From the family of possible quadratic curves the one that matched the Arrhenius-type conductivity at a temperature $(T_0 + T_1)/2$ was chosen. The numerical results were then compared with the experimental results and with predictions obtained by an extension of Bradley's method [10] to a stabilizing temperature distribution ($R < 0$) and are presented in Tables 2-6.

For transformer oil ($d = 0.001$ m; $T_1 - T_0 = 12$°C) oscillatory modes were predicted at a critical voltage about twenty times larger than that at which Gross and Porter observed convective instability (cf. Table 2). By taking a lower value of conductivity, e.g., $\sigma(T_0) \simeq 1.1 \times 10^{-11}$ S/m and thus a higher value of $\bar{K}$ ($\simeq 0.1$), it was possible to find convective instability, but only for a sufficiently strong quadratic variation of conductivity (e.g., $A = 0.11$ and $B = 1$). Such a variation is, however, not of the type usually observed. This would suggest, therefore, that another instability mechanism,

Table 4 Critical values for the preferred mode of linear instability in corn oil ($d = 0.0508$m, $\mathrm{Pr} = 460$, $\bar{K} = 9 \times 10^{-6}$)

$T_1 - T_0$ (°C)	$\sigma(T_1)$ S/m)	R		M_c	k_c	ω_c
5	1.85×10^{-10}	-6.5×10^5	B	9.95×10^5	3.513	25.6
			L	1.50×10^6	6.534	25.0
			Q	1.44×10^6	6.432	24.0
			A	1.45×10^6	6.430	24.0
			E	5.45×10^5	-	-
10	2.40×10^{-10}	-1.3×10^6	A	1.05×10^6	6.859	33.2
			E	4.58×10^5	-	11.9
15	3.15×10^{-10}	-2.0×10^6	A	8.27×10^5	8.352	39.7
			E	4.13×10^5	-	14.9
20	4.80×10^{-10}	-2.6×10^6	A	5.24×10^5	16.30	34.6
			E	3.71×10^5	-	13.4

Table 5 Critical values for the preferred mode of linear instability in castor oil ($d = 0.0254$m, $\mathrm{Pr} = 10^4$, $\bar{K} = 6 \times 10^{-5}$)

$T_1 - T_0$ (°C)	$\sigma(T_1)$ (S/m)	R		M_c	k_c	ω_c
5	1.2×10^{-10}	-6.4×10^3	B	5.04×10^5	3.240	0.613
			L	1.79×10^5	5.627	0.140
			Q	1.43×10^5	5.120	0.109
			A	1.43×10^5	5.116	0.109
			E	5.79×10^4	-	0.101
10	1.5×10^{-10}	-1.3×10^4	A	8.26×10^4	5.239	0.115
			E	3.46×10^4	-	0.162
15	2.0×10^{-10}	-1.9×10^4	A	5.14×10^4	5.263	0.113
			E	3.06×10^4	-	0.182
20	2.5×10^{-10}	-2.6×10^4	A	3.98×10^4	5.466	0.117
			E	2.34×10^4	-	0.223

Table 6 Critical values for the preferred mode of linear instability in castor oil ($d = 0.0508$m, $\mathrm{Pr} = 10^4$, $\bar{K} = 2 \times 10^{-5}$)

$T_1 - T_0$ (°C)	$\sigma(T_1)$ (S/m)	R		M_c	k_c	ω_c
5	1.2×10^{-10}	-5.1×10^4	B	1.24×10^6	3.381	1.541
			L	5.51×10^5	7.527	0.439
			Q	4.69×10^5	6.944	0.378
			A	4.68×10^5	6.937	0.378
			E	-	-	-
10	1.5×10^{-10}	-1.0×10^5	A	3.15×10^5	7.946	0.456
			E	1.38×10^5	-	0.405
15	2.0×10^{-10}	-1.5×10^5	A	2.14×10^5	9.142	0.478
			E	1.22×10^5	-	0.405
20	2.5×10^{-10}	-2.1×10^5	A	1.71×10^5	10.40	0.500
			E	1.08×10^5	-	0.486

perhaps charge injection, was dominant in their experiment, a possibility supported by their observation of a slightly different behavior on reversing the polarity of the d-c voltage and of no instability with an a-c applied potential at 50 Hz.

For the Turnbull corn oil and castor oil experiments ($d = 0.0254$ and 0.0508 m; $T_1 - T_0 = 5$, 10, 15, and 20°C) numerical investigation revealed no convective instabilities (cf. Tables 3–6). Again, for the three types of conductivity variation the predicted critical voltages for oscillatory instability were consistently higher than the experimental values but at worst by a factor of two. The discrepancy was least for a 20°C temperature difference. Dimensionless oscillation frequencies ω_c in castor oil were well predicted, whilst those for corn oil were high by a factor of at most three. There was little difference between predictions using an Arrehnius-type conductivity and a matching quadratic one, whilst a linear conductivity produced small deviations particularly, as expected, for the highest temperature difference. On the other hand, predictions using Bradley's method were in general much less accurate except for critical voltages in corn oil, with 5, 10 and 15°C temperature differences.

Concluding Remarks

We have shown that the dissociation and recombination of a single impurity in a dielectric liquid results, in an Ohmic limit, in a conductivity dependent only on temperature, if the number density of positive and negative ions in the absence of an electric field is temperature independent. Experimental observations [4, 12] suggest that the second derivative of liquid resistivity with respect to temperature is positive. This, combined with a parcel exchange argument, suggests that a conductivity model will not predict convective instability in a thermally stabilized liquid layer. Numerical investigations support this conjecture, except in the case of a sufficiently strong quadratic variation of conductivity with temperature, as considered by Takashima and Aldridge [9]. However, this case is unrealistic since it results in a negative second derivative of liquid resistivity contrary to experimental evidence. It thus seems that the convective instability of Gross and Porter [3] cannot be predicted by a simple conductivity model, whereas Martin and Richardson [7] have shown that a unipolar charge injection model predicts convective instability

at about the right critical voltage for an ionic mobility of 3×10^{-10} m^2/Vs and a nondimensional emitter space-charge density value lying between 1 and 10. Since the exact value of C_0 depends on the value chosen for residual conductivity (e.g., $C_0 \simeq 1$ for $\sigma_0 = 1.1 \times 10^{-12}$ S/m or $C_0 \simeq 10^3$ for $\sigma_0 = 1.1 \times 10^{-9}$ S/m) the true picture is probably between these two extremes, with an instability driven by injection, perhaps even bipolar, but modified by residual conduction.

In Turnbull's experiments [4], the wider electrode spacing means that parameter C_0 is large (e.g., for corn oil $C_0 \simeq 600$ and for castor oil $C_0 \simeq 12{,}000$ in the case of a 0.0508 m gap) so that the Ohmic conduction current is likely to dominate any current due to charge injection. Nevertheless, the injection model of Martin and Richardson [7], in the case of corn oil with a 15°C temperature difference across a 0.0254 m gap, predicts the preferred overstable mode at about the right critical voltage and oscillation frequency for an ionic mobility of 10^{-9} m^2/Vs and a nondimensional emitter space-charge density value lying between 0.1 and 1. As expected the numerical predictions of the critical voltages and frequencies from a conductivity model agree reasonably well with experimental values. The oscillatory modes found numerically depended only slightly on the form assumed for conductivity variation with temperature. An Arrhenius-type dependence however has the advantage over linear and quadratic variations of fitting experimental measurements over a wider temperature range.

A more controlled experiment might involve a very pure dielectric liquid doped perhaps with a single known dissociable impurity and contained between electrodes with a larger aspect ratio to reduce edge effects. On the other hand the conductivity model could be improved by including a temperature-dependent viscosity and unipolar or bipolar injection. There is a danger, however; without more reliable experimental information a more detailed analysis could easily be misguided.

References

1 Fernandez, J. L., "Electrohydrodynamic Enhancement of Forced Convection Heat Transfer in Tubes," Ph.D. thesis, University of Bristol, 1975.

2 Poulter, R., and Richardson, A. T., "The Electrohydrodynamic Enhancement of Heat Transfer With Single-Phase Dielectric Fluid in Tubes," A.R.C. Heat and Mass Transfer Subcommittee, Report No. ARC36395/HMT392, 1975.

3 Gross, M. J., and Porter, J. E., "Electrically Induced Convection in Dielectric Liquids," Nature, Vol. 212, 1966, pp. 1343–1345.

4 Turnbull, R. J., "Electroconvective Instability With a Stabilising Temperature Gradient. II. Experimental Results," *Phys. Fluids*, Vol. 11, 1968, pp. 2597–2603.

5 Worraker, W. J., and Richardson, A. T., "The Effect of Temperature Induced Variations in Charge Carrier Mobility on a Stationary Electrohydrodynamic Instability," *Journal of Fluid Mechanics*, Vol. 93, 1979, pp. 29–45.

6 Worraker, W. J., and Richardson, A. T., "A Nonlinear Electrohydrodynamic Stability Analysis of a Thermally Stabilized Plane Layer of Dielectric Liquid," *Journal of Fluid Mechanics*, Vol. 109, 1981, pp. 217–237.

7 Martin, P. J., and Richardson, A. T., "Overstable Electrothermal Instabilities in a Plane Layer of Dielectric Liquid," *Proceedings of Seventh International Conference on Conduction and Breakdown in Dielectric Liquids*, Berlin, West Germany, 1981, pp. 314–317.

8 Roberts, P. H., "Electrohydrodynamic Convection," *Quart. J. Mech. Appl. Math.*, Vol. 22, 1969, pp. 211–220.

9 Takashima, M., and Aldridge, K. D., "The Stability of a Horizontal Layer of Dielectric Fluid Under the Simultaneous Action of a Vertical D.C. Electric Field and a Vertical Temperature Gradient," *Quart. J. Mech. Appl. Math.*, Vol. 29, 1976, pp. 71–87.

10 Bradley, R., "Overstable Electoconvective Instabilities," *Quart. J. Mech. Appl. Math.* Vol. 31, 1978, pp. 381–390.

11 Turnbull, R. J., "Electroconvective Instability with a Stabilising Temperature Gradient. I. Theory," *Phys. Fluids*, Vol. 11, 1968, pp. 2588–2596.

12 Yasufuku, S., Umemura, T., and Tanii, T., "Electric Conduction Phenomena and Carrier Mobility Behavior in Dielectric Fluids," *IEEE Trans. Electr. Insul.*, Vol. EI-14, No. 1, 1979, pp. 28–35.

Thermal Convective Instabilities in a Porous Medium

M. Kaviany
Mechanical Engineering Department,
University of Wisconsin—Milwaukee,
Milwaukee, Wis. 53201
Mem. ASME

The onset of convection due to a nonlinear and time-dependent temperature stratification in a saturated porous medium with upper and lower free surfaces is considered. The initial parabolic temperature distribution is due to uniform internal heating. The medium is then cooled by decreasing the upper surface temperature linearly with time. Linear stability theory is applied to the more formally developed governing equations. In order to obtain an asymptotic solution for transient problems involving very long time scales, the critical Rayleigh number for steady-state, nonlinear temperature distribution is also obtained. The effects of porosity, permeability, and Prandtl number on the time of the onset of convection are examined. The steady-state results show that the critical Rayleigh number depends only on the ratio of porosity to permeability and when this ratio exceeds a value of one thousand, the critical Rayleigh number is directly proportional to this ratio.

1 Introduction

The onset of convection in a saturated porous medium subject to potentially unstable, steady-state and linear temperature distribution has been studied both analytically [1-9] and experimentally [1, 4, 7]. The analytical investigations have been based on application of linear stability theory. However, the conservation equations that have been applied, which are extensions of Darcy's law, have not been unique. The formalism of local volume averaging that has been developed by Slattery [10] and Whitaker [11] leads to additional terms in the conservation equations. Further assumptions and approximations are needed in order to make these equations solvable. Vafai and Tien [12] have combined the results of local volume averaging and empirical results and thus have been able to include the inertia and boundary effects in the equation for conservation of momentum.

The prediction of the time of the onset has been made via the amplification theory [13] and also by the application of the amplitude equation and a forcing function [14]. The latter allows for the study of the convection patterns as well as the determination of the time of the onset, but it requires specification of the forcing function which is determined for the experimental results [14]. The amplification theory [13] also requires empirical determination of the initial conditions and the amplification factor marking the time of the onset. However, good agreement with the experimental data is found using this method [15].

The problem considered in this study is the prediction of the onset of convection due to a nonlinear and time-dependent temperature stratification in a saturated porous medium with upper and lower free surfaces. The amplification theory [13] is applied to the more formally developed governing equations recommended by Vafai and Tien. The critical Rayleigh number for steady-state nonlinear temperature distribution is also obtained.

Figure 1 shows the details of the problem considered. The initial parabolic temperature distribution is due to uniform internal heating. The medium is then cooled by decreasing the upper surface temperature linearly with time. The uniform heat generation can be due to either radiative decay or chemical reaction. The cooling from above, which in principle is the same as heating from below due to the identical hydrodynamic boundary conditions at both surfaces, can be caused by evaporative cooling.

Contributed by the Heat Transfer Division for publication in the JOURNAL OF HEAT TRANSFER. Manuscript received by the Heat Transfer Division December 13, 1983.

2 Analysis

The following are the governing equations for thermal convection in a porous medium saturated with fluid, as given by Vafai and Tien [12], but modified to include the time dependency and Boussinesq approximation.

$$\nabla \cdot <\mathbf{u}> = 0 \tag{1}$$

$$\frac{\rho_f}{\delta}\frac{\partial <\mathbf{u}>}{\partial t} + \frac{\rho_f}{\delta} <(\mathbf{u}\cdot\nabla)\mathbf{u}> = -\frac{1}{\delta}\nabla <P> + \frac{\mu_f}{\delta}\nabla^2 <\mathbf{u}> - \frac{\mu_f}{K} <\mathbf{u}> - \rho_f F \frac{\delta}{K^{1/2}} [<\mathbf{u}>\cdot <\mathbf{u}>]\mathbf{l} + \frac{\rho_f}{\delta} g\mathbf{k}, \tag{2}$$

where $\mathbf{l} = \mathbf{u}_p / |\mathbf{u}_p|$ and $F = f(K, \mathrm{Re}_K, \text{geometry})$ is an empirical function

$$\frac{\partial <T>}{\partial t} + \frac{\rho_f C_f \delta}{\rho_f C_f \delta + \rho_s C_s (1-\delta)} <\mathbf{u}> \cdot \nabla <T> = \alpha_e \nabla^2 <T> + \tag{3}$$

where $\alpha_e = \dfrac{k_f \delta + k_s (1-\delta)}{\rho_f C_f \delta + \rho_s C_s (1-\delta)}$

In the above equations the local volume average of quantity, ψ, over a small volume of fluid, V_f, is defined as

$$<\psi> = \frac{1}{V}\int_{V_f} \psi dV$$

where V_f is that portion of V that is occupied by the fluid. Since the analysis that follows is for infinitesimal perturbations in the absence of any mean motion, the nonlinear terms in equation (2) do not influence the results obtained in this study. However, this is not the case for the terms containing the time derivative and the boundary effect. The time derivative term is expected to be valid when the porosity is high. As shown in Fig. 1, a rectangular coordinate system with the z-axis in the direction of gravity and the origin located at the upper free surface of the porous media is considered. The depth of the saturated porous media is L. By dropping the brackets indicating the local volume average and by separating the averaged quantities into mean and perturbation components, the variables become

$$\mathbf{u} = u\mathbf{i} + v\mathbf{j} + w\mathbf{k},$$
$$T = \bar{T}(z,t) + \theta$$

where all the perturbation quantities are functions of t, x, y, and z. By neglecting the terms containing the products of the

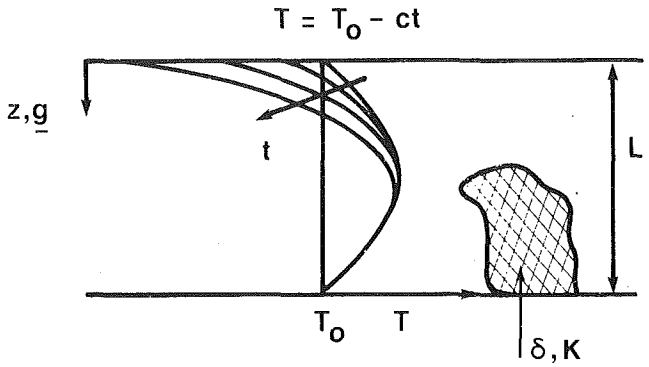

Fig. 1 A schematic of the problem considered

perturbation components and in the absence of any mean motion, the equation for the horizontally averaged mean component of temperature becomes

$$\frac{\partial \bar{T}}{\partial t} = \alpha_e \frac{\partial^2 \bar{T}}{\partial z^2} + S \tag{4}$$

where it is assumed that the source is not a function of perturbation variables. For the perturbation component, we have

$$\frac{\partial \theta}{\partial t} + \frac{\rho_f C_f \delta}{\rho_f C_f \delta + \rho_s C_s (1-\delta)} w \frac{\partial \bar{T}}{\partial z} = \alpha_e \nabla^2 \theta \tag{5}$$

Following Pellew and Southwell [16] and Foster [13], the pressure term in equation (2) is eliminated as follows. By taking the x-derivative of the first component of equation (2) and the y-derivative of the second component, adding the resulting equations, invoking the continuity equation, and taking the z-derivative of the outcome, the result becomes

$$-\rho_f \frac{\partial}{\partial t} \frac{\partial^2 w}{\partial z^2} = -\frac{\partial}{\partial z} \nabla_1{}^2 P - \mu_f \nabla^2 \frac{\partial^2 w}{\partial z^2} + \frac{\mu_f \delta}{K} \frac{\partial^2 w}{\partial z^2} \tag{6}$$

Next, the $-\nabla_1^2$ of the third component of equation (2) is taken and the result is added to equation (6). The outcome is

$$\left(\frac{\partial}{\partial t} - \nu_f \nabla^2 + \frac{\nu_f \delta}{K}\right) \nabla^2 w = -\beta_f g \nabla_1{}^2 \theta \tag{7}$$

where a linear equation of state is used. Now, the perturbation component of temperature in equation (7) is removed by applying equation (5). This is done by taking

$$\left(\frac{\partial}{\partial t} - \alpha_e \nabla^2\right)$$

of equation (7) and

$$-\beta_f g \nabla_1{}^2$$

of equation (5) and adding the resulting equations. The result is

$$\left(\frac{\partial}{\partial t} - \alpha_e \nabla^2\right)\left(\frac{\partial}{\partial t} - \nu_f \nabla^2 + \frac{\nu_f \delta}{K}\right) \nabla^2 w = \frac{\rho_f C_f \delta}{\rho_f C_f \delta + \rho_s C_s (1-\delta)} \beta_f g \nabla_1{}^2 w \frac{\partial \bar{T}}{\partial z} \tag{8}$$

The following form is assumed for the perturbation component of velocity

$$w = w(z,t) e^{i(a_x x + a_y y)}$$

A similar distribution is assumed for θ.

By introducing the above expression into equation (8), the following equation results

$$\left[\frac{\partial}{\partial t} - \alpha_e \left(\frac{\partial^2}{\partial z^2} - a^2\right)\right]\left[\frac{\partial}{\partial t} - \nu_f \left(\frac{\partial^2}{\partial z^2} - a^2\right) + \frac{\nu_f \delta}{K}\right]\left(\frac{\partial^2}{\partial z^2} - a^2\right) w = -\frac{\rho_f C_f \delta}{\rho_f C_f \delta + \rho_s C_s (1-\delta)} \beta_f g a^2 w \frac{\partial \bar{T}}{\partial z} \tag{9}$$

where $a^2 = a_x{}^2 + a_y{}^2$ is the horizontal wave number.

The variables in equation (9) are made dimensionless using the following definitions

$$z^* = \frac{z}{L},\ t^* = \frac{t\alpha_e}{L^2},\ w^* = \frac{wL}{\alpha_e},\ \bar{T}^* = \frac{(\bar{T} - T_o)\alpha_e}{SL^2},$$

$$\mathrm{Ra} = \frac{g\beta_f S L^5}{\nu_f \alpha_e{}^2} \frac{\rho_f C_f \delta}{\rho_f C_f \delta + \rho_s C_s (1-\delta)},$$

$$\theta^* = \frac{g\beta_f \theta L^3}{\nu_f \alpha_e},\ K^* = \frac{K}{L^2},\ a^* = aL \tag{10}$$

The boundary conditions for w in the case of shear free upper and lower surfaces are (after dropping the asterisks)

$$w = \frac{\partial^2 w}{\partial z^2} = 0 \quad \text{for } z = 0, 1 \tag{11a}$$

It should be noted that Lapwood [17] and Kulacki and Ramchandani [18] have considered the case of constant pressure surfaces, which is more realistic than the constant streamline considered here. In this study, equation (11a) is applied. The boundary conditions for θ and w are coupled through equation (7). By assuming that the temperature perturbations vanish at the free surfaces, equation (7) results in

Nomenclature

a = wave number
A_m = defined in equation (12)
c = the temporal rate at which the temperature of the upper surface is decreased
C = specific heat
g = gravitational constant
I_{mr} = defined in equation (14)
$\mathbf{i},\mathbf{j},\mathbf{k}$ = unit vectors
k = thermal conductivity
K = permeability
L = depth of the layer
P = pressure
Pr = Prandtl number
Ra = Rayleigh number defined in equation (10)
Re_K = Reynolds number
S = heat source
t = time
T = temperature
T_o = temperature of the lower and upper surfaces at $t=0$ and the temperature of the lower surface for $t>0$
$\mathbf{u}$ = velocity vector
$\mathbf{u}_p$ = pore velocity vector
u,v,w = perturbation velocity components
V = elemental volume
x,y,z = Cartesian coordinate axes

Greek

α_e = effective thermal diffusivity
β = coefficient of thermal expansion
δ = porosity
δ_{mr} = 0 for $m \neq r$
= 1 for $m = r$
$\nabla_1{}^2 = \frac{\partial^2}{\partial x^2} + \frac{\partial^2}{\partial y^2}$
θ = perturbation component of temperature
μ = dynamic viscosity
ν = kinematic viscosity
ρ = density
ψ = a scalar

Subscript

c = critical
f = fluid
s = solid

Superscript

$\bar{\ }$ = horizontally averaged
* = dimensionless

$$\frac{\partial^4 w}{\partial z^4} = 0 \quad \text{for } z = 0, 1 \tag{11b}$$

Furthermore, the following series solution that satisfies the boundary conditions given by equations (11*a*) and (11*b*) is assumed

$$w(z,t) = \sum_{m=1}^{\infty} A_m(t) \sin(m\pi z) \tag{12}$$

Upon introducing equation (12) into the nondimensionalized form of equation (9) and by multiplying both sides of the equation by $\sin(r\pi z)$ and then integrating for z between zero to unity, the following results

$$\frac{d^2 A_r}{dt^2} = -\frac{dA_r}{dt}\left[(\mathrm{Pr}+1)(r^2\pi^2+a^2)+\frac{\mathrm{Pr}\delta}{K}\right] - A_r \mathrm{Pr}\left(r^2\pi^2+a^2\right)\left(r^2\pi^2+a^2+\frac{\delta}{K}\right) + \sum_{m=1}^{\infty} A_m I_{mr} \frac{2\mathrm{RaPr}\, a^2}{r^2\pi^2+a^2} \quad r=1,2\ldots \tag{13}$$

where

$$I_{mr} = \int_0^1 \frac{\partial \bar{T}}{\partial z} \sin(m\pi z)\sin(r\pi z)\, dz \tag{14}$$

Equation (13) consists of an infinite number of coupled second-order ordinary differential equations in $A_r(t)$. The initial conditions for these equations will be discussed later. In order to solve this system of equations, the gradient of mean temperature must be specified.

The temperature distribution considered in this study is due initially (i.e., $t=0$) to a constant uniform heat generation, S, with both upper and lower surfaces at a constant temperature, T_o. For $t>0$, the upper surface temperature is reduced at a constant rate and the heat generation term is set at zero. These initial and boundary conditions are

$$\bar{T}(z, t=0) = \frac{(1-z)z}{2} \tag{15a}$$

$$\bar{T}(0, t>0) = -ct \tag{15b}$$

$$\bar{T}(1, t>0) = 0 \tag{15c}$$

The solution to equation (4) with $S=0$ for $t>0$, subject to conditions given by equations (15*a-c*), is found by separating the variables and applying Duhamel's theorem, and the details are given in [19]. The mean temperature distribution is

$$\bar{T} = c(z-1)t + \frac{2}{\pi^2}\sum_{n=1}^{\infty}\frac{\sin(n\pi z)}{n^3}\{[1-(-1)^n - c]e^{-n^2\pi^2 t} + c\} \tag{16}$$

By substituting the above equation into equation (14), one obtains

$$I_{mr} = \begin{cases} \dfrac{1}{2\pi^2}\left\{\dfrac{[1-(-1)^{m-r}-c]e^{-(m-r)^2\pi^2 t}+c}{(m-r)^2} - \dfrac{[1-(-1)^{m+r}-c]e^{-(m+r)^2\pi^2 t}+c}{(m+r)^2}\right\}, & \text{for } m \neq r \\ \dfrac{ct}{2} + \dfrac{c[e^{-(m+r)^2\pi^2 t}-1]}{2\pi^2(m+r)^2}, & \text{for } m = r \end{cases} \tag{17}$$

Equation (13), along with equation (17), describes the behavior of an infinitesimal vertical velocity perturbation introduced into a stagnant layer of fluid which has saturated a porous medium and is subjected to a potentially unstable mean temperature stratification.

The initial parabolic temperature distribution is potentially unstable. Therefore, for very low cooling rates, the onset of convection due to the initial temperature distribution is of interest. For this reason the critical Rayleigh numbers corresponding to a steady-state temperature distribution are found next. The results for transient temperature distributions then follow the steady-state results.

3 Steady-State Results

Equation (15*a*) describes the steady-state temperature distribution due to uniform internal heating and constant and equal temperatures at the upper and lower surfaces. For time-dependent temperature distribution, according to Pellew and Southwell [16], the limiting conditions of stability are obtained when all the time derivatives are made zero. Thus, the characteristic equations, i.e., equation (13), become

$$A_r(r^2\pi^2+a^2)^2\left(r^2\pi^2+a^2+\frac{\delta}{K}\right) - 2\sum_{m=1}^{\infty} A_m I_{mr} a^2 \mathrm{Ra} = 0 \quad r=1,2\ldots \tag{18}$$

which is independent of the Prandtl number. This equation can be written as

$$\sum_{m=1}^{\infty} A_m\left[\delta_{mr}(r^2\pi^2+a^2)^2\left(r^2\pi^2+a^2+\frac{\delta}{K}\right) - 2I_{mr}a^2\mathrm{Ra}\right] = 0 \quad r=1,2 \tag{19}$$

which is a system of linear algebraic equations. In order to obtain nontrivial solutions for this system, the infinite order determinant of equation (19) must vanish, i.e.,

$$\left\|\delta_{mr}(r^2\pi^2+a^2)^2\left(r^2\pi^2+a^2+\frac{\delta}{K}\right) - 2I_{mr}a^2\mathrm{Ra}\right\| = 0 \tag{20}$$

Equation (20) is solved for a given δ/K, and the minimum value of Ra with respect to a is sought. Equation (14), for the temperature distribution given by equation (15*a*), becomes

$$I_{mr} = \begin{cases} \dfrac{1}{2\pi^2}\left[\dfrac{(-1)^{m+r}-1}{(m+r)^2} - \dfrac{(-1)^{m-r}-1}{(m-r)^2}\right], & \text{for } m \neq r \\ 0, & \text{for } m = r \end{cases} \tag{21}$$

The results given below are for a determinant of order ten; no further increase in the order was necessary.

The limit at which the solid matrix has no influence on the momentum equation is given by $\delta/K \to 0$, i.e., very large permeabilities, and the influence of the solid matrix increases as δ/K becomes larger. The results of equation (20) for $\delta/K=0$ are presented in Fig. 2. The Rayleigh number reaches a minimum value of 16,992 at a wave number of 3.02, which is identical to the value obtained by Kulacki and Goldstein [20]. Therefore, the limit for a very large permeability is given by

$$Ra_c = 16992 \quad , \quad \text{for } \delta/K = 0 \tag{22}$$

As the value of δ/K increases, the critical Rayleigh number increases. Figure 3 shows this trend. The results are locii of critical Rayleigh numbers found in a manner similar to that shown in Fig. 2. For $\delta/K<10$, the critical Rayleigh number is rather insensitive to the value of δ/K. On the other hand, for

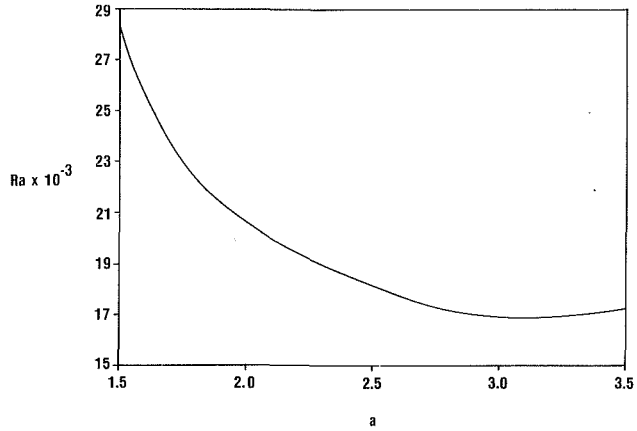

Fig. 2 Steady state – the variation of the Rayleigh number with respect to the wave number for $\delta/K = 0$

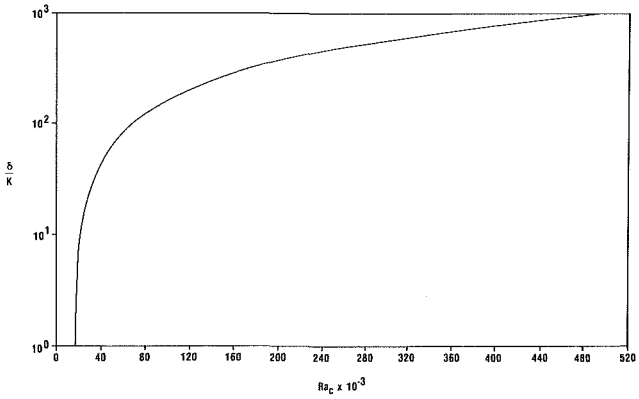

Fig. 3 Steady state – the effect of the parameter δ/K on the critical Rayleigh number

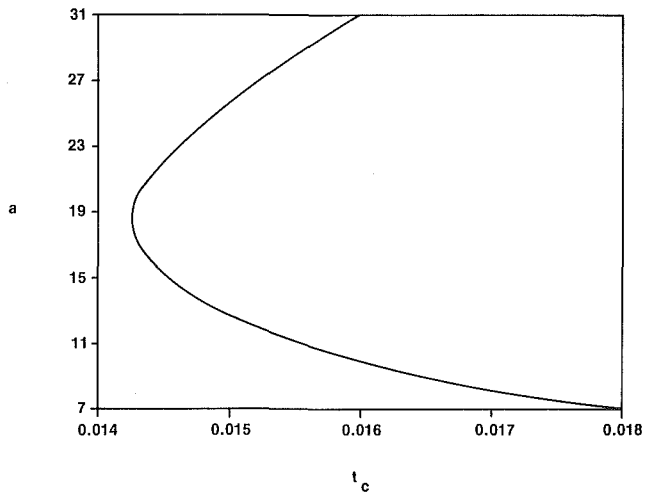

Fig. 4 The effect of the wave number on the critical time: the parameters are $Ra = 10^5$, $Pr = 0.1$, $\delta/K = 10^4$ and $c = 10^4$

$\delta/K > 10^3$, the critical Rayleigh number varies linearly with δ/K, such that

$$Ra_c = 471.75(\delta/K), \quad \text{for} \quad \delta/K > 10^3 \tag{23}$$

However, for the range $10 < \delta/K < 10^3$, the relationship between δ/K and Ra_c is nonlinear, as given by equation (20). Most of the investigators have used momentum equations that have resulted in equations similar to equation (23) which is valid only for $\delta/K > 10^3$. However, this is not the case for the results obtained by Katto and Masuoka [4] and Walker and Homsy [8]; these results support the trend shown in Fig. 3.

4 Transient Results

The one-dimensional and time-dependent horizontally averaged temperature distribution for the special situation considered in this study is given by equation (16). The steady-state solutions discussed in the last section were for temperature distributions corresponding to the initial condition used to arrive at equation (16). Therefore, the stability of the time-dependent temperature distributions corresponding to Rayleigh numbers less than the steady-state critical Rayleigh number is now examined.

The system of ordinary differential equations given by equation (13), with I_{mr} as given by equation (17), are solved numerically using Runge-Kutta-Gill's fourth order approximation as described by Romanelli [21]. In general, more than fifteen terms are required for low values of nondimensional time, but for large values of nondimensional time, fewer terms suffice. The first twenty terms in the Fourier series were retained and a value of unity was assigned for the initial values of all A_r, and a value of zero was assigned for the initial value of all dA_r/dt. More details about the scheme are given in [13, 19]. The growth rate of the average velocity perturbation is defined as

$$\bar{w}(t) = \left[\frac{\int_0^1 w^2(z,t)dz}{\int_0^1 w^2(z,t=0)dz} \right]^{1/2} \tag{24}$$

The time at which the magnitude of this quantity reaches a value of 1000 is assumed to be the time of the onset of convection [13]. This choice appears to be arbitrary; but since for $w > 10^2$ the growth is rather exponential, the choice of a larger value of w does not alter the critical time significantly. It should be noted that Foster [13] has suggested that the results of linear stability theory may be valid even after the magnitudes of the disturbances are no longer infinitesimal.

The criterion for marking the onset of convection and to a lesser degree the choice of the initial conditions may result in some error. However, the choices made here have proven to be satisfactory in predicting onset of convection [15].

The parameters of the system considered in this study are Ra, Pr, δ/K, and c. The wave number of the perturbations, a, also affects the critical time. However, for a given Rayleigh number, Prandtl number, cooling rate, and δ/K, the critical time has a minimum at a particular wave number. Figure 4 shows the variation of the critical time as a function of wave number. The parameters are $Ra = 10^5$, $Pr = 0.1$, $\delta/K = 10^4$, and $c = 10^4$. The wave number corresponding to the minimum critical time, i.e., the wave number that grows the fastest, is called the critical wave number.

The shape of the curve shown in Fig. 4 changed depending on the magnitude of Ra, δ/K, and Pr. In general, for smaller magnitudes for these parameters, the curve showed a sharp minimum and as these magnitudes increased, the minimum was more shallow.

The variation of critical time with Prandtl number is shown in Fig. 5. The parameters are $Ra = 10^5$, $\delta/K = 10^4$, $c = 10^4$, and the wave numbers which correspond to the minimum critical time. The results show that as the Prandtl number decreases – which is equivalent to increasing the thermal diffusivity – the critical time increases. As the effect of the upper surface cooling penetrates further and further into the layer, its ability as a destabilizing force decreases. Figure 5 also shows that critical time does not vary significantly with Prandtl number as long as $Pr > 2$. The Prandtl number applied here is based on an effective thermal diffusivity of the saturated porous medium. For example, in the experimental study of Katto and

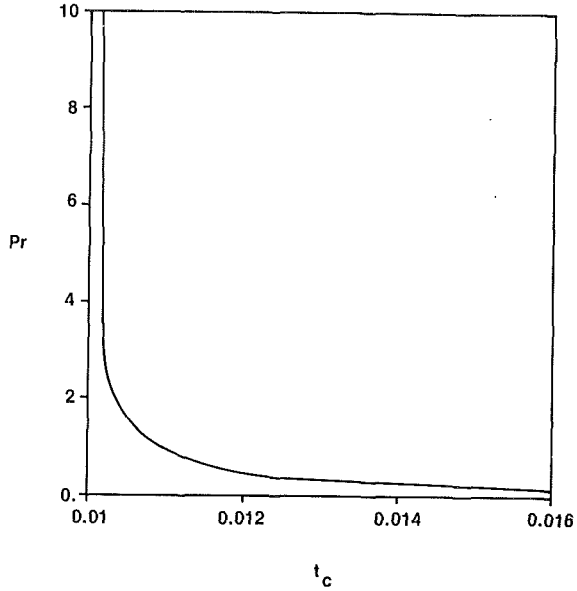

Fig. 5 The variations of the critical time with respect to the Prandtl number: the parameters are $Ra = 10^5$, $\delta/K = 10^4$, $c = 10^4$, and the critical wave numbers

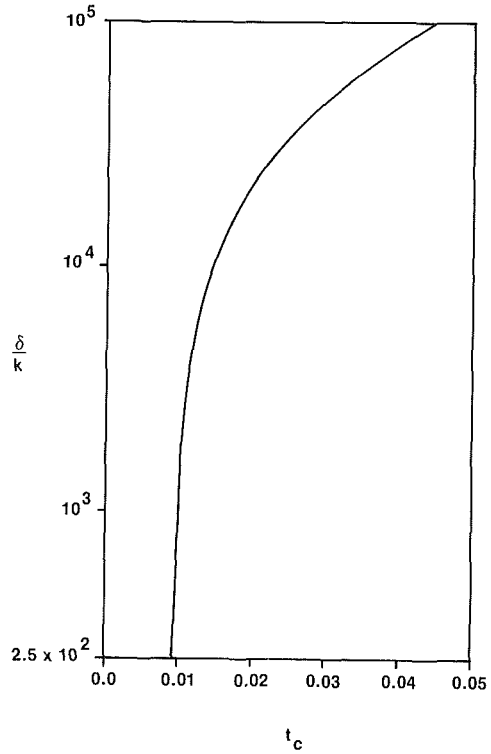

Fig. 6 The effect of the parameter δ/K on the critical time: the other parameters are $Ra = 10^5$, $Pr = 0.1$, $c = 10^4$ and the critical wave numbers

Masuoka [4] with gases, a typical value for Prandtl number was 0.1.

The presence of the solid matrix delays the onset of convection. This is illustrated in Fig. 6. The parameters are $Ra = 10^5$, $Pr = 0.1$, $c = 10^4$, and the critical wave number. The variation of the critical time with respect to δ/K is relatively insignificant as long as $\delta/K < 10^4$.

The increase in the cooling rate of the upper surface, c, accelerates the onset of convection when other parameters are kept constant. Figure 7 shows the variation of the critical time with respect to the Rayleigh number for various cooling rates.

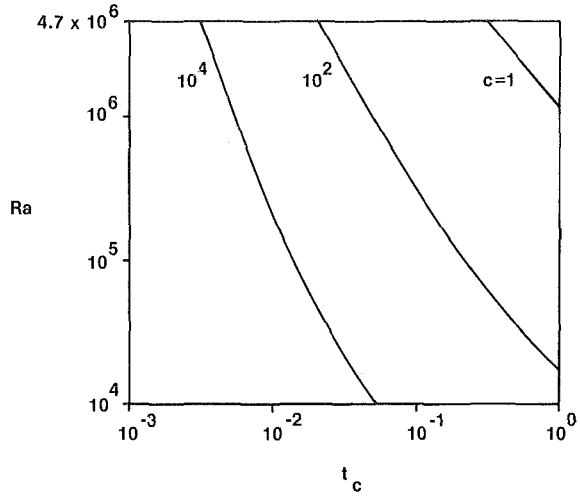

Fig. 7 The effect of the cooling rate on the critical time: the parameters are $\delta/K = 10^4$, $Pr = 0.1$, and the critical wave numbers

The parameters are $\delta/K = 10^4$, $Pr = 0.1$, and the critical wave numbers. For Rayleigh numbers less than the critical Rayleigh number for steady-state temperature distribution, i.e., 471.75 (δ/K), the transient cooling is the cause of instability. This is shown in Fig. 7, where the acceleration in the onset of convection is evident as the cooling rate increases.

5 Conclusion

The equations governing thermal convection in a saturated porous medium are developed using a combination of local volume averaging and empirical results [12]. The amplification theory is applied to cases of free upper and lower surfaces. The time-dependent unstable temperature distribution is due to transient cooling of the upper surface with initial internal heating. The analysis is divided into two parts and the following summary is made

1 Steady State:

The critical Rayleigh number is found as a function of δ/K. The value of the critical Rayleigh number increases with increases in the value of δ/K with the following limits:

$$Ra_c = 16992 \quad , \qquad \text{for} \quad \delta/K = 0$$

$$Ra_c = 471.75\,(\delta/K), \quad \text{for} \quad \delta/K > 10^3$$

2 Transient:

The stability of the time-dependent temperature distributions with Rayleigh numbers less than the steady-state critical Rayleigh numbers is also considered, and it was found that:

(*a*) The critical time incresaes as the Prandtl number decreases.

(*b*) For a given Ra, there exists a value of δ/K below which the magnitude of δ/K does not alter the critical time significantly.

(*c*) The effect of the cooling rate on the time of the onset of convection is shown quantitatively for a specific set of parameters.

Acknowledgment

The support of the National Science Foundation (Grant: MEA 82-04837) is greatly appreciated.

References

1 Wooding, R. A., "Steady-State Free Thermal Convection of Liquid in Saturated Medium," *Journal of Fluid Mechanics*, Vol. 2, 1957, pp. 273–285.

2 Elder, J. W., "Steady Free Convection in a Porous Medium Heated From Below," *Journal of Fluid Mechanics*, Vol. 27, 1967, pp. 29–48.

3 Gheorghitza, St. I., "On the Marginal Stability in Porous Media," *J. Math. Phys. Sci.*, Vol. 3, 1969, pp. 269–279.

4 Katto, Y., and Masuoka, T., "Criterion for the Onset of Convective Flow in a Fluid in a Porous Medium," *International Journal of Heat and Mass Transfer*, Vol. 10, 1967, pp. 297–309.

5 Nield, D. A., "Onset of Thermohaline Convection in a Porous Media," *Water Resources Research*, Vol. 4, No. 3, 1968, pp. 553–560.

6 Weber, J. E., "Convection in a Porous Medium With Horizontal and Vertical Temperature Gradient," *International Journal of Heat and Mass Transfer*, Vol. 17, 1974, pp. 241–248.

7 Horne, R. N., and O'Sullivan, M. J., "Oscillatory Convection in a Porous Medium Heated from Below," *Journal of Fluid Mechanics*, Vol. 66, 1974, pp. 339–352.

8 Walker, K., and Homsy, G. M., "A Note on Convective Instabilities in Boussinesq Fluids and Porous Media," ASME JOURNAL OF HEAT TRANSFER, Vol. 99, 1977, pp. 338–339.

9 Somerton, C. W., and Catton, I., "On the Thermal Instability of Superposed Porous and Fluid Layers," ASME JOURNAL OF HEAT TRANSFER, Vol. 104, 1982, pp. 160–165.

10 Slattery, J. C., *Momentum, Energy and Mass Transfer in Continua*, McGraw-Hill, 1972.

11 Whitaker, S., "Simultaneous Heat, Mass and Momentum Transfer in Porous Media: A Theory of Drying," *Advances in Heat Transfer*, Vol. 13, edited by T. F. Irvine and J. P Hartnett, 1977.

12 Vafai, K., and Tien, C. L., "Boundary and Inertia Effects on Flow and Heat Transfer in Porous Media," *International Journal of Heat and Mass Transfer*, Vol. 24, 1981, pp. 195–203.

13 Foster, T. D., "Stability of a Homogeneous Fluid Cooled Uniformly From Above," *Physics of Fluids*, Vol. 8, No. 7, 1965, pp. 1249–1257.

14 Ahlers, G., Cross, M. C., Hohenberg, P. C., and Safran, S., "The Amplitude Equation Near the Convective Threshold: Application to Time-Dependent Heating Experiments," *Journal of Fluid Mechanics*, Vol. 110, 1981, pp. 297–334.

15 Foster, T. D., "Onset of Manifest Convection in a Layer of Fluid With a Time-dependent Surface Temperature," *Physics of Fluids*, Vol. 12, 1969, pp. 2482–2487.

16 Pellew, A., and Southwell, R. V., "On Maintained Convective Motion in Fluid Heated From Below," *Proc. Roy. Soc. A*, Vol. 176, 1940, pp. 312–343.

17 Lapwood, E. R., "Convection of a Fluid in a Porous Medium," *Proceedings of the Cambridge Philosophical Society*, Vol. 44, 1948, pp. 508–521.

18 Kulacki, F. A., and Ramchandani, R., "Hydrodynamic Instability in Porous Layer Saturated with Heat Generating Fluid," *Warme-und-Stoffubertagung*, Vol. 8, 1975, pp. 179–185.

19 Kaviany, M., "Onset of Convection in a Fluid Layer With Time-Dependent Temperature Distribution," to appear in *International Journal of Heat and Mass Transfer*, 1983.

20 Kulacki, F. A., and Goldstein, R. J., "Hydrodynamic Instability in Fluid Layers with Uniform Volumetric Energy Sources," *Appl. Sci. Res.*, Vol. 31, 1975, pp. 81–109.

21 Romanelli, M. J., *Mathematical Methods for Digital Computers*, edited by A. Ralston and H. S. Wilf, John Wiley, 1960, pp. 110–120.

22 Nield, D. A., "The Thermohaline Rayleigh-Jeffreys Problem," *Journal of Fluid Mechanics*, Vol. 29, 1967, pp. 545–558.

Higher-Order Approximations for Darcian Free Convective Flow About a Semi-Infinite Vertical Flat Plate

P. Cheng
Department of Mechanical Engineering,
University of Hawaii at Manoa,
Honolulu, Hawaii, 96822
Mem. ASME

C. T. Hsu
Fluid Mechanics Department,
TRW Systems and Energy,
Redondo Beach, Calif. 90278

Higher-order effects of Darcian free convection boundary-layer flow adjacent to a semi-infinite vertical flat plate with a power law variation of wall temperature (i.e., $\hat{T}_w \propto \hat{x}^\lambda$ for $\hat{x} \geq 0$) are examined theoretically in this paper. The method of matched asymptotic expansions is used to construct inner and outer expansions. The small parameter of the perturbation series is the inverse of the square root of the Rayleigh number. The leading term in the inner expansions is taken to be the boundary layer theory with the second-order term due to the entrainment effect, and the third-order term due to the transverse pressure gradient and the streamwise heat conduction. The ordering of the term due to the leading edge effect depends on the wall temperature distribution; this term is determinate within a multiplicative constant owing to the appearance of an eigenfunction in the inner expansion. Thus, the perturbation solutions are carried out up to this term. For the case of an isothermal vertical plate ($\lambda = 0$), the second-order corrections for both the Nusselt number and the vertical velocity are zero, with the leading edge effect appearing in the third-order term. For $\lambda > 0$, both the second- and third-order corrections in the Nusselt number are positive. The increase in surface heat flux is due to the fact that the higher-order effects increase the velocity parallel to the heated surface. The boundary layer theory for the prediction of the Nusselt number is shown to be quite accurate even at small Rayleigh number for $0 \leq \lambda \leq 1/3$. The higher order effects tend to have a stronger influence on the velocity distribution than the temperature distribution. These effects become more pronounced as λ is increased from $\lambda = 1/3$, or as the Rayleigh number is decreased.

Introduction

In the past decade, higher-order effects of convection boundary layer in a Newtonian fluid have received considerable attention. For example, higher-order approximations for free convection boundary layers about a vertical flat plate at constant temperature have been analyzed by Yang and Jerger [1], Hieber [2], and Riley and Drake [3], while that for constant surface heat flux has been studied by Mahajan and Gebhart [4]. Riley [5] as well as Hieber and Nash [6] have obtained higher-order theories for free convection about a horizontal line source of heat.

Recent interest on the utilization of geothermal energy has led to an upsurge in research activities on convection heat transfer in a porous medium. Based on the boundary layer approximation, Cheng and Minkowycz [7] have obtained similarity solutions for free convection about a semi-infinite vertical flat plate with a power variation of wall temperature, i.e., $T_w \propto x^\lambda$, where $\lambda = -1/3$, 0, and 1/3 correspond to the cases of a horizontal line source, constant wall temperature, and constant surface heat flux, respectively. As in the classical boundary layer theory, these solutions are valid for large Rayleigh numbers with effects of entrainments from the outer flow, the streamwise heat conduction, and the transverse pressure gradient neglected. The present paper is motivated by a desire to examine the magnitude of these higher-order effects on the heat transfer and fluid flow characteristics especially at low to moderate values of the Rayleigh number.

In the following, the method of matched asymptotic expansions will be used to construct inner and outer expansions. It will be shown that the small parameter of the perturbation series is the inverse of the square root of the Rayleigh number. The leading term of the series is the boundary layer approximation, and the higher-order terms are obtained by matched asymptotic expansions. It will be shown that the second-order inner problem takes into consideration the entrainment effects, while the third-order inner problem takes into account the effects of the transverse pressure gradient and the streamwise heat conduction. A study of the eigenvalues and the eigenfunctions of the associated homogeneous problem shows that the leading edge effect appear at the second-, third- and fourth-order terms for $\lambda = -1/3$, $-1/3 \leq \lambda \leq 0$ and $0 < \lambda < 1$, respectively. For the case of an isothermal vertical flat plate ($\lambda = 0$), the second-order corrections for both the Nusselt number and the vertical velocity are zero, whereas for $\lambda > 0$, both second- and the third-order corrections in Nusselt number are positive. For $0 \leq \lambda \leq 1/3$, the boundary layer approximation is shown to be accurate even at small Rayleigh numbers. In general, the boundary layer theory is found to be underestimating the Nusselt number, with the higher-order effects becoming more pronounced as λ is increased from $\lambda = 1/3$ or as the Rayleigh number is decreased. The entrainment along the edge of the boundary layer has a stronger effect on the increase of the surface heat flux than that of the combined effects of the transverse pressure gradient and the streamwise heat conduction. The higher-order terms tend to have a strong influence on the velocity distribution, and a lesser effect on the temperature distribution and the surface heat flux.

Analysis

The governing equations for steady, two-dimensional,

Contributed by the Heat Transfer Division for publication in the JOURNAL OF HEAT TRANSFER. Manuscript received by the Heat Transfer Division August 30, 1982.

constant-property, buoyancy-induced Darcian flow about a vertical impermeable heated surface in a porous medium are [8]

$$\hat{\psi}_{\hat{x}\hat{x}} + \hat{\psi}_{\hat{y}\hat{y}} = \frac{\rho_\infty \beta g K}{\mu} \hat{T}_{\hat{y}} \tag{1}$$

$$\alpha(\hat{T}_{\hat{x}\hat{x}} + \hat{T}_{\hat{y}\hat{y}}) = \hat{T}_{\hat{x}}\hat{\Psi}_{\hat{y}} - \hat{T}_{\hat{y}}\hat{\Psi}_{\hat{x}} \tag{2}$$

where $\hat{x}$ and $\hat{y}$ are the coordinates along and perpendicular to the plate; ρ_∞, μ, and β are the fluid density at infinity, the viscosity, and thermal expansion coefficient of the fluid; K and α are the permeability and the equivalent thermal diffusivity of the porous medium; g is the gravitational acceleration; $\hat{T}$ is the temperature and $\hat{\psi}$ is the stream function which is defined as

$$\hat{u} = \hat{\psi}_{\hat{y}}, \quad \text{and} \quad \hat{v} = -\hat{\psi}_{\hat{x}} \tag{3}$$

where $\hat{u}$ and $\hat{v}$ are the Darcian velocities in the $\hat{x}$- and $\hat{y}$-directions.

The boundary conditions at the heat surface with a power law variation of wall temperature are

$$\hat{y}=0: \quad \hat{\psi}_{\hat{x}} = 0, \quad \hat{T}_w = \hat{T}_\infty + A\hat{x}^\lambda, \quad \hat{x} \geq 0 \tag{4a,b}$$

while that at infinity are

$$\hat{y} \to \infty \quad \hat{\psi}_{\hat{y}} = 0, \quad \hat{T} = \hat{T}_\infty \tag{5a,b}$$

where $\hat{T}_\infty$ is the temperature at infinity with $A > 0$ and $-1/3 \leq \lambda < 1$ being the prescribed constants. The boundary condition for $\hat{x} < 0$ are

$$\hat{y}=0: \hat{T} = \hat{T}_\infty, \hat{\psi} = 0 \tag{6a,b}$$

We now introduce the following dimensionless variables

$$\psi = \frac{\mu\hat{\psi}}{\rho_\infty g K \beta A L^\lambda}, \quad \theta = \frac{\hat{T} - \hat{T}_\infty}{AL^\lambda} \tag{7a,b}$$

$$x = \hat{x}/L, \quad y = \hat{y}/L \tag{7c,d}$$

where L is a characteristic length. In terms of the dimensionless variables, the governing equations and boundary conditions are

$$\psi_{xx} + \psi_{yy} = \theta_y \tag{8}$$

$$\epsilon^2(\theta_{xx} + \theta_{yy}) = \theta_x\psi_y - \theta_y\psi_x \tag{9}$$

and

$$\psi_x(x,0) = 0, \ \theta(x,0) = x^\lambda, \ x \geq 0 \tag{10}$$

$$\psi_y(x,\infty) = 0, \ \theta(x,\infty) = 0, \ x \geq 0 \tag{11}$$

where $\epsilon = 1/\sqrt{\text{Ra}}$ with Ra denoting the Rayleigh number defined as $\text{Ra} = \rho_\infty K\beta g A L^{\lambda+1}/\mu\alpha$. In the following we shall obtain a perturbation solution to equations (8–10) for which ϵ is small.

The Inner Expansions

For $\epsilon << 1$, we seek the inner expansion of the form

$$\psi(x,y,\epsilon) = \epsilon[\Psi_0(X,Y) + \epsilon\Psi_1(X,Y) + \epsilon^2\Psi_2(X,Y) + \ldots] \tag{12a}$$

$$\theta(x,y,\epsilon) = \Theta_0(X,Y) + \epsilon\Theta_1(X,Y) + \epsilon^2\Theta_2(X,Y) + \ldots \tag{12b}$$

where the inner variables are given by

$$X = x, \quad \text{and} \quad Y = y/\epsilon \tag{13}$$

Rewriting equations (8–11) in terms of the inner variables and substituting equations (12) in the resulting equations leads to the following subproblems

The First-Order Inner Problem:

$$\Psi_{0YY} = \Theta_{0Y} \tag{14}$$

$$\Theta_{0YY} = \Theta_{0X}\Psi_{0Y} - \Theta_{0Y}\Psi_{0X} \tag{15}$$

with boundary conditions

$$\Psi_{0X}(X,0) = 0, \quad \Theta_0(X,0) = X^\lambda \tag{16a,b}$$

$$\Psi_{0Y}(X,\infty) = 0, \quad \Theta_0(X,\infty) = 0 \tag{16c,d}$$

Note that equations (14–17) are the boundary layer theory for

Nomenclature

A = constant defined in equation (4*b*)
A_m = constants defined in equation (75*a*)
B_m = constants defined in equation (75*b*)
$c_1, c_2, \ldots$ = constants defined in equation (42)
D = constants defined in equation (48*a*)
f_0, f_1, f_2 = dimensionless perturbation stream functions
g = acceleration due to gravity
g_0, g_1, g_2 = dimensionless perturbation temperature functions
h = local heat transfer coefficient
K = permeability of the porous medium
κ = constant defined in equation (53*b*)
k = thermal conductivity of the saturated porous medium
L = a characteristic length
Nu_x = local Nusselt number
p = pressure
q = local heat transfer rate
r = radial distance from the origin
Ra_x = local Rayleigh number
T = dimensionless temperature
u = dimensionless Darcian velocity in the x-direction
v = dimensionless Darcian velocity in the y-direction
X = dimensionless inner coordinate
x = dimensionless coordinate
Y = dimensionless inner coordinate
y = dimensionless coordinate

Greek Symbols

α = equivalent thermal diffusivity
α_m = exponent of the perturbation parameter
β = coefficient of thermal expansion
ϵ = perturbation parameter
η = similarity variable
Θ = dimensionless inner temperature
θ = dimensionless temperature
Λ = constant defined in equation (46)
λ = constant defined in equation (4*b*)
ρ = density of the fluid
μ = viscosity of the fluid
Ψ = dimensionless inner stream function
ψ = dimensionless stream function

Superscript

$\hat{}$ = dimensional variables

Subscripts

∞ = condition at infinity
w = condition at the wall

the problem [7], which has neglected the effects of entrainment from the edge of the boundary layer, the transverse pressure gradient, and the streamwise heat conduction.

The Second-Order Inner Problem:

$$\Psi_{1YY} = \Theta_{1Y} \tag{17}$$

$$\Theta_{1YY} = (\Theta_{0X}\Psi_{1Y} + \Theta_{1X}\Psi_{0Y}) - (\Theta_{0Y}\Psi_{1X} + \Theta_{1Y}\Psi_{0X}) \tag{18}$$

with boundary conditions

$$\Psi_{1X}(X,0) = 0,\ \Theta_1(X,0) = 0 \tag{19a,b}$$

and $\Psi_{1Y}(X,\infty)$ and $\Theta_1(X,\infty)$ match with the outer expansions which remain to be carried out.

The Third-Order Inner Problem:

$$\Psi_{2YY} = \Theta_{2Y} - \Psi_{0XX} \tag{20}$$

$$\Theta_{2YY} = (\Theta_{0X}\Psi_{2Y} + \Theta_{2X}\Psi_{0Y}) - (\Theta_{0Y}\Psi_{2X} + \Theta_{2Y}\Psi_{0X}) + \Theta_{1X}\Psi_{1Y} - \Theta_{1Y}\Psi_{1X} - \Theta_{0XX} \tag{21}$$

subject to the boundary conditions

$$\Psi_{2X}(X,0) = 0,\ \Theta_2(X,0) = 0 \tag{22a,b}$$

and $\Psi_{2Y}(X,\infty)$ and $\Theta_2(X,\infty)$ are to be matched with the outer expansions. Equations (20) and (21) show that the transverse pressure gradient (Ψ_{0XX}) and the streamwise heat conduction (Θ_{0XX}) are taken into consideration in the third-order inner problem.

The Eigenvalue Problem. It is noted that the higher-order theory as given by equations (17), (18), (20), and (21) are linear and homogeneous. Thus, any nontrivial solution that satisfies these equations and their associated homogeneous boundary conditions is also a solution to the higher-order theory. To find the possible existence of these solutions, we add the terms $\epsilon^{\alpha_m}\theta_m(X,Y)$ and $\epsilon^{\alpha_m}\psi_m(X,Y)$ in equations (12*a*,*b*) to give

$$\psi(x,y,\epsilon) = \epsilon[\Psi_0(X,Y) + \epsilon\Psi_1(X,Y) + \epsilon^2\Psi_2(X,Y) + \epsilon^{\alpha_m}\Psi_m(X,Y) + \ldots]$$

$$\theta(x,y,\psi) = \Theta_0(X,Y) + \epsilon\Theta_1(X,Y) + \epsilon^2\Theta_2(X,Y) \epsilon^{\alpha_m}\Theta_m(X,Y) + \ldots \tag{23a,b}$$

where α_m is the eigenvalue that will be shown to depend on λ. Rewriting equations (8–11) in terms of the inner variables and substituting equations (23) in the resulting equations gives the following homogeneous equations for ψ_m and Θ_m

$$\Psi_{mYY} = \Theta_{mY} \tag{24}$$

$$\Theta_{mYY} = (\Theta_{0X}\Psi_{mY} + \Theta_{mX}\Psi_{0Y}) - (\Theta_{0Y}\Psi_{mX} + \Theta_{mY}\Psi_{0X}) \tag{25}$$

Equations (24) and (25) are to be solved subject to the following homogeneous boundary conditions

$$\Psi_m(X,0) = \Theta_m(X,0) = 0 \tag{26a,b}$$

$$\Psi_{mY}(X,\infty) = \Theta_m(X,\infty) = 0 \tag{27a,b}$$

Equations (24–27) constitute an eigenvalue problem. The determination of the eigenvalue α_m and the eigenfunctions ψ_m and Θ_m will follow the procedures given by Chang and Cheng [9].

The Outer Expansions

We now write the straightforward outer expansions of ψ and θ as

$$\psi(x,y,\epsilon) = \epsilon[\psi_0(x,y) + \epsilon\psi_1(x,y) + \epsilon^2\psi_2(x,y) + \epsilon^{\alpha_m}\psi_m(x,y) + 0(\epsilon^n)] \tag{28a}$$

$$\theta(x,y,\epsilon) = \epsilon^2[\theta_0(x,y) + \epsilon\theta_1(x,y) + \epsilon^2\theta_2(x,y) + \epsilon^{\alpha_m}\theta_m(x,y) + 0(\epsilon^n)] \tag{28b}$$

where the terms $0(\epsilon^{\alpha m})$ are corrections due to the eigensolutions of the inner expansions with $n \geq \alpha_m$. Again, the ordering of these terms depends on the value of the eigenvalue α_m, which, in turn, depends on λ. It can be shown that there are no eigensolutions associated with the outer expansion for the present problem.

Substituting equations (28) into equations (8–11) yields the following subproblems:

The First-Order Outer Problem:

$$\nabla^2\psi_0 = 0 \tag{29}$$

$$\theta_{0x}\psi_{0y} - \theta_{0y}\psi_{0x} = 0 \tag{30}$$

with the boundary conditions $\psi_0(x,0)$ and $\theta_0(x,0)$ match with the inner expansions at the edge of the boundary layer, and the infinity conditions

$$\psi_{0y}(x,\infty) = 0 \quad \text{and} \quad \theta_0(x,\infty) = 0 \tag{31a,b}$$

The Second-Order Outer Problem:

$$\nabla^2\psi_1 = \theta_{0y} \tag{32}$$

$$\theta_{0x}\psi_{1y} - \theta_{0y}\psi_{1x} + \theta_{1x}\psi_{0y} - \theta_{1y}\psi_{0x} = \nabla^2\theta_0 \tag{33}$$

with the boundary conditions $\psi_{1y}(x,0)$ and $\theta_1(x,0)$ match with the inner expansions at the edge of the boundary layer, and the infinity conditions

$$\psi_{1y}(x,\infty) = 0 \quad \text{and} \quad \theta_1(x,\infty) = 0 \tag{34a,b}$$

It is pertinent to note that the nonhomogeneous boundary conditions for higher order inner and outer problems are the results of matching.

Solutions by the Asymptotic Matching Procedures

We now obtain the solutions of the higher-order theory by the method of matched asymptotic expansions.

The First-Order Inner Solution. Equations (14–17) admit similarity solutions of the form [7]

$$\Psi_0 = X^{\frac{\lambda+1}{2}} f_0(\eta) \tag{35}$$

$$\Theta_0 = X^{\lambda} g_0(\eta) \tag{36}$$

where

$$\eta = YX^{\frac{\lambda-1}{2}} \tag{37}$$

with $f_0(\eta)$ and $g_0(\eta)$ determined from

$$f_0'' = g_0' \tag{38}$$

$$g_0'' = \lambda f_0' g_0 - \frac{\lambda+1}{2} f_0 g_0' \tag{39}$$

subject to boundary conditions

$$f_0(0) = 0, \quad g_0(0) = 1 \tag{40a,b}$$

$$f_0'(\infty) = g_0(\infty) = 0 \tag{41a,b}$$

which has been numerically integrated by Cheng and Minkowycz [7], who show that $\lambda = -1/3$, 0, and 1/3 correspond to the cases of a horizontal line source, and a vertical plate with uniform wall temperature and with uniform heat flux, respectively. However, for higher-order theory, the cases of $\lambda = -1/3$ and 1/3 do not correspond to the cases of horizontal line source and uniform surface heat flux.

Table 1 Values of α_m, $f_0(\infty)$, $g_1'(0)$, $g_2'(0)$, and $f_2'(0)$ for selected values of λ

	$\lambda=-1/3$	$\lambda=0$	$\lambda=0.1$	$\lambda=1/3$	$\lambda=1/2$	$\lambda=3/4$
α_m	1.0	2.0	2.181	2.500	2.666	2.857
$f_0(\infty)$	2.449	1.614	1.495	1.300	1.200	1.086
$g_1'(0)$	*	0	−0.1328	−0.3272	−0.4236	−0.5381
$g_2'(0)$	*	*	−0.1942	−0.2030	−0.2452	−0.4469
$f_2'(0)$	*	*	0.0121	0.0970	0.2023	0.5656

*Values cannot be determined without a detailed analysis of the leading edge effect.

The asymptotic behavior of $g_0(\eta)$ and $f_0(\eta)$ can be found from equations (38), (39) and (41) to give

$$g_0(\eta) \sim c_1 e^{-\gamma\eta}, \text{ as } \eta\to\infty \tag{42a}$$

$$f_0(\eta) \sim f_0(\infty) + c_2 e^{-\gamma\eta}, \text{ as } \eta\to\infty \tag{42b}$$

where $\gamma \equiv (\lambda+1)/2f_0(\infty)$. It follows from equations (35), (36), and (42) that

$$\Psi_0(X,Y) = f_0(\infty) X^{\frac{\lambda+1}{2}}, \text{ as } Y\to\infty \tag{43a}$$

and

$$\Theta_0(X,Y) \to 0, \text{ as } Y\to\infty \tag{43b}$$

Equations (43) are the matching conditions for ψ_0 and θ_0 in the outer expansions.

The First-Order Outer Solution. Equation (43*b*) shows that there is no temperature correction to the outer expansion. Consequently

$$\theta_0(x,y) = 0 \quad \text{everywhere} \tag{44}$$

The function ψ_0 is to be solved from equation (29) subject to the matching condition

$$\psi_0(x,0) = \begin{cases} f_0(\infty) x^{\frac{\lambda+1}{2}}, & x \geq 0 \\ 0, & x < 0 \end{cases} \tag{45}$$

and the infinity conditions (31). It can be shown that the solution for ψ_0 in terms of the polar coordinate (r,Λ) is

$$\psi_0(r,\Lambda) = \frac{f_0(\infty) r^{\frac{\lambda+1}{2}}}{\operatorname{Sin}\left[\left(\frac{\lambda+1}{2}\right)\pi\right]} \sin\left[\frac{\lambda+1}{2}(\pi-\Lambda)\right] \tag{46}$$

where $r = \sqrt{x^2+y^2}$ and $\Lambda = \tan^{-1}(y/x)$. Equation (46) is the induced streamlines in the outer flow due to a semi-infinite vertical plane sink along the x-axis. As seen from the outer flow, the vertical plate appears to be a semi-infinite plane sink with nonuniform sink strength. This can be shown by obtaining the expression of the velocity perpendicular to the plate from equation (45) and noting that $f_0(\infty)$ is positive (see Table 1). The induced flow imposes a positive velocity slip along the surface. Expanding equation (46) for $\Lambda\to 0$, one obtains

$$\psi_0(r,0) = f_0(\infty) x^{\frac{\lambda+1}{2}} \left\{1 - \epsilon \frac{(1+\lambda)}{2} \frac{Y}{x} \cot\left[\frac{(1+\lambda)}{2}\pi\right] + \epsilon^2 \frac{(1-\lambda^2)}{8} \frac{Y^2}{x^2} + 0(\epsilon^3)\right\} \tag{47a}$$

and

$$\psi_{0y}(r,0) = f_0(\infty) x^{\frac{\lambda+1}{2}} \left\{ -\frac{(1+\lambda)}{2} \frac{Y}{x} \cot\left[\frac{1+\lambda}{2}\pi\right] + \frac{(1-\lambda^2)}{4} \frac{y}{x^2} + \ldots \right\} \tag{47b}$$

The Second-Order Inner Solution. The governing equations for Ψ_1 and Θ_1 are given by equations (18-21) with the matching condition

$$\Psi_{1Y}(X,\infty) = DX^{\frac{\lambda-1}{2}} \tag{48a}$$

$$\Theta_1(X,\infty) = 0 \tag{48b}$$

where $D = -(1+\lambda)/2 \cot[(1+\lambda)/2\pi] f_0(\infty)$. Note that equation (48*a*) is the matching condition from equation (47*b*). Thus, the second-order inner problem takes into consideration the induced velocity at the outer of the boundary layer and the interaction of the outer irrotational isothermal flow and the inner boundary layer flow. It can be shown that the solutions of Ψ_1 and Θ_1 are of the form

$$\Psi_1 = Df_1(\eta) \tag{49a}$$

$$\Theta_1 = DX^{\frac{\lambda-1}{2}} g_1(\eta) \tag{49b}$$

where $f_1(\eta)$ and $g_1(\eta)$ are determined from

$$f_1''' = g_1' \tag{50a}$$

$$g_1'' + \frac{\lambda+1}{2} f_0 g_1' - \frac{\lambda-1}{2} f_0' g_1 = \lambda g_0 f_1' \tag{50b}$$

subject to the boundary conditions

$$f_1(0) = g_1(0) = 0 \tag{51a,b}$$

$$f_1'(\infty) = 1 \text{ and } g_1(\infty) = 0 \tag{52a,b}$$

For the case of $\lambda=0$, the solution to equations (50–51) is $g_1(\eta)=0$ and $f_1(\eta)=\eta$. However since $D=0$ for $\lambda=0$, consequently $\Psi_1=\Theta_1=0$ for $\lambda=0$. For other values of λ, $g_1(\eta)$ and $f_1(\eta)$ must be solved from equations (50) and (51) numerically. The asymptotic behavior of f_1 and g_1 can be obtained from equations (50) with the aid of equations (42) and (52) to give

$$g_1(\eta) \sim e^{-\gamma\eta}, \text{ as } \eta\to\infty \tag{53a}$$

and

$$f_1(\eta) \sim \eta + \kappa, \text{ as } \eta\to\infty \tag{53b}$$

where κ is a constant (whose value depends on λ) and can be determined only after equations (50–52) have been solved numerically. It follows from equations (49) and (53) that

$$\Psi_1(X,Y) = D\left[YX^{\frac{\lambda-1}{2}} + \kappa\right], \quad \text{as } Y\to\infty \tag{54a}$$

$$\Theta_1(X,Y) \to 0, \text{ as } Y\to\infty \tag{54b}$$

and

$$\Psi_{1Y}(X,Y) = DX^{\frac{\lambda-1}{2}}, \quad \text{as } Y\to\infty \tag{54c}$$

The Second-Order Outer Solution. Solution to equation (33) with the matching condition (54*b*), the infinity condition (34*b*) and with the aid of equation (44) is

$$\theta_1(x,y) = 0 \text{ everywhere} \tag{55}$$

In view of equations (44) and (32), the governing equation for ψ_1 is

Table 2 Local Nusselt numbers versus local Rayleigh numbers at selected values of λ

Ra_x	$\lambda=0$			$\lambda=0.1$			$\lambda=1/3$			$\lambda=1/2$			$\lambda=3/4$		
	1st approx.	2nd approx.	3rd approx.	1st approx.	2nd approx.	3rd approx.	1st approx.	2nd approx.	3rd approx.	1st approx.	2nd approx.	3rd approx.	1st approx.	2nd approx.	3rd approx.
10	1.403	1.403	(a)	1.655	1.672	1.734	2.140	2.306	2.371	2.434	2.817	2.896	2.821	4.060	4.208
20	1.984	1.984	(a)	2.341	2.358	2.402	2.982	3.194	3.240	3.443	3.826	3.882	3.990	5.229	5.333
50	3.137	3.137	(a)	3.701	3.719	3.746	4.787	4.955	4.984	5.444	5.828	5.864	6.309	7.548	7.614
100	4.437	4.437	(a)	5.235	5.252	5.272	6.770	6.940	6.961	7.700	8.085	8.110	8.923	10.15	10.20
200	6.274	6.274	(a)	7.403	7.421	7.434	9.574	9.747	9.762	10.88	11.27	11.29	12.61	13.85	13.89
500	9.921	9.921	(a)	11.70	11.72	11.73	15.13	15.31	15.32	17.21	17.60	17.61	19.95	21.18	21.20
1000	14.03	14.03	(a)	16.55	16.57	16.57	21.40	21.59	21.59	24.34	24.74	24.74	28.21	29.45	29.45

(a) Values cannot be determined without a detailed analysis of the leading edge effect

$$\nabla^2\psi_1 = 0 \tag{56}$$

which is to be solved with the infinite condition equation (34*a*) and the following matching condition

$$\psi_1(x,0) = \begin{cases} D\kappa, x \geq 0 & (57a) \\ 0, x < 0 & (57b) \end{cases}$$

where equation (57*a*) is obtained from equation (54*a*). It can be shown that the solution for ψ_1 in the polar coordinate $(r.\Lambda)$ is

$$\psi_1(r,\Lambda) = D\kappa\left(1 - \frac{\Lambda}{\pi}\right) \tag{58}$$

Expressing equation (58) in terms of (x,y) and expanding for small y yields

$$\psi_1(x,y) = D\kappa\left[1 - \frac{y}{\pi x} + \ldots\right]$$

$$= D\kappa\left[1 - \frac{\epsilon Y}{\pi x} + 0(\epsilon^2)\right], \text{ as } y \to 0 \tag{59a}$$

and

$$\psi_{1y}(x,y) = -D\kappa/\pi x + \ldots, \text{ as } y \to 0 \tag{59b}$$

The Third-Order Inner Solution. The governing equations for Ψ_2 and Θ_2 are given by equations (21–23) with the matching conditions

$$\Theta_2(X,\infty) = 0 \tag{60a}$$

and

$$\frac{\partial \Psi_2}{\partial Y}(X,\infty) = \frac{(1-\lambda^2)}{4} f_0(\infty) Y X^{\frac{\lambda-3}{2}} - \frac{D\kappa}{\pi X} \tag{60b}$$

where equation (60*b*) is obtained by matching with equations (47*b*) and (59*b*). It can be shown that the solution for Ψ_2 and Θ_2 are of the form

$$\Psi_2(X,Y) = X^{-\frac{\lambda+1}{2}} f_2(\eta) \tag{61a}$$

$$\Theta_2(X,Y) = g_2(\eta)/X \tag{61b}$$

where $f_2(\eta)$ and $g_2(\eta)$ are determined from

$$f_2'' - g_2' = \frac{1-\lambda}{2}\left[\frac{1+\lambda}{2} f_0 + \frac{3\lambda-1}{2}\eta f_0' + \frac{\lambda-1}{2}\eta^2 f_0''\right] \tag{62}$$

$$g_2'' + \frac{\lambda+1}{2} f_0 g_2' + f_0' g_2 = \lambda g_0 f_2' + \frac{\lambda+1}{2} f_2 g_0'$$

$$+ (1-\lambda)\left[\frac{\lambda-1}{4}\eta^2 g_0'' + \left(\frac{5\lambda-3}{4}\right)\eta g_0' + \lambda g_0\right] + D^2\frac{(\lambda-1)}{2} f_1' g_1 \tag{63}$$

subject to the boundary conditions

$$f_2(0) = g_2(0) = 0 \tag{64a,b}$$

$$\eta \to \infty: f_2'(\infty) = \frac{1-\lambda^2}{4} f_0(\infty)\eta - \frac{D\kappa}{\pi}, \; g_2(\infty) = 0 \tag{65a,b}$$

Eigenvalues and Eigenfunctions

Following the procedures described by Chang and Cheng [9], the solution of the eigenfunctions Ψ_m and Θ_m associated with the inner expansions as determined from equations (24–27) are

$$\Psi_m = X^{\left(\frac{\lambda+1}{2}\right)(1-\alpha_m)} f_m(\eta) \tag{66}$$

$$\Theta_m = X^{\lambda-\left(\frac{\lambda+1}{2}\right)\alpha_m} g_m(\eta) \tag{67}$$

where f_m and g_m are determined from

$$f_m''' = g_m' \tag{68}$$

$$g_m'' + \frac{\lambda+1}{2} f_0 g_m' - \left(\lambda - \frac{\lambda+1}{2}\alpha_m\right) f_0' g_m = \lambda g_0 f_m'$$

$$- \frac{\lambda+1}{2}(1-\alpha_m) g_0' f_m \tag{69}$$

subject to the boundary conditions

$$f_m(0) = g_m(0) = 0 \tag{70a,b}$$

$$f_m'(\infty) = g_m(\infty) = 0 \tag{71a,b}$$

As in the classical boundary layer theory [2, 4], it will now be shown the Ψ_{0X} *and* Θ_{0X} turn out to be one of the eigenfunctions. To show this, we first differentiate equations (14) and (15) with respect to X. The resulting equation is identical to equations (24) and (25) if $\Psi_m = \Psi_{0X}$ and $\Theta_m = \Theta_{0X}$. Thus

$$\Psi_m = \Psi_{0X} = \frac{X}{2}^{\frac{\lambda-1}{2}}[(\lambda+1)f_0 + (\lambda-1)\eta f_0'] \tag{72a}$$

$$\Theta_m = \Theta_{0X} = X^{\lambda-1}\left[\lambda g_0 + \frac{\lambda-1}{2}\eta g_0'\right] \tag{72b}$$

With the aid of equations (41) and (42), it can be shown that equations (72) satisfy the boundary conditions (26) and (27) only if $\lambda = 0$. It follows from equations (72) that for $\lambda = 0$

$$\Psi_m = (f_0 - \eta f_0')/2\sqrt{X} \tag{73a}$$

$$\Theta_m = -\eta g_0'/2X \tag{73b}$$

Comparing equations (73) with equations (66) and (67) with $\lambda = 0$, one obtains

$$\alpha_m = 2 \tag{74a}$$

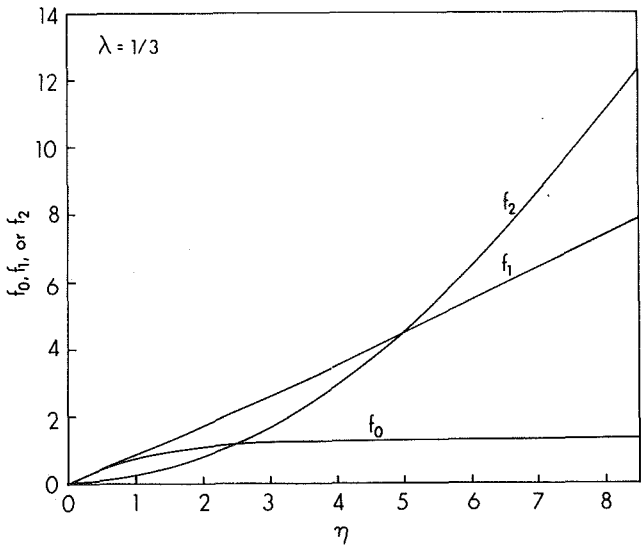

Fig. 1 f_i versus η for $\lambda = 1/3$

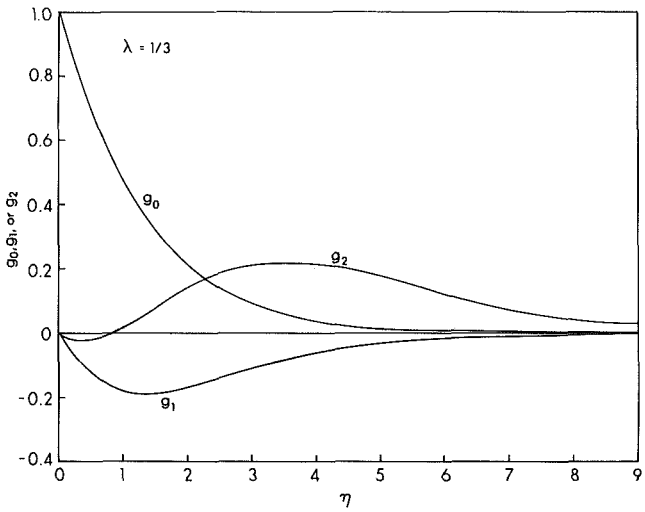

Fig. 2 g_i versus η for $\lambda = 1/3$

$$f_m = (f_0 - \eta f_0')/2 \tag{74b}$$

$$g_m = -\eta g_0'/2 \tag{74c}$$

which are the eigenvalue and eigenfunctions for $\lambda = 0$. For other values of λ, the eigenvalues, α_m, and the eigenfunctions, f_m and g_m, must be found numerically from equations (68–72). Similar procedures can be used to show that although Ψ_{0Y} and Θ_{0Y} satisfy equations (24) and (25), they cannot satisfy the boundary conditions (26) and (27) and therefore are not eigenfunctions of the problem.

Numerical Results and Discussion

Eigenvalues. The eigenvalues α_m were determined numerically from equations (68) and (69) subject to boundary conditions (70) and (71) and with the normalization condition $f_m(\infty) = 1$. The numerical integration were carried out by the Runge-Kutta method which integrated from $\eta \to \infty$ backward to $\eta = 0$ at the wall. The results for the smallest eigenvalue for each selected value of λ is presented in Table 1.

Higher-Order Theories for the Stream Function and Temperature. Equations (12) with equations (35), (36), (49), and (61) give

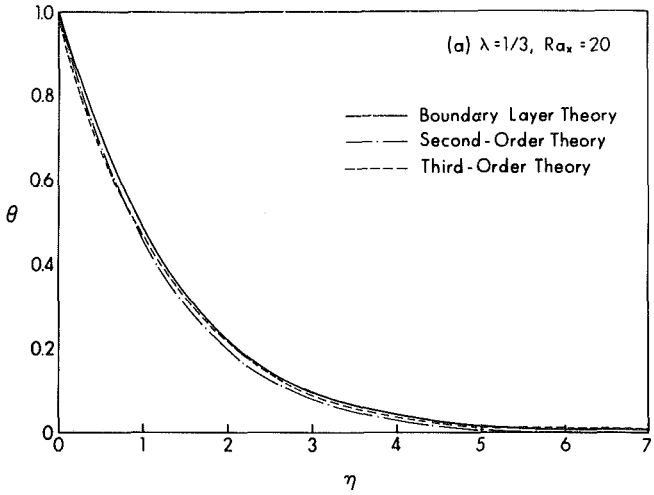

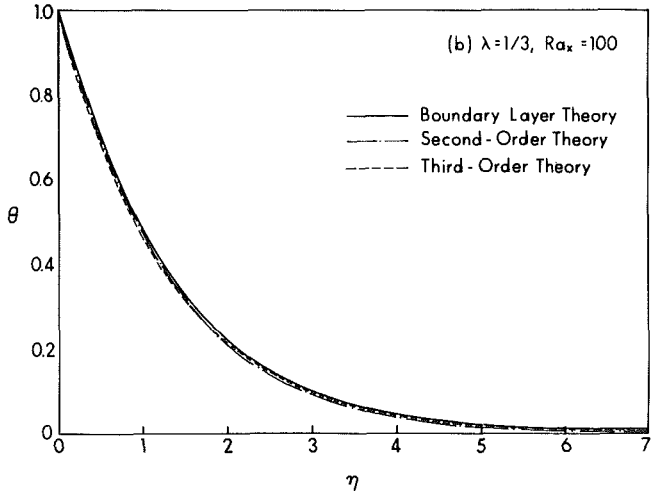

Fig. 3 Dimensionless Temperature Profiles for $\lambda = 1/3$: (*a*) $Ra_x = 20$ and (*b*) $Ra_x = 100$

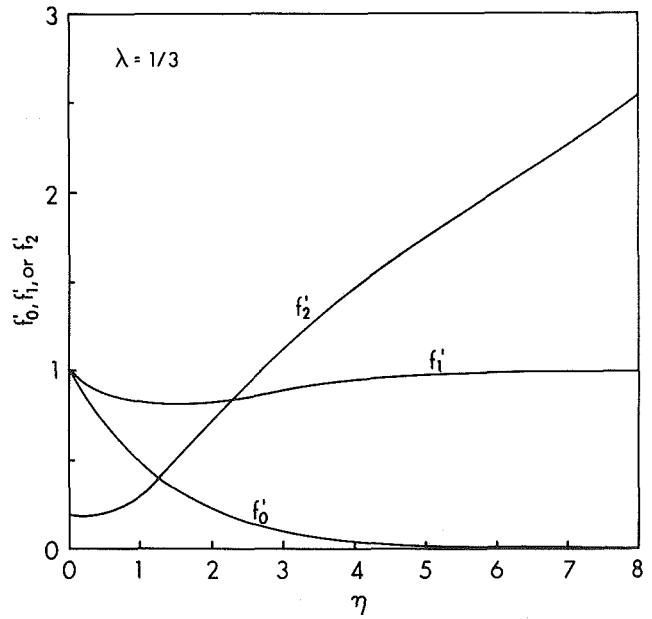

Fig. 4 f_i' versus η for $\lambda = 1/3$

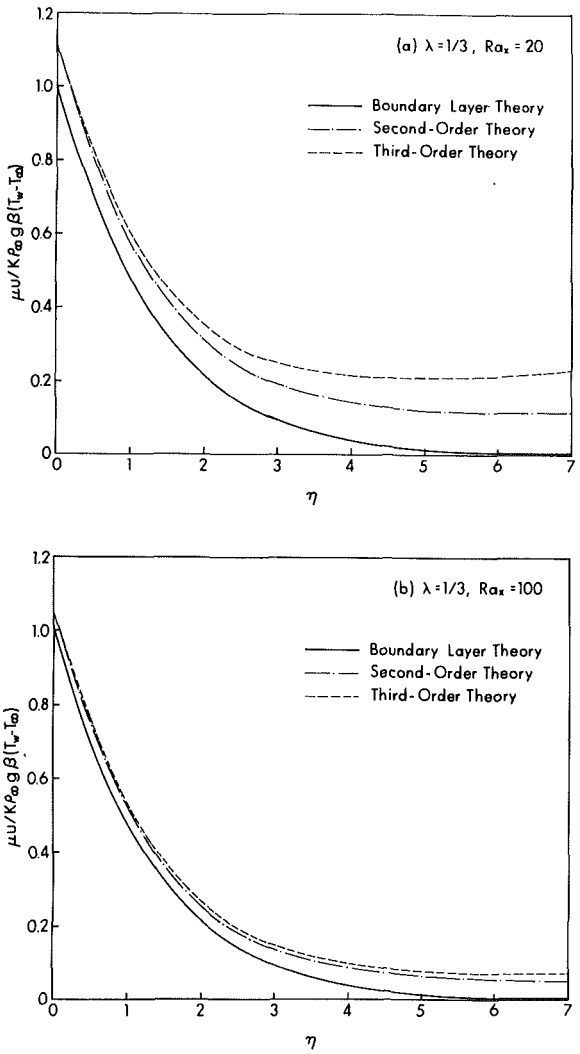

Fig. 5 Dimensionless Vertical Velocity Profile for $\lambda = 1/3$: (*a*) $Ra_x = 20$ and (*b*) $Ra_x = 100$

$$\psi=\epsilon\left[x^{\frac{\lambda+1}{2}} f_0(\eta)+\epsilon D f_1(\eta)+\epsilon^2 x^{\frac{\lambda+1}{2}} f_2(\eta)\right.$$
$$\left.+\epsilon^{\alpha_m} A_m x^{\left(\frac{\lambda+1}{2}\right)(1-\alpha_m)} f_m(\eta)+0(\epsilon^n)\right] \tag{75a}$$

$$\theta=x^{\lambda} g_0(\eta)+\epsilon D x^{\frac{\lambda+1}{2}} g_1(\eta)+\epsilon^2 g_2(\eta)/x$$
$$\left.+\epsilon^{\alpha_m} B_m x^{\lambda-\left(\frac{\lambda+1}{2}\right)\alpha_m} g_m(\eta)+0(\epsilon^n)\right] \tag{75b}$$

where $D=0$ for $\lambda=0$. Note that the ordering of the term $0(\epsilon^{\alpha_m})$ depends on the value of α_m which in turn depends on λ as indicated in Table 1. The constants A_m and B_m in equations (75) cannot be determined without a detailed analysis of the leading edge effects [10, 11], which are beyond the scope of the present paper. As a result, the perturbation series is truncated to the term $0(\epsilon^n)$ where n is an integer with $n \leq \alpha_m$. Thus

(*i*) for $\lambda = -1/3$ (with $\alpha_m = 1$)

$$\psi=\epsilon[x^{1/3} f_0(\eta)+0(\epsilon)] \tag{76a}$$
$$\theta=x^{-1/3} g_0(\eta)+0(\epsilon) \tag{76b}$$

(*ii*) for $\lambda=0$ (with $\alpha_m=2$)

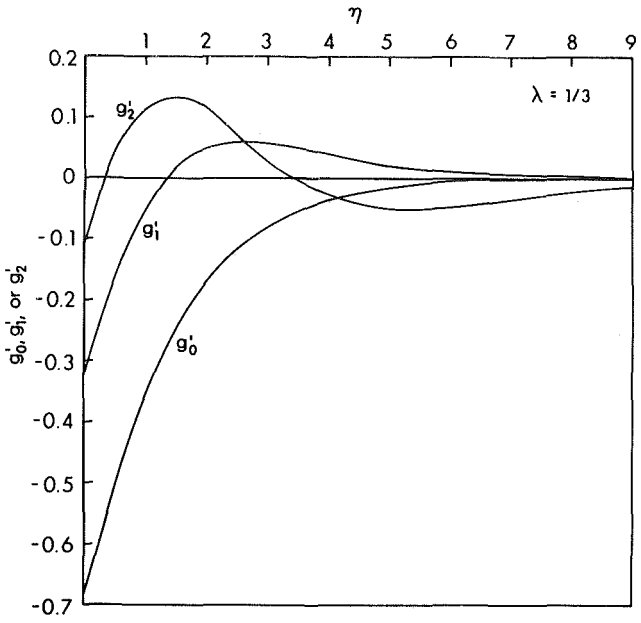

Fig. 6 g_i' versus η for $\lambda = 1/3$

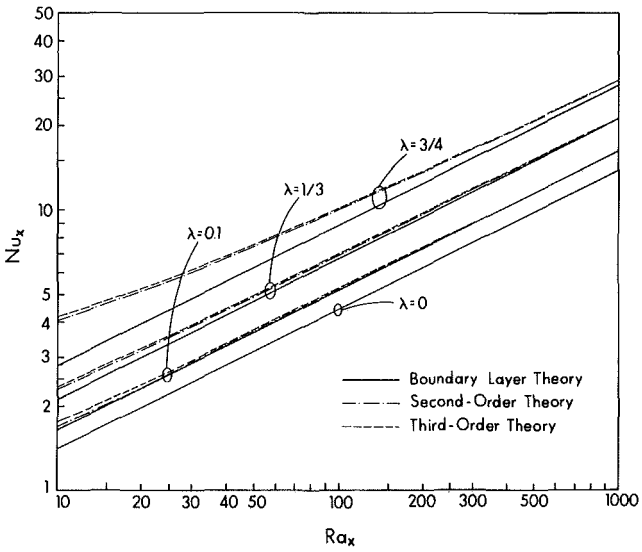

Fig. 7 Local Nusselt number versus local Rayleigh number for selected values of λ

$$\psi=\epsilon[x^{1/2} f_0(\eta)+0(\epsilon^2)] \tag{77a}$$
$$\theta=g_0(\eta)+0(\epsilon^2) \tag{77b}$$

(*iii*) for $0<\lambda<1$ (with $\alpha_m>2$)

$$\psi=\epsilon\left[x^{\frac{\lambda+1}{2}} f_0(\eta)+\epsilon D f_1(\eta)+\epsilon^2 x^{-\frac{\lambda+1}{2}} f_2(\eta)+0(\epsilon^n)\right] \tag{78a}$$

$$\theta=x^{\lambda} g_0(\eta)+\epsilon D x^{\frac{\lambda-1}{2}} g_1(\eta)+\epsilon^2 x^{-1} g_2(\eta)+0(\epsilon^n) \tag{78b}$$

where $n \leq \alpha_m$

Equations (77) show that for $\lambda = 0$ the boundary layer theory is actually accurate to the second order.

The numerical results of the first-order perturbation functions $f_0(\eta)$ and $g_0(\eta)$ for selected values of λ have been obtained by Cheng and Minkowycz [7]. The higher-order

perturbation functions (f_1, f_2, g_1, and g_2) as given by equations (50–52) and by equations (62–65) for selected values of λ were numerically integrated backward from $\eta \to \infty$ to $\eta = 0$ (at the wall) by means of the Runge-Kutta method. Table 1 summarizes the results of $g_i'(0)$, $f_2'(0)$, and $f_0(\infty)$ for selected values of λ. Because of space limitations, only the results for $\lambda = 1/3$ are displayed in Figs. 1–6.

Figures 1 and 2 show the perturbation functions of f_i and g_i ($i=0, 1, 2$) versus η for the case of $\lambda = 1/3$. It is noted that the functions $f_i(\eta)$ are all positive with $f_0(\infty)$ approaching a constant while $f_1(\infty)$ increasing linearly with η, as dictated by equations (42*b*) and (52*b*). On the other hand, while the function $g_0(\eta)$ is positive for all η, the functions g_1 and g_2 are negative near the wall (see Fig. 2). This implies that the temperature distribution near the wall is smaller for higher-order theory resulting in a steeper temperature gradient at the wall. The dimensionless temperature distribution, θ, as given by the higher-order theory is plotted in Figs. 3(*a*) and 3(*b*) for $\mathrm{Ra}_x = 20$ and $\mathrm{Ra}_x = 100$, respectively. It is noted that the magnitude of the higher-order corrections in temperature is small even at small Rayleigh number (i.e., $\mathrm{Ra}_x = 20$).

Higher-Order Theory for Velocity and Surface Heat Flux

Higher-order theory for the vertical velocity and surface heat flux can be obtained by differentiating equations (75) with respect to y, which gives

$$\frac{\mu u}{K\rho_\infty g\beta(T_w - T_\infty)} = \begin{cases} f_0'(\eta) + 0(\epsilon), & \text{for } \lambda = -1/3 \quad (79a) \\ f_0'(\eta) + 0(\epsilon^2), & \text{for } \lambda = 0 \quad (79b) \\ f_0'(\eta) - \dfrac{1}{\sqrt{\mathrm{Ra}_x}}\left(\dfrac{\lambda+1}{2}\right)\cot\left[\dfrac{\lambda+1}{2}\pi\right] f_0(\infty) f_1'(\eta) \\ \quad + \dfrac{1}{\mathrm{Ra}_x} f_2'(\eta) + 0(\epsilon^{\alpha_m}), & \text{for } 0 < \lambda < 1 \quad (79c) \end{cases}$$

$$\frac{\mathrm{Nu}_x}{\sqrt{\mathrm{Ra}_x}} = -\begin{cases} g_0'(0) + 0(\epsilon), & \text{for } \lambda = -1/3 \quad (80a) \\ g_0'(0) + 0(\epsilon^2), & \text{for } \lambda = 0 \quad (80b) \\ g_0'(0) - \dfrac{1}{\sqrt{\mathrm{Ra}_x}}\left[\left(\dfrac{\lambda+1}{2}\right)\cot\left(\dfrac{\lambda+1}{2}\pi\right) f_0(\infty) g_1'(0)\right] \\ \quad + \dfrac{1}{\mathrm{Ra}_x} g_2'(0) + 0(\epsilon^{\alpha_m}), & \text{for } 0 < \lambda < 1 \quad (80c) \end{cases}$$

where $\mathrm{Nu}_x = qx/k(T_w - T_\infty)$ is the local Nusselt number.

The perturbation functions f_1' ($i=0,1,2$) for the case of $\lambda = 1/3$ are plotted in Fig. 4, which shows that their values are positive for the whole range of η. It is relevant to note that $f_1'(\eta)$ for this case is almost constant for the whole range of η, indicating that the entrainments from the outer irrotational flow induce an almost constant vertical velocity across the boundary layer. Thus the higher-order effects increase the vertical velocity in the boundary layer. This is shown in Figs. 5(*a*) and 5(*b*) for the case of $\mathrm{Ra}_x = 20$ and 100, respectively. As expected the magnitude of the higher-order corrections decreases as the Rayleigh number is increased. In comparison of Figs. 3 and 5, it is apparent that the higher-order terms have a stronger effect on the velocity than the temperature distribution.

The corresponding perturbation functions, g_i' ($i=0,1,2$), are plotted in Fig. 6 which shows that the temperature gradient at the wall (at $\eta = 0$) and its higher-order corrections are negative (see also Table 2). The steeper temperature gradient at the wall given by the second- and the third-order theory is due to the increased vertical velocity within the boundary layer. As shown in Fig. 7, this leads to an increase in surface heat flux. For $0 \le \lambda \le 1/3$, the boundary layer theory is shown to be accurate even at small Rayleigh numbers. The boundary layer theory becomes less accurate as λ is increased from $\lambda = 1/3$.

It is interesting to observe the differences and similarities of the higher-order boundary layer theory between a Darcian fluid (as obtained in the present paper) and that of a Newtonian fluid [1–3, 10–12]. In contrast to the Navier-Stokes equations, the viscous effect along the impermeable heated surface is neglected in the Darcy law. In view of this difference, it is rather surprising to find that higher order theory for free convection adjacent to a semi-infinite vertical plate in a Newtonian fluid and a Darcian fluid has much in common. For example, consider the case of an isothermal plate in a Newtonian and a Darcian fluid. The second-order correction to temperature in the boundary layer is due to entrainments from the outer edge of the boundary layer, which are found to be zero (i.e., $g_1(\eta) = \Theta_1(X,Y) = 0$ for $\lambda = 0$). Thus the expression for the local Nusselt number as obtained from the boundary layer theory is actually accurate to the second-order. In addition, for $\lambda = 0$, the eigensolutions in both cases turn out to be the x-derivative of the first-order solution. As in the Newtonian fluid, it is likely that a term of $0(\epsilon^2 \ln \epsilon)$ must be added in the inner expansion for $\lambda = 0$ if we should be interested in carrying out the complete solution for the third-order theory in the present problem. Note that in the classical case, the logarithmic terms are closely related to the behavior of the flow near the leading edge [11, 12]. The possible existence of the logarithmic terms and the details of the leading edge effect are beyond the scope of the present investigation.

Concluding Remarks

The problem of higher-order effects for Darcian free convection about a vertical heated plate with a power law variation of wall temperature is studied by the method of matched asymptotic expansions. The following conclusions may be drawn:

1 The boundary layer theory tends to underestimate the local Nusselt number. For $0 \le \lambda \le 1/3$, higher-order corrections in the local Nusselt number is small even at small Rayleigh numbers.

2 The effect of the entrainment from the outer irrotational flow along the edge of the boundary layer is of second-order. This effect induces a positive vertical velocity within the boundary layer, thus increases the local surface heat flux or the local Nusselt number.

3 The effects of streamwise heat conduction and the transverse pressure gradient are of third-order. The combined effect tend to further increase the vertical velocity within the boundary layer, resulting in a further increase in the local surface heat flux or the local Nusselt number.

4 The higher-order effects are stronger on the velocity than the temperature distribution. Their influence is more pronounced for $\lambda > 1/3$ and at smaller Rayleigh numbers.

Acknowledgments

This work was supported by the National Science Founsation through Grant No. MEA81-00437.

References

1 Yang, K. T., and Jerger, E. W., "First-Order Perturbations of Laminar Free-Convection Boundary Layers on a Vertical Plate," ASME *Journal of Heat Transfer*, Vol. 86, 1964, pp. 107–115.

2 Hieber, C. A., "Natural Convection Around a Semi-Infinite Vertical Plate: Higher-Order Effects," *International Journal of Heat and Mass Transfer*, Vol. 17, 1974, pp. 785–790.

3 Riley, D. S., and Drake, D. G., "Higher Approximations to the Free Convection Flow from a Heated Vertical Flat Plate," *Applied Sci. Res.*, Vol. 30, 1975, pp. 193–207.

4 Mahajan, R. L., and Gebhart, B., "Higher-Order Approximations to the Natural Convection Flow Over a Uniform Flux Vertical Surface," *International Journal of Heat and Mass Transfer*, Vol. 21, 1978, pp. 549–556.

5 Riley, N., "Free Convection From a Horizontal Line Source of Heat," *ZAMP*, Vol. 25, 1974, pp. 817–828.

6 Hieber, C . A., and Nash, E. J., "Natural Convection Above a Line Heat Source: Higher-Order Effects and Stability," *International Journal of Heat and Mass Transfer*, Vol. 18, 1975, pp. 1473–1479.

7 Cheng, P., and Minkowycz, W. J., "Free Convection About a Vertical Flat Plate Embedded in a Porous Medium with Application to Heat Transfer from a Dike," *J.G.R.*, Vol. 82, 1977, pp. 2040–2044.

8 Cheng, P., "Heat Transfer in Geothermal Systems," *Advances in Heat Transfer*, Vol. 14, 1978, pp. 1–105.

9 Chang, I-Dee, and Cheng, P., "Matched Asymptotic Expansion for Free Convection About an Impermeable Horizontal Surface in a Porous Medium," *International Journal of Heat and Mass Transfer*, Vol. 26, 1983, pp. 163–174.

10 Stewartson, K., *The Theory of Laminar Boundary Layers in Compressible Fluids*, Sec. 3.5, Oxford University Press, Oxford, 1964.

11 Messiter, A. F., and Linan, A., "A Vertical Plate in Laminar Free Convection: Effects of Leading and Trailing Edges and Discontinuous Temperature," *ZAMP*, Vol. 27, 1976, pp. 633–651.

12 Stewartson, K., "On Asymptotic Expansions in the Theory of Boundary Layers," *J. Math. Phys.*, Vol. 36, 1957, pp. 173–191.

Natural Convection in a Rectangular Porous Cavity With Constant Heat Flux on One Vertical Wall

V. Prasad[1]

F. A. Kulacki
Mem. ASME

Department of Mechanical and Aerospace Engineering, University of Delaware, Newark, Del. 19711

Numerical solutions for two-dimensional, steady, free convection are presented for a rectangular cavity with constant heat flux on one vertical wall, the other vertical wall being isothermally cooled. The horizontal walls are insulated. Results are presented in terms of streamlines and isotherms, local and average Nusselt numbers at the heated wall, and the local heat flux at the cooled wall. Flow patterns are observed to be quite different from those in the case of a cavity with both vertical walls at constant temperatures. Specifically, symmetry in the flow field is absent and any increase in applied heat flux is not accompanied by linearly proportional increase in the temperature on the heated wall. Also, for low Prandtl number, the heat transfer rate based upon the mean temperature difference is higher as compared to experimental results for the isothermal case. Heat transfer results, further, indicate that the average Nusselt number is correlated by a relation of the form $\overline{Nu} = \text{constant } Ra^{*m} A^n$, *where* Ra^* *is the Rayleigh number and* A *the height-to-width ratio of the cavity.*

Introduction

Natural convection in a porous medium has several important geophysical and engineering applications. These include regenerative heat exchangers containing porous materials, high performance insulation for building and cold storage, solar power collection, underground spread of pollutants, and convection in the earth's crust [1, 2, 3]. Natural convection effects on heat transfer in a differentially heated rectangular porous cavity, with top and bottom walls insulated, is of fundamental interest in each of these areas. Several investigators [3–16, 22, 27] have presented analytical and experimental results for the case when both the vertical walls are at constant temperature. Analytical work includes numerical solutions, boundary layer solutions, integral analyses, and series solutions. Based on these past studies, various correlations, covering a wide range of Rayleigh number and cavity height-to-width (aspect) ratios, have been presented for heat transfer coefficients [3, 5, 9, 12, 14].

The purpose of the present paper is to examine the effects of free convection in a vertical porous cavity when a constant heat flux is applied at one vertical wall, while the other vertical wall is maintained at a constant temperature and the top and bottom are insulated (Fig. 1). The problem has been analyzed numerically for two-dimensional flow via finite difference solution to the governing equations. Flow patterns obtained over a wide range of Rayleigh number and aspect ratio exhibit a distinct difference from those when both the vertical walls are at constant temperatures. The effects of Rayleigh number and aspect ratio are qualitatively similar, but correlations for average Nusselt number are different from those in constant temperature case.

For two-dimensional, steady free convection in a porous media where Darcy's law holds, the governing differential equations [1, 18] are

$$\frac{\partial u}{\partial x} + \frac{\partial v}{\partial y} = 0 \tag{1}$$

$$\frac{\partial p}{\partial x} + \frac{\mu}{K} u = 0 \tag{2}$$

$$\frac{\partial p}{\partial y} + \rho g + \frac{\mu}{K} v = 0 \tag{3}$$

$$\nabla \cdot (\bar{V} T) = \alpha \nabla^2 T \tag{4}$$

$$\rho = \rho_r [1 - \beta (T - T_r)] \tag{5}$$

Here, it has been assumed that the fluid properties are constant, except for the density variation in producing the buoyancy force. Viscous drag and inertia terms are neglected because their magnitudes are of small order compared to other terms. Thus, velocity slip at the bounding surfaces is permitted. Also, heat transfer by radiation is assumed to be small compared to conduction and convection, and hence is neglected in the formulation of the problem.

Using dimensionless variables, equations (1–5) are transformed to the stream function form

$$A^2 \frac{\partial^2 \psi}{\partial X^2} + \frac{\partial^2 \psi}{\partial Y^2} = \mathrm{Ra}^* A \frac{\partial \theta}{\partial X} \tag{6}$$

$$\frac{\partial}{\partial Y}\left(\theta \frac{\partial \psi}{\partial X}\right) - \frac{\partial}{\partial X}\left(\theta \frac{\partial \psi}{\partial Y}\right) = \frac{\partial^2 \theta}{\partial X^2} + \frac{1}{A^2} \frac{\partial^2 \theta}{\partial Y^2} \tag{7}$$

where Ra^* is the Rayleigh number defined in terms of the heat flux applied to the vertical wall, and A is the aspect ratio, L/D.

The relevant hydrodynamic boundary conditions for no mass flux through the boundaries [14, 15] and the thermal boundary conditions are

$$\psi = 0, \frac{\partial \theta}{\partial X} = -1 \text{ at } X = 0 \tag{8}$$

$$\psi = 0, \theta = 0 \qquad \text{at } X = 1 \tag{9}$$

$$\psi = 0, \frac{\partial \theta}{\partial Y} = 0 \quad \text{at } Y = 0 \text{ and } Y = 1 \tag{10}$$

Numerical Method

Finite difference equations are derived for equations (6)

Contributed by the Heat Transfer Division for publication in JOURNAL OF HEAT TRANSFER. Manuscript received by the Heat Transfer Division June 8, 1982.

[1] Present address: Mechanical Engineering Department, Clemson University, Clemson, S.C. 29631.

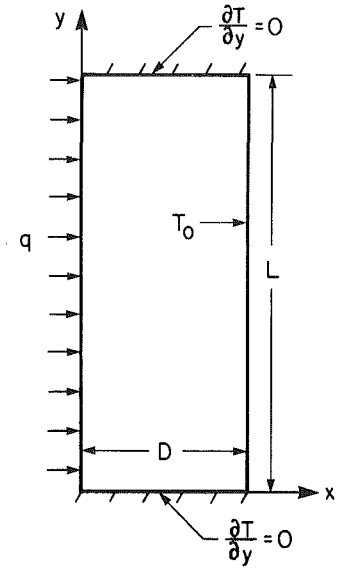

Fig. 1 Vertical cavity, coordinate system, and thermal boundary conditions

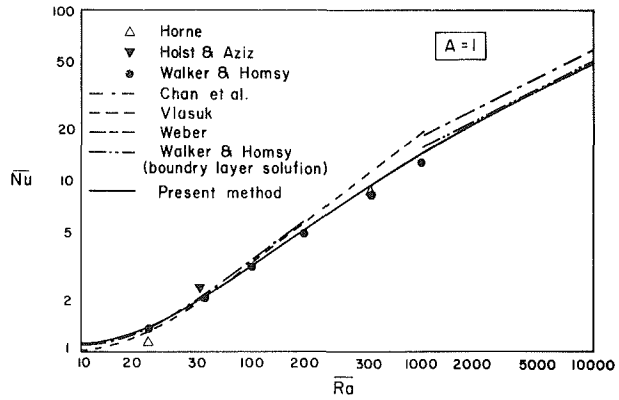

Fig. 2 Results obtained by various workers for a square cavity with side walls maintained at constant temperatures

and (7) by integration over finite area elements. This approach ensures that the conservation laws are obeyed over arbitrarily large or small portions of the domain and lends itself better to physical interpretation [20, 21]. Integration of the equations in a way as outlined by Gosman et al. [20] introduces upwind differences for the convective terms in the energy equation and is equivalent to second upwind differencing [21]. The successive substitution formula derived in this way satisfies the convergence criterion and is quite stable for many circumstances [20]. The method has been widely used by investigators to solve natural convection problems and is well documented in literature [20].

For solving the simultaneous algebraic equations thus obtained, a point iterative method is used which makes use of the new values as soon as they are available. Boundary conditions for the specified temperature gradients, to be consistent with the integral formulation for the system, are applied using two-point formula for the derivative.

To test the present method of formulation and the finite difference scheme, calculations were run for the case where both the vertical walls are at constant temperatures. Various combinations of mesh sizes were used to select one which give better accuracy and requires less computational time. It was observed that the use of varying grids with fine mesh near the walls is advantageous and more reasonable for high Rayleigh numbers, owing to boundary layers on the vertical walls and significant changes in the magnitude and direction of velocities near the horizontal walls. To make a proper choice of mesh sizes, computations were done with 11×11 to 31×31 uniform and nonuniform grid fields, for $A = 1$. It was observed that a 21×21 mesh is a reasonably good choice. This has resulted in obtaining heat transfer results in excellent agreement with the reported values (Fig. 2)

For $\overline{Ra} < 200$, the present results agree well with the numerical solutions of Chan et al. [5] and Vlasuk [7]. The agreement with Walker and Homsy's solution, using regular expansion in $\overline{Ra}$, is quite good for $\overline{Ra} \leq 1000$, though Valsuk's numerical results are a little higher for $\overline{Ra} > 200$. Similarly, the comparison with Walker and Homsy's boundary layer

Nomenclature

A = aspect ratio, L/D
c = specific heat of fluid at constant pressure, J/kg-K
D = width of porous cavity, m
g = acceleration due to gravity, m/s^2
h = heat transfer coefficient, W/m^2-K
$\bar{h}$ = average heat transfer coefficient on heated wall, W/m^2-K
K = permeability of porous medium, m^2
k_m = effective thermal conductivity of the saturated porous medium, W/m-K
L = height of porous cavity, m
n = direction perpendicular to wall
Nu_y = local Nusselt number on heated wall, hy/k_m
$\overline{Nu}$ = average Nusselt number, $\bar{h}D/k_m$
p = pressure, Pa
Pr = Prandtl number, ν/α
q = heat flux at $x = 0$, W/m^2
q_L = local heat flux at cooled wall, $x = D$, W/m^2
Ra* = Rayleigh number, $(\rho g \beta K q D^2)/(\mu \alpha k_m)$
$\overline{Ra}$ = Rayleigh number, $(\rho g \beta K D)(T_{hm} - T_0)/(\mu\alpha)$, for present case; and $(\rho g \beta K D \Delta T)/(\mu\alpha)$, for constant temperature walls
T = temperature, K
T_0 = temperature at cooled wall, K
ΔT = temperature difference across cavity for constant temperature wall case.
u = fluid velocity in x-direction, $(-\alpha/D)(\partial\psi/\partial Y)$
v = fluid velocity in y-direction, $(\alpha L/D^2)(\partial\psi/\partial X)$
$\bar{V}$ = velocity vector
x,y = Cartesian coordinates, m
X = dimensionless distance on x-axis, x/D
Y = dimensionless distance on y-axis, y/L

Greek Symbols

α = thermal diffusivity of porous medium, $k_m/\rho c$
β = isobaric coefficient of thermal expansion of fluid, K^{-1}
θ = dimensionless temperature, $(T - T_0)/(qD/k_m)$
μ = dynamic viscosity of fluid, kg/m-s
ν = kinematic viscosity of fluid, m^2/s
ρ = density of fluid, kg/m^3
ψ = stream function

Subscripts

h = heated wall
m = mean value
r = reference point for Eq. (5)
W = wall
y = local value on vertical wall
max = maximum value

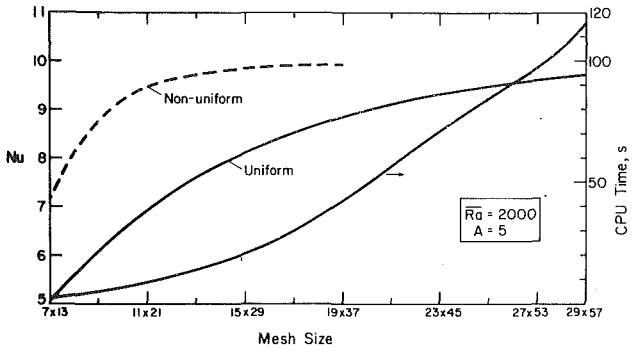

Fig. 3 Effects of mesh size on Nusselt number and CPU time, for $\overline{Ra} = 2000$, $A = 5$

solution [14] seems to be quite favorable for $\overline{Ra} > 1000$. At $\overline{Ra} = 10{,}000$ the present value is only 3 percent lower than theirs. This agreement at high $\overline{Ra}$, particularly with boundary layer solutions, is encouraging and shows that the solution procedure is acceptable.

For the present problem, a 21 × 21 grid was used for $A = 1$, low Ra*, and a nonuniform grid was used for $Ra^* \geq 500$. For a high aspect ratio, a proper choice of mesh size depends upon the values of Ra* and A. For small Rayleigh numbers ($Ra^* < 500$), a grid of 11 × 15 yields as accurate results (within 2.5 percent) as a grid of 15 × 17 yields for $Ra^* = 10{,}000$, for $A = 5$. In general, the grid sizes selected for various combinations of Ra* and A are based upon a good compromise between the accuracy and computation time. For all test cases, the selected mesh size yields Nusselt numbers within 2 percent of the values obtained by using very fine grid sizes (see Fig. 3). The following are the grid fields used for the several aspect ratios considered in the present work.

A	Grid field
0.5	31 × 21
1	21 × 21
>1	11 × 15 to 15 × 31

A detailed discussion on mesh size is presented in [22].

For large Rayleigh number, the contribution of the source term in the momentum equation, equation (6), becomes larger, and hence convergence is affected. Use of successive underrelaxation for the stream function and overrelaxation for the temperature helps in overcoming this difficulty. For low Rayleigh number, suitable values for the relaxation parameters for ψ and θ vary between 0.7 and 1.0, and 1.5 and 1.9, respectively, whereas for high Ra*, these vary between 0.5 and 0.7 for ψ, and 1 and 1.4 for θ.

The upwind differencing used here is known to introduce damping by adding false diffusion to the solution. This effect in the present case is of very small order as compared to the true diffusion, owing to the upwind scheme being used for only one equation (the energy equation) and the small ratio of false to true diffusion. As suggested by Gosman et al. [20], this ratio may be approximated by

$$\epsilon \simeq 0.36 \left(\frac{VD}{\alpha}\right)\left(\frac{h}{D}\right) \sin(2\phi) \qquad (11)$$

where V is the velocity, h the grid size, and ϕ is the angle the streamlines (or velocity vectors) make with coordinate system. With nonuniform grids where V is large (near the walls), h and sin (2ϕ) are very small (streamlines almost parallel to walls), and vice versa (in the core). This always leads to $\epsilon << 1$.

For the present problem, 100 to 300 iterations are sufficient to satisfy an iterative convergence criterion of 0.1 percent for both ψ and θ, which required a CPU time of 20 s to 90 s on a DEC-10 computer. It may be mentioned here that the number of iterations required in the present case is 1.5 to 2 times greater than those required for an isothermal heated wall problem, for the same grid size used in both the cases. To check the accuracy of the results, an overall energy balance has been used for the system. This energy balance compares heat transfer at $x = D$ to input at $x = 0$. Generally energetic closure is achieved to within 3 percent for $A \geq 1$ and to within 4 percent for $A = 0.5$. At $x = 0$, agreement between the applied heat transfer rate and the heat transfer rate into the porous media is within 0.05 percent.

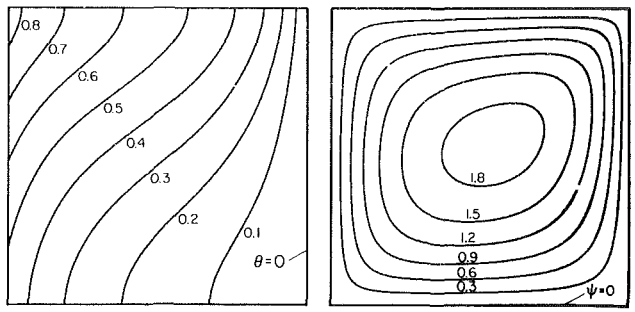

Fig. 4 Isotherms and streamlines for a porous cavity for $Ra^* = 50$ and $A = 1$

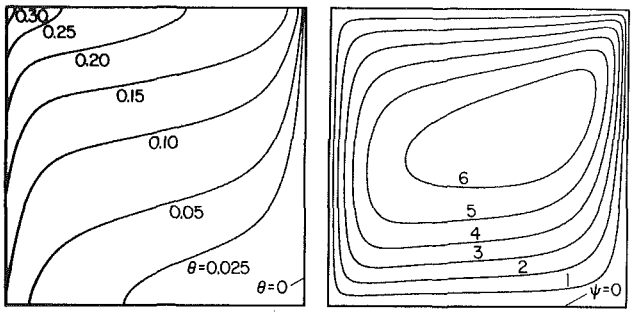

Fig. 5 Isotherms and streamlines for a porous cavity for $Ra^* = 1000$ and $A = 1$

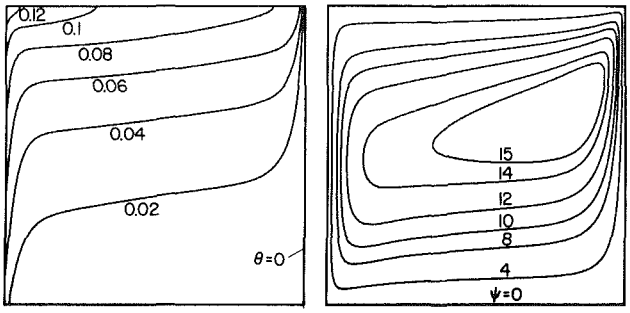

Fig. 6 Isotherms and streamlines for a porous cavity for $Ra^* = 10{,}000$ and $A = 1$

Results and Discussion

Computations were conducted for a wide range of Rayleigh number, $10 \leq Ra^* \leq 10{,}000$, with aspect ratios from 0.5 to 50. Flow patterns and temperature fields for some typical values of Rayleigh number and aspect ratio are presented in Figs. 4–7. Compared to the case of constant temperatures at both vertical walls, temperature fields in the present case are quite different. Here, isotherms for any size of cavity start either from the heated wall or from the bottom and end at the top wall. Similar isotherm patterns have been reported for free convection in a nonporous vertical cavity by Said and Trupp

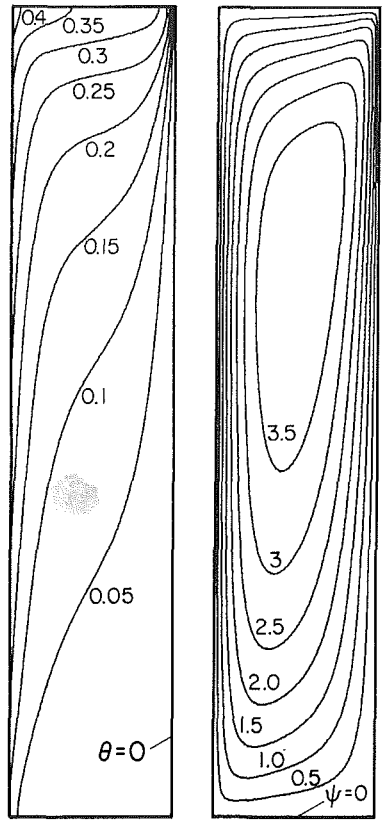

Fig. 7 Isotherms and streamlines for a porous cavity for Ra* = 1000 and $A = 5$

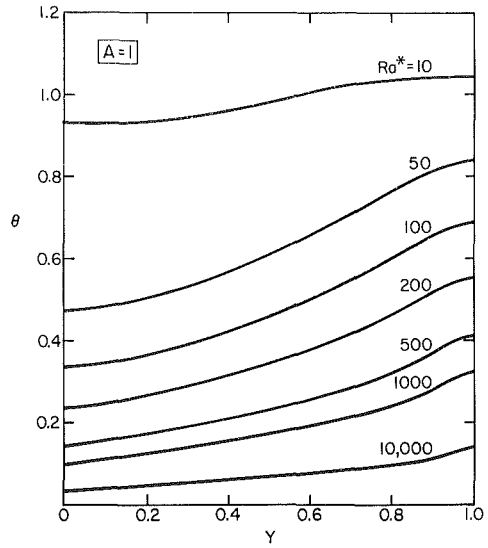

Fig. 8 Temperature distribution on the heated wall for a porous cavity with $A = 1$

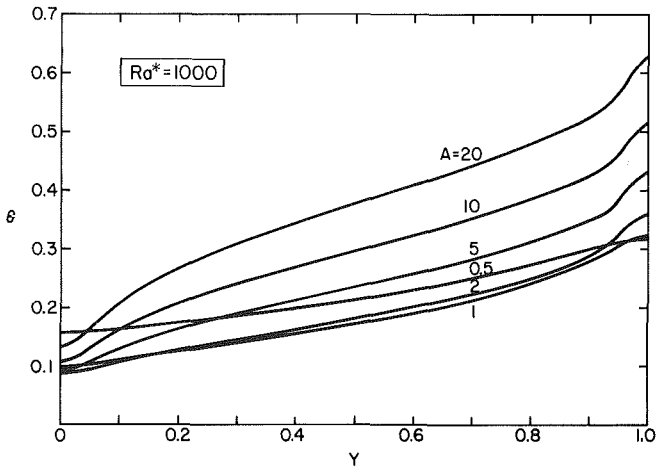

Fig. 9 Temperature distribution on the heated wall for several aspect ratios for Ra* = 1000

[23] and Balvanz and Kuehn [24], though no adverse temperature gradients or "S"-shaped isotherms [23] are observed for the present case. This change in the temperature field brings a noticeable change to the flow patterns near the heated wall as compared to those for the cavity with isothermal vertical walls [5]. The thermal boundary layer thickness increases upward on the hot wall and downward on the cold wall. Though the velocity boundary layer thickness on the cold wall increases in the same way as for the isothermal case on the heated wall, the growth is different and is largely due to the change in buoyancy effect. Streamlines close to the heated wall are observed to run parallel to the wall over significantly large portion of its extent. This behavior becomes more prominent as the aspect ratio is increased (Fig. 7). Flow patterns reported for nonporous cavities exhibit a very similar qualitative behavior [23, 24]. Further, owing to the strong boundary layer flow on the cooled wall, a shift in streamlines towards the right-hand top corner is observed.

As expected, the temperature and velocity fields are strong functions of Rayleigh number and aspect ratio. As Ra* is increased (Figs. 4 to 6), isotherms shift toward the constant flux wall and left top corner, and streamlines move towards the top of the cold wall. This results in an asymmetric core flow. An increase in aspect ratio (Figs. 5 and 7) further pushes the isotherms towards the top of the heated wall, indicating a higher velocity near the upper boundary (e.g., compare streamline density at top and bottom of the cavity).

The temperature distribution at the heated wall is presented in Figs. 8 and 9. At large Ra*, the temperature profile becomes almost linear over most of the wall, except for a change near the top and bottom. The effect is more prominent for large aspect ratio (Fig. 9). The reasons for this appear to be low velocity in the top left corner and the insulated top wall. Also, the increase in aspect ratio is seen to reduce the flow near the bottom left corner (Fig. 7). This, along with the insulated bottom surface, changes the temperature profile significantly near the botton edge for large aspect ratio (Fig. 9).

As expected, the ratio of maximum temperature to the minimum temperature on the heated wall increases as the Rayleigh number and/or aspect ratio increases (Figs. 8 and 9). Though the dimensionless temperature is indirectly proportional to the applied heat flux, it is not reduced in the same proportion as the heat flux is increased. This is a result of higher velocities at high Rayleigh numbers.

The local Nusselt number on the heated wall in terms of the local temperature difference, $T_{hy} - T_0$, is given by

$$\mathrm{Nu}_y = A\,Y/\theta_{hy} \tag{12}$$

Values of Nu_y are plotted in Fig. 10 against dimensionless height for various values of Rayleigh number with $A = 1$. It can be seen that the local Nusselt number first increases and then drops near the top wall for Ra* > 100. By recalling the results for local temperature on the heated wall, one can see that the local Nusselt number directly reflects the variation of $\theta(Y)$. The maximum in the Nusselt number occurs at larger values of Y as Ra* is increased. However, it must always decrease at $Y = 1$, owing to lower convective velocities there. Similar behavior in the local Nusselt number is obtained when the aspect ratio is increased beyond unity.

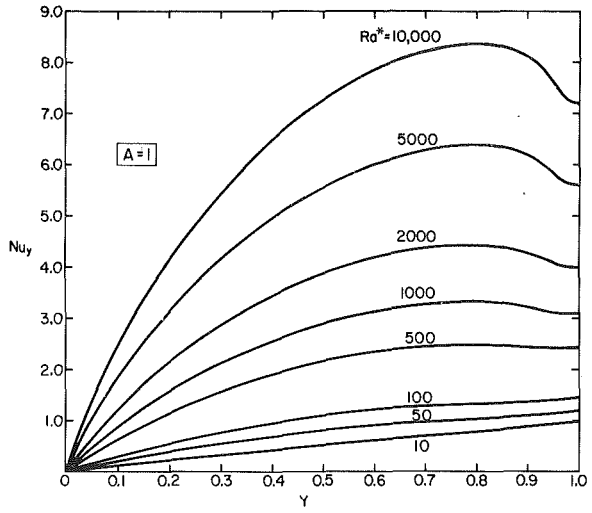

Fig. 10 Local Nusselt numbers at the heated wall for various Rayleigh numbers in a porous cavity with $A = 1$

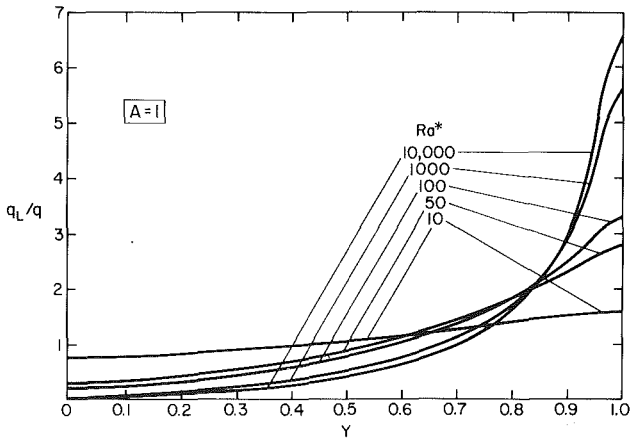

Fig. 11 Distribution of heat flux at the cooled wall for a porous cavity with $A = 1$

Another quantity of practical value is the local heat flux relative to the applied heat flux at the cooled wall, that is,

$$q_L/q = -\left.\frac{\partial\theta}{\partial X}\right|_{X=1}. \tag{13}$$

In Fig. 11, the distribution of local heat flux ratio is presented for a square cavity. It is seen that in the convection regime, a large percentage of heat is rejected along the upper 20 percent of the wall, with $q_L/q > 5$ for $\mathrm{Ra}^* > 1000$, close to the top. This behavior in the local heat flux is consistent with the observed higher convective flow in the upper right-hand corner of the cavity (Figs. 4 to 7).

Based upon the average temperature on the heated wall

$$\theta_m = \int_0^1 \theta(0, Y)dY \tag{14}$$

the mean Nusselt number is obtained as

$$\overline{\mathrm{Nu}} = \frac{1}{\theta_m} \tag{15}$$

This value of Nusselt number is important for design purposes because it directly gives the value of the average temperature, T_{hm}, for any applied heat flux which, in turn, gives the order of temperatures to be encountered for any particular values of Ra^* and A. The bound of temperature is then known. It has been observed that for $\mathrm{Ra}^* < 10{,}000$ and $0.5 < A < 50$, the ratio of the maximum temperature in the medium and the mean temperature on the heated wall, $\theta_{\max}/\theta_m$, never exceeds 2.0.

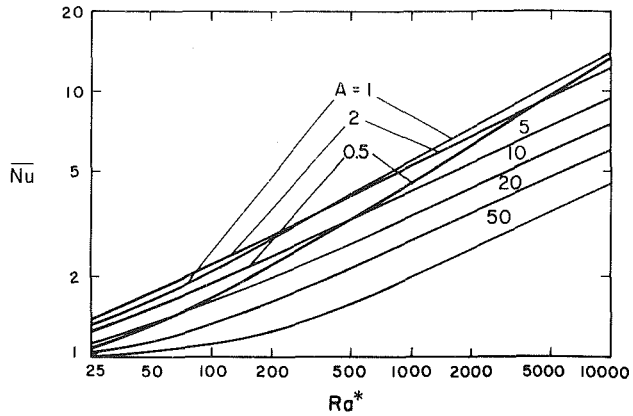

Fig. 12 Variation of average Nusselt number for various values of aspect ratio

The results for average Nusselt number, $\overline{\mathrm{Nu}}$, for the $25 < \mathrm{Ra}^* < 10^4$ and $0.5 < A < 50$, are presented in Fig. 12. In the so-called conduction regime, $\overline{\mathrm{Nu}}$ approaches unity for all values of aspect ratio. An increase in heat flux is always associated with the increase in average heat transfer coefficient. In the boundary layer regime, $\mathrm{Ra}^* > 500$, the mean Nusselt number can always be expressed by the relations of the form

$$\mathrm{Nu} = \text{Constant } \mathrm{Ra}^{*m} \tag{16}$$

for any particular value of the aspect ratio.

The dependence of mean Nusselt number on the aspect ratio is not easily stated. For a tall cavity, i.e., $A > 2$, the value of $\overline{\mathrm{Nu}}$ always decreases as A is increased. Conversely, for $A < 1$, any decrease in A below unity also decreases $\overline{\mathrm{Nu}}$. It appears that the mean Nusselt number attains a maximum value for $1 < A < 2$. For nonporous media, Said and Trupp [23] have observed a similar behavior and have reported that the Nusselt number reaches a maximum and remains constant for $1.4 < A < 2$. Chan et al. [5] report this maximum to occur at $A \approx 1.5$ for the constant temperature case. Based on these results, it appears that the case of aspect ratio close to unity requires additional and special consideration (see Bejan [17]).

With the present heat transfer results (Fig. 12), correlations for the mean Nusselt number can be expressed as

$$\overline{\mathrm{Nu}} = 0.312\ \mathrm{Ra}^{*0.413},\ A = 1,\ \mathrm{Ra}^* > 100 \tag{17}$$

$$\overline{\mathrm{Nu}} = 0.662\ \mathrm{Ra}^{*0.345} A^{-0.328},\ A > 2,\ \mathrm{Ra}^* \geq 200 \tag{18}$$

These correlations predict the mean Nusselt number within 2 percent of the data obtained from numerical computation.

The above correlations may be readily converted from Ra^* to $\overline{\mathrm{Ra}}$, the Rayleigh number based upon the mean temperature on the heated wall. Thus, equation (18) becomes

$$\overline{\mathrm{Nu}} = 0.533\overline{\mathrm{Ra}}^{0.527} A^{-0.501} \tag{19}$$

where $\mathrm{Ra}^* \geq 200$ and $A > 2$. It is worth mentioning, also, that equation (19) is quite close to the correlation given by Walker and Homsy [14]

$$\overline{\mathrm{Nu}} = (0.51 \pm 0.01)\overline{\mathrm{Ra}}^{0.5} A^{-0.5} \tag{20}$$

for isothermal case. Owing to the variation of temperature on the heated wall, this agreement between equations (19) and (20) is considered fortuitous.

Since no experimental or analytical results are available for the problem considered here, a direct comparison is not possible. To analyze the difference between the isothermal vertical walls case and present one, a comparison with the results of Walker and Homsy [14], Weber [12], and Seki et al.

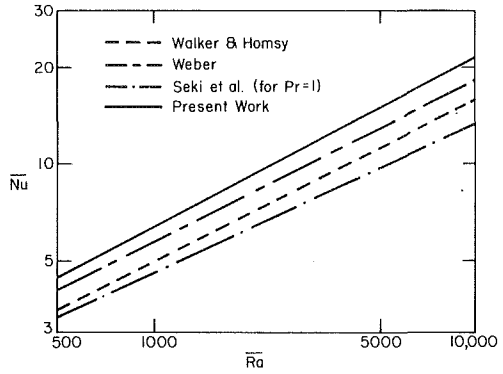

Fig. 13 Present heat transfer results compared with the results for the isothermal case, for $A = 10$

[3] is presented. For tall cavities ($A > 2$), the present results for Nu are 8 percent higher than Weber's results for $\overline{Ra} = 500$. This difference increases as $\overline{Ra}$ increases, and for $\overline{Ra} = 10{,}000$, the present results are 15 percent higher. Compared to Walker and Homsy's results, the differences are 20 percent and 26 percent, respectively. With respect to the work of Seki et al. [3], which is an experimental study for the case of isothermal walls and a tall cavity ($5 < A < 26$), including Prandtl number effect, the present results show a difference of 25 percent at $\overline{Ra} = 500$ and 38 percent at $\overline{Ra} = 10{,}000$ for $Pr = 1$. As the Prandtl number increases, this difference is greatly reduced. For $Pr = 20$, the heat transfer is lower by 10 percent at $\overline{Ra} = 500$, but for $\overline{Ra} = 10{,}000$, it is higher by 9 percent. Thus, it appears that the Nusselt number is always larger in the present case compared to the analytical results for isothermal walls and is larger, at least, for low Prandtl number ($Pr < 20$), compared to the experimental results of Seki et al. It may be noted that this effect of the Prandtl number on average Nusselt number has not been observed, to the authors' knowledge, in any previous analytical or numerical study of problems of this type. A similar conclusion has been derived for free convection in air-filled cavity by Said and Trupp [23]. Also, the experimental results of MacGregor and Emery [25], for mixed boundary conditions, and Emery and Chu [26], for isothermal boundary conditions, for nonporous media, point to the same conclusion. A comparison of heat transfer results has been presented in Fig. 12 for $A = 10$.

Conclusion

The numerical results obtained for free convection in a rectangular porous cavity with constant heat flux on one wall show a distinctly different flow pattern as compared to the case with isothermal vertical walls. Any increase in applied heat flux is found to increase the convective effects, but the temperatures are not observed to increase proportionately. Based on the mean temperature at the heated wall, it is possible to fix a bound for the maximum temperature in the porous medium. It is also observed that a large fraction of heat is rejected within a very small distance from the top edge of the cooled wall. Average Nusselt number is always higher, in the present case, than for the case with two isothermal walls. For a given heat flux, the Nusselt number is observed to attain a maximum value for $1 < A < 2$. Based upon these results, two correlations can be derived for the average nusselt number, equations (17) and (18). However, experimental data are needed to verify the present results and the form of these correlations.

Acknowledgment

We wish to acknowledge the helpful discussions with M. Keyhani and S. I. Guceri, and the support of the University of Delaware Computing Center.

References

1 Combarnous, M. A., and Bories, S. A., "Hydrothermal Convection in Saturated Porous Media," *Advances in Hydroscience*, Vol. 10, Academic Press, 1975, pp. 231-307.

2 Buchberg, H., Catton, I., and Edwards, D. K., "Natural Convection in Enclosed Spaces—A Review of Application to Solar Energy Collection," ASME JOURNAL OF HEAT TRANSFER, Vol. 98, 1976, pp. 182-188.

3 Seki, N., Fukusako, S., and Inaba, H., "Heat Transfer in a Confined Rectangular Cavity Packed With Porous Media," *International Journal of Heat and Mass Transfer*, Vol. 21, 1978, pp. 985-989.

4 Schneider, K. J., "Investigation of the Influence of Free Thermal Convection on Heat Transfer Through Granular Material," *Proceedings, 11th International Congress on Refrigeration*, 1963, Paper No. 11-4.

5 Chan, B. K. C., Ivey, C. M., and Barry, J. M., "Natural Convection in Enclosed Porous Media With Rectangular Boundaries," ASME JOURNAL OF HEAT TRANSFER, Vol. 2, 1970, pp. 21-27.

6 Klarsfeld, S., "Champs de Temperature Associes aux Mouvements de Convection Naturelle Dans Un Milieu Poreux Limite," *Revue Gen. Thermique*, Vol. 9, 1970, pp. 1403-1424.

7 Vlasuk, M. P., "Transfert de Chaleur par Convection Dans une Couche Poreuse," *Proceedings, 4th All-Union Heat and Mass Transfer Conference*, Minsk., 1972.

8 Holst, P. H., and Aziz, K., "A Theoretical and Experimental Study of Natural Convection in a Confined Porous Medium," *Canadian Journal of Chemical Engineering*, Vol. 50, 1972, pp. 232-241.

9 Bories, S. A., and Combarnous, M. A., "Natural Convection in a Sloping Porous Layer," *Journal of Fluid Mechanics*, Vol. 57, 1973, pp. 63-79.

10 Bankvall, C. G., "Natural Convection in Vertical Permeable Space," *Warme-und Stoffubertragung*, Vol. 7, 1974, pp. 22-30.

11 Horne, R., "*Transient Effects in Geothermal Convective Systems,*" Ph.D. thesis, University of Auckland, New Zealand, 1975.

12 Weber, J. E., "The Boundary Layer Regime for Convection in a Vertical Porous Layer," *International Journal of Heat and Mass Transfer*, Vol. 18, 1975, pp. 569-573.

13 Burns, P. J., Chow, L. C., and Tien, C. L., "Convection in a Vertical Slot Filled with Porous Insulation," *International Journal of Heat and Mass Transfer*, Vol. 20, 1976, pp. 919-926.

14 Walker, K. L., and Homsy, G. M., "Convection in a Porous Cavity," *Journal of Fluid Mechanics*, Vol. 97, 1978, pp. 449-474.

15 Bejan, A., "On the Boundary Layer Regime in a Vertical Enclosure Filled with a Porous Medium," *Letters in Heat and Mass Transfer*, Vol. 6, 1979, pp. 93-102.

16 Simpkins, P. G. and Blythe, P. A., "Convection in a Porous Layer," *International Journal of Heat and Mass Transfer*, Vol. 23, 1980, pp. 881-887.

17 Bejan, A., "Progress in Natural Convection Heat Transfer," University of Colorado, Report No. CUMER 80-1, 1980.

18 Wooding, R. A., "Steady Free Thermal Convection of Liquid in a Saturated Permeable Medium," *Journal of Fluid Mechanics*, Vol. 2, 1957, pp. 273-285.

19 Elder, J. W., "Steady Free Convection in a Porous Layer Heated from Below," *Journal of Fluid Mechanics*, Vol. 27, 1967, pp. 609-623.

20 Gosman, A. D., Pun, W. M., Runchal, A. K., Spalding, D. B., and Wolfshtein, M., *Heat and Mass Transfer in Recirculating Flows*, Academic Press, 1969.

21 Roache, P. J., *Computational Fluid Dynamics*, Hermosa Publishers, 1976.

22 Prasad, V., "Natural Convection in Porous Media – An Experimental and Numerical Study for Vertical Annular and Rectangular Enclosures," Ph.D. dissertation, University of Delaware, 1983.

23 Said, M. N. A., and Trupp, A. C., "Laminar Free Convection in Vertical Air-Filled Cavities with Mixed Boundary Conditions," ASME Paper No. 79-HT-110, 1979.

24 Balvanz, J. L., and Kuehn, T. H., "Effect of Wall Conduction and Radiation on Natural Convection in a Vertical Slot With Uniform Heat Generation on the Heated Wall," *Natural Convection in Enclosures*, edited by K. E. Torrance and I. Catton, HTD Vol. 8, ASME, 1980, pp. 55-62.

25 MacGregor, R. K., and Emery, A. F., "Free Convection Through Vertical Plane Layers," ASME JOURNAL OF HEAT TRANSFER, Vol. 91, 1969, pp. 391-401.

26 Emery, A. F., and Chu, N. C., "Heat Transfer Across Vertical Layers," ASME JOURNAL OF HEAT TRANSFER, Vol. 87, 1965, pp. 110-114.

27 Prasad, V., and Kulacki, F. A., "Convective Heat Transfer in a Rectangular Porous Cavity-Effect of Aspect Ratio on Flow Structure and Heat Transfer," ASME Paper No. 83-HT-66, 21st National Heat Transfer Conference, Seattle, 1983, ASME JOURNAL OF HEAT TRANSFER, (in press).

Convective Heat Transfer in a Rectangular Porous Cavity—Effect of Aspect Ratio on Flow Structure and Heat Transfer

V. Prasad

F. A. Kulacki
Mem. ASME

Department of Mechanical and Aerospace Engineering,
University of Delaware
Newark, Del. 19711

Two-dimensional steady natural convection in a porous rectangular cavity bounded by isothermal vertical walls at different temperatures and adiabatic horizontal walls has been studied numerically for aspect ratios less than unity and Rayleigh numbers up to 10^4. Results indicate the presence of multicellular flow. Also, the average Nusselt number based on cavity width is observed to be a maximum in a restricted range of aspect ratio, depending on the Rayleigh number. Effects of aspect ratio are summarized by a family of curves for constant Rayleigh number, based on cavity height, for aspect ratios from 0.05 to 100. For a cavity with fixed height, the heat transfer rate always increases as the aspect ratio is increased, except when the flow exhibits boundary layers on the vertical walls. Criteria in terms of aspect ratio and Rayleigh number have been established for the existence of different flow regimes.

Introduction

Natural convection in porous media has recently received considerable attention due to the increasing interest in high performance building insulation and geothermal operations. A wide range of application, such as to heat exchangers, solar power collectors, energy efficient drying processes, underground spread of pollutants, and the like, has led to the large number of publications in this area. Convective heat transfer in a rectangular porous cavity, whose vertical walls are maintained at two different temperatures and horizontal walls are insulated, is a problem fundamental to this area, which has received attention by many investigators [1–15]. Analytical work reported includes numerical results by Chan et al. [1], Vlasuk [3], Holst and Aziz [4], Bankvall [6], Burns et al. [8], Hickox and Gartling [14], and Prasad and Kulacki [15], and boundary layer analyses by Weber [7], Walker and Homsy [9], and Bejan [12]. Simpkins and Blythe [13] have presented integral solutions, whereas approximate solutions have been obtained by Walker and Homsy [9], and Bejan and Tien [10]. Important experimental results are due to Klarsfeld [2], Holst and Aziz [4], Bories and Combarnous [5] and Seki et al. [11]. Based on these studies, various correlations have been reported for the average Nusselt number for square ($A = 1$) and tall ($A > 2$) cavities [5, 7, 9, 11, 15].

Though the published results for the rectangular cavity cover wide ranges of Rayleigh number and aspect ratio, most of them have been limited to $A \geq 1$. For low aspect ratio, $A < 1$, very few reports are available in the literature. Chan, Ivey, and Barry [1] were the first to present heat transfer results, obtained via finite difference solutions, for $A \geq 0.2$ and $\mathrm{Ra}^* = 20$, 50, and 100. Bejan and Tien [10] have recently reported an approximate analytical method valid for $A << 1$. Walker and Homsy [9] have also suggested a method for long shallow cavities which employs a matched asymptotic expansion in the aspect ratio when $A \to 0$. The most recent work is due to Hickox and Gartling [14], who have used a finite element solution technique to obtain heat transfer results for $0.1 \leq A \leq 0.5$ and $25 \leq \mathrm{Ra}_L^* \leq 200$. Heat transfer results for low Rayleigh number are also due to Bankvall [6] and Burns, Chow, and Tien [8], both via numerical solutions. To our knowledge, no experimental results are available for low aspect ratio cavities.

In spite of the aforementioned work for the shallow cavity and quite a good number of reports for tall cavities, there is a gap in the heat transfer literature for low aspect ratios in the vicinity of $A = 1$. This is due to the fact that analytical results are accurate for either $A >> 1$ [7, 8, 9, 12] or $A << 1$ [9, 10], and the available numerical results do not provide enough information for $A < 1$ for a wide range of Rayleigh number.

The object of the present study is to fill this gap and provide a basis for the validity of the approximate analyses presented by Bejan and Tien [10] and by Walker and Homsy [9]. Further, the effects of aspect ratio on flow behavior and heat transfer rates have not been reported thus far, say, in the case where a long shallow cavity is changed to a tall one. Knowledge of this behavior is very important for the design of thermal insulation systems and other applications. For example, one may be interested in knowing the proper thickness of insulation if heat transfer is to be reduced. For a tall cavity, an increase in the width will decrease heat transfer unless a combination of Rayleigh number and aspect ratio are reached where a boundary layer flow is established on the vertical walls. Beyond this point, average Nusselt numbers are weakly dependent on aspect ratio [15]. If the cavity width, D, is further increased, thus lowering the aspect ratio even more, information is lacking on any subsequent changes in the flow structure and heat fluxes to the walls. Consequently, the effects of aspect ratio on heat transfer and flow behavior have been investigated for $0.05 \leq A \leq 100$. It is observed that the Rayleigh number based upon cavity height, Ra_L^*, is more appropriate parameter than Ra^* to study the effects of aspect ratio on heat transfer rates.

Formulation and Solution

Consider a fluid-saturated porous layer enclosed by two isothermal vertical walls at temperatures T_h and T_c, $T_h > T_c$, and two adiabatic horizontal walls (Fig. 1). All walls of the cavity are further assumed to be impermeable. In the porous medium, Darcy's law is assumed to hold, the fluid is assumed to be a normal Boussinesq fluid, and the viscous drag and inertia terms of the momentum equations are neglected because their magnitudes are of small order compared to

Contributed by the Heat Transfer Division for publication in the JOURNAL OF HEAT TRANSFER. Manuscript received by the Heat Transfer Division November 16, 1982.

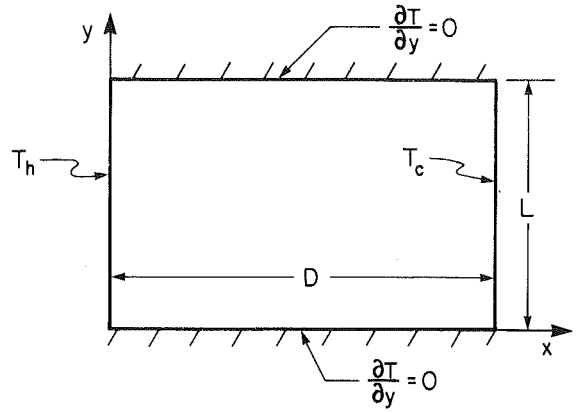

Fig. 1 Two-dimensional porous layer subjected to an end-to-end temperature difference

other terms for low Darcy numbers and low particle Reynolds numbers. Owing to the last assumption, velocity slip at the wall is permitted.

With these assumptions, the conservation equations for mass, momentum, and energy for steady, two-dimensional flow in an isotropic porous medium are [16]

$$\frac{\partial u}{\partial x} + \frac{\partial v}{\partial y} = 0 \tag{1}$$

$$\frac{\partial p}{\partial x} + \frac{\mu}{K} u = 0 \tag{2}$$

$$\frac{\partial p}{\partial y} + \rho g + \frac{\mu}{K} v = 0 \tag{3}$$

$$u\frac{\partial T}{\partial x} + v\frac{\partial T}{\partial y} = \alpha\left[\frac{\partial^2 T}{\partial x^2} + \frac{\partial^2 T}{\partial y^2}\right] \tag{4}$$

where

$$\rho = \rho_r[1 - \beta(T - T_r)] \tag{5}$$

Expressed in dimensionless variables and transformed to the stream function form equations (1-5) can be rewritten as

$$A^2\frac{\partial^2 \psi}{\partial X^2} + \frac{\partial^2 \psi}{\partial Y^2} = \mathrm{Ra}^* A\frac{\partial \theta}{\partial X} \tag{6}$$

$$\frac{\partial \psi}{\partial X}\frac{\partial \theta}{\partial Y} - \frac{\partial \psi}{\partial Y}\frac{\partial \theta}{\partial X} = \frac{\partial^2 \theta}{\partial X^2} + \frac{1}{A^2}\frac{\partial^2 \theta}{\partial Y^2} \tag{7}$$

where Ra^* is the Rayleigh number based on cavity width.

The relevant hydrodynamic and thermal boundary conditions are

$$\psi = 0,\ \theta = 1 \quad \text{at } X = 0 \tag{8}$$

$$\psi = 0,\ \theta = 0 \quad \text{at } X = 1 \tag{9}$$

$$\psi = 0,\ \frac{\partial \theta}{\partial Y} = 0 \text{ at } Y = 0 \text{ and } Y = 1 \tag{10}$$

Equations (6) and (7)[1] are transformed into finite difference equations using the scheme developed by Gosman et al. [17]. The method is based on integrations of the equations over finite area elements and ensures that the conservation laws are obeyed over suitably large or small portions of the domain. The solution technique is well described in the literature [17, 18] and has been widely used for natural convection problems. The applicability of the method and the accuracy of the results for heat transfer in a porous rectangular cavity had already been discussed by the authors [19, 20].

For the present work, a mesh of 41 × 21 has been used for very low aspect ratios, whereas for $A > 0.5$, a mesh of 31 × 31 was used. These mesh sizes gave an average Nusselt number within 2 percent of the asymptotic value predicted by calculations with a much finer mesh. In each case, varying grids were used in both x- and y- directions for $\mathrm{Ra}^* > 200$, whereas for lower Rayleigh numbers uniform grids were employed. In the case of varying mesh size, very fine grids were used near the walls, which increased gradually toward the center of the cavity. This was found to be quite helpful, especially at high Rayleigh numbers, owing to boundary layers on the vertical walls and significant changes in the magnitude and direction of velocities near the horizontal walls. Mesh sizes of the order of 0.005 were used near the vertical walls for $\mathrm{Ra}^* \geq 2000$. A point iterative scheme was used to solve the system of algebraic equations, with the help of relaxation parameters. For low Rayleigh numbers, overrelaxation of temperature helped in obtaining faster

[1] For derivation of the finite difference equations the divergence form of equations (4) and (7) is used.

Nomenclature

A = aspect ratio, L/D
c = specific heat of fluid at constant pressure, J/kg-K
D = width of porous cavity, m
g = acceleration due to gravity, m/s^2
$\bar{h}$ = average heat transfer coefficient on heated wall, $q/(T_h - T_c)$, W/m^2-K
K = permeability of porous medium, m^2
k_m = effective thermal conductivity of the saturated porous medium, W/m-K
L = height of porous cavity, m
Nu = Nusselt number based on cavity width, $\bar{h}D/k_m$
Nu_L = Nusselt number based on cavity height, $\bar{h}L/k_m$
p = pressure, Pa
q = heat transfer rate per unit area, W/m^2
Ra^* = Rayleigh number based on cavity width, $\frac{\rho g \beta K D \Delta T}{\mu \alpha}$
Ra_L^* = Rayleigh number based on cavity height, $\frac{\rho g \beta K L \Delta T}{\mu \alpha}$
T = temperature, K
ΔT = temperature difference, $T_h - T_c$, K
u = Fluid velocity in x-direction, $-(\alpha/D)(\partial\psi/\partial Y)$, m/s
v = fluid velocity in y-direction, $(\alpha L/D^2)(\partial\psi/\partial X)$, m/s
x,y = Cartesian coordinates, m
X = dimensionless distance on x-axis, x/D
Y = dimensionless distance on y-axis, y/L

Greek Symbols

α = thermal diffusivity of porous medium, $k_m/\rho c$, m^2/s
β = isobaric coefficient of thermal expansion of fluid, K^{-1}
θ = dimensionless temperature, $(T - T_c)/(T_h - T_c)$
μ = dynamic viscosity of fluid, kg/m-s
ρ = density of fluid, kg/m^3
ψ = stream function

Subscripts

c = cooled wall
h = heated wall
r = reference value for equation (5)

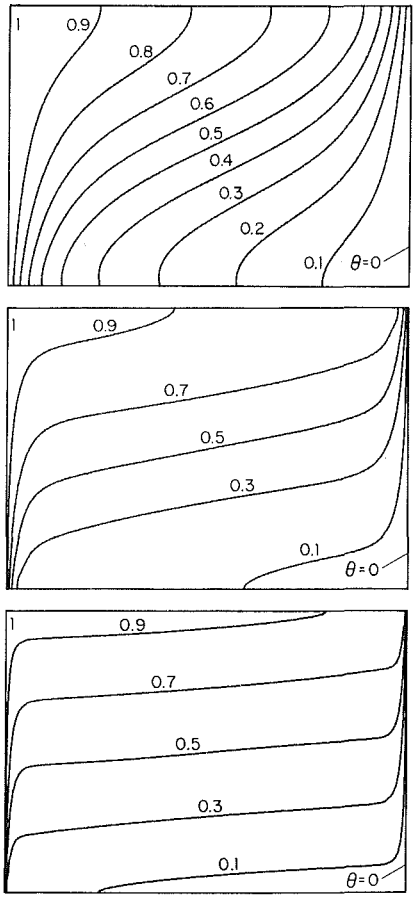

Fig. 2(a) Isotherms for $A = 0.7$, $Ra^* = 100$, 1000, and 10,000 (from top to bottom)

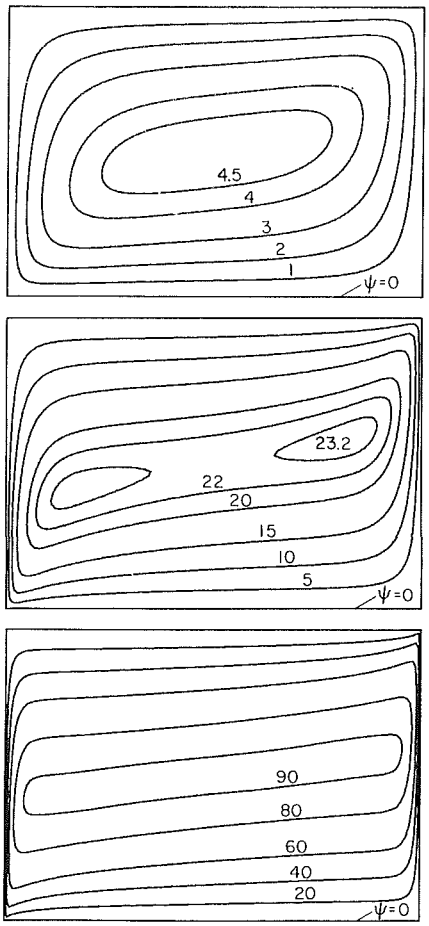

Fig. 2(b) Streamlines for $A = 0.7$, $Ra^* = 100$, 1000, and 10,000 (from top to bottom)

convergence whereas for high Rayleigh numbers, underrelaxation of stream function, ψ, was more helpful. The value of overrelaxation parameter used was as high as 1.9, and a suitable value of underrelaxation parameter was between 0.6 and 1. A detailed discussion on mesh sizes and relaxation parameters is presented in [20].

To check the accuracy of the results, an energy balance was used for the system. This energy balance compares heat transfer at $x = D$ to input at $x = 0$. For 70 percent of the cases reported here, the energy balance was satisfied within 1 percent, whereas for the rest, it was within 3 percent. Furthermore, a close agreement between our results and that reported by Hickox and Gartling [14], and other investigators [1, 6, 9, 10] shows that the present numerical scheme yields very good results for the shallow cavity (see Fig. 6). A detailed comparison of the results will be presented later.

To satisfy the convergence criterion of 0.1 percent for both ψ and θ throughout the domain, 250 iterations were sufficient in most cases. In some instances, the number of iterations required for convergence was less than 100. The CPU time required for convergence was always less then 50s on a DEC-10 computer.

Results and Discussion

Flow Regimes. Before the results for various ranges of aspect ratio and Rayleigh number are presented, it is worthwhile to discuss the different flow regimes encountered in free convection in porous enclosures. Convective heat transfer in a porous cavity is usually classified as belonging to the conduction, the asymptotic, and the boundary layer flow regimes.

As the temperature of the hot wall begins to rise, energy is first transported to the cold wall by pure (i.e., molecular) conduction, and the Nusselt number is unity. A larger temperature difference results in a moderate circulatory parallel flow, the core temperature still being independent of y. This situation is achieved either for $Ra^* \to 0$ and finite A or for $A \to 0$ and finite Ra^*, and is referred to as conduction flow regime. This flow regime may also be encountered for any fixed Ra^* if $A \to \infty$. A convenient limit for this regime may be when the temperature gradient at the cavity center differs by 10 percent from its value at $Ra^* = 0$ [21]. This usually results in about 10 percent increase in average Nusselt number for the present case.

Any further increase in the Rayleigh number enhances the stratification in the core, and the contribution of heat transfer by convection near the walls increases. This situation is termed asymptotic flow.

Finally, a sufficiently large temperature difference across the cavity causes a boundary layer flow in which the dominant mode of heat transfer is convection. A convenient characterization is usually based upon the slope of the Nusselt number curve on ln (Nu) versus ln (Ra^*) plot, the slope being constant for the boundary layer regime. Another criterion can be obtained from the tall cavity results, which show that the aspect ratio effect is very weak in this flow regime [15]. The criterion that the horizontal temperature gradient at the cavity center equals to zero, as used for newtonian fluids [21], cannot be employed here. This is because $\partial\theta/\partial X(0.5,0.5)$ is negligible only at very high Rayleigh numbers, whereas the boundary layer effects dominate the heat transfer at much lower values of Ra^*. This has been adequately demonstrated

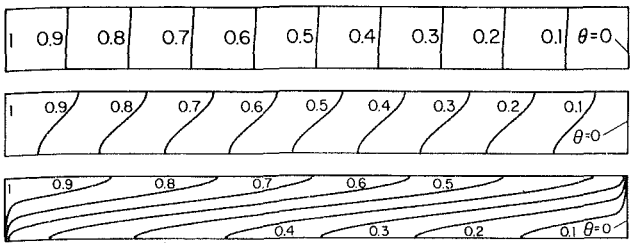

Fig. 3(*a*) Isotherms for $A = 0.1$, $Ra^* = 100$, 1000, and 10,000 (from top to bottom)

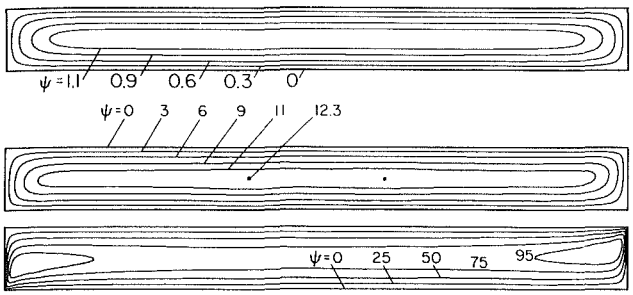

Fig. 3(*b*) Streamlines for $A = 0.1$, $Ra^* = 100$, 1000, and 10,000 (from top to bottom)

by the experimental results of Klarsfeld [2]. The present calculation shows that the temperature gradient, $\partial\theta/\partial X$, at the cavity center is -0.261 for $Ra^* = 500$ and -0.096 for $Ra^* = 1000$ when the aspect ratio is 5.

A somewhat different situation arises when $A \leq 0.5$. For the shallow cavity, the conduction in the core is not negligible even at high Rayleigh numbers (see Figs. 3(*a*) and 4), although the heat transfer is mainly by convection through the boundary layers on the hot and cold walls. Hence, between the conduction regime and the boundary layer flow regime, two different situations (for $A \leq 0.5$) can exist: one when the boundary layer effects are small and the other when the boundary layer effects on heat transfer are not small but conduction in the core is also not negligible. The former will continue to be designated as asymptotic flow whereas the later will be referred as the "pseudo boundary layer" regime. The significance of this designation is that heat transfer is mainly by convection through wall boundary layers and by conduction through the core.

Multicellular Flow. Results obtained for $0.05 \leq A \leq 0.9$ and $25 \leq Ra^* \leq 10^4$ show a distinct change in the flow structure as compared to that in square and tall cavities. In the present case, more than one convective cell has been observed, whereas no such behavior has been reported so far for $A \geq 1$.

Figures 2 to 4 show that the flow field comprises a primary cell of relatively high velocity, circulating around the entire enclosure and, for specific combinations of A and Ra^*, secondary cells near each vertical wall appear, e.g., $A = 0.7$ and $Ra^* = 1000$. The secondary cells are located outside the boundary layers and are separated by an almost stagnant core. As a consequence, the secondary flow velocity is much lower than that of the primary circulation. Streamlines for the secondary flows are skewed toward the starting corners for the wall boundary layers owing to the existence of adiabatic horizontal boundaries. In the range $0.1 \leq A \leq 0.9$ and for $Ra^* \leq 10{,}000$, the flow patterns exhibit two secondary cells, whereas for somewhat lower aspect ratios, a few more such cells may be expected to appear. The flow pattern obtained for $A = 0.05$ and $Ra^* = 10{,}000$ (Fig. 4) shows the presence of four secondary cells and supports this idea.

Multicellular flow appears immediately after aspect ratio is reduced below unity. Two locations for the maximum value of the stream function appear at $Ra^* = 1000$ for $A = 0.9$, and at $Ra^* = 2000$, the flow is found to be multicellular. This flow structure does not persist, and as $Ra^* \to 5{,}000$ unicellular flow reappears. A similar behavior is observed for $A = 0.7$. The multicellular patterns start appearing as soon as the Rayleigh number is increased beyond 100 and is well developed at $Ra^* = 1000$. If Ra^* is further increased beyond 5000, the secondary flow weakens and at $Ra^* = 10{,}000$ unicellular flow again prevails (Fig. 2(*b*)).

At $A = 0.5$, the flow becomes multicellular for $Ra^* > 50$, but any further decrease in aspect ratio delays the appearance of more than one recirculating cell (see Table 1). For $A = 0.3$, multicellular flow emerges for $Ra^* > 75$. Flow patterns reported by Hickox and Gartling [14], for $A = 0.3$ show that the maximum value for the stream function exists at two locations for $Ra^* = 167$, and convective cells are well developed at $Ra^* = 667$. For $A = 0.1$, the multicellular behavior appears at $Ra^* = 200$, but even at $Ra^* = 1000$, these cells are very small (Fig. 3(*b*)).

The emergence of two locations for the maximum value of the stream function and the start of multicellular flow strongly depend on the aspect ratio as does the return to unicellular flow. At least for $A < 0.7$, multicellular flow is initiated in the asymptotic flow regime and continues to the pseudo boundary layer regime. Based upon the results obtained in this study, one can state a criterion for the start of multicellular flow as

$$Ra^* > 22.5/A, \quad A \leq 0.5 \tag{11}$$

The length and scope of the present work do not permit a thorough discussion on the effect of multicellular flow on the heat transfer and the reason for the appearance of more than one recirculating cell. It is speculated that a multicellular flow reduces the Nusselt number at a constant value of $Ra^*(A)$ via an increase in the dissipation of kinetic energy; also, the recirculating flows near the vertical walls tend to deliver nearby fluid back to the wall and, thus, decrease the average temperature gradient there. Since the present calculations are not extensive enough to permit an investigation of local stability, one cannot speculate on the mechanism or reason for appearance of the multicellular flow.

Temperature Field. In the so-called conduction regime, the isotherms are almost parallel to the vertical wall but start

Table 1 Rayleigh number at which flow structure changes from unicellular to multicellular and vice versa

A	Multicellular flow starts at Ra* greater than	Flow is again unicellular when Ra* is
0.9	1000	5000
0.7	100	10,000
0.5	50	
0.3	75	
0.2	100	greater than 10,000
0.1	200	

Table 2 Selected values of average Nusselt number, Nu, for various Rayleigh numbers and aspect ratios

A \ Ra*	50	200	1000	5000	10,000
0.9	1.96	5.13	14.19	35.49	50.20
0.7	1.69	4.70	13.51	38.95	55.52
0.5	1.43	3.81	14.21	43.68	62.58
0.3	1.13	2.33	10.66	41.46	67.00

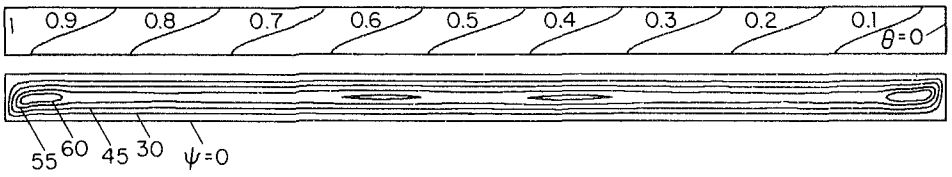

Fig. 4 Isotherms and streamlines for $A = 0.05$ and $Ra^* = 10{,}000$

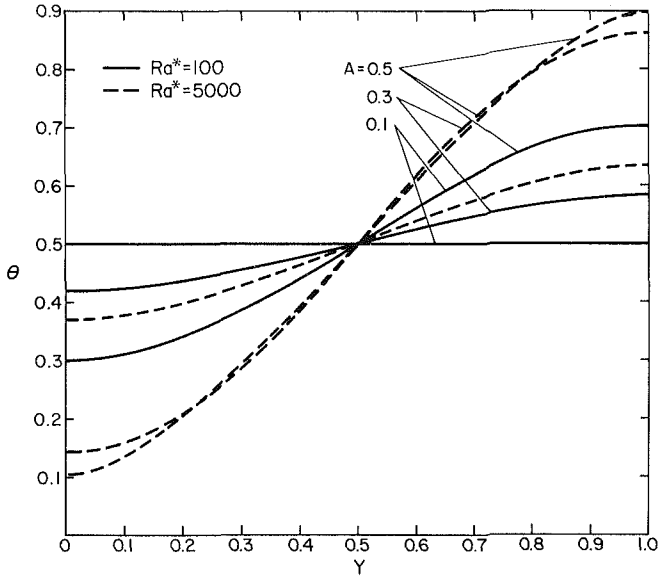

Fig. 5 Temperature distribution at vertical midplane, $X = 0.5$

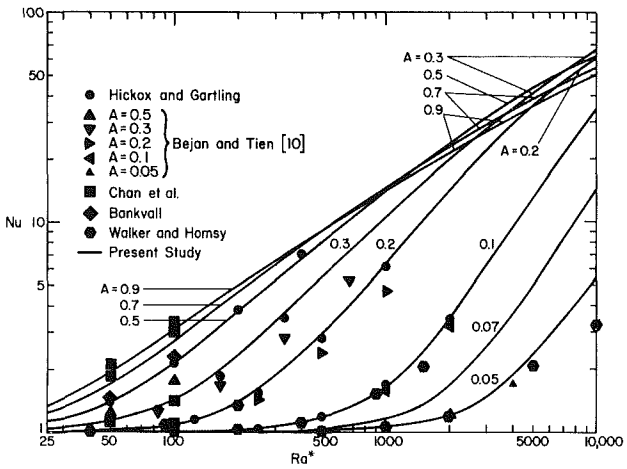

Fig. 6 Variation in Nusselt number for shallow rectangular cavities, $A < 1$, and comparison with previous results

changing direction when the Rayleigh number is increased such that the flow proceeds to the boundary layer regime. At large Ra*, horizontal temperature gradients in the core region are quite modest, and the flow field appears to be nearly stratified, for $A \gtrsim 0.5$ (see Fig. 2(*a*)). As the aspect ratio is reduced, $\partial\theta/\partial X$ at any height increases for a fixed Rayleigh number (Figs. 2 to 4). This is true even for very high Ra* and shows that the pseudo-boundary-layer flow regime is extended as A is decreased. However, the Rayleigh number where the nearly stratified situation prevails depends on the aspect ratio.

For low Rayleigh number, the temperature profiles at midheight, $Y = 0.5$, are almost linear and very close to each other in the core region. As Ra* is increased, the character of the profiles changes, and sharp drops in temperatures are observed near the walls due to boundary layer effects. Generally, when $A > 0.1$, temperature profiles are nonlinear in both the wall and core regions, for moderately high Rayleigh numbers. This points out a limitation inherent in the approximate approaches [9, 10], which use a linear temperature distribution in x and are thus inaccurate in predicting temperatures in the core region, at least for high Rayleigh numbers.

Temperature distributions at $X = 0.5$ have been plotted for $Ra^* = 100$ and 5000, and for $A = 0.1$, 0.2, and 0.5 in Fig. 5. In each case, the temperature profile is linear in a small portion of the core region, but the gradient is a function of Ra* and A. A variation in the aspect ratio for low Rayleigh number is associated with a large change in slope, whereas for large Ra*, the gradient changes fast when A is increased beyond 0.1. As $A \to 0.3$, the variation of the gradient is slight. The temperature profiles for $A = 0.3$ and 0.5 are very close at $Ra^* = 5000$. The dimensionless temperature at the cavity center ($X = 0.5$ and $Y = 0.5$) is very close to 0.5 and agrees with the condition used in the approximate analyses of Walker and Homsy [9] and Bejan and Tien [10] based upon the centrosymmetric property of the system.

Heat Transfer. Heat transfer results in terms of Nusselt number are presented in Fig. 6 and Table 2. In the conduction regime, $Nu \to 1$ for all values of A. This is followed by the asymptotic and boundary layer flow regimes for $A > 0.5$ and by the asymptotic, pseudo boundary layer and boundary layer flow regimes for $A \lesssim 0.5$. As discussed previously, the start of these flow regimes is strongly dependent on aspect ratio. The Rayleigh number at which any of the above regimes starts, increases very rapidly as the aspect ratio is decreased.

First, the conduction regime gets extended very rapidly with a reduction in height to width ratio. For $A = 0.2$, this regime ends at $Ra^* \simeq 100$, whereas for $A = 0.05$ it continues up to $Ra^* \simeq 1500$. Similarly, the Rayleigh number ranges for asymptotic and pseudo boundary layer flows are also extended. Consequently, pure boundary layer flow starts at much higher Rayleigh number. For $A = 0.3$ this situation arises at $Ra^* \simeq 2000$ whereas for $A = 0.2$ the appropriate Ra* is greater than 7000.

The curves for Nusselt number versus Rayleigh number are seen to cross depending upon Ra* and A (Fig. 6). Generally, the role of aspect ratio is the dominant factor for any constant Ra*. The implication is that there are certain critical values of A for which Nu is a maximum with Ra* fixed. This critical value, or range of critical values, is a strong function of Ra* and does not support the idea that Nusselt number is always maximum for $1 < A < 2$ [1].

In general, the slope of the Nusselt number curve (Fig. 6) is higher in the asymptotic flow regime and is lower for the boundary layer flow. For $0.5 < A < 1$, the slope of the curve is observed to further decrease at very high Rayleigh numbers. Qualitatively, this is similar to the observation made by Shiralkar, Gadgil, and Tien [22] that the slope of this curve decreases as the Rayleigh number is increased for high Rayleigh number convective heat transfer in nonporous shallow cavity. For lower aspect ratios the change in slope is

Table 3 Values of C and m for equation (12)

A	C	m	For Ra* greater than
0.1	2.5×10^{-4}	1.27	2000
0.07	8.1×10^{-6}	1.57	3000
0.05	7.9×10^{-5}	1.21	4000

due to the change in flow regime (from pseudo boundary layer to boundary layer flow).

Further, in the psuedo boundary layer regime the slope of the curve for Nusselt number increases as the aspect ratio is decreased. The behavior does not continue forever. The slope at $A = 0.05$ is lower than that for $A = 0.07$, which indicates that the slope is maximum between these values (see Table 3). From Fig. 6, it can also be observed that the slope of the Nusselt number curve remains almost constant for a larger part of the pseudo boundary layer regime. Hence, it is possible to predict the Nusselt number by a relation

$$\mathrm{Nu} = C\,\mathrm{Ra}^{*m} \tag{12}$$

where C depends on the apsect ratio. For $A = 0.1$, 0.07, and 0.05, the values of C and m with lower bounds of Rayleigh number, are given in Table 3. The upper bounds of Ra* depend upon the extent of pseudo boundary layer regime.

Also in Fig. 6, the present heat transfer results are compared to the results of several prior studies [1, 6, 9, 10, 14]. Though the values obtained by Hickox and Gartling [14] are very limited, they are in excellent agreement with the present Nusselt numbers. For $A = 0.1$, their Nusselt numbers agree almost exactly and at other values of A, the agreement is within 5 percent. The Nusselt numbers obtained by Chan et al. [1] for $A \geq 0.2$ and $\mathrm{Ra} \leq 100$ also agree well despite their use of a coarse mesh. Agreement between the results of Bankvall [6] and the present work is also quite good.

The values of Nusselt number obtained by Bejan and Tien [10] have been compared to the present results for $A \leq 0.5$. For low Rayleigh number and/or very low aspect ratio, the difference between the present results and theirs is quite small, but for high Ra*, it is quite appreciable. For example, at $\mathrm{Ra}^* = 1000$ and $A = 0.2$, Nusselt numbers differ by 35 percent. This is most probably a result of the assumptions of parallel flow in the core and a linearly varying core temperature, which are, in retrospect, best applied to low Ra* and very low A. Recalling the prior discussion of the flow field, one can see that streamlines are not parallel to the insulated walls even at moderate Ra*. Also, the presence of multicellular flow does not produce a negligible vertical velocity in the core flow (e.g., Fig. 2(*b*) and 3(*b*)).

Similar arguments are applicable to the assumptions made by Walker and Homsy [9] for solving the problem by asymptotic expansions. A reasonable agreement could be obtained only for $A = 0.2$, 0.1, and 0.05 for Rayleigh numbers up to 1000, 2000, and 4000, respectively. In the case of the work of Bejan and Tien [10], a comparison of their results with those of Hickox and Gartling [14] and the present work suggests that their method would yield reasonable results for $A < 0.1$. Generally, the solution method of both Walker and Homsy and of Bejan and Tien would give excellent results in the conduction regime and reasonably good results in the asymptotic flow regime for $A < 0.2$ but would fail to provide satisfactory results for high Rayleigh numbers.

Criteria for Flow Regimes. To analyze the effects of aspect ratio, on flow structures, consider a redefinition of the Rayleigh and Nusselt numbers in terms of the cavity height, L. This is suggested because a better picture can be obtained of how the flow regime and heat transfer rates change with a change in aspect ratio. Also, for the design of thermal insulation and other similar systems wherein the cavity height may be fixed, any change in the Nusselt number can be directly interpreted as a change in the heat transfer coefficient. A family of curves for Nusselt number based on L is presented in Fig. 7. The values plotted are a combination of results from the present study and those of prior work [15, 20]. As the correlations presented for a tall cavity [7, 9, 15] show no aspect ratio dependence in the boundary layer regime [15], the values obtained by those correlations have not been used in Fig. 7 so that one does not lose sight of even the weak effects of the aspect ratio.

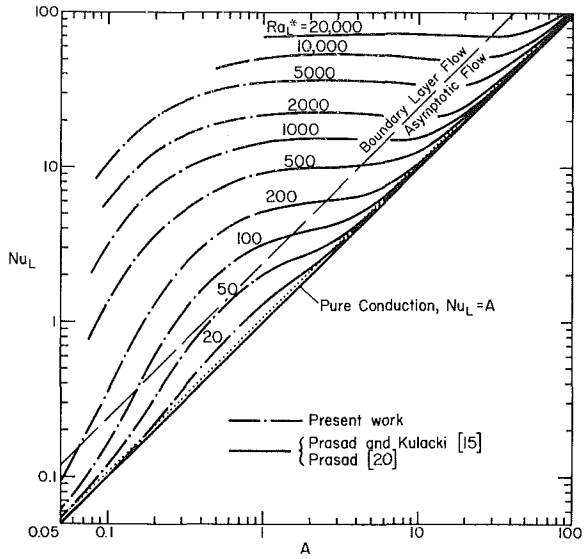

Fig. 7 Effects of aspect ratio on Nusselt number based on cavity height, Nu_L ..... Separates conduction and asymptotic flow regimes. For $A \leq 0.5$, – – separates asymptotic and pseudo boundary layer flow regimes.

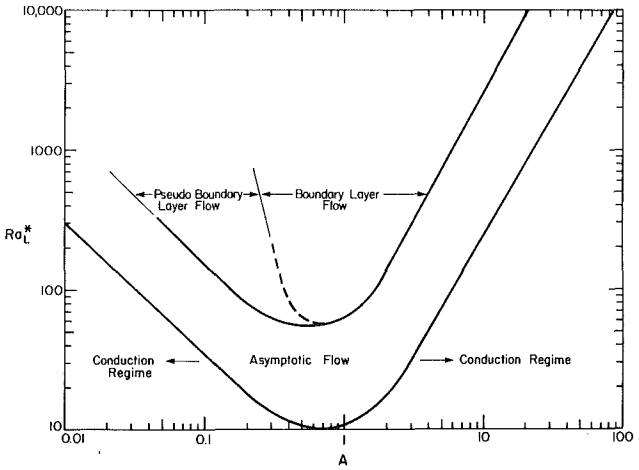

Fig. 8 Critical Rayleigh number for change of convective flow regimes

First, using the results obtained by previous investigators for $A \geq 1$ and the present results, Rayleigh number ranges have been estimated for the conduction, asymptotic, pseudo boundary layer, and boundary layer flow regimes. Fortuitously, two lines parallel to the pure conduction line, $\mathrm{Nu}_L = A$, are sufficient to predict the various flow regimes for a larger part of the aspect ratio range considered here. This is important considering the difficulty in obtaining precise and accurate values of Rayleigh number to delimit the flow regimes. These two lines are expected to predict within 10 percent the critical values for Ra_L^* (Fig. 7).

For $A \leq 0.5$, the dashed line in Fig. 7 separates the asymptotic and the pseudo boundary layer flows. As discussed earlier, a much higher value of Ra* is required to satisfy the criterion for the boundary layer flow in this range of aspect ratio.

Further, the values of Ra_L^* lying on these two lines (Fig. 7) lead to the two curves shown by the full lines in Fig. 8, where Ra_L^* is presented as a function of A. To separate the pseudo boundary layer with pure boundary layer flow, a curve with dashed line is also drawn for a small range of aspect ratio. Since the present numerical scheme does not yield satisfactory results for a higher range of Rayleigh number than what has been reported, no attempt has been made to extend this line further. The curve for the start of asymptotic flow has been extended for $A < 0.05$ with the values obtained from the solution of Walker and Homsy [9]. Generally, each curve in Fig. 8 can be divided into three ranges of aspect ratio, one for a tall cavity, $A > 2$, another for a long shallow cavity, and a third for an intermediate range.

For tall and long shallow cavities, both curves are straight lines on logarithmic coordinates and can be represented by an expression of the form $Ra_L^* = \text{Constant} \times A^m$, where the constant and exponent depend on the line under consideration and the aspect ratio. It may be mentioned here, that for a shallow cavity, Bejan and Tien [23] has earlier suggested a regime map similar to Fig. 8.

Based upon the curve obtained in Fig. 8, the criteria obtained for the start of asymptotic flow are

$$Ra_L^* > (4.65 \pm 0.15) A^{1.73}, \quad A > 2 \tag{13}$$

$$Ra_L^* > (3.9 \pm 0.2) A^{-0.95}, \quad A < 0.2 \tag{14}$$

and

$$Ra_L^* > (33.5 - 115.7A + 218.2A^2 - 198.4A^3 + 88.1A^4 - 15.0A^5), \quad 0.2 \leq A \leq 2 \tag{15}$$

For the tall cavity the boundary layer regime starts at

$$Ra_L^* > (37.2 \pm 0.8) A^{1.85}, \quad A > 2 \tag{16}$$

whereas, for the aspect ratio close to one the criterion is obtained as

$$Ra_L^* > (155.4 - 578.6A + 1229.7A^2 - 1216.5A^3 + 573.8A^4 - 100.8A^5), \quad 0.5 < A \leq 2 \tag{17}$$

For a long shallow cavity, the criterion for the start of the pseudo boundary layer regime is

$$Ra_L^* > 15/A, \quad A < 0.2 \tag{18}$$

whereas equation (17) can be used to separate the asymptotic and pseudo boundary layer regimes for $0.2 < A < 0.5$.

It may be mentioned here that the validity of the approximate solution for the shallow cavity [9] suggests that the asymptotic flow criterion should be $Ra_L^* \sim A^{-1}$. The exponent of A obtained by us is -0.95 (equation (14)). Similarly, the boundary layer solutions for tall cavity [7] are valid for $\delta << D/2$ (where δ is the boundary layer thickness), which yields $Ra_L^* >> 4A^2$, indicating that Ra_L^* should be proportional to A^2 for the boundary layer regime. The present correlation has an exponent of 1.85 (equation (16)). This close agreement between the exponents of A for these two cases shows that the criteria for choosing the values of the critical Rayleigh number are satisfactory.

Effects of Aspect Ratio. As can be seen in Fig. 7, for a fixed Rayleigh number ($Ra_L^* > 60$), any change in the aspect ratio from a very low value to a high value changes the flow structure as follows: Pure conduction → conduction → asymptotic flow → pseudo boundary layer flow → boundary layer flow → asymptotic flow → conduction → pure conduction.

For $Ra_L^* < 60$, either only conduction or conduction and asymptotic flow regimes may be encountered depending upon the Rayleigh number. The presence of pseudo boundary layer may not be distinguished if the aspect ratio greater than 0.5 is considered.

Further, for any fixed Ra_L^*, the heat transfer rate increases as the aspect ratio is increased, except when the boundary layer flow is encountered. As can be seen in Fig. 7, this rate of increase is a maximum near the pure conduction line and is a minimum as the boundary layer flow is approached. Actually, the numerical results show a small decrease in Nusselt number for any increase in A if the boundary layer flow is maintained, which is contrary to the experimental observation of Seki et al. [11], but substantiates the experimental results of Klarsfeld [2], and Bories and Combarnous [5]. It may be noted that the boundary layer analyses of Weber [7] and Walker and Homsy [9] do not show any aspect ratio dependence.

With reference to Fig. 6, one can now observe that the lower values of Nusselt number, Nu, for higher aspect ratios (at high Ra*) do not mean that the heat transfer rate increases as A is reduced. In fact, the heat transfer rate always decreases if the cavity width is increased keeping its height fixed, except for the range of Rayleigh number when the boundary layer flow is maintained.

Conclusion

Flow fields, temperature fields, and average Nusselt numbers at the side walls have been obtained for steady convection in a porous cavity bounded by isothermal vertical walls and insulated horizontal walls for $0.05 \leq A \leq 0.9$ and $Ra^* \leq 10{,}000$. Various flow regimes, such as conduction, asymptotic, and boundary layer, usually encountered with the convective heat transfer in a porous enclosure, have been defined. For long shallow cavity, the asymptotic flow has been separated into two parts. The first part is still referred to as asymptotic flow, whereas the second part has been designated as pseudo boundary layer flow. This name has been given because heat transfer is mainly by convection through wall boundary layers and by conduction through the core. With the results of the present study and previous investigations for $A \geq 1$, two lines parallel to the pure conduction line (Fig. 7) are able to predict the different flow regimes. Equations (13) to (18) set the Rayleigh number criteria in terms of the aspect ratio.

Multicellular flow has been found for $A < 1$, and the flow structure comprises a primary recirculating cell with smaller secondary cells inside. For $A < 0.7$, more than one secondary cell appears in the asymptotic flow regime. This structure gives way to a boundary layer regime in which the flow is again unicellular. Equation (11) gives a criterion for the start of the multicellular flow.

Nusselt numbers based on the cavity width are not necessarily a maximum for $1 < A < 2$. Depending on the value of aspect ratio, more than one maximum can be found when Ra* is fixed. Moreover, the effects of aspect ratio on heat transfer have been summarized through a family of curves for constant Ra_L^*. For any $Ra_L^* > 60$, the flow is seen to have the following structures as the aspect ratio is varied from a very low to very high value: pure conduction → conduction → asymptotic flow → pseudo boundary layer flow → boundary layer flow → asymptotic flow → conduction → pure conduction. Except for the boundary layer regime, Nusselt number based on the cavity height, Nu_L, always increase when A is increased, and this increase is more rapid in shallow cavities ($A < 1$) than in tall cavities.

Acknowledgment

Acknowledgments are due to M. Keyhani for helpful

discussion and to the University of Delaware Computing Center for computational facilities.

References

1 Chan, B. K. C., Ivey, C. M., and Barry, J. M., "Natural Convection in Enclosed Porous Media with Rectangular Boundaries," ASME JOURNAL OF HEAT TRANSFER, Vol. 2, 1970, pp. 21-27.

2 Klarsfeld, S., "Champs de Temperature Associes aux Mouvements de Convection Naturelle Dans Un Milieu Poreux Limite," *Revue Gen. Thermique*, Vol. 9, 1970, pp. 1403-1424.

3 Vlasuk, M. P., "Transfert de Chaleur par Convection Dans une Couche Poreuse," *Proceedings, 4th All-Union Heat and Mass Transfer Conference*, Minsk., 1972.

4 Holst, P. H., and Aziz, K., "A Theoretical and Experimental Study of Natural Convection in a Confined Porous Medium," *Canadian Journal of Chemical Engineering*, Vol. 50, 1972, pp. 232-241.

5 Bories, S. A., and Combarnous, M. A., "Natural Convection in a Sloping Porous Layer," *Journal of Fluid Mechanics*, Vol. 57, 1973, pp. 63-79.

6 Bankvall, C. G., "Natural Convection in Vertical Permeable Space," *Warme-und Stoffubertragung*, Vol. 7, 1974, pp. 22-30.

7 Weber, J. E., "The Boundary Layer Regime for Convection in a Vertical Porous Layer," *International Journal of Heat and Mass Transfer*, Vol. 18, 1975, pp. 569-573.

8 Burns, P. J., Chow, L. C., and Tien, C. L., "Convection in a Vertical Slot Filled with Porous Insulation," *International Journal of Heat and Mass Transfer*, Vol. 20, 1976, pp. 919-926.

9 Walker, K. L., and Homsy, G. M., "Convection in a Porous Cavity," *Journal of Fluid Mechanics*, Vol. 97, 1978, pp. 449-474.

10 Bejan, A., and Tien, C. L., "Natural Convection in a Horizontal Porous Medium Subjected to an End-to-End Temperature Difference," ASME JOURNAL OF HEAT TRANSFER, Vol. 100, 1978, pp. 191-198.

11 Seki, N., Fukusako, S., and Inaba, H., "Heat Transfer in a Confined Rectangular Cavity Packed with Porous Media," *International Journal of Heat and Mass Transfer*, Vol. 21, 1978, pp. 985-989.

12 Bejan, A., "On the Boundary Layer Regime in a Vertical Enclosure Filled with a Porous Medium," *Letters in Heat and Mass Transfer*, Vol. 6, 1979, pp. 93-102.

13 Simpkins, P. G., and Blythe, P. A., "Convection in a Porous Layer," *International Journal of Heat and Mass Transfer*, Vol. 23, 1980, pp. 881-887.

14 Hickox, C. E., and Gartling, D. K., "A Numerical Study of Natural Convection in a Horizontal Porous Layer Subjected to an End-to-End Temperature Difference," ASME JOURNAL OF HEAT TRANSFER, Vol. 103, 1981, pp. 797-802.

15 Prasad, V., and Kulacki, F. A., "Natural Convection in a Vertical Porous Annulus," *International Journal of Heat and Mass Transfer*, (in press).

16 Combarnous, M. A., and Bories, S. A., "Hydrothermal Convection in Saturated Porous Media," *Advances in Hydroscience*, Vol. 10, Academic Press, 1975, pp. 231-307.

17 Gosman, A. D., Pun, W. M., Runchal, A. K., Spalding, D. B., and Wolfshtein, M., *Heat and Mass Transfer in Recirculating Flows*, Academic Press, 1969.

18 Roache, P. J., *Computational Fluid Dynamics*, Hermosa Publishers, 1976.

19 Prasad, V., and Kulacki, F. A., "Natural Convection in a Rectangular Porous Cavity with Constant Heat Flux on One Vertical Wall," *ASME HTD-Vol. 22*, edited by J. V. Beck and L. S. Yao, pp. 35-41; also to appear in ASME JOURNAL OF HEAT TRANSFER.

20 Prasad, V., "Natural Convection in Porous Media—An Experimental and Numerical Study for Vertical Annular and Rectangular Enclosures." Ph.D. dissertation, University of Delaware, 1983.

21 Thomas, R. W., and de Vahl Davis, G., "Natural Convection in Annular and Rectangular Cavity - A Numerical Study," *Proceedings, 4th International Heat Transfer Conference*, Paris, Vol. 4, NC 2.4, Elsevier, Amsterdam, 1970.

22 Shiralkar, G., Gadgil, A., and Tien, C. L., "High Rayleigh Number Convection in Shallow Enclosures with Different End Temperatures," *International Journal of Heat and Mass Transfer*, Vol. 14, 1981, pp. 1621-1629.

23 Bejan, A., and Tien, C. L., "Laminar Natural Convection Heat Transfer in a Horizontal Cavity with Different End Temperatures," ASME JOURNAL OF HEAT TRANSFER, Vol. 100, 1978, pp. 641-647.

Low Rayleigh Number Thermal Convection in a Saturated Porous Medium Bounded by Two Horizontal, Eccentric Cylinders

H. H. Bau
Department of Mechanical Engineering
and Applied Mechanics,
University of Pennsylvania,
Philadelphia, Pa. 19104
Assoc. Mem. ASME

A two-term regular perturbation expansion is presented for two-dimensional, steady-state thermal convection in a fully saturated porous medium bounded by two horizontal, eccentric cylinders. Both cylinders are impermeable to fluid motion and are maintained at different, uniform temperatures. The complicated boundary conditions are handled through the use of bicylindrical coordinates. Three geometrical configurations are considered: an eccentric annulus; a pipe buried in a semi-infinite medium; and two cylinders, one outside the other, imbedded in an infinite medium. Detailed results, however, are presented only for the first case. It is demonstrated that eccentric insulations may be more effective under certain conditions and therefore more economical than the currently used concentric ones.

1 Introduction

Natural convection in porous media is germane to many technologies involving thermal insulators such as: steam lines, gas lines in gas cooled nuclear reactors, cryogenics, and storage of thermal energy, to name just a few. The thermal insulator typically consists of a fibrous material, which is permeable to fluid motion. Consequently, natural convection may develop in the insulating material and contribute significantly to the heat transfer process, as has been demonstrated by Caltagirone [3], Burns and Tien [2], Brailovskaya et al. [1], and others. Currently, concentric insulations are widely used. Clearly, an eccentric insulation may be more efficient and more economical than a concentric one, since the heat transfer process in the insulation consists of natural convection and conduction. An increase in the eccentricity so that the center of the inner, hotter cylinder is above the center of the outer one reduces the effective Rayleigh number, and therefore the impact of the convective heat transfer. On the other hand, the resulting reduction in the local thickness of the insulation may increase the conductive heat losses. Hence, one may expect that an optimal value of eccentricity exists for which the heat losses are minimized.

Although the problem of thermal convection in a porous, eccentric annulus has not been considered before, the analogous problem of thermal convection in an eccentric annulus containing viscous fluid (a nonporous medium) has attracted some attention in the recent literature. Kuehn and Goldstein [5] have conducted an experimental study which included flow visualization and heat transfer measurements. Yao [11] developed a perturbation solution for slightly eccentric cylinders, using two parameter expansion in terms of the eccentricity and the Rayleigh number. For this purpose, Yao [11] used a special coordinate transformation in which the inner circle was transformed into a pole. More recently, Prusa and Yao [8] constructed a finite difference numerical simulation using Yao's [11] transformed coordinates. Additional numerical simulations of viscous fluid in an eccentric annulus have been provided by Projahn, et al. [7] and by Cho et al. [4]. The former applied nonorthogonal body fitted coordinates, while the latter used bicylindrical coordinates.

The bicylindrical coordinates (Fig. 2) system is the most natural for this type of problem, since the two cylinders' surfaces coincide with constant value coordinates. Indeed, the coordinate system allows convenient description of three geometrical configurations (Fig. 1): (*a*) an eccentric gap, (*b*) a buried pipe, and (*c*) two cylinders, one outside the other.

In what follows, we construct a regular perturbation expansion of Rayleigh numbers for the stream function, temperature field, and the Nusselt number. The analytical results are compared with numerical solutions. We discuss in detail the case of the eccentric annulus in which we examine the effect of rotation in the gravity field as well as the effect of the Rayleigh number. In contrast to Yao [11] our expansion is valid for all values of eccentricity. Our solution is also valid for the case of the buried pipe; however, we defer presentation of these results to another occasion. Finally, we also comment about the case of the two cylinders, one outside the other. Although in this case a formal perturbation expansion can be constructed, the results are of no physical significance.

2 The Mathematical Model

Consider a saturated porous medium bounded between two horizontal, eccentric cylinders of radii, r_1 and r_2. Here we use the term eccentricity liberally, applying it in connection with an eccentric annulus (Fig. 1(*a*)), a buried pipe (Fig. 1(*b*)) and two cylinders, one outside the other (Fig. 1(*c*)). The line connecting the centers of these two cylinders forms angle, θ, with the gravity vector (**g**). In all these cases, the cylinders' surfaces are impermeable and maintained at constant uniform temperatures, T_1 and T_2, respectively. As a result of the foregoing temperature difference, fluid motion is induced in the medium.

We assume that the fluid motion can adequately be described by Darcy-Oberbeck-Boussinesq's equations, which can be written in cartesian coordinates (x, y, Fig. 2) as

$$\nabla^2\psi = \mathrm{R}\left(\frac{\partial T}{\partial x}\sin\theta - \frac{\partial T}{\partial y}\cos\theta\right)$$

$$\nabla^2 T = \frac{\partial\psi}{\partial y}\frac{\partial T}{\partial x} - \frac{\partial\psi}{\partial x}\frac{\partial T}{\partial y} \tag{1}$$

Where ψ and T are the stream function and the temperature, R, is the Darcy-Rayleigh number

$$\mathrm{R} = \frac{\beta^* g \lambda r_1 (T_1 - T_2)}{\alpha_{\mathrm{eq}}\nu} \tag{2}$$

In equation (2), β^* is the thermal expansion coefficient of the

Contributed by the Heat Transfer Division and presented at the ASME Winter Annual Meeting, Boston, Massachusetts, November 13-18, 1983. Paper No. 83-WA/HT-66. Manuscript received by the Heat Transfer Division April, 11, 1983.

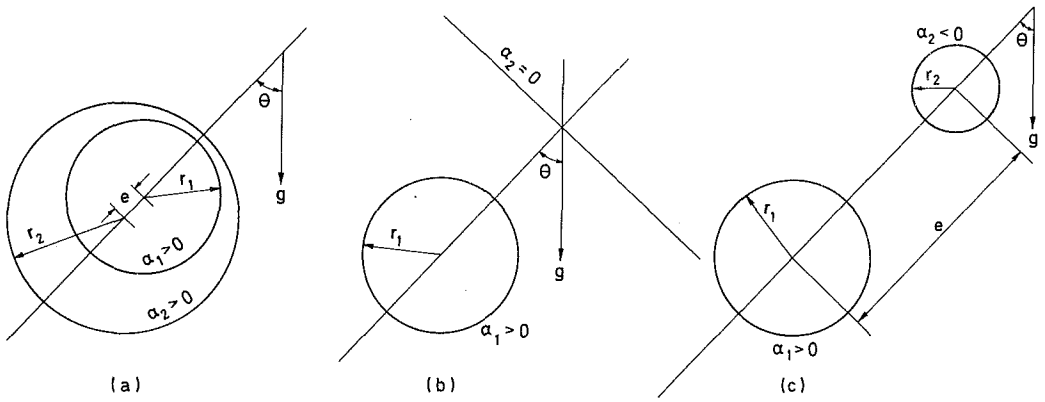

Fig. 1 The geometrical configurations considered: (*a*) the eccentric annuli; (*b*) the buried pipe; and (*c*) two cylinders, external to each other

fluid, λ is the medium permeability, α_{eq} is the thermal diffusivity, ν is the kinematic viscosity, and r_1 is the radius of the inner cylinder. All quantities are in nondimensional form. The length scale is r_1, the velocity scale is α_{eq}/r_1, and the temperature scale is $(T_1 - T_2)$.

For mathematical convenience, we have defined the Rayleigh number (R) based on the radius (r_1) of the inner cylinder. It should be noted, however, that the effective Rayleigh number should be based on the thickness of the gap between the two cylinders.

The corresponding boundary conditions are

$$T=1, \quad \psi=0 \quad \text{on } r=1$$
$$T=0, \quad \psi=0 \quad \text{on } r=r_2/r_1 \tag{3}$$

The complicated boundary conditions are handled in an elegant manner through the introduction of bicylindrical coordinates (Fig. 2). The conversion into this coordinate system is achieved through the transformation (Moon and Spencer, 1971)

$$x+iy=a\coth\frac{\alpha-i\beta}{2} \tag{4}$$

where constant α lines are the circles

$$(x-a\coth\alpha)^2+y^2=\frac{a^2}{\sinh^2\alpha} \tag{5}$$

Via this transformation, the two cylinders (Fig. 1) can be described by two constant α coordinates: α_1 and α_2 ($a = \sinh\alpha_1$).

The eccentric annulus (Fig. 1(*a*)) is obtained by specifying two nonzero coordinates of the same sign, say, $\alpha_1 > \alpha_2 > 0$. The corresponding radii ratio is $r_2/r_1 = \sinh\alpha_1/\sinh\alpha_2$, and the eccentricity $e/r_1 = \sinh(\alpha_1-\alpha_2)/\sinh\alpha_2$. We note that

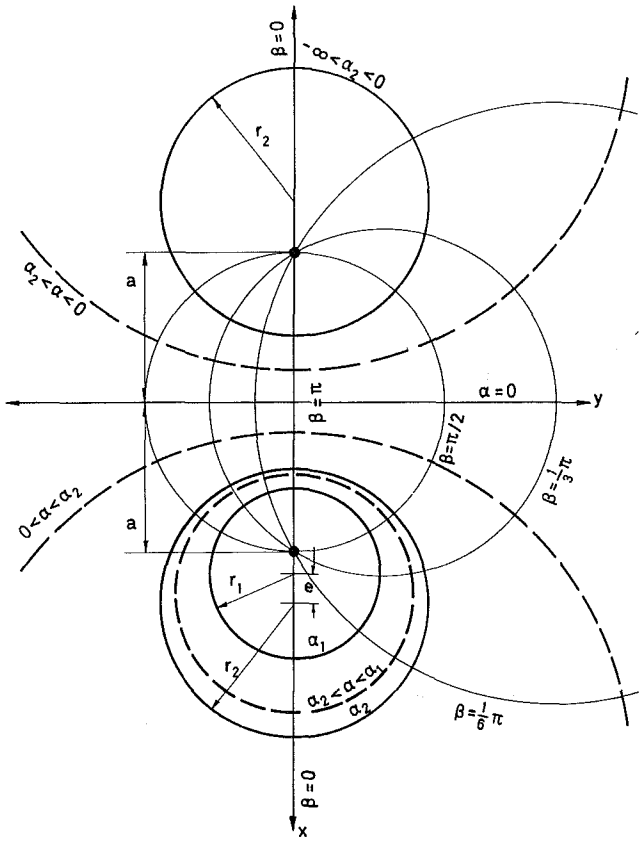

Fig. 2 The coordinate system

Nomenclature

a = scale factor in bicylindrical coordinates ($=\sinh\alpha_1$)
g = gravity vector
G,H = functions (equation 8)
N_s = a coefficient in the expansion for the Nusselt number
Nu = Nusselt number
Q = heat flow
q = heat flux
R = Rayleigh-Darcy number $\left(=\dfrac{\beta^* g\lambda r_1(T_1-T_2)}{\alpha_{eq}\nu}\right)$
r = the cylinder radius
T = temperature
x,y = Cartesian coordinates

Greek Symbols

α,β = bicylindrical coordinates
α_{eq} = equivalent thermal diffusivity of the saturated porous medium
β^* = thermal expansion coefficient
θ = inclination angle
λ = permeability
ρ = density
ψ = stream function

Subscripts

1 = the inner cylinder surface
2 = the outer cylinder surface

for any given radii ratio and eccentricity, two corresponding values of α_1 and α_2 can be found. One drawback of this coordinate system is that it does not provide for concentric cylinders. However, one may decrease the eccentricity as much as one desires. Thus, from the practical point of view, this limitation is not a serious one.

By setting $\alpha_2 = 0$, we extend the radius of the outer cylinder to infinity, which implies that the corresponding surface is a plane. We thus obtain the case of the buried pipe (Fig. 1(*b*)).

Finally, by allowing α_1 and α_2 to be of different signs (i.e., $\alpha_2 < 0$, $\alpha_1 > 0$), we obtain the case of the two cylinders, one external to the other (Fig. 1(*c*)). The eccentricity, e, in this case is the distance between the cylinders' centers.

The transformed equations (1) are

$$\nabla^2_{\alpha\beta}\psi = aR\left\{[H(\alpha,\beta)\sin\theta + G(\alpha,\beta)\cos\theta]\frac{\partial T}{\partial\alpha} + [H(\alpha,\beta)\cos\theta - G(\alpha,\beta)\sin\theta]\frac{\partial T}{\partial\beta}\right\} \tag{6}$$

$$\nabla^2_{\alpha\beta}T = \frac{\partial\psi}{\partial\alpha}\frac{\partial T}{\partial\beta} - \frac{\partial\psi}{\partial\beta}\frac{\partial T}{\partial\alpha}$$

where $\nabla^2_{\alpha\beta} = \frac{\partial^2}{\partial\alpha^2} + \frac{\partial^2}{\partial\beta^2}$ and the boundary conditions are

$$\begin{aligned} &\psi = 0 \quad T = 1 \text{ at } \alpha = \alpha_1 \\ &\psi = 0 \quad T = 0 \text{ at } \alpha = \alpha_2 \\ &\psi, T(\alpha,\beta+2\pi) = \psi, T(\alpha,\beta) \end{aligned} \tag{7}$$

and

$$H(\alpha,\beta) = \frac{1-\cosh\alpha\cos\beta}{(\cosh\alpha-\cos\beta)^2}$$

$$G(\alpha,\beta) = \frac{\sinh\alpha\sin\beta}{(\cosh\alpha-\cos\beta)^2} \tag{8}$$

Once the temperature field and the stream function are determined, the local heat flux (q) at the surfaces, α_1 and α_2, can be readily obtained.

$$q = \frac{\cosh\alpha-\cos\beta}{a}\frac{\partial T}{\partial\alpha} \text{ at } \alpha = (\alpha_1 \text{ or } \alpha_2) \tag{9}$$

The total heat flow is obtained by integrating q over either one of the cylinder's surfaces.

$$Q = \int_{-\pi}^{\pi}\left(\frac{\partial T}{\partial\alpha}\right)d\beta, \quad \alpha = \alpha_1 \text{ or } \alpha_2 \tag{10}$$

and the Nusselt number (Nu) is

$$\text{Nu} = \frac{(\alpha_1-\alpha_2)}{2\pi}Q \tag{11}$$

3 The Solution Procedure

In this paper, we construct a solution by applying a regular perturbation expansion in the form

$$T = \sum_{s=0}^{\infty}(aR)^s T_s; \quad \psi = \sum_{s=0}^{\infty}(aR)^s\psi_s;$$

$$\text{and Nu} = \sum_{s=0}^{\infty}(aR)^s N_s \tag{12}$$

Next, we introudce this expansion into the differential equations (6). Before doing that, however, we find it convenient to expand the functions H and G from (8) into their corresponding Fourier series (Appendix A). Some care must be exercised in this respect since different series result for $\alpha > 0$ and $\alpha < 0$.

The resulting perturbation equations are

$$\nabla^2_{\alpha\beta}\psi_s = \pm 2\sum_{k=1}^{\infty} ke^{\mp k\alpha}\left[\frac{\partial T_{s-1}}{\partial\alpha}\sin(k\beta\mp\theta) \mp \frac{\partial T_{s-1}}{\partial\beta}\cos(k\beta\mp\theta)\right]$$

$$\nabla^2_{\alpha\beta}T_s = \sum_{j=1}^{s}\left(\frac{\partial\psi_j}{\partial\alpha}\frac{\partial T_{s-j}}{\partial\beta} - \frac{\partial\psi_j}{\partial\beta}\frac{\partial T_{s-j}}{\partial\alpha}\right) \tag{13}$$

where the upper and lower signs in (13(*a*)) correspond to $\alpha > 0$ and $\alpha < 0$, respectively.

The boundary conditions are

$$\left.\begin{aligned} &T_o = 1, \quad \psi_o = 0 \\ &T_s = 0, \quad \psi_s = 0 (s>0) \end{aligned}\right\} \alpha = \alpha_1$$

$$T_s = 0, \quad \psi_s = 0 (s \geq 0) \qquad \alpha = \alpha_2 \tag{14}$$

and

$$N_s = \frac{\alpha_1-\alpha_2}{2\pi}\int_{-\pi}^{\pi}\left(\frac{\partial T_s}{\partial\alpha}\right)d\beta, \quad \alpha = (\alpha_1 \text{ or } \alpha_2) \tag{15}$$

In the following sections, we shall discuss separately each of the cases: the eccentric annulus, the buried pipe and the two separated cylinders.

4 The Eccentric Annulus ($\alpha_1 > \alpha_2 > 0$, Fig. 1(*a*))

4.1 The Zero-Order Solution ($s = 0$). The zero-order solution corresponds to the state of pure conduction (no fluid motion)

$$T_o = \frac{\alpha-\alpha_2}{\alpha_1-\alpha_2}; \quad \psi_o = 0; \quad N_o = 1 \tag{16}$$

4.2 First-Order Solution ($s = 1$). For the first-order equations in (13) become

$$\nabla^2_{\alpha\beta}\psi_1 = \frac{2}{\alpha_1-\alpha_2}\sum_{k=1}^{\infty} ke^{-k\alpha}\sin(k\beta-\theta)$$

$$\nabla^2_{\alpha\beta}T_1 = \frac{-1}{\alpha_1-\alpha_2}\frac{\partial\psi_1}{\partial\beta} \tag{17}$$

with boundary conditions (14). The solution is readily obtained in the form

$$\psi_1 = \sum_{n=1}^{\infty} g_{1n}\sin(n\beta-\theta)$$

$$T_1 = \sum_{n=1}^{\infty} f_{1n}\cos(n\beta-\theta) \tag{18}$$

where

$$g_{1n} = e^{-n\alpha_1}\frac{\sinh n(\alpha-\alpha_2)}{\sinh n(\alpha_1-\alpha_2)} - \frac{\alpha-\alpha_2}{\alpha_1-\alpha_2}e^{-n\alpha}$$

$$f_{1n} = \frac{1}{4}e^{-n\alpha_1}\left\{1 + \frac{1}{n(\alpha_1-\alpha_2)} + 2\coth[n(\alpha_1-\alpha_2)]\right\}\times \frac{\sinh n(\alpha-\alpha_2)}{\sinh n(\alpha_1-\alpha_2)} - \frac{1}{2}\left(\frac{\alpha-\alpha_2}{\alpha_1-\alpha_2}\right)e^{-n\alpha_1}\frac{\cosh n(\alpha-\alpha_2)}{\sinh n(\alpha_1-\alpha_2)} - \frac{1}{4}\left[\left(\frac{\alpha-\alpha_2}{\alpha_1-\alpha_2}\right)^2 + \frac{1}{n}\frac{\alpha-\alpha_2}{(\alpha_1-\alpha_2)^2}\right]e^{-n\alpha}$$

$$(0 < \alpha_2 < \alpha < \alpha_1) \tag{19}$$

We observe that the expressions for g_{1n} and f_{1n} consist of two types of terms, those containing $e^{-n\alpha_1}$ and those without it. The expressions containing $e^{-n\alpha_1}$ are expected to converge rapidly for most practical cases (i.e., for a situation of $r_2/r_1 = 2$ and relative eccentricity $e/(r_2-r_1) = 0.1$; $\alpha_1 \sim 3.4$). The terms without this exponent may converge slowly for cases in which $\alpha > \alpha_2$ is small. Fortunately, the potentially slowly converging series can be identified with known analytical functions (see Appendix A), thereby allowing us to rewrite the expressions for ψ_1 and T_1 in the following form

$$\psi_1 = -\frac{1}{2}\left(\frac{\alpha-\alpha_2}{\alpha_1-\alpha_2}\right)\frac{\sin(\beta-\theta)+e^{-\alpha}\sin\theta}{\cosh\alpha-\cos\beta} + \sum_{n=1}^{\infty} e^{-n\alpha_1}\frac{\sinh n(\alpha-\alpha_2)}{\sinh n(\alpha_1-\alpha_2)}\sin(n\beta-\theta)$$

$$T_1 = -\frac{1}{8}\left(\frac{\alpha-\alpha_2}{\alpha_1-\alpha_2}\right)^2\frac{\cos(\beta-\theta)-e^{-\alpha}\cos\theta}{\cosh\alpha-\cos\beta} - \frac{1}{4}\frac{\alpha-\alpha_2}{(\alpha_1-\alpha_2)^2}\left\{\cos\theta\left[\frac{\alpha}{2}-\frac{1}{2}\ln 2(\cosh\alpha-\cos\beta)\right] + \sin\theta\tan^{-1}\left(\frac{\sin\beta}{e^{\alpha}-\cos\beta}\right)\right\} + \sum_{n=1}^{\infty} e^{-n\alpha_1}\left\{\frac{1}{4}\left[1+\frac{1}{n(\alpha_1-\alpha_2)} + 2\coth n(\alpha_1-\alpha_2)\right]\frac{\sinh n(\alpha-\alpha_2)}{\sinh n(\alpha_1-\alpha_2)} - \frac{1}{2}\frac{\alpha-\alpha_2}{\alpha_1-\alpha_2}\frac{\cosh n(\alpha-\alpha_2)}{\sinh n(\alpha_1-\alpha_2)}\right\}\cos(n\beta-\theta) \tag{20}$$

Now we have quickly converging expressions for all values of $\alpha > \alpha_2 > 0$.

Note that the first-order solution for the stream function has the property

$$\psi_1(\alpha,\beta,\theta) = -\psi_1(\alpha,\beta,\theta+\pi)$$

which implies that the first-order flow field is essentially invariant to rotation of the annulus through 180 deg, except, of course, to a change in the direction of the flow.

Although the first-order solution modifies the local heat flux on the cylinders' surfaces, there is no net contribution to the total heat flow. That is

$$N_1 = 0 \tag{21}$$

In order to assess the contribution of the convection to the heat transfer, we have to turn to the second-order solution.

4.3 Second-Order Solution ($s = 2$). The second-order equations are obtained from (13) by introducing $s = 2$ and replacing T_1 and ψ_1 with (18). The equation for the stream function becomes

$$\nabla^2_{\alpha\beta}\psi_2 = 2\sum_{i=1}^{\infty}\sum_{k=1}^{\infty} ke^{-k\alpha}\left\{\frac{df_{1,i}}{d\alpha}\cos(i\beta-\theta)\sin(k\beta-\theta) + if_{1,i}\sin(i\beta-\theta)\cos(k\beta-\theta)\right\} \tag{22}$$

with a solution of the form

$$\psi_2 = \sum_{n=1}^{\infty}\left\{g^I_{2,n}\sin n\beta + g^{II}_{2,n}\sin(n\beta-2\theta)\right\} \tag{23}$$

The corresponding equation for the temperature is

$$\nabla^2_{\alpha\beta}T = -\frac{1}{\alpha_1-\alpha_2}\sum_{i=1}^{\infty}[ig^I_{2,i}\cos i\beta + ig^{II}_{2,i}\cos(i\beta-2\theta)] - \frac{1}{2}\sum_{i=1}^{\infty}\sum_{j=1}^{\infty}\left\{\left(jf_{1,j}\frac{dg_{1,i}}{d\alpha} + ig_{1,i}\frac{df_{1,j}}{d\alpha}\right)\cos(i-j)\beta - \left(jf_{1,j}\frac{dg_{1,i}}{d\alpha} - ig_{1,i}\frac{df_{1,j}}{d\alpha}\right)\cos[(i+j)\beta-2\theta]\right\} \tag{24}$$

with a solution of the form

$$T_2 = \sum_{n=0}^{\infty}[f^I_{2,n}\cos n\beta + f^{II}_{2,n}\cos(n\beta-2\theta)] \tag{25}$$

with $f^{II}_{2,0} = 0$.

Although the resulting equations for g_2 and f_2 are simple second-order ODE, the algebra is rather lengthy. Thus, we present the results only for the former (see Appendix B).

We note, however, that in order to obtain the second-order correction to the Nusselt number (N_2) no knowledge of the second order solution is required since

$$N_2 = (\alpha_1-\alpha_2)\frac{df^I_{2,0}}{d\alpha}\bigg|_{\alpha=\alpha_1 \text{ or } \alpha_2} = \frac{1}{2}\sum_{i=1}^{\infty} i\int_{\alpha_1}^{\alpha_2} f_{1,i}\,g_{1,i}\,d\alpha \tag{26}$$

Calculated values for (a^2N_2) are presented in Fig. 3 for radii ratio $r_2/r_1 = 1.5$, 2, 5, and 10 and for various eccentricities. We extrapolate our results to zero eccentricity and compare them with those calculated by Burns and Tien [2] for the case of two concentric cylinders; their results are denoted by triangles in Fig. 3. Clearly, we reproduce the results of a concentric annulus for the limiting case of $e \to 0$.

A somewhat peculiar characteristic of the second-order correction to the Nusselt number is its independence of the inclination angle (θ). This suggests that the range of validity of the second-order solution will quickly deteriorate as the eccentricity increases.

4.4 Third-Order Solution ($s = 3$). The algebra involved in constructing this order of solution is tedious indeed. Here, our goal is merely to assess the effect of the inclination angle (θ) on the Nusselt number. As in the previous section, this correction is constructed from the lower order solution, and fortunately detailed knowledge of the third-order solution is not required.

$$N_3\cos\theta = \frac{1}{2}\cos\theta\sum_{i=1}^{\infty} i\int_{\alpha_1}^{\alpha_2}[f_{1,i}(g^I_{2,i}+g^{II}_{2,i}) + g_{1,i}(f^I_{2,i}+f^{II}_{2,i})]\,d\alpha \tag{27}$$

Calculated values for a^3N_3 are depicted in Fig. 3 for radii ratios $r_2/r_1 = 1.5$, 2, 5, and 10 and for various eccentricities. We expect N_3 to decrease as the eccentricity decreases and to go to zero as $e \to 0$. That is, for two concentric cylinders we predict $N_3 = 0$ since the Nusselt number should be independent of θ. This trend is well reflected in Fig. 3.

4.5 Higher Order Solutions. Analytical continuation of the foregoing is extremely tedious; therefore, we shall quit at this stage. In a separate paper, we use a somewhat different procedure which can be readily delegated to the computer. In the latter case we extend the expansion to many terms.

A sample of these results is presented in Table 1, where we list the 24 first terms in the Nusselt number expansion for $r_2/r_1 = 2$, $\theta = 0$, $e = 0.001$, and $\theta = 0.2$. We estimate the radius of convergence (R_c) of the series by using the criteria (Titchmarsh, 1942)

$$R_c = \lim_{s\to\infty} |a^sN_s|^{-1/s}$$

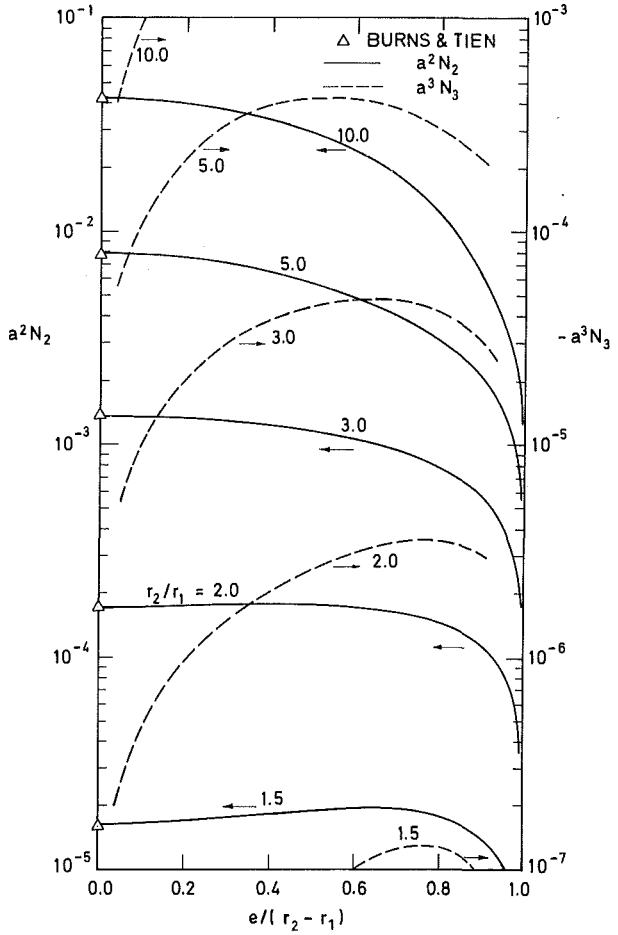

Fig. 3 The coefficients a^2N_2 and a^3N_3 in the perturbation expansion for the Nusselt number as a function of the relative eccentricity $e/(r_2 - r_1)$

and consider separately the even and odd terms in each set.

By extrapolating the values in Table 1, we estimate $R_c \geq 50$ and 35 for $e = 0.001$ and $e = 0.2$, respectively. These estimates are not accurate due to the slow convegence of the sequence $|a^sN_s|^{-1/s}$. We present the foregoing values here to demonstrate that the perturbation series is valid for finite values of R and is not restricted to $R < 1$. This fact will be further amplified in section 7.1 where we compare the results of the perturbation expansion with those of a finite difference numerical simulation (Fig. 5). We obtain an excellent agreement for $R = 20$ and for $-0.8 \leq e \leq 0.8$. As the Rayleigh number increases, the deviation between the perturbation expansion and the numerical simulation increases for large $|e|$. This fact suggests that the radius of convergence decreases with increasing eccentricity, and it is in agreement with the trend observed in Table 1.

5 The Case of the Buried Pipe ($\alpha_1 > \alpha_2 = 0$)

The case of the buried pipe is obtained by setting $\alpha_2 = 0$. The expressions presented in section 4 are valid for this case. We note that infinity in the physical plane corresponds to $\alpha = \beta = 0$ in the mapped plane (the bicylindrical coordinates). At infinity ($\alpha = \beta = 0$), both components of the velocity vector (the normal and the tangential) vanish. It is this fact that makes this solution physically acceptable. A detailed discussion of this case will be given elsewhere.

6 The Case of Two Cylinders One Outside the Other ($\alpha_1 > 0, \alpha_2 < 0$)

When α_1 and α_2 have different signs, the case of the two cylinders one outside the other is obtained (Fig. 1(*c*)).

In this particular case one encounters two difficulties. First, suppose the two cylinders are at the same temperature. Our model will predict isothermal medium which does not give rise to buoyancy driven flow. Clearly, this is not the case in actuality where buoyant plumes always exist.

Second of all, although a regular perturbation expansion can be constructed for the case of two cylinders having different temperatures, this expansion predicts behavior which is physically unacceptable.

In order to demonstrate that this is the case, let us focus on a special example of $\theta = 0$, and $\alpha_2 = -\alpha_1$. The perturbation

Table 1 The first 26 terms (a^sN_s) in the series expansion for the Nusselt number

s	$e=0.001$ a^sN_s	$e=0.2$ a^sN_s
0	1.	1.
1	0.	0.
2	.172 757 −003	.174 025 −003
3	−.481 692 −008	−.983 492 −006
4	−.167 702 −007	−.132 370 −007
5	.171 879 −011	.360 647 −009
6	.757 615 −012	.446 437 −011
7	−.254 092 −015	.177 153 −013
8	.292 879 −015	.478 085 −015
9	.173 860 −019	−.767 600 −017
10	−.144 064 −018	.132 619 −018
11	.269 621 −022	−.146 783 −019
12	.208 478 −022	.837 533 −021
13	−.149 852 −025	−.269 552 −022
14	.480 353 −026	.431 801 −024
15	−.412 495 −029	.665 302 −026
16	.197 535 −029	−.742 865 −027
17	.134 362 −032	.285 746 −028
18	−.120 757 −032	−.627 258 −030
19	.191 950 −035	.215 962 −032
20	−.881 199 −036	.485 951 −033
21	−.172 917 −039	−.242 596 −034
22	.375 106 −039	.661 411 −036
23	−.497 283 −042	−.806 894 −038
24	.125 434 −042	−.227 872 −039
25	.655 986 −046	.175 243 −040
26	−.799 421 −046	−.594 768 −042

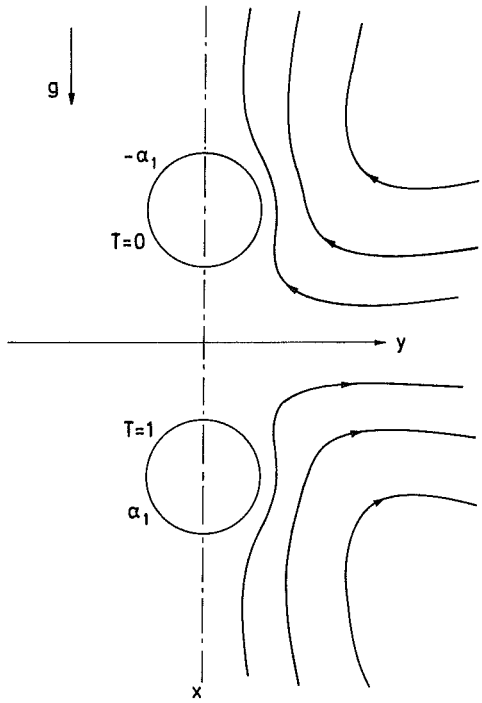

Fig. 4 The streamlines (ψ_1) predicted by the perturbation expansion for the case of two cylinders, equal in size and external to each other

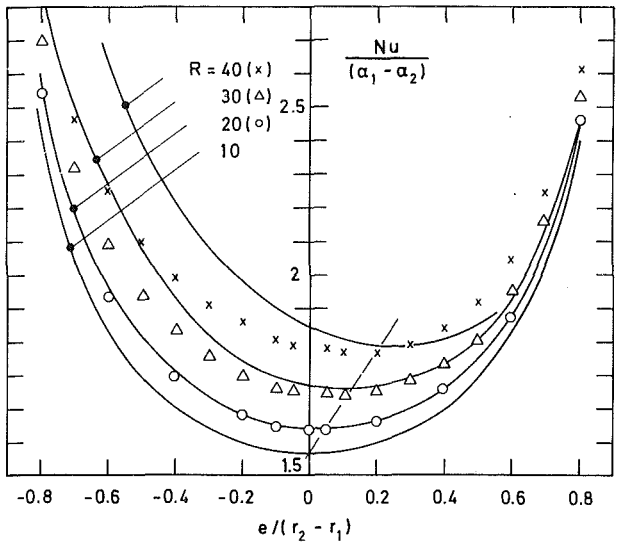

Fig. 5 The heat flow as a function of the relative eccentricity for an annulus of radii ratio $r_2/r_1 = 2$. Results are presented for Rayleigh numbers R = 10, 20, 30, and 40. The solid lines are the analytical solution, while the symbols (o, Δ and +) represent the results of a numerical simulation.

equation for ψ_1 in this case will be

$$\nabla^2\psi_1 = \frac{1}{2\alpha_1}\frac{\sinh\alpha\sin\beta}{(\cosh\alpha-\cos\beta)^2} \tag{28}$$

with the boundary condition $\psi_1 = 0$ at $\pm\alpha_1$. Note, that we avoid using equation (17) since the Fourier expansions for G and H may not be uniformly convergent at $\alpha = 0$.

Clearly, the forcing term in (28) is antisymmetric; hence, we expect the solution to have the property $\psi_1(\alpha,\beta) = -\psi_1(-\alpha,\beta)$. The foregoing result implies that $\psi_1 = 0$ on $\alpha = 0$. That is the plane $\alpha = 0$ appears as a solid boundary. In other words, the perturbation solution yields a solution which is identical to the case of two cylinders buried on both sides of an impermeable surface. In order to further clarify the idea, we sketch the predicted streamlines in Fig. 4. Similar results will be obtained for the more general case of $|\alpha_1| \neq |\alpha_2|$, $\theta \neq 0$. Clearly these results have no physical significance, and thus we conclude that in general the perturbation solution cannot be used in the case of two cylinders, one external to the other.

7 Results for the Eccentric Annulus

In this section, we present a few results for the heat transfer, flow and temperature fields in an eccentric annulus. We choose a particular case of radii ratio $r_2/r_1 = 2$, and we denote the eccentricity as positive or negative according to whether the center of the inner cylinder is located above ($\theta = 0$) or below ($\theta = \pi$) the center of the outer cylinder.

7.1 Heat Transfer. As a conclusion of our derivation in section 4, we obtain

$$\mathrm{Nu} = 1 + (a\mathrm{R})^2 N_2 + (a\mathrm{R})^3 N_2\cos\theta + (a\mathrm{R})^4 (N_{4,1} + N_{4,2}\cos 2\theta) + 0(a\mathrm{R})^5 \tag{29}$$

where values for a^2N_2 and a^3N_3 are presented in Fig. 3. In this section, we investigate the dependence of the heat flow on the eccentricity. As a measure of the heat transfer, we use the quantity $\mathrm{Nu}/(\alpha_1-\alpha_2)$, where $1/(\alpha_1-\alpha_2)$ is proportional to the conductive heat flow. The dependence of $\mathrm{Nu}/(\alpha_1-\alpha_2)$ on the relative eccentricity $e/(r_2-r_1)$ is depicted (solid curves) in Fig. 5, for $r_2/r_1 = 2$, R = 10, 20, 30, and 40 and $-.8 < e/(r_1-r_2) < .8$.

For R = 10 conduction heat transport is dominating, and the convective effects are very weak. Consequently, the curve is almost symmetric with respect to $e = 0$. The minimum heat losses are obtained in the concentric situation. Any deviation from the concentricity results in decreased effective thickness of the insulation and thus an increase in the conductive heat flow. As $e/(r_2-r_1) \to \pm 1$ we approach a situation in which both cylinders are almost touching each other, and the heat transfer goes to infinity.

As the Rayleigh number increases about 10, the convective effects become more pronounced. Clearly the intensity of the convective motion (i.e., the effective Rayleigh number) can be decreased or increased by moving the center of the inner cylinder upwards or downwards. At the same time, however, the conductive resistance is reduced. Hence, there is some optimal value of the eccentricity ($e/(r_2-r_1) > 0$) for which the heat flow is minimized. The magnitude of the optimal value will increase as the Rayleigh number increases. This trend is schematically shown by a dashed line in Fig. 5. Our analytical results are valid only for relatively small Rayleigh numbers, for which the reduction in the total heat transfer achieved by using eccentric insulation is minor, i.e., less than 1 percent for R = 30 and less than 4 percent for R = 40. However, the reduction in the heat losses is likely to become more significant as the Rayleigh number increases.

In the present work, we obtained only rough estimates for the radius of convergence of the series for the Nusselt number (section 4.5). It is interesting, therefore, to compare our analytical results with those obtained from a finite difference numerical simulation (Fig. 5) in which we used Patankar's [9] power law scheme. We note a good agreement between the analytical and numerical results for R = 20 and 30 (discrepancies smaller than 2 and 8 percent, respectively). However, as the Rayleigh number increases, the accuracy of the analytical solution deteriorates. For R = 40, the analytical solution is valid only for small eccentricities.

7.2 The Flow and Temperature Fields. In Figs. 6, 8, and 9 we exhibit the flow and temperature fields calculated by using the first-order term in the perturbation series (i.e., ψ_1 and $T_o + a\mathrm{R}\,T_1$).

We examine first the effect of the eccentricity on the temperature and flow field. In Fig. 6 we depict the streamlines (the righ-hand side of the annulus) and the isotherms (left-hand side) for $r_2/r_1 = 2$, $\theta = 0$ and $e/(r_2-r_1) = 0.01, 0.35$, and 0.70. The increment between streamlines is constant and equal to $|\psi_{\max}|/6$. The (+) denotes the location of $|\psi_{\max}|$. The isotherms correspond to R = 20, and the increment between them equals 0.2. In this particular case ($\theta = 0$), the flow and temperature fields are symmetric with respect to the line interconnnecting the cylinders' centers. The flow consists of two counter rotating convective cells. That is, hot fluid rises near the inner, hotter, cylinder and descends next to the outer, cooler cylinder. We have depicted the flow field for positive eccentricities only ($\theta = 0$), since the situation for negative eccentricities can be obtained simply by inverting the figure. We have already mentioned (section 4.1) that the flow field predicted by ψ_1 is invariant to rotation by θ, except, of course, for a change in the direction of the flow. As a result of this invariance the center of rotation (+) is always located at the midplane of the outer cylinder.

The dashed lines in Fig. 6 depict the isotherms in the absence of convection (T_o), while the solid lines represent the actual temperature field ($T_o + a\mathrm{R}\,T_1$). The distortion of the temperature field due to convection is self evident. We also note that at these low Rayleigh numbers there is no evidence of the emergence of a plume at the top of the inner cylinder, as we expect to observe at higher Rayleigh numbers (which are beyond the range of validity of our expansion).

In order to investigate the effect of the Rayleigh number on the structure of the flow field, we depict in Fig. 7 the

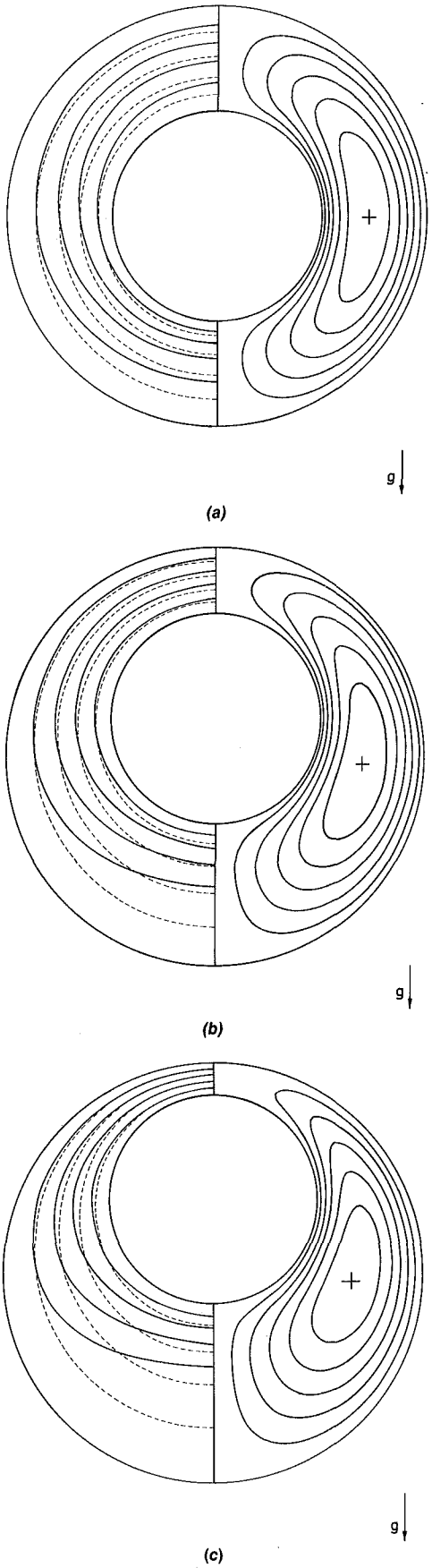

Fig. 6 The streamlines (ψ_1) and the isotherms ($T_o + aR\,T_1$) are shown for the eccentric annulus $r_2/r_1 = 2$ and for different relative eccentricities $e/(r_2 - r_1)$ = (a) 0.01, (b) 0.35, and (c) 0.70. The streamlines and the isotherms occupy the right- and left-hand sides of the annulus, respectively. The dashed lines represent the conductive solution (T_o).

streamlines obtained by the two term expansion ($aR\psi_1 + a^2R^2\psi_2$) for R = 1, 10, 40, and 100. We note that up to R $\leq$ 40, the increase in the Rayleigh number does not change significantly the structure of the flow. The only effect is the upward shifting of the center of circulation (the location of $|\psi_{max}|$). This trend is represented by a dashed line in Fig. 7. A dramatic change is observed for R > 50. For example, for R = 100 (Fig. 7(*d*)), we observe the emergence of a secondary cell at the bottom of the annulus. This result, however, may not have any physical significance since the corresponding value of R = 100 is well beyond the range of validity of our analytical results. As a matter of fact, neither our flow visualization experiments nor our numerical simulation predict this type of bifurcation.

Next, we examine the effect of the eccentricity on the maximum value of the stream function $|\psi_{max}|$. The dashed and solid curves in Fig. 8 represent the value of $|\psi_{max}|$ obtained by using the first term in the expansion ($|aR\,\psi_1|_{max}$) and the sum of the two first terms ($|aR\,\psi_1 + (aR)^2\,\psi_2|_{max}$), respectively. The circles are results of a finite difference numerical simulation. Results are presented for R = 20 and 30.

The first term expansion $|aR\,\psi_1|_{max}$ predicts results which are symmetric with respect to $e = 0$. This, of course, is physically incorrect since we expect more intense circulation for negative eccentricities than for positive ones. The situation is, however, corrected by the second term in the expansion. The value of $|\psi_{max}|$ calculated from the two term expansion decreases monotonically with increasing eccentricity as, indeed, should be the case. Our analytical results compare well with those of the finite difference simulation for R = 20 (deviation smaller than 4 percent). For higher Rayleigh numbers, this deviation increases (i.e., less than 10 percent for R = 30).

Finally, we examine the effect of the angle of inclination (θ) on the flow field. In Fig. 9 we depict streamlines (solid lines) and isotherms (dashed lines) for $e/(r_2 - r_1) = 0.35$ and for $\theta = \pi/2$ and $3\pi/4$. In Fig. 10 we depict the case of $e/(r_2 - r_1) = 0.70$ and $\theta = \pi/4$ and $\pi/2$. In both cases we use the first term in the perturbation expansion (ψ_1). The streamlines are equally spaced with an increment of $|\psi_{max}|/4$.

Since, with the exception of the direction of the flow, the flow field (ψ_1) is invariant to π rotation, the case of $\theta = \pi/4$ can be obtained by π rotation of Fig. 9(*b*) and mirror image projection. Similarly, the case of $\theta = 3\pi/4$ can be obtained from $\theta = \pi/4$ in Fig. 10(*a*).

The flow field predicted by ψ_1 is good qualitative agreement to flow visualization experiments we have conducted in a Hele-Shaw cell.

We note that the structure of the two convective cells we have observed in the symmetric case (Fig. 6) is preserved. The symmetry is, however, destroyed when the two cells align themselves in the gravity field.

8 Conclusion

A regular perturbation expansion has been derived for the flow and temperature fields as well as for the Nusselt number for the case of the eccentric annulus. The results are applicable also for the case of the buried pipe. For the case of two cylinders external to each other, in general a meaningful regular pertubration series cannot be constructed.

The results for the eccentric annulus demonstrate that the heat flow involved therein can be reduced compared to the concentric case. The magnitude of the above reduction in the heat losses is proportional to the magnitude of the Rayleigh number. Similarly, in the case of the buried pipe there exists an optimal burial depth for which heat losses are minimized.

Acknowledgment

This material is based upon work supported, in part, by the

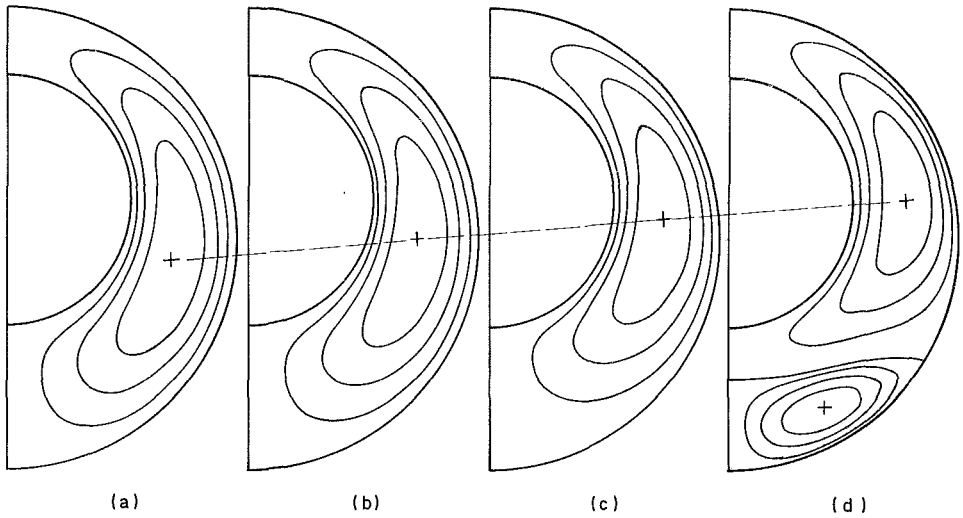

Fig. 7 The effect of the Rayleigh number on the structure of the flow field. The flow field in the eccentric annulus (α_1 = 2.01961, α_2 = 1.440775 and $e/(r_2 - r_1)$ = 0.35) is depicted for Rayleigh numbers: R = 1, 10, 40, and 100 in parts (*a*), (*b*), (c), and (*d*), respectively.

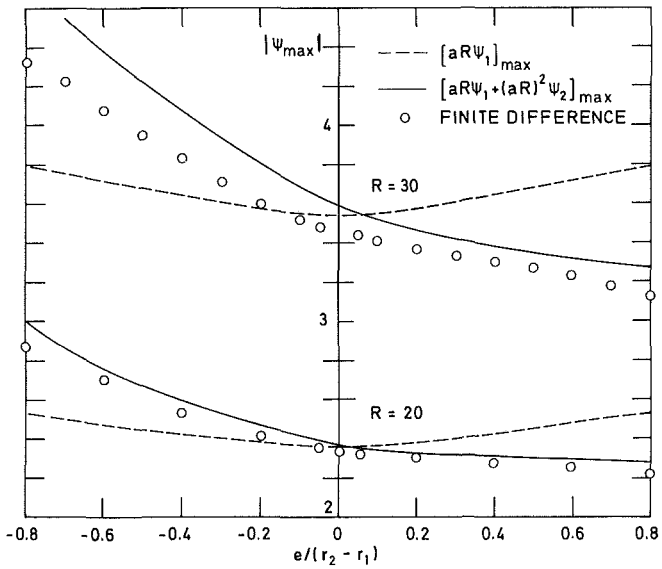

Fig. 8 The maximum value of the stream function $|\psi_{max}|$ is depicted as a function of the eccentricity. The dashed lines and the solid lines represent respectively the first and the two first terms in the expansion. The circles are the results of numerical simulation.

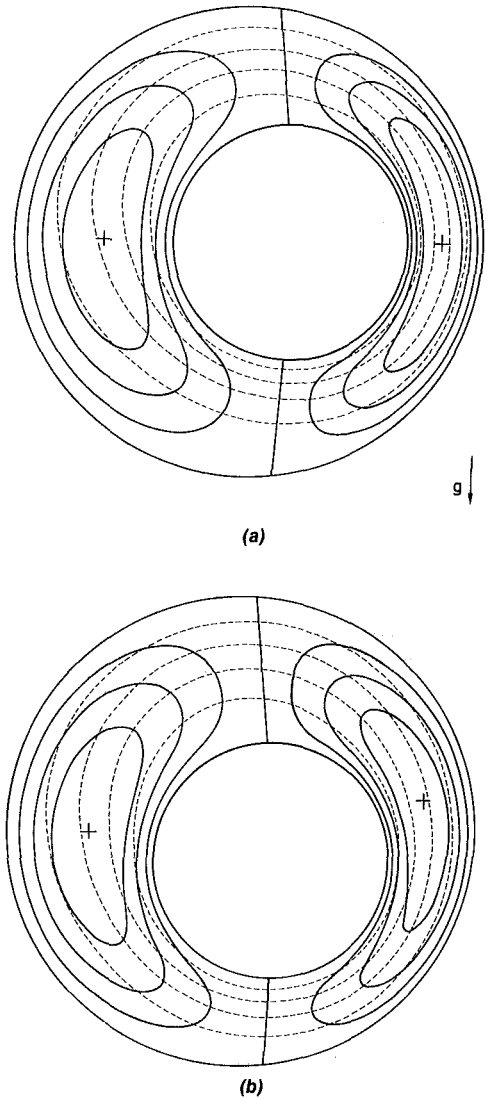

Fig. 9 The flow and temperature field are depicted in solid lines and dashed lines respectively for relative eccentricity $e/(r_2 - r_1)$ = 0.35 and inclination angles (*a*) $\theta = \pi/2$ and (*b*) $\theta = 3\pi/4$

National Science Foundation under Grant No. MEA 8217565. I also gratefully acknowlege a summer award from the University of Pennsylvania which provided partial support for the research.

References

1 Brailovskaya, V. A., Petrazhitskii, G. B., and Polezhaev, V. I., "Natural Convection and Heat Transfer in Porous Interlayers Between Horizontal Coaxial Cylinders," *Journal of Applied Mechancis and Technical Physics*, Vol. 19, 1978, pp. 781–785.

2 Burns, P. J., and Tien, C. L., "Natural Convection in Porous Media Bounded by Concentric Spheres and Horizontal Cylinders," *International Journal of Heat and Mass Transfer*, Vol. 22, 1979, pp. 929–939.

3 Caltagirone, J. P., "Thermoconvective Instabilities in a Porous Medium Bounded by Two Concentric Horizontal Cylinders," *Journal of Fluid Mechanics*, Vol. 2, 1976. pp. 337–362.

4 Cho, C. H., Chung, K. S., and Park, K. H., "Numerical Simulation of Natural Convection in Concentric and Eccentric Horizontal Cylindrical Annuli," ASME JOURNAL OF HEAT TRANSFER, Vol. 104, 1982, pp. 624–630.

5 Kuehn T. H., and Goldstein, R. J., "An Experimental Study of Natural

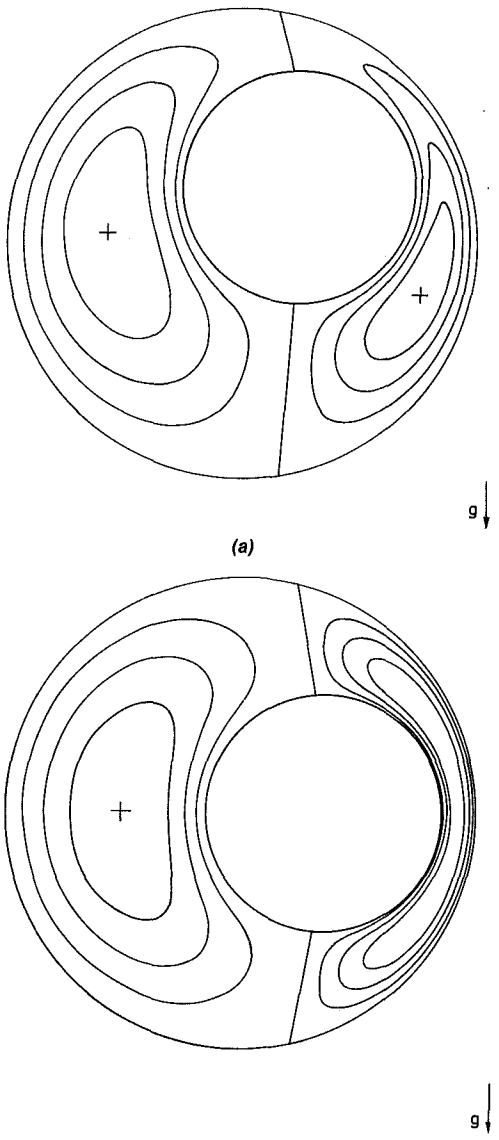

Fig. 10 The flow field is shown for an annulus with relative eccentricity $e/(r_2 - r_1) = 0.70$ and inclination angles (a) $\theta = \pi/4$ and (b) $\theta = \pi/2$

Convection Heat Transfer in Concentric and Eccentric Horizontal Cylindrical Annuli," ASME JOURNAL OF HEAT TRANSFER, Vol. 100, 1978, pp. 635-640.

6 Moon, P., and Spencer, D. E., *Field Theory Handbook*. Springer-Verlag, 1971.

7 Projahn, U., Rieger, H., and Beer, H., "Numerical Analysis of Laminar Natural Convection Between Concentric and Eccentric Cylinders," *Numerical Heat Transfer*, Vol. 4, pp. 131-146.

8 Prusa, J., and Yao, L. S., "Natural Convection Heat Transfer Between Eccentric Horizontal Cylinders," ASME JOURNAL OF HEAT TRANSFER, Vol. 105, pp. 108-116.

9 Patankar, S. V., *Numerical Heat Transfer and Fluid Flow*, Hemisphere, 1980.

10 Titchmarsh, E. C., *The Theory of Functions*, Oxford University Press, 1942, p. 213.

11 Yao, L. S., "Analysis of Heat Transfer in Slightly Eccentric Annuli," ASME JOURNAL OF HEAT TRANSFER, Vol. 102, 1980, pp. 279-284.

APPENDIX A

In this Appendix we expand functions G and H (equation (8)) into the corresponding Fourier series. Later in the Appendix, we manipulate these results so that we can identify some of the inifinte series in equation (19) with known analytic functions. The derivation is for $\alpha > 0$. The derivation for $\alpha < 0$ will follow along similar lines and is not given here.

Let

$$G(\alpha,\beta) = \sum_{n=1}^{\infty} A_n \sin n\beta \tag{A1}$$

Thus

$$A_n = \frac{1}{\pi}\int_{-\pi}^{\pi} \frac{\sinh\alpha \sin\beta \sin n\beta}{(\cosh\alpha - \cos\beta)^2}\, d\beta \tag{A2}$$

and integration by parts yields

$$A_n = \frac{n\sinh\alpha}{\pi}\int_{-\pi}^{\pi} \frac{\cos n\beta}{\cosh\alpha - \cos\beta}\, d\beta \tag{A3}$$

Next, we focus on the integral

$$I_n = \int_{-\pi}^{\pi} \frac{e^{in\beta}\, d\beta}{\cosh\alpha - \cos\beta} \tag{A4}$$

We denote $z = e^{i\beta}$ and carry the integration over the contour enclosing $|z| \le 1$. Consequently

$$I_n = 2i\oint \frac{z^n\, dz}{(z - e^{\alpha})(z - e^{-\alpha})} \tag{A5}$$

The integrand has a simple pole at $z = e^{-\alpha}$. Using Cauchy's integral formula, we obtain

$$I_n = \frac{2\pi e^{-n\alpha}}{\sinh\alpha} \tag{A6}$$

Note that equation (A3) can be written as

$$A_n = \frac{n\sinh\alpha}{\pi}\,\mathrm{Re}\{I_n\} = 2ne^{-n\alpha} \tag{A7}$$

where $\mathrm{Re}\{I_n\}$ is the real part of I_n.
Therefore the Fourier series expansion for

$$G(\alpha,\beta) = 2\sum_{n=1}^{\infty} ne^{-n\alpha}\sin n\beta \tag{A8}$$

The expansion of $H(\alpha,\beta)$ is obtained through a similar procedure. Let

$$H(\alpha,\beta) = \sum_{n=0}^{\infty} B_n \cos n\beta \tag{A9}$$

Thus

$$B_n = \frac{\delta_n}{\pi}\int_{-\pi}^{\pi} \frac{1 - \cosh\alpha\cos\beta}{(\cosh\alpha - \cos\beta)^2}\cos n\beta\, d\beta$$

$$= \frac{\delta_n}{\pi}\frac{\partial}{\partial\alpha}[\sinh\alpha\,\mathrm{Re}\{I_n\}] \tag{A10}$$

where I_n is calculated in equation (A6) and

$$\delta_n = \begin{cases} 1/2 \text{ for } n = 0 \\ 1 \text{ for } n > 0 \end{cases} \tag{A11}$$

Consequently

$$H(\alpha,\beta) = -2\sum_{n=1}^{\infty} ne^{-n\alpha}\cos n\beta \tag{A12}$$

By integrating (A8) with respect to β or (A12) with respect to α, we obtain

$$\frac{\sinh\alpha}{\cosh\alpha - \cos\beta} = 2\,\delta_n\sum_{n=0}^{\infty} e^{-n\alpha}\cos n\beta \tag{A13}$$

Similarly, integration of (A8) with respect to α or (A12) with respect to β yields

$$\frac{\sin\beta}{\cosh\alpha-\cos\beta}=2\sum_{n=1}^{\infty}e^{-n\alpha}\sin n\beta \tag{A14}$$

Integration of (A13) with respect to α or (A14) with respect to β yields

$$\ln\left[2(\cosh\alpha-\cos\beta)\right]=\alpha-2\sum_{n=1}^{\infty}\frac{1}{n}e^{-n\alpha}\cos n\beta \tag{A15}$$

where the factor 2 inside the ln is due to a constant of integration.

Integration of (A13) with respect to β or (A14) with respect to α yields

$$\tan^{-1}\frac{\sin\beta}{e^{\alpha}\cos\beta}=\sum_{n=1}^{\infty}\frac{1}{n}e^{-n\alpha}\sin n\beta \tag{A16}$$

Expressions (A13–A16) were used in converting equation (19) into equation (20).

APPENDIX B

We present here the analytical expressions for the second term in the expansion for ψ_2. Recall equation (23)

$$\psi_2=\sum_{n=1}^{\infty}\left\{g^{I}_{2,n}\sin n\beta+g^{II}_{2,n}\sin(n\beta-2\theta)\right\} \tag{B1}$$

We find it convenient to express $g^{I}_{2,n}$ and $g^{II}_{2,n}$ in the following form

$$g^{I}_{2,n}=(gg_1(\alpha,n)+C_2+C_4)\,e^{-n\alpha}+(gg_2(\alpha,n)+C_1+C_3)\,e^{n\alpha} \tag{B2}$$

and

$$g^{II}_{2,n}=(gg_3(\alpha,n)+C_5)e^{-n\alpha}+C_6e^{n\alpha} \tag{B3}$$

where

$$gg_1(\alpha,n)=\frac{1}{8}\left(\frac{\alpha-\alpha_2}{\alpha_1-\alpha_2}\right)^2\frac{1}{e^{2\alpha-1}}+\sum_{i=1}^{\infty}\left\{\frac{(n+2i)\,e^{-2i\alpha}}{16i(n+i)\,(\alpha_1-\alpha_2)^2}\left[\frac{1}{(n+i)}+2(\alpha-\alpha_2)\right]+\frac{e^{-i(\alpha_1-\alpha_2)}}{8\sinh[i(\alpha_1-\alpha_2)]}\left[\frac{n+i}{n}\left(\frac{\alpha-\alpha_2}{\alpha_1-\alpha_2}\right)e^{-2i\alpha_2}+\frac{1}{2}e^{-2i\alpha}\left(1+\frac{n+2i}{i(n+i)\,(\alpha_1-\alpha_2)}+2\coth[i(\alpha_1-\alpha_2)]+2\frac{\alpha-\alpha_2}{\alpha_1-\alpha_2}\right)\right]\right\} \tag{B4}$$

$$gg_2(\alpha,n)=\frac{1}{8}\left(\frac{\alpha-\alpha_2}{\alpha_1-\alpha_2}\right)^2\frac{e^{-2n\alpha}}{e^{2\alpha-1}}+\sum_{i=n+1}^{\infty}\left\{\frac{(2i-n)\,e^{-2i\alpha}}{16i(i-n)\,(\alpha_1-\alpha_2)^2}\left[\frac{1}{(i-n)}+2(\alpha-\alpha_2)\right]+\frac{e^{-i(\alpha_1-\alpha_2)}}{8\sinh[i(\alpha_1-\alpha_2)]}\left[\frac{n-i}{n}\left(\frac{\alpha-\alpha_2}{\alpha_1-\alpha_2}\right)e^{-2i\alpha_2}+\frac{1}{2}e^{-2i\alpha}\left(1+\frac{n}{i(n-i)\,(\alpha_1-\alpha_2)}+2\coth[i(\alpha_1-\alpha_2)]+2\frac{\alpha-\alpha_2}{\alpha_1-\alpha_2}\right)\right]\right\} \tag{B5}$$

$$gg_3(\alpha,n)=\frac{1}{8}\sum_{i=i}^{n-1}\left\{\frac{n-i}{n}\left(\frac{\alpha-\alpha_2}{\alpha_1-\alpha_2}\right)\left[\frac{e^{-i(\alpha_1-\alpha_2)}}{\sinh[i(\alpha_1-\alpha_2)]}+\frac{1}{i(\alpha_1-\alpha_2)}+\frac{1}{n(\alpha_1-\alpha_2)}\right]+\frac{n-i}{n}\left(\frac{\alpha-\alpha_2}{\alpha_1-\alpha_2}\right)^2-\frac{1}{2}e^{2i\alpha}\frac{e^{-i(\alpha_1+\alpha_2)}}{\sinh[i(\alpha_1-\alpha_2)]}\left[1+\frac{2i-n}{i(1-n)\,(\alpha_1-\alpha_2)}+2\coth[i(\alpha_1-\alpha_2)]-2\frac{\alpha-\alpha_2}{\alpha_1-\alpha_2}\right]\right\} \tag{B6}$$

$$C_1=\frac{gg_1(\alpha_2,n)-gg_1(\alpha_1,n)}{e^{2n\alpha_1}-e^{2n\alpha_2}} \tag{B7}$$

$$C_2=\frac{gg_1(\alpha_1,n)\,e^{-n(\alpha_1-\alpha_2)}-gg_1(\alpha_2,n)\,e^{n(\alpha_1-\alpha_2)}}{2\sinh[n(\alpha_1-\alpha_2)]} \tag{B8}$$

$$C_3=\frac{gg_2(\alpha_1,n)-gg_2(\alpha_2,n)}{e^{-2n\alpha_2}-e^{-2n\alpha_1}} \tag{B9}$$

$$C_4=\frac{gg_2(\alpha_2,n)^{-n(\alpha_1-\alpha_2)}-gg_2(\alpha_1,n)\,e^{n(\alpha_1-\alpha_2)}}{2\sinh[n(\alpha_1-\alpha_2)]} \tag{B10}$$

$$C_5=\frac{gg_3(\alpha_1,n)\,e^{-n(\alpha_1-\alpha_2)}-gg_3(\alpha_2,n)\,e^{n(\alpha_1-\alpha_2)}}{2\sinh[n(\alpha_1-\alpha_2)]} \tag{B11}$$

$$C_6=\frac{gg_3(\alpha_1,n)-gg_3(\alpha_2,n)}{e^{2n\alpha_2}-e^{2n\alpha_1}} \tag{B12}$$

We note that although infinite series are involved, they converge quickly (exponentially) for $\alpha_2 > 0$. A difficulty is encountered only in the limiting case of $\alpha = \alpha_2 = 0$ (the buried pipe). In the latter case, the first term in both the infinite series (B4) and (B5) converges algebraically (like $1/i^2$). We note, however, that in the case of $\alpha = \alpha_2 = 0$, the algebraically converging terms can be summed up in a rather simple fashion. For example, in (B5) the algebraically converging term at $\alpha = \alpha_2 = 0$ is

$$\sum_{i=1}^{\infty}\frac{(n+2i)}{i(n+1)^2}=\frac{\pi^2}{6}-\sum_{i=1}^{n}\left[\frac{1}{n(n-i+1)}-\frac{1}{i^2}\right]$$

Hence, the difficulty of slow convergence can be eliminated even for the case of the buried pipe, except for those circumstances when one insists on evaluating ψ_2 very close to the plane $\alpha_2 = 0$.

Due to the lengthy expressions involved we do not present here the corresponding equations for the temperature field.

S. W. Jones
Reactor Analysis and Safety Division,
Argonne National Laboratory,
Argonne, Ill. 60439

M. Epstein
Fauske and Associates, Inc.,
Encino, Calif. 91316
Mem. ASME

S. G. Bankoff
Chemical Engineering Department,
Northwestern University,
Evanston, Ill. 60521
Mem. ASME

D. R. Pedersen
Reactor Analysis and Safety Division,
Argonne National Laboratory,
Argonne, Ill. 60439

Dryout Heat Fluxes in Particulate Beds Heated Through the Base

A laboratory study of dryout heat fluxes in particulate beds heated through the base is reported. More than two hundred experimental heat flux data points were measured. Semi-empirical correlations of the dryout heat flux data for both deep and shallow particulate beds are developed, based on flooding in countercurrent flow in deep beds and a boiling crises in shallow beds. The role of capillary forces in bed dryout is discussed and an explanation for the variation of dryout heat flux with bed height in volumetrically heated particulate beds is presented.

Introduction

In nuclear reactor safety applications, it is of importance to be able to determine the maximum heat flux carried upward from a liquid-filled, heated particulate bed by evaporation (saturated liquid boiling). When this limiting heat flux is exceeded, a portion of the bed is observed to dry as manifested by the local bed temperature rising above the liquid saturation temperature. The term "dryout" heat flux has been employed to describe the maximum heat transfer capacity of the boiling liquid coolant.

Within the last ten years, numerous publications dealing with dryout in particulate beds have appeared in the literature. In general, these papers report on dryout heat flux data obtained by volumetrically heating beds of metal particulates or set forth models, most of which are semi-empirical, for prediction of dryout heat fluxes.

Experimenters have obtained data using various sizes of particles in debris beds composed of uranium dioxide, steel, copper, and lead [1-9]. At least four methods of volumetric heating have been used. Gabor et al. [1], generated heat in the coolant phase by resistive heating. Dhir and Catton [5] used an induction furnace to generate heat in the solid phase, a technique subsequently used by Gabor et al. [3], Squarer and Peoples [6], and Barleon and Werle [7]. Trenberth and Stevens [8] produced volumetric heating in the solid phase by electrical resistance. Rivard [9] and Lipinski, Gronager, and Schwartz [10] have conducted in-pile tests in which volumetric heating was produced by fission due to neutron bombardment.

The numerous predictive models and correlations that have been set forth include those of Ostensen and Lipinski [11], Henry and Fauske [12], and Dhir and Barleon [13] for beds composed of particles sufficiently large (large being defined here as about one millimeter or more) to permit turbulent flow in the interstitial volume of the bed. Models for predicting dryout heat fluxes during laminar flow in beds of smaller particles ($\lesssim$ 1 mm) include those of Dhir and Catton [5], Hardee and Nilson [14], Jones et al. [15], and Gabor et al. [3]. Lipinski [16] extended the laminar-flow model of Hardee and Nilson to include turbulent flow and capillary effects.

For the present, it seems sufficient to say that, owing to the immense scatter in the data, none of the models that have been presented yield accurate values for the dryout heat flux of all systems that have been studied, although most of the models do agree qualitatively with data, with the model of Hardee and Nilson [13], including the Scheidegger [21] specific permeabilities giving the best quantitative agreement with data taken using volume-heated beds (see below) of small particulate. Lipinski [16] has collected the majority of available data and compared various models with it. Very recently, Squarer et al. [17] have also made such a comparison between predicted and measured dryout heat fluxes. It would seem that a variation of almost an order of magnitude in the experimental data exists. Sizeable differences not only arise between the data taken by various investigators in various apparatus, but also between data taken with different materials in the same equipment.

A rather limited amout of dryout heat flux data have also been obtained with particle beds heated from below the bed container (bottom heating). Gabor et al. [1] heated the base of the bed with a swirling flame source and measured the dryout heat fluxes for sodium or water-cooled UO_2 beds of irregularly shaped particles of a wide size distribution. Dhir and Barleon [13] employed and inductively heated copper block as a bottom heat source and obtained dryout heat flux data in beds of large glass particles saturated with water or Freon-113 in turbulent flow. The dryout heat flux for bottom-heated particle beds is found to be somewhat lower than that for volume-heated particle beds. This finding is somewhat disturbing, since in most of the modeling work reported so far, except for Gabor et al. [3], no distinction is made between dryout in a volumetrically heated particulate bed and in a bottom-heated particulate bed. There is another difference between dryout data taken from beds heated through the base and from beds heated volumetrically. The data for volumetrically heated beds of intermediate height show a dependence on bed height, whereas the dryout data from beds heated through the base do not exhibit this dependence.

The various experimenters agree as to the general features of boiling and dryout in liquid-filled particulate beds. Tests with dyed water showed that the liquid moves downward through the bed while its vapor moves upward, resulting in a vertical counterflow of steam and water [1]. Shallow beds of

Contributed by the Heat Transfer Division for publication in the JOURNAL OF HEAT TRANSFER. Manuscript received by the Heat Transfer Division December 9, 1982.

fine particles are prone to localized channeling. As the boiling rate is increased, instead of the bed expanding uniformly, the upward flowing vapor moves some particles aside and opens up channels through the particulate bed. Except for some channeling near the very top of the bed, very deep beds of high-density particulate behave much like packed beds. Formation of distinct channels in beds composed of particles having diameters substantially greater than one millimeter does not seem to occur.

In particulate beds heated through the base, a sharp reduction in the dryout heat flux is observed as the bed depth exceeds the channel penetration depth [18, 19]. The dryout heat flux for beds deeper than the channel depth, h, is found to be independent of bed depth. A deep bed is here considered to be a particulate bed of sufficient depth so that the dryout heat flux remains constant with further increase in bed depth. A shallow bed is a bed shallow enough to allow the penetration of channels completely through to the base. In volumetrically heated beds, the measured dryout heat flux decreases gradually as bed height increases and approaches the deep-bed limit at depths considerably greater than h, indicating some intermediate bed-height behavior that falls between the deep and shallow limits. An expression that successfuly predicts the depth of channel penetration in bottom-heated beds of high-density particulate was recently reported by Jones et al. [19].

The present effort was designed to substantially increase the available body of experimental data on dryout heat fluxes in particulate beds heated through the base under well-controlled conditions. Such information will complement the abundance of available dryout data on volume-heated particle beds and is necessary for a comprehensive evaluation of existing or future dryout theories and to provide a firm empirical basis for their improvement. Experimental data were taken for both deep and shallow beds and semi-empirical correlations of the data were developed. In addition, questions pertaining to the effect of capillary forces on dryout are debated and an explanation of the observed dryout heat flux versus bed height data trend for volume-heated particle beds is presented. Only beds of small particles of one millimeter or less in diameter were studied, not only because this is the upper limit on particle size in liquid-cooled fast-reactor applications, but because the two-phase flow in debris beds composed of particles with diameters greater than one millimeter appears to be turbulent, and channels do not form in beds composed of large particles since the vapor cannot push the large particles aside.

Theories for Correlation of Data

Deep Beds. Most of the current models [5, 14, 15] for the limiting heat flux at incipient dryout are similar, the only difference resulting from the choice of a "specific permeability" for the *laminar* flow of each phase through the bed. The one-dimensional model development begins by assuming that the liquid flows downward and the vapor generated by boiling flows upward in the form of descending liquid columns (or globules) and ascending vapor columns (or bubbles). The vapor is formed on the surfaces of the particles in the case of volume-heated beds and at the lower boundary of a bottom-heated bed by boiling, and the entire bed is assumed to be at the liquid saturation temperature. Consider two arbitrary vertical locations in the bed separated by a distance Δz, which is small compared with the height of the bed, L. The pressures, P_1 and P_2, at the two locations are related by

$$P_1 - P_2 = \frac{\mu_v \epsilon U_v}{\kappa_v(\alpha)\kappa} \cdot \Delta z + \rho_v g \cdot \Delta z \tag{1}$$

for the upward flow of vapor and

$$\rho_l g \cdot \Delta z = P_1 - P_2 + \frac{\mu_l \epsilon U_l}{\kappa_l(\alpha)\kappa} \cdot \Delta z \tag{2}$$

for the downward flow of liquid. Note that we assume that the flow of both liquid (denoted by subscript l) and vapor (denoted by subscript v) satisfy a modified form of Darcy's law where κ is the single-phase bed permeability which can be estimated from the Kozeny equation; namely [20]

$$\kappa = \frac{D^2}{180} \cdot \frac{\epsilon^3}{(1-\epsilon)^2}$$

and where $\kappa_v(\alpha)$ and $\kappa_l(\alpha)$ are the specific permeabilities, which correct the single-phase permeability of the bed for the effect of each phase on the flow of the other. The specific permeabilities are functions of the volume (void) fraction, α, of the pore space occupied by vapor. A mass balance between vapor and liquid requires that

$$\rho_l U_l (1-\alpha) = \rho_v U_v \alpha \tag{3}$$

and the heat flux from the bed, q, is related to the mass flux of vapor $\rho_v U_v$ at the top of the bed by

$$q = \epsilon \rho_v h_{vl} U_v \alpha \tag{4}$$

Adding equations (1) and (2) and eliminating the velocities U_v and U_l in favor of the heat flux, q, via equations (3) and (4) leads to the result

Nomenclature

D = diameter of particles in bed
$F(\nu_v/\nu_l)$ = kinematic viscosity ratio function, equation (6)
g = gravitational acceleration constant
h = maximum channel penetration depth, equation (11)
h_{vl} = heat of vaporization
K = dimensionless (Kutatedadze) constant
L = total bed height
L' = vertical distance between top of volume-heated bed and flooding plane
n = channel density
P = pressure
q = heat flux above bed
q_{max} = limiting (dryout) heat flux above bed
$q_{max,deep}$ = dryout heat flux from the deepest volume-heated bed in a given data set, obtained from experiment
Q_{max} = dimensionless dryout heat flux, equation (7)
U = local, vertical velocity of vapor or liquid through particulate bed
α = vapor void fraction
Δz = small vertical distance in particulate bed
ϵ = porosity of bed
κ = permeability (or specific permeability with subscripts l or v)
λ = wavelength
μ = absolute viscosity
ρ = density
σ = interfacial surface tension
ν = kinematic viscosity
ν_v/ν_l = kinematic viscosity ratio

Subscripts

b = applies to particulate bed
c = denotes critical wavelength
D = denotes most dangerous wavelength
l = liquid phase
s = applies to solid
v = vapor phase

$$\frac{q\nu_v}{h_{vl}\kappa(\rho_l-\rho_v)g}=\left[\frac{1}{\alpha\kappa_v(\alpha)}+\frac{\nu_l}{\nu_v}\frac{1}{(1-\alpha)\kappa_l(\alpha)}\right]^{-1} \tag{5}$$

The maximum or limiting heat flux may be obtained by selecting the value of α which maximizes q; i.e., we compute α from the "flooding" condition $dq/d\alpha=0$. The value of α so obtained is then used in equation (5) to find the dryout heat flux, $q_{\max}$. Therefore, we are led to the conclusion that the dryout heat flux must be of the functional form

$$\frac{q_{\max}\nu_v}{h_{vl}\kappa(\rho_l-\rho_v)g}=F(\nu_v/\nu_l) \tag{6}$$

and thus the dimensionless dryout heat flux for a deep bed, namely

$$Q_{\max}\equiv\frac{q_{\max}\nu_v}{h_{vl}\kappa(\rho_l-\rho_v)g} \tag{7}$$

depends only on the kinematic viscosity ratio, ν_v/ν_l. This ratio has various values according to the liquid coolant of interest, ranging from ~5.0 for organic liquids to ~325 for liquid metals.

The functional form of $F(\nu_v/\nu_l)$ depends, of course, on how one chooses the specific permeabilities $\kappa_v(\alpha)$ and $\kappa_l(\alpha)$, which in turn depends on one's choice of the two-phase flow configuration. In the flow pattern proposed by Hardee and Nilson [14], the diameter of each fluid column is large in comparison with the size of the spherical packing so that the pressure drop due to interfacial shear where liquid is in contact with vapor is negligible compared with that due to the interaction between fluid and particles. This choice leads to $\kappa_v(\alpha)=\kappa_l(\alpha)=1.0$. Hardee and Nilson also derived another expression for $F(\nu_v/\nu_l)$ based on the following empirical expressions suggested by Scheidegger [21] for cocurrent flow only

$$\kappa_v(\alpha)=\frac{(1-\alpha)^3}{\alpha},\kappa_l(\alpha)=\frac{1.1\alpha-0.1}{1-\alpha} \tag{8}$$

Lipinski [16] extended the Hardee-Nilson model that incorporates equation (8) to include the effects of capillary forces and turbulent flow (large particles). In the flow regime suggested by Jones et al. [14], the two phases are in intimate contact, and one considers the mutal "frictional force" between the two phases as well as how one phase changes the pore space available to the other phase. The work of Jones et al. results in $\kappa_v(\alpha)=\alpha(1-\alpha)$ and $\kappa_l(\alpha)=(1-\alpha)^2$. Dhir and Catton [5] proposed that the heat transfer is limited only by the rate of liquid downflow in deep (packed) beds. This is equivalent to letting $\kappa_v(\alpha)\to\infty$ in equation (5). In this limit, q does not exhibit a maximum on a plot of q versus α, so that an expression for the limiting heat flux must be developed in terms of an unknown constant which must be established from experimental data. Most recently, Jones [18] expressed the specific permeabilities in terms of the perimeters around the flow areas of each phase and searched over all admissible values of perimeters, employing laboratory observations and geometrical constraints, in an attempt to bound the specific permeabilities. He showed that reasonable guesses for perimeters result in reasonable agreement with the dryout heat flux data.

It is important to note that equation (6) in combination with any of the various functional forms of $F(\nu_v/\nu_l)$ invoked by researchers is obtained without reference to the method of heating the bed. Later on we will use equation (6) as a guide to the presentation of data on dryout heat flux for particle beds heated through their bases.

Shallow Beds. Visual observations made during this study indicate that when beds become sufficiently shallow to allow channels to penetrate completely to their bases, the number of channels increases. There is in conjunction with this increase

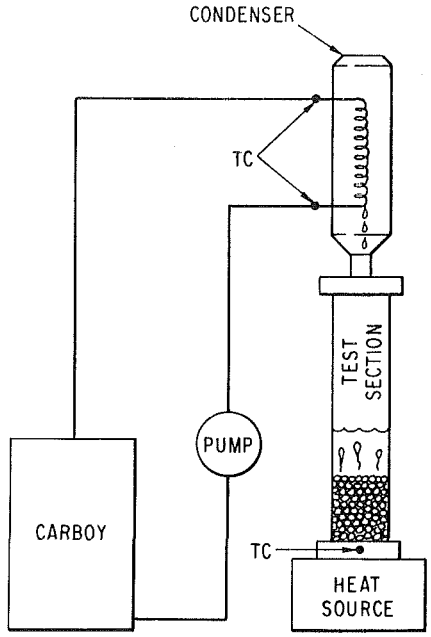

Fig. 1 Schematic of the experimental apparatus

in the number of channels, an observable increase in the motion of the particles. As the bed depth becomes less than the maximum obtainable channel depth, incipient fluidization seems to be reached. Although there is little vigorous movement of particles except when the bed is very shallow, the bed (particles plus liquid) seems to behave as a single fluid.

In deep beds a noticeable jump in vapor fraction, which can be observed at the test section wall, occurs between the channeled zone, where vapor is predominantly in the channels, and the region below. Although the vapor fraction measurements (described in the next section) exhibit much scatter, they indicate that about 50 percent of the interstitial volume of the deep bed region is occupied by vapor. Observations of channel size and density, however, indicate that vapor occupies no more than 10 percent of the interstitial volume in the channeled region. It is reasonable to suppose that, in bottom-heated beds, a very sharp change in the vapor and liquid fractions also occurs just below the base of the channels when the total bed depth becomes less than the maximum channel depth. This observed and postulated jump in vapor fraction for deep and shallow beds, respectively, serves as a horizontal interface between a lower vapor phase and a heavier liquid-particle (slurry) phase. In fact, as will be demonstrated in a following subsection, in analogy with pool boiling from a horizontal surface, one finds that the vapor channels are spaced in a pattern which is predicted by the consideration of Taylor instability. Consequently, an analysis based on a method similar to that used for predicting critical boiling heat fluxes from horizontal surfaces seems a reasonable way to approach the modeling of dryout heat fluxes from shallow beds which are channeled completely through. This involves using Taylor instability theory to predict the spacing between channels and Kelvin-Helmholtz instability theory to predict the maximum allowable vapor velocity through the channels. This procedure, which is reported in detail in [18], results in the following modified form of Zuber's [22] or Kutateladzes' [23] expression for the peak heat flux in pool boiling for use in predicting dryout heat fluxes in shallow particulate beds

$$\frac{q_{\max}}{h_{vl}\rho_v^{1/2}[\sigma g(\rho_b-\rho_v)]^{1/4}}=K=\text{constant} \tag{9}$$

where the constant K was determined by the experiments to be 0.035 (see below).

Note that equation (9) differs from the classical boiling correlation in that a hydrostatic force based on the bed density

$$\rho_b = \rho_s(1-\epsilon) + \rho_l\epsilon \tag{10}$$

is used in place of the liquid hydrostatic force. This substitution is a direct consequence of the assumption that the pressure drop through a shallow particulate bed corresponds to that at incipient fluidization. Dryout in shallow beds was also postulated by Dhir and Catton [5] to occur when the vapor velocity in the channels exceeds the Kelvin-Helmholtz critical velocity. However, the channel spacing was *not* determined by these workers to be due to Taylor instability. Instead, they applied a potential energy principle to arrive at the channel density and presented an expression for dryout heat flux as a function of bed height.

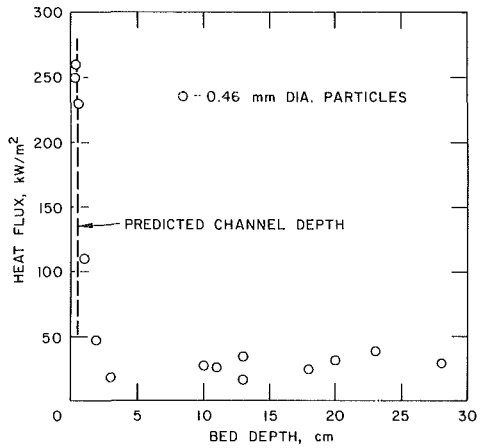

Fig. 2 Dryout heat fluxes from lead particulate beds in methanol as a function of bed height, showing the sharp transition from shallow to deep beds

Experiment

Details of the experimental apparatus, procedure, and error analysis are found in [18] and therefore only a brief description is provided in this section and in the following section. The apparatus utilized for collection of limiting heat flux data is depicted in Fig. 1. In general, the apparatus consisted of a heat source, a test section, a condenser and coolant circulation system, and instrumentation for thermocouple readout.

A 1500-W hot plate, a gas-oxygen flame, or an oxygen-acetylene torch provided heat through the base of the bed. The test section was a glass pipe having an i.d. of either 25.4 mm, 50.8 mm, or 101.6 mm. It was secured at the bottom to a copper flange, and at the top to a brass flange fitted with an adapter to a 29/42 standard taper fitting. Cooling water was supplied to the spiral, glass condenser from a 5-gal carboy by means of a peristaltic pump. Chromel-alumel thermocouples were used to monitor the inlet and outlet coolant temperatures at the condenser, the temperature of the copper flange which supported the bed, and in some experiments, the temperatures in the bed at heights of approximately 3 mm and approximately 25 mm above the copper flange. Chart records, accurate to ± 1 percent in the 0–5 mV range, were used to record thermocouple readings.

Considerable effort was spent to construct beds of particles having uniform shape and size. Details concerning the size distributions of the particles used and a discussion of the effects of particle nonuniformity are given in [18]. Porosity measurements were made both within the apparatus and outside the apparatus in a graduated cylinder. The measured porosity seemed to be dependent on the way the particles align themselves as they were poured into the test section, but all porosity measurements were repeatable to $\pm$ 7 percent of their mean.

The dryout limit was measured by monitoring the temperature difference between the inlet and outlet of the condenser. If, following an increase in heat flux added to the bed, both the temperature difference and the coolant flow rate remained approximately constant for several minutes, the heat flux was significantly increased to determine if a true dryout had been reached. If, after another several minutes, the temperature difference measured from the condenser remained essentially the same or decreased, and no change in coolant flow rate occurred, the maximum heat flux obtained during this time was taken as corresponding to incipient dryout. The dryout heat flux was then calculated from the heat balance over the condenser using this temperature difference.

In addition, during experiments in which the heat flux into the bed exceeded the dryout heat flux for a significant period of time, dryout could be observed visually, and was verified by a sharp rise in the temperature near the bottom of the bed, which normally remained at the liquid saturation temperature. The heat flux measured from the condenser during these post-dryout conditions, when liquid was actually being expelled from the lower portions of the bed, was not, in deep beds, significantly different from the heat flux measured when flooding conditions, as indicated by the plateau in the amount of heat removed through the condenser, were first reached in the bed. This indicates that flooding in deep beds was a phenomenon dependent on local conditions restricting the flow and not limited to the bottom of the bed where the vapor was generated. In a few experiments, the heat transfer surface at the base of the bed was increased by a factor of four while holding the bed diameter fixed to determine if heat transfer was limited at the base. No significant change in the dryout heat flux resulted from extending the heat transfer surface, lending additional support to a two-phase flow model for dryout (or flooding) within the interior of deep beds. Experiments with deep beds were conducted in which the bed diameter was increased by a factor of four. Scale effects were determined to be negligible.

Determination of channel depth, density, and vapor fraction were based on direct visual measurements. Channel depths were measured at the wall of the test section at various times during a given experiment. The channel depths remained fairly constant, but the apparent depth of various channels in a bed differed, depending on their orientation with respect to the test section walls. The distance between the top of the bed and a noticeable jump in vapor fraction at the base of the channels was approximately constant around the entire perimeter of the test section. Measurements of channel density were accomplished by counting the channels in a thin region adjacent to the test section wall. This localized channel density was assumed to be identical to that of the entire bed. The total volume of vapor present at incipient dryout could be determined by measurement of the total expansion of the coolant pool. To obtain the total vapor volume in the bed, the volume of vapor in the coolant pool above the bed, estimated from existing data and correlations on bubbling in liquid columns, was subtracted from the total vapor volume obtained by measuring the boil-up height.

Estimates of channel diameter were also made by visual comparison with the diameter of nearby particles. In general, the channel diameter did not appear to vary with particle size and seemed to be very nearly proportional to the spacing between channels. Channel diameters were usually on the

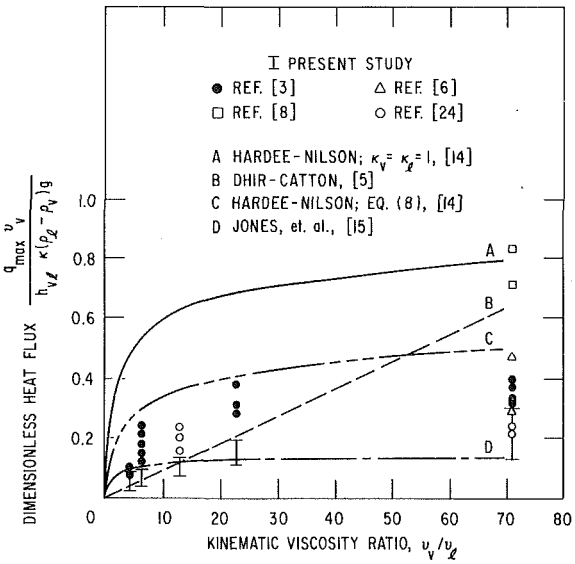

Fig. 3 Comparison of theories with deep bed data taken from bottom-heated beds (this study) and volume (induction) heated beds

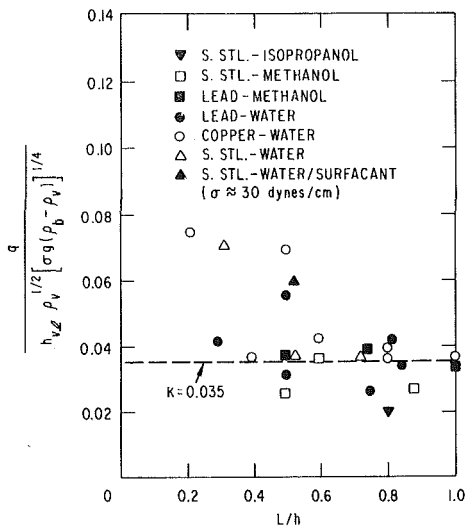

Fig. 4 Correlation of dryout heat flux data from shallow beds versus ratio of bed depth to predicted channel depth

order of, but somewhat larger than, the larger diameter particles used in this study.

Experimental Results and Discussion

A vast quantity of experimental data was obtained, and pertinent parameters were varied over a wide range. The average particle diameter varied from about 400 to about 1100 μm. Water, isopropanol, acetone, methanol, and Freon-113 were used to obtain deep bed data, providing an order or magnitude variation both in the heat of vaporization and in the ratio of kinematic viscosities, ν_v/ν_l. Deep bed data were taken with beds composed of glass, steel, copper, and lead particles. Studies in which the bed height was varied from very shallow to very deep were conducted with fourteen various liquid-solid systems. All the data in tabular form can be found in Ref. [18].

Height-Dependent Studies. A representative plot showing the results of the height-dependent studies is presented in Fig. 2, the dryout heat flux being plotted against bed height for lead particulate beds in methanol. A similar plot for copper particulate beds in water can be found in [19]. Additional plots of this type for other liquid-solid pairs are available in [18].

The vertical (dashed) line in Fig. 2 corresponds to the penetration of the channels as predicted by using the Jones et al. formula [19]

$$h = \frac{6\sigma}{(\rho_s - \rho_l)g\epsilon D} \tag{11}$$

The formula gives a good indication of the bed height that divides shallow bed behavior from deep bed behavior. Despite the scatter in the data, it can be concluded that the dryout heat flux for deep beds is independent of bed height. The sharp increase in heat flux shown in the figure as the bed depth falls below the maximum channel depth, h, and enters the shallow-bed regime is typical of the bottom-heated system.

The data scatter in Fig. 2 is a result of several experimental difficulties. While precise information on the pertinent properties of the liquid and vapor phases are available in the literature, the solid is difficult to characterize. Not only is the overall permeability difficult to predict, but local variations of permeability within a given bed can significantly alter the dryout heat flux. The extent of errors in the dryout heat flux measurements resulting from these local variations is very difficult, if not impossible, to estimate. Accordingly, an enormous number of data points were taken to better quantify the limits of reliability.

In deep bed studies the principal errors incurred were probably due to heat losses through the apparatus walls, especially in experiments throughout which visibility was desired and the apparatus was uninsulated. In experiments with beds immersed in methanol, acetone, or Freon 113, maximum possible heat losses were estimated at less than 25 percent of the dryout heat flux. However, maximum possible heat losses during experiments with isopropanol or water were estimated to be as much as 50 percent. Thus some of the data taken from very deep beds tends to be low.

In experiments with shallow beds, the heat fluxes are sufficiently high so that heat losses are negligible. In this case, however, the boiling heat flux that first increases with the applied heat flux reaches a peak value and falls abruptly to a minimum, passing quickly through a "transition" boiling regime. This minimum corresponds to the establishment of a vapor film above the base of the bed. The condenser response time is too slow to follow this transition, and thus mixing in the condenser leads to some distortion of the peak and minimum heat flux measurements. It is interesting to note that when the particulate bed is quite deep, the heat flux above the bed reaches a maximum value and remains at the value despite great increases in the applied bottom heat flux (or base temperature). These observations illustrate that the mechanism controlling the dryout heat flux in a shallow bed is similar to that for the peak heat flux in pool boiling of a pure liquid and quite different from the mechanism that limits the heat flux in a deep bed.

Deep Beds. All the deep bed data collected in this study are plotted in dimensionless form in Fig. 3 as a function of the kinematic viscosity ratio, along with the models by Dhir and Catton [5], Hardee and Nilson [14], and Jones et al. [15] for very deep beds composed of small particles. Each of the five data flags represents a different coolant, but consists of at least 18 data points taken from beds composed of various size particles of glass, stainless steel, copper, and lead. A limited number of data points obtained with induction (volume) heating of deep beds are also included for comparison purposes [3, 6, 8, 24].

Except perhaps for the semi-empirical correlation recommended by Dhir and Catton [5] for deep beds, the

Table 1 Comparison of predicted channel densities with observed channel densities (channels/cm^2)

Type of particles	Coolant	Predicted channel density (equation (13))	Predicted channel density (equation (14))	Observed channel density (shallow beds)	Observed channel density (deep beds)
Stainless steel	Water	2	1	2	2
Stainless steel	Water/ surfactant[a]	4–8	2–3	-	10–15
Stainless steel	Methanol	7	2	11	5
Stainless steel	Isopropanol	8	3	6	4
Copper	Water	2	1	5	2
Lead	Water	3	1	4	3
Lead	Methanol	10	3	12	5
Lead	Isopropanol	11	4	-	11

[a]The surface tension of this solution in the bed was not known exactly. Capillary rise measurements indicated a surface tension of 15–30 dynes/cm.

models seem to yield curves which fit the form of the deep-bed data quite well. As mentioned previously, the exact numerical result depends on how one chooses specific permeabilities. As is evident from the data in Fig. 3, dryout heat fluxes obtained with bottom heating are generally lower than fluxes obtained with volume heating.

For deep, bottom-heated beds, the dimensionless grouping of the limiting flux as suggested by equation (6) does an excellent job of eliminating trends in the data with particle diameter, bed porosity, and properties of the solids for all the liquid constants used in this study except Freon-113. There seems to be an unexpected variation of the dimensionless heat flux, Q_{max}, with particle size in the data taken with Freon. This might result from vapor velocities that are sufficiently large so that the assumption of laminar flow could result in an incorrect diameter dependence. Particle Reynolds numbers for the Freon-113 systems correspond to flow intermediate between laminar and turbulent. An exponent of one (corresponding to near turbulent flow) in defining the dependence of permeability on the mean particle diameter, rather than two, would better reduce the data for Freon-113.

The dryout heat flux data obtained in this study using the bottom-heating technique can be adequately represented by the correlation

$$Q_{max} = \frac{0.015(\nu_v/\nu_l)^{0.8}}{[1+0.003(\nu_v/\nu_l)^2]^{0.25}} \tag{12}$$

which passes through the centroid of the data.[1] Caution should be exercised in using this correlation outside the kinematic viscosity ratio range $4.0 \le \nu_u/\nu_l \le 75$.

Channel Density. Recall that equation (9) for the peak heat flux above a shallow particulate bed assumes that the channels arise in boiling in particulate beds from Taylor instability. In deriving equation (9), a modified "effective wavelength" is postulated for the vapor-liquid/particulate interface by substituting a hydrostatic force based on the bed density ρ_b [see equation (10)] for the liquid hydrostatic force used in classical analyses of interfacial instability. This procedure results in the following modifications of the critical and "most dangerous wavelengths" for use in predicting channel density, as given by Zuber [22], and Bellman and Pennington [25]

$$\lambda_c = 2\pi\left(\frac{\sigma}{g(\rho_b-\rho_v)}\right)^{1/2} \tag{13}$$

and

$$\lambda_D = 2\pi\left(\frac{3\sigma}{g(\rho_b-\rho_v)}\right)^{1/2} \tag{14}$$

Here λ_c is the critical wavelength and λ_D is the most dangerous (or most unstable) wavelength. If we now carry our analogy with pool boiling from a horizontal surface a step further and suppose that just one channel rises from each unique square on a grid composed of squares with sides equal in length to one wavelength, a calculation of channel densities can be made as follows

$$n = \frac{1}{\lambda^2} \tag{15}$$

where n is the channel density and λ is the spacing between channels.

Table 1 is a comparison of predicted channel densities with the average observed channel densities listed in [18], each observation having been given equal weight. Observed channel densities listed for shallow beds include only data from beds that were channeled completely to the base. Those listed for deep beds include only data for beds at least two centimeters deeper than the channel depth. Channel densities are predicted using both the critical and most dangerous wavelengths. A bed porosity of 0.4 is assumed.

Table 1 indicates that, generally, channel densities in deep beds range between the values predicted using the modified critical and most unstable wavelengths, given by combining equations (13) or (14), respectively, with equation (15). Channel densities in shallow beds appear to be approximately equal to, or perhaps slightly greater than, the channel densities predicted using the modified critical wavelength. Thus a correlation of dryout heat fluxes from shallow beds might be based upon the notion of instability at an interface with the critical wavelength defined by equation (13). Certainly the most convincing argument for the utility of equation (13) or (14) and equation (15) in this regard is the massive increase in the number of channels obtained in stainless steel particulate beds immersed in solutions of water with a commercial surfactant.

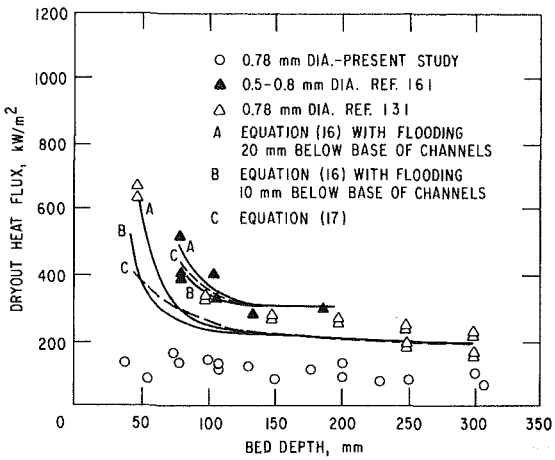

Fig. 5 Dependence of dryout heat flux on bed depth for inductively heated steel particulate beds in water

[1] To avoid "overcrowding" in Fig. 3, a plot of equation (12) is not shown.

Shallow Beds. Figure 4 is a plot of the shallow bed dryout data, with the heat flux reduced as in equation (9), against the ratio of bed depth to predicted channel depth [see equation (11)]. The five data points lying above the remainder of the data all correspond to very shallow beds immersed in water. Owing to the fact that each of these five data points was produced with the shallowest bed studied using a given size and type of particles in *water*, which is a vigorously boiling liquid, it is thought that fluidization and bed expansion resulted in higher heat fluxes. Otherwise the data show no dependence on bed height. The independence on bed height exhibited by these data is in agreement with equation (9). In addition, the correlation eliminates trends with respect to both the type of particles and type of coolant used. The bulk of the data is fitted best with equation (9) by setting $K = 0.035$.

Effects of Interfacial Forces and Differences Between Dryout Heat Fluxes Resulting from Heating Technique

As Fig. 3 demonstrates (see also Fig. 5), dryouts in beds heated inductively or electrically consistently occur at higher heat fluxes than do dryouts in bottom-heated beds, even for very deep beds. The numerous models presented in Fig. 3 serve to demonstrate how a change in the effective permeability of either phase can alter the magnitude of the heat flux at incipient dryout. It is not unlikely that boiling on the particle surfaces results in somewhat different hydrodynamics than boiling on a flat plate below the bed. The nature of these differences remains uncertain. One possibility is that, in volumetrically heated beds, the plane of flooding is sufficiently near the bed surface for the local porosity to be significantly greater than it would be at the base of the bed. Also, a reduction in the interfacial area of liquid and vapor due to localized areas of higher vapor generation, or a flow regime change due to boiling on the surface of particles, might result in an increase in dryout heat flux similar to that which is experimentally observed. The data of Gabor et al. [1] for volumetrically heated beds of uranium dioxide with vapor generated by electrical resistance heating in the sodium coolant rather than in the solid may support such a hypothesis. Although their beds contained particles of various sizes (from 100 μm to 1 mm) and had high porosities, their dryout data for deep beds seem to converge to the results they obtained by bottom heating similar sodium-uranium dioxide systems. Perhaps resistance heating of the liquid phase resulted in more uniform vapor generation or in a less turbulent two-phase flow.

As seen in Fig. 5, the dryout data for volumetrically heated beds show a dependence on bed height. This is especially true for beds immersed in high-surface tension coolants such as water or liquid sodium. This tendency toward greater dryout heat fluxes from beds of intermediate height has been explained by Lipinski [16, 26] as being a result of capillary forces that maintain a pressure difference between liquid and vapor throughout the bed. At a definite interface capillary forces can act on the liquid phase, pulling liquid toward the interface in a manner similar to that observed in capillary rise experiments. Such an interface exists at the base of the channeled zone and has been discussed herein and in [19] and is believed to be a dominant factor in channel behavior. The basis for including capillary pressure terms in a deep-bed dryout-heat flux model (as done, e.g., by Lipinski) is that there must also exist sizeable changes in vapor volume fraction α along the vertical axis of the bed in the region well below the channeled zone. Visual observations for both bottom- and volume-heated beds, however, do not indicate marked changes in vapor fraction in the deep-bed region where flooding seems most likely to occur. Therefore, an alternative explanation of the data trend in Fig. 5 has been devised.

Consider a volumetrically heated bed with uniform heat generation. The vapor flux increases linearly with axial distance above the bottom of the bed. Thus the vapor flux is highest at the top of the bed. If the bed is unchanneled, flooding should then occur at the top. However, due to the presence of channels, the top of the bed can sustain much higher fluxes than lower portions of the bed without experiencing flooding. From our bottom-heated dryout data from beds of various metals submerged in water, we find that dryout heat fluxes begin to rise above the deep bed values at bed depths 1 to 2 cm greater than the estimated channel depth. Suppose that flooding occurs in a volumetrically heated bed on a horizontal plane just below the bed depth which is capable of sustaining larger vapor fluxes. Then the vapor flux responsible for flooding is not that generated by the entire bed, but only the fraction of the vapor flux due to heat generation and boiling below the flooding plane. Thus if the dryout heat flux for a very deep bed is known, as well as the distance between the flooding plane and the top of the bed, a prediction of dryout heat fluxes at intermediate bed depths can be made as follows

$$q_{\max} = \frac{L}{L - L'} \cdot q_{\max,\text{deep}} \tag{16}$$

where $q_{\max}$ is the dryout heat flux measured at the top of the volume - heated bed in question, $q_{\max.\text{deep}}$ is the dryout heat flux measured from a very deep volume-heated bed of the same material, L is the total height of the bed, and L' is the vertical distance between the flooding plane and the top of the bed.

In Fig. 5, dryout data from volumetrically heated beds [3, 6] are compared with dryout heat fluxes calculated from equation (16). Additional comparisons with all the existing data showing the height dependence of dryout heat fluxes from volumetrically heated beds composed of small, reasonably uniform particles are found in [18]. The dark curves labeled A and B result from equation (16) and the assumptions that the flooding plane lies one and two centimeters below the base of the channels (i.e., $L' = h + 1$ or 2 cm), with the channel depth calculated from equation (11). The dashed curves labeled C in Fig. 5 result from Lipinski's [16] inclusion of capillary terms in the momentum equations

$$q_{\max} = \left[1 + \frac{6\sigma(1-\epsilon)}{D\epsilon(\rho_l - \rho_v)gL}\right] \cdot q_{\max,\text{deep}} \tag{17}$$

In all cases, $q_{\max}$ is obtained by solving equations (16) or (17) with $q_{\max,\text{deep}}$ evaluated as the dryout heat flux from the deepest bed in the data set.

Reviewing Fig. 5, it appears that an interpretation of volumetrically heated dryout data based on equation (16) is quite reasonable except, of course, in the limit $L \to L'$. Note that the dependence of surface tension is preserved in this interpretation due to the effect of this parameter on channel depth. It should be noted that the ideas presented in the foregoing are similar to those used by Gabor et al. [1] to predict dryout data from volumetrically heated beds (with electrical resistance heating in the liquid) using dryout data from identical beds heated through the base. This cannot be done in our case, however, since dryout heat fluxes from beds with volumetric heating in the solid phase appear to be greater than those from bottom-heated beds, even in the deep bed limit.

A few more words should be said about the effects of capillary forces on dryout heat fluxes before concluding. Trenberth and Stevens [8] report very low dryout heat fluxes resulting from the addition of a surfactant to the coolant. In efforts to repeat such experiments in our bottom-heated apparatus, the heat flux at incipient dryout could not be

accurately measured. Dryout seemed to occur at very low heat fluxes. However, the *post-dryout* heat fluxes measured from beds immersed in a surfactant solution having a surface tension approximately one-half that of water were quite similar to those measured from beds immersed in water. In addition, foaming was observed in the liquid coolant above the particulate bed. Thus, it is suspected that dryout occurred prematurely due to a drastic change in flow regime within the bed, rather than being due to a reduction in "capillary pressure" difference between liquid and vapor as expressed by equation (17).

Conclusions

The major conclusions of this study are:

1 The dependence of the dryout heat flux (dimensionless) on the vapor-liquid kinematic viscosity ratio exhibited by the existing models for prediction of dryout heat fluxes in deep particulate beds seems nearly identical to the trend observed in the experimental data. Current understanding, however, is insufficient to provide accurate models for prediction of dryout heat fluxes from volume- or bottom-heated deep beds composed of small particles.

2 Dryout heat fluxes above bottom-heated, shallow beds composed of small particles may be correlated by analogy with the boiling crisis which occurs in pool boiling from a horizontal surface.

3 The trend of dryout heat fluxes with bed height for volumetrically heated particulate beds can be explained by assuming that flooding occurs locally just below the channeled zone. By comparing with the available data, the plane of flooding in most beds may be estimated at 20 mm below the base of the channels.

Acknowledgment

This work was performed under the auspices of the U.S. Department of Energy.

References

1 Gabor, J. D., Sowa, E. S., Baker, L., Jr., and Cassulo, J. C., "Studies and Experiments on Heat Removal from Fuel Debris in Sodium," *Proc. of ANS Fast Reactor Safety Meeting*, Beverly Hills, Calif. CONF-740401, Apr. 2-4, 1974, pp. 823-844.

2 Sowa, E. S., Gabor, J. D., Baker, L., Jr., Pavlik, J. R., Cassulo, J. C., and Holloway, W., "Studies of the Formation and Cooling of Particulate Fuel Debris Beds in Sodium," *Proceedings of International Meeting on Fast Reactor Safety and Related Physics*, Chicago, Ill. CONF-761001, Oct. 5-8, 1976, pp. 2036-2046.

3 Gabor, J. D., Cassulo, J. C., Jones, S. W., and Pedersen, D. R., "Studies on Heat Removal from Fuel Debris," *ANS Transactions*, Vol. 39, 1981, pp. 642-643.

4 Keowin, R. S., "Dryout of a Fluidized Particle Bed with Internal Heat Generation, M.S. thesis, University of California at Los Angeles, 1974.

5 Dhir, V., and Catton, I., "Dryout Heat Fluxes for Inductively Heated Particulate Beds," ASME JOURNAL OF HEAT TRANSFER, Vol. 99, 1977, pp. 250-256.

6 Squarer, D., and Peoples, J. A., "Dryout in Inductively Heated Bed With and Without Forced Flow," *ANS Transactions*, Vol. 34, 1980, pp. 535-537.

7 Barleon, L., and Werle, H., "Dependence of Debris Bed Dryout Heat Flux on Particle Diameter," *ANS Transactions*, Vol. 38, 1981, pp. 382-383.

8 Trenberth, R., and Stevens, G. F., "An Experimental Study of Boiling Heat Transfer and Dryout in Heated Particulate Beds," AEEW-R1342, U.K. Atomic Energy Authority, Winfrith, 1980.

9 Rivard, J. B., "In-Reactor Experiments on the Cooling of Fast Reactor Debris," *Nucl. Tech.*, Vol. 46, 1979, pp. 344-349.

10 Lipinski, R. J., Gronager, J. E., and Schwartz, M., "Particle Bed Heat Removal with Subcooled Sodium: D-4 Results and Analysis," *Nucl. Tech.*, Vol. 58, 1982, pp. 369-378.

11 Ostensen, R. W., and Lipinski, R. J., "A Particle Bed Dryout Model Based on Flooding," *Nucl. Sci. and Eng.*, Vol. 79, 1981, pp. 110-113.

12 Henry, R. E. and Fauske, H. K., "Core Melt Progression and the Attainment of a Permanently Coolable State," presented at Am. Nuc. Soc./European Nuc. Soc. Topical Meeting on Reactor Safety Aspects of Fuel Behavior, Sun Valley, Idaho, Aug. 2-6, 1981.

13 Dhir, V. K., and Barleon, L., "Dryout Heat Flux in a Bottom-Heated Porous Layer," *ANS Transactions*, Vol. 38, 1981, pp. 385-386.

14 Hardee, H. C., and Nilson, R. H., "Natural Convection in Porous Media with Heat Generation," *Nuc. Sci. and Eng.*, Vol. 63, 1977, pp. 119-132.

15 Jones, S. W., Epstein, M., Gabor, J. D., Cassulo, J. C., and Bankoff, S. G., "Investigation of Limiting Boiling Heat Fluxes from Debris Beds," *ANS Transactions*, Vol. 35, 1980, pp. 361-363.

16 Lipinski, R. J., "A Particle-Bed Dryout Model with Upward and Downward Boiling," *ANS Transactions*, Vol. 35, 1980, pp. 358-360.

17 Squarer, D., Pieczynski, A. T., and Hochreiter, *L. E.*, "Effect of Debris Bed Pressure, Particle Size, and Distribution on Degraded Core Coolability," ASME Paper No. 81-WA/HT-16, presented at ASME winter annual meeting, Nov. 15-20, 1981.

18 Jones, S. W., "A Study of Dryout Heat Fluxes," Ph.D thesis, Northwestern University, June 1982.

19 Jones, S. W., Baker, L., Jr., Bankoff, S. G., Epstein, M., and Pedersen, D. R., "A Theory for Prediction of Channel Depth in Boiling Particulate Beds," ASME JOURNAL OF HEAT TRANSFER, Vol. 104, 1982, pp. 806-808.

20 Bear, J., *Dynamics of Fluids in Porous Media*, Elsevier, New York, 1972.

21 Scheidegger, A. E., *The Physics of Flow Through Porous Media*, University of Toronto Press, Toronto, 1974.

22 Zuber, N., "On the Stability of Boiling Heat Transfer," ASME *Transactions*, Vol. 80, 1958, pp. 711-720.

23 Kutateladze, S. S., "A Hydrodynamic Theory of Changes in the Boiling Process Under Free Convection Conditions," *Izv. Akad. Nauk*, USSR, Otd. Tech. Nauk, No. 4, 1951, p. 529.

24 Dhir, V. K. and Catton, I., "Dryout Heat Fluxes in Very Deep Debris Beds," *ANS Transactions*, Vol. 35, 1980, pp. 360-361.

25 Bellman, R., and Pennington, R. H., "Effects of Surface Tension and Viscosity on Taylor Instability," *Quarterly of Applied Mathematics*, Vol. 12, 1954, pp. 151-162.

26 Lipinski, R. J., "A One-Dimensional Particle Bed Dryout Model," *ANS Transactions*, Vol. 38, 1981, pp. 386-387.

Prediction of Nucleate Pool Boiling Heat Transfer Coefficients of Refrigerant-Oil Mixtures

M. K. Jensen
Department of Mechanical Engineering,
University of Wisconsin-Milwaukee,
Milwaukee, Wis. 53201
Mem. ASME

D. L. Jackman
Water Technologies Division,
Aqua-Chem, Inc.,
Milwaukee, Wis. 53201

This paper describes an experimental investigation to determine the mechanism governing nucleate pool boiling heat transfer in refrigerant-oil mixtures, the role diffusion plays in this process, and the influence of the fluid mixture properties. Boiling heat transfer data were taken in mixtures of up to 10 percent oil by weight in R-113. Thermophysical properties of the mixtures (density, viscosity, surface tension, specific heat, and contact angle) were measured. The decrease in heat transfer coefficient with increasing oil concentration is attributed to diffusion in an oil-enriched region surrounding the growing vapor bubbles. A correlation based on the postulated mechanism is presented which shows fair agreement with the experimental data from this study and with data obtained from the literature.

Introduction

When designing the evaporator of a refrigeration system, one must be able to accurately predict the boiling heat transfer coefficients of the refrigerants used. However, the fluids being circulated within these refrigeration systems generally are not pure refrigerants, but are refrigerant-oil mixtures. Even with pure liquids, the prediction of the boiling heat transfer coefficient is difficult because of all the variables involved. The addition of a miscible liquid to the pure fluid further complicates the problem by producing an extremely complex process whose governing mechanisms might differ from those of the pure liquid.

The literature dealing with the effect of oil contamination on boiling of refrigerants in pool boiling heat transfer is quite limited. Various studies, e.g., [1–5], have shown that the nucleate boiling heat transfer coefficients decrease with increasing oil concentration. Increasing oil viscosity also appears to decrease the heat transfer coefficient [2, 4]; however, this is contradicted by the data in [3] which found the opposite to be true. No explanation was offered for this contradiction. In some instances at low oil concentrations (< 3 percent), the heat transfer coefficients actually increased compared to the pure refrigerant data [1–3]. This result was attributed to the effects of foaming of the mixture, which occurred in the mixtures when boiled at low saturation temperatures (−18°C).

Only one model of the governing processes involved in boiling of refrigerant-oil mixtures was found. Stephan [1] suggests that as a refrigerant-oil mixture boils, the liquid layer near the superheated surface becomes oil-enriched as the more volatile refrigerant component evaporates into the interior of the bubbles which are forming adjacent to the heated surface. Thus, the exterior surface of these bubbles is composed of an oil-enriched layer. This higher oil concentration results in a higher surface tension, thus requiring the growing bubbles to do more work. Hence, the bubbles grow more slowly, and the heat transfer rate, which is dependent on the rate at which bubbles depart from the heated surface, decreases. Recently, Stephan [6] has presented a review paper in which this idea is expanded and clarified.

Sauer and Chongrungreong [4] developed a dimensional, nonmodel based correlation from the data in [1–5]. The equation

$$h = 0.05253\left[\frac{q''D}{\mu_l h_{fg}}\right]^{0.569}\left[\frac{\mu_l c_{pl}}{k_l}\right]^{0.395}$$
$$[P]^{1.695}\left[\frac{D}{0.01588}\right]^{-0.444}\left[\phi_r\frac{\rho_l}{\rho_v}\right]^{1.579} \quad (1)$$

uses bulk mixture properties, which were calculated by assuming that the mixtures behaved as ideal mixtures (e.g., equations (3), (4), and (5)). No confirming mixture property data were obtained. While equation (1) predicts the same trends as found in the experimental results, there appears to be a systematic overprediction as the oil concentration increases. This was attributed to poor prediction of the mixture viscosity.

The work done on other binary mixtures, such as those surveyed by Van Stralen [7], have applicability to refrigerant-oil mixtures. In these mixtures, with either two relatively volatile liquids or with one liquid much more volatile than the other, the heat transfer coefficients are lower than those obtained during boiling of the pure components. Diffusion at the vapor/liquid interface in the bubble plays an important role in reducing the bubble growth rate. This can lead to lower heat transfer rates. This situation appears to be similar to that experienced in nucleate pool boiling of refrigerant-oil mixtures.

The objectives of this study, thus, were to determine the effect of oil on the refrigerant thermophysical properties, to investigate the role of diffusion on the boiling heat transfer coefficients in refrigerant-oil mixtures, and to examine the mechanisms controlling nucleate pool boiling of refrigerant-oil mixtures.

Experimental Apparatus

Heat transfer data were obtained by boiling the pure R-113 and R-113-oil mixtures on the outside of an electrically (d-c) heated tube which was immersed in a saturated pool of the liquids at one atmosphere (see Fig. 1). All test sections were constructed with 321 stainless steel seamless tubing 12.7 mm in diameter. The heated length was 102 mm. Direct current power was supplied to the test section by a silicon rectifier d-c power supply (1 percent ripple).

Six copper-constantan thermocouples, evenly spaced around the circumference of the test section, were used to measure the inside wall temperatures of the test section. The thermocouple beads were electrically insulated from the test section and were held in tight contact with the inner tube wall using a simple mechanical expansion device. Four ther-

Contributed by the Heat Transfer Division for publication in the JOURNAL OF HEAT TRANSFER. Manuscript received by the Heat Transfer Division October 21, 1982.

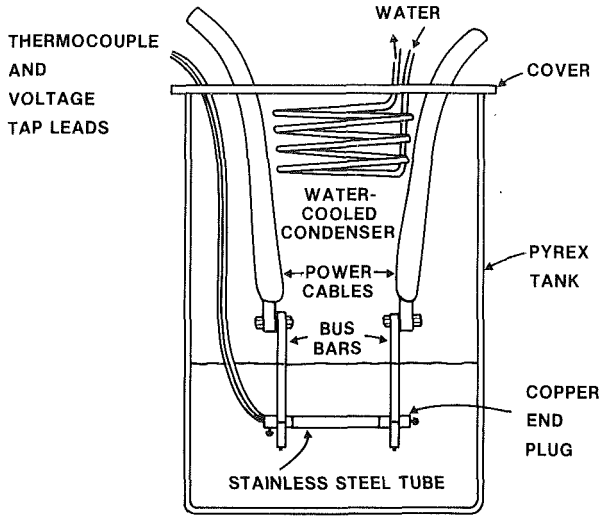

Fig. 1 Schematic of boiling apparatus

mocouples were placed in the pool near the test section to measure the bulk pool temperatures. An auxiliary electric immersion heater was used only to preheat and deaerate the pool prior to taking data.

Thermophysical properties of the pure oil, pure R-113, and R-113-oil mixtures were measured with a variety of instruments which were first calibrated with fluids with known properties. A Lauda-Brinkmann constant temperature bath maintained the mixture to ± 0.02°C for all property measurements. Densities were obtained by recording the volumes of a known mass of fluid at a fixed, known temperature. As determined through a propagation-of-error analysis, the estimated uncertainty in the density is ± 1 percent. The calibration fluids were R-113 and distilled water [8].

Dynamic viscosities were measured with a Hoeppler Precision Falling Ball Viscometer. An external water jacket regulated the temperature of the sample. Viscosities could be measured to an accuracy of approximately ± 0.02 centipoises. The calibration fluid was distilled water [8].

Surface tension was measured with a Cenco-du-Nuny Tensiometer. This device utilized the ring method for determining surface tension. The accuracy of the tensionmeter was within ± 0.3 dynes/cm. The calibration fluid was distilled water [8].

Specific heats were measured using a calorimeter and the method of mixtures. Specific heats could be determined with an accuracy of approximately ± 10 percent. The calibration fluids were distilled water and acetone [8].

To measure the dynamic contact angle, photographs of bubbles growing from a single isolated nucleation site were taken using a stroboscopic flash to stop the bubble action. Using photographs enlarged 30 times their original size, the contact angle then could be directly measured using a protractor. To obtain a single nucleation site, a small, flat electrically heated stainless steel test section was built. One artificial nucleation site approximately 0.25 mm in diameter was machined into this surface using electro-discharge machining. The accuracy of the dynamic bubble contact angles obtained with this procedure was estimated to be ± 5 deg.

Instrumentation necessary for measuring the thermal conductivities of liquids was not avaibable for this study. Therefore, the Filippov and Novoselova [9] correlation was used to predict the thermal conductivities of the mixtures when the thermal conductivities of the pure components of the mixtures are known. This correlation is

$$k_m = k_{rl}(1-C) + k_{ol}C - 0.72(k_{ol} - k_{rl})(1-C)C \qquad (2)$$

Four different refrigeration oils were used to form the R-113-oil mixtures. Three oils were from one manufacturer and had nominal viscosities of 22.5, 36.5, and 71.0 cp at 47.7°C. The fourth oil was from a second manufacturer and had a viscosity (39.0 cp) close to that of one of the other oils. The two oils with similar viscosities were used to determine whether the measured thermophysical properties were sufficient to characterize the effects of oil on pool boiling heat transfer, or whether other oil additives need to be considered.

Experimental Procedure

Pure refrigerant boiling data were obtained for reference so that a direct evaluation of the effect of the oil could be made. After filling the tank with pure R-113, an electrical immersion heater was used to degas and preheat the pool to saturation temperature; upon reaching the desired temperature, the electric immersion heater was switched off and the d-c power supply was turned on. The power supplied to the test section was gradually increased in increments of approximately 10,000 W/m^2 to a maximum of about 100,000 W/m^2. After the maximum power level was reached, the power was gradually decreased in increments and then was again in-

Nomenclature

C = oil concentration (kg oil/kg mixture), $m_0/(m_o + m_r)$
C_1, C_2 = constants in equations (12) and (14), respectively
c_p = specific heat (kJ/kg K)
d = bubble break-off diameter (m)
D = test section diameter (m)
G_d = vaporized mass diffusion fraction
h = heat transfer coefficient (W/m^{2}K)
h_{fg} = heat of vaporization (kJ/kg)
k = thermal conductivity (W/mK)
m = mass (kg)
M = molecular weight
n = mole fraction
P = pressure (atm)
ΔP = pressure difference corresponding to ΔT_{sat} (Pa)
q'' = wall heat flux (W/m^2)
$\dot{R}$ = bubble growth rate (m/s)
t = time (s)
T = temperature (°K)
ΔT = temperature difference (°K)
V = volume (m^3)
X = mass fraction of refrigerant at the bubble wall
Y = mass fraction of refrigerant in the vapor bubbles
z = diffusion boundary layer thickness (m)
α = thermal diffusivity (m^2/s)
δ = mass diffusivity (m^2/s)
θ = contact angle (deg)
μ = dynamic viscosity (centipoises, cp, 10^{-3} N-s/m^2)
ρ = density (g/cm^3)
σ = surface tension (dyne/cm)
ϕ = volume fraction

Subscripts

eff = based on effective oil concentration
l = liquid
m = mixture
o = oil
r = refrigerant
sat = saturation
v = vapor
z = Forster-Zuber equation (8)

Table 1 Summary of thermophysical properties at 47.7°C

Fluid	C	ρ (g/cm^3)	μ (10^{-3}N−s/m^2)	c_p (kJ/kgK)	σ (dyne/cm)	θ (deg)	k^a (W/mK)
R-113	0.0	1.545	0.48	0.996	15.3	60	0.0706
R-113-Oil #1	0.02		0.50		16.6	63	0.0709
	0.05		0.58		17.1	61	0.0715
	0.10	1.355	0.68		18.1	64	0.0725
	0.25			1.234			
	0.50				21.8		
	1.00	0.853	22.5	1.795	25.2		0.1249
R-113-Oil #2	0.02		0.50		17.1	61	0.0709
	0.05		0.59		17.7	60	0.0714
	0.10	1.388	0.69		18.4	60	0.0725
	0.25			1.297			
	0.50				22.1		
	1.00	0.908	36.5	1.807	25.1		0.1237
R-113-Oil #3	0.02		0.52		16.5		0.0709
	0.05		0.60		18.0	63	0.0714
	0.10	1.388	0.75		18.5	63	0.0724
	0.25			1.218			
	0.50				22.5		
	1.00	0.878	71.0	1.753	25.7		0.1230
R-113-Oil #4	0.02		0.50		15.7		0.0709
	0.05		0.58		17.2	62	0.0714
	0.10	1.381	0.74		18.0	66	0.0725
	0.25			1.226			
	0.50				22.0		
	1.00	0.903	39.0	1.745	25.1		0.1237

[a] Obtained using Eq. 2 and data from [14, 15].

creased, in order to replicate the data obtained during the decreasing power sweep. After each level of power was attained, the system was allowed to reach steady state and then all the data were recorded.

At the completion of all the tests, the liquid level was checked to see if the amount of refrigerant had changed. Because of the water-cooled condenser, refrigerant loss was negligible. After a run using pure R-113 was completed, a known amount of oil was added to the known quantity of refrigerant in the pool in order to bring the oil concentration in the refrigerant to 2 percent oil by weight. The 2 percent by weight oil in R-113 run proceeded as outlined above for the pure refrigerant. However, before any testing began with the oil mixtures or of different oil concentrations, the test section as removed from the pool, cleaned thoroughly in a hot water/detergent solution and rinsed with pure R-113, and allowed to air dry between runs. No polishing, sanding, etc., was done to the test section. After the 2 percent oil by weight run was completed, more oil was added to the refrigerant-oil mixture already in the tank, so that the 5 percent oil by weight and 10 percent oil by weight tests could be run. After all runs for one oil were completed, the entire tank was cleaned thoroughly by washing with soap and water, drying the tank, and by rising with pure R-113. This was done in order to remove all oily residue. Then the tank was refilled with fresh R-113 and the runs for the other oiis proceeded as outlined above.

The heat transfer coefficients were calculated using the heat flux, an average of the six outer wall temperatures, and the measured saturation temperature. Uncertainties in the heat transfer coefficients were estimated to be about ±8 percent as determined through a propagation-of-error analysis. Further details of the apparatus, procedure, and data reduction can be found in [10].

Experimental Results

Thermophysical Properties. Experimental data were obtained for the density, viscosity, surface tension, dynamic bubble contact angle, and specific heat of pure R-113, pure oil, and R-113-oil mixtures. Table 1 is a listing of the experimentally measured properties at 47.7°C.

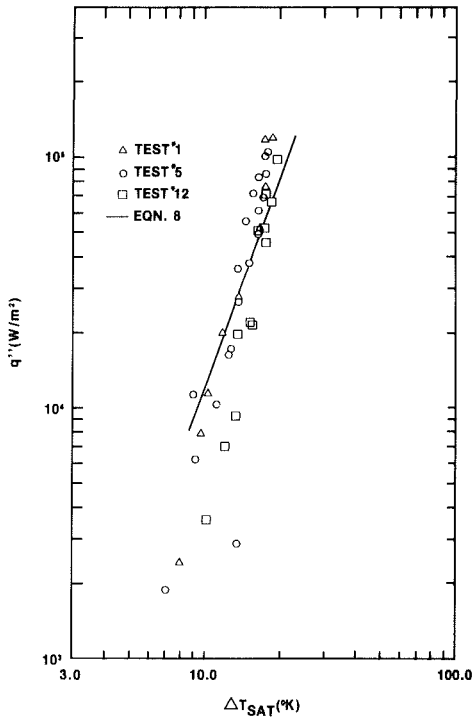

Fig. 2 Pure R-113 boiling data

The predictive equations for calculating ideal mixture densities and specific heats

$$\frac{1}{\rho_m} = \frac{C}{\rho_{ol}} + \frac{1-C}{\rho_{rl}} \tag{3}$$

$$c_{pm} = (1-C)c_{prl} + Cc_{pol} \tag{4}$$

both agreed to within ±4 percent of the experimental values. However, the viscosity of the mixtures could not be predicted with the ideal mixture equation suggested by Daniels [12]. This equation

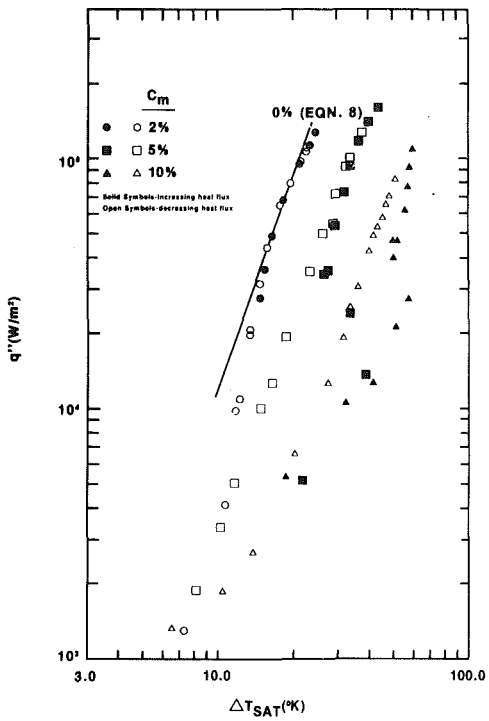

Fig. 3 R-113-Oil No. 1 boiling data

$$\frac{1}{\mu_m} = \frac{\phi_{rl}}{\mu_{rl}} + \frac{\phi_{ol}}{\mu_{ol}} \tag{5}$$

tended to substantially underpredict the experimental data. Therefore, the following interpolating equation was developed

$$\mu_m = \mu_r e^{C\left(\frac{\mu_o}{\mu_r}\right)^{0.3}} \tag{6}$$

and agreed to within an average of ±2 percent of the experimental data.

No predictive equations could be found in the literature for the surface tension of two component mixtures. Neither mass-weighted no volume-weighted mixture equations, similar in form to equations (3), (4), or (5), predicted the experimental data adequately. However, the following equation predicted the mixture surface tension to within an average of ±1.6 percent for all of the data.

$$\sigma_m = \sigma_r + (\sigma_o - \sigma_r)\sqrt{C} \tag{7}$$

No firm conclusions can be drawn about the effect of oil on the dynamic bubble contact angle. While there appears to be a trend toward a slightly increasing angle with increasing oil concentration, there is too much uncertainty in the data to conclusively state this as true. The measured angle in the pure R-113 agrees well with the data from [13]. For a clean nickel surface, they obtained an angle of 60 deg which decreased to about 45 deg as the surface aged.

The present experimental data for θ, ρ, μ, c_p, and σ of the oils and R-113 were compared to various sources in the literature [13–16], and good agreement was obtained in all cases.

Boiling Heat Transfer Characteristics. Representative heat transfer data are shown in Fig. 2. The different tests were taken all on the same test section, with Test #5 and Test #12 taken after thoroughly cleaning the test section after refrigerant-oil mixtures had been boiled on the surface. Hysteresis effects were observed which are consistent with the findings of other investigations. Typical boiling curves which show the effect of oil concentration on the nucleate pool boiling are shown in Fig. 3. The qualitative results of these experiments agree well with the results of previous studies [1–4]. It should be noted that the saturation temperature increased with increasing oil concentration; for a 10 percent oil mixture, the increase was approximately 1.8–2°K. The actual saturation temperature was used in the evaluation of all fluid properties.

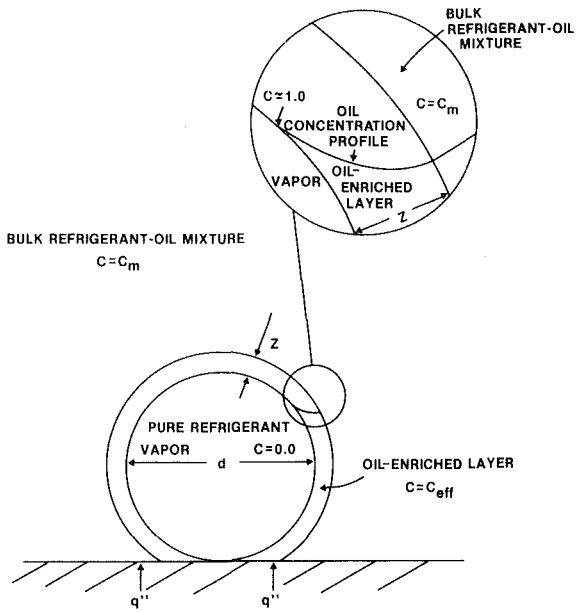

Fig. 4 Idealized model of bubble growth in refrigerant-oil mixture

With increasing oil concentration and viscosity, the heat transfer coefficient decreases. While some augmentation of the heat transfer coefficient was observed at low oil concentration (< 3 percent) in [1–3], no such enhancement was obtained in this study. Note that the slopes of the nucleate boiling portions of the boiling curves for both pure R-113 and the R-113-oil mixtures decrease slightly with increasing oil concentration. This agrees with a paper referenced by Stephan [6]. The "knee" of the boiling curve (that portion of the boiling curve where natural convection effects are becoming negligible compared to the nucleate boiling effects) of the R-113-oil mixtures appears to be shifted upward and to the right compared to the pure R-113 curve. It should also be noted that for a given oil concentration, the percent decrease in the heat transfer coefficient compared to the pure refrigerant data increases with increasing wall superheat. Hysteresis effects are not shown on the faired-in curves, since the regime of interest is the fully-developed nucleate boiling section of the pool boiling curve.

Wall temperature measurements indicated large (up to about 4°C) variations in the circumferential wall temperatures at any one heat flux in the R-113-oil mixtures. There was no set pattern as to which location had the highest or lowest wall temperature. Other researchers also have noted this problem. This temperature variation was averaged out, and the presented data reflect this averaging. Much smaller circumferential variations in wall temperature were noted in the pure boiling R-113. Hysteresis effects appear to be much more pronounced as the oil concentration increases when compared to the pure refrigerant data. At the higher oil concentrations, the hysteresis transition occurred in several small steps, whereas for the pure refrigerant, the hysteresis occurred in one or two large steps.

Development of Model and Correlation

The mixture properties were used in the pure refrigerant

correlation (equation (8)) to try to predict the mixture heat transfer coefficients. The data were grossly overpredicted with the deviation increasing as the oil concentration increases. Thus, it was concluded that the mechanisms involved with boiling of refrigerant-oil mixtures are significantly different than with pure refrigerants. Therefore, the following model is suggested to govern the nucleate boiling heat transfer in refrigerant-oil mixtures. This mechanism occurs on the microscopic level during the growth of the vapor bubble. As a bubble, such as shown in Fig. 4, grows on a heated surface, the refrigerant evaporates from the superheated liquid phase near the wall into the bubble interior. Since the oil in the mixture is much less volatile than the refrigerant, the oil does not evaporate into the interior of the bubble, but rather, is left behind at the liquid-vapor interface. Diffusion of the oil into the liquid refrigerant-oil mixture and the diffusion of the refrigerant through the oil into the vapor bubble decreases the bubble growth rate and contributes to a decreased heat transfer rate. The region immediately adjacent to the surface of the vapor bubble becomes enriched with the oil as the bubble grows.

If we can assume that the boiling process occurs as a combination of macroscopic and microscopic effects, then the use of an existing heat transfer correlation for nucleate pool boiling of a pure refrigerant should account for the macroscopic effects. That correlation combined with the above model of the microscopic effects should allow the data to be correlated. The pure refrigerant equation chosen to represent the macroscopic effects was developed by Forster and Zuber [17].

$$h_z = 0.00122\left(\frac{k_l^{0.79} c_{pl}^{0.45} \rho_l^{0.49} g_c^{0.25}}{\sigma^{0.5} \mu_l^{0.29} h_{fg}^{0.24} \rho_v^{0.24}}\right) \Delta T_{\text{sat}}^{0.24} \Delta P_{\text{sat}}^{0.75} \tag{8}$$

The microscopic effects are represented by a dimensionless "effective" oil concentration, C_{eff}, in the vicinity of the bubble interface to represent the mass diffusion process.

The effective oil concentration in the vicinity of the growing bubble can be determined using a simple geometric model. If it is assumed that only refrigerant evaporates into the growing vapor bubble (which is reasonable since refrigerants are much more volatile than most oils), then the oil component of the refrigerant-oil mixture accumulates at the vapor-liquid interface and diffuses into the liquid refrigerant-oil mixture. Assuming that the oil accumulates in a layer of thickness, z, around a spherical bubble of diameter, d, then the effective oil concentration can be calculated through the use of the definition of the oil concentration, $C = m_o/(m_o + m_r)$, and the volume of the layer z: $V = (4\pi/3)(((d+2z)/2)^3 - (d/2)^3)$. The mass of the oil, in this case, is determined by adding the oil present in the layer z before enrichment occurs ($C\rho_m V$) and the oil left after the refrigerant has evaporated to form the bubble ($C\rho_v \pi d^3/6(1-C)$). The mass of the refrigerant is equal to $(1-C)\rho_m V$. Substituting these expressions into the definition of C results in the following equation for the effective oil concentration, C_{eff}.

$$C_{\text{eff}} = \frac{\dfrac{C\rho_v d}{1-C} + C\rho_m(6d^2 z + 12dz^2 + 8z^3)}{\dfrac{C\rho_v d^3}{1-C} + \rho_m(6d^2 z + 12dz^2 + 8z^3)} \tag{9}$$

The bubble diameter, d, is assumed to be the break-off bubble diameter. An equation presented by Thome [18], which takes into account the effect of diffusion on the bubble growth, can be used, but as noted below, will not be required.

The enriched oil layer thickness, z, can be estimated by assuming it is equal to the diffusion boundary layer thickness. This thickness is dependent on the mass diffusivity of the oil

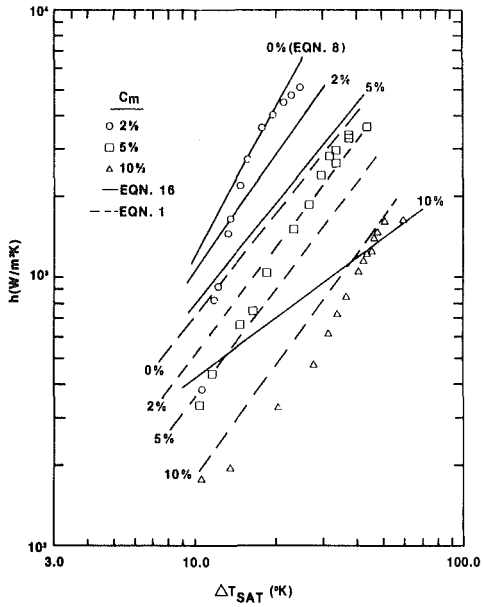

Fig. 5 comparison of predicted heat transfer coefficients with experiment R-113-Oil No. 1 data

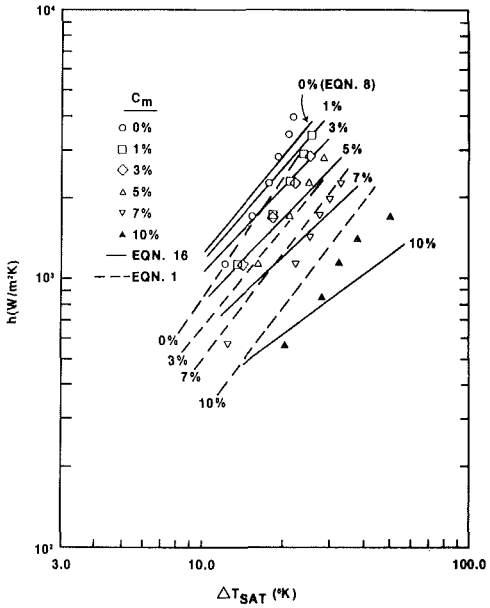

Fig. 6 Comparison of predicted heat transfer coefficients with experimental R-11-Oil No. 1 data at 1 atm. from [2]

in the refrigerant and the time required to reach the bubble break-off diameter and can be calculated by

$$z = \left(\frac{\pi}{3}\right)^{1/2} (\delta t)^{1/2} \tag{10}$$

This equation is an approximation and assumes a thin boundary layer. Using an equation developed by Van Stralen [7] (pp. 222-224), which estimates the bubble growth rate in a binary mixture where diffusion plays an important role, the time, t, can be determined.

The bubble growth equation is

$$\dot{R} = \frac{\Delta T_{\text{sat}}}{\left(\dfrac{\rho_v}{\rho_l}\right)\left[\dfrac{h_{fg}}{c_{Pl}} + \left(\dfrac{\alpha_l}{\delta}\right)^{1/2} \dfrac{\Delta T}{G_d}\right]} \left(\frac{3\alpha_l}{\pi t}\right)^{1/2} \tag{11}$$

Table 2 Effect of wall superheat and oil viscosity on effective oil concentration

Refrigerant	Oil	C	C_{eff} $\Delta T=10K$	$\Delta T=20K$	$\Delta T=40K$
R113	#1	0.01	0.0117	0.0130	0.0150
	#1	0.10	0.1193	0.1324	0.1515
	#3	0.01	0.0118	0.0131	0.0151
	#3	0.10	0.1207	0.1345	0.1545
R11	#1	0.01	0.0116	0.0128	0.0146
	#1	0.10	0.1186	0.1314	0.1499
	#3	0.01	0.0116	0.0129	0.0147
	#3	0.10	0.1209	0.1349	0.1548

By integrating this equation, the time required to reach the break-off diameter is obtained.

$$t=\left(\frac{d}{4C_1}\right)^2 \tag{12}$$

where

$$C_1=\frac{\Delta T_{sat}}{\left(\frac{\rho_v}{\rho_l}\right)\left[\frac{h_{fg}}{c_{Pl}}+\left(\frac{\alpha_l}{\delta}\right)^{1/2}\frac{\Delta T}{G_d}\right]}\left(\frac{3\alpha_l}{\pi}\right)^{1/2}$$

The term $\Delta T/G_d$, which represents a reduction in the effective superheat conducting heat to the bubble wall, is given by Van Stralen as

$$\frac{\Delta T}{G_d}=\left(\frac{\delta}{\alpha_l}\right)^{1/2}\left(\frac{h_{fg}}{c_{pl}}\right)\left(\frac{\Delta T_{sat}}{\Delta T}-1\right) \tag{13}$$

where

$$G_d=\frac{(1-C)-X}{Y-X}$$

Note that the bubble departure diameter factors out of the effective concentration equation (9) when equations (10) and (12) are used. Thus, C_{eff} is a function of C, ρ_v/ρ_m, and $(\pi\delta/48C_1^2)^{1/2}$.

Assuming X, the mass fraction of refrigerant at the bubble interface, approaches zero and Y, the mass fraction of refrigerant in the vapor bubble, is unity, then

$$G_d=1-C$$

By rearranging equation (13), a quadratic equation in ΔT is obtained. Since a negative ΔT is meaningless, dividing the positive root of the equation by G_d gives

$$\frac{\Delta T}{G_d}=\frac{-C_2+\sqrt{C_2+4\Delta T_{sat}C_2}}{2(1-C)} \tag{14}$$

where

$$C_2=(1-C)\left(\frac{\delta}{\alpha_l}\right)^{1/2}\left(\frac{h_{fg}}{c_{Pl}}\right)$$

The remaining quantity to be determined is the mass diffusivity of the oil in the refrigerant. Since no specific literature values for refrigerant-oil mixtures could be found, a relation recommended [19] for estimating the mass diffusivity, δ, of one liquid in another for nonassociated (nonpolar) nonideal liquid solutions is used. With some manipulation and simplification this relation is

$$\delta=\frac{T}{\mu_m}\left[n\frac{(M_o)^{0.5}}{\left(\frac{M_r}{\rho_{lr}}\right)^{0.6}}+(1-n)\frac{(M_r)^{0.5}}{\left(\frac{M_o}{\rho_{lo}}\right)^{0.6}}\right]\times 7.4\times 10^{-12} \tag{15}$$

where the mole fraction of oil in the refrigerant, n, is given by

$$n=\frac{\frac{C}{M_o}}{\frac{C}{M_o}+\frac{1-C}{M_r}}$$

Combining equations (9, 10, 12, 14) and (15), the effective oil concentration can be calculated (see Table 2). C_{eff} increases with increasing wall superheat and to a lesser extent by an increasing oil viscosity.

R-113 data from this study, R-11 and R-113 data from [2], and R-11 data from [4] were used in developing the correlation. Data from [3] were not used, since this data showed decreasing heat transfer coefficients with decreasing oil viscosity which is the opposite effect found in all other studies. The data from [2] and [4] were obtained by drawing smooth curves through the fully developed nucleate boiling data and then picking off five to seven representative data points. Only data at temperature differences greater than 10°K were used to ensure that they were in the fully developed nucleate boiling regime. In all, 381 refrigerant-oil mixture data points were used. Pressures of one and two atmospheres were covered with saturation temperatures varying from 23 to 72°C. The resulting correlation is

$$\frac{h}{h_z}=e^{-4.095C_{eff}-55.11C_{eff}^2} \tag{16}$$

where h_z, is obtained from equation (8) using pure refrigerant properties. Compared to the data at the same wall superheat, the correlation has a mean absolute error of 29.6 percent. The error can be attributed to normal scatter in the data and possibly poor prediction of the mixture properties. Using equation (8) to predict the pure refrigerant data (79 data points), the mean absolute error was 19.2 percent. (Equation (8) consistently overpredicted the R-11 data by a substantial amount; therefore, to obtain a much improved prediction, the R-11 data were multiplied by 0.70.) Figures 5 and 6 compare the present correlation (equation (16)) with the experimental data. As can be seen, fair agreement is obtained for most cases. The Sauer and Chongrungreong [4] correlation (equation (1)) predicts the pure refrigerant data with a mean absolute error of 30.2 percent, and the refrigerant-oil mixture data with a mean absolute error of 35.2 percent

The effective oil concentration also was correlated

$$C_{eff}=C(1+0.0317\Delta T^{0.753}) \tag{17}$$

with ΔT in °K. This equation, when used with equation (16), predicts the data with an average deviation of ±30.3 percent. As can be seen, if equations (16) and (17) are used, the mixture properties do not need to be known. In addition, the pure refrigerant correlation which best fits the data could be used in equation (16) to give a better prediction of the heat transfer coefficients in refrigerant-oil mixtures. Note that the proposed correlation (equation (16)) does indicate decreasing slope of the boiling curve with an increasing oil concentration. This can be seen by examining equation (17). In addition,

Table 2 shows a small increase in the effective oil concentration with increasing viscosity; this would lead to a slightly smaller heat transfer coefficient with increasing oil viscosity. Thus, the trends between the prediction and data are the same.

Conclusion

An experimental study has been conducted to investigate the effect of oil contamination on the nucleate boiling heat transfer coefficients of refrigerant oil mixtures. The following conclusions can be drawn from this study.

1 As the weight percent concentration of oil in the refrigerant increases, the boiling heat transfer coefficient, h, decreases. At a given oil concentration, there is a larger decrease in h at high wall superheats than at small wall superheats when compared to the pure refrigerant data.

2 Diffusion plays a significant role in the reduction in the boiling heat transfer coefficients in refrigerant-oil mixtures when compared to pure refrigerants. The effective oil concentration concept models the mechanisms governing this process well, predicting increasing C_{eff} with increasing bulk oil concentration and with increasing wall superheat.

3 While density and specific heat behave ideally in refrigerant-oil mixtures, viscosity and surface tension do not. Up to 10 percent oil by weight has little effect on the dynamic bubble contact angle.

4 A correlation has been developed which satisfactorily models the heat and mass transfer processes occurring in nucleate pool boiling of refrigerant-oil mixtures.

Additional pool boiling experiments should be performed for a wider range of refrigerants, oils, and operating conditions, including oil concentration and operating pressure. More extensive measurements of the relevant thermophysical properties of refrigerant-oil mixtures at a wider range of temperatures and pressures are needed. A better technique for estimating the mass diffusivity is required.

Acknowledgments

The investigation was supported by the Department of Mechanical Engineering and the Graduate School at the University of Wisconsin-Milwaukee.

References

1 Stephan, K., "Influence of Oil on the Heat Transfer of Boiling Freon 12 and Freon 22," *Proceedings of the International Congress of Refrigeration*, Vol. 1, 1963, pp. 369-379.

2 Sauer, H. J., and Dougherty, R. L., "Nucleate Pool Boiling of Refrigerant-Oil Mixtures from Tubes," *ASHRAE Transactions*, Vol. 80, pt. 2, 1974, pp. 175-193.

3 Sauer, H. J., Gibson, R. K., and Chongrungreong, S., "Influence of Oil on the Nucleate Boiling of Refrigerants," *Proceedings from the 6th International Heat Transfer Conference*, Toronto, Vol. 1, 1978, pp. 181-186.

4 Sauer, H. J. and Chongrungeong, S., "Nucleate Boiling Performance of Refrigerants and Refrigerant-Oil Mixtures," ASME JOURNAL OF HEAT TRANSFER, Vol. 102, 1980, pp. 701-705.

5 Stephan, K., "The Computation of Heat Transfer to Boiling Refrigerants," *Kaeltetechnik*, Vol. 15, 1963, pp. 231-234.

6 Stephan, K., and Mitrovic, J., "Heat Transfer in Natural Convective Boiling of Refrigerant-Oil Mixtures," *Proceedings of the Seventh International Heat Transfer Conference*, Vol. 4, Hemisphere Publishing Corporation, Washington, D.C., 1982, pp. 73-87.

7 Van Stralen, S., and Cole, R., *Boiling Phenomena*, Vol. 1, Hemisphere Publishing Corporation, Washington, D.C., 1979, pp. 57-63.

8 *Handbook of Chemistry and Physics*, 57th ed., Op. F-51, CRC Press, Cleveland, 1976.

9 Filippov, L. P., and Novoselova, N. S., *Vestn. Mosk. Univ., Ser. Fiz. Mat. Estestv. Nauk.*, (3) 10(2), 1955, pp. 37-40; *Chem. Abstr.*, Vol. 49, 1955, p. 11366.

10 Jackman, D. L., "Effect of Oil Contamination of Nucleate Pool Boiling of Refrigerant-113," M.S. thesis, University of Wisconsin—Milwaukee, 1981.

11 *ASHRAE Handbook and Product Directory*, Vol. II, ASHRAE, New York, 1973, p. 32.8.

12 Daniels, F., *Outlines of Physical Chemistry*, Wiley and Sons, Inc., New York, 1951, p. 189.

13 Corty, C., and Foust, A. S., "Surface Variables in Nucleate Boiling," *Chemical Engineering Progress Symposium Series*, No. 17, Vol. 51, 1955, pp. 1-10.

14 *Thermophysical Properties of Refrigerants*, ASHRAE, New York, 1973, pp. 60.

15 Personal communication with the Sun Oil Company, manufacturers of Suniso Refrigeration Oils, 1981.

16 Sinitsyn, Y. N., Muratov, G. N., and Skripov, V. P., "The Surface Tension of F-11, 21, and 113," *Heat Transfer-Soviet Research*, Vol. 4, No. 4, 1972, pp. 79-80.

17 Forster, H. K., and Zuber, N., "Dynamics of Vapor Bubbles and Boiling Heat Transfer," *AIChE Journal*, Vol. 1, 1955, pp. 531-535.

18 Thome, J. R., "Nucleate Boiling of Binary Mixtures—An Analytical Equation," *AIChE Symposium Series No. 208*, Vol. 77, 1981, pp. 238-250.

19 *Chemical Engineers Handbook*, 5th ed., McGraw-Hill, New York, pp. 3-224-3-225.

The Effect of Vapor Velocity Profile Shape on Flow Film Boiling From Submerged Bodies[1]

L. C. Witte
Mem. ASME

J. Orozco
Heat Transfer/Phase Change Laboratory,
Department of Mechanical Engineering,
University of Houston,
Houston, Texas 77004

An analysis of subcooled flow film boiling from submerged bodies that includes the effect of nonlinearity of the vapor film velocity profile is performed. The angle at which vapor flow reversal occurs on the back of the body is predicted by the analysis. A comparison of the predicted vapor flow reversal angle to the wake formation angle observed for flow boiling over spheres indicates that wake formation occurs a few degrees downstream of the vapor flow reversal point. A comparison of the analysis to available experimental data shows that heat transfer results based on a quadratic vapor velocity profile compare much better with experiments than do previous analyses. The heat transfer results for linear and quadratic vapor velocity profiles become virtually identical as subcooling increases.

Introduction

Film boiling heat transfer from spheres and cylinders submerged in a flowing, saturated liquid can be calculated easily if the vapor velocity is assumed to vary linearly across the film (see [1]). However, it is known that a nonlinear vapor velocity profile results if it is assumed that the liquid pressure is "impressed" upon the vapor film (see Kobayasi [2], Epstein and Hauser [3], and Witte and Orozco [4].) In the absence of surface tension effects, this assumption is physically realistic.

The shape of the vapor velocity profile affects the heat transfer from the body because it influences the vapor film thickness over the body surface. In this paper, an analysis is performed that accounts for the nonlinearity of the vapor velocity profile around spheres and cylinders. A result of the analysis is a prediction of the point of vapor flow reversal on the rear of the body.

Theoretical Model

The basic flow model is shown in Fig. 1. It allows for a variation of vapor thickness with angle, and is similar to one used by Witte [1]. Appropriate expressions for the velocity and temperature distributions can be found by using the following assumptions:

- Pure, incompressible liquid and vapor
- Smooth liquid-vapor interface with laminar vapor flow
- Uniform body surface temperature
- Vapor film thin compared to radius of the body
- Negligible buoyant forces
- Negligible inertia and convection effects in the vapor
- Uniform vapor and liquid thermophysical properties
- Liquid velocity at the liquid-vapor interface unaffected by vapor drag
- Negligible thermal radiation
- Negligible viscous dissipation in the vapor film

The following development is for a sphere. The corresponding development for a cylinder is virtually identical and is not presented here for the sake of brevity.

Liquid Region. The liquid velocity at the liquid-vapor interface is

$$u_l(\theta) = (3/2)V\sin\theta \tag{1}$$

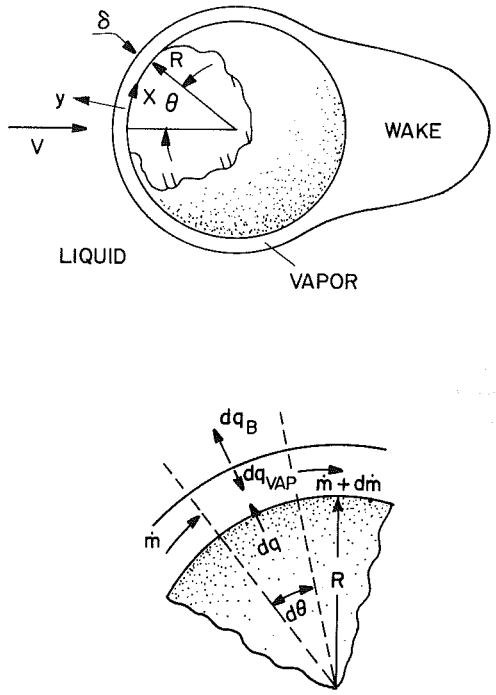

Fig. 1 Model for flow boiling from a submerged sphere

because the liquid is assumed to move unaffected by vapor drag. This assumption means that the shear stresses at the liquid-vapor interface are not matched. Sparrow and Cess [5] used this assumption for laminar film boiling over a flat plate and showed that as long as the parameter

$$\frac{c_{p_v}\Delta T_{\text{sat}}}{h_{fg}\text{Pr}_v}\,\frac{(\rho\mu)_l}{(\rho\mu)_v} \tag{2}$$

was large heat transfer results are accurate to within less than 1 percent compared to the results obtained when vapor drag on the liquid is included. In fact, even for values of the parameter (2) down to 10, heat transfer results based on potential flow for the liquid are only slightly more than 1 percent higher than for the theory in which vapor drag is included. Realistically, values of the parameter (2) which are encountered in the laboratory and in practice are much larger than 10. Epstein and Hauser [3] also showed that heat transfer results are rather insensitive to the potential flow assumption for flow over spheres and cylinders, even for the subcooled liquid case.

[1] Work on this paper was supported by NSF Grant MEA 8008036.
Contributed by the Heat Transfer Division for publication in the JOURNAL OF HEAT TRANSFER. Manuscript received by the Heat Transfer Division January 3, 1983.

The energy equation for the liquid is

$$u\frac{\partial T}{\partial x}+v\frac{\partial T}{\partial y}=\alpha\frac{\partial^2 T}{\partial y^2} \tag{3}$$

where x and y are curvilinear coordinates attached to the sphere surface. The solution of equation (3) will be discussed later.

Vapor Region. The assumption of laminar vapor flow is justified if velocity and body diameter are moderate in magnitude. For example, the vapor velocity would have to be greater than 15 m/s for DV/ν_{vapor} to be greater than 300,000 for Freon-113 film boiling from a 6.35-mm-dia cylinder. Most film boiling data fall into the laminar vapor flow category.

In light of the assumptions, the vapor momentum equation reduces to

$$\frac{dp}{dx}=\mu_v\frac{\partial^2 u}{\partial y^2} \tag{4}$$

Equation (4) is integrated, subject to the no-slip condition at both the liquid-vapor interface and the solid surface. Then equation (1) is used to describe the velocity at the liquid-vapor interface and Bernoulli's equation allows the pressure gradient along the liquid-vapor interface to be written in terms of the liquid velocity. The resulting expression for the vapor velocity profile is

$$u_v=\frac{9}{8}\frac{\rho_l V^2}{\mu_v R}\sin\theta\,\cos\theta\{y\delta-y^2\}+\frac{3}{2}V\sin\theta\left(\frac{y}{\delta}\right) \tag{5}$$

The only unknown in equation (5) is δ, the film thickness, which depends upon a mass-energy balance on the system.

For the case where a substantial wake forms behind the sphere, equation (5) is not strictly applicable not only in the immediate vicinity of the wake but relatively far upstream on the sphere. The effect of the wake on the liquid pressure field would probably be much like the effect of a separated laminar boundary layer in single phase flow. In that case, the pressure can deviate from that predicted by potential flow all the way back to about 45 deg from the stagnation point [6].

The effect of the wake has largely been ignored in studies of flow film boiling over submerged bodies. Thus, our ability to include deviations from the pressure distribution predicted by potential flow theory is limited by a lack of knowledge on the size and shape of vapor wakes generated by boiling. Any error involved in using equation (5) over the entire spherical surface would be greatest for a saturated liquid because of the larger wake that is formed, and the error would decrease as the level of subcooling is increased because subcooling decreases the size of the wake.

The effect of the y-component of vapor velocity, v, on the temperature distribution across the vapor film is assumed to be small, thereby yielding a linear temperature profile.

Mass-Energy Balance. The heat balance on a differential film element as shown in Fig. 1 is

$$dq=dq_{\text{vap}}+dq_B \tag{6}$$

where dq_{vap} is the energy required to form vapor, and dq_B is the energy conducted into the subcooled liquid when $T_B<T_{\text{sat}}$. Equation (6) can be expanded as

$$k_v\frac{\Delta T}{\delta}dA_s=h'_{fg}d\dot{m}+\left(-k_l\frac{\partial T}{\partial y}\right)_\delta dA_s \tag{7}$$

where $dA_s=2\pi R^2\sin\theta\,d\theta$. The differential flow rate resulting from the mass balance on the differential film element, $d\dot{m}$, is written in terms of δ as

$$d\dot{m}=2\pi R\rho_v d\left\{\frac{9}{8}\frac{V^2}{R}\frac{\rho_l}{\mu_v}\sin^2\theta\cos\theta\left(\frac{\delta^3}{6}\right)+3/2V\sin^2\theta\left(\frac{\delta}{2}\right)\right\} \tag{8}$$

Equation (8) is based on the assumption of constant vapor density around the body surface. The variation of vapor density because of the liquid pressure gradient is small; only a 3 percent variation occurs for a 2.5-cm sphere in a 2.5 m/s flow. Thus, the use of constant density is justified.

The heat transferred into the bulk liquid is found by using the solution to the energy equation according to Sideman [7]. Sideman's solution is based on potential flow and also on the notion that the heat transfer in the liquid is confined to a thin layer near the liquid-vapor interface. Using this gives

$$\left.\frac{\partial T}{\partial y}\right|_\delta=\frac{-\Delta T_B\sin^2\theta}{\left\{\pi\frac{2}{3}\frac{R\alpha}{V}\left(\frac{2}{3}-\cos\theta+\frac{1}{3}\cos^3\theta\right)\right\}^{1/2}} \tag{9}$$

Equation (7) can now be recast in dimensionless form, giving the variation of δ with the angle θ as

$$\frac{d(\delta/D)}{d\theta}=\frac{1}{1+\frac{3}{2}\frac{\rho_l}{\rho_v}\text{Re}_v\left(\frac{\delta}{D}\right)^2\cos\theta}\left\{\frac{2}{3}\frac{\text{Ja}_v}{\text{Pe}_v\left(\frac{\delta}{D}\right)\sin\theta}-2\left(\frac{\delta}{D}\right)\cot\theta-\frac{1}{2}\frac{\rho_l}{\rho_v}\text{Re}_v\left(\frac{\delta}{D}\right)^3\left\{\frac{3\cos^2\theta-1}{\sin\theta}\right\}\right.$$

Nomenclature

A_s = body surface area
c_p = specific heat
D = body diameter
h_{fg} = latent heat of vaporization
h'_{fg} = latent heat of vaporization, including the effects of vapor superheat
Ja = Jakob Number, see equation (11)
k = thermal conductivity
$\dot{m}$ = vapor mass flow rate
Nu = local Nusselt Number
$\overline{\text{Nu}}$ = average Nusselt Number
Pe = Peclet Number, see equation (11)
p = pressure
q = heat transfer rate
q'' = heat flux
Re = Reynolds Number, see equation (11)
R = body radius
T = temperature
ΔT = temperature difference, T_w-T_{sat}
ΔT_B = temperature difference, $T_{\text{sat}}-T_B$
u = velocity in the x-direction
v = velocity in the y-direction
V = liquid velocity, see Fig. 1
x = curvilinear coordinate, see Fig. 1
y = curvilinear coordinate, see Fig. 1
α = thermal diffusivity
δ = vapor film thickness
θ = angle measured from stagnation point
μ = viscosity
ρ = density
ν = kinematic viscosity

Subscripts

B = bulk
l = liquid
O = $y=0$
v = vapor region
r = vapor flow reversal
sat = saturation
s = separation
w = wall

Table 1 Characteristics of spherical and cylindrical systems

	Sphere	Cylinder
Potential flow velocity	$3/2V\sin\theta$	$2V\sin\theta$
Vapor velocity distribution	$\frac{9}{8}\frac{\rho_l V^2}{\mu_v R}\sin\theta\cos\theta[y\delta - y^2] + \frac{3}{2}V\sin\theta\left(\frac{y}{\delta}\right)$	$2\frac{\rho_l V^2}{\mu_v R}\sin\theta\cos\theta]y\delta - y^2] + 2V\sin\theta\left(\frac{y}{\delta}\right)$
$\left(\frac{\partial T}{\partial y}\right)_l$ at $y=\delta$	$\frac{-\Delta T_B \sin^2\theta}{\left[\pi\frac{2}{3}\frac{R\alpha}{V}\left(\frac{2}{3}-\cos\theta+\cos^3\theta\right)\right]^{1/2}}$	$\frac{-\Delta T_B \sin\theta}{\left[\pi\frac{R\alpha}{2V}\left(1-\cos\theta\right)\right]^{1/2}}$
$\frac{d(\delta/D)}{d\theta}$	See equation (10)	$\frac{d(\delta/D)}{d\theta} = \frac{1}{1+2\mathrm{Re}_v\frac{\rho_l}{\rho_v}\left(\frac{\delta}{D}\right)^2\cos\theta}\left[\frac{\mathrm{Ja}_v}{2\mathrm{Pe}_v\sin\theta\left(\frac{\delta}{D}\right)} - \frac{\delta}{D}\cot\theta - \frac{2}{3}\frac{\mathrm{Re}_v\rho_l/\rho_v\left(\frac{\delta}{D}\right)^3(2\cos^2\theta-1)}{\sin\theta} - \frac{\mathrm{Ja}_l\rho_l/\rho_v}{\sqrt{\mathrm{Pe}_l}}\frac{1}{[\pi(1-\cos\theta)]^{1/2}}\right]$
$\cos\theta_r$	$-\frac{4}{3}\frac{\mu_v R}{\rho_l V\delta_r{}^2}$	$-\frac{\mu_v R}{\rho_l V\delta_r{}^2}$

$$-\frac{2}{3}\frac{\rho_l/\rho_v \mathrm{Ja}_l\sin\theta}{\sqrt{\mathrm{Pe}_l}\sqrt{\pi}\left\{\frac{1}{3}\left(\frac{2}{3}-\cos\theta+\frac{1}{3}\cos^3\theta\right)\right\}^{1/2}}\Bigg\} \quad (10)$$

where

$$\mathrm{Ja}_v = \frac{(c_p\Delta T)_v}{h'_{fg}} \qquad \mathrm{Pe}_v = \frac{DV}{\alpha_v}$$

$$\mathrm{Ja}_l = \frac{(c_p\Delta T_B)_l}{h'_{fg}} \qquad \mathrm{Pe}_l = \frac{DV}{\alpha_l} \quad (11)$$

$$\mathrm{Re}_v = \frac{\rho_v VD}{\mu_v}$$

These dimensionless numbers would be the same for cylinders. A numerical solution of equation (10) is required; once solved for δ/D, the heat transferred from the body can be easily calculated as shown in a later section of the paper.

Vapor Flow Reversal/Wake Formation

Equation (5) can be written to demonstrate the effect of the impressed liquid pressure gradient upon the vapor velocity distribution at various angles,

$$\frac{u_v}{3/2V\sin\theta} = \frac{u_v}{u_\delta} = \frac{y}{\delta} + \frac{3}{4}\frac{\rho_l V}{\mu_v R}\cos\theta\{y\delta - y^2\} \quad (12)$$

Figure 2 shows how the vapor velocity responds to the liquid pressure gradient for boiling of subcooled water. An interesting feature of the plot is that the velocity profile exhibits flow reversal at some angle past the 90 deg point. Flow separation occurs because, although the liquid moves in an inviscid manner, the vapor flow is viscosity-dominated.

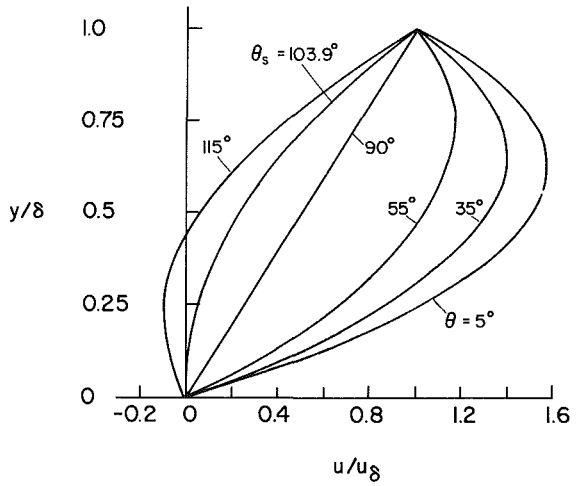

Fig. 2 Velocity profiles for subcooled water flowing over a 6.35-mm sphere at 4.26 m/s: $T_w = 400°C$, $\Delta T_B = 40°C$

Differentiating equation (12) with respect to y and setting it to zero at $y = 0$ yields the point of vapor flow separation as

$$\cos\theta_r = -\frac{4}{3}\frac{\mu_v R}{\rho_l V\delta_r^2} \quad (13)$$

Equation (13) alone does not predict the angle of separation; rather, it gives the relationship between the separation angle and the thickness of the vapor film at separation for a given boiling case. The relationship shows that the separation will occur in the range $\pi/2 < \theta < \pi$. The separation angle is found by solving equations (10) and (13) simultaneously. For the

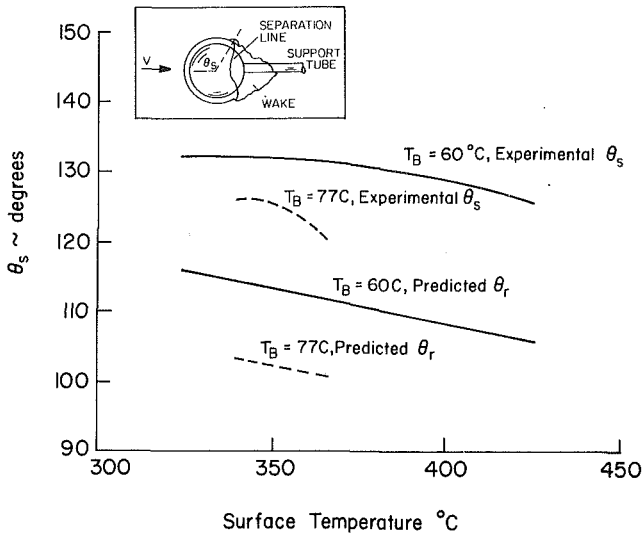

Fig. 3 Comparison of wake formation angles, θ_s, to predicted vapor flow reversal angles, θ_r, for water flowing over 24-mm spheres at 1.52 m/s. The vapor wake shown here is for illustrative purposes and does not necessarily represent the actual size or shape of the wake.

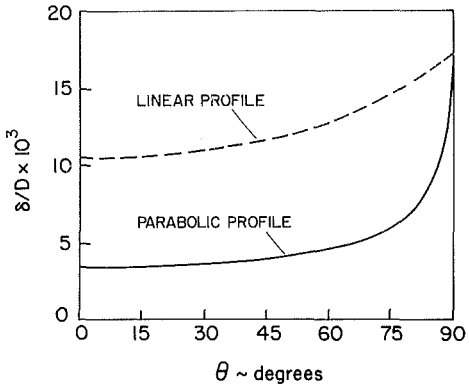

Fig. 4 Comparison of vapor film thickness for linear and quadratic velocity profiles for a 6.35-mm sphere in saturated water: $V = 4.26$ m/s, $T_{sat} = 100°C$, $T_w = 678°C$.

case plotted in Fig. 2, the separation point θ_r, turns out to be 103.9 deg.

Heat Transfer

The local heat transfer is given by

$$q'' = k_v \frac{(T_w - T_{sat})}{\delta} \tag{14}$$

because the temperature profile is linear. The local heat transfer coefficient is

$$h = \frac{q''}{(T_w - T_{sat})} \tag{15}$$

so that

$$h = k_v/\delta \tag{16}$$

The definition of a local Nusselt number as $\mathrm{Nu} = hD/k_v$ gives

$$\mathrm{Nu} = D/\delta \tag{17}$$

Thus, the integration of equation (10) yields the local nondimensional heat transfer directly. The average Nusselt number based on total sphere area, $4\pi R^2$, is

$$\overline{\mathrm{Nu}} = \frac{1}{2}\int_0^{\theta_r} \mathrm{Nu}(\theta)\sin\theta d\theta \tag{18}$$

since T_w is constant with θ. Equation (18) ignores the heat transfer in the wake region. In effect, it is assumed that $\mathrm{Nu}(\theta)$ remains defined only up to the point where vapor flow reversal is described by equation (13).

Radiation heat transfer is typically very small compared to the heat transferred by conduction across the vapor film. It is generally less than 1 percent of the total heat transfer even for fairly high surface temperatures.

The method of analysis for a cylinder is identical, with the appropriate cylindrical velocities, areas, temperature gradients, etc., being substituted for their corresponding spherical quantities. Table 1 is a summary of corresponding spherical and cylindrical quantities for the two cases.

Comparison to Experimental Data

Spheres. Only a few experimental investigations of flow film boiling from spheres have been made. Stevens and Witte [8], Walford [10], Jacobson and Shair [11], Dhir and Purohit [12], and Ungar [13] have performed quenching tests using spheres of various sizes and materials, moving through various liquids. Most of these data are unsuitable for comparison to theory because they lack certain required details, such as instantaneous surface temperature and heat flux. Walford's data, for example, are averaged over an entire quench; consequently, they represent averages of film and nucleate boiling. Jacobson and Shairs' data are for extremely low flow velocities and do not include surface temperature measurements, nor do those of Stevens and Witte, rendering both sets unsuitable for theoretical comparison. Ungar's data extend into the film regime, but were not reduced to heat transfer versus ΔT form.

The data of Dhir and Purohit are perhaps the best documented; although obtained during quenching, they have been carefully reduced to instantaneous heat flux versus surface temperature. Figure 6 shows a comparison of nondimensionalized data of Dhir and Purohit to the results of our analysis. The data are for the minimum film boiling condition; consequently, some liquid-solid contact could be occurring, which is not accounted for in our analysis. Also plotted is the average Nusselt number predicted by using a linear vapor velocity profile.

Dhir and Purohit also performed experiments at 0.3 and 0.1 m/s. Those data are not presented because of the possibility that buoyancy effects could have been present in those experiments. Their data for 0.45 m/s comply more closely with the assumptions used in our analysis.

For a given boiling liquid, body size, and liquid velocity, equation (13) indicates that a smaller δ_r corresponds to a larger θ_r. Subcooling of the liquid tends to decrease film thicknesses around the body; thus, the separation angle should show a corresponding increase for higher subcooling. Consequently, the influence of subcooling on the size of the wake can be included in the film boiling analysis.

The photographic evidence of Stevens and Witte, reported in [8, 9], allows some insight into the influence of the flow reversal angle on the formation of a vapor wake. Motion pictures were made at approximately 5000 frames/s of boiling around a 24-mm silver sphere during flow quenching in water. Surface temperatures for these data were not measured directly. Stevens, however, calculated from his experimental data the average heat transfer coefficient as a function of sphere temperature using a lumped capacity assumption. For 60°C and 77°C water in the film boiling regime, the heat transfer coefficients are relatively low, so that the lumped capacity procedure yields a reasonably accurate history of sphere surface temperature.

From Stevens's photographs the angle at which the wake formed was measured frame-by-frame. This yielded a θ_s versus time plot for a quench at a given velocity, where θ_s is the angle where the wake can be visibly seen. Then, the

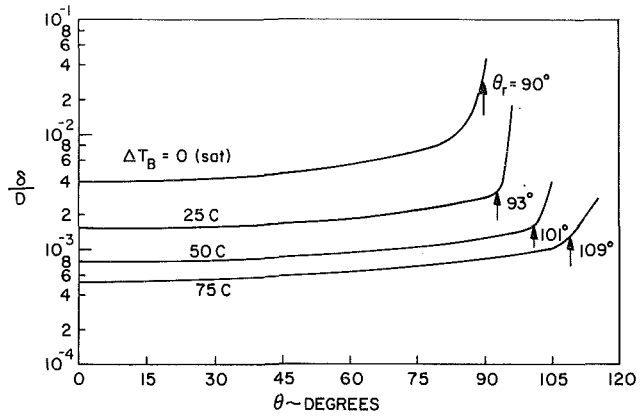

Fig. 5 The effect of liquid subcooling on vapor film thickness for quadratic profiles for 6.35-mm sphere in water: $V = 4.26$ m/s, $T_{sat} = 100°C$, $T_W = 678°C$. θ_r indicates the point of vapor flow reversal.

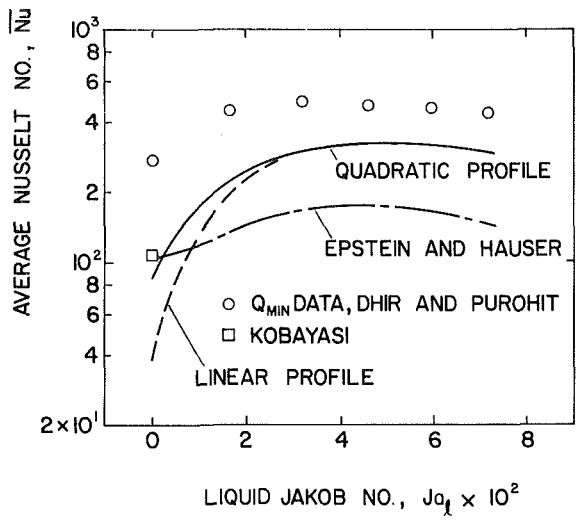

Fig. 6 Comparison of theory to the minimum heat flux data of Dhir and Purohit for water boiling around a 19-mm sphere: $T_{sat} = 100°C$

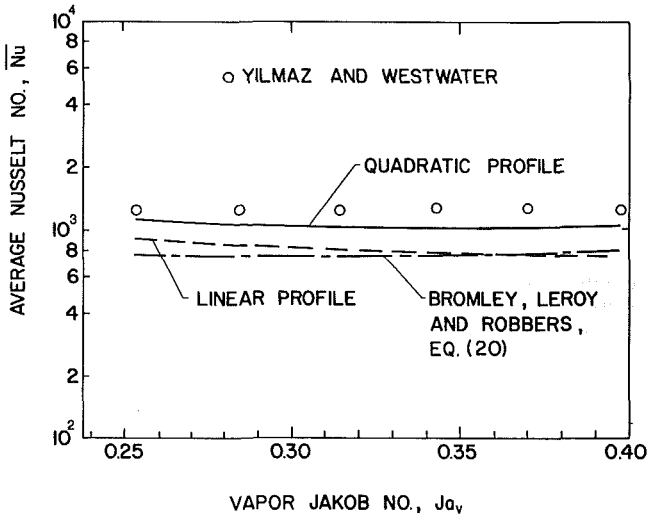

Fig. 7 Comparison of theory to experiment for 6.35-mm-dia cylinder in Freon-113: $V = 2.4$ m/s, $T_B = 45.6°C$

surface temperature histories were calculated, thus allowing a plot of θ_s versus T_w to be made. Figure 3 shows a comparison of the best-estimate measurements of θ_s histories for two such cases. The $T_B = 60°C$ curve is a composite of values from four sets of motion pictures taken during various parts of the quench, while the $T_B = 77°C$ curve is based on three sets. Both curves are for a velocity of 1.52 m/s. The curve for 77°C water covers a quench time of 0.426 s while the 60°C curve covers a time of 0.480 s. The sphere temperature falls much less for 77°C water than for 60°C water, because the heat transfer coefficient is much less for 77°C water.

Some uncertainty exists in the determination of θ_s because of the tendency of the wake to form asymmetrically on the rear of the sphere, as shown in the inset on Fig. 3. It is estimated that possible variations of ±2.5 deg are involved in the measurements of Fig. 3.

The θ_s for 60°C water is greater than that for 77°C water at any given T_w. This is indicative of thinner film thicknesses for the more highly subcooled case. This trend agrees with equation (13) for θ_r. Also, θ_s increases as the quench proceeds (as T_w decreases). The film thickness is decreasing as the quench proceeds, so that equation (13) would correctly predict this observed trend as well.

A comparison of θ_r to θ_s in Fig. 3 shows that the predicted point of vapor flow reversal and the observed point of wake formation show the same trends as dictated by equation (13), although the observed θ_s is 15 to 20 deg larger than θ_r. It appears that θ_r is a precursor of the formation of an observable vapor wake on the rear of the sphere. This effect is discussed further in the next section.

Film Thickness

The integration of equation (10) for the film thickness was carried out for a few specific cases to show the influence of various parameters. A fourth-order Runge-Kutta technique was employed, with the initial thickness being established by the condition $d\delta/d\theta = 0$ at $\theta = 0$.

The film thickness over the forward portion of the sphere based on the quadratic profile – equation (5) – which is obtained by the solution of equation (10), is much smaller than that obtained using a linear profile. This effect is shown in Fig. 4 for flow boiling of saturated water and implies that the quadratic vapor layer allows more vapor flow through it, allowing a smaller thickness, over the forward portion of the sphere.

Figure 5 shows the effect of subcooling on the film thickness based on quadratic vapor velocity profiles – specifically, a thinning of the vapor film as the water temperature is decreased. Figure 5 illustrates that following the point where vapor flow reversal occurs, the vapor film does indeed grow rapidly in thickness. The curves in Fig. 5 are carried a few degrees past the point of vapor flow reversal. A rapid increase of the predicted vapor film thickness occurs just past θ_r.

Strictly speaking, the hydrodynamic assumptions used in a thin film boundary layer analysis begin to lose their validity in the region where the film thickness grows rapidly. On the other hand, the behavior of the vapor film is dominated by heat transfer and evaporation effects so that the violation of some of the assumptions regarding hydrodynamic behavior should not destroy the applicability of the heat transfer results. As long as δ remains considerably smaller than the body radius *and* as long as the δ variation with angle does not violate physical reality, this type of heat transfer analysis should be applicable.

For certain combinations of liquid velocity and subcooling, the solution equation (10) past θ_r shows oscillations of δ, and even predicts that δ would decrease over certain angular regions past θ_r. Observations of flow film boiling from spheres [9] indicate that this is physically unrealistic behavior. Because of this, the applicability of our analysis is restricted to the region $0 \le \theta \le \theta_r$.

Similar calculations were made for the cylindrical

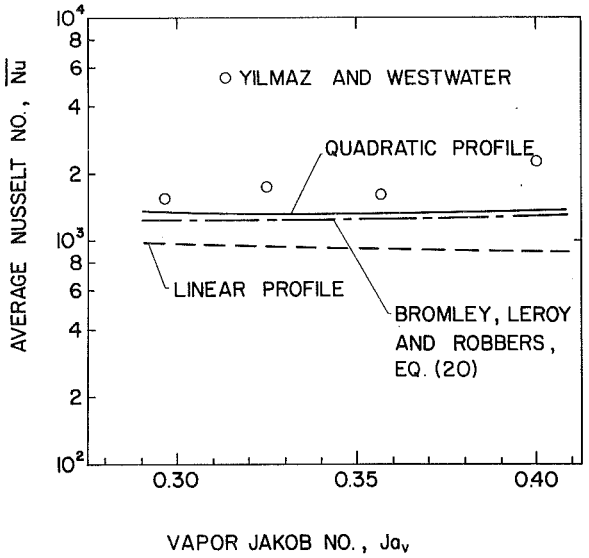

Fig. 8 Comparison of theory to experiment for 6.35-mm-dia cylinder in Freon-113: $V = 6.8$ m/s, $T_B = 45.6°C$

geometry, but are not presented for the sake of brevity. Reference [4] contains plots similar to Figs. 4 and 5 for subcooled flow boiling around cylinders.

The prediction of Kobayasi for saturated boiling [2], as corrected by Hesson and Witte [14], is shown on Fig. 6. Epstein and Hauser's [3] theoretical result is also plotted. Their result is based on a uniform film thickness around the sphere – the film thickness being the value predicted near the forward stagnation point. They assume that separation occurs at $\theta = \pi/2$. At saturation, Kobayasi's and Epstein and Hauser's predictions are virtually identical and compare with the saturated data of Dhir and Purohit slightly better than our result based on a quadratic vapor velocity profile. However, as subcooling is imposed on the liquid, our results using the quadratic profile provide a much better prediction of heat transfer than Epstein and Hauser's results. At 50°C of subcooling, our quadratic profile result is only 30 percent lower than Dhir's data, whereas Epstein and Hauser's result is 67.5 percent lower than the data.

As subcooling increases, the last term (due to subcooling) begins to dominate the right side of equation (10). Thus the energy used to form vapor becomes a smaller fraction of the total energy transferred from the sphere. The hydrodynamics of the vapor flow takes on lesser importance as the liquid bulk temperature is decreased. Consequently, the difference between the heat transfer results for linear and quadratic vapor velocity profiles tends to disappear as subcooling increases. Figure 6 shows that the two curves are virtually identical for ΔT_B greater than about 15°C, $Ja_l \simeq 2.5 \times 10^{-2}$.

Cylinders. Figures 7 and 8 are a comparison of the results of this analysis to the recent measurements of Yilmaz and Westwater [15] for film boiling from cylinders in crossflowing Freon-113. Heat transfer results based on the quadratic profile clearly predict the data better than that based on the linear profile.

Bromley, LeRoy, and Robbers [16] performed an approximate analysis of flow film boiling of saturated liquids around horizontal cylinders. Their analysis provided dimensionless groups upon which a correlation of experimental data could be based. Their correlation for heat transfer is

$$q'' = 2.7\left\{\frac{Vk_v\rho_v h'_{fg}\Delta T_{sat}}{D}\right\}^{1/2} \tag{19}$$

or in dimensionless terms

$$\overline{Nu} = 2.7\{Pe/Ja\}_v^{1/2} \tag{20}$$

where the constant 2.7 was selected to fit data for benzene, ethyl alcohol, n-hexane, and carbon tetrachloride boiling from graphite tubes of the range 0.983 cm $\leq D \leq$ 1.621 cm at velocities up to 4.25 m/s. Equation (20) is plotted on Figs. 7 and 8 for comparison to the results of this analysis and to Yilmaz and Westwater's data.

For the lower velocity, 2.4 m/s in Fig. 7, the present analysis predicts the data of Yilmaz much better than the Bromley et al. equation. At the higher velocity, the results of Bromley's theory and the present analysis tend toward each other especially at higher wall temperatures, although both are about 20 percent too low in their predictions.

Concluding Remarks

The theory for flow film boiling from submerged bodies that accounts for the nonlinearity of the vapor velocity profile gives vapor film thicknesses that are considerably thinner than the results for a linear velocity profile for saturated and slightly subcooled liquids. For moderate to high subcoolings, the heat transfer results for the linear and quadratic profiles are virtually identical. However, the use of the quadratic profile yields a prediction of the point of vapor flow reversal on the rear of the sphere, whereas the use of a linear profile does not.

A comparison of the predicted angles of vapor reversal, θ_r, to angles at which a wake becomes visible, θ_s, during flow film boiling from a sphere indicates that the point of vapor film reversal is a precursor to the point of wake formation. This conclusion is based on the fact that both θ_s and θ_r behave qualitatively in accordance with the condition for vapor flow reversal, equation (13).

The results of this analysis using a quadratic vapor velocity profile, although somewhat lower than the results of previous analyses at saturation for spheres, provide a far better prediction of heat transfer over the entire range of subcooling than the results of previous analyses. Still, the results are lower than experimental data, indicating that there are effects in flow film boiling that are not being included. Certainly, there is some heat transfer in the wake region that is being neglected. If this heat transfer could be adequately calculated, the theory would be brought closer to experimental data.

The reason that the analysis predicts heat transfer better for cylinders than for spheres may be attributable to the geometry. The analysis applied to spheres predicts vapor flow reversal angles smaller than observed wake formation angles; the same trend would be expected for cylinders. The percentage of area that is affected by this underprediction of the wake formation angle is larger for a sphere than it is for a cylinder. Thus, the neglect of heat tranfer in the wake behind a sphere is greater on a percentage basis than for a cylinder.

Acknowledgments

The authors appreciate the support of NSF Grant MEA 8008036 during this study.

References

1 Witte, L. C., "Film Boiling From a Sphere," *I. and E.C.-Fundamentals*, Vol. 7, No. 3, Aug. 1968, p. 517.

2 Kobayasi, K., "Film Boiling Heat Transfer Around a Sphere in Forced Convection," *Journal of Nuclear Science and Technology*, Vol. 2, No. 2, 1965, pp. 62–67.

3 Epstein, M., and Hauser, G., "Subcooled Forced Convection Film Boiling in the Forward Stagnation Region of a Sphere or Cylinder," *International Journal of Heat and Mass Transfer*, Vol. 23, 1980, pp. 179–189.

4 Witte, L. C., and Orozco, J., "The Effect of Vapor Velocity on Film Boiling From Cylinders," ASME Paper 82-HT-28, presented at the

ASME/AIAA Joint Thermophysics, Heat Transfer, and Fluid Mechanics Conference, St. Louis, Mo., June 1982.

5 Sparrow, E. M., and Cess, R. D., "Film Boiling in a Forced Convection Boundary Layer Flow," ASME JOURNAL OF HEAT TRANSFER, Aug. 1961, pp. 370-376.

6 Schlicting, H., *Boundary Layer Theory*, 4th ed., McGraw-Hill, New York, 1960, p. 20.

7 Sideman, S., "The Equivalence of the Penetration Theory and Potential Flow Theories," *I. and E.C.*, Vol. 58, No. 2, 1966, pp. 54-68.

8 Stevens, J. W., and Witte, L. C., "Destabilization of Vapor Film Boiling Around Spheres," *International Journal of Heat and Mass Transfer*, Vol. 16, 1973, pp. 669-678.

9 Stevens, J. W., "Transient Film and Transition Boiling from a Sphere," Ph.D. dissertation, University of Houston, 1972.

10 Walford, F. J., "Transient Heat Transfer From a Hot Nickel Sphere Moving Through Water," *International Journal of Heat and Mass Transfer*, Vol. 12, 1969, pp. 1621-1625.

11 Jacobson, R. N., and Shair, F. M., "Film Boiling From a Sphere During Forced Convection of Subcooled Water," *I. and E.C.-Fundamentals*, Vol. 9, 1970, p. 183-185.

12 Dhir, V. K., and Purohit, G. P., "Subcooled Film-Boiling Heat Transfer From Spheres," *Nucl. Engi. and Des.*, Vol. 47, 1978, pp. 49-66.

13 Ungar, E. K., "Construction and Initial Testing of an Apparatus for Studying Flow Boiling From a Heated Sphere," MS thesis, University of Kentucky, 1981.

14 Hesson, J. C., and Witte, L. C., "Comment on 'Film Boiling Heat Transfer From a Sphere in Forced Convection' by Kobayasi," *Journal of Nuclear Science and Technology*, Vol. 3, No. 10, 1966, pp. 448-449.

15 Yilmaz, S., and J. W. Westwater, "Effect of Velocity on Heat Transfer to Boiling Freon-113," ASME JOURNAL OF HEAT TRANSFER, Vol. 102, No. 1, Feb., 1980, pp. 26-32.

16 Bromley, L. A., LeRoy, N. R., and Robbers, J. A., "Heat Transfer in Forced Convection Film Boiling," *I. and E.C.*, Vol. 45, No. 12, 1953, pp. 2639-2646.

P. Saha
Department of Nuclear Energy,
Brookhaven National Laboratory,
Upton, N.Y. 11973
Mem. ASME

N. Abuaf
Research and Development Center,
General Electric Co.,
Schenectady, N.Y. 12301
Mem. ASME

B. J. C. Wu
Lawrence Livermore National Laboratory,
Livermore, Calif. 94550,

A Nonequilibrium Vapor Generation Model for Flashing Flows

A nonequilibrium vapor generation model for flashing flows is presented. The model consists of a flashing inception point, a bubbly flow regime followed by a bubbly-slug regime, an annular or annular-mist regime, and finally a dispersed-droplet regime. Existence of superheated liquid at the inception point and beyond is recognized. The vapor generation rate is calculated from the flow-regime dependent interfacial area density and net interfacial heat flux. However, the bubble number density at the flashing inception point was varied to obtain optimum fits with the void fraction data taken in a vertical converging-diverging nozzle. The interfacial area density at the inception point, thus determined, showed a rapid increase with the decrease in the liquid superheat at that point. This trend is plausible, since in the limit of thermal equilibrium flow where the liquid superheat approaches zero, the interfacial area for heat and mass transfer should be very large.

Introduction

Flashing of liquid to a two-phase mixture through pipes and nozzles is an important phenomenon in the area of nuclear reactor safety, energy conversion, and space propulsion, among others. The analysis of such flows becomes difficult, particularly for short pipes and nozzles, because of the nonequilibrium aspect of phase change [1].

Flashing in commercial pipes is most likely initiated by heterogeneous nucleation of vapor bubbles in the bulk liquid and/or at crevices or microcavities along the wall with preexisting gas phase. Following Oswatitsch's treatment of condensation in supersonic nozzles [2], Zuber et al. [3] proposed a model which led to an expression for the calculation of the mass flow rate of vapor, G_g, over a cross section located at a point, Z, along a duct of constant cross section, A

$$G_g(Z) = \frac{1}{A}\int_{Z_o}^{Z} \xi_h m(Z,\zeta) J(\zeta) d\zeta \tag{1}$$

where ξ_h is the perimeter of the duct, $J(\zeta)$ is the nucleation rate per unit wall area at point ζ along the pipe, $m(Z,\zeta)$ is the mass at Z of a vapor bubble nucleated at ζ, and Z_o is a point upstream from the nucleation zone. The integration effectively sums the vapor mass of all the bubbles nucleated before point Z. Although Oswatitsch's model has been applied to the study of condensation in high-speed flows with remarkable success [4], its extension to flashing flow has been difficult, mainly because of the lack of understanding of the heterogeneous nucleation process, and of the nucleation rates (J) for flashing flows.

Rohatgi and Reshotko [5] carried out such a calculation for flashing flow of liquid nitrogen and compared their results with the experimental data of Simoneau [6]. There were two unknown parameters in their heterogeneous nucleation equations, one being the number of effective nucleation sites per unit area, and the other being the contact angle between liquid nitrogen and the surface of the heterogeneity. They determined these unknown parameters by "best-fits" to the experimental data, but they did not apply the analysis to any steam-water data.

To circumvent the above difficulty, Wu et al. [7] treated the nucleation and bubble growth separately and proposed a conduction controlled vapor generation model, which was first applied to the experimental data of Reocreux [8]. The local vapor generation rate was assumed to depend primarily on the following three quantities:

(*a*) The onset of flashing or inception point, Z_{NVG}
(*b*) The initial void fraction, α_0, at the point of inception
(*c*) A quantity, C_Γ, which is related to the number of bubbles generated at the inception point

The values of these three parameters were determined independently by the "best-fit" to the void fraction data [7]. In reality, they are all related to one another. For example, if the liquid superheat at the inception point is specified, both the flashing onset location, Z_{NVG} and the critical bubble radius at the onset location can be determined. The value of the initial void fraction, α_0, is then uniquely related to the bubble number density at the inception point.

Semi-empirical correlations [9 and 10] are now available for determining the liquid superheat at the flashing inception point. This paper will, therefore, concentrate on discussing a mechanistic nonequilibrium vapor generation model applicable for the flashing two-phase flows. The model requires a priori knowledge of the liquid superheat at the flashing inception point and uses the bubble number density at the inception point as a "free" parameter. This parameter is then evaluated from the flashing experiment conducted in a vertical converging-diverging nozzle [11].

Present Model

The heat transfer dominated vapor generation rate per unit volume following flashing inception can be given by

$$\Gamma_v = a_i \dot{q}_i''/L \tag{2}$$

where a_i is the total liquid-vapor interfacial area per unit volume of the mixture, $\dot{q}_i''$ is the net heat flux to the interface, and L is the latent heat of vaporization. Both a_i and $\dot{q}_i''$ are flow-regime-dependent, and are functions of the thermodynamic state and flow variables. Therefore, to calculate a_i and $\dot{q}_i''$, it is necessary to know a priori in which flow regime the system is expected to be. In this model, a simple flow regime map for vertical pipe flows is assumed where the flow regime is a function of the local void fraction only.[1] Thus, a

Contributed by the Heat Transfer Division for publication in the JOURNAL OF HEAT TRANSFER. Manuscript received by the Heat Transfer Division June 7, 1982.

[1] A more elaborate flow regime map may be used in the future if deemed necessary.

bubbly flow, a bubbly-slug, an annular and/or annular-mist regime, and finally a dispersed droplet flow are assumed to occur at successively higher void fraction ranges. The void fractions at the transition points are assumed to be

$$\alpha_{b,\max}=0.3, \quad \alpha_{s,\max}=0.8, \quad \alpha_d=0.95$$

The selected flow regime was based on the observation in straight pipes with constant cross-sectional area and is in-line with the flow regime maps being used in the advanced water reactor safety codes such as TRAC and RELAP5 [12. 13]. It is also either similar to, or more sophisticated than, the flow regime maps used in the relatively recent analyses of critical flows [14, 15, 16].

In the present paper, only the flow with void fraction less than 0.8 will be considered. Therefore, the interfacial area densities and the interfacial heat transfer coefficients applicable for bubbly and bubbly-slug flow regimes are discussed in the following section.

Bubble Nucleation Zone, $0 < \alpha < \alpha_o$. The bubble nucleation zone is the point of flashing inception, and it serves as the starting point of the vapor generation calculation. It is assumed that a certain number of bubbles are nucleated in this "narrow" zone and the net vapor generation at a location downstream will be dominated by the bubbles nucleated in this zone. This assumption is supported by the work of Jones and Zuber [17], who found that the rate of bubble volume growth is a strong function of growth time. Therefore, the contributions of the bubbles nucleated downstream of the bubble nucleation zone or the flashing inception point are neglected in this study. This is similar to the assumption used by many of the earlier researchers (e.g., Edwards [18]).

The location of flashing inception may be determined either from the flashing inception correlations [9 and 10] or from experimental observation. At the inception point, the vapor is assumed to be in the form of critical sized bubbles, with radius R_{cr}

$$R_{cr}=2\sigma/(p_{sat}(T_l)-p) \tag{3}$$

The critical radius is of the order of a few microns for typical liquid superheat (or pressure undershoot) values found experimentally at flashing inception. At these sizes the bubbles can certainly be considered to be spherical and to move with the liquid without slip. Thus, the following expressions can be written to start the calculation for vapor generation

$$\alpha_o=\frac{4\pi}{3}R_{cr}^3N_{b,o} \tag{4}$$

$$a_{i,o}=3\alpha_o/R_{cr} \tag{5}$$

$$X_o\cong\alpha_o\rho_g/\rho_l \tag{6}$$

where X_o is the initial quality and $N_{b,o}$ is the number of bubbles per unit mixture volume at the inception point which may be related to the packing density [9] through the flow geometry.

Bubbly Flow. For $\alpha_o < \alpha < \alpha_{b,\max}$, the flow is assumed to be in the bubble regime. The vapor exists in the form of bubbles of uniform size, although not necessarily spherical. However, an equivalent sphere radius, ω, can be defined such that the bubble volume is written as

$$V=4\pi\omega^3/3 \tag{7}$$

In general, the bubbles will move faster than the surrounding liquid. Because of the complexity of implementing a general form of the bubble rise velocity as prescribed by Wallis [19], a simplified form of the vapor drift velocity is adopted here

$$v_{gj}=1.41\left[\frac{g\sigma(\rho_l-\rho_g)}{\rho_l^2}\right]^{1/4} \tag{8}$$

if $\omega > 0.5\sqrt{\sigma/(\rho_l g)}$. For $\omega < 0.5\sqrt{\sigma/(\rho_l g)}$, a linear interpolation between zero and the above value is used. The relative velocity between the bubbles and the surrounding liquid is then calculated from

$$v_{gl}=v_{gj}/(1-\alpha) \tag{9}$$

It is recognized that a two-fluid model would probably be superior to the above drift-flux model for calculating relative velocity in an accelerating and/or decelerating flow. The drift-flux model has been used in this paper only as a first approach, which may be revised in the future.

For the interfacial heat transfer coefficient, it has been found [20] that even for bubble growth during a variable liquid superheat condition, the Plesset-Zwick [21] or Forster-Zuber [22] type of heat transfer coefficient may be used for short time. However, for a bubbly flow with relative velocity, these expressions should be modified in such a way that the convective heat transfer due to the relative velocity is also accounted for. The general expression should satisfy the limiting behavior of the heat transfer process at both $t \to 0$ and $t \to \infty$, where t is the time from bubble nucleation. At the inception point, the transient conduction dominates the heat transfer process so that the general expression should approach the Plesset-Zwick of Forster-Zuber expression at $t \to 0$. However, as the bubbles "age," the convective heat transfer due to the relative velocity between the bubbles and

Nomenclature

A = cross-sectional area, m^2
a = thermal diffusivity, m^2/s
a_i = interfacial area density, m^2/m^3
c = vapor mass concentration or static quality
c_p = specific heat at constant pressure, J/kg K
D = pipe or channel diameter, m
G = mass flux, kg/m^2s
G_g = vapor mass flux, kg/m^2s
g = acceleration due to gravity, m/s^2
h = specific enthalpy, J/kg; heat transfer coefficient, W/m^2K
J = nucleation rate, $1/m^2s$
k = thermal conductivity, W/mK
L = latent heat of vaporization, J/kg
N_b = bubble number density, $1/m^3$
p = pressure, N/m^2
$\dot{q}_i''$ = interfacial heat flux, W/m^2
R_{cr} = critical bubble radius, m
T = temperature, K
t = time, s
V = volume, m^3
v = velocity, m/s
v_{gl} = relative velocity between vapor and liquid, m/s
v_{gj} = vapor drift velocity, m/s
X = flow quality
Z = axial coordinate, m
α = void fraction
Γ_v = volumetric rate of vapor mass generation, kg/m^3s
ξ_h = perimeter, m
ρ = density, kg/m^3
σ = surface tension, N/m
ω = equivalent sphere radius, m

Subscripts

b = bubble or bubbly flow regime
d = droplet
g = saturated vapor
i = vapor-liquid interface
l = liquid
m = mixture
o = flashing inception point
s = bubbly-slug flow regime
sat = saturation
ss = steady-state
T = throat, Taylor or large bubble
v = vapor

liquid starts to dominate, as shown by Wolfert [23]. Therefore, at $t \to \infty$, the general expression should yield the steady-state convective heat transfer coefficient to the bubbles.

Two simple expressions are found in the literature which provide a smooth transition from the Plesset-Zwick expression at $t \to 0$ to the steady-state heat transfer coefficient at $t \to \infty$. These are

$$h_l = \frac{\sqrt{3}k_l}{\sqrt{\pi a_l t}}\left[1 + \frac{2}{3}\frac{v_{gl}t}{\omega}\right]^{1/2} \tag{10}$$

and

$$h_l = \frac{\sqrt{3}k_l}{\sqrt{\pi a_l t}}\left[1 + \sqrt{\frac{2}{3}\frac{v_{gl}t}{\omega}}\right] \tag{11}$$

The first is due to Aleksandrov et al. [24] as modified by Saha [20] and the second to Wolfert [23]. Since both of these expressions were based on intuitive physical arguments, it is not clear which one is more realistic. Note, however, that Wolfert's expression always yields a greater value for h_l. For the present calculations, the modified Aleksandrov expression (Equation (10)) is used.

The interfacial area density is calculated from the following expression

$$a_{i,b} = 3\,\alpha/\omega \tag{12}$$

regardless of whether the bubbles are spheres or not. However, a method of calculating the variation of equivalent bubble radius, ω, and the void fraction, α, is required.

In the bubble flow regime, it is assumed that no bubble coalescence or disintegration takes place. Thus, the bubble radius changes only as a result of vaporization or condensation at the interface

$$\frac{d\omega}{dt} = \frac{\dot{q}_i''}{L\rho_g} = \frac{h_l(T_l - T_{\text{sat}})}{L\rho_g} \tag{13}$$

This equation is equivalent to equation (2) written on the basis of unit interfacial area rather than unit volume. Also, the vapor phase is assumed to be at saturation.

To calculate the void fraction, α, an equation for the conservation of bubble number for the bubbly flow regime was utilized. For steady-state, this equation results in the following simple expression

$$N_b v_g A = \text{constant} = (N_b v_g A)_o \tag{14}$$

The bubble density, N_b, can now be calculated at any cross section, and the void fraction can then be calculated from

$$\alpha = \frac{4}{3}\pi\omega^3 N_b \tag{15}$$

The liquid superheat is calculated from the mixture energy equation by assuming the vapor phase to be at saturation, and the flow to be adiabatic

$$h_m + \frac{1}{2}\left(\frac{G}{\rho_m}\right)^2 = \text{constant} \tag{16}$$

Note that the effect of relative velocity has been neglected in the foregoing equation. This is valid for the low-quality, high-speed flow considered in the present study.

Bubbly-Slug Flow. As the void fraction increases, bubble coalescence becomes significant. Following Dukler and Taitel [25], it is assumed here that when $\alpha = \alpha_{b,\max} = 0.3$ some of the bubbles begin to coagulate to form larger bubbles, while the others continue to grow by vaporization according to the rate and mechanism previously discussed. Thus, two classes of bubbles coexist in this flow regime; the larger bubbles formed by coagulation and the smaller original bubbles. As a result of vaporization at the interface, both classes of bubbles

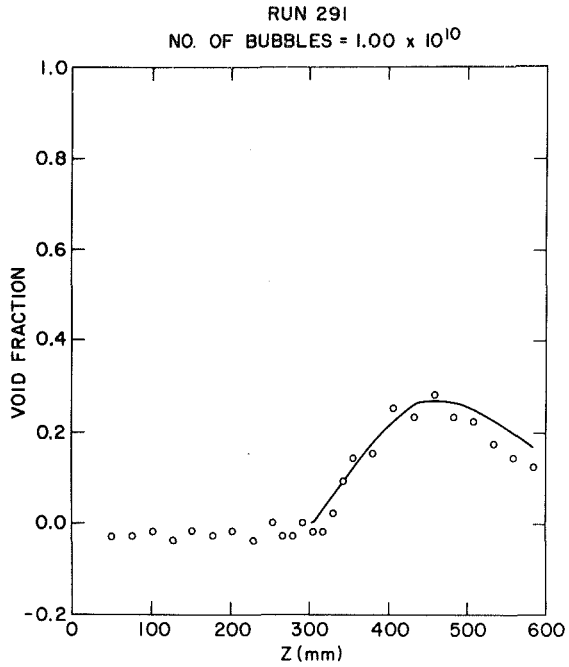

Fig. 1 Comparison between the area-averaged void fraction data (0) for run 291 and the "best-fit" calculation (—) using the present model

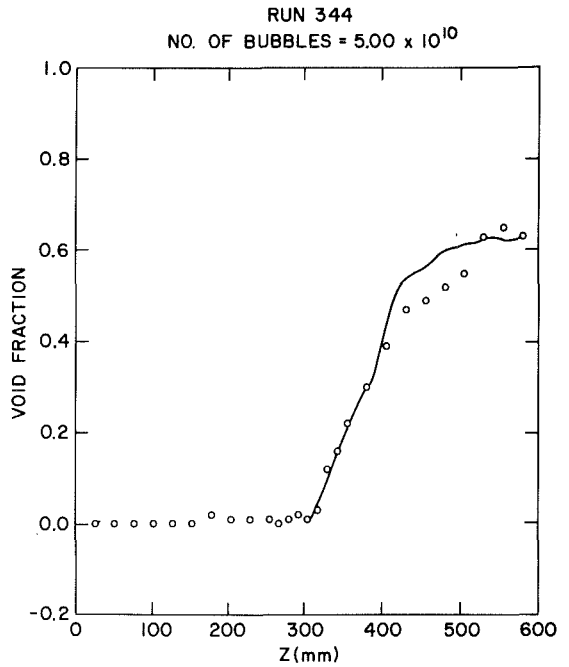

Fig. 2 Comparison between the area-averaged void fraction data (0) for run 344 and the "best-fit" calculation (—) using the present model

grow, although at different rates. A detailed model for this flow regime was developed by the present authors and has been reported in [11] and [26].

One of the basic assumptions in formulating the model was that the bubbles nucleated at the wall would migrate into the center of the channel and coalesce there. This is to be expected for flashing flow in a converging or straight pipe. However, in a diverging nozzle, the bubbles seem to coalesce near the wall and only a few bubbles seem to migrate into the center region [11]. Thus the model for the bubbly-slug flow needs improvement for flashing flow in a diverging nozzle. However, the model for the bubbly flow is valid even for the diverging nozzle (until the bubble coalescence begins) and the same for

Table 1 Summary of test conditions and present model calculations[a]

Run no.	T_{in}(°C)	G_o(kg/m^{2}s)	p_o(bar)	$\Delta T_{l,o}$(°C)	$N_{b,o}$(No./m^3)	R_{cr}(μm)	$a_{i,o}$(m^2/m^3)
353	100.0	18974	0.955	1.65	1×10^{10}	20.3	25.5
358	100.0	25116	0.950	1.80	1×10^{10}	18.7	23.5
362	99.7	28314	0.929	2.13	1×10^{10}	16.3	20.27
145	121.2	15566	1.742	5.31	2×10^{10}	3.48	3.043
133	121.2	18658	1.634	7.28	1×10^{10}	2.63	0.865
137	121.2	24801	1.482	11.82	0.3×10^{10}	1.71	0.11
344	121.3	27935	1.922	2.23	5×10^{10}	7.88	39.0
291	148.9	13336	4.03	5.0	1×10^{10}	1.71	0.367
284	149.2	15061	4.047	5.2	2×10^{10}	1.63	0.557
273	148.7	18048	4.192	3.4	5×10^{10}	2.46	3.79
278	148.7	24119	4.257	2.94	8×10^{10}	2.82	8.04
296	148.8	27148	4.17	3.7	8×10^{10}	2.27	4.52
268	148.9	18091	4.057	4.91	3×10^{10}	1.73	1.13
304	148.9	18133	3.997	5.25	4×10^{10}	1.64	1.35
309	149.1	18217	3.935	6.12	0.5×10^{10}	1.41	0.125

[a]The subscript "o" refers to the flashing inception point

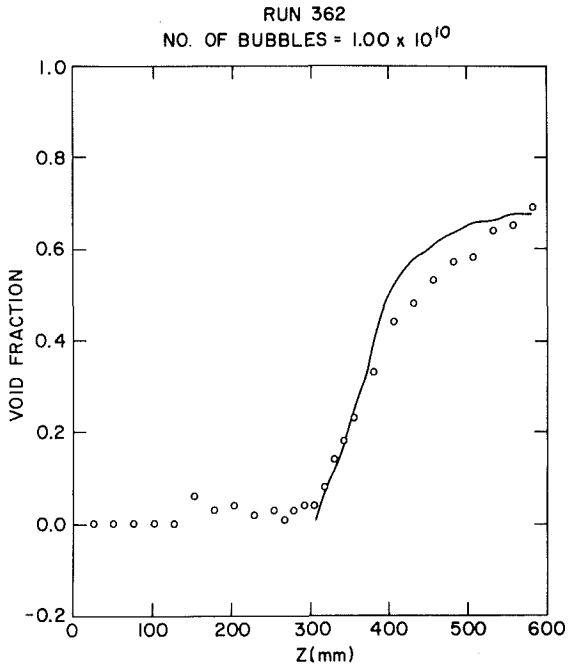

Fig. 3 Comparison between the area-averaged void fraction data (0) for run 362 and the "best-fit" calculation (—) using the present model

the bubbly-slug flow as reported earlier [11, 26] is applicable for straight and converging nozzles.

Comparison With Experimental Data

Ideally, the present model should have been first applied to steady-state flashing experiments conducted in a straight pipe with uniform cross-sectional area. However, no such experiment with detailed void fraction measurements was available. Therefore, the model was applied to steady-state experiments conducted in a vertical converging-diverging nozzle [11] for which detailed void fraction measurements were available. The test section was made of stainless steel with a total length of 0.787 m, including a symmetrical converging-diverging portion of 0.56 m in length. The inside diameters at both ends were 0.051 m and the throat inside diameter was 0.025 m. Initially subcooled water at low pressures (2–8 bar) entered the test section at the bottom and flowed upwards. As the pressure decreased, flashing began near the throat and two-phase mixture flowed through the diverging part of the nozzle. Pressures and area-averaged void fractions were measured along the length of the test section. The accuracy of the pressure measurement was within 1 percent of the reading and that for void fraction was within 0.05. The accuracy for the fluid temperature measurement was within 0.1°C.

A computer program was written for the present model described earlier. Steady-state balance equations for mass and energy were employed. No momentum equation was used; instead, the experimental axial pressure distribution was imposed. Since the maximum void fraction in the experiments simulated was less than 0.8, the models developed for the bubbly and the bubbly-slug regimes were sufficient to cover the range of the data. The following mixture mass and mixture energy equations were used for both of these regimes

$$GA = \text{constant} \tag{17}$$

and

$$h_m + \frac{1}{2}\left(\frac{G}{\rho_m}\right)^2 = \text{constant} \tag{18}$$

Assuming the vapor phase to be at saturation, the specific enthalpy for the liquid phase was calculated from

$$h_l = \frac{h_m - ch_g}{(1-c)} \tag{19}$$

where c is the vapor mass concentration and is defined by $c = \alpha\rho_g/\rho_m$. The liquid superheat was then calculated from

$$T_l - T_{\text{sat}} = \frac{h_l - h_f}{c_{pl}} \tag{20}$$

For the void fraction calculation, equations (13–15) were used for the bubbly flow regime where bubbles were tracked as they grew. However, in the bubbly-slug regime, a more general form of the vapor mass equation was used. The equation employed was

$$G\frac{dX}{dZ} = \Gamma_v = \frac{(h_T a_{i,T} + h_b a_{i,b})(T_l - T_{\text{sat}})}{L} \tag{21}$$

The void fraction was then calculated from

$$\alpha = \frac{X}{[X + (1-X)\rho_g/\rho_l] + \rho_g v_{gj}/G} \tag{22}$$

For a given simulation, the input consisted of

1 The effective geometry of the converging-diverging nozzle [11]

2 The nozzle inlet conditions, i.e., pressure, temperature, and velocity or flow rate

3 The experimental pressure distribution along the length of the nozzle [11]

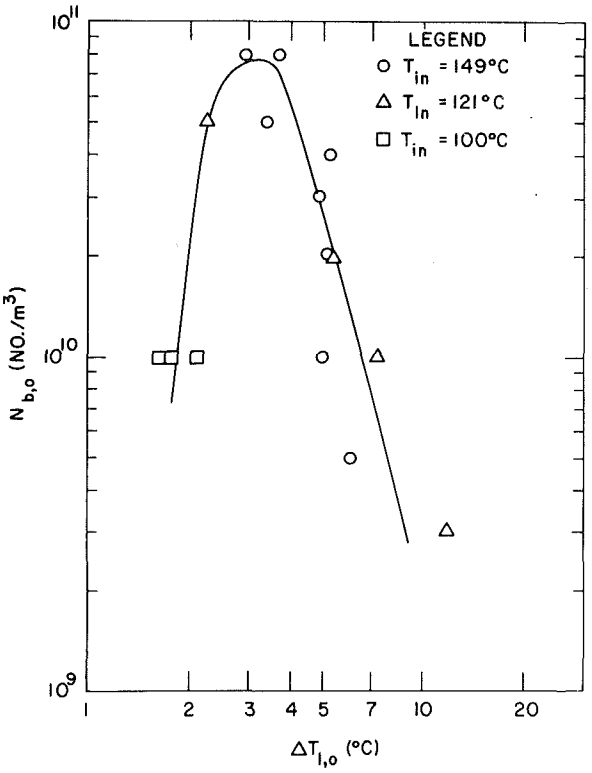

Fig. 4 The optimum bubble number density at the inception point versus the liquid superheat at the inception point

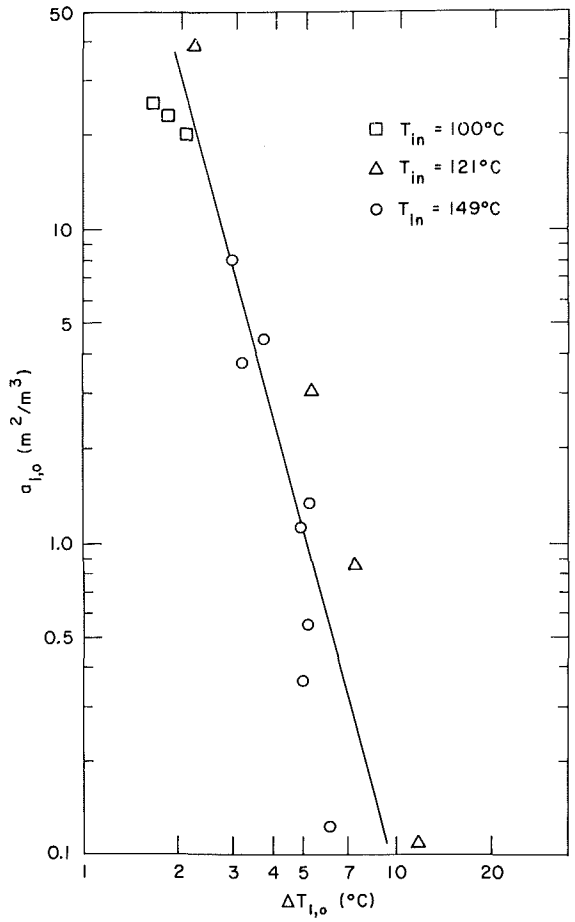

Fig. 5 The interfacial area density at the inception point versus the liquid superheat at the inception point

For all the runs considered here, the flashing inception point was taken to be at the nozzle throat. This is based on the experimental void fraction data as well as the study of Abuaf et al. [11, 27], which showed that the flashing inception point according to the Alamgir-Lienhard correlation [9] was indeed very close to or at the nozzle throat. The critical bubble radius at the throat pressure was calculated by using equation (3) and a bubble number density at the inception point, $N_{b,o}$, was assumed to start the calculation. A marching technique was used to calculate all the variables (except pressure which was input) along the length of the nozzle. Axial steps or mesh sizes were small enough to assure a converged result. The axial void fraction profile calculated by the computer program was then compared with the area-averaged void fraction data. In case of unsatisfactory agreement, the free parameter, $N_{b,o}$, was varied until a "best-fit" between the calculated and the measured void fraction was obtained.

A total of 15 runs were simulated with the present model. Results of the calculation with the "optimum" values of bubble number density at the inception point are presented elsewhere [11, 26]. Three typical comparisons are shown in Figs. 1-3. The agreement in the bubbly flow regime, i.e., $\alpha < 0.3$, is quite reasonable. However, there is still room for improvement in the bubbly-slug regime, i.e., $0.3 < \alpha < 0.8$. As mentioned earlier, an examination of the chordal void fraction measurements [11] at various axial elevations revealed that, in general, there were more voids near the wall than at the center of the diverging section of the nozzle. These imply that for a diverging nozzle, most of the vapor bubbles, nucleated at the wall, can not migrate into the center of the nozzle; instead, they start to coalesce near the wall. An improved model, applicable for the diverging nozzles, must take this into account.

Table 1 provides a summary of the test conditions and the optimum values of the bubble number density at the flashing inception point. No clear relationship between the mass flow rate and the liquid superheat at the flashing inception point can be found. However, when the optimum values for the bubble number density at the inception point, $N_{b,o}$, are plotted against the liquid superheat at the inception point, $\Delta T_{l,o}$, a clear trend can be found as shown in Fig. 4. The optimum number of bubbles at the inception point seems to increase until a liquid superheating of 3°C is reached. Thereafter, the heat transfer rate to the bubble interface is so large that fewer number of bubbles are needed to be nucleated as the liquid superheating at the inception point increases. The phenomenon can be better understood when the interfacial area density at the inception point, i.e., $a_{i,o}$, which is equal to $4\pi R_{cr}^2 N_{b,o}$, is plotted against the liquid superheating at the inception point. This is shown in Fig. 5. It is interesting to note that although the bubble number density decreased as the liquid superheating dropped below 3°C, the interfacial area density continued to increase monotonically as the liquid superheating decreased even below 3°C. This is consistent with the requirement that as the flow approaches a thermal equilibrium flow, i.e., as the liquid superheat becomes smaller, the interfacial area for heat and mass transfer, a_i, must increase to produce more vapor. However, it should also be noted that as $\Delta T_{l,o} \rightarrow 0$, the critical bubble radius, R_{cr} becomes very large in accordance with equation (3), although the pipe or nozzle diameter does impose an upper limit on R_{cr}. Therefore, the bubble number density, $N_{b,o}$, which is equal to $a_{i,o}/(4\pi R_{cr}^2)$, does not have to continue to increase as $\Delta T_{l,o} \rightarrow 0$. This explains the apparent contradiction between Figs. 4 and 5.

Although Fig. 4 may serve as a guidance for the selection of the optimum bubble number density at the inception point once that point is determined, it must be realized that the data

base for Fig. 4 is quite limited. Only one nozzle size was used, and the experiments were conducted only at low pressures and temperatures. Therefore, the data base must be expanded first to develop a general correlation for the bubble number density or the interfacial area density at the inception point.

Summary and Conclusion

1 A model of vapor generation following flashing inception has been proposed including estimates for the interfacial area density, interfacial heat transfer coefficients and relative velocity in the bubbly and bubbly-slug flow regimes covering the void fraction range $0 < \alpha < 0.8$.

2 Comparison of the model predictions with the experimental area-averaged void fraction distributions obtained in a vertical converging-diverging nozzle showed a reasonable agreement in the bubbly flow regime. However, the model for the bubbly-slug regime needs improvement for flows in diverging nozzles.

3 The optimum bubble number density at inception, $N_{b,o}$, determined from the "best-fit" considerations, increased with the liquid superheat at inception, $\Delta T_{l,o}$, until a liquid superheat of 3°C was reached. However, the bubble number density decreased as the liquid superheat increased beyond 3°C.

4 The interfacial area density calculated from the critical bubble radius and the optimum bubble number density at inception increased monotonically with a decreasing liquid superheat. This trend is consistent with the interfacial area requirement for a thermal equilibrium flow.

Acknowledgments

This work was performed at Brookhaven National Laboratory under the auspices of the U.S. Nuclear Regulatory Commission. Special thanks are due to Mrs. Y. Sanborn for her help in developing and running the computer program used in this study, and to Mrs. Ann C. Fort for her help in preparing the manuscript.

References

1 Jones, O. C., Jr., and Saha, P., "Nonequililbrium Aspects of Water Reactor Safety," *Symposium on the Thermal and Hydraulic Aspects of Nuclear Reactor Safety*, Vol. 1, *Light Water Reactors*, edited by O. C. Jones, Jr. and S. G. Bankoff, ASME, New York, 1977, pp. 249–288.

2 Oswatitsch, J., "Kondensationserscheinungen in Ubverschalldusen," *Z. angew. Math. Mech.* Vol. 22, 1942, p. 1.

3 Zuber, N., Staub, F. W., and Bijwaard, G., "Vapor Void Fraction in Subcooled Boiling and in Saturated Boiling Systems," *Proceedings Third International Heat Transfer Conference*, Vol. 5, 1966, p. 24.

4 Wegener, P. P., and Wu, B. J. C., "Gasdynamics and Homogeneous Nucleation," *Nucleation Phenomena*, edited by A. C. Zettlemoyer, Elsevier, New York, 1977, p. 325.

5 Rohatgi, U. S., and Reshotko, E., "Nonequilibrium One-Dimensional Flow in Variable Area Chennels," *Nonequilibrium Two Phase Flow*, edited by R. T. Lahey, Jr. and G. B. Wallis, ASME, New York, 1975, pp. 47–54.

6 Simoneau, R. J., "Pressure Distribution in a Converging-Diverging Nozzle During Two-Phase Choked Flow of Subcooled Nitrogen," NASA TMX-71762, 1975.

7 Wu, B. J. C., Saha, P., Abuaf, N., and Jones, O. C., Jr., "A One-Dimensional Model of Vapor Generation in Steady Flashing Flow," BNL-NUREG-25709, 1979; also, *ANS Transactions*, Vol. 32, 1979, pp. 490–491.

8 Reocruex, M., "Contribution a l'etude des Debits Critiques en Ecoulement Diphasique Eau-Vapeur," PhD thesis, Universite Scientifique et Medicale de Grenoble, France, 1974.

9 Alamgir, Md., and Lienhard, J. H., "Correlation of Pressure Undershoot During Hot-Water Depressurization," *Journal of Heat Transfer*, Vol. 103, February 1981, pp. 52–55.

10 Lackme, C., "Autovaporisation Dans une Conduite d'un Liquide Satre ou Sous-Refroidi a l'Entree," CEA-R-4957, 1979.

11 Abuaf, N., Zimmer, G. A., Wu, B. J. C., and Saha, P., "A Study of Non-equilibrium Flashing of Water in a Converging-Diverging Nozzle," BNL-NUREG-51317, NUREG/CR-1864, June 1981.

12 Safety Code Development Group, "TRAC-PF1: An Advanced Best Estimate Computer Program for Pressurized Water Reactor Analysis," Los Alamos National Laboratory Draft Report, Nov. 1981.

13 Ransom, V. H., et al., "RELAP5/MOD1 Code Manual," NUREG/CR-1826, EGG-2070, Mar. 1982.

14 Ardron, K. H., "A Two-Fluid Model for Critical Vapor-Liquid Flow," *International Journal of Multiphase Flow*, Vol. 4, 1978, pp. 323–337.

15 Rivard, W. C., and Travis, J. R., "A Nonequilibrium Vapor Production Model For Critical Flow," *Nuclear Science and Engineering*, Vol. 74, 1980, pp. 40–48.

16 Richter, H. J., "Separated Two-Phase Flow Model: Application to Critical Two-Phase Flow," EPRI NP-1800, Apr. 1981.

17 Jones, O. C., Jr., and Zuber, N., "Evaporation in Variable Pressure Fields," ASME JOURNAL OF HEAT TRANSFER, Vol. 100, 1978, pp. 453–459.

18 Edwards, A. R., "Conduction Controlled Flashing of a Fluid, and the Prediction of Critical Flow Rates in One-Dimensional System," U. K. Atomic Energy Authority Report, AHSB (SD) R 147, 1968.

19 Wallis, G. B., *One Dimensional Two-Phase Flow*, ch. 9 and 12, McGraw-Hill, N.Y., 1969.

20 Saha, P., "Analytical Modeling: Effect of Pressure Change," *Reactor Safety Research Program*, Quarterly Progress Report for the Period Apr.–June 1977, BNL-NUREG-50683, 1977, pp. 145–155.

21 Plesset, M. S., and Zwick, S. A., "The Growth of Vapor Bubbles in Superheated Liquids," *Journal of Applied Physics*, Vol. 25, No. 4, 1954, pp. 493–500.

22 Forster, H. K., and Zuber, N., "Growth of a Vapor Bubble in a Superheated Liquid," *Journal of Applied Physics*, Vol. 25, No. 4, 1954, pp. 474–478.

23 Wolfert, K., "The Simulation of Blowdown Processes with Consideration of Thermodynamic Nonequilibrium Phenomena," presented at OECD Specialists' Meeting on Transient Two-Phase Flow, Toronto, 1976.

24 Aleksandrov, Y. A., Voronov, G. S., Gorbunkov, V. M., Delone, N. B., and Nechayev, Yu, I., *Bubble Chambers*, Indiana University Press, Bloomington, Ind. 1967, pp. 72–76.

25 Dukler, A. E., and Taitel, Y., "Flow Regime Transitions for Vertical Upward Gas-Liquid Flow: A Preliminary Approach Through Physical Modeling," NUREG-0162, 1977.

26 Saha, P., Abuaf, N., and Wu, B. J. C., "A Nonequilibrium Vapor Generation Model for Flashing Flows," ASME Paper No. 81-HT-84, 1981.

27 Abuaf, N., Jones, O. C., Jr., and Wu, B. J. C., "Critical Flashing Flows in Nozzles with Subcooled Inlet Conditions," BNL-NUREG-27512, 1980.

Application of the Local Assumption for the Design of Compact Heat Exchangers for Boiling Heat Transfer

C. C. Chen

J. W. Westwater
Mem. ASME

Department of Chemical Engineering,
University of Illinois,
Urbana, Ill. 61801

The design technique of interest here is the use of the local assumption, namely, that the local heat transfer coefficient during flow boiling is uniquely fixed by the local metal-to-liquid, ΔT, and the local fluid velocity. The object of this paper is to show the performance of two new compact heat exchangers that are specifically designed for boiling duty by this technique. These exchangers, from different manufacturers, were brazed aluminum, crossflow devices having core sizes of about 8 × 8 × 8 cm. The equivalent diameter of the flow passages on the boiling side, based on the wetted perimeter, was 0.167 cm. Offset fins gave excellent mixing of the boiling fluid, so homogeneous flow was assumed to prevail. Tests were made with Refrigerant-113 (R-113) at atmospheric pressure in these exchangers installed as thermosiphon reboilers. Heat was provided by condensing steam. The measured mass velocity of the R-113 was from 14 to 750 kg/s m^2, the inlet velocity was 0.008 to 0.45 m/s, the calculated homogeneous exit velocity was 0.5 to 20 m/s, the calculated metal-liquid, ΔT, varied from 15 to 120 K, and the heat duty varied from 5.5 to 57 kW. On a volumetric basis, this upper duty is 120,000 kW/m^3, a remarkably high duty for the exchange of heat between two fluids. For both exchangers, the agreement between predicted and measured duties was satisfactory as long as no dryout occurred. When dryout occurred, flow oscillations were observed, and the observed heat duty was as much as 40 percent below the predicted value.

Introduction

Compact heat exchangers have been popular for some years in aircraft and in cryogenic industries to transfer heat between single-phase fluids. Acceptable design methods are available for such applications [1, 2]. The usage of compact heat exchangers has expanded recently [3–15] to include boiling, vaporization, and condensation. The design techniques for these phase-change operations, which cannot be the same as for single-phase flow, are still being developed. Some recent work [14, 15] showed that the performance of a commercial, off-the-shelf compact heat exchanger originally intended for aircraft use could be predicted when used as a condensation/boiling exchanger. The prediction involved a homogeneous flow model coupled with the local assumption. This exchanger was not the optimum for boiling. Definitely the fin height (3.89 mm) was too great, based on previous studies of boiling on fins [16–18]. The object of the present paper is to report on the results of tests made with two additional compact heat exchangers. These were designed by the authors specifically for boiling heat transfer using the technique described. It was intended that they required the lowest wall superheat to reach a particular heat duty, compared to other exchangers. The optimum selection was done by calculating the expected performance for different possible heat exchangers made by standard procedures from standard materials with standard dimensions. It was expected that for the best choices, the heat duty, energy transferred per unit volume, would exceed any value previously published for a two-fluid exchanger; this turned out to be the case.

Experimental

Each compact heat exchanger was installed as a thermosiphon reboiler. The test fluid was R-113 (CCl_2F-$CClF_2$, normal boiling point 47.6°C). Heat was provided by condensing steam which flowed horizontally in a single-pass, crossflow pattern. The test equipment is illustrated in Figs. 1 and 2, which show the R-113 side and the steam side. On the R-113 side, all piping was stainless steel. On the steam side, it was stainless steel up to the heat exchanger. Complete details are available [19].

One new brazed aluminum, plate-type, finned, compact heat exchanger was obtained from the Stewart-Warner Corporation (SW) and another was obtained from the

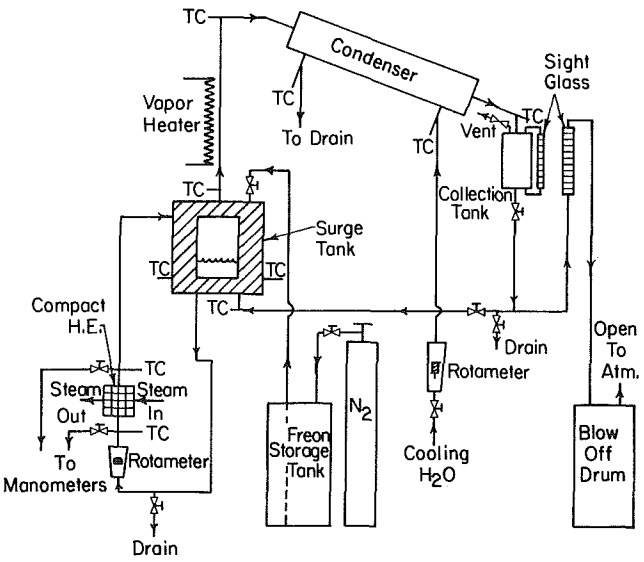

Fig. 1 Sketch of apparatus for the boiling side

Contributed by the Heat Transfer Division for publication in the JOURNAL OF HEAT TRANSFER. Manuscript received by the Heat Transfer Division December 13, 1982.

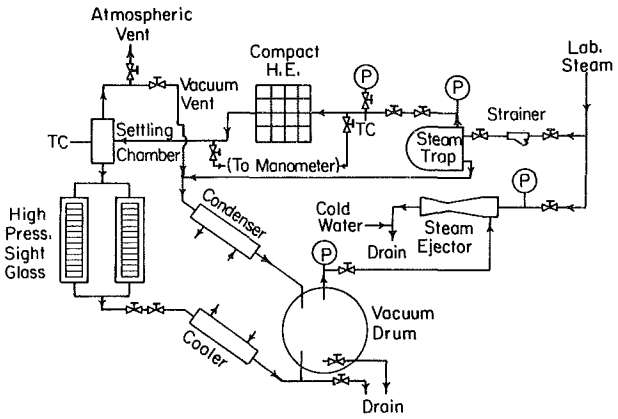

Fig. 2 Sketch of apparatus for condensing steam

LIMCO Manufacturing Corporation (LIMCO). Each was a one-of-a-kind item constructed to our specifications. They were intended to be nearly identical. Their performances turned out to be very similar. Each had a core size of about 8 × 8 × 8 cm, similar to that of the exchanger reported earlier [13–15] that was made by AiResearch Manufacturing Company (AiR). The new exchangers contained 14 boiling and 13 condensation single-stack passages. Figure 3(*a*) shows the offset fins in each passage, and Fig. 3(*b*) shows the crossflow pattern of the two streams. Each boiling side fin was 0.203 mm thick, 2.54 mm high, and 3.175 mm long in the flow direction. The pitch for the new exchangers was 709 and 630 fins/m (18 and 16 fins/in.). The clearance between adjacent fins was about 1.3 mm. These fins were 100 percent thicker and 54 percent shorter than those in the AiR compact heat exchanger. These two changes were predicted to be advantageous. Table 1 lists the fin dimensions, free-flow cross-sectional area, fin area, and total heat transfer area for the boiling side of the three tested heat exchangers.

The boiling loop was charged with about 34 L of R-113 before each run. The thermosiphon action induced different circulating flows from the surge tank to the compact heat exchanger, depending on the steam temperature. The R-113 flow rate was measured with a calibrated rotameter. Vapor formed in the heat exchanger was condensed in a tube-and-shell condenser, metered, and returned to the surge tank. A vent insured that the boiling side was at about atmospheric pressure. The liquid R-113 entered the compact heat ex-

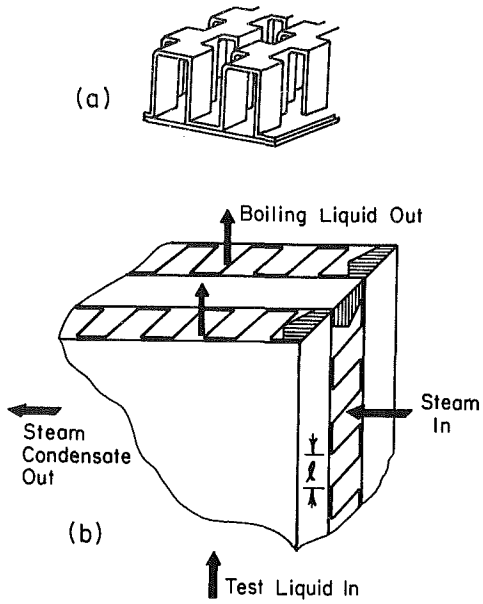

Fig. 3 Sketches of offset (or serrated) fins used in compact heat exchanger and the cross flow pattern of the two streams

Table 1 Comparison of the boiling-side fin dimensions of the three tested heat exchangers

Heat exchangers	AiR	SW	LIMCO
Passages	14 (Double-stack)	14 (Single-stack)	14 (Single-stack)
Fin height (mm)	3.89	2.54	2.54
Fin pitch (mm)	1.59	1.41	1.59
Fin thickness (mm)	0.102	0.203	0.203
Offset (mm)	4.67	3.175	3.175
Equiv. dia (mm)	2.13	1.59	1.74
Free flow cross section (cm^2)	37.8	19.8	20.4
Fin area (cm^2)	4549	3245	2912
Total area (cm^2)	5295	3911	3577

Nomenclature

A = base plate area between two passages, m^2
C_L = heat capacity of liquid, J/(kg•°C)
D = equivalent diameter, $4x$ (cross-sectional area)/(wetted perimeter), m
f = friction factor defined by equation (4), dimensionless
g = gravitational acceleration, m/s^2
G = mass velocity, $kg/(m^2•s)$
h = heat transfer coefficient, $kW/(m^2•°C)$
j = Colburn j-factor defined by equation (5), dimensionless
k = thermal conductivity, W/(m•°C)
l = clearance between two adjacent fins, m
L = flow length on boiling side, m
ΔP = total pressure drop on boiling side, kPa
ΔP_f = two-phase friction pressure drop on boiling side, kPa
ΔP_s = total pressure drop on condensation side, kPa
Q = total heat duty, kW
Re = Reynolds number, dimensionless
T_s = average steam temperature, °C
T_w = base plate temperature, °C
ΔT = average steam temperature minus base plate temperature, °C
ΔT_{sub} = boiling liquid temperature minus inlet R-113 temperature, °C
ΔT_w = base plate temperature minus boiling liquid temperature, °C
v = specific volume, m^3/kg
V = homogeneous velocity, m/s
V_i = liquid velocity at the inlet, m/s
W = induced thermosiphon flow rate, kg/hr
W_c = R-113 condensate rate, kg/hr
x = fluid quality
z = coordinate in the flow direction
λ = latent heat, J/kg
μ = dynamic viscosity, kg/(m•S)
ρ = density, kg/m^3
$\bar{\rho}$ = average density in compact heat exchanger, kg/m^3

Subscripts

e = exit
G = gas phase
L = liquid phase
TP = two-phase

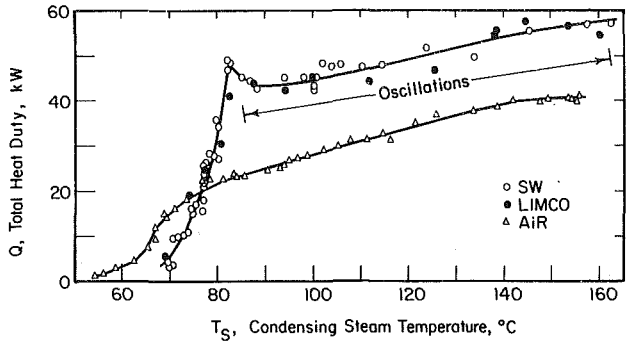

Fig. 4 Comparison of heat transfer results for a compact exchanger having long, thin fins (AiR) versus two exchangers having short, thick fins (SW and LIMCO)

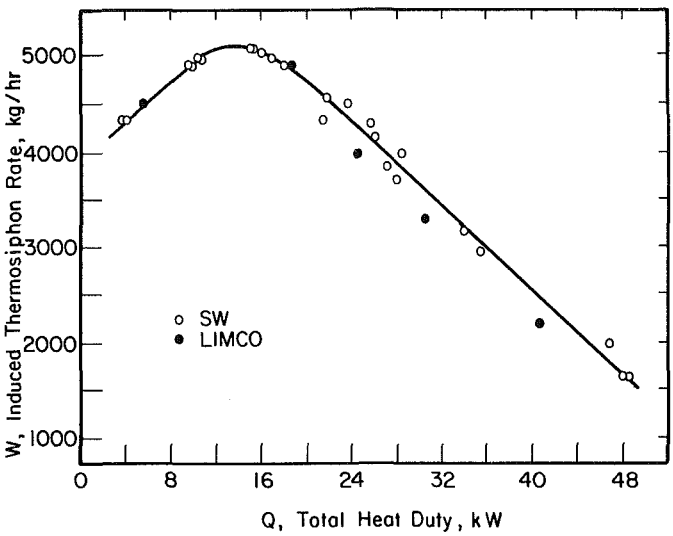

Fig. 5 Dependence of liquid flow rate on the heat transfer rate as a result of the thermosyphon reboiler effect

changer subcooled by about 6°C. The measured mass velocity was from 14 to 750 kg/s m^2, corresponding to inlet velocities from 0.008 to 0.45 m/s. The exit fluid was a two-phase mixture or superheated vapor. The calculated exit homogeneous velocity varied from 0.5 to 20 m/s, ΔT_w was from 18 to 120°C, and the heat duty was from 3.5 to 57.4 kW.

On the condensation side, the steam was condensed and metered. The steam pressure and temperatures, in and out, were monitored. The measurements indicated that the entering steam was saturated or near saturated at absolute pressures between 30 and 730 kPa. A steam ejector was used as shown in Fig. 2 to provide the necessary vacuums for low ΔT_w runs.

The heat duty of the compact heat exchanger was measured three ways: (*i*) from the steam condensate rate, (*ii*) the R-113 condensate rate, and (*iii*) the heat absorbed by the cooling water in the condenser. These three heat duties agreed within 10 percent for nonoscillating runs and within 20 percent for oscillating runs. In this paper, the heat duty based on condensed steam is used as being correct because there was less chance of heat loss along the steam line than from the rest of the system.

Results

Figure 4 shows the performance of the three compact heat exchangers. The two new "optimized" exchangers (SW and LIMCO) performed similarly, as they should. They transferred 48 kW at a steam temperature of 82°C, whereas the old nonoptimum exchanger (AiR) transferrred 23 kW at this same temperature. The AiR exchanger reached its maximum duty,

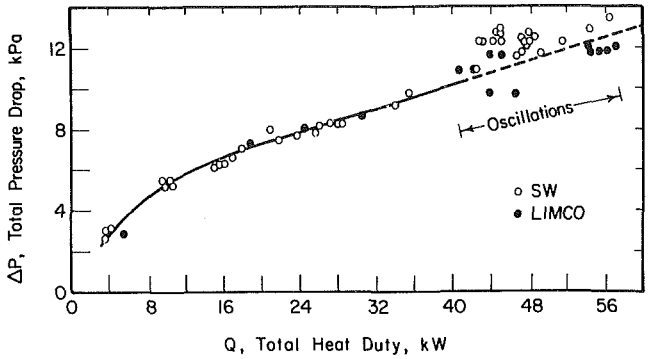

Fig. 6 Total pressure drop across the offset fins in compact heat exchangers

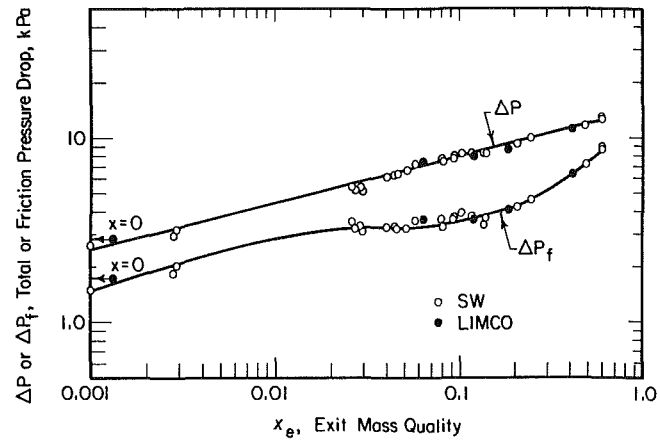

Fig. 7 Total pressure drop and two-phase friction pressure drop as functions of the exit quality

40kW, at a steam temperature of about 150°C. All three cited heat duties are remarkable for exchangers of such small size, 8×8×8 cm. They indicate that heat exchangers of compact design are desirable for industrial applications in which they are unknown. They are attractive only for clean, nonfouling fluids, because the flow passages are small.

The "optimized" exchangers give steep lines for the main branch (nucleate boiling) of their curves in Fig. 4. This is a result of using short fins. This main branch stops abruptly at a steam temperature of 82°C, because oscillations (density-wave oscillations) begin at this point. They persisted for all higher steam temperatures. This second branch of the performance curve, beyond the 82°C temperature, corresponds to but little change in heat duty. The metal wall temperature in this region is hot enough to support transition and some film boiling. The vapor generation became cyclical, pulsing at about 1 to 5 Hz. The amplitude of the pulses reached its maximum at a steam temperature of about 140°C, before film boiling became dominant.

The circulating flow induced by the thermosiphon effect is a balance between the buoyant hydrostatic head and the demands of friction and acceleration. All three forces increase at different rates with fluid quality, and this implies the existence of a maximum in the induced flow rate as the heat duty is increased. Figure 5 shows this characteristic for the optimized exchangers. The maximum flow of 5000 kg/hr (750kg/s m^2) occurred when the heat duty was about 27 percent of the maximum value of 48.6 kW in Fig. 5. Oscillating flows are not included in this graph. A flow versus heat duty curve such as Fig. 5 depends on the hydrostatic head and thus on the amount of liquid in the surge tank. For Fig. 5, the liquid level was 1.2 m above the inlet to the compact heat exchanger. A lower level would give a smaller maximum flow rate and a flatter curve.

Figure 6 shows the total pressure drop across the heat exchanger core on the boiling side. In the region of smooth flow, there was little scatter of data. As dryout began and oscillations appeared, the scatter of data became noticeable.

Figure 7 shows that the pressure drop is a smooth function of exit quality. The quality was calculated by the following equation.

$$x_e = \frac{W_c}{W} - \frac{C_L\ \Delta T_{\text{sub}}}{\lambda} \tag{1}$$

Here W is the measured liquid flow rate entering the compact heat exchanger. W_c is the measured flow rate of R-113 leaving the condenser, and λ is the latent heat of R-113. Equation (2) was used to calculate the two-phase friction pressure drop ΔP_f.

$$\Delta P_f = \Delta P - \bar{\rho} g L - G^2 \Delta v \tag{2}$$

Here $\bar{\rho}$ is the average fluid density in the heat exchanger, Δv is the difference in the inlet and outlet specific volume, and G is the total flow rate divided by the free cross section. The friction pressure drop is graphed also in Fig. 7. This line is neither straight nor parallel to that for the total ΔP. The total ΔP fits a correlating equation with ΔP proportional to $x_e^{0.25}$.

Equations (3) and (4) were used to reduce the friction data to dimensionless forms of friction factor, f, versus two-phase Reynolds number Re_{TP} [20]. The results are shown in Fig. 8.

$$\text{Re}_{TP} = \frac{DG}{\mu_{TP}} \tag{3}$$

$$f = \frac{\Delta P_f}{4(L/D)\,(G^2/2\rho_L)} \tag{4}$$

Here $1/\mu_{TP} = x_e/\mu_G + (1-x_e)/\mu_L$, and D is the equivalent diameter of the finned passages. When the flow was nearly all liquid (x_e = approximately zero and Re_{TP} = approximately 2100) the values of f are rather flat and agree with those in [1] for single-phase flow. At higher Reynolds numbers, the friction factor rises sharply, meaning that two-phase pressure drops are larger than single-phase (liquid phase) pressure drops.

Fluid friction of course occurs on the surface of the fins as well as on the surface of the base plate. The experimental pressure drop used in equation (4) presumably accounts for the total area. In calculating a j-factor for heat transfer, equation (5) is used.

$$j = \frac{(Q/A\Delta T_w)}{G\ C_L} \left(\frac{\mu_L\ C_L}{k_L}\right)^{2/3} \tag{5}$$

A difficulty arises in choosing the heat tranfer area and the ΔT, because the ΔT varies from point to point, particularly on the fins. One procedure is to use the base plate area only and the average ΔT existing there, ΔT_w. If this is done, the curve for j shown in Fig. 8 is the result. If we use instead the fin area plus the base plate area, the new j-factor is given by 0.39 (the proper area ratio) multiplied by the j in Fig. 8. Neither j-factor is exact, because the fin efficiency is not 100 percent and furthermore varies from one row to the next. Thus, even though the f and j curves in Fig. 8 are roughly parallel, the usefulness of the curves is open to question. If one wishes to assume a constant ratio of f to j, that is use the Colburn analogy, caution is needed. Experiments with other liquids are needed to discover whether the rough parallelism of f and j noted in Fig. 8 occurs in general.

Inasmuch as no practical means was available to measure the base plate temperature, T_w, values were estimated by using computed values of the heat transfer coefficient on the steam side, equation (6) and then combining this with the known heat duty, Q, and known area, A, to get the steam film ΔT in equation (7) and finally the desired wall temperature, T_w, by equation (8). An easy trial-and-error procedure is required to find h and ΔT values to satisfy both equation (6) and (7).

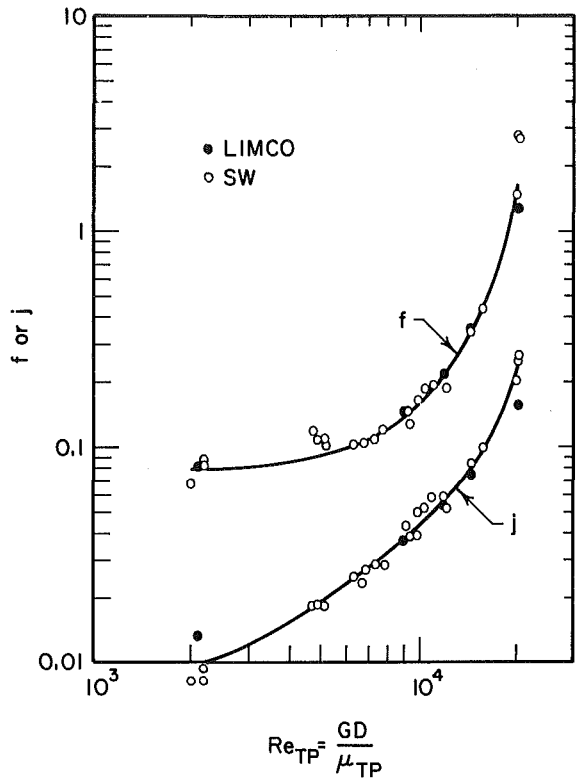

Fig. 8 Dimensionless representation of the friction and heat transfer

$$h = 0.943\left[\frac{k_L^{\,3}\rho_L(\rho_L-\rho_G)g\lambda}{\mu_L\ l\ \Delta T}\right]^{1/4} \tag{6}$$

$$Q = h\ A\ \Delta T \tag{7}$$

$$T_w = T_s - \Delta T \tag{8}$$

The foregoing procedure is fairly good when the steam-film heat transfer coefficient is large compared to the boiling-side heat transfer coefficient, as for most of the present runs. It would be less dependable if the two coefficients were comparable. The steam-film coefficient varied from 32 to 73 kW/m^2 °C, and the boiling R-113 coefficient varied from 1.3 to 15 kW/m^2 °C.

Equation (6) is the Nusselt equation for condensation on a vertical surface [21]. The base plates were vertical, and l is the clearance between fins (see Fig. 3). Equation (6) ignores such complications as steam velocity, possible flooding, and surface tension effects at corners. The contribution to heat transfer of fins on the steam side likewise is ignored here.

The Model

The main features of the model are the local assumption, the stepwise procedure, and the homogeneous flow assumption. These are summarized briefly below; they are discussed in detail elsewhere [15]. Computations are done on a digital computer.

Local Assumption. This is the assumption that the heat transfer coefficient during flow boiling is fixed by the local fluid velocity and the local metal-to-liquid temperature difference. The local h varies from the base of a fin to its tip, because of varying ΔT_w. The local h varies with distance along the line of flow, because of varying velocity. For this paper, the flow-boiling curves of Yilmaz and Westwater [22]

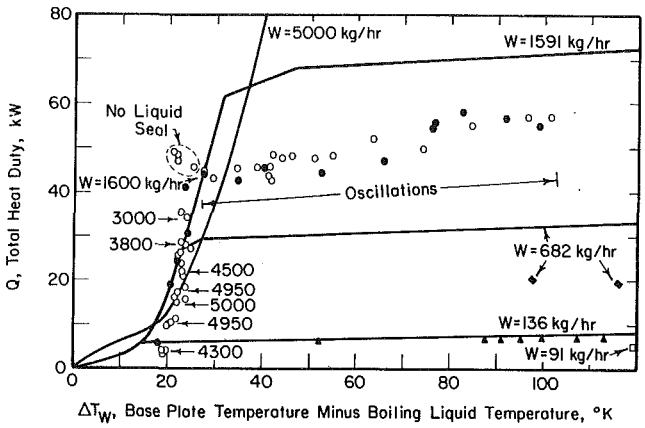

Fig. 9 Comparison of measured and predicted flow-boiling performance

were used. It was assumed that these only existing complete curves for boiling R-113 flowing normal to a 6.5 mm tube are applicable to the finned exchangers used herein [15].

Stepwise Procedure. The fluid quality changes as the fluid travels through the heated passages. This causes the velocity to increase. A stepwise procedure is used to account for this variation. The size of each step was selected to be 3.175 mm; thus 24 steps were used to proceed from the inlet to the exit. Thermodynamic equilibrium is assumed at all positions; thus the local fluid quality can be calculated from heat balance equations.

Homogeneous Flow. The flow is assumed to be homogeneous, that is, the liquid and vapor are intimately mixed and travel at the same velocity. Note that the flow path is not straight nor smooth. The flow is split every 3.175 mm downstream. Well-developed boundary layers cannot build up. Many other flow regimes and models have been proposed for two-component, two-phase flow in straight round tubes [23], but they do not seem applicable for small interrupted passages as used herein. Collier [23] concludes that the homogeneous model is preferred for cases of high mass velocities, whereas the separated-flow model is better for low velocities. For the present study, the flow was as high as 750 kg/s m^2, which is much greater than that of other studies [7, 8]. Yung et al. [11] found that their separated flow model (annular flow) failed when the Reynolds number DG/μ_L exceeded 1000. For the present study, the Reynolds number varied from 800 to 2500 (with no oscillations). The homogeneous model seems suitable here. With it, the velocity is calculated by

$$V = G[xv_G + (1-x)v_L] \tag{9}$$

Figure 9 shows the prediction curves (solid lines) and the actual data points. The predictions curves are constructed for arbitrary flow rates. The actual flow rate was fixed by the thermosiphon action and was not under independent control. Some observed flow rates are indicated. There is satisfactory agreement between predictions and experimental data up to a heat duty of 36 kW. This includes flows from 1591 to 5000 kg/hr and ΔT_w values up to 28°C. The inlet steam velocity at 36 kW was 30 m/s. In fact, for four runs at high heat duties, it was impossible to maintain a liquid seal in the steam condensate line to prevent the escape of uncondensed steam, so the vapor velocity was even greater than 30 m/s. Thus the condensing-steam, h, calculated from equation (7) is probably too low, inasmuch as it was computed for negligible vapor velocity. If h for steam were increased as the velocity increased, the abscissa in Fig. 9 for the data would be shifted in such a way as to improve the match between the data and the lines.

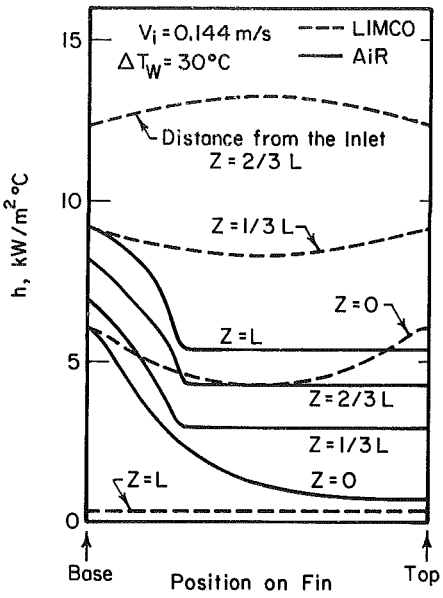

Fig. 10 Variation of local h over the fin surface as fluid travels through AiR and LIMCO heat exchangers

It is interesting to compare the two prediction curves for flow rates of 1591 and 5000 kg/hr in Fig. 9. The larger flow rate gives higher heat duties as expected when ΔT_w is below 17°C and forced convection is dominant. But at ΔT_w values higher than 17°C the additional subcooled liquid which accompanies high flow rate delays the onset of efficient nucleate boiling. Thus the lower flow gives superior performance in the ΔT_w range from 17 to 38°C. At about $\Delta T_w = 38$°C the lower flow liquid has all evaporated, whereas the high flow system still has wetted surfaces.

The regions of oscillations is indicated in Fig. 9. It is believed that during oscillations the heated surface is not wetted continuously. The actual liquid flow rates during oscillations could not be measured accurately with the rotameter. The proposed model is not applicable during oscillatory flow.

A few special runs were made with high ΔT_w and smaller amounts of R-113 in the loop to see whether all film boiling could be achieved. These were carried out by the dry-charge method, that is, the heat exchanger was hot before liquid was introduced. The thermosiphon head was deliberately low, and the flow rates were small. Film boiling was dominant, and no oscillations were observed. The data are evident in Fig. 9 at high ΔT_w and low heat duty. Runs with 91 and 136 kg/hr agree well with prediction. It was possible to add liquid, which increased the head and caused the flow rate to increase. At a flow of 682 kg/hr, the homogeneous model overestimated the local velocities and predicted a too high heat duty. Thus for this one case of low velocity, the separated flow model can be proved to be superior [19].

In this study, the variation of boiling heat transfer coefficient over the fin surfaces is strongly emphasized. Figure 10 shows this variation (calculated values) for fins in the AiR and LIMCO heat exchangers with ΔT_w of 30°C as the fluid travels through the heat exchanger. The inlet velocity is 0.144 m/s, and the inlet liquid is saturated. This inlet velocity corresponds to a mass flow rate of 1591 kg/hr for the LIMCO exchanger. In the AiR heat exchanger, the h over the fin varies by a ratio of 8.5 at the entrance and 1.7 at the exit. With higher ΔT_w, the ratio can go as high as 20.5 [19]. Definitely, the constant-h assumption often used in single-phase heat transfer is unrealistic under these conditions. The "optimized" LIMCO heat exchanger reduces the variation to 1.4 at the inlet because of the shorter and thicker fins. At the exit,

the fluid is all vaporized and the change in h along the fin is trivial. The conventional fin efficiency concept for constant h may be used with caution here to obtain a first approximate design. The local assumption is the best way to handle the complex temperature-dependent boiling heat transfer coefficient for more accurate design purposes.

Conclusions

1 Chemical process industries should consider finned, compact heat exchangers for flow boiling of clean fluids.

2 The local assumption provides a successful design technique, as long as no oscillations occur.

3 Fin dimensions can be optimized, and this leads to higher heat duties.

4 Dimensionless f- and j-factors show promise for flow boiling; these should receive further attention.

Acknowledgments

Financial assistance came from the National Science Foundation. One compact heat exchanger was furnished by the South Wind Division of Stewart-Warner Corporation, Indianapolis, Indiana, and one was furnished by LIMCO Manufacturing Corporation, Glen Cove, New York.

References

1 Kays, W. M., and London, A. L., *Compact Heat Exchangers*, 2d ed., McGraw-Hill, New York, 1964.

2 Shah, R. K., "Compact Heat Exchangers," *Heat Exchangers: Thermal-Hydraulic Fundamentals and Design*, edited by S. Kakac, A. E. Bergles and F. Mayinger, Hemisphere Publishing Co., Washington, D.C., 1981, pp. 111-151.

3 Collier, J. G., Kennedy, T. D. S., and Ward, J. A., "Thermal Design of Plate-Fin Reboilers," *Cryotech 73 Proceedings Use Industrial Gases Processors Conference*, IPC Technol Press, Guildford, England, 1974, pp. 95-100.

4 Shorin, C. N., Sukhov, V. I., Shevyakova, S. A., and Orlov, V. K., "Experimental Investigation of Heat Transfer With Boiling Oxygen in Vertical Channels During Condensation Heating," *International Chemical Engineering*, Vol. 14, 1974, pp. 517-521.

5 Galezha, V. B., Usyukin, I. P., and Kan, K. D., "Boiling Heat Transfer with Freons in Finned-Plate Heat Exchangers," *Heat Transfer—Soviet Research*, Vol. 8, No. 3, 1976, pp. 103-110.

6 Gopin, S. R., Usyukin, I. P., and Aver'yanov, I. G., "Heat Transfer in Condensation of Freons on Finned Surfaces," *Heat Transfer—Soviet Research*, Vol. 8, No. 6, 1976, pp. 114-119.

7 Robertson, J. M., "Boiling Heat Transfer with Liquid Nitrogen in Brazed Aluminium Plate-Fin Heat Exchangers," *AIChE Symposium Series*, Vol. 75, No. 189, 1979, pp. 151-164.

8 Robertson, J. M., and Lovegrove, P. C., "Boiling Heat Transfer With Freon-11 in Brazed Aluminium Plate-Fin Heat Exchangers," ASME JOURNAL OF HEAT TRANSFER, Vol. 105, 1983, pp. 605-610.

9 Haseler, L. E., "Condensation of Nitrogen in Brazed Aluminium Plate-Fin Heat Exchangers," ASME Paper No. 80-HT-57, 1980.

10 Robertson, J. M., "Review of Boiling, Condensation and Other Aspects of Two-Phase Flow in Plate-Fin Heat Exchangers," *Compact Heat Exchangers*, HTD-Vol. 10, ASME, New York, 1980, pp. 17-27.

11 Yung, D., Lorenz, J. J., and Panchal, C., "Convective Vaporization and Condensation in Serrated-Fin Channels," *Heat Transfer in Ocean Thermal Energy Conversion (OTEC) Systems*, HTD-Vol. 12, ASME, New York, 1980, pp. 29-37.

12 Robertson, J. M., and Clarke, R., "The Onset of Boiling of Liquid Nitrogen in Plate-Fin Heat Exchanger," *AIChE Symposium Series*, Vol. 77, No. 208, 1981, pp. 86-95.

13 Westwater, J. W., "Boiling and Condensation in Compact Finned Heat Exchangers," *Proceedings 1982 NATO Research Workshop on Advances in Two-Phase Flow and Heat Transfer*, Martinus Nijhoff Publisher, Netherlands, 1983, Vol. II, pp. 827-857.

14 Panitsidis, H., Gresham, R. D., and Westwater, J. W., "Boiling of Liquids in a Compact Plate-Fin Heat Exchanger," *International Journal of Heat and Mass Transfer*, Vol. 18, 1975, pp. 37-42.

15 Chen, C. C., Loh, J. V., and Westwater, J. W., "Prediction of Boiling Heat Transfer Duty in a Compact Plate-Fin Heat Exchanger Using the Improved Local Assumption," *International Journal of Heat and Mass Transfer*, Vol. 24, 1981, pp. 1907-1912.

16 Haley, K. W., and Westwater, J. W., "Boiling Heat Transfer From Single Fins," *Proceedings of 3rd International Heat Transfer Conference*, Vol. 3, New York, 1966, pp. 245-253.

17 Bondurant, D. L., and Westwater, J. W., "Performance of Transverse Fins for Boiling Heat Transfer," *Chemical Engineering Progress Symposium Series*, Vol. 67, No. 113, 1971, pp. 30-37.

18 Siman-Tov, M., "Analysis and Design of Extended Surfaces in Boiling Liquids," *Chemical Engineering Progress Symposium Series*, Vol. 66, No. 102, 1970, pp. 174-184.

19 Chen, C. C., "Improved Design Method for Boiling Heat Transfer in Compact Heat Exchangers," Ph.D. thesis, University of Illinois, Urbana, Ill., 1983.

20 Hewitt, G. F., and Hall-Taylor, N. S., *Annular Two-Phase Flow*, Pergamon Press, New York, 1970, p. 30.

21 Nusselt, W., "Die Oberflachenkondensation des Wasserdampfes," *Zeitschr. Ver. deutsch. Ing.*, Vol. 60, 1916, p. 541.

22 Yilmaz, S., and Westwater, J. W., "Effect of Velocity on Heat Transfer to Boiling Freon-113," ASME JOURNAL OF HEAT TRANSFER, Vol. 102, 1980, pp. 26-31.

23 Collier, J. G., *Convective Boiling and Condensation*, McGraw-Hill, New York, 1981, pp. 37-51; 72-77.

Study of Heat and Mass Transfer in a Vertical-Tube Evaporative Cooler[1]

H. Perez-Blanco
Assoc. Mem. ASME

W. A. Bird

Oak Ridge National Laboratory
Oak Ridge, Tenn. 37830

Evaporative coolers are three-fluid heat exchangers used to reject heat to the environment. A mixture of air and recirculating water is used as the cooling medium. In this paper, the heat and mass transfer processes taking place in a vertical-tube evaporative cooler are studied. A steady-state, one-dimensional model of cooler performance is formulated and is validated by experimental measurements, taken in a single-tube exchanger, of the controlling heat and mass transfer coefficients. These coefficients occur at the air-water interface. Heat fluxes and enhancement ratios for conditions of interest are measured and calculated, and the results are compared and discussed. The model is found to adequately predict heat exchanger performance.

Introduction

Heat rejection to the environment is usually accomplished via a heat exchanger that has a hot fluid on one side and atmospheric air or water on the other. When both air and water are used as the cooling medium, mass and sensible heat transfer take place, and the exchanger is referred to as an evaporative cooler. This type of exchanger is of interest due to two important characteristics: (*i*) at typical summer design conditions, the exchange of mass increases the heat flux considerably over that obtainable in a dry heat exchanger of the same configuration and (*ii*) these heat exchangers reject heat in principle to the air wet-bulb temperature. Thus, if properly designed, they may reject heat at lower temperatures than dry heat exchangers. Also, they may achieve lower rejection temperatures than the combination of water-cooled heat exchanger–cooling tower when the cooling tower is designed for the same wet bulb approach. These design possibilities, associated with evaporative coolers, may lead to improvements in the thermal efficiency of power or refrigerating cycles [1–3].

Previous work in the area of evaporative coolers focused mainly on determining performance of horizontal-tube coolers, with and without fins. Mizushima et al. studied experimentally the performance of a horizontal-tube cooler without fins. Heat and mass transfer coefficients were determined and correlated as functions of the Reynolds numbers of the cooling water and of the air flows, and a method of calculating performance was presented [4–5]. A step-by-step method of performance calculation for a plate-fin, tube-type evaporative condenser was presented by Leidenfrost et al. under the assumption of a Lewis number equal to 1 [2]. The effect of spraying a fine mist of water on air flowing over a compact tube-and-fin-type heat exchanger was also studied experimentally [6]. Good improvements in heat transfer performance were measured: essentially no increase in the pressure drop of the air phase occurred across the heat exchanger.

The overall heat transfer coefficient in evaporative coolers is a function of the resistance to heat transfer on each side of the tube wall and the resistance of the wall itself. The latter is, in most cases, relatively low. Previous work on water-cooled condensers has shown that vertical fluted tubes may enhance the heat transfer coefficient on the refrigerant side by up to six times the smooth tube value [7, 8]. It is of interest, therefore, to study the vertical tube condenser performance in the coolant fluid side, since additional improvements in the refrigerant side yield diminishing returns. No previous studies on vertical tube heat exchangers were found.

In this paper, a smooth vertical tube exchanger is studied in order to formulate a mathematical model of the evaporative cooler performance and to validate this model experimentally. A steady-state, one-dimensional model of the heat and mass transfer process that takes place in the exchanger is formulated and is validated by experimental measurements performed in a single-tube exchanger. The controlling resistance to heat dissipation is identified, and the heat fluxes and enhancement ratios obtainable using this type of cooler are determined in order to provide a basis for evaluation of its potential.

Mathematical Model

In formulating a one-dimensional model of cooler performance, two routes may be chosen: formulation of an overall heat transfer coefficient based on air enthalpy as the driving force or formulation of equations for mass and heat transfer at the air-water interface.Here we choose the second route for the sake of generality, since it does not call for a specific link between the heat and mass transfer coefficients.

In a vertical-tube evaporative cooler, the hot fluid flows inside an outer shell which surrounds vertical tubes. Inside each tube, a water film falls counterflow to a stream of air. Figure 1 shows the three fluids and the changes in mass and intensive variables as they flow through a differential length of one tube of the heat exchanger.

To formulate the mathematical model, we focus on the differential of length, dz, in Fig. 1. One-dimensional, steady-state flow is assumed. The equations are formulated according to the following sign convention: flows of matter or energy going into a control volume have opposite signs to those coming out from it. A mass balance for the air and water falling film yields

$$\frac{dm_w}{dz} = m_a \frac{dW}{dz} \tag{1}$$

At the air-water interface, a mass transfer process occurs which can be expressed as [9], p. 153, equation (5.4))

$$\frac{dm_w}{dz} = 2\pi M_w (R_3 - \delta) K \ln\left[\frac{1 - Y_{w,a}}{1 - Y_{w,i}}\right] \tag{2}$$

[1]Research sponsored by Office of Coal Utilization, U.S. Department of Energy, under subcontract W-7405-eng-26 with the Union Carbide Corporation.

Contributed by the Heat Transfer Division and presented at the ASME Winter Annual Meeting, Phoenix, Arizona, November 14-19, 1982. Manuscript received by the Heat Transfer Division December 9, 1982. Paper No. 82-WA/HT-75.

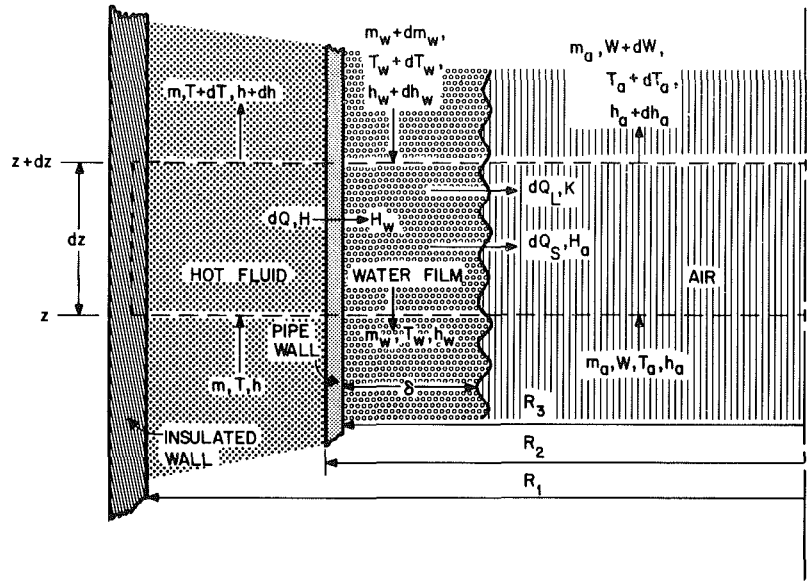

Fig. 1 Schematic of a differential of tube length, illustrating the transfer processes among the three fluids. The axial coordinate is denoted by *z*, the mass flow rates by *m*, the temperature by *T*, the enthalpies by *h*, and the heat transferred by *dQ*. The air humidity ratio is denoted by *W*, and m_a indicates dry air mass flow. Convective heat transfer coefficients are denoted by *H*, and mass transfer coefficients by *K*. Water and air flows are indicated by the subscripts *w* and *a*, and the subscripts *L* and *S* indicate latent and sensible heat, respectively.

A heat balance on the hot fluid yields

$$\frac{dT}{dz} = -\frac{2\pi R_2}{mC_p} U(T - T_w) \tag{3}$$

where U is the overall heat transfer coefficient between the hot fluid and the water film, given by

$$\frac{1}{U} = \frac{1}{H} + \frac{R_2}{k} \ln \frac{R_2}{R_3} + \frac{R_2}{R_3 H_w} \tag{4}$$

The enthalpy change of the hot fluid is given by

$$\frac{dh}{dz} = C_p \frac{dT}{dz} \tag{5}$$

A heat balance on the air phase yields

$$m_a[C_{p,a} T_a + W(C_{p,s} T_a + \Delta h_{w,0})] + dQ_S + dQ_L = m_a\{C_{p,a}(T_a + dT_a) + (W + dW)[C_{p,s}(T_a + dT_a) + \Delta h_{w,0}]\} \tag{6}$$

We assume that for well-mixed water films, the temperature

Nomenclature

C_p = heat capacity at constant pressure (kJ/kG•K)
d = molecular diffusivity of steam in air (m^2/s)
De = equivalent diameter (m)
g = acceleration of gravity (m/s^2)
h = specific enthalpy (kJ/kg)
H = convective heat transfer coefficient ($W/m^2 \cdot K$)
$\Delta h_{w,0}$ = enthalpy of vaporization of water at 0°C (kJ/kg)
k = thermal conductivity (W/m•K)
K = mass transfer coefficient (kg mol/m^2•s)
L = tube length (m)
m = mass flow rate (kg/s)
M = molecular weight (kg/kg mol)
Nu = Nusselt number = $2R_\delta H/k$
P = pressure (N/m^2)
Pr = Prandtl number
q = heat flux (kW/m^2)
Q = heat flow (kW)
R = radius (m)
R_2 = center tube radius (m)
R_3 = inner tube radius (m)
R_δ = radius (m) = $R_3 - \delta$
Re_a = air Reynolds number = $(w_w + w_a)\, 2R_\delta/v_a$
Re_w = water Reynolds number = $4\Gamma/\mu_w$
Ru = universal gas constant (kg m^2/s^2•kg mole•K)
Sc = Schmidt number = v/d
Sh = Sherwood number = $\dfrac{2R_\delta K R_u T}{\mathrm{Pd}}$
T = temperature (K or °C)
U = overall hot fluid-water film heat transfer coefficient ($kW/m^2 \cdot K$)
w = average velocity (m/s)
W = air humidity ratio (kg/kg)
Y = mole fraction
z = axial coordinate (m)
δ = film thickness (m)
Δ = change
Γ = film mass flow rate per unit of tube perimeter (kg/s•m)
μ = absolute viscosity (N•s/m^2)
ν = kinematic viscosity (m^2/s)
ρ = density (kg/m^3)

Superscripts and Subscripts

a = air
b = bottom of cooler
H = heat transfer
i = air-water film interface
L = latent
m = air-steam mixture
s = steam
S = sensible
t = top of cooler
w = water
$*$ = dimensionless

at the air-water interface is equal to the film temperature, T_w. Accordingly, the symbols in this equation are defined as

$$dQ_s = 2\pi(R_3 - \delta)H_a(T_w - T_a)dz$$

$$dQ_L = h_{s,i}dm_w$$

$$h_{s,i} = C_{p,s}T_w + \Delta h_{w,0}$$

From the four immediately proceding equations and equation (1), neglecting second-order differentials, one gets

$$\frac{dT_a}{dz} = \left[\frac{2\pi(R_3 - \delta)}{m_a C_{p,m}} H_a + \frac{C_{p,s}}{C_{p,m}} \frac{dW}{dz}\right](T_w - T_a) \qquad (7)$$

where

$$C_{p,m} = C_{p,a} + WC_{p,s}$$

Equation (7) shows that the air temperature change along the cooler depends not only on the sensible heat transferred but on the mass exchanged as well.

The air enthalpy change is given by

$$\frac{dh_a}{dz} = C_{p,m}\frac{dT_a}{dz} + \frac{dW}{dz}(C_{p,s}T_a + \Delta h_{w,0}) \qquad (8)$$

From an enthalpy balance around the control volume of Fig. 1, indicated by broken lines, one gets

$$\frac{dT_w}{dz} = \left[m\frac{dh}{dz} + m_a\frac{dh_a}{dz} - h_w\frac{dm_w}{dz}\right]/(m_w C_{p,w}) \qquad (9)$$

and, finally, the water enthalpy change is given by

$$\frac{dh_w}{dz} = C_{p,w}\frac{dT_w}{dz} \qquad (10)$$

The system formed by equations (1-3), (5), and (7-10) has eight unknowns, namely

$$T_w, h_w, m_w, T_a, h_a, W, T, h$$

Denoting with subscripts b and t at the bottom and the top of the cooler, the following boundary conditions are known at b ($z=0$), T_b, h_b for the hot fluid; $T_{a,b}$, $W_{a,b}$, $h_{a,b}$ for the air; and at $t(z=L)$, $T_{w,t}$, $h_{w,t}$ for the water.

This boundary problem was solved using a digital computer. A fourth-order Runge Kutta subroutine (RKF45) for solving initial-value problems in ordinary differential equations [10], together with a shooting technique, was used to obtain a solution. To run the program, values of the inlet humidities and temperatures must be provided. These values are given at $z = 0$ or at $z = L$, as previously explained. It is then necessary to employ a shooting technique, since the Runge-Kutta method requires that all inlet conditions be given at the same location, namely at $z = 0$ or at $z = L$. Thus guesses at $z = L$ of the final hot-fluid temperature and of the final air temperature and moisture must be provided. The solution obtained with these guesses, proceeding from $z=L$ to $z = 0$, is compared to the inlet conditions given, and if the solution is not within 1 percent of the inlet values, the procedure is repeated using new guesses obtained by a bisection technique. This is repeated until convergence to the inlet values is obtained. The local heat and mass transfer coefficients and property values are calculated by subroutines.

To reproduce the experimental conditions of our testing facility, water, instead of a condensing refrigerant, was chosen as the hot fluid. In principle, the computer code can be easily adapted to handle a condensing fluid instead of hot water. To solve the preceding system of equations, values of the fluid properties and of the heat and mass transfer coefficients must be provided. A complete description of these correlations may be found in [11].

The thermal properties of the fluids at atmospheric pressure are, in general, a function of temperature. Their local values were calculated employing the correlations in [12]. The thermal diffusivity of steam in air was calculated as recommended in ([13] p. 3.2). The heat transfer coefficients for the water flowing in an annular space and for the falling film were taken from [14] and [15], respectively. The mass transfer coefficient from the falling film to the air as calculated as in ([9], p. 214), and the corresponding heat transfer coefficient was calculated via the Chilton-Colburn analogy [9]. The falling film thickness and velocity were estimated as in [16]. In general, the falling film thickness increases with the water flow rate. Low flow rates lead to dry spots in the heat exchanger, thus reducing its performance and proving deposition of dissolved chemicals. High flow rates lead to waves on the film surface, which, in turn, may increase entrainment at high air velocities. In our experiments, an average falling film thickness of 0.25 mm was found to be adequate for ensuring complete wetting and for minimizing entrainment at air velocities of up to 10 m/s.

Test Loop and Data Analysis

Figure 2 is a schematic of the test section showing overall dimensions. The water film is fed via a porous 40-μm sintered ring and flows down the vertical 72.9-mm-dia Monel tube, completely wetting the tube wall. Air flows counterflow to the falling film after going through a honeycomb 4.2 dia long. The water film is extracted at the bottom of the tube through a 3-mm gap. Hot water flows inside a circular annulus that has a 11.1-mm radial clearance. The test section is well insulated, and glass portholes at the top and bottom ensure good flow visibility.

In each experiment, air moisture is adjusted by means of a steam humidifier, and hot water temperature is adjusted by an in-line steam heater. The flow rates and inlet and outlet

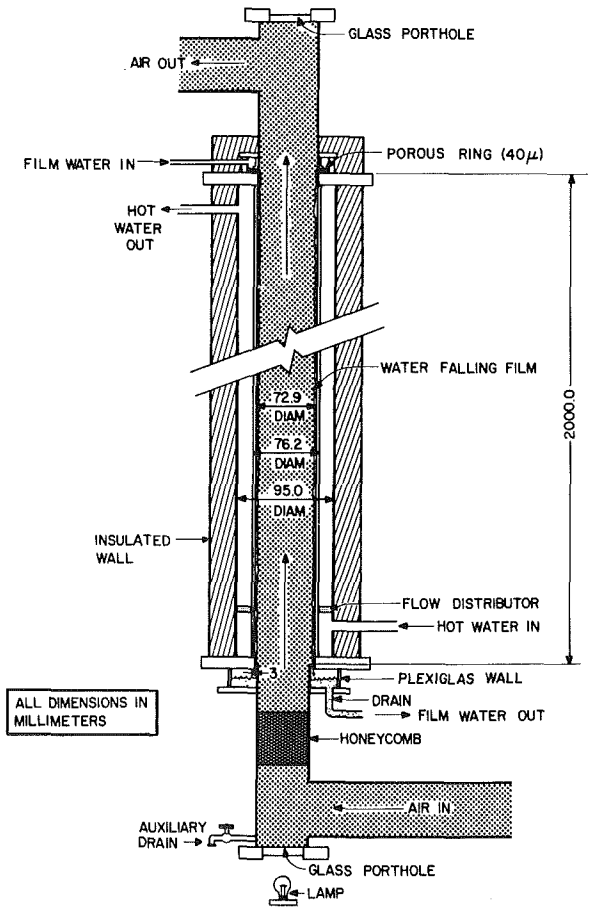

Fig. 2 Schematic of the test section, showing overall dimensions

temperatures of all fluids are measured. The air moisture content is determined both at the inlet and outlet of the test section by two methods: using a dewpoint meter and using the wet-bulb measurement together with the dry-bulb measurement. This repetition is necessary to ensure reliable moisture measurements. A complete description of the test facility and instrumentation may be found in [11].

The mass and heat transfer coefficients at the air-water interface control tube performance, as shown in the next section. It is thus important to calculate these transfer coefficients from experimental data to validate our model.

Equations (1) and (2) can be combined and rearranged, expressing the air humidity ratio as a function of the air mole fraction, to give

$$m_a \frac{M_w}{M_a} \frac{d(1/Y_a)}{\ln[(1/Y_{a,i})/(1/Y_a)]} = 2\pi(R_3 - \delta)KM_w dz \tag{11}$$

If the temperature of the water falling film is nearly constant, its vapor pressure will be constant, and the air mole fraction at the interface will hence remain nearly constant. Under those conditions, equation (11) may be integrated to give the mass transfer coefficient, K, as a function of the inlet and outlet air mole fractions

$$K = \frac{m_a}{2\pi(R_3 - \delta)M_a L}\left[\ln\ln\frac{Y_{a,b}}{Y_{a,i}} - \ln\ln\frac{Y_{a,t}}{Y_{a,i}} - \ln\frac{Y_{a,b}}{Y_{a,i}} + \ln\frac{Y_{a,t}}{Y_{a,i}} + \frac{\left[\ln\frac{Y_{a,b}}{Y_{a,t}}\right]^2 - \left[\ln\frac{Y_{a,t}}{Y_{a,i}}\right]^2}{(2)(2!)} - \frac{\left[\ln\frac{Y_{a,b}}{Y_{a,i}}\right]^3 - \left[\ln\frac{Y_{a,t}}{Y_{a,i}}\right]^3}{(3)(3!)} + \ldots\right] \tag{12}$$

Convergence of this series is quite fast and was assumed to take place when the absolute value of the last term calculated between brackets was smaller than 1×19^{-9}.

To calculate the heat transfer coefficient, equation (7) is integrated similarly to give

$$H_a = \left[-\ln\frac{(T_w - T_{a,t})}{(T_w - T_{a,b})} + \frac{C_{p,s}}{C_{p,m}}(W_b - W_t)\right]\frac{m_a C_{p,m}}{2\pi(R_3 - \delta)L} \tag{13}$$

Using equations (12) and (13), values of the average water film temperature and values of the initial and final dry-bulb temperature and moisture content, the heat and mass transfer coefficients can be calculated. In deriving these equations, it was assumed that the specific heat of air and steam remain constant and that the water film temperature is nearly constant. To produce this assumed condition as closely as possible in our experiments, the water film was injected at the same temperature as the hot water in the shell. The hot water was run at high mass flows to minimize its temperature drop. For these conditions, the change in the falling film temperature from top to bottom of the cooler did not exceed 2°C in most runs.

Results and Discussion

In a vertical-tube heat exchanger such as this one, heat is transferred from the hot water across the tube wall to the water film because of temperature gradients. Heat is transferred from the water film to the air in latent forms as a consequence of mass concentration and in sensible forms as a consequence of temperature gradients. For a given heat flux, the maximum temperature gradient will take place at the interface where the resistance to heat transfer is largest.

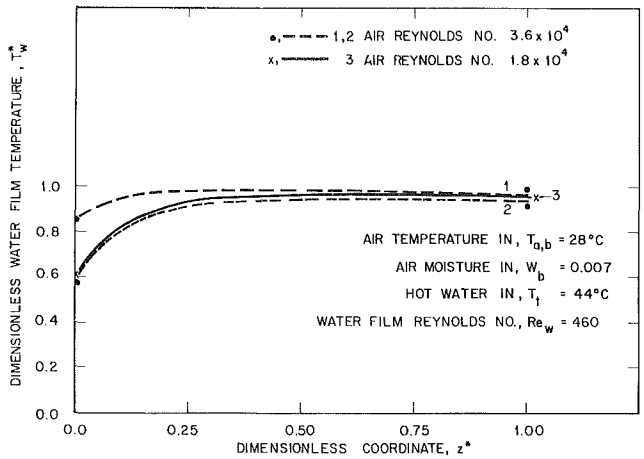

Fig. 3 Dimensionless water film temperature versus dimensionless axial coordinate

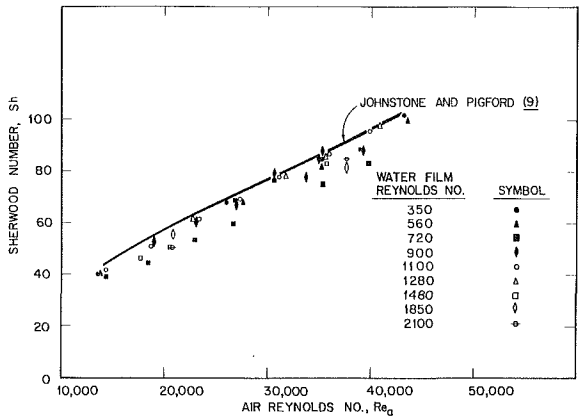

Fig. 4 Sherwood number versus air Reynolds number for different water film flows

From theoretical and experimental results, it can be readily shown that the resistance to heat transfer at the air-water interface predominates over all other resistances, since the maximum temperature drop occurs at this interface. This is illustrated in Fig. 3, where the ratio of the film temperature to the hot water temperature, T_w, (both temperatures in degrees Celsius) is plotted versus the dimensionless vertical coordinate, z, (axial coordinate divided by tube length, $z = 0$ at top of the tube) for the two different air Reynolds numbers, as obtained from the mathematical model. The experimentally determined inlet and outlet values of T_w are also shown. The hot water was run at high mass flows to keep its temperature constant. Regardless of the inlet water film temperature, an equilibrium temperature close to the hot water temperature is reached near the point of injection, and the maximum temperature drop is thus concentrated at the air-water interface.

Figure 3 shows that the water film temperature may be kept nearly constant by injecting it at the same temperature as the hot water flowing on the shell. To validate the model, the heat and mass transfer coefficients were calculated from experimental data as explained in the proceding section.

Tests were run at water film Reynolds numbers (Re_w) ranging from 350 to 2100 and at air Reynolds numbers (Re) from 1×10^4 to 4×10^4. The film was injected at the same temperature as the hot water (about 43°C), which was run at a

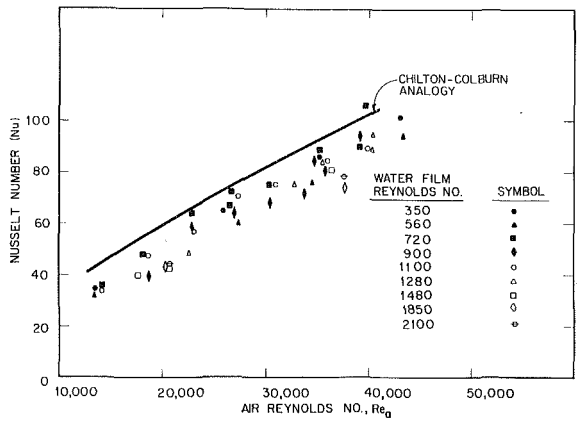

Fig. 5 Nusselt number versus air Reynolds number for different water film flows

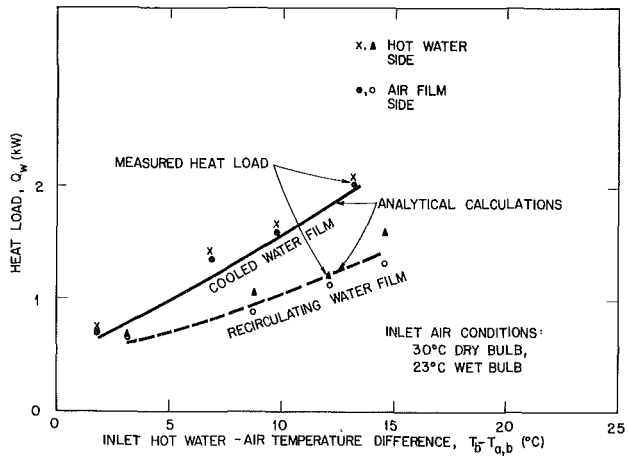

Fig. 6 Heat flux obtained in the evaporative condenser mode versus inlet temperature difference. The experimental points show the heat load as measured in the hot water (or shell) side and in the air-water film (or tube) side. The vertical distance between corresponding points is proportional to the heat balance error.

high flow rate (1.4 kg/s). The air inlet moisture was maintained at a low value (0.006 kg/kg) to increase the accuracy of the determination of the mass transfer coefficient. Air inlet temperatures ranged from 25 to 30°C.

The Sherwood and Nusselt numbers were calculated from these experimental data. Figure 4 shows the Sherwood number versus the air Reynolds number. Note that the air Reynolds number is calculated with the relative air-water film velocity. The experimental data and the correlation from [9], using a Schmidt number equal to 0.6, are displayed. Most of the experimental points fall within 10 percent of the existing correlation.

Figure 5 shows the Nusselt number versus the air Reynolds number. The experimental data fall somewhat below the values predicted by the Chilton-Colburn analogy; the differences between the existing correlation and the experimental points are within 25 percent. Note that the scattering of the experimental points in this figure is greater than that of those shown in Fig. 4 (for the Sherwood number). An uncertainty analysis employing equations (11) and (12) and the methodology presented in [17] shows that whereas the uncertainty interval for the Nusselt number is typically 29 percent, it is 15 percent for the Sherwood number. The uncertainty interval for each individual variable employed for this analysis was the manufacturer's specified accuracy of each transducer/readout combination, with only one exception, the average film temperature, which was determined to have an uncertainty interval of ±1°C with an 80 percent degree of confidence. Since this error is for both cases (Nu and Sh), the major contributor to the uncertainty of the results, it can be ascertained that their uncertainties (29 and 15 percent) are known with an 80 percent degree of confidence.

The good agreement between the correlation employed in the computer program and the values of the experimentally determined Sherwood number is very important for accurate calculations of cooler performance. This statement is justified because, as will be shown, the contribution of latent heat to the total heat dissipated is much larger than the contribution of sensible heat. Thus the correlations employed in the model were not modified to account for the differences displayed in heat transfer coefficients (Fig. 5).

Perhaps one of the most important applications of evaporative coolers is for condensation of a refrigerant in the shell side. During condensation, it is reasonable to assume a nearly constant wall temperature. To study performance under simulated condensing conditions, the hot water flow inside the shell was maintained at 0.95 kg/s. This flow rate produced a temperature drop of 1 to 2°C in the hot water. The water film flow was kept at 0.0127 kg/s, corresponding to a Reynolds number of 350. This is the minimal flow that will keep the tube wall wet for all conditions in our experimental facility. Small water film flows are of interest since they minimize the possibility of water carryover and decrease water pumping power [11]. The air flow rate was 0.037 kg/s, which corresponds to an air Reynolds number of 3.6×10^4. This flow is relatively large, but it does not produce any liquid carryover.

As stated, the controlling resistance to heat transfer is concentrated at the air-water interface. Since the resistance to heat transfer from the tube wall to the water film is small, it seems that the heat load could increase if the water were cooled before recirculation. Thus, two inlet water film temperatures were simulated: one for water cooled in an auxiliary wet cooling tower at 2.5°C above the air wet bulb and another for water recirculated without intermediate cooling at 2°C below the hot water temperature inside the shell. Air dewpoint, dry, and wet-bulb temperatures were 21.1, 30, and 23°C, respectively, corresponding to the 5 percent design condition for the Knoxville, Tennessee, area [13], p. 24.13).

Figure 6 displays the heat dissipated versus the inlet hot water-air temperature difference. As this difference increases, the heat load increases approximately linearly. As expected, cooling the water film increases the heat load; the increase ranges from about 14 to 55 percent as the hot water temperature increases from 3 to 15°C above the dry bulb. Interestingly, this plot shows that for evaporative coolers designed to operate at temperatures close to the design dry bulb, the gains obtained by cooling the water are relatively small. In such cases, providing an auxiliary system for cooling the water may not be warranted. It can be seen in Fig. 6 that the results given by the model and the experiment agree well.

To compare the performance for wet conditions to the performance for dry conditions, the enhancement ratio, q, was calculated for the typical summer conditions of Fig. 6 by dividing the heat exchanged when the water film flows by the heat exchanged when no water film is injected. The experimental and theoretical results are shown in Fig. 7. The most important conclusion that can be extracted from this figure is that when hot water temperatures are close to the dry-bulb temperatures, an evaporative cooler can dissipate substantially more heat than a dry one. For an initial dimensionless temperature difference of 0.1, the heat transferred in an evaporative cooler is about 14 to 18 times that transferred in an air-cooled exchanger of the same configuration. Small approach temperatures are thus possible without a corresponding increase of the exchanger area. It is

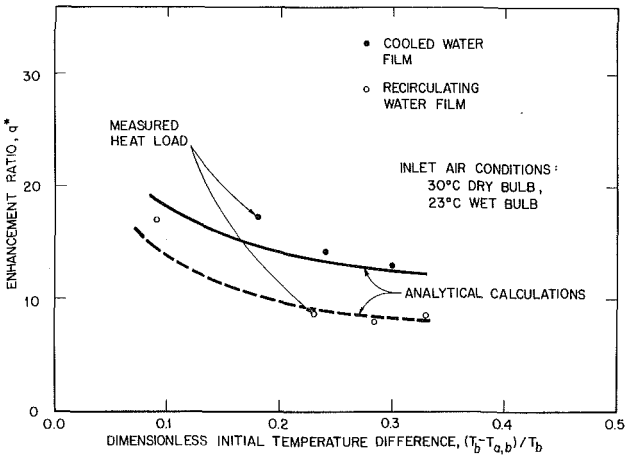

Fig. 7 Enhancement ratio versus inlet temperature difference

possible to operate the cooler at temperatures below the dry bulb, but this was not attempted.

The comparison given in Fig. 7 must be viewed with caution, since a smooth tube is not an effective configuration for heat transfer under dry conditions. However, the increase in heat flux obtained under wet conditions is remarkable because the additional pressure drop is small. One way of accounting for the pressure drop is to calculate the ratio of the heat flow to the power required to circulate the air and to compare that ratio for the wet and dry cases. For our experimental conditions, at an inlet temperature difference of 0.1 (Fig. 7), about 11 times more heat per unit of power spent in circulating the air is dissipated in the evaporative cooler than in the dry cooler. Complete measurements of pressure drop in the air phase are given in [11].

Conclusions

From this work, it is possible to conclude that the controlling resistance to heat dissipation in a vertical-tube evaporative cooler takes place at the air-water interface. Enhancement mechanisms should thus focus on improving the transfer process at this interface. The enhancement devices may be either repeated roughness or swirling flows, with the primary emphasis being on maximum enhancement with a minimum pressure drop increase of the air phase. The model of cooler performance developed here is flexible and can handle a wide range of fluids and inlet conditions. It can accept heat and mass transfer coefficients determined experimentally, and thus serve as a useful tool in studying heat transfer enhancement for this type of equipment. The empirical correlation for smooth tubes found in the literature are entirely adequate for performance calculation of this type of equipment.

References

1 Holzhauer, R., "Cooling System Condensers," *Plant Engineering*, Vol. 32, No. 9, 1979, pp. 74–81.

2 Leidenfrost, W., and Korenic, B., "Analysis of Evaporative Cooling and Enhancement of Condenser Efficiency and of Coefficient of Performance," *Warme -und Stoffubertragung*, Vol. 12, 1979, pp. 5–23.

3 Guinn, G. R., and Novel, G. J., "Operating Performance of a Water Spray on an Air Type Condensing Unit," *ASHRAE Transactions*, Vol. 87, Pt. 2, 1981, pp. 373–381.

4 Mizushima, T., Ito, R., and Miyashita, H., "Experimental Study of an Evaporative Cooler," *International Chemical Engineering*, Vol. 7, No. 9, 1967, pp. 727–732.

5 Mizushima, T., Ito, R., and Miyashita, H., "Characteristics and Methods of Thermal Design of Evaporative Coolers," *International Chemical Engineering*, Vol. 8, No. 3, 1968, pp. 532–38.

6 Jang, W. J., and Clark, D. W., "Spray Cooling of Air-Cooled Compact Heat Exchangers," *International Journal of Heat Mass Transfer*, Vol. 18, 1975, pp. 311–317.

7 Combs, S. K., "An Experimental Study of Heat Transfer Enhancement for Ammonia Condensing on Vertical Fluted Tubes," ORNL-5536, Oak Ridge, Tenn., 1978.

8 Combs, S. K., Mailen, G. S., and Murphy, R. W., "Condensation of Refrigerants on Vertical Fluted Tubes, ORNL/TM-5848, Oak Ridge, Tenn., 1978.

9 Sherwood, T. K., Pigford, R. L., and Wilke, C. R., *Mass Transfer*, McGraw-Hill, New York, 1975.

10 Forsyte, G. E., Malcom, M. A., and Moler, C. B., *Computer Methods for Mathematical Computations*, Prentice-Hall, Englewood Cliffs, N. J., 1977.

11 Perez-Blanco, H., and Bird, W. A., "Study of Heat and Mass Transfer in Evaporative Coolers," ORNL/TM-8150, Oak Ridge, Tenn., 1982.

12 *Thermophysical Properties of Refrigerants*, ASHRAE, New York, 1976.

13 *ASHRAE Handbook, 1981 Fundamentals*, ASHRAE, New York, 1977.

14 McAdams, W. H., *Heat Transmission*, McGraw-Hill, New York, 1954.

15 Edwards, D. K., Dumy, V. E., and Mills, A. F., *Transfer Processes*, Hemisphere Publishing Corp., Washington, 1979.

16 Blaß, E., "Gas/Film-Stromung in Rohren," *Chemical Engineering Technology*, Vol. 49, Pt. 2, 1977, pp. 95–105.

17 Kline, S. J., and McClintock, F. A., "Describing Uncertainties in Single-Sample Experiments," ASME *Mechanical Engineering*, 1953, pp. 3–8.

The Representation of Regenerator Fluid Carryover by Bypass Flows

P. J. Banks
Division of Energy Technology, Commonwealth Scientific and Industrial Research Organization, Highett, Victoria 3190, Australia

A regenerator transfers sensible heat between two fluid streams by means of a porous matrix through which the streams are passed alternately. The fluid contained in the matrix passages is carried over from one fluid stream to the other, and contributes to the heat transfer process. It has been suggested that this contribution may be predicted by treating the fluid carryover as fluid flows bypassing the matrix. The validity of this representation is explained, and its accuracy is explored in a case for which numerical solutions of the governing equations are available. A published analysis of the representation is discussed and completed.

1 Introduction

A regenerative heat exchanger or regenerator transfers sensible heat between two fluid streams by means of a porous matrix through which the streams are passed alternately. Transfer occurs via energy storage in the matrix and also via the fluid contained in the matrix passages. The contribution of the contained fluid has been presented recently by the author [1] on a design chart, obtained using finite difference solutions of the governing equations, including and neglecting it. The contribution is termed the effect of carryover, since the contained fluid is carried from one fluid stream to the other with the matrix.

The formulation of the chart was stimulated by the similarity between fluid carryover and fluid flows in a regenerator that bypass the matrix and pass between the fluid streams at matrix faces. These cross bypass flows may be caused by pressure differences driving leakage through seals and by the trapping of fluid in header volumes between seals and matrix [2–5]. Prior to the availability of a solution of the governing equations, including carryover, Dunkle [6] had suggested that the effect of carryover on the effectiveness of a regenerator with high performance is close to that of cross bypass flows into matrix outlets, each with flow rate a half that of the carryover. Shah [7] has recently drawn the author's attention to the approximate theory of Klopfer [2, 5] which represents carryover by such bypass flows with flow rate equal to that of the carryover.

Klopfer's theory [2, 5] is directed to regenerators for gas turbine engines, and so considers the thermal capacity (specific heat times density) of each fluid stream to be different, whereas the author [1, 3] considered these capacities to be the same, an assumption applicable to air-conditioning regenerators.

Accurate prediction of the effect of carryover on regenerator effectiveness requires solution of the governing equations by a numerical method. The results of such solution are available, to the author's knowledge, only for fluid thermal capacity the same in each fluid stream. Therefore, the accuracy of Klopfer's theory for this capacity different in each stream cannot be checked.

In this paper, the validity of the representation of carryover by bypass flows is explained, and the accuracy of such representation is explored using the design chart [1], which applies to a symmetric balanced counterflow regenerator with fluid thermal capacity the same in each fluid stream. The conclusions serve to indicate the possible applicability of such representation more generally, particularly for this capacity different in each fluid stream, as in Klopfer's theory.

The theoretical analysis of cross bypass flows into matrix outlets [2, 3, 5] is adapted in this paper to provide representation of carryover. Fluid specific heat is assumed to be the same in each fluid stream, as in [1–3, 5], so that different fluid density gives different fluid thermal capacity. The discussion and analysis in sections 2 to 4 consider a symmetric balanced counterflow regenerator with fluid density the same in each fluid stream, and without "purge" arrangement [1], as in [1, 3]. Different fluid density in each fluid stream is considered in section 5, as in Klopfer's theory [2, 5], which is discussed critically in sections 5 and 6.

2 Comparison of Carryover and Cross Bypass Flows

Figure 1 represents the matrix of a symmetric balanced counterflow regenerator on a distance-time diagram and shows paths followed by fluid elements carried over from one fluid stream to the other by the matrix. The fraction of each fluid stream carried over is termed the carryover ratio, and given by

$$\kappa = L/v\tau \tag{1}$$

where L is the matrix dimension in the fluid flow direction, v is the mean velocity of fluid flow through a matrix passage, and τ is the flow period, the time that the matrix spends in each fluid stream.

In Fig. 1, the relative magnitudes are shown of the masses of fluid leaving the matrix during period 1, as carryover from

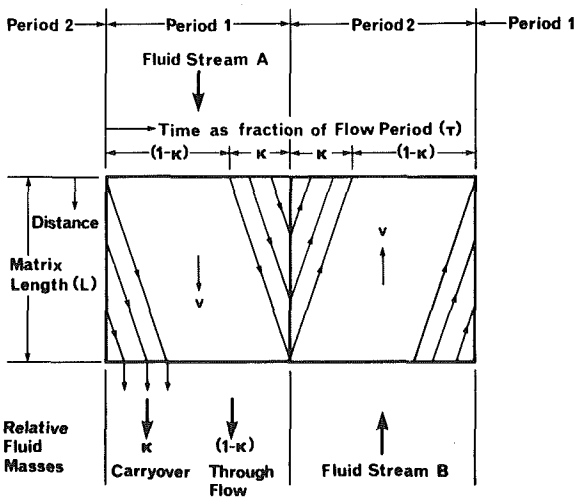

Fig. 1 Distance-time diagram for matrix of a symmetric balanced counterflow regenerator, showing paths of fluid elements carried over from one fluid stream to the other by the matrix

Contributed by the Heat Transfer Division for publication in the JOURNAL OF HEAT TRANSFER. Manuscript received by the Heat Transfer Division, June 1, 1982.

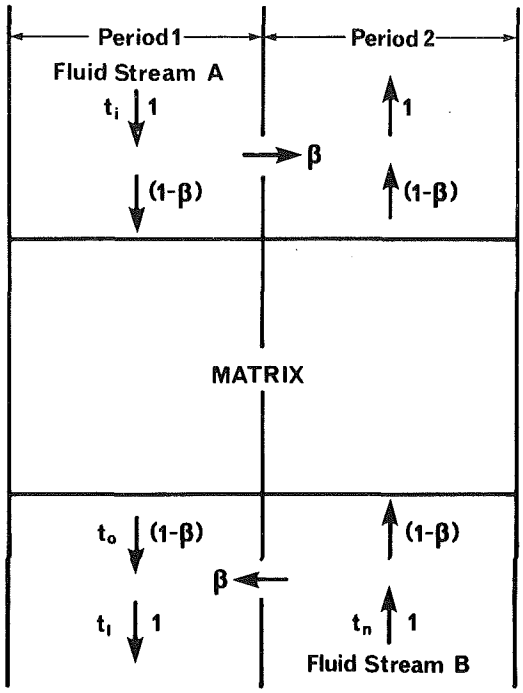

Fig. 2 Matrix of a balanced counterflow regenerator with fluid flows occurring for equal cross bypass flows into matrix outlets. Temperatures and relative mass flow rates are shown.

fluid stream B and as through flow from fluid stream A. These masses become mass flow rates when divided by the flow period.

Figure 2 shows the matrix of a balanced counterflow regenerator with the fluid flows occurring for equal cross bypass flows into the matrix outlets. The relative mass flow rates are shown, with bypass mass flow rate as a fraction of that of each fluid stream denoted β. Comparison with Fig. 1 shows the similarity between these flows and carryover, as both are seen to pass a fraction of each fluid stream into the other fluid stream.

In the case of no heat transfer between fluid streams and matrix, the carryover has the same effect as the cross bypass flows in passing isothermally a fraction of each stream into the other. Hence, in this case, the effect of carryover on regenerator effectiveness is given by that of the bypass flows, each with flow rate equal to that of the carryover.

In the general case, with heat transfer between fluid streams and matrix, the effect of carryover differs from that of the bypass flows in two respects. First, the carryover changes in temperature while resident in the matrix, thus affecting its equivalence in effect to the bypass flows. Second, the periodic energy storage in the matrix is effectively increased due to energy storage in the fluid contained in the matrix passages, thus increasing the effectiveness of the regenerator for transfer via the matrix. The first difference can be accommodated by modeling the carryover by nonisothermal bypass flows. However, the second difference makes such a model fictitious, and so representative only, since this difference is not associated with the passage of the matrix-contained fluid between the fluid streams. This question is explained further in section 4.

With regard to the second difference, it is noted that Maclaine-cross [8] shows the usefulness of representing carryover by increases in matrix specific heat and matrix to fluid heat transfer coefficient, and this design method has been compared [1] with the use of the author's design chart [1].

The effect of nonisothermal cross bypass flows into matrix outlets on regenerator effectiveness is now derived and compared with that of carryover.

3 Analysis

The effectiveness of a regenerator is defined as the ratio of the heat transfer rate achieved and the maximum possible transfer rate, and thus for a balanced regenerator is given by

$$\epsilon = (t_o - t_i)/(t_n - t_i) \tag{2}$$

where t_i and t_o denote the temperature of one of the fluid streams at inlet to and outlet from the matrix, respectively, and t_n that of the other fluid stream at inlet, as shown in Fig. 2. The outlet temperature of the other fluid stream is not

Nomenclature

c_f = specific heat of fluid
C = thermal capacity rate of a fluid stream [5]
C^* = C_A/C_B
C_r^* = matrix to fluid stream thermal capacity rate ratio [1, 5]
E_β = bypass flow effect, equation (5)
E_κ = carryover effect, equation (3)
f = change in temperature during passage of a bypass flow representing carryover, as a fraction of the difference between the temperatures of the fluid stream from which it originates and the fluid stream into which it mixes
L = matrix dimension in fluid flow direction
$N_{tu,o}$ = modified number of heat transfer units [1, 5]
P = pressure of a fluid stream at inlet
P^* = P_A/P_B
r = thermal capacity ratio of the fluid streams, equation (9)
t = temperature of fluid; t_i, t_o, and t_1, for one fluid stream at inlet to matrix, at outlet from matrix, and on leaving regenerator after mixing with bypass flow into matrix outlet, respectively; t_n, for other fluid stream at inlet
T = absolute temperature of a fluid stream at inlet
T^* = T_B/T_A
v = mean velocity of fluid flow through matrix passage
Y = parameter, equation (15)
β = mass flow rate of each bypass flow as a fraction of that of each fluid stream
ϵ = regenerator effectiveness [5], equation (2) for balanced flow
ϵ_m = value of ϵ due to transfer via the matrix
ϵ_o = effectiveness of a balanced regenerator including the effect of equal cross bypass flows into matrix outlets, equation (4)
κ = fluid carryover ratio, the fraction of a fluid stream carried over into the other stream, equation (1)
ρ_f = density of fluid
τ = flow period, the time that the matrix spends in a fluid stream

Subscripts

a = with carryover considered as cross bypass flows into matrix outlets
A = fluid stream A, cold stream, $C_A < C_B$
B = fluid stream B

specified, since it is not used in the analysis. The outlet temperatures are bulk mean values because of the periodic nature of energy storage in the matrix.

The effectiveness is denoted ϵ_m when t_o is evaluated considering only transfer via the matrix, that is, the effect of carryover is neglected. For a symmetric balanced regenerator, ϵ_m is determined by two parameters, and the two parameters used here are the modified number of heat transfer units $N_{tu,o}$ and the matrix to fluid stream thermal capacity-rate ratio, C_r^* [1, 5]. Effectiveness ϵ, that includes the effect of carryover, depends also on a parameter describing the rate of carryover, for which carryover ratio κ is used here.

The quantity "carryover effect," defined by

$$E_\kappa = (\epsilon - \epsilon_m)/\kappa \tag{3}$$

has been shown [1] to be independent of κ for practical designs of symmetric balanced counterflow regenerator for gas streams, that is for $(C_r^*/\kappa) > 50$.

With bypass flow into a matrix outlet, the mean temperature t_o in a fluid stream leaving the matrix differs from that t_1 at the regenerator outlet, after the bypass flow has mixed with the fluid stream, as shown for fluid stream A in Fig. 2. The overall effectiveness of the regenerator, with the effect of such bypass flows included, becomes

$$\epsilon_o = (t_1 - t_i)/(t_n - t_i) \tag{4}$$

The effect of the bypass flows on regenerator effectiveness may be described by a quantity "bypass flow effect," defined by

$$E_\beta = (\epsilon_o - \epsilon)/\beta \tag{5}$$

where β is the mass flow rate of each bypass flow as a fraction of that of each fluid stream.

Temperature, t_1, in equation (4) is given by conservation of energy in the mixing of a bypass flow into a matrix outlet with the outlet fluid stream. This mixing is illustrated for fluid stream A in Fig. 2. Following the explanation in section 2, the bypass flow is considered to change in temperature by a fraction, f, of the difference between the temperature, t_n, of the fluid stream from which it originates and the temperature, t_o, of the fluid stream into which it mixes. Therefore, the bypass flow enters this mixing process with temperature $[(t_n - f(t_n - t_o)]$, and from energy conservation in the process

$$t_1 = \beta[t_n - f(t_n - t_o)] + (1-\beta)t_o \tag{6}$$

From equations (2) and (4-6), the effect of such bypass flows on regenerator effectiveness is given by

$$E_\beta = (1-f)(1-\epsilon) \tag{7}$$

The result of the approximate theory for carryover effect of Klopfer ([5], equation (176)) becomes equation (7), with $f = 0$ for fluid density the same in each fluid stream.

Equation (7) is plotted in Fig. 3 for several values of f. The line for $f = 0$ corresponds to actual isothermal bypass flows, and the other lines to nonisothermal bypass flows that can be equivalent in effect to carryover. The determination of f for a particular regenerator operating condition is described in the next section.

4 Equivalence Between Bypass Flows and Carryover

When cross bypass flows into matrix outlets represent carryover, effectivenesses ϵ_o and ϵ, considering and neglecting these bypass flows, respectively, correspond to effectivenesses ϵ and ϵ_m, considering and neglecting carryover, respectively. Therefore, the form of equation (7) prompted the author to plot carryover effect, E_κ, versus regenerator effectiveness, ϵ_m, neglecting carryover, [1, Fig. 3] of which a simplified form is presented in Fig. 4. Comparing Figs. 3 and 4, the departure of the plot from a straight line between $\epsilon_m = 0$, $E_\kappa = 1$ and $\epsilon_m = 1$, $E_\kappa = 0$ shows a general lack of equivalence in effect

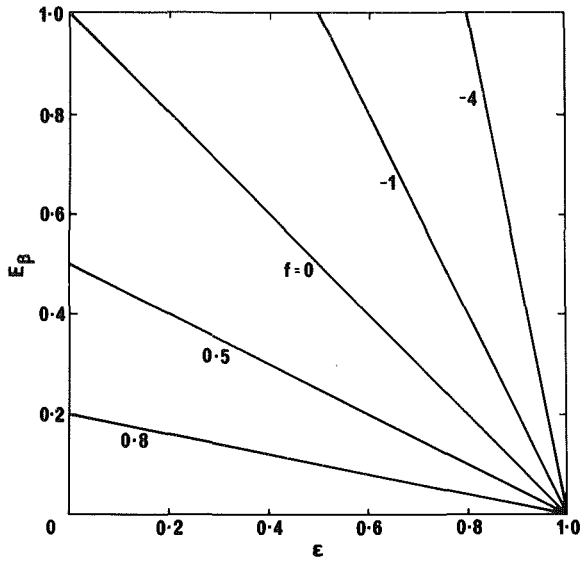

Fig. 3 Bypass flow effect, E_β, for several values of the bypass temperature change fraction, f, for a balanced couterflow regenerator with equal cross bypass flows into matrix outlets

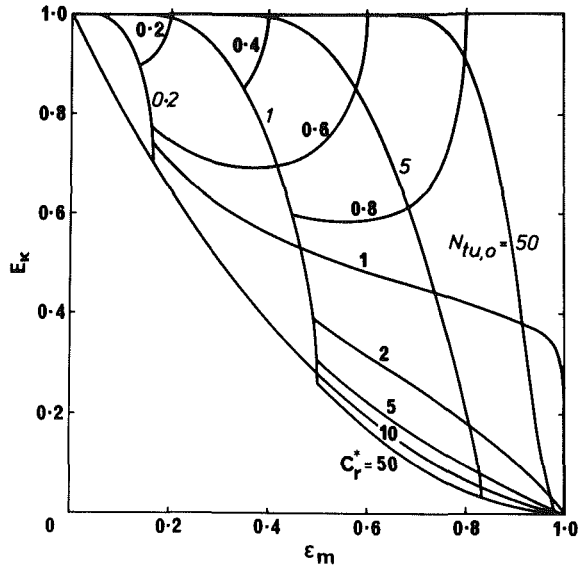

Fig. 4 Carryover effect, E_κ, for $(C_r^*/\kappa) > 50$ [1], for a symmetric balanced couterflow regenerator

between carryover and cross bypass flows that are isothermal, that is, with $f = 0$.

Isothermal equivalence is seen to apply for $\epsilon_m = 0$ (no heat transfer), as noted in section 2, for $\epsilon_m = 1$ (ideal heat transfer), and for $\epsilon_m > 0.7$ with C_r^* near 2 (as in practical regenerator operation). For $\epsilon_m > 0.7$ with $C_r^* > 2$, comparison of Figs. 3 and 4 shows that equivalence requires $0 < f < 1$. For example, for $\epsilon_m > 0.7$, $f = 0.5$, 0.65, and 0.8 with $C_r^* \cong 5$, 10 and 50 respectively. This result is in accord with the suggestion by Dunkle [6] mentioned in section 1.

Equivalence in effect between carryover and cross bypass flows is seen to apply in general provided a suitable value is chosen for f. This equivalence is fictitious and so representative only, as explained in section 2, and as is apparent for $f \leq 0$. $f < 0$ corresponds to the bypass flow reaching a temperature outside the range between the inlet temperatures of the two fluid streams. $f = 0$ implies no heat transfer between bypass flow and matrix, yet can apply with high $N_{tu,o}$. For $f = 0$, the two differences in effect between carryover and cross

bypass flows mentioned in section 2 must be equal and opposite.

The factor $(1-f)$ in equation (7) may be considered to change the carryover flow rate to that of the equivalent bypass flow rate. The specification of f as a function of C_r^* and $N_{tu,o}$ is possible using Figs. 3 and 4, enabling carryover to be accurately represented by bypass flows for all operating conditions. However, this design method is not easier than the direct use of Fig. 4.

The representation of fluid carryover by bypass flows provides a convenient design method in the absence of accurate results, as in the case of different fluid density in each fluid stream, for which Klopfer [2, 5] provides analysis like that in section 3 with $f = 0$.

5 Fluid Density Different in Each Stream

5.1 Representation of Carryover by Bypass Flows. Klopfer [2, 5] represents carryover by cross bypass flows into matrix outlets, each with flow rate equal to that of the carryover. Such representation is shown in the previous section to be accurate for a symmetric balanced regenerator with fluid density and specific heat the same in each fluid stream over a range of practical operating conditions. This result indicates the possible applicability of Klopfer's theory in the case of fluid density different in each fluid stream. However, in this case there is an effect of carryover additional to those discussed in section 2, that on the fluid stream thermal capacity rates, which is not considered by Klopfer.

5.2 Effect of Carryover on Fluid Stream Capacity Rates. It is apparent from Fig. 1, that a fluid stream in its passage through the matrix progressively loses fluid by carryover to the other stream and gains fluid by carryover from the other stream. The volume flow rate of loss is equal to that of gain, since the matrix passages may be considered invariant in volume. Hence, for fluid density and specific heat the same in each fluid stream, the thermal capacity rates of the fluid streams are unaffected by carryover.

For different fluid density or specific heat in each stream, the capacity rates of loss and gain are unequal, and the capacity rate of one fluid stream will increase as it passes through the matrix, while that of the other stream will decrease. With carryover represented by cross bypass flows into matrix outlets, the change in each fluid stream capacity rate occurs at inlet, Fig. 2. With this representation, the capacity rates C_A and C_B of fluid streams A and B are modified by consideration of carryover to rates C_{Aa} and C_{Ba} given by

$$C_{Aa} = C_A(1-\kappa_A) \quad \text{and} \quad C_{Ba} = C_B(1-\kappa_B) \tag{8}$$

The carryover ratios κ_A and κ_B of the fluid streams are related as a result of the equality of carryover volume flow rates, from which

$$\kappa_B C_B / \kappa_A C_A = c_{fB}\rho_{fB} / c_{fA}\rho_{fA} = r \tag{9}$$

where ρ_f and c_f denote fluid density and specific heat, respectively, and r is the thermal capacity ratio of the fluid streams.

Considering fluid stream A to have the minimum thermal capacity rate, $C_A = C_{min}$ [5], and the maximum thermal capacity, $r < 1$, in accord with Klopfer [2, 5], the regenerator parameters when modified by consideration of carryover may be derived using equations (8) and (9) to be

$$C_a^* = C_{Aa}/C_{Ba} = C^*(1-\kappa_A)/(1-rC^*\kappa_A) \tag{10}$$

$$C_{ra}^* = C_r^*/(1-\kappa_A) \tag{11}$$

$$N_{tu,oa} = N_{tu,o}/(1-\kappa_A) \tag{12}$$

Since r and C^* are less than unity, the effect of this modification of parameters will be to increase regenerator effectiveness, that is, to give $\epsilon_{ma} > \epsilon_m$.

Klopfer's theory [2, 5] gives the decrease in regenerator effectiveness resulting from the separation and mixing of the cross bypass flows representing carryover. The result is given for $c_{fA} = c_{fB}$ and gas streams, so that

$$r = 1/P^*T^* \tag{13}$$

where $P^* = P_A/P_B$ and $T^* = T_B/T_A$ are the ratios of pressure and absolute temperature, respectively, of the fluid streams at inlet, with stream A being the cold stream. The result [5, equation (176)] may be expressed in the form

$$(\epsilon_{ma} - \epsilon_a)/\kappa_A = (Y-1)(1-\epsilon_{ma})/(1-\kappa_A Y) \tag{14}$$

with

$$Y = [T^* - (1/P^*)]/(T^*-1) \tag{15}$$

$T^* > 1$, and in gas turbine regenerators, to which Klopfer's theory is directed, $P^* > 1$ so that $Y > 1$ and $\epsilon_{ma} > \epsilon_a$, since $\kappa_A << 1$. However, this decrease in regenerator effectiveness due to carryover acting as bypass flows should be combined with the increase due to reduced fluid stream capacity rates discussed above in determining the effect of carryover. This effect is now shown to be an increase in effectiveness for a typical operating condition.

The data of the numerical example by Klopfer [5, Fig. 20], $C_r^* = 200\,\kappa_A$, $P^* = 4$ and $T^* = 2$, are used together with the parameter values

$$C^* = 1,\ C_r^* = 10 \text{ and } N_{tu,o} = 5.$$

Hence, $\kappa_A = 5$ percent and the values of the parameters, when modified by consideration of carryover are, from equations (10) to (13),

$$C_a^* = 0.956,\ C_{ra}^* = 10.53 \text{ and } N_{tu,oa} = 5.26$$

The computer program of Maclaine-cross [9] for regenerator effectiveness neglecting carryover with these parameter values gives

$$\epsilon_m = 0.832 \text{ and } \epsilon_{ma} = 0.854 \text{ so that } \epsilon_{ma} - \epsilon_m = 0.022$$

For the above data and parameter values, Klopfer's theory gives, from equations (14) and (15),

$$\epsilon_{ma} - \epsilon_a = 0.006$$

It follows that the change in regenerator effectiveness due to carryover is predicted to be

$$\epsilon_a - \epsilon_m = 0.016$$

which is seen to be a significant increase.

Klopfer [2, 5] presents the effect of carryover on regenerator effectiveness as $\epsilon_{ma} - \epsilon_a$, a decrease equal to 0.006 in the example given in the previous paragraph. The actual effect of carryover predicted by his model is $\epsilon_a - \epsilon_m$, an increase equal to 0.016 in the example given. Therefore, the indication by Klopfer [5, Fig. 20] that the effect of carryover is to reduce regenerator effectiveness and be negligible for $C_r^* < 10$ is misleading.

6 Effect of Header Volumes

In some regenerator designs, particularly those of fixed-matrix type, the matrix fluid flow passages are switched between the fluid streams in groups, so that header volumes exist between seals and matrix faces. On switching, the fluid in each such volume is trapped and mixes with the fluid stream that subsequently passes through the volume. Thus, the header volumes provide cross bypass flows in both directions at a matrix face [3].

Klopfer treats these bypass flows as a contribution to carryover, by adding header volume to matrix passage volume in determining carryover flow rate [5, equation (174)]. Since carryover is treated as cross bypass flows into matrix outlets,

the opposite bypass flows at each matrix face due to header volumes are neglected. The resulting error for a balanced regenerator with equal header volumes and fluid thermal capacity the same in each stream is shown by comparing Figs. 6 and 8 in [3] and seem to be negligible for the practical case of β small and ϵ_m near unity. The error becomes negligible in this range of operation because the effects of the neglected bypass flows, shown in Figs. 4 and 5 of [3], cancel in this range. For fluid thermal capacity different in each fluid stream, the neglected bypass flows differ for equal header volumes and cancellation will not occur. Therefore, in general, an analysis like that in [3] is required to predict the effect of header volumes.

7 Conclusions

The representation of regenerator fluid carryover by cross bypass flows into matrix outlets has been seen not to model the actual processes occurring, but to provide an approximate method for predicting the effect on regenerator effectiveness of the fluid contained in the matrix, which is useful when results from numerical solution of the governing equations are not available.

For a symmetric balanced counterflow regenerator with fluid thermal capacity the same in each fluid stream, the representation of carryover by such cross bypass flows with equal flow rate has been shown to be accurate in the limit of no heat transfer, $\epsilon_m = 0$, and for the practical operating conditions, $\epsilon_m > 0.7$ and $C_r^* \cong 2$. However, for other operating conditions, the equivalent bypass flows need to differ in flow rate from the carryover.

These conclusions indicate the possible applicability of the theory of Klopfer [2, 5] that represents carryover by such cross bypass flows in the case of different fluid thermal capacity in each fluid stream, for which results from numerical solution are not known to be available. However, the indication by Klopfer that the effect of carryover in this case is to reduce regenerator effectiveness and be negligible for $C_r^* < 10$ is shown to be misleading, because a component of the effect predicted by his model is omitted. Also, the inclusion by Klopfer of header volumes in his model is shown to be approximate, particularly in this case.

Acknowledgments

The author is grateful to Dr. R. K. Shah of General Motors Corporation for prompting this work and for helpful comments, to his colleague Mr. R. V. Dunkle for stimulating suggestions, and to Dr. I. L. Maclaine-cross of the University of New South Wales for helpful discussions.

References

1 Banks, P. J., "Effect of Fluid Carryover on Regenerator Performance," ASME JOURNAL OF HEAT TRANSFER, Vol. 104, No. 1, Feb. 1982, pp. 215–217 (Errata: Vol. 104, No. 4, Nov. 1982, p. 820 and Vol. 105, No. 3, Aug. 1983, p. 683).

2 Klopfer, G. H., "The Design of Periodic-Flow Heat Exchangers for Gas Turbine Engines," Technical Report HE-1, Department of Mechanical Engineering, Stanford University, Stanford, California, Aug. 1969.

3 Banks, P. J., and Ellul, W. M. J., "Predicted Effects of By-Pass Flows on Regenerator Performance," *Mechanical & Chemical Engineering Transactions of The Institution of Engineers, Australia*, Vol. MC9, Nos. 1 & 2, 1973, pp. 10–14.

4 Maclaine-cross, I. L., and Ambrose, C. W., "Predicted and Measured Pressure Drop in Parallel Plate Rotary Regenerators," ASME *Journal of Fluids Engineering*, Vol. 102, No. 1, Mar. 1980, pp. 59–63.

5 Shah, R. K., "Thermal Design Theory for Regenerators," *Heat Exchangers—Thermal-Hydraulic Fundamentals and Design*, edited by S. Kakac, A. E. Bergles and F. Mayinger, Hemisphere/McGraw-Hill, Washington, D.C., 1981, pp. 721–763.

6 Dunkle, R. V., personal communication, CSIRO Division of Mechanical Engineering, 1969.

7 Shah, R. K., personal communication, Harrison Radiator Division, General Motors Corporation, Lockport, N.Y., March 1982.

8 Maclaine-cross, I. L., "Effect of Interstitial Fluid Heat Capacity on Regenerator Performance," ASME JOURNAL OF HEAT TRANSFER, Vol. 102, No. 3, Aug. 1980, pp. 572–574. (The figures are reversed with respect to captions.)

9 Maclaine-cross, I. L., "A Theory of Combined Heat and Mass Transfer in Regenerators, Ph.D. thesis, Department of Mechanical Engineering, Monash University, Australia, 1974.

An Investigation of Steady Wall-Ceiling and Partial Enclosure Fires

C.-P. Mao

A. C. Fernandez-Pello
Mem. ASME

J. A. C. Humphrey
Mem. ASME

Department of Mechanical Engineering,
University of California,
Berkeley, Calif. 94720

A numerical model has been developed to: (a) study the buoyancy-driven combusting flows of partial enclosure fires and (b) to help assess the fire hazards of different burning materials. The calculations provide the flow patterns and distributions of velocity, temperature, species concentration, and flame location in the flow. The model assumes steady laminar flow and makes use of the flame sheet approximation to describe the gas-phase chemical reaction. In corresponding experiments, photographic determinations of flame location were made. Two different cases were studied: (i) a fire occurring in a wall-ceiling configuration with variable pyrolyzing length (of PMMA material); and (ii) a partial enclosure fire with variable soffit and pyrolyzing lengths (the latter of PMMA or POM materials). Good agreement was obtained between measurements and calculations of the flame location for the first case. However, a significant discrepancy was found for the second case and is attributed to the neglect of turbulence and radiation transport in the model. Notwithstanding these limitations, it is found that a simple laminar flow model provides a correct qualitative description of the evolution of partial enclosure fires. For example, stratified (layered) motions, recirculation zones and the so-called "firewind" are correctly predicted as a function of pyrolysis and soffit lengths. The present approach, of incorporating physico-chemical parameters and boundary conditions of practical systems into a numerical model for assessing fire hazards, is very attractive due to its relative ease of execution. The accuracy of the numerical prediction approach can be improved by including radiation and turbulent transport.

1 Introduction

The development of fires and the assessment of fire hazards in partial enclosures are important problems in fire research. The study of fire behavior provides useful information for the design of transportation vehicles and buildings, the implementation of improved flammability tests of new materials, and for fire prevention. Mathematical models of fires in enclosures can provide an effective supplement to large-scale fire testing. The growing interest in mathematical models for assessing potential fire hazards is reflected in excellent surveys on the topic by Emmons [1, 2], Kawagoe [3], Thomas [4], Friedman [5], and Hathaway [6].

There are at least two different approaches to the mathematical modeling of the behavior of an enclosure fire: zone (control-volume) models, and field (partial differential equation) models. The zone model divides a compartment into control volumes of different but uniform properties which are interrelated by means of heat and mass fluxes across their respective boundaries. While this approach provides relative computational simplicity, it requires fairly arbitrary assumptions for specifying the heat and mass generation rates, the behavior of each zone, and the exchanges between zones. Notable examples of this type of mathematical modeling are the works of Reeves and MacArthur [7], Quintiere et al. [8, 9], Tanaka [10, 11], Emmons et al. [12, 13], Zukoski and Kubota [14], and Pape and Waterman [15, 16].

To date, the field model approach has received considerably less attention. This is probably due to the lack of a full understanding of turbulent combustion combined with the need for large computer storage and time requirements for performing calculations. The mathematical analysis actually solves, by numerical methods, the partial differential conservation equations that describe the gas and solid phase behavior during the development of a fire. In principle, this approach can provide an accurate and detailed description of the velocity, temperature, and species concentration distributions in an enclosure. Among the few studies using field model approaches are the works of Ku et al. [17], Hasemi [18], Matsushima and Yoshimura [19], and Baum et al. [20, 21]. All these analyses consider a nonreacting gaseous flow. The actual combustion process in an enclosure configuration is simulated in the models by specifying spacially distributed heat sources from which are calculated the detailed time-dependent velocity and temperature fields.

The present work uses the field model approach to predict the behavior of a fully developed fire in a partial enclosure. By fully developed fire, we mean that the fire and its associated flow have reached a steady state governed by the appropriate boundary conditions. In some respects, the model is similar to that of Ku et al. [17], but the present analysis considers the actual burning of a fuel surface as the source of the fire and, therefore, does not require making arbitrary assumptions concerning the nature of the fire. For purposes of simplifying the calculations, and as a first step towards a more accurate prediction of large compartment fires, it is assumed here that the flow is laminar, two-dimensional and that the chemical reaction rate is infinitely fast. Radiation from the flame and the enclosure walls is neglected. Therefore, the model is only applicable to small-scale fires and for conditions removed from extinction.

In parallel with the numerical model development, experiments were performed to measure flame location in two basic fire configurations. Comparisons between measured and predicted flame locations show very encouraging agreement.

2 Experiment

Experimental measurements of the flame location were performed for two different small-scale configurations. These correspond respectively to: (*i*) a wall-ceiling fire and (*ii*) a partial enclosure or compartment fire. Schematic diagrams of these configurations are respectively given in Figs. 1(*a*) and 1(*b*). The floor, vertical wall, and ceiling were constructed of

Contributed by the Heat Transfer Division for publication in the JOURNAL OF HEAT TRANSFER. Manuscript received by the Heat Transfer Division October 8, 1982.

Marinite 2.54-cm thick, 16-cm deep, and with cross-sectional lengths as indicated in the figures. Pyrex windows were installed on both sides of the test section to permit optical access to the interior of the enclosure while containing the flow. The combustible material consisted of a slab of Polymethylmethacrylate (PMMA) 1.27-cm thick and 15-cm deep embedded in the Marinite. The PMMA slab was positoned on the vertical wall with its lower edge 18 cm from the ceiling and protruding slightly from the Marinite surface to compensate for the regression of the fuel surface while it attained steady burning state. The height, X_P, of the PMMA was a variable in order to investigate the dependence of the flame location on the length of the pyrolyzing material.

In the wall-ceiling configuration the vertical Marinite wall was extended 0.2 m past the PMMA sample, to allow for the smooth entrainment of air from below. An insulated wall placed at the outer edge of the ceiling was used to guide the combustion products up and way from the burning zone. In the partial enclosure configuration, the floor was extended horizontally outwards from the compartment opening. The soffit, made of cement-asbestos material 0.3-cm thick, extended vertically upwards a distance of 10-cm from the ceiling edge. These dimensional characteristics were chosen since they are particularly convenient for experimentation and relatively simple to model numerically.

Flame location measurements were made in the wall-ceiling configuration for pyrolyzing lengths varying from X_P = 1-cm to X_P = 38-cm. This last case corresponds to burning of both the vertical and ceilng surfaces. For the compartment fire, tests were made with a single pyrolyzing length of 7-cm and a soffit 10-cm high. The PMMA samples were ignited as uniformly and quickly as possible with a propane torch. Frontal visualization of the developing flame envelope, and of convected soot particles, revealed a flow of predominantly two-dimensional spanwise characteristics in the center 2/3 of the test section.

The fuel burning process was presumed to have reached steady state when visual observations confirmed an unchanged mean flame location with time. At this point, between 10 to 20 photographs were taken at intervals of 2 s to determine the mean flame shape from its luminous boundary. Variations in flame location were also obtained from the photographs and are shown as tolerance bars on the profiles to be discussed in section 4. In the experiments, ASA 400 Kodak Tri-X film and a Nikon FM camera were used. The shutter speed was set to 1/30 s for an f/4 aperture setting. Photographs were taken of the flame against a black background in a darkened room. While the photographic technique only allows an estimate of the true flame location, the results obtained were considered to be sufficiently accurate for the purpose of this study. Since photography records information from the luminous regions of the reaction zone, it is expected that the present results indicate flames that are shorter and closer to the fuel surface than in reality.

For both configurations, particularly at the ceiling surface, it was observed that the luminous boundary fluctuated randomly due to combined turbulent and buoyant effects. In addition, nonturbulent, low-frequency oscillations driven by gravitational effects may have been present in the compartment configuration because of the possibility of both stably and unstably stratified gases trapped by the soffit at the top of the compartment. The unstable condition arises when the ceiling is cooler than the combusting mixture. The experimental results are discussed together with the calculations in section 4.

3 Model Formulation

The analysis consider the steady burning of a combustible surface that forms part of the walls of the partial enclosures shown in Figs. 1(*a*) and 1(*b*), respectively. The rest of the enclosure surfaces are prescribed as noncombustible and nonconducting. Because of the present unavailability of a model capable of simulating accurately the buoyancy-affected

Nomenclature

b_T = energy-species coupling variable, $-h/Q - Y_o/\nu'_o M_o$
b_{Tw} = b_T at pyrolyzing fuel surface
b_s = species coupling variable, $Y_F/\nu'_F M_F - Y_o/\nu'_o M_o$
b_{sw} = b_s at pyrolyzing fuel surface
B = mass transfer number, $(Q\ Y_{o\infty}/\nu'_o M_o - h_w)/L_v$
C_P = specific heat, [KJ kg^{-1}K^{-1}]
$\mathfrak{D}$ = species diffusivity, [m^2 s^{-1}]
D_c = dimensionless heat of combustion, $(Q\ Y_{o\infty}/\nu'_o M_o\ h_w)$
f = normalized Shvab-Zeldovich function, $(b_T - b_{T\infty})/(b_{Tw} - b_{T\infty}) = (b_s - b_{s\infty})/(b_{sw} - b_{s\infty})$
g = gravitational acceleration, [m s^{-2}]
Gr = Grashof number, $\rho_l{}^2 g H^3 (T_f - T_\infty)/\mu_f{}^2 T_f$
H = specific enthalpy, [KJ kg^{-1}]
h_c = heat transfer coefficient, [W m^{-2} K^{-1}]
h = height of open cavity
L_v = effective latent heat of pyrolysis, [KJ kg^{-1}]
L = width of open cavity
$\dot{m}_i'''$ = volumetric mass generation rate, [kg s^{-1} m^{-3}]
$\dot{m}''$ = rate of fuel gasification, [kg s^{-1} m^{-2}]
n = coordinate direction normal to a surface
M_i = molecular weight of species i, [kg mol^{-1}]
Pr = Prandtl number, $C_P\mu/\lambda$
P = pressure [atm]
$\dot{q}'''$ = volumetric heat generation rate, [KJ s^{-1} m^{-3}]
Q = heat of combustion per ν'_F moles of fuel consumed [KJ mol^{-1}]
r = mass consumption number, $Y_{o\infty}\nu'_F M_F/Y_{FW}\nu'_o M_o$
R = gas content, [KJ kg^{-1} K^{-1}]
T = temperature, [K]
T_v = pyrolysis temperature of combustible material [K]
U = velocity vector, [m s^{-1}]
U = velocity component of gas mixture in the x-direction, [m s^{-1}]
V = velocity component of gas mixture in the y-direction, [m s^{-1}]
x = coordinate along the vertical wall, [m]
X_P = length of pyrolysis region, [m]
X_s = length of soffit, [m]
y = coordinate along the ceilng, [m]
Y_i = mass fraction of species i

Greek Symbols

Γ = transport coefficient in difference equation, [kg m^{-1} s^{-1}], $\Gamma = \lambda/C_P$
λ = thermal conductivity of the gas, [KJ s^{-1} m^{-1} K^{-1}]
μ = dynamic viscosity, [kg s^{-1} m^{-1}]
ν' = stoichiometric coefficient of reactant
ν'' = stoichiometric coefficient of product
ρ = mixture density, [kg m^{-3}]

Subscripts

f = film
fl = flame
F = fuel
i = species
I = inert
O = oxidant
P = product
R = reference conditions
W = wall conditions
∞ = ambient value

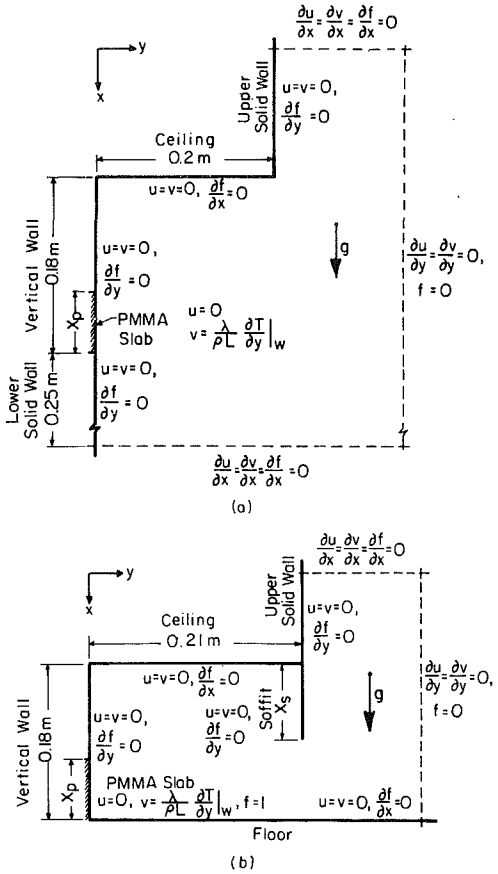

Fig. 1 Schematic diagram of fire configuration showing dimensions and boundary conditions: (a) wall-ceiling; (b) partial enclosure or compartment

turbulent diffusion processes arising in the configurations of interest, emphasis has been placed here on deriving useful numerical results for the laminar regime. Thus, for the steady, two-dimensional, laminar, nonradiative, buoyant flow of a combusting perfect gas mixture, the transport equations describing the idealized problem are as given by, for example, Pagni [22]

continuity
$$\nabla \cdot (\rho \mathbf{u}) = 0 \tag{1}$$

momentum
$$\rho \mathbf{u} \cdot \nabla \mathbf{u} = -\nabla (P - P_\infty) + \mathbf{g}(\rho - \rho_\infty) + \nabla \cdot (\mu \nabla \mathbf{u}) \tag{2}$$

energy
$$\rho \mathbf{u} \cdot \nabla h = \nabla \cdot \left(\frac{\lambda}{C_P} \nabla h \right) + \dot{q}''' \tag{3}$$

species
$$\rho \mathbf{u} \cdot \nabla Y_i = \nabla \cdot (\rho \mathfrak{D} \nabla Y_i) + \dot{m}_i''' \tag{4}$$

In equation (4) the subscript, i, stands for: fuel (F), oxidant (O), product (P) and inert (I). By assuming that a one-step chemical reaction takes place, it follows

$$\nu_F' F + \nu_O' O \rightarrow \nu_P'' P(+Q) \tag{5}$$

This relation provides the following equality between mass consumption and heat generation

$$\frac{-\dot{m}_F'''}{\nu_F' M_F} = \frac{-\dot{m}_o'''}{\nu_o' M_o} = \frac{\dot{q}'''}{Q} \tag{6}$$

The equation of state for the gas phase is

$$P = \rho R T \tag{7}$$

The above seven equations are the governing equations for the system.

Boundary conditions are needed to complete the specification of the model. At the pyrolyzing surface, energy and species conservation are given by

$$\dot{m}'' L_v = \lambda \left(\frac{\partial T}{\partial y} \right)_w \tag{8}$$

$$(\rho V)_w = (\rho V)_w Y_{Fw} - \left(\rho \mathfrak{D} \frac{\partial Y_F}{\partial y} \right)_w \tag{9}$$

$$(\rho V)_w Y_{iw} = \left(\rho \mathfrak{D} \frac{\partial Y_i}{\partial y} \right)_w \tag{10}$$

Also required are: the constant and known pyrolysis temperature of the fuel $(T)_w = T_v$; the no-slip condition $(U)_w = 0$ for velocity; and mass conservation $\dot{m}'' = (\rho V)_w$. The noncombustible surfaces are considered to be adiabatic to the transport of mass and heat, i.e., $U = 0$, $V = 0$, $\partial Y_i/\partial n = 0$, $\partial T/\partial n = 0$.

The source terms $\dot{q}'''$ and $\dot{m}_i'''$ can be eliminated from the energy equation (3) and the species equation (4) by defining the following Shvab-Zeldovich functions

$$b_T = -\frac{h}{Q} - \frac{Y_o}{\nu_o' M_o}, \quad b_s = \frac{Y_F}{\nu_F' M_F} - \frac{Y_o}{\nu_o' M_o} \tag{11}$$

Equations (3) and (4) then reduce to

$$\rho \mathbf{u} \cdot \nabla f = \nabla \cdot \left(\frac{\lambda}{C_P} \nabla f \right) \tag{12}$$

where f is the normalized Shvab-Zeldovich function defined as

$$f \equiv \frac{b_T - b_{T\infty}}{b_{Tw} - b_{T\infty}} \equiv \frac{b_s - b_{s\infty}}{b_{sw} - b_{s\infty}} \tag{13}$$

The boundary conditions for equation (13) becomes $f = 1$ at the pyrolyzing fuel surface, $\partial f/\partial n = 0$ at the noncombustible surfaces and $f = 0$ at the ambient surroundings. The variable f is a conserved scalar quantity in the flow field.

Far-field boundary conditions for the velocity components and for f were imposed by setting

$$\frac{\partial (U, V, f)}{\partial n} = 0 \tag{14}$$

along imaginary surfaces enclosing the calculation domains as shown in Figs. 1(a) and 1(b). The use of this type of boundary condition for velocity in the cavity configuration has been discussed by LeQuere et al. [23] and compares favorably with a more rigorous boundary condition specification investigated by them. However, these authors also found, and subsequent experiments by Humphrey et al. [24] have verified, that the flow inside a strongly heated cavity is determined principally by local heat transfer events and is fairly insensitive to perturbations in the far-field boundary values of the velocity components.

Under the flame sheet approximation, both the fuel vapor and the oxidizer vanish at the flame. Thus, the value of f at the flame location becomes $f_{fl} = r/(1 + r)$ where r is the mass consumption number [22], $r = Y_{o\infty} \nu'_F M_F / (Y_{FW} \nu'_o M_o)$. The value of $f = f_{fl}$ indicates the position of the flame in the flow field.

The set of partial differential equations (1), (2), and (12) with their boundary conditions was solved numerically using the REBUFFS code described by LeQuere et al. [23]. This numerical scheme solves time dependent variable property laminar flows without invoking the Boussinesq approximation. High frequency pressure oscillations are not resolved due to the neglect of spacial variations of pressure and of dissipation in the energy equation. This was not a limitation for the present study.

In this work, the REBUFFS code was adapted and extended to consider the existence of a pyrolyzing surface and of a gas phase reaction. Because details relating to the formulation of the finite difference equations and to features of the numerical algorithm are provided in [23], only a brief summary is given here. Computations are carried out on a staggered nonuniform grid. Once the coefficients for the

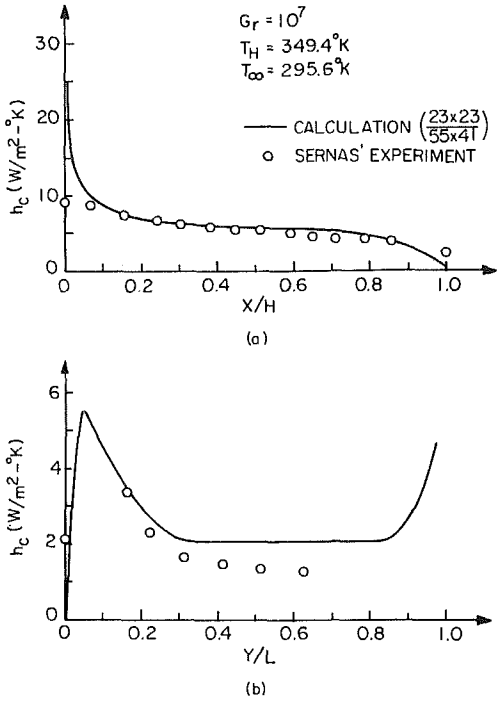

Fig. 2 Comparison of predicted and measured [27] local heat transfer coefficients along: (*a*) inner vertical wall; (*b*) ceiling

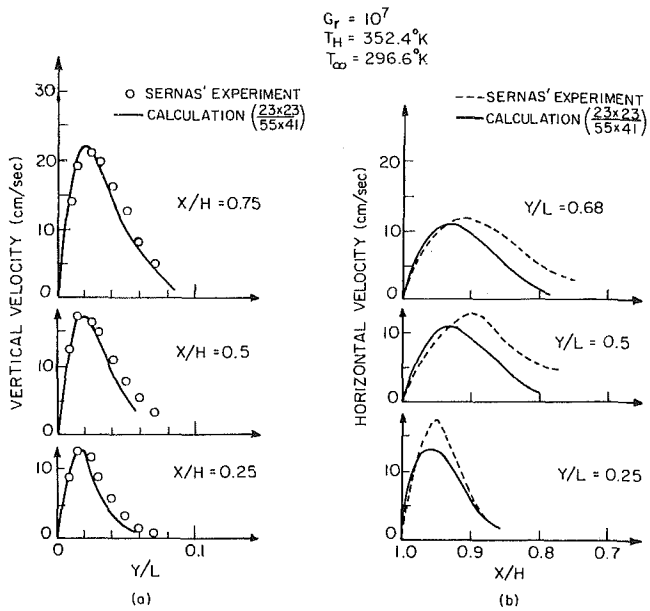

Fig. 3 Comparison of predicted and measured [27] velocity profiles along: (*a*) inner vertical wall; (*b*) ceiling

finite difference equations have been evaluated for each cell in the calculation domain, a line-by-line procedure using the tri-diagonal matrix algorithm solves iteratively for U,V,P, and f. The pressure is calculated by means of the SIMPLE algorithm [23] by solving a Poisson-type equation for pressure. At every iteration, the coefficients at each node in the grid and the physical properties are updated, the residual sources (denoting imbalances) of the dependent variables are checked, and iteration is continued until a predetermined convergence criterion is met. The blowing velocity along the pyrolyzing surface is guessed initially. It is checked every iteration and recomputed from the surface energy balance given by equation (8), until the relative change in its value between consecutive iterations is less than 10^{-4}. Because the Boussinesq approximation is not used in the analysis, the viscosity of the mixture is calculated from a formula suggested by Reichenberg [25] based on the value for nitrogen at a reference temperature $T_R = (T_{fl} + T_\infty)/2$. Other properties of the mixture are obtained by fixing the Prandtl number to Pr = 0.7 and the specific heat to $C_P = 1.25$ KJ/kg-K. The data used for PMMA in the computations were: $T_v = 663$ K, $L_v = 1.59 \times 10^3$ kJ/Kg, $B = 1.7$, $D_c = 6.45$ and $r = 0.22$ [22].

The present calculations were performed using the HYBRID differencing scheme. This scheme combines the stability of upwind differencing (for a cell Peclet number larger than 2) with the accuracy of central differencing (for a cell Peclet number less than 2). Central differencing is used for all diffusion terms. While, globally, the scheme is only first-order accurate, it is robust and has been used successfully to predict high-temperature, buoyancy-driven flows in partial enclosures [23, 26]. Calculations on several grids were performed to establish the level of refinement required for essentially grid-independent results. These were found to correspond to (x, y) grids of (54, 41) nodes in Case 1, and (62, 55) nodes in Case 2. The finer grid required by Case 2 was due to the more complex spacial variation of the flow, induced by the presence of a soffit. All of the calcuations were performed on the CDC 7600 machine at the Lawrence Berkeley Laboratory. Typical calculation time and storage requirements for Case 2 using a (62, 55) grid were 700 CPU s and 149 k_8 words, respectively. About 400 iterations, with an average of three sweeps per calculated variable, were required to meet the convergence criterion; this was that the largest of the normalized residual sources for momentum, energy, or mass should be less than 10^{-3}.

Among the early tests perfomed with the calculation procedure was the establishment of appropriate locations for the far-field boundaries (the imaginary planes). Numerical experimentation showed that the partial enclosure flow characteristics were fairly insensitive to the position of the far-field boundaries as long as they were located approximately two ceiling widths away from the configuration openings.

Prior to performing the calculations of interest, the numerical scheme was tested with respect to the experimental study of Sernas and Kyriakides [27]. These authors measured the steady flow and heat transfer characteristics in a two-dimensional cavity in which the bottom wall was kept at ambient temperature ($T_\infty \simeq 296$ K) with the back wall and ceiling maintained at $T_H \simeq 350$ K. The Grashof number in their experiment was Gr $\simeq 10^7$ based on a film temperature for air of $T_f \simeq 323$ K. Figures 2 and 3 show comparisons between measured and predicted profiles of the heat transfer coefficient and of the velocity components at various positions in the cavity. In general, the agreement between measurements and calculations is very good. The discrepancies observed in Fig. 3(*b*) are partly due to unquantified errors present in the horizontal velocity component measurements [28], and to the coarseness of the grid used within the cavity for these predictions (23, 23). However, the good agreement found for the vertical component of velocity suggests that the experimental error may have been principally responsible for the discrepancies shown in Fig. 3(*b*). Further grid refinement was deemed to be unnecessary for concluding that the numerical scheme had been adequately and successfully tested, for nonisothermal flow, especially with respect to a suitable implementation of the far field boundary conditions. Predictions of constant temperature contours and of the vector velocity field for this test case (not shown here) revealed a marked qualitative resemblance with the wall-ceiling burning configuration subsequently predicted.

4 Results and Discussion

The numerical procedure, extended as discussed above, was

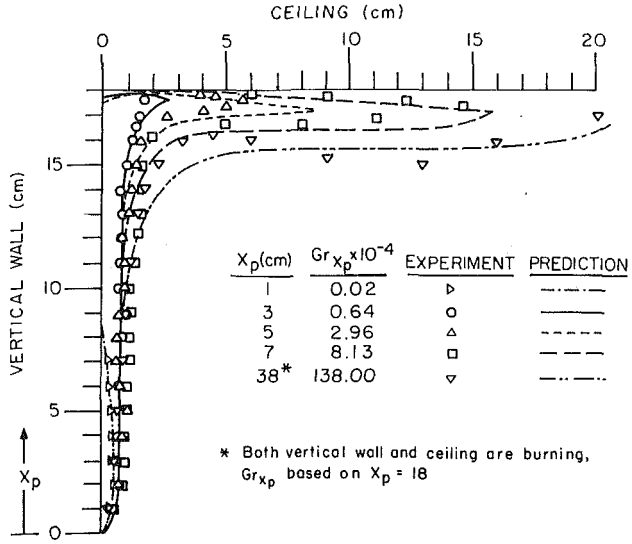

Fig. 4 Comparison between measured and computed flame locations for the vertical wall-ceiling configuration

applied to the calculation of the velocity and normalized Shvab-Zeldovich function distributions for PMMA burning surfaces with different lengths arranged in a vertical wall-ceiling configuration and in a compartment configuration. For the latter configuration a POM burning surface was also investigated. A discussion of the numerical predictions and of their comparisons with the experimental measurements follows below.

4.1 Wall-Ceiling Fire Results. Figure 4 shows a comparison between measured and computed flame locations in the case of vertical wall-ceiling configurations with different pyrolyzing lengths. In general, the agreement is quite good, although the laminar model tends to overpredict the length of the flame. That the length of the flame increases with pyrolyzing length, X_P, should be expected from the results of [22]. For $X_P \sim 3$ cm, the flame tip reaches the ceiling. For longer pyrolysis lengths the flame partially covers the ceiling, attaining its maximum forward distance displaced from the ceiling surface. THis is contrast with the case where the flame is adjacent and limited to the vertical surface, for which the flame tip is located at the wall. The reason for the flame overshoot in the ceiling region appears to be related to the existence of a recirculation region at the wall-ceiling corner (Figs. 5(*a*) and 5(*b*)) that removes fuel vapor from the ceiling surface. This fuel vapor is returned to the main flow stream, giving rise to a concentration distribution with the maximum displaced from the ceiling surface and of the same shape as the horizontal velocity profile. Whereas wall-quenching of the combustion process would also work to displace the flame tip from the ceiling, such an effect cannot be predicted by the present model.

In order to display more clearly the calculated flame structure and its associated flow patterns, a typical steady velocity field and constant f profiles for a fixed pyrolyzing length of 7 cm are shown in Figs. 5(*a*) and 5(*b*), respectively. For $X_P >$ cm, a corner recirculation zone was experimentally confirmed by the presence of heavy soot deposition on the Pyrex walls and the fact that the fuel, for this configuration, did not pyrolyze in the top corner region. The recirculation zone was about 1-cm long along the ceiling and about 3-cm long along the vertical wall. The predictions show that after the flow impinges on and is deflected by the ceiling, it turns into a strong ceiling jet. Although the flow in the center region of the wall-ceiling configuration is essentially stagnant, air is actually being entrained through the bottom free-stream boundary. The predicted blowing velocity decreases weakly

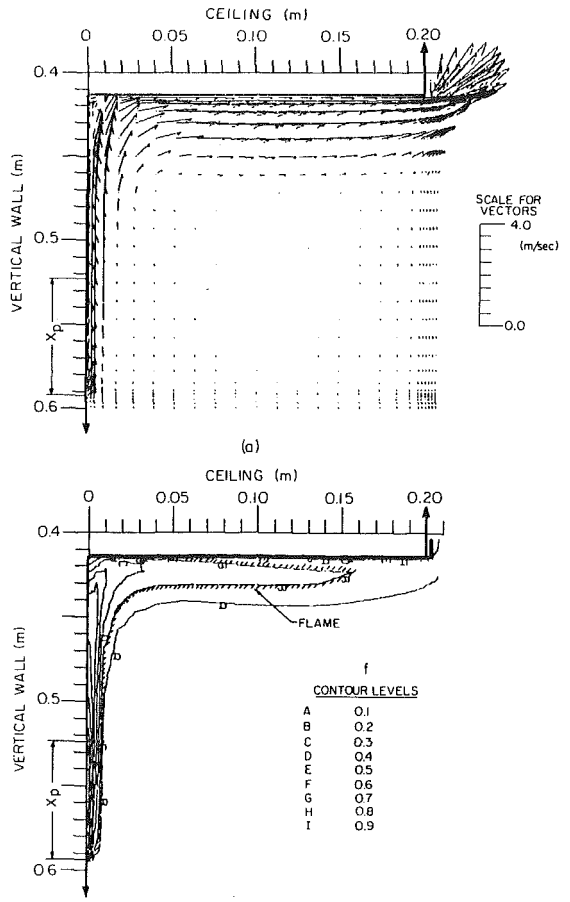

Fig. 5 Vertical wall-ceiling predictions for a PMMA fire with a pyrolyzing length of 7 cm: (*a*) vector velocity field; (*b*) constant *f* profiles and flame location

along the length of the pyrolyzing surface. This is in agreement with theoretical predictions of burning rates in laminar boundary layer flows [22]. The appearance in Fig. 5(*a*) of finite nonzero velocity components on the far-field boundaries is due to having used a residual convergence criterion of 10^{-3} as opposed to a smaller number. Relative to the magnitude of the buoyancy-driven flow, it is clear that the free boundary values are negligibly small.

In Fig. 5(*b*) the hatched profile indicates the predicted flame location. Under the flame sheet approximation, the variable f (equation (13)) is proportional to the temperature or the fuel concentration in the region between the surface and the flame. Therefore, f-contour lines in this region can be viewed either as isotherms or as lines of constant fuel concentration. Between the flame location and ambient, the f-contour lines represent constant concentration oxygen profiles. The distribution of excess fuel vapor convected away from the pyrolyzing region can be found from the f profiles. The shapes of the constant f profiles show clearly the effect of the recirculating flow in the corner region of this configuration.

In general, the laminar flow model adequately predicts the flame shape of the wall-ceiling configuration at least for the present small-scale experiment. This success may be partly due to the lack of a pronounced turbulence activity, a fact supported by the experiments conducted for this case. For large-scale fires, it is expected that turbulence and radiation will be more important [29], thus reducing the predicting capabilities of the present model.

4.2 Small-Scale Partial Enclosure Fire. In this section, three sets of computations were carried out for: (*i*) comparison with measurements of the flame location and

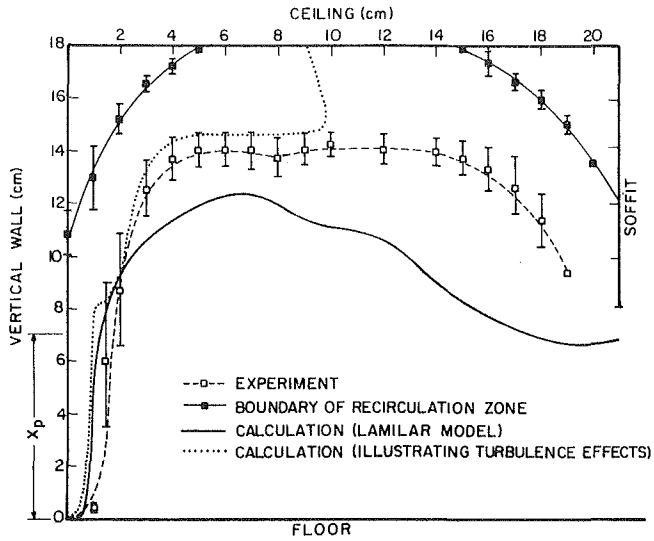

Fig. 6 Comparison between measured and predicted flame locations in a partial enclosure PMMA fire with a pyrolyzing length of 7 cm and a soffit length of 10 cm

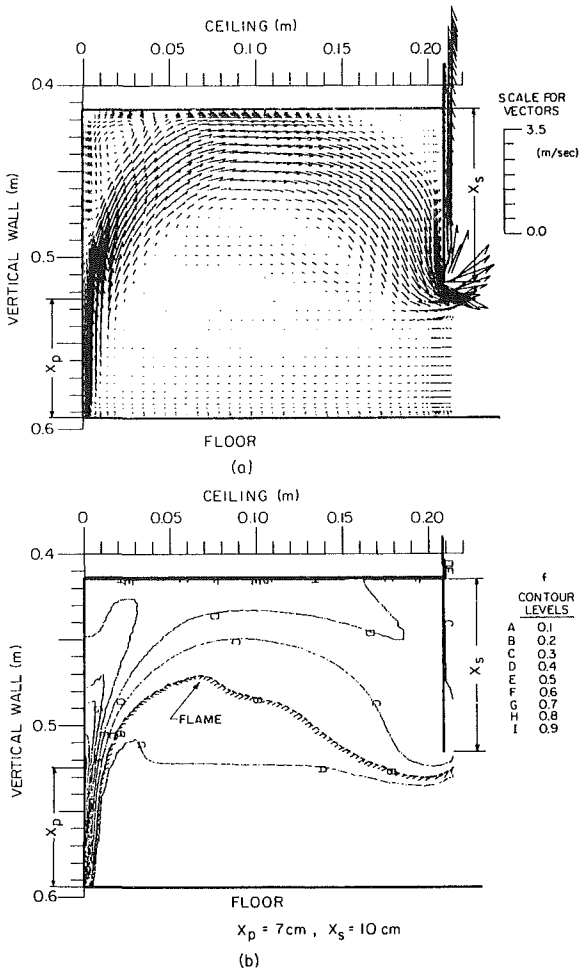

Fig. 7 Partial enclosure predictions for a PMMA fire with a pyrolyzing length of 7 cm and a soffit length of 10 cm: (*a*) vector velocity field; (*b*) constant *f* profiles and flame location

recirculation zone; (*ii*) checking the influence of pyrolyzing and soffit lengths on the flame structure; (*iii*) estimating potential fire hazards with different burning materials. Figure 6 provides a comparison between measurements and calculations of flame location in a partial enclosure with a pyrolyzing length of X_P = 7 cm and a soffit length of X_s = 10 cm. The blank squares drawn in the figure show the measured flame location. The bars on these points denote the range of possible positions of the flame front as it oscillated in the vertical direction. The dark squares indicate experimentally determined approximate boundaries (dividing streamlines) separating the corner recirculation zones from the rest of the flow in the compartment. The solid line is the calculated flame position. The calculation overestimates the flame length as well as the flame location by a factor of 1.5 to 2. The flame is predicted to extend outside the compartment. However, in the experiment the flame was observed to reach just to the bottom edge of the soffit. The computed velocity field and constant *f* profiles for this case are shown in Figs. 7(*a*) and 7(*b*). The velocity field shows a layer of inflow and another of outflow at the enclosure aperture plane. However, in the interior of the enclosure a four-layer structure of alternating flow directions is observed of which the two central layers are very weak. These results are similar to those reported in the work of Ku et al. [17]. It is shown below that the strength and sense of flow in the stratified layers depend on the lengths of the pyrolyzing surface and soffit and on the burning material properties. The unsteadiness observed in the experiments was probably due to the tendency to stable stratification of hot gases in the compartment. Two recirculation zones were predicted at the compartment top corners. Their size and shape were consistent with the corresponding regions visualized in the experiments. In Fig. 7(*b*), the flame has moved farther away from the ceiling relative to the case shown in Fig. 5(*b*), due to the substantial change in flow structure induced by the soffit. The burning rate is also smaller, because the heat flux from the flame to the compartment surfaces is less in the partial enclosure fire.

The discrepancies between measurements and predictions of the foregoing case (Fig. 6) are attributed primarily to buoyancy affected turbulent diffusion and radiation feedback from the compartment walls, which were not modeled. Turbulent mixing will cause the flame to become shorter and will move its location closer to the ceiling. In contrast, for the vertical wall-ceiling case the absence of a soffit precludes stratification of the flow and of associated low-frequency internal waves, which helps stabilize the flame on the ceiling. Radiation transport between walls is small due to the large opening in this configuration. Furthermore, for the wall-ceiling fire there is an ample supply of air which results in a more complete combustion and less soot formation in the vicinity of the flame.

The influence of turbulence in the compartment fire was demonstrated qualitatively by increasing by a factor of 100 the transport property $\Gamma = \lambda/C_P = \rho\mathfrak{D}$ for species and heat in the near-wall flow region, along the periphery of the vertical wall-ceiling-soffit. The choice of enhancing diffusion in the peripheral wall-region only was not arbitrary, it recognizes the importance of wall-induced turbulence in confined flows. As shown in Fig. 6, the flame becomes considerably shorter and moves closer to the ceiling as a consequence of the enhanced diffusion.

To analyze the effect of pyrolysis length on the flow structure and flame location in a compartment, the case of a pyrolysis length of X_P = 13 cm and a soffit length of X_s = 10 cm was calculated for comparison with the previous case. From the predicted velocity field presented in Fig. 8(*a*), it is seen that the flow structure is different from that of Fig. 7(*a*). In this case, the velocity field exhibits only a two layer structure but the recirculating corner flow has been strengthened substantially and enlarged. It is observed that part of the pyrolyzing region is covered by the recirculating flow. The predicted blowing velocity decreases along the vertical wall, reaching a minimum value, and subsequently increases at the top end of the pyrolyzing region. The variation is explained by the return of hot gas, trapped in the

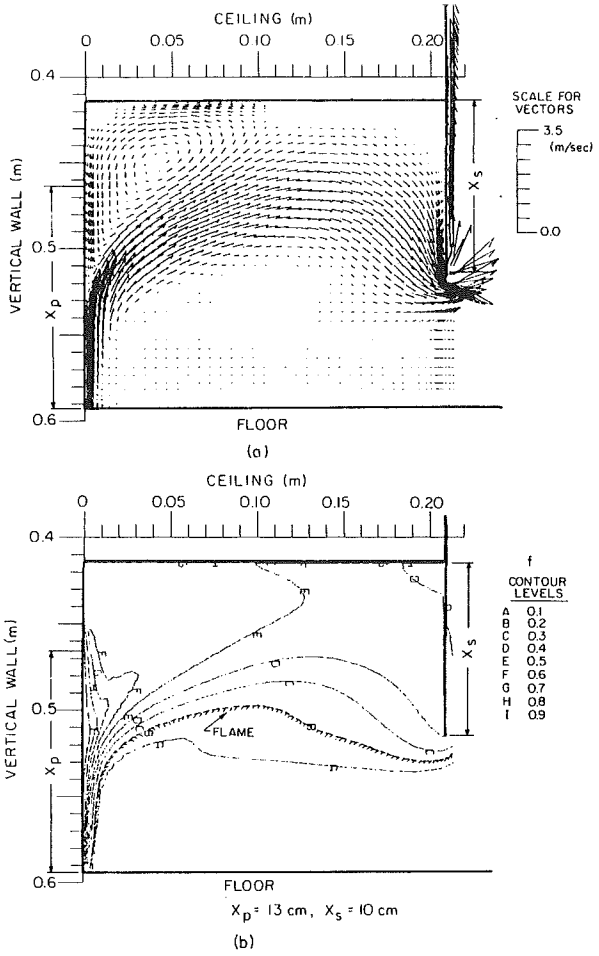

Fig. 8 Partial enclosure predictions for a PMMA fire with a pyrolyzing length of 13 cm and a soffit length of 10 cm: (*a*) vector velocity field; (*b*) constant *f* profiles and flame location

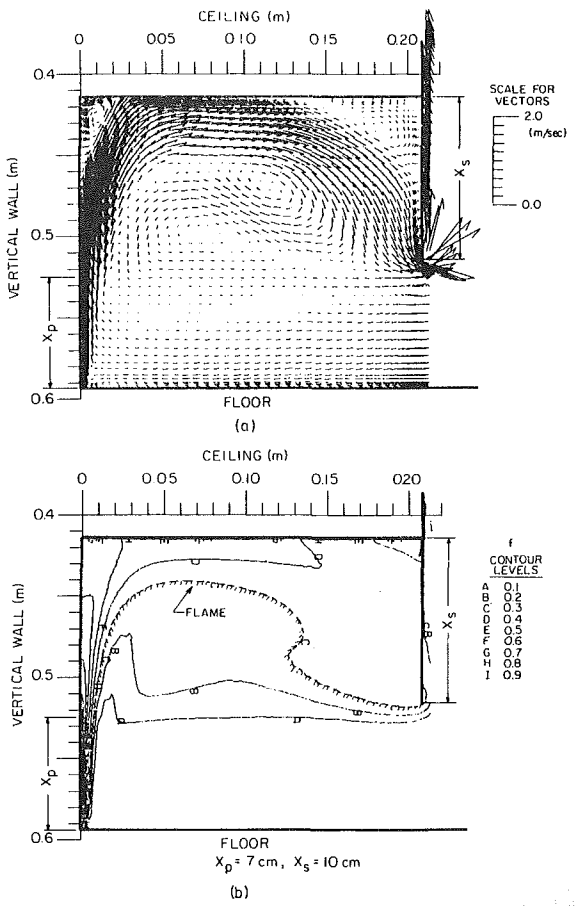

Fig. 9 Partial enclosure predictions for a POM fire with a pyrolyzing length of 7 cm and a soffit length of 10 cm: (*a*) vector velocity field; (*b*) constant *f* profiles and flame location

recirculating corner flow, along the side wall of the compartment. The minimum blowing velocity occurred at the position on the side wall where the upward flow collides with the downward recirculating flow. At this position the flame is observed to have a rather large turning angle. Figure 8(*b*) shows the constant *f* profiles. A large amount of fuel vapor has gathered beneath the ceiling and the flame location is displaced closer to the floor. This has the effect of reducing the amount of fresh air entering the compartment. Further increases in the length of burning material should eventually choke the fire, leading to a situation of fuel rich vapor trapped in the partial enclosure. As discussed below, this situation is altered simply by reducing the length of the soffit.

To study the effect of soffit length on the fire behavior, a case with a pyrolysis length of 13 cm and a soffit length of 3 cm was calculated for comparison with the case presented in Fig. 8. The results obtained (not shown here but available in [30]) show that a short soffit results in a velocity field with a three-layer structure; two layers of outflow near the floor and ceiling, respectively, and one of inflow in the middle. The weak floor-jet appears to be the result of the strong "fire wind" [17] predicted for this case. The inward motion of the middle layer of air, which is finally entrained by the vertical flame, pushes part of the air toward the floor, thus inducing a recirculation region that drives the bottom outflow layer. The upper corner recirculation regions are very small in this case. A comparison between flame locations for these two cases showed that the flame is much higher and removed from the floor in the case of the shorter soffit.

To investigate the connection between the properties of the fuel and the dynamic behavior of flames in partial enclosure fires, calculations were made using Polyoxymethylene (POM) as the combustible material. The predictions were performed for the same conditions as those calculated in Figs. 7(*a*) and 7(*b*) for PMMA. The data for POM used in the calculation are: T_v = 585 K, L_v = 2.43 × 10^3 KJ/kg, B = 1.22, D_c = 9.0 and r = 0.48 [22]. The velocity field for a POM compartment fire with a pyrolysis length of 7 cm and a soffit length of 10 cm is shown in Fig. 9(*a*). While the flow structure is quite similar between the PMMA fire and the POM fire, a comparison with Fig. 7(*a*) shows that the two vortices in the center region of the compartment are stronger in the case of the POM fire. These vortices tend to keep the gaseous flow closer to the solid surfaces and to reduce the amount of gases escaping through the compartment opening. Constant *f* contours for the POM fire are shown in Fig. 9(*b*). The hatched profile delineates the location of the flame. It is seen that in this case the flame is rolled backward by the top vortex, is closer to the compartment ceiling, and does not emerge through the compartment opening as was predicted for the PMMA fire. From the fire safety standpoint, this suggests that a POM fire is less dangerous than a PMMA fire for the configuration tested.

The prediction that the POM flame size is smaller and the fire less hazardous is in agreement with the calculations of Pagni [22] for flame heights on vertical walls. In that work, it was concluded that the parameter, r, was critical in determining the flame height and consequently the potential hazard of the fire; small r implies large hazard. PMMA has a smaller r than POM, and as predicted here, appears to be a more hazardous material than POM.

Velocity profiles at the enclosure aperture have been plotted in [30] for all the cases reported above. A comparison among the velocity profiles showed that, contrary to what might be

expected, for equal soffit length the inward flow rate to the enclosure is smaller for the case of longer pyrolysis length. This is primarily because a larger recirculation zone arises for the case with longer pyrolysis length, resulting in a shorter flame and, consequently, in smaller amounts of fuel and oxidizer consumed. Inspection of the profiles showed that the soffit length is a determining factor for the existence of two or three flow layers at the enclosure opening. Increasing the length of the soffit reduced the number of aperture plane flow layers. It was also found that, in spite of POM having a larger stoichiometric ratio than PMMA, the incoming air flow rate was larger for the POM case than for the corresponding PMMA case. This is the result of the longer flame length predicted for the POM case (Fig. 9). The lower average temperature of the exhaust gases for POM explains the smaller outgoing volumetric flow rate observed for this case in comparison with the PMMA case. Checks for the balance of mass at the aperature plane showed that it was within 1 percent for all calculated cases.

5 Conclusions

The numerical model proposed provides a basis for describing the steady burning of surfaces in small-scale partial enclosure fires. In principle, the possibility of changing physico-chemical parameters and of including different and relatively arbitrary boundary conditions make the numerical model a highly flexible tool for assessing the fire hazard potential of different combustible materials. The inclusion of time dependence and fully enclosed compartment boundary conditions constitute fairly straightforward modifications to the model.

The numerical model has been successfully tested by reference to an experimentally documented nonisothermal flow of similar characteristics to the two configurations analyzed here. Laminar regime calculations of the steady burning of surfaces in a partial enclosure have yielded good predictions of flame location for the wall-ceiling fire and acceptable results for the partial enclosure fire. In practice, buoyancy affected turbulence and radiation transport are influential in determining the flame shape and flow structure. Neither of these two effects has been accounted for in the present calculations, leading to a predicted flame location for the compartment fire which is in error. Notwithstanding, significant physical insight has been gleaned from the present qualitative study of partial enclosure fires. The influence on fire behavior of pyrolyzing length, soffit length, and available ventilation areas have also been demonstrated.

The informatin provided by this investigation, and similar time-dependent information which can readily be predicted with the numerical model, should be of value to designers concerned with the problem of potential fire hazards and fire spread in compartments. However, improved predictions will require the inclusion of radiation, turbulent transport and solid phase heat conduction.

Acknoweldgments

Special thanks are due to Mr. W. M. To for the assistance provided in adapting the numerical scheme to the present problem. Discussions with Professor P. J. Pagni were of great value to the work. This research was supported by the National Bureau of Standards under Grant NB80NADA1064 awarded to A.C.F.P., and by Sandia National Laboratories through Contract No. 20-1012 awarded to J.A.C.H. The authors welcome the opportunity to express their appreciation for this support. Thanks are due to Ms. L. Donahue for the typing of this manuscript.

References

1 Emmons, H. W., "The Prediction of Fires In Buildings," *Proceedings of the Seventeenth Symposium (International) on Combustion*, The Combustion Institute, Pittsburgh, Pa. 1978, pp. 1101-1111.

2 Emmons, H. W., "The Growth of Fire Science," *Fire Safety Journal*, Vol. 3, 1980/81, pp. 95-106.

3 Kawagoe, K., "Recent Advances in Fire Physics in Japan," *Fire Safety Journal*, Vol. 3, 1980/81, pp. 149-162.

4 Thomas, P. H., "Fire Modeling and Fire Behavior in Rooms" *Proceedings of the Eighteenth Symposium (International) On Combustion*, The Combustion Institute, Pittsburgh, Pa., 1981, pp. 503-518.

5 Friedman, R., "Status of Mathematical Modeling of Fires," First Specialists Meeting (International) of the Combustion Institute, University of Bordeaux, France, LXXV, July 1981.

6 Hathaway, W. T., "Survey of Fire Modeling Efforts with Application to Transportation Vehicles," DOT Report No. DOT-TSC-OST-81-4, 1981.

7 Reeves, J. B., and MacArthur, C. D., "Dayton Aircraft Cabin Fire Model," *Vol. I-Basic Mathematical Model*, FAA Report No. FAA-RD-76-120, 1976.

8 Quintiere, J. G., "The Growth of Fire in Building Compartments," *Fire Standards and Safety*, ASTM-STP 614, 1977, pp. 131-167.

9 Quintiere, J. G., McCaffrey, B. J., and Den Braven, K., "Experimental and Theoretical Analysis of Quasi-Steady Small-Scale Enclosure Fires," *Proceedings of the Seventeenth Symposium (International) on Combustion*, The Combustion Institute, Pittsburgh, Pa. 1978, pp. 1125-1137.

10 Tanaka, T., "A Mathematical Model of a Compartment Fire," BRI Res. Paper No. 70, Building Research Institute, Japan, 1977.

11 Tanaka, T., "A Model of Fire Spread in Small Scale Buildings," BRI Res. Paper No. 84, Building Research Institute, Japan, 1980.

12 Emmons, H. W., Mitler, H. E., and Trefethen, L. N., "Computer Fire Code III, Harvard University Home Fire Project Technical Report No. 25, 1978.

13 Emmons, H. W., "The Calculation of Fire in a Large Building," Paper No. 81-HT-2, ASME 20th National Heat Transfer Conference, Milwaukee, Wis., 1981.

14 Zukoski, E. E., and Kubota, T., "A Computer Model for Fluid Dynamic Aspects of a Transient Fire in a Two Room Structure," California Institute of Technology, NBS Grant No. 5-9004, 1978.

15 Pape, R., and Waterman, T. E., "Understanding and Modeling Preflashover Compartment Fires," *Design of Buildings for Fire Safety*, ASTM STP 685, 1979, pp. 106-138.

16 Pape, R., "Preflashover Room Fire Model: Parametric Sensitivity Analysis and Development of a Submodel for Burning Furniture Items," NBS Report No. NBS-GCR-81-300, 1981.

17 Ku, A. C., Doria, M. L., and Lloyd, J. R., "Numerical Modeling of Unsteady Buoyant Flows Generated by Fire in a Corridor," *Proceedings of the Sixteenth Symposium (International) on Combustion*, The Combustion Institute, Pittsburgh, Pa., 1976, pp. 1373-1384.

18 Hasemi, Y., "Numerical Calculation of the Natural Convection in Fire Compartment," BRI Res. Paper No. 69, Building Research Institute, Japan, 1977.

19 Matsushima, O., and Yoshimura, M., "Numerical Experiment of Hot Layer Forming Process in Fire," Symposium on the Application of Computers to Building Science, Mar. 1980.

20 Baum, H., and Rehm, R. G., "Finite Difference Calculations of Buoyant Convection in an Enclosure, Part I: The Basic Algorithm," NBS Report NBSIR 81-2385, 1981.

21 Baum, H., Rehm, R. G., and Mulholland, G. W., "Computation of Fire Induced Flow and Smoke Coagulation," *Proceedings of the Nineteenth Symposium (International) on Combustion*, The Combustion Institute, Pittsburgh, Pa., 1982 (in press).

22 Pagni, P. J., "Diffusion Flame Analyses," *Fire Safety Journal*, Vol. 3, 1980/81, pp. 273-285.

23 LeQuere, P., Humphrey, J. A. C., and Sherman, F. S., "Numerical Calculation of Thermally Driven Two-Dimensional Unsteady Laminar Flow in Cavities of Rectangular Cross Section," *Numerical Heat Transfer*, Vol. 4, 1981, pp. 249-283.

24 Humphrey, J. A. C., Sherman, F. S., and Chen, K.-S., "Experimental Study of Free and Mixed Convective Flow of Air in a Heated Cavity," Final report (on experiments) to Sandia National Laboratories for Contract No. 20-1012; also available as Report No. FM-83-1, Department of Mechanical Engineering, University of California, Berkeley, 1983.

25 Reichenberg, D., DSC Report II, National Physical Laboratory, Teddington, England, Aug. 1971; also *AIChE Journal*, Vol. 19, 1973, pp. 854-856.

26 Humphrey, J. A. C., Sherman, F. S., Chen, K.-S., and To, W.-M., "Investigation of Free-Forced Convection Flows in Cavity-Type Receivers," Contract report pertaining to year two of research under Contract No. 20-1012, Sandia National Laboratories, July 1982.

27 Sernas, V., and Kyriakides, I., "Natural Convection in an Open Cavity," Vol. 2, *Proceedings of the Seventh International Heat Transfer Conference*, Munchen, West Germany, 1982, pp. 275-280.

28 Sernas, V., personal communication, July 1982.

29 DeRis, J., "Fire Radiation—A Review," *Proceedings of the Seventeenth Symposium (International) on Combustion*, The Combustion Institute, Pittsburgh, Pa., 1978, pp. 1003-1016.

30 Mao, C.-P., Fernandez-Pello, A. C., and Humphrey, J. A. C., "An Investigation of Steady Wall-Ceiling and Partial Enclosure Fires," Report No. FM-82-6, Mechanical Engineering Department, University of California, Berkeley, Calif., Aug. 1982.

Effect of Free-Stream Velocity Vector and Aspect Ratio on the Output of a Free-Standing Circular Disk Heat Flux Gage

M. F. Young
Department of Mechanical Engineering,
University of California,
Irvine, Calif. 92717
Mem. ASME

The effects of free-stream velocity, angle of attack, and aspect ratio on the output of a free-standing circular disk heat flux gage subjected to a combined radiative and convective heat flux are reported. The Reynolds number range investigated extends from 6000 to 25,000, while the gage angle of attack was varied from 0 to 90 deg. Results for three gage aspect ratios, 5.85, 8.77, and 11.76, are presented. The Nusselt number is used to represent the effects of convection on the gage output. The Nusselt number was found to increase with increasing Reynolds number and angles of attack. At an angle of attack of about 90 deg, however, a significant reduction in the Nusselt number was noted. A correlation relating the Nusselt number (based on the disk diameter) to the Reynolds number (based on the gage outside diameter) and the angle of attack is reported. This correlation represents the data to within ±5 percent.

Introduction

A circular thin-foil (Gardon) gage is often used to measure the total heat flux incident on a surface. These gages are simple to construct, relatively small, inexpensive, and characterized by short time constants. The incident or absorbed heat flux is found to be directly proportional to the temperature difference between the center and the edge of the foil [1]. The linearity of the gage is due to the linear thermal conductivity of the constantan foil (disk).

Heat flux gages are often exposed (sometimes inadvertently) to convective and radiative environments. If only the radiative flux is desired, gages insensitive to convection should be used or corrections to the gage output for convection must be made. On the other hand, there are applications that may require knowledge of the individual convective and radiative contributions to the total heat flux. Such applications include: (*i*) mapping of the radiative and convective heat fluxes over the inside liner of a rocket nozzle during ignition [2], (*ii*) measurement of the radiative and convective heat transfers to or from the interior surfaces of an open top atrium [3], and (*iii*) measurement of the heat loss distribution at the opening of a cavity solar central receiver [4]. In the first two examples, heat flux gages are normally built into the surfaces of interest and the combined heat flux measured. In the third example, however, a gage can be used as a free-standing probe to traverse the cavity opening. The use of a heat flux gage as a free-standing probe is addressed in the present study.

In a combined convective and radiative environment when only the radiative component is of interest, a heat flux gage with a lens over the gage surface can be used. The radiation spectrum of the incident heat flux should be known a priori, however, so that a suitable lens, transparent to the incident radiation, can be chosen. For applications that require a knowledge of the individual heat flux components, a heat flux gage that measures the total heat flux, along with a radiometer to measure only radiation or an aspirated heat flux gage to measure only convection, can be used. The difference between the total heat flux and the radiative or convective contribution is the other component of the heat flux. Another approach for the accurate measurement of convection and radiation in a combined convective and radiative environment is to use a single heat flux gage to measure the total heat flux and reliable estimates of the convective heat transfer coefficients.

The purpose of the present study is to investigate the effects of free-stream velocity (magnitude and direction) and gage aspect ratio on the output of a free-standing circular disk heat flux gage when it is subjected to a radiative and convective heat flux. The aspect ratio is defined as the outside gage diameter divided by the disk diameter. Convective heat transfer coefficients in terms of Nusselt numbers are presented for the calculation of the convective contribution or to make convection corrections when the total heat flux is measured. The heat flux gage and its relative angular positions are shown in Fig. 1.

Experimental Procedure

Apparatus. Four water-cooled (Thermogage Inc., Model 1000-1) circular disk heat flux gages were tested in the present study. Their important dimensions are listed in Table 1. Four 300-W tungsten filament projector lamps were used to provide the radiant heat flux, while the air flow source was a low-speed, 76.2-mm (3-in.)-dia nozzle assembly. The experimental apparatus is shown in Fig. 2. The potential core, velocity uniform to within ±1 percent extended about three nozzle diameters downstream of the nozzle exit. The tests were conducted about 38.1 mm (1.5 in.) from the nozzle exit. A potential core of about 50.8 mm (2 in.) in diameter was found at this location. Turbulence intensities at this location were less than 0.01 percent. The free-stream temperature was constant at about 20°C.

The gages and the heat lamps were mounted on a horizontal rotary table with angular uncertainly of ± 0.10 deg. Since the gages and lamps were rotated as a unit, the radiative heat flux was independent of the gage angle of attack. The sensitivity coefficients of the gages, as checked in a vacuum chamber[1],

Contributed by the Heat Transfer Division for publication in the JOURNAL OF HEAT TRANSFER. Manuscript received by the Heat Transfer Division February 3, 1983.

[1]The gages were placed in a Plint and Partners (Model TE 85) vacuum chamber and subjected to a known heat source.

Table 1 Circular disk heat flux gage characteristics

Gage o. d. mm(in.)	Disk dia mm(in.)	Gage thickness mm(in.)	Aspect ratio	Sensitivity $kW/m^2/mV$
25.4(1.0)	4.34(0.171)	0.013(0.0005)	5.85	6.24
38.1(1.5)	4.34(0.171)	0.013(0.0005)	8.77	9.65
25.4(1.0)	2.16(0.085)	0.013(0.0005)	11.76	20.89
25.4(1.0)	4.34(0.171)	0.025(0.0010)	5.85	32.93

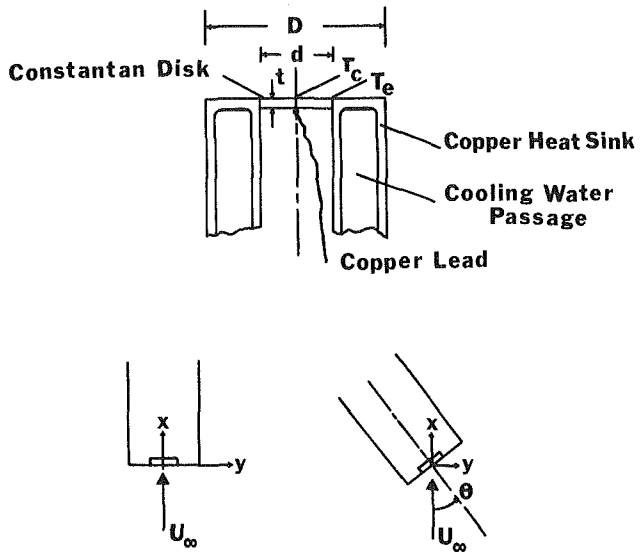

Fig. 1 Heat flux gage configuration, upper diagram; heat flux gage orientation, lower diagram. The airflow is in the *x*-direction.

were within ± 3 percent of the values provided by the manufacturer. Gage sensitivity values are listed in Table 1. The heat lamps were placed above, below, to the left, and to the right of the gages (see Fig. 2). Since the lamps were placed outside the flow field, their outputs were unaffected by velocity currents. The outputs of the lamps were maintained constant by adjusting, when needed, the line voltage with a powerstat. The radiant heat flux over each gage surface, as measured with a thermocouple probe[2], was uniform to within ±3 percent. Cooling water was circulated around the disk edges at a relatively high flow rate of about 190 cm^3/s (3 gpm). The edge temperature of the disk was thus measured by placing a thermocouple in the cooling water line.

Data Reduction. The calculation of the average convective heat transfer coefficient will be outlined below. For a radiation with no convection condition, the heat flux sensed by the gage is[3]

[2] Assuming that the radiation properties of the thermocouple, e.g., emissivity, absorptivity, etc., are independent of its location on the disk surface, the output of the thermocouple gives an indication of the relative heat flux over the disk.

[3] The absorbed heat flux is used since the gage was calibrated for this condition.

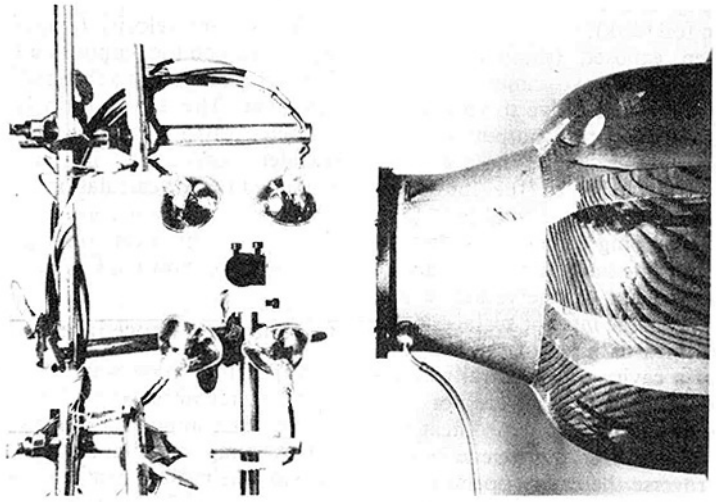

Fig. 2 Experimental test set-up that includes nozzle assembly, radiant heat lamps, and heat flux gage

Nomenclature

d = diameter of disk
D = outside diameter of gage
E = output of gage
F_{s-r} = configuration factor from gage to radiation lamps
$\bar{h}_c$ = average convective heat transfer coefficient
k_f = thermal conductivity of surrounding fluid
$\bar{\mathrm{Nu}}_d$ = Nusselt number based on $d = \bar{h}_c d/k_f$
$\dot{q}$ = heat flux
Re_D = Reynolds number based on $D = U_\infty D/\nu_f$
S = gage sensitivity
t = gage thickness
T = temperature
U_∞ = free-stream velocity
ϵ = emissivity
θ = angle between gage surface normal and free-stream velocity vector
σ = Stefan-Boltzmann constant
ν_f = kinematic viscosity of surrounding fluid

Subscripts

c = center
e = edge
L = lamps
r = radiation only
s = effective disk quantity
T = total (radiation and convection)
∞ = free-stream

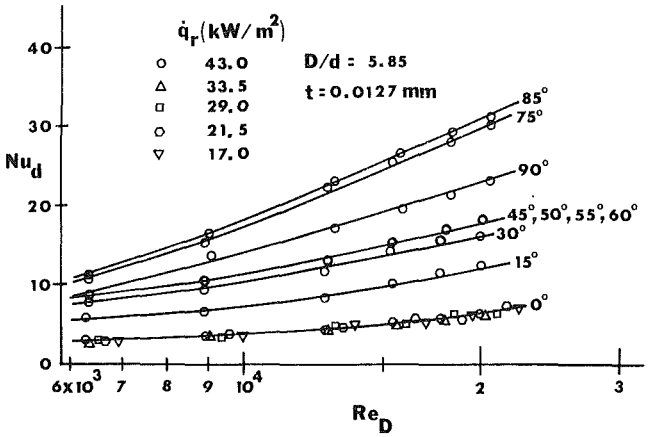

Fig. 3 Nusselt numbers for a circular disk heat flux gage with an aspect ratio of 5.85

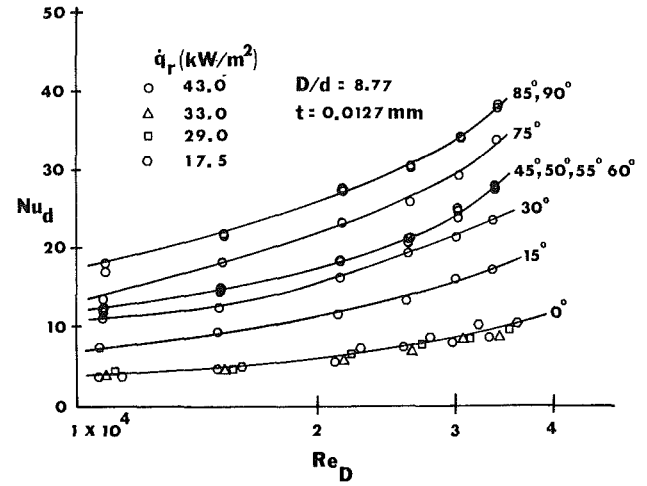

Fig. 4 Nusselt numbers for a circular disk heat flux gage with an aspect ratio of 8.77

$$SE_r = F_{s-r}\epsilon\sigma(T_L{}^4 - T_s{}^{*4}) \tag{1}$$

where T_s^* is the effective gage surface temperature for a radiation condition only. For combined radiation and convection, the heat flux sensed is[3]

$$SE_T = F_{s-r}\epsilon\sigma(T_L{}^4 - T_s{}^4) + \bar{h}_c(T_\infty - T_s) \tag{2}$$

The average convective heat transfer coefficient, $\bar{h}_c$, is obtained by subtracting equation (1) from (2)

$$\bar{h}_c = \frac{S(E_T - E_r) + F_{s-r}\epsilon\sigma(T_s{}^4 - T_s{}^{*4})}{(T_\infty - T_s)} \tag{3}$$

Exact specification of the second term in the numerator of equation (3), and hence the gage emissivity, is not required, since it represents only about 2 percent of $\bar{h}_c$. The configuration factor, F_{s-r}, can be estimated from case 15 of Appendix C in Siegel and Howell [5]. It is assumed in the present calculations that natural convection effects are negligible. This was demonstrated by recording the gage output for the gage facing upwards and then downwards while exposed to the same radiative heat flux. The gage outputs for these two positions were almost identical.

The convective heat transfer coefficient is presented in terms of the Nusselt number based on the disk diameter, d

$$\mathrm{Nu}_d = \bar{h}_c d/k_f \tag{4}$$

The Nusselt number is parameterized by the Reynolds number which is based on the outside gage diameter

$$\mathrm{Re}_D = U_\infty D/\nu_f \tag{5}$$

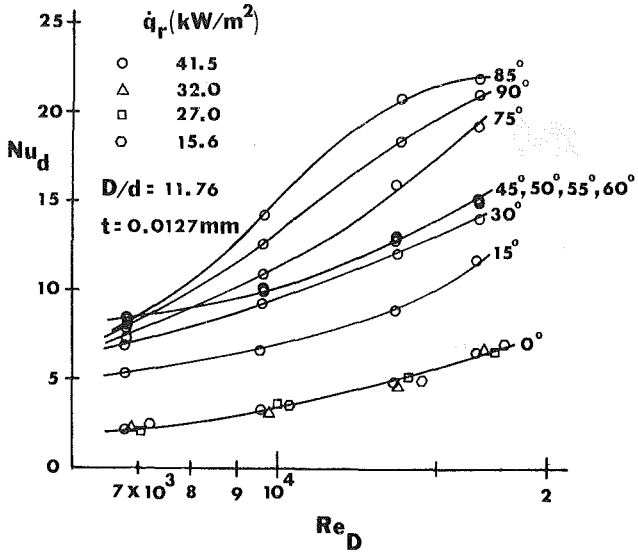

Fig. 5 Nusselt numbers for a circular disk heat flux gage with an aspect ratio of 11.76

The fluid properties in equations (4) and (5) are based on the film temperature, T_f

$$T_f = (T_s + T_\infty)/2 \tag{6}$$

where T_s (and T_s^*), the effective disk surface temperature, is defined as (see [6])

$$T_s = 0.75\,T_c + 0.25T_e \tag{7}$$

Note that equation (7) is a convenient approximation of the effective disk temperature. The center temperature, T_c, can be calculated from a NBS [8], fourth-order, emf-temperature polynomial. The accuracy of this relationship is stated as ± 0.17°C. Representative magnitudes of T_∞, T_c, and T_e are 20, 120, and 20°C, respectively. The selection of characteristic lengths on which to base the Nusselt and Reynolds numbers will be discussed in the following section.

Results and Discussion

The Nusselt number is plotted in Figs. 3, 4, and 5 as a function of the Reynolds number based on the outside gage diameter for gage angles of attack between 0 (normal incidence) and 90 deg. The aspect ratios represented in Figs. 3, 4, and 5 are 5.85, 8.77, and 11.76, respectively. The disk thickness for these results is 0.013 mm (0.0005 in.). At all angles of attack, the results show little dependence on radiant heat flux. The data for several radiant heat fluxes are shown for the normal incidence cases only. The results at other angles of attack are similar. The results indicate that the Nusselt number in the central region of the gage increases with angle of attack. The increase in Nusselt number is initially due to movement of the stagnation region relative to the constantan disk and at angles of attack greater than 45 deg could be due to a decrease in boundary layer thickness over the disk. For the normal incidence case, the disk is in the stagnation zone, and lower heat transfer coefficients are expected. As the gage is rotated, i.e., as the right edge is thrust forward in the direction of the oncoming flow, the stagnation region moves towards the upstream edge of the gage. These results are verified by flow visualization studies using the oil/lampblack technique. The test surface was covered with white contact paper and a thin film of oil and lampblack applied to the surface. A twelve to one mixture (weight proportions) of manometer fluid (S.G. = 0.826) to lampblack was used (see [8] for further details of this technique). The pattern of streaks over the test surface reveals the fluid flow directions, while black areas without streaks are stagnation or very low

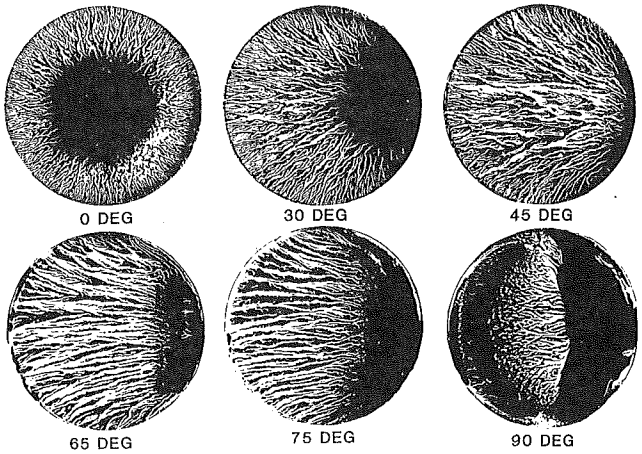

Fig. 6 Fluid flow patterns over the gage surface for Re_D = 30,000

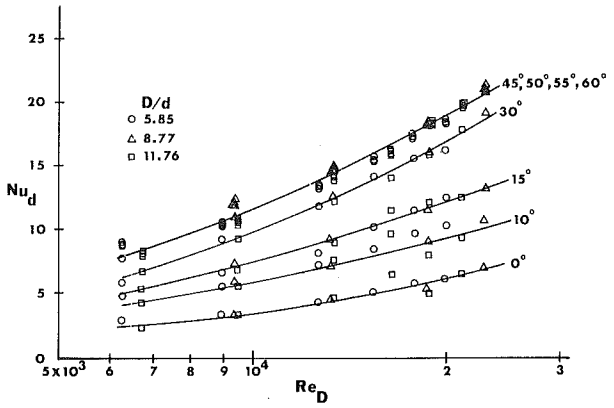

Fig. 7 Nusselt numbers for aspect ratios of 5.85, 8.77, and 11.76

velocity regions. Figure 6 shows fluid flow patterns for a Reynolds number based on the gage outside diameter of 30,000 and for several angles of attack. The gage o. d. is 38.1 mm (1.5 in.) and represents the gage with an aspect ratio of 8.77. The photographs are ordered from left to right, which corresponds to increasing angles of attack. Consider the top row of photographs in Fig. 6. For the case when the gage is placed normal to the flow (left photo), the stagnation zone is in the center of the gage, directly over the disk. As the angle of attack is increased (right edge moving forward), the stagnation zone moves towards the upstream edge of the gage. The flow outside the stagnation region is in the outward radial direction. As the stagnation region moves further from the center of the gage, more of the disk is exposed to the developing boundary layer, which results in higher Nusselt numbers.

For angles of attack greater than 65 deg, there is a noticeable change in the flow field, which is inferred from the unsteadiness in the gage output and which corresponds to a substantial increase in Nusselt number. The unsteadiness in the flow field is believed due to an increased interaction between the vortex structure produced on the cylindrical sides of the gage, the separated flow field on the downstream side of the gage, and the flow over the front surface of the gage. The Nusselt number continues to increase with angle of attack until about 90 deg. Flow separation at 90 deg may be responsible for the decrease in the Nusselt number. At all angles of attack, increasing the Reynolds number leads to an increase in the Nusselt number. The flow patterns shown in Fig. 6 (lower photos) indicate that the stagnation region is moving back towards the disk for angles of attack greater than 60 deg. For angles greater than about 85 deg, the stagnation region begins to partially cover the disk surface and results in lower Nusselt numbers. At a 90 deg angle of attack, there is a horseshoe-shaped separation bubble (or region) on the forward portion of the gage, followed by a backflow region, reattachment zone, and a developing boundary layer (see lower right photo in Fig. 6). This pattern is similar to the flow description given by Sparrow and Samie [9] for the tip region of a long vertical cylinder in a crossflow. The lengths of the gages in the present study are only about 38.1 to 50.8 mm (1.5 to 2.0 in). Consequently, it is believed that the lengths of the gages do not significantly affect the heat transfer results.

The selection of characteristic lengths on which to base the Nusselt and Reynolds numbers warrants some discussion. In the results of Tien [10] as reported in Sparrow, Ramsey, and Mass [8], the convective heat transfer coefficient was found to differ by as much as 300 percent between the center and edge regions of a square plate. They also reported that while the spatially averaged heat transfer coefficient is a weak function of angle of attack, the heat transfer coefficient at the center of the plate decreases significantly with increasing angle of attack. To reflect this sensitivity to angle of attack, the disk diameter is used as the characteristic length dimension in the Nusselt number. The velocity field, however, is highly dependent on the gage outside diameter. The stagnation zone, backflow region, etc., are all proportional in size to the outside gage diameter. Consequently, for gages with the same disk size but different outside diameter, different portions of the disk will be covered by the stagnation zone. To reflect the flow field's sensitivity to the gage o. d., the Reynolds number is based on this length dimension. Figure 7 is a plot of the Nusselt number based on the disk diameter versus the Reynolds number based on the gage outside diameter for all three aspect ratios. For angles between 0 and 60 deg, the results are somewhat independent of the aspect ratio. This result lends support to basing the heat transfer parameter on the disk diameter and the velocity field parameter on the gage o. d. A correlation[4] is developed by performing a least-squares curve fit through the data. The resulting correlation is

$$\mathrm{Nu}_d = 0.039\ \mathrm{Re}_D^{1/2}[1 + 2.16\sin 2\theta] \tag{8}$$

This correlation is valid for $6{,}000 < \mathrm{Re}_D < 25{,}000$, aspect ratios between 5.85 and 11.76, angles of inclination, $0 \le \theta \le 60$ deg, and for radiative heat fluxes between 17 and 43 kW/m^2. The correlation represents the data to within ±5 percent. It should be noted that the convective component was about 10 to 15 percent of the total heat flux.

The results in Figs. 3, 4, 5, and 7 are for a gage thickness of 0.013 mm (0.0005 in.). A test was performed to determine the effect of gage thickness on the heat transfer results. Tests were conducted on a gage with an aspect ratio of 5.85 and a gage thickness of 0.025 mm (0.0010 in.). Increasing the gage thickness decreases the gage's sensitivity, i.e., it increases the gage's sensitivity coefficient (see Table 1). The heat transfer results for a disk thickness of 0.025 mm were compared to results for a gage with the same aspect ratio but with a disk thickness of 0.013 mm. The results were within ± 5 percent of each other provided that the radiation input resulted in a gage output of at least 2 mV. For outputs less than 2 mV, the results differed substantially, and no correlation relating disk thickness was found. Consequently, the gages should be operated well within their linear output ranges if reliable results are to be expected.

A heat transfer correlation was proposed by Sogin [11], for an isothermal circular disk oriented perpendicular to an oncoming airflow. The correlation, which is recast here in

[4] The power of the Reynolds number was selected by comparison to existing correlations for $\theta = 0$ deg, e.g., [8] and [11], while the quantity 2θ resulted from the least-squares curve fit.

terms of the Nusselt number based on the outside diameter of the gage, is

$$Nu_D = 1.08\ Re_D^{1/2} \tag{9}$$

If the present results are based on the outside gage diameter, the coefficient (0.039) in equation (8) becomes 0.459. This result is for an aspect ratio of 11.76. This aspect ratio is chosen for comparison because of the three aspect ratios tested it most closely approximates the constant temperature boundary condition used by Sogin. For the normal incidence case (θ = 0 degrees), equation (8) when based on the outside gage diameter, is approximately 58 percent lower than Sogin's results. This difference is expected, since the stagnation region, which is in the central region of the gage, has lower heat transfer coefficients than at the edge regions of the disk where there is a developing boundary layer. A second reason is that the temperature distribution at the disk surface is not uniform as in the experiments of Sogin.

Another correlation was proposed by Sparrow, Ramsey, and Mass [8] for isothermal finite width rectangular plates inclined at various angles of attack to an oncoming airflow. The form of their correlation is similar to equation (9), except that the multiplicative constant is 0.86. Their data indicate a slight dependence on angle of attack when a narrow plate was tested, but no dependence was found for a wide plate; i.e., the flow over a narrow plate is more three-dimensional than that over a wide plate. The present geometry leads to a highly three-dimensional flow field with a corresponding dependence on angle of attack. In addition, the present thermal boundary conditions are in part responsible for this angular dependence.

Conclusions

In the present study, convective heat transfer coefficients for a free-standing circular disk heat flux gage exposed to a radiative and convective heat flux were calculated for several free-stream velocities, aspect ratios, and angles of attack. The results indicate that the Nusselt number increases with increasing angle of attack up until about 90 deg. At 90 deg, a significant reduction in the Nusselt numbers was noted. The results suggest that care should be taken when using a heat flux gage in a convective and radiative environment. In particular, for angles of attack greater than 60 deg, flow instabilities can lead to large measurement uncertainties and increased convective heat transfer coefficients. For angles between 0 and 60 deg, the following correlation is suggested for the calculation of the convective contribution

$$Nu_d = 0.039\ Re_D^{1/2}[1 + 2.16 \sin 2\theta] \tag{8}$$

This correlation is valid for $6{,}000 < Re_D < 25{,}000$, aspect ratios between 5.85 and 11.76, and for angles of inclination, $0 \le \theta \le 60$ deg. It represents the data to within ± 5 percent.

References

1 Gardon, R., "An Instrument for the Direct Measurement of Intense Thermal Radiation," *The Review of Scientific Instruments*, Vol. 24, No. 5, 1953, pp. 366–370.

2 Wool, M. R., Schaefer, J. W., and Baker, D. L., "Measurement of Convective and Radiative Heat Fluxes at the Surface of an Ablative Material," *ISA Transactions*, Vol. 9, No. 2, 1970, pp. 94–103.

3 Leung, S. K., Young, M. F., Pierson, R. E., Kazama, D., Trenschel, D., and Tam, T., "Heating and Cooling Applications in Atriums and Attached Greenhouses—A State of the Art Report," Report for the Department of Energy, Eureka Laboratories, Report No. 80-EN-11, Apr. 1981.

4 Kraabel, J. S., and Meyer, B., "An Experimental Investigation of the Convective Heat Losses from Cavity Type Central Receivers," *Proceedings of Convective Losses From Solar Central Receivers Workshop*, Sandia National Laboratories, SAND81-8014, 1981, pp. 119–124.

5 Siegel, R., and Howell, J. R., *Thermal Radiation Heat Transfer*, McGraw-Hill, New York, 1972.

6 Malone, E. W., "Design and Calibration of Thin-Foil Heat Flux Sensors," *ISA Transactions*, Vol. 7, No. 3, 1968, pp. 175–180.

7 "Thermocouple Reference Tables Based on the IPTS-68," NBS Monograph 125, 1974.

8 Sparrow, E. M., Ramsey, J. W., and Mass, E. A., "Effect of Finite Width on Heat Transfer and Fluid Flow about an Inclined Rectangular Plate," ASME JOURNAL OF HEAT TRANSFER, Vol. 101, 1979, pp. 199–204.

9 Sparrow, E. M., and Samie, F., "Measured Heat Transfer Coefficients at and Adjacent to the Tip of a Wall-Attached Cylinder in Crossflow—Application to Fins," ASME JOURNAL OF HEAT TRANSFER, Vol. 103, 1981, pp. 778–784.

10 Tien, K. K., "Heat/Mass Transfer Characteristics and Fluid Flow Patterns for Airflow about an Inclined and Yawed Flat Plate," Ph.D. thesis, Department of Mechanical Engineering, University of Minnesota, Minneapolis, Minn., 1978.

11 Sogin, H. H., "Sublimation From Disks to Air Streams Flowing Normal to Their Surfaces," *Transactions ASME*, Vol. 80, 1958, pp. 61–69.

ERRATA

Corrections to "The Optimum Dimensions of Convective Pin Fins," by P. Razelos, published in the May 1983 issue of the ASME JOURNAL OF HEAT TRANSFER, pp. 441–413:

1 On pages 412, line 16 from the bottom in the second column should read "while the length is inversely proportional to the quantity."

2 In Table 1 on page 412, the expression for D in the last column should be replaced by

$$\frac{2u/3}{1+(1+4u^2/9)^{1/2}}$$

Journal of Heat Transfer

Technical Notes

This section contains shorter technical papers. These shorter papers will be subjected to the same review process as that for full papers.

The Accuracy of Perfect Contact Fin Analyses

M. Manzoor,[1] D. B. Ingham,[1] and P. J. Heggs[1]

Nomenclature

Aug = Q/Q_0, augmentation factor
Bi_1 = $h_1 P/k_w$, Biot number
Bi_2 = $h_2 P/k_w$, Biot number
h = heat transfer coefficient, W/m^2K
k = thermal conductivity, W/mK
l = fin length, m
L = l/P, aspect ratio
P = half fin pitch, m
Q = fin assembly heat flow rate
Q_0 = unfinned wall heat flow rate
t = half fin thickness, m
T = t/P, aspect ratio
w = wall thickness, m
W = w/P, aspect ratio
ϵ = ratio of actual contact area to apparent contact area
κ = k_f/k_w
θ_1, θ_2 = fluid temperatures, K
θ = temperature distribution, K
φ = $(\theta-\theta_2)/(\theta_1-\theta_2)$, dimensionless temperature distribution

Subscripts

1 = plain side
2 = fin side
f = fin
w = wall

Introduction

The heat flow within finned surfaces is usually analysed on the basis of several simplifying assumptions, the most questionable being (*a*) invariant thermal conductivity, (*b*) purely convective heat transfer with uniform heat transfer coefficient, (*c*) unidirectional heat flow, and (*d*) perfect contact between fin and supporting surface. Of these four assumptions, the validity of the first three has been extensively investigated by examining the effects of temperature-dependent thermal conductivity, e.g., [1]; radiative heat transfer, e.g., ,[2]; nonuniform heat transfer coefficients, e.g., [3]; and multidirectional heat flow, e.g., [4]. However, prior to the present investigation, the validity of the perfect contact assumption has received relatively little attention. In fact, there are only three published articles on this subject [5–7], and these have all considered the problem of spiral fins wound onto a cylindrical tube where contact is completely relaxed as a consequence of differential expansion. Unfortunately, the results of these investigations are of limited value because in most applications some form of bonding is used in order to ensure that contact is never completely relaxed.

In situations where the fins are bonded to the supporting surface, the inevitable roughness of the contacting surfaces precludes the possibility of perfect contact, although contact is maintained at discrete zones along the contact interface. In this study a theoretical technique is developed in order to predict the effects of surface roughness on the performance of extended surface heat exchangers. This technique does not attempt to model the complex features which govern contact, but instead examines the effects of prescribed contact-zone distributions on the overall performance.

The main aim of the present study is to investigate the validity of the perfect contact assumption in the context of fin assembly heat transfer. Attention is restricted to the case of longitudinal fins attached to a plane wall. However, the work presented here can easily be extended to the annular geometry and to include fins with tapered or curved fin profile.

Contact Interface Model

Consider an assembly of equally spaced longitudinal rectangular fins attached to a plane wall as depicted schematically in Fig. 1. For mathematical treatment, it is necessary to develop a theoretical representation of this assembly. In the case where the fins are in perfect contact with the base surface, symmetry considerations indicate that only that section of the assembly bounded by the contour OABC-DEFO need be examined. However, if the fins are bonded to the base surface then thermal symmetry is improbable since this would require a uniform symmetric distribution of the surface irregularities which form the contact zones. Therefore, in order to facilitate a mathematically tractable formulation, attention is restricted to contact zones distributions which are symmetric about the axis BCD, Fig. 1.

The total heat flow across the contact interface is a combination of conduction across the contact zones, and conduction, convection, and radiation through the gaps adjacent to the contact zones. The convection contribution to the gap heat transfer is negligible by virtue of the microscopically small separation of the surfaces. In fact, if the fluid entrapped within the gaps has relatively high thermal conductivity, then the gap heat transfer is primarily conductive, whilst at high temperature or in vacua, the gap heat transfer is mainly radiative. In this study, a first approximation of the contact interface is introduced; it is assumed that there is perfect

[1] University of Leeds, Leeds LS2 9JT England
Contributed by the Heat Transfer Division for publicaton in the JOURNAL OF HEAT TRANSFER. Manuscript received by the Heat Transfer Division January 4, 1983.

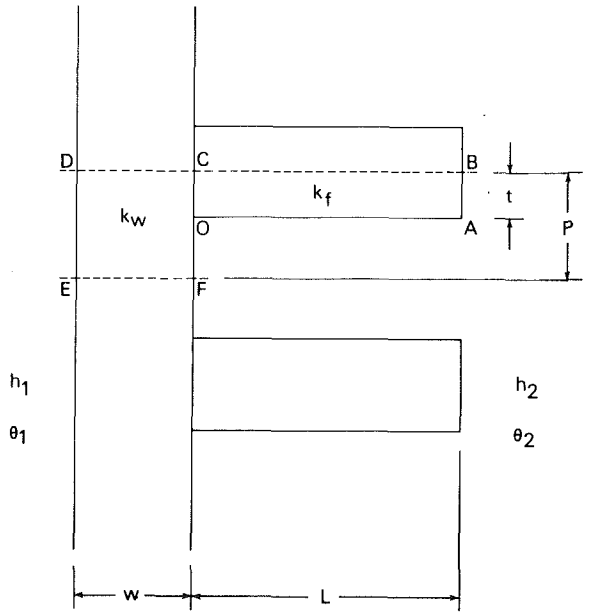

Fig. 1 Schematic representation of the fin assembly

contact at the contact zones, and zero heat flux through the adjacent gaps. Thus, for any given contact zone distribution, this model will give a lower bound on the overall heat transfer across the contact interface, i.e., the actual heat transfer will invariably be higher than that predicted by this model.

In comparison with the relevant dimensions of the fin assembly section OABCDEFO, the dimensions of the microscopic surface irregularities which cause reduced contact are negligible. Therefore, in the following analysis the contact interface OC is treated as a perfectly flat surface consisting of segments across which there is perfect contact, interspersed with segments across which there is no heat flux.

Analysis

Mathematical Formulation. The primary concern of the present investigation is to determine the errors in the prediction of the fin assembly heat transfer rate arising as a consequence of employing the perfect contact assumption. Therefore, it is essential to ensure that the heat flow is modeled accurately so that any errors which are detected may be attributed solely to the effects of reduced contact. Since numerous recent investigations, e.g., [4], have shown that the addition of fins induces quite significant two-dimensional effects within the supporting surface, it would be most advisable to employ a multidirectional analysis in order to preclude errors resulting from the use of the one-dimensional approximation. Thus, the determination of the overall heat flow rate through the fin assembly requires the simultaneous solution of

$$\nabla^2 \varphi_f = 0 \text{ within the fin (OABCO, Fig. 1),} \tag{1}$$

and

$$\nabla^2 \varphi_w = 0 \text{ within the wall (OCDEFO, Fig. 1),} \tag{2}$$

subject to the boundary conditions

on OA

$$\varphi_f' = -\frac{\mathrm{Bi}_2}{\kappa}\varphi_f \tag{3a}$$

on AB

$$\varphi_f' = -\frac{\mathrm{Bi}_2}{\kappa}\varphi_f \tag{3b}$$

on BC

$$\varphi_f' = 0 \tag{3c}$$

on CD

$$\varphi_w' = 0 \tag{3d}$$

on DE

$$\varphi_w' = \mathrm{Bi}_1(1-\varphi_w) \tag{3e}$$

on EF

$$\varphi_w' = 0 \tag{3f}$$

on FO

$$\varphi_w' = -\mathrm{Bi}_2\varphi_w \tag{3g}$$

on OC

$$\varphi_w = \varphi_f \text{ and } \varphi_w' = -\kappa\varphi_f' \text{ on each contact zone} \tag{3h}$$

and

$$\varphi_f' = 0 \text{ and } \varphi_w' = 0 \text{ on each gap} \tag{3i}$$

where the prime (′) denotes the derivative in the direction of the outward normal to the associated surface.

The boundary conditions (3*c*), (3*d*), and (3*f*) arise from the geometrical and thermal symmetry of the fin assembly configuration and stipulate that there is no heat flux across the fictitious boundaries BC, CD and EF, respectively. The boundary conditions (3*h*) and (3*i*) represent the regions of perfect contact and the adjacent gaps across which it is assumed that there is no heat flux. The remaining boundary conditions describe the convective heat exchange at the exposed surfaces FOAB and DE, Fig. 1.

Method of Solution. The solution of plane potential boundary-value problems, such as that described by the equations (1), (2), and (3), can be computed employing various numerical techniques of which the finite difference, finite element, and boundary integral equation methods are the most popular. A recent paper by Heggs et al. [8] has shown that the boundary integral equation method offers several computationally advantageous properties over the other two methods for the solution of fin assembly problems. Furthermore, the flexibility of the boundary integral equation discretization process is such that it can most easily handle the computational complexities associated with the interface boundary conditions (3*h*) and (3*i*). Therefore, it appears that it would be most appropriate to tackle the problem described by equations (1), (2), and (3) employing the boundary integral equation method.

Although it would be beneficial, from the point of view of completeness, to present details of the boundary integral equation method here, this information would be superfluous because there is now an extensive range of published literature describing the application of the boundary integral equation methods to problems of heat transfer analysis, e.g., see [8]. It will suffice to note that the boundary integral equation program used to generate the data presented in this paper was validated by comparison with finite-element results presented by Stones [9] and series truncation results given by Heggs et al. [10].

Heat Exchanger Performance

The heat flow rate through the fin assembly is given by

$$Q = (k_w/P)(\theta_1 - \theta_2)\int_{\mathrm{DE}} \varphi_w'(s)\,ds \tag{4}$$

where *ds* denotes a differential increment of the boundary segment DE. In order to facilitate a concise parametric study, it is most convenient to introduce a dimensionless representation for the fin assembly heat flow rate. This

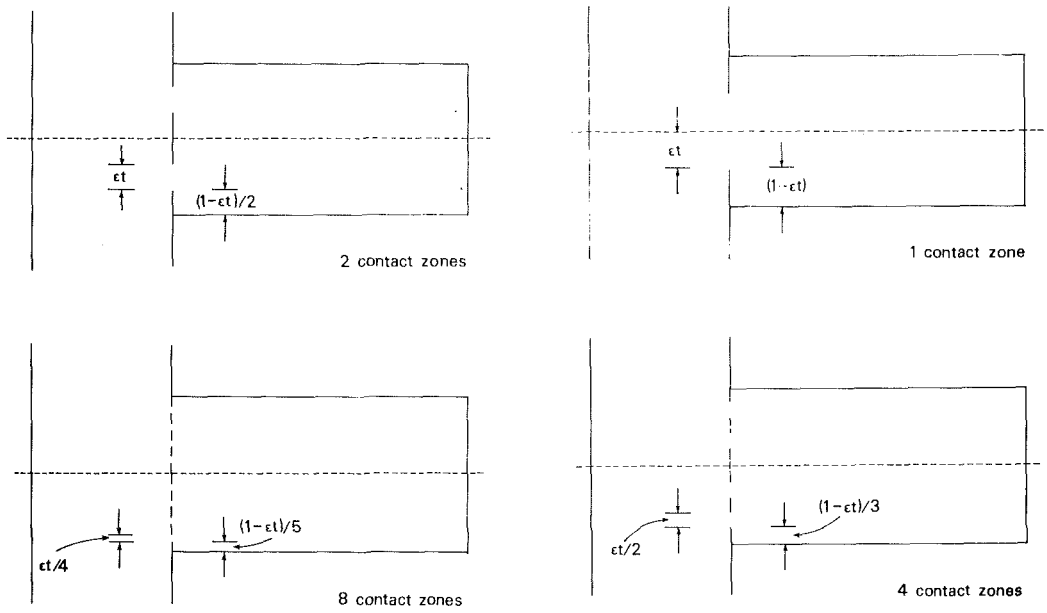

Fig. 2 Contact zone distributions

dimensionless representation is referred to as the augmentation factor, Aug, and is defined as the ratio of the heat flow rate of the fin assembly (Q) to that of the unfinned wall operating under the same conditions (Q_0), i.e.,

$$\text{Aug} = Q/Q_o = \left(\frac{1}{\text{Bi}_1} + W + \frac{1}{\text{Bi}_2}\right)\int_{\text{DE}} \varphi'_w(s)\,ds \qquad (5)$$

Thus, the augmentation factor is a measure of the improvement in the *overall* heat flow rate resulting from the addition of fins. Therefore, it is more useful for design purposes than the widely used *fin efficiency* which only gives an indication of the *fin* heat dissipation. Furthermore, it differs from the conventional *fin effectiveness* in that the later fails to account for the heat flow within the supporting surface.

Results and Discussion

From the equations (1), (2), and (3) it may be deduced that the heat flow through the fin assembly may be parameterized by the Biot numbers, Bi_1 and Bi_2; the ratio of the thermal conductivities, κ; the aspect ratios, L, T, and W; and the size and distribution of the contact zones. In order to minimize the number of independent parameters necessary to completely define the fin assembly heat flow, a computationally orientated procedure is adopted for parameterizing the size and distribution of the contact zones. With this procedure the contact interface is parameterized by a single variable, namely ϵ, which indicates the ratio of the actual contact area to the apparent contact area. Then, for each prescribed value of ϵ, solutions are computed for four different contact zone distributions. These correspond to the cases of 1, 2, 4, and 8 contact zones as shown in Fig. 2.

Results have been obtained for an extensive range of the system parameters Bi_1, Bi_2, κ, L, T, and W. For each particular problem, solutions were computed for the cases ϵ = 0.0, 0.1, 0.2, 0.5, and 1.0, i.e., with the amount of contact varying from 0 to 100 percent. The solutions for the case $\epsilon = 0.0$ were computed without solving for the temperature distribution within the fin, whilst the solutions for the case $\epsilon = 1.0$ were computed employing the usual perfect contact formulation, see [8]. Furthermore, solutions for these two special cases were also computed employing the extremely accurate but rather cumbersome series truncation method [10]; these solutions were found to be in excellent agreement with those predicted by the boundary integral equation method.

Representative results for three particular problems are given in Tables 1, 2, and 3. These tables show the values of the augmentation factor for the various values of ϵ and the four different contact zone distributions. These results correspond to the problems

	Bi_1	Bi_2	κ	L	T	W
(1)	1.00	0.01	1.0	10.0	0.5	5.0
(2)	1.00	0.01	10.0	4.0	0.3	0.5
(3)	0.10	0.001	2.0	5.0	0.4	1.0

Problems (1) represents the performance of a stainless steel heat exchanger with forced convection of air on the plain side and free convection of air on the fin side. Problem (2) corresponds to a heat exchanger comprising of a stainless steel wall with aluminum fins, whilst problem (3) relates to a heat exchanger composed of an aluminum wall with copper fins.

The results presented in Tables 1, 2, and 3 illustrate various features of reduced wall-to-fin contact and are characteristic of results obtained for other values of the system parameters. The dominant feature of these results is that, irrespective of the distribution of contact zones, provided contact occurs over at least 10 percent of the apparent contact area then the reduction in the overall heat flow rate through the fin assembly is virtually negligible. However, if the actual contact area is reduced below 10 percent then the overall heat flow rate begins to deteriorate quite markedly. Fortunately, in most industrial applications 10 percent contact is accomplished with ease.

Closer inspection of the results presented in Tables 1, 2, and 3 reveals that for a given amount of actual contact area, i.e., for a prescribed value of ϵ, increasing the number of contact zones facilitiates an improvement in the overall heat flow rate even though the size of the individual contact zones is reduced. A reduction in the size of the contact zones should act to constrict the heat flow. However, with the contact interface model developed in this paper, these smaller contact zones are distributed over a larger portion of the contact

Table 1 The effects of surface roughness for problem (1)

Number of contact zones	Augmentation-factor				
	$\epsilon=0.0$	$\epsilon=0.1$	$\epsilon=0.2$	$\epsilon=0.5$	$\epsilon=1.0$
1	0.51	4.62	4.77	4.99	5.11
2	0.51	4.74	4.88	5.05	5.11
4	0.51	4.98	5.02	5.09	5.11
8	0.51	5.06	5.08	5.10	5.11

Table 2 The effects of surface roughness for problem (2)

Number of contact zones	Augmentation-factor				
	$\epsilon=0.0$	$\epsilon=0.1$	$\epsilon=0.2$	$\epsilon=0.5$	$\epsilon=1.0$
1	0.70	4.30	4.41	4.51	4.57
2	0.70	4.44	4.51	4.56	4.57
4	0.70	4.52	4.54	4.57	4.57
8	0.70	4.56	4.56	4.57	4.57

Table 3 The effects of surface roughness for problem (3)

Number of contact zones	Augmentation-factor				
	$\epsilon=0.0$	$\epsilon=0.1$	$\epsilon=0.2$	$\epsilon=0.5$	$\epsilon=1.0$
1	0.60	4.99	5.12	5.26	5.34
2	0.60	5.19	5.25	5.32	5.34
4	0.60	5.28	5.30	5.33	5.34
8	0.60	5.32	5.33	5.34	5.34

interface and therefore counteract the constriction by allowing the heat flow to disperse over a larger area.

In order to ensure that the phenomena observed were not a consequence of the particular contact zone distributions described above, results were also obtained for various other contact zone distributions. These results substantiated the original observations.

Conclusions

The validity of the perfect contact assumption has been investigated in the context of fin assembly heat transfer employing a sophisticated two-dimensional analysis coupled with a relatively simple theoretical model of surface roughness. The results predicted by this analysis indicate, in particular, that provided contact can be achieved over at least 10 percent of the contact interface then the difference between the nonperfect and perfect contact solutions is virtually negligible. Thus, it may be concluded that the perfect contact assumption will suffice for design calculations provided wall-to-fin contact is greater than 10 percent.

Finally, it must be emphasized that the authors do not advocate the complex theoretical model described by equations (1), (2), and (3) as a design technique; the two-dimensional analysis and the associated surface roughness model were only necessary in order to perform a meaningful theoretical investigation into the applicability of the perfect contact assumption. In fact, from the results obtained it is evident that the conventional methods of analysis are perfectly sufficient for design purposes.

References

1 Aziz, A., and Na, T. Y., "Periodic Heat Transfer in Fins With Variable Thermal Parameters," *Int J Heat Mass Transfer*, Vol. 24, 1981, pp. 1397-1404.

2 Eslinger, R. G., and Chung, B. T. F., "Periodic Heat Transfer in Radiating Fins or Fin Arrays," *AIAA Journal*, Vol. 17, 1979, pp. 1134-1140.

3 Heggs, P. J., and Stones, P. R., "Improved Design Methods for Finned Tube Heat Exchangers," Trans Inst Chem Engrs, Vol. 58, 1980, pp. 147-154.

4 Suryanarayana, N. V., "Two-Dimensional Effects on Heat Transfer From an Array of Straight Fins," ASME JOURNAL OF HEAT TRANSFER, Vol. 99, 1977, pp. 129-132.

5 Gardener, K. A., and Carnovos, T. C., "Thermal Contact Resistance in Finned Tubing," ASME JOURNAL OF HEAT TRANSFER, Vol. 82, 1960, pp. 279-284.

6 Young, E. H., and Briggs, D. E., "Bond Resistance of Bimetallic Finned Tubes," *Chem Enging Progress*, Vol. 61, 1965, pp. 71-76.

7 Kulkarni, M. W., and Young, E. H., "Bimetallic Finned Tubes," *Chem Enging Progress*, Vol. 62, 1966, pp. 69-74.

8 Heggs, P. J., Ingham, D. B., and Manzoor, M., "The Boundary Integral Equation Analysis of Fin Assembly Heat Transfer," *Numerical Heat Transfer*, Vol. 4, 1981, pp. 285-301.

9 Stones, P. R., PhD thesis, University of Leeds, England, 1980.

10 Heggs, P. J., Ingham, D. B., and Manzoor, M., "The Analysis of Fin Assembly Heat Transfer by a Series Truncation Method," ASME JOURNAL OF HEAT TRANSFER, Vol. 104, 1982, pp. 210-212.

Solidification Interface Shape for Continuous Casting in an Offset Mold—Two Analytical Methods

R. Siegel[1]

Nomenclature

A = dimensionless parameter and dimensionless length, $a\bar{u}\rho\lambda/k(t_f-t_c) = a/\gamma$
a = half-width of slab ingot
B_n, D_n = coefficients in Fourier series
h = offset of mold; $H = h/\gamma$
k = thermal conductivity of solidified material
n = normal to interface; $N = n/\gamma$
S = dimensionless coordinate along solidification interface
t = temperature
$\bar{u}$ = casting velocity of ingot
x,y = coordinates in physical plane; $X = x/\gamma$, $Y = y/\gamma$

Greek symbols

γ = length scale parameter, $k(t_f-t_c)/\bar{u}\rho\lambda$
Θ = angle between interface normal and x-axis
λ = latent heat of fusion per unit mass of solid
ρ = density of solid
Φ = potential function, $(t_f-t)/(t_f-t_c)$
Ψ = heat flow function orthogonal to Φ

Subscripts

c = at cooled boundary
f = at solidification temperature
s = at solidification interface
1,2...8 = locations around ingot boundary
I,II = two solutions in superposition

Introduction

When a slab ingot is being formed as a continuous casting by pulling it from a mold with parallel sides, the solidification interface is a "free" boundary that adjusts with the heat flow

[1] National Aeronautics and Space Administration, Lewis Research Center, Cleveland, Ohio 44135, Fellow ASME

Contributed by the Heat Transfer Division for publication in the JOURNAL OF HEAT TRANSFER. Manuscript received by the Heat Transfer Division, May 11, 1983.

Table 1 The effects of surface roughness for problem (1)

Number of contact zones	Augmentation-factor				
	$\epsilon=0.0$	$\epsilon=0.1$	$\epsilon=0.2$	$\epsilon=0.5$	$\epsilon=1.0$
1	0.51	4.62	4.77	4.99	5.11
2	0.51	4.74	4.88	5.05	5.11
4	0.51	4.98	5.02	5.09	5.11
8	0.51	5.06	5.08	5.10	5.11

Table 2 The effects of surface roughness for problem (2)

Number of contact zones	Augmentation-factor				
	$\epsilon=0.0$	$\epsilon=0.1$	$\epsilon=0.2$	$\epsilon=0.5$	$\epsilon=1.0$
1	0.70	4.30	4.41	4.51	4.57
2	0.70	4.44	4.51	4.56	4.57
4	0.70	4.52	4.54	4.57	4.57
8	0.70	4.56	4.56	4.57	4.57

Table 3 The effects of surface roughness for problem (3)

Number of contact zones	Augmentation-factor				
	$\epsilon=0.0$	$\epsilon=0.1$	$\epsilon=0.2$	$\epsilon=0.5$	$\epsilon=1.0$
1	0.60	4.99	5.12	5.26	5.34
2	0.60	5.19	5.25	5.32	5.34
4	0.60	5.28	5.30	5.33	5.34
8	0.60	5.32	5.33	5.34	5.34

interface and therefore counteract the constriction by allowing the heat flow to disperse over a larger area.

In order to ensure that the phenomena observed were not a consequence of the particular contact zone distributions described above, results were also obtained for various other contact zone distributions. These results substantiated the original observations.

Conclusions

The validity of the perfect contact assumption has been investigated in the context of fin assembly heat transfer employing a sophisticated two-dimensional analysis coupled with a relatively simple theoretical model of surface roughness. The results predicted by this analysis indicate, in particular, that provided contact can be achieved over at least 10 percent of the contact interface then the difference between the nonperfect and perfect contact solutions is virtually negligible. Thus, it may be concluded that the perfect contact assumption will suffice for design calculations provided wall-to-fin contact is greater than 10 percent.

Finally, it must be emphasized that the authors do not advocate the complex theoretical model described by equations (1), (2), and (3) as a design technique; the two-dimensional analysis and the associated surface roughness model were only necessary in order to perform a meaningful theoretical investigation into the applicability of the perfect contact assumption. In fact, from the results obtained it is evident that the conventional methods of analysis are perfectly sufficient for design purposes.

References

1 Aziz, A., and Na, T. Y., "Periodic Heat Transfer in Fins With Variable Thermal Parameters," *Int J Heat Mass Transfer*, Vol. 24, 1981, pp. 1397-1404.

2 Eslinger, R. G., and Chung, B. T. F., "Periodic Heat Transfer in Radiating Fins or Fin Arrays," *AIAA Journal*, Vol. 17, 1979, pp. 1134-1140.

3 Heggs, P. J., and Stones, P. R., "Improved Design Methods for Finned Tube Heat Exchangers," Trans Inst Chem Engrs, Vol. 58, 1980, pp. 147-154.

4 Suryanarayana, N. V., "Two-Dimensional Effects on Heat Transfer From an Array of Straight Fins," ASME JOURNAL OF HEAT TRANSFER, Vol. 99, 1977, pp. 129-132.

5 Gardener, K. A., and Carnovos, T. C., "Thermal Contact Resistance in Finned Tubing," ASME JOURNAL OF HEAT TRANSFER, Vol. 82, 1960, pp. 279-284.

6 Young, E. H., and Briggs, D. E., "Bond Resistance of Bimetallic Finned Tubes," *Chem Enging Progress*, Vol. 61, 1965, pp. 71-76.

7 Kulkarni, M. W., and Young, E. H., "Bimetallic Finned Tubes," *Chem Enging Progress*, Vol. 62, 1966, pp. 69-74.

8 Heggs, P. J., Ingham, D. B., and Manzoor, M., "The Boundary Integral Equation Analysis of Fin Assembly Heat Transfer," *Numerical Heat Transfer*, Vol. 4, 1981, pp. 285-301.

9 Stones, P. R., PhD thesis, University of Leeds, England, 1980.

10 Heggs, P. J., Ingham, D. B., and Manzoor, M., "The Analysis of Fin Assembly Heat Transfer by a Series Truncation Method," ASME JOURNAL OF HEAT TRANSFER, Vol. 104, 1982, pp. 210-212.

Solidification Interface Shape for Continuous Casting in an Offset Mold—Two Analytical Methods

R. Siegel[1]

Nomenclature

A = dimensionless parameter and dimensionless length, $a\bar{u}\rho\lambda/k(t_f-t_c) = a/\gamma$
a = half-width of slab ingot
B_n, D_n = coefficients in Fourier series
h = offset of mold; $H = h/\gamma$
k = thermal conductivity of solidified material
n = normal to interface; $N = n/\gamma$
S = dimensionless coordinate along solidification interface
t = temperature
$\bar{u}$ = casting velocity of ingot
x,y = coordinates in physical plane; $X = x/\gamma$, $Y = y/\gamma$

Greek symbols

γ = length scale parameter, $k(t_f-t_c)/\bar{u}\rho\lambda$
Θ = angle between interface normal and x-axis
λ = latent heat of fusion per unit mass of solid
ρ = density of solid
Φ = potential function, $(t_f-t)/(t_f-t_c)$
Ψ = heat flow function orthogonal to Φ

Subscripts

c = at cooled boundary
f = at solidification temperature
s = at solidification interface
1,2...8 = locations around ingot boundary
I,II = two solutions in superposition

Introduction

When a slab ingot is being formed as a continuous casting by pulling it from a mold with parallel sides, the solidification interface is a "free" boundary that adjusts with the heat flow

[1] National Aeronautics and Space Administration, Lewis Research Center, Cleveland, Ohio 44135, Fellow ASME

Contributed by the Heat Transfer Division for publication in the JOURNAL OF HEAT TRANSFER. Manuscript received by the Heat Transfer Division, May 11, 1983.

conditions. For a symmetric mold the unknown interface was found by a conformal mapping method in [1], where background information is given that will not be repeated here. In [2] an alternate analysis was given using a Cauchy boundary value method that required less algebra than the mapping method. The usefulness of this method is demonstrated here in analyzing the more difficult situation of a nonsymmetric horizontal mold where the walls may be offset to support the lower ingot boundary. Another solution method for the casting problem, involving a product solution in the potential plane and the use of conjugate harmonic functions, is also presented. As shown later, for some types of geometries this may be more direct than the Cauchy boundary value method.

Analysis

Since this analysis is a generalized case of that considered in [1] and [2], the physical description and boundary conditions can be abbreviated here and the references consulted for details. As shown in Fig. 1(*a*), the ingot is formed at velocity, $\bar{u}$, from an insulated mold where $\partial t/\partial y = 0$ at the mold boundaries. The sides of the ingot are cooled to t_c and the solidification interface is at t_f. The heat flow condition in the solid along the solidification interface is $k\partial t/\partial n = \rho\bar{u}\lambda\cos\Theta$ and the interface is an unknown "free" boundary. Within the ingot the heat conduction equation, $\nabla^2 t = 0$, is to be satisfied.

Referring to the Nomenclature, the temperatures are expressed in terms of a potential, Φ, and all lengths are divided by the characteristic dimension, γ. Then $\Phi = 1$ at the cooled boundaries, $\Phi = 0$ at the unknown interface, and $\partial\Phi/\Phi Y = 0$ at the mold. At the interface $-\partial\Phi/\partial N = \cos\Theta$. The Ψ is a heat flow function orthogonal to Φ so that the Cauchy-Riemann equations can be applied at the interface to yield $-\partial\Phi/\partial N = \partial\Psi/\partial S$ and $\partial\Psi/\partial N = \partial\Phi/\partial S = 0$ (since S is at constant Φ). Then, along the interface, $\partial\Psi/\partial Y|_s = (\partial\Psi/\partial S)(\partial S/\partial Y) + (\partial\Psi/\partial N)(\partial N/\partial Y) = (-\partial\Phi/\partial N)(\partial S/\partial Y) = \cos\Theta(1/\cos\Theta) = 1$. If Ψ is set equal to zero at $Y = 0$, then $\Psi = Y$ along the interface. It follows that Ψ equals 0 and $2A$ along the lower and upper mold boundaries, and the ingot region is contained within two constant Φ and two constant Ψ boundaries. In the Ψ-Φ plane, the ingot then occupies a rectangle: $0 \le \Psi \le 2A$, $0 \le \Phi \le 1$, as shown in the upper part of Fig. 2. The Ψ_2 dashed line in Fig. 1(*b*) is the divider between heat flows to the upper and lower boundaries. The heat of fusion for the portion of the interface below this line all flows out of the lower boundary.

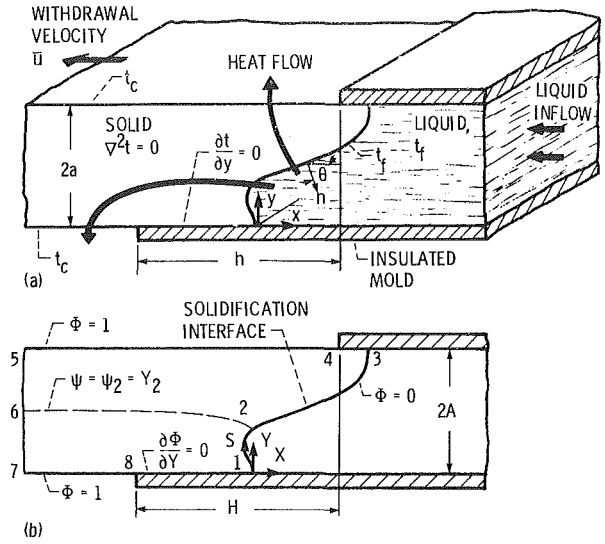

Fig. 1 Slab ingot being cast by continuous withdrawal from an offset horizontal mold: (*a*) physical geometry; (*b*) geometry and boundary conditions in dimensionless variables

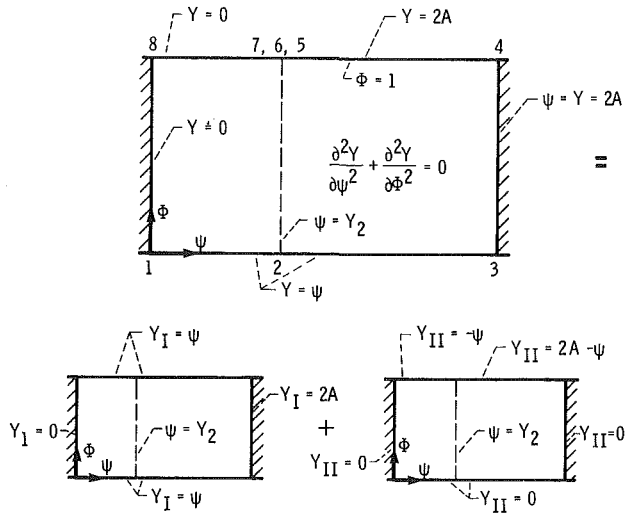

Fig. 2 Solid region in potential plane and superposition of boundary conditions for alternate method

Cauchy Boundary Value Method. As shown in [2], if the functions $X_s(\Psi)$ and $Y_s(\Psi)$ are known along the solidification interface, $S(\Phi = 0)$, then within the rectangle of Fig. 2

$$X(\Psi,\Phi) = \mathrm{Re}X_s(\Psi + i\Phi) - I\mathrm{m}Y_s(\Psi + i\Phi) \qquad (1a)$$

$$Y(\Psi,\Phi) = I\mathrm{m}X_s(\Psi + i\Phi) + \mathrm{Re}Y_s(\Psi + i\Phi) \qquad (1b)$$

Since at the interface $Y_s(\Psi) = \Psi$, the $Y_s(\Psi + i\Phi) = \Psi + i\Phi$ and equations (1) reduce to

$$X(\Psi,\Phi) = \mathrm{Re}X_s(\Psi + i\Phi) - \Phi \qquad (2a)$$

$$Y(\Psi,\Phi) = I\mathrm{m}X_s(\Psi + i\Phi) + \Psi \qquad (2b)$$

Let the unknown interface be expressed as a Fourier series

$$\frac{X_s(Y)}{A} = B_o + \sum_{n=1}^{\infty} B_n \cos\frac{n\pi Y}{2A} \quad 0 \le Y \le 2A \qquad (3)$$

The unknown B_n will be found from conditions relating the regions in Figs. 2 and 1. Since $Y = \Psi$ along the interface S, equation (3) directly yields $X_s(\Psi)$ which is inserted into equations (2) to yield

$$\frac{X(\Psi,\Phi)}{A} = B_o + \sum_{n=1}^{\infty} B_n \cos\frac{n\pi\Psi}{2A}\cosh\frac{n\pi\Phi}{2A} - \frac{\Phi}{A} \qquad (4a)$$

$$\frac{Y(\Psi,\Phi)}{A} = -\sum_{n=1}^{\infty} B_n \sin\frac{n\pi\Psi}{2A}\sinh\frac{n\pi\Phi}{2A} + \frac{\Psi}{A} \qquad (4b)$$

Along the boundary 7-8, $\Phi = 1$ and $Y = 0$, and along 4-5, $\Phi = 1$ and $Y = 2A$. This yields from equation (4*b*)

$$\frac{\Psi}{A} = \sum_{n=1}^{\infty} B_n \sin\frac{n\pi\Psi}{2A}\sinh\frac{n\pi}{2A} \qquad 0 \le \Psi \le \Psi_2 (= Y_2) \qquad (5a)$$

$$\frac{\Psi}{A} - 2 = \sum_{n=1}^{\infty} B_n \sin\frac{n\pi\Psi}{2A}\sinh\frac{n\pi}{2A} \qquad Y_2 \le \Psi \le 2A \qquad (5b)$$

As in a standard application of Fourier series, each of equations (5) is multiplied by $\sin(m\pi\Psi/2A)$ and integrated over its applicable range of Ψ. The two equations are then added, and after integration this yields

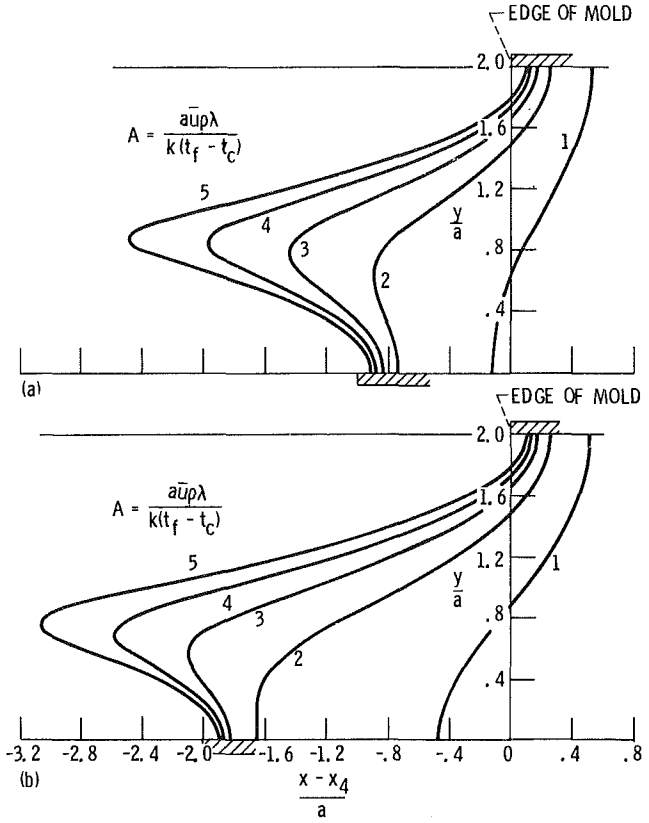

Fig. 3 Interface shapes as a function of parameter *A*: (*a*) mold offset, *h*/*a* = 1; (*b*) mold offset, *h*/*a* = 2

$$B_n = -\frac{4}{\pi}\frac{1}{n\sinh(n\pi/2A)}\cos\left(\frac{n\pi Y_2}{2A}\right) \tag{6}$$

Inserting the B_n into equation (3) yields the shape (but not the horizontal position) of the solidification interface if Y_2 in (6) can be obtained. The Y_2 is found from the geometric constraint of the mold offset that $X_4 - X_8 = H$. The X_4 is found from (4*a*) at $\Psi = 2A$ and $\Phi = 1$, and X_8 is at $\Psi = 0$ and $\Phi = 1$. After inserting B_n from (6) and some rearrangement to improve convergence

$$\left(\text{by use of the identity } \sum_{n=1,3,5\ldots}^{\infty}\frac{1}{n}\cos\frac{n\pi Y_2}{2A} = \frac{1}{2}\ln\cot\frac{\pi Y_2}{4A}\right)$$

this gives,

$$\frac{H}{A} = \frac{4}{\pi}\ln\cot\frac{\pi Y_2}{4A} + \frac{16}{\pi}\sum_{n=1}^{\infty}\frac{1}{2n-1}\frac{e^{-(2n-1)\pi/A}}{1-e^{-(2n-1)\pi/A}}\cos\frac{(2n-1)\pi Y_2}{2A} \tag{7}$$

This yields the following Y_2/A values used for the results in Fig. 3:

	Y_2/A	
A	$H/A=1$	$H/A=2$
1	0.59768	0.30476
2	.75270	.51292
3	.83341	.66706
4	.87500	.75001
5	.90000	.80000

To locate the interface horizontally within the mold, the X-values will be obtained relative to $X_4 = X(2A, 1)$ located at one edge of the mold. Then by use of equations (3), (4*a*), and (6), after some rearrangement

$$\left(\text{note that } \sum_{n=1}^{\infty}\frac{(-1)^n}{n}\cos\frac{n\pi Y_2}{2A} = -\ln\left[2\cos\frac{\pi Y_2}{4A}\right]\right)$$

$$\frac{X_s(Y)-X_4}{A} = \frac{1}{A} - \frac{4}{\pi}\ln\left(2\cos\frac{\pi Y_2}{4A}\right) + \frac{4}{\pi}\sum_{n=1}^{\infty}\frac{1}{n}\frac{\cos(n\pi Y_2/2A)}{\sinh(n\pi/2A)}\left[(-1)^n e^{-n\pi/2A} - \cos\frac{n\pi Y}{2A}\right] \tag{8}$$

Product Solution Method. The expressions for $X(\Psi, \Phi)$ and $Y(\Psi, \Phi)$ can be found in another way that may be useful in some instances, such as for the parallel-sided type of geometry being analyzed here. From the boundary condition $Y = \Psi$ along the solidification interface and from the parallel-sided configuration of the ingot and mold, the values of Y are known in terms of the quantities Ψ, 0, or A on all sides of the upper rectangle in Fig. 2. This boundary value problem for Y can be represented as a superposition of two solutions, $Y = Y_{\mathrm{I}} + Y_{\mathrm{II}}$ as shown in the figure. The solution for Y_{I} that satisfies $\partial^2 Y_{\mathrm{I}}/\partial\Psi^2 + \partial^2 Y_{\mathrm{I}}/\partial\Phi^2 = 0$ is $Y_{\mathrm{I}} = \Psi$. The Y_{II} satisfying the same equation can be found by separation of variables (see [3] p. 422, for example) to yield,

$$Y_{\mathrm{II}}(\Psi,\Phi) = \sum_{n=1}^{\infty} D_n \sin\frac{n\pi\Psi}{2A}\frac{\sinh(n\pi\Phi/2A)}{\sinh(n\pi/2A)} \tag{9a}$$

$$D_n = \frac{1}{A}\left[\int_0^{Y_2}(-\Psi)\sin\frac{n\pi\Psi}{2A}d\Psi + \int_{Y_2}^{2A}(2A-\Psi)\sin\frac{n\pi\Psi}{2A}d\Psi\right] = \frac{4A}{n\pi}\cos\frac{n\pi Y_2}{2A} \tag{9b}$$

The sum $Y = Y_{\mathrm{I}} + Y_{\mathrm{II}}$ gives the same result as equations (4*b*) and (6). The $X(\Psi, \Phi)$ is then found as the conjugate harmonic function of Y by integrating the Cauchy-Riemann equations $\partial X/\partial\Psi = \partial Y/\partial\Phi$ and $\partial X/\partial\Phi = -\partial Y/\partial\Psi$. With $X(\Psi, \Phi)$ and $Y(\Psi, \Phi)$ known the completion of the solution follows through as before.

Results and Discussion

The "free" boundary solidification interface for continuous casting in an offset mold was found by two methods: a Cauchy boundary value procedure and by separation of variables in the complex potential plane. Both methods lead to the solution with a small amount of algebra and may be useful for similar types of problems. The solutions are in terms of analytical expressions that can be easily evaluated.

Typical interface shapes are shown in Fig. 3. The curves depend on the mold offset and on the parameter, A, that contains the ingot withdrawal velocity, latent heat of fusion, and thermal conductivity of the solid. Increasing A such as by increasing $\bar{u}$ causes the interface to extend further to the left to provide a shape of the solid with less resistance for heat conduction from the interface to the cooled surfaces of the ingot. When the mold offset is zero the results reduce to those in [1] and [2].

As shown in Fig. 1(*b*), the constant Ψ-line that divides the heat flow between the lower and upper cooled boundaries intersects the solidification interface at Y_2, and the Ψ is equal to Y_2. Since the maximum Ψ is $2A$, the fraction of the total solidification energy flowing out the lower cooled boundary is $Y_2/2A$, which can be obtained from the values in the table given in the Analysis. As A increases, the effect of the offset

on the interface shape diminishes, and the interface tends to become symmetric; the $Y_2/2A$ then tends to approach 1/2.

The numerical results given here are only illustrative; other cases can be easily evaluated from the analytical solutions.

References

1 Siegel, R., "Analysis of Solidification Interface Shape During Continuous Casting of a Slab," *International Journal of Heat and Mass Transfer*, Vol. 21, Nov. 1978, pp. 1421–1430.

2 Siegel, R., "Cauchy Method for Solidification Interface Shape During Continuous Casting," ASME JOURNAL OF HEAT TRANSFER, Vol. 105, Aug. 1983, pp. 667–671.

3 Hildebrand, F. B., *Advanced Calculus for Engineers*, Prentice-Hall, New York, 1949.

Mixed Convection Over a Horizontal Plate

N. Afzal[1] and T. Hussain[2]

1 Introduction

Mixed convection on a horizontal plate has been studied by several workers. It is well known that the problem for an isothermal plate does not admit similarity [1-4]. Recently Schneider [5] has shown the existence of similarity provided the wall temperature is prescribed as the inverse square root of the distance from the leading edge. The solutions [5] cover a limited range of buoyancy to forced convection parameter (say, K) that do not include the strongly buoyant flows in aiding situations and nearly separating flows in opposing situations. Likewise, the work of Dey [6], dealing with an extension of [5] to mass transfer, also considers almost the same limited range of K. One of the limitation of these works [5, 6] is that the nature of the solution in the neighborhood of separation remains unexplored [5, 6]. It is shown here that the solutions to the Schneider [5] problem in the neighborhood of separation are dual.

The aim of this work is to present the dual solutions to the problem of Schneider and also to examine the solution for the entire domain, beginning from purely free convection dominated to separated flows.

2 Equations

The self-similar boundary layer equations for mixed convection on a flate plate, in the notions of Schneider [5], are

$$\begin{aligned} &2f''' + ff'' + K\eta\theta = 0 \\ &\frac{2}{\sigma}\theta'' + (f\theta)' = 0 \\ &f(0) = f'(0) = 0,\ \theta(0) = 1 \\ &f'(\infty) = 1, \quad \theta(\infty) = 0 \end{aligned} \tag{1}$$

Here $f(\eta)$ and $\theta(\eta)$ nondimensional stream function and temperature, respectively, and η is the similarity (Blasius) variable. K is a parameter, representing the relative effects of free to forced convection, and σ is the Prandtl number of the fluid. The global heat flux expressed in terms of Stanton number, St, is given by

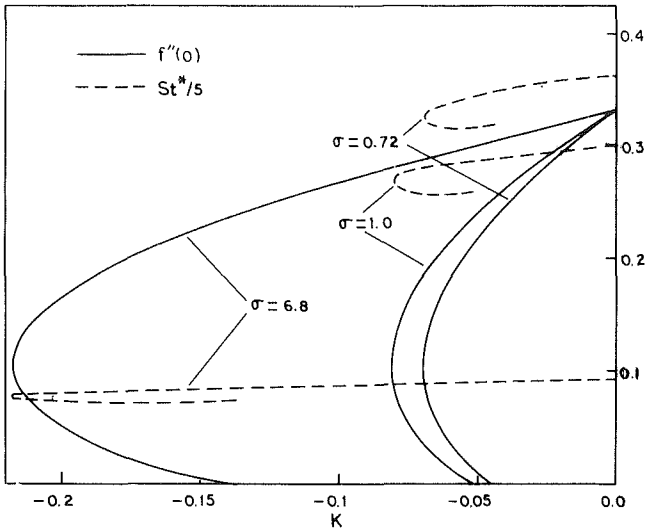

Fig. 1 Adverse case: skin friction and global heat flux in self-similar mixed convection flow on a flat plate

$$\mathrm{St}^* = \mathrm{St}\sqrt{\mathrm{Re}} = \int_0^\infty f'\theta d\eta \tag{2}$$

where Re is the Reynolds number. For free convection dominated flow, $K \to \infty$, appropriate variables are

$$\zeta = K^{1/5}\eta \tag{3a}$$

$$\mathrm{F}(\zeta) = f(\eta)K^{-1/5} \tag{3b}$$

In terms of variables (3), the problem (1) becomes

$$\begin{aligned} &2F''' + FF'' + \zeta\theta = 0 \\ &\frac{2}{\sigma}\theta'' + (F\theta)' = 0 \\ &F(0) = F'(0) = 0, \quad \theta(0) = 1 \\ &F'(\infty) = \epsilon,\ \theta(\infty) = 0 \end{aligned} \tag{4}$$

where $\epsilon = K^{-2/5}$ (5)

The global heat flux (2) reduces to

$$\mathrm{St}^*/K^{1/5} = \int_0^\infty F'\theta d\zeta \tag{6}$$

The cases $K = 0$ and $\epsilon = 0$ correspond respectively to purely forced and free convection flows.

3 Results

The boundary value problems governed by ordinary differential equations (1) and (4) had been integrated by the Runge-Kutta method with the Gill improvement on a VAX-11/780 at Aligarh Muslim University, Aligarh. The missing boundary condition was guessed such that the boundary condition on streamwise velocity at infinity was satisfied by minimum error criteria in the least-square sense. In the favorable case, K (or ϵ) was fixed, and $f''(0)$ [or $F''(0)$] was guessed. In the adverse case near separation, it was found more convenient to fix values of $f''(0)$ and guess the value of K. The values of Prandtl numbers considered correspond to air $\sigma = 0.72$ and water $\sigma = 6.8$; the case of $\sigma = 1.0$, for $K < 0$ is also considered for comparison with [5].

For the adverse case $K < 0$, where buoyancy opposes the forced convection, the solutions for skin friction, $f''(0)$, and global Stanton number, St*, are displayed in Fig. 1. Figure 1 shows that as magnitude of K increases, the skin friction, $f''(0)$, decreases until a value of $K(=K_o(\sigma)$; say) is reached where $df''(\sigma)/dK$ is minus infinity; consequently, the curve turns back and as the magnitude of K decreases, the skin

[1]Department of Mechanical Engineering, Aligarh Muslim University, Aligarh, 202001, India

[2]Department of Mathematics, Aligarh Muslim University, Aligarh, 202001, India

Contributed by the Heat Transfer Division for publication in the JOURNAL OF HEAT TRANSFER. Manuscript received by the Heat Transfer Division December 3, 1982.

on the interface shape diminishes, and the interface tends to become symmetric; the $Y_2/2A$ then tends to approach 1/2.

The numerical results given here are only illustrative; other cases can be easily evaluated from the analytical solutions.

References

1 Siegel, R., "Analysis of Solidification Interface Shape During Continuous Casting of a Slab," *International Journal of Heat and Mass Transfer*, Vol. 21, Nov. 1978, pp. 1421–1430.

2 Siegel, R., "Cauchy Method for Solidification Interface Shape During Continuous Casting," ASME JOURNAL OF HEAT TRANSFER, Vol. 105, Aug. 1983, pp. 667–671.

3 Hildebrand, F. B., *Advanced Calculus for Engineers*, Prentice-Hall, New York, 1949.

Mixed Convection Over a Horizontal Plate

N. Afzal[1] and T. Hussain[2]

1 Introduction

Mixed convection on a horizontal plate has been studied by several workers. It is well known that the problem for an isothermal plate does not admit similarity [1–4]. Recently Schneider [5] has shown the existence of similarity provided the wall temperature is prescribed as the inverse square root of the distance from the leading edge. The solutions [5] cover a limited range of buoyancy to forced convection parameter (say, K) that do not include the strongly buoyant flows in aiding situations and nearly separating flows in opposing situations. Likewise, the work of Dey [6], dealing with an extension of [5] to mass transfer, also considers almost the same limited range of K. One of the limitation of these works [5, 6] is that the nature of the solution in the neighborhood of separation remains unexplored [5, 6]. It is shown here that the solutions to the Schneider [5] problem in the neighborhood of separation are dual.

The aim of this work is to present the dual solutions to the problem of Schneider and also to examine the solution for the entire domain, beginning from purely free convection dominated to separated flows.

2 Equations

The self-similar boundary layer equations for mixed convection on a flate plate, in the notions of Schneider [5], are

$$\begin{aligned} &2f''' + ff'' + K\eta\theta = 0 \\ &\frac{2}{\sigma}\theta'' + (f\theta)' = 0 \\ &f(0) = f'(0) = 0,\ \theta(0) = 1 \\ &f'(\infty) = 1, \quad \theta(\infty) = 0 \end{aligned} \tag{1}$$

Here $f(\eta)$ and $\theta(\eta)$ nondimensional stream function and temperature, respectively, and η is the similarity (Blasius) variable. K is a parameter, representing the relative effects of free to forced convection, and σ is the Prandtl number of the fluid. The global heat flux expressed in terms of Stanton number, St, is given by

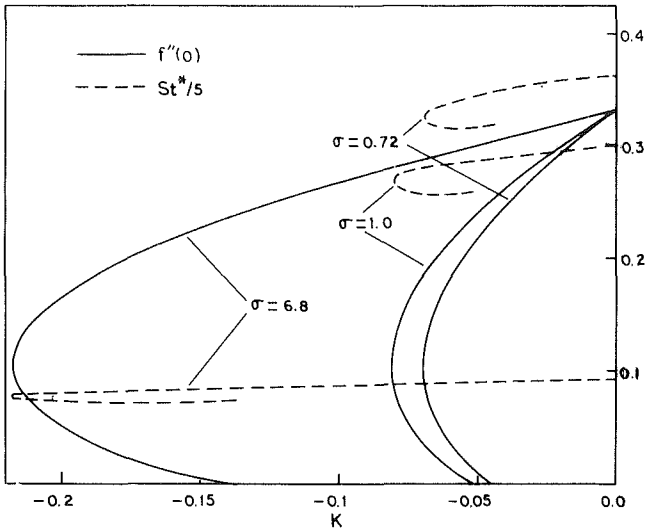

Fig. 1 Adverse case: skin friction and global heat flux in self-similar mixed convection flow on a flat plate

$$\mathrm{St}^* = \mathrm{St}\sqrt{\mathrm{Re}} = \int_0^\infty f'\theta d\eta \tag{2}$$

where Re is the Reynolds number. For free convection dominated flow, $K \to \infty$, appropriate variables are

$$\zeta = K^{1/5}\eta \tag{3a}$$

$$\mathrm{F}(\zeta) = f(\eta)K^{-1/5} \tag{3b}$$

In terms of variables (3), the problem (1) becomes

$$\begin{aligned} &2F''' + FF'' + \zeta\theta = 0 \\ &\frac{2}{\sigma}\theta'' + (F\theta)' = 0 \\ &F(0) = F'(0) = 0, \quad \theta(0) = 1 \\ &F'(\infty) = \epsilon,\ \theta(\infty) = 0 \end{aligned} \tag{4}$$

where $\epsilon = K^{-2/5}$ (5)

The global heat flux (2) reduces to

$$\mathrm{St}^*/K^{1/5} = \int_0^\infty F'\theta d\zeta \tag{6}$$

The cases $K = 0$ and $\epsilon = 0$ correspond respectively to purely forced and free convection flows.

3 Results

The boundary value problems governed by ordinary differential equations (1) and (4) had been integrated by the Runge-Kutta method with the Gill improvement on a VAX-11/780 at Aligarh Muslim University, Aligarh. The missing boundary condition was guessed such that the boundary condition on streamwise velocity at infinity was satisfied by minimum error criteria in the least-square sense. In the favorable case, K (or ϵ) was fixed, and $f''(0)$ [or $F''(0)$] was guessed. In the adverse case near separation, it was found more convenient to fix values of $f''(0)$ and guess the value of K. The values of Prandtl numbers considered correspond to air $\sigma = 0.72$ and water $\sigma = 6.8$; the case of $\sigma = 1.0$, for $K < 0$ is also considered for comparison with [5].

For the adverse case $K < 0$, where buoyancy opposes the forced convection, the solutions for skin friction, $f''(0)$, and global Stanton number, St*, are displayed in Fig. 1. Figure 1 shows that as magnitude of K increases, the skin friction, $f''(0)$, decreases until a value of $K(=K_o(\sigma)$; say) is reached where $df''(\sigma)/dK$ is minus infinity; consequently, the curve turns back and as the magnitude of K decreases, the skin

[1]Department of Mechanical Engineering, Aligarh Muslim University, Aligarh, 202001, India

[2]Department of Mathematics, Aligarh Muslim University, Aligarh, 202001, India

Contributed by the Heat Transfer Division for publication in the JOURNAL OF HEAT TRANSFER. Manuscript received by the Heat Transfer Division December 3, 1982.

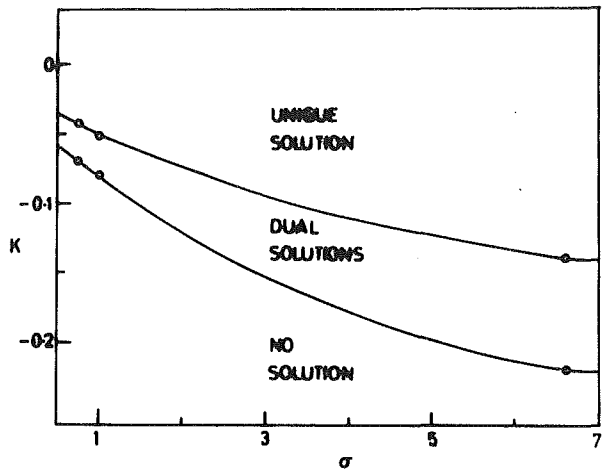

Fig. 2 The nature of solutions for the adverse case where buoyancy opposes the oncoming stream

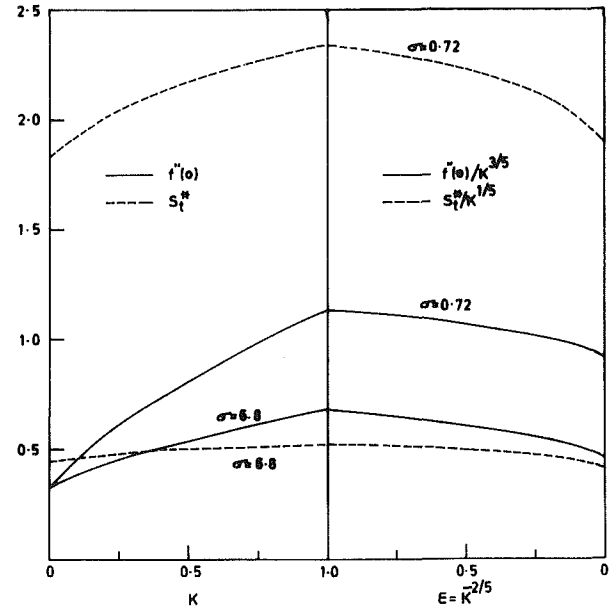

Fig. 3 Favourable case: skin friction and global heat flux in (a) forced convection dominated flow, $0 \le K \le 1$; (b) free-convection dominated flow, $0 \le \epsilon \le 1$

friction further decreases to become zero. Figure 1 shows that for $K > K_o(\sigma)$, the solutions to the problem are nonexistent, and at $K < K_o(\sigma)$ there is a domain where solutions are dual. The dual solutions have not been reported earlier [1-6]. The heat transfer results are qualitatively similar to skin friction, and no additional comment is needed. The nature of the solutions in $K-\sigma$ plane displayed in Fig. 2 shows the boundary of the domains where solutions are unique, dual, and nonexistent.

The dual nature of present solutions is qualitatively similar to the one reported by Cohen and Reshotko for a compressible boundary layer on a cold surface under adverse pressure gradient near separation [7, 8]. In the present similarity analysis, the wall temperature, $T_w \sim x^{-1/2}$, is singular near the leading edge and the similarity solution cannot be completely reproduced by a real flow. When a temperature field is imposed on the wall, the developing boundary layer after local adjustments would approach to one of the similar solutions for $K<0$. Therefore, it seems plausible that depending on the manner in which a temperature field is imposed, one or the other solution could be approached after different adjustment phases. It may not be out of place to point out that in the experimental work on turbulent boundary layer under strong adverse pressure gradient Spangenberg, Rowland and Mease [9] have found the dual solutions, depending on the way in which the pressure gradient is applied.

For $K>0$, where buoyancy accelerates the forced convection flow, the entire domain of K is of interest. For computational convenience the domain is divided in two subdomains. In the first subdomain, $0 \le K \le 1$, corresponding to forced convection dominated flows, the equations (1) are employed, and in the second subdomain, $1 \ge \epsilon \ge 0$ ($\epsilon = K^{-2/5}$), corresponding to free convection dominated flows, the equations (4) are employed, with a change over at $\epsilon = K = 1$. The solutions for skin friction and heat transfer for $0 \le K \le 1$ and $1 \ge \epsilon \ge 0$ are displayed in Fig. 3. The figure shows that as K increases, the skin friction and heat transfer rate increases. This is because that for $K>0$ the buoyancy accelerates the flow in the boundary layer. As K becomes sufficiently large, the skin friction, $f''(0)$, and heat transfer, St*, become large, respectively, like $K^{3/5}$ and $K^{2/5}$. As $K \to \infty$ ($\epsilon \to 0$), the results approach to purely free convection flow.

In summary, the present work describes the solution for self-similar mixed convection flow, covering the entire range, beginning from purely free convection to the separating flows. In the adverse flow situation where buoyancy opposes the forced convection, the solutions in the neighborhood of separation are dual.

Acknowledgment

T. Hussain is thankful to the University Grants Commission, New Delhi, for the award of a research fellowship.

References

1 Sparrow, E. M., and Minkowyez, W. J., "Buoyancy Effects on Horizontal Boundary Layer Flow and Heat Transfer," *International Journal of Heat and Mass Transfer*, Vol. 5, 1962, pp. 505-511.

2 Hieber, C. A., "Mixed Convection Above a Heated Horizontal Surface," *International Journal of Heat and Mass Transfer*, Vol. 16, 1973, pp. 769-782.

3 Chen, T. S., Sparrow, E. M., and Mucoglu, A., "Mixed Convection in Boundary Layer Flow on a Horizontal Plate," ASME JOURNAL OF HEAT TRANSFER, Vol. 99, 1977, pp. 66-71.

4 Banthiya, N. K., and Afzal, N., "Mixed Convection Over a Semi-Infinite Horizontal Plate," *Z. Angew. Math. Phys.*, Vol. 31, 1980, pp. 646-652.

5 Schneider, W., "A Similarity Solution for Combined Forced and Free Convection Flow Over a Horizontal Plate," *International Journal of Heat and Mass Transfer*, Vol. 22, 1979, pp. 1401-1406.

6 Dey, J., "Mixed Convection Flow Over a Semi-Infinite Horizontal Plate With Vectored Mass Transfer," ASME JOURNAL OF HEAT TRANSFER, Vol. 104, 1982, pp. 558-560.

7 Cohen, C. B., and Reshotko, E., "Similar Solutions for Compressible Laminar Boundary Layer With Heat Transfer and Pressure Gradient," NACA Report 1293, 1956.

8 Schlichting, H., *Boundary Layer Theory*, McGraw-Hill, 6th ed. 1968, pp. 332-334.

9 Spangenberg, W. G., Rowland, W. R., and Mease, N. E., *Fluid Mechanics of Internal Flows*, edited by G. Sovran, Elsevier, 1967, pp. 110-150.

Natural Convection in a Volumetrically Heated Porous Layer

C. W. Somerton,[2] J. M. McDonough,[1] and I. Catton[1]

a = wave number
C_p = specific heat
Da = Darcy number, ψ/h^2

[1] University of California, Los Angeles, Los Angeles, Calif. 90024
[2] Louisiana State University, Baton Rouge, La. 70803

Contributed by the Heat Transfer Division for publication in the JOURNAL OF HEAT TRANSFER. Manuscript received by the Heat Transfer Division September 9, 1982.

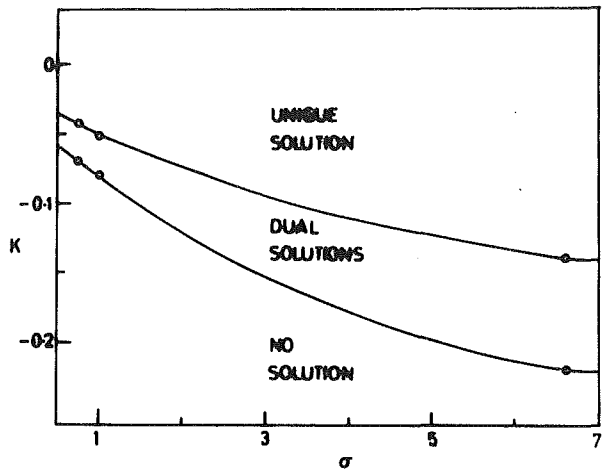

Fig. 2 The nature of solutions for the adverse case where buoyancy opposes the oncoming stream

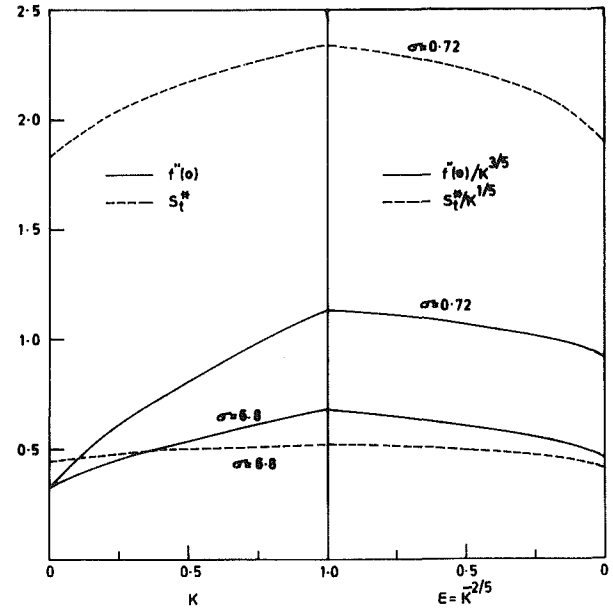

Fig. 3 Favourable case: skin friction and global heat flux in (a) forced convection dominated flow, $0 \le K \le 1$; (b) free-convection dominated flow, $0 \le \epsilon \le 1$

friction further decreases to become zero. Figure 1 shows that for $K > K_o(\sigma)$, the solutions to the problem are nonexistent, and at $K < K_o(\sigma)$ there is a domain where solutions are dual. The dual solutions have not been reported earlier [1-6]. The heat transfer results are qualitatively similar to skin friction, and no additional comment is needed. The nature of the solutions in $K-\sigma$ plane displayed in Fig. 2 shows the boundary of the domains where solutions are unique, dual, and nonexistent.

The dual nature of present solutions is qualitatively similar to the one reported by Cohen and Reshotko for a compressible boundary layer on a cold surface under adverse pressure gradient near separation [7, 8]. In the present similarity analysis, the wall temperature, $T_w \sim x^{-1/2}$, is singular near the leading edge and the similarity solution cannot be completely reproduced by a real flow. When a temperature field is imposed on the wall, the developing boundary layer after local adjustments would approach to one of the similar solutions for $K<0$. Therefore, it seems plausible that depending on the manner in which a temperature field is imposed, one or the other solution could be approached after different adjustment phases. It may not be out of place to point out that in the experimental work on turbulent boundary layer under strong adverse pressure gradient Spangenberg, Rowland and Mease [9] have found the dual solutions, depending on the way in which the pressure gradient is applied.

For $K>0$, where buoyancy accelerates the forced convection flow, the entire domain of K is of interest. For computational convenience the domain is divided in two subdomains. In the first subdomain, $0 \le K \le 1$, corresponding to forced convection dominated flows, the equations (1) are employed, and in the second subdomain, $1 \ge \epsilon \ge 0$ ($\epsilon = K^{-2/5}$), corresponding to free convection dominated flows, the equations (4) are employed, with a change over at $\epsilon = K = 1$. The solutions for skin friction and heat transfer for $0 \le K \le 1$ and $1 \ge \epsilon \ge 0$ are displayed in Fig. 3. The figure shows that as K increases, the skin friction and heat transfer rate increases. This is because that for $K>0$ the buoyancy accelerates the flow in the boundary layer. As K becomes sufficiently large, the skin friction, $f''(0)$, and heat transfer, St*, become large, respectively, like $K^{3/5}$ and $K^{2/5}$. As $K \to \infty$ ($\epsilon \to 0$), the results approach to purely free convection flow.

In summary, the present work describes the solution for self-similar mixed convection flow, covering the entire range, beginning from purely free convection to the separating flows. In the adverse flow situation where buoyancy opposes the forced convection, the solutions in the neighborhood of separation are dual.

Acknowledgment

T. Hussain is thankful to the University Grants Commission, New Delhi, for the award of a research fellowship.

References

1 Sparrow, E. M., and Minkowyez, W. J., "Buoyancy Effects on Horizontal Boundary Layer Flow and Heat Transfer," *International Journal of Heat and Mass Transfer*, Vol. 5, 1962, pp. 505-511.

2 Hieber, C. A., "Mixed Convection Above a Heated Horizontal Surface," *International Journal of Heat and Mass Transfer*, Vol. 16, 1973, pp. 769-782.

3 Chen, T. S., Sparrow, E. M., and Mucoglu, A., "Mixed Convection in Boundary Layer Flow on a Horizontal Plate," ASME JOURNAL OF HEAT TRANSFER, Vol. 99, 1977, pp. 66-71.

4 Banthiya, N. K., and Afzal, N., "Mixed Convection Over a Semi-Infinite Horizontal Plate," *Z. Angew. Math. Phys.*, Vol. 31, 1980, pp. 646-652.

5 Schneider, W., "A Similarity Solution for Combined Forced and Free Convection Flow Over a Horizontal Plate," *International Journal of Heat and Mass Transfer*, Vol. 22, 1979, pp. 1401-1406.

6 Dey, J., "Mixed Convection Flow Over a Semi-Infinite Horizontal Plate With Vectored Mass Transfer," ASME JOURNAL OF HEAT TRANSFER, Vol. 104, 1982, pp. 558-560.

7 Cohen, C. B., and Reshotko, E., "Similar Solutions for Compressible Laminar Boundary Layer With Heat Transfer and Pressure Gradient," NACA Report 1293, 1956.

8 Schlichting, H., *Boundary Layer Theory*, McGraw-Hill, 6th ed. 1968, pp. 332-334.

9 Spangenberg, W. G., Rowland, W. R., and Mease, N. E., *Fluid Mechanics of Internal Flows*, edited by G. Sovran, Elsevier, 1967, pp. 110-150.

Natural Convection in a Volumetrically Heated Porous Layer

C. W. Somerton,[2] J. M. McDonough,[1] and I. Catton[1]

a = wave number
C_p = specific heat
Da = Darcy number, ψ/h^2

[1] University of California, Los Angeles, Los Angeles, Calif. 90024
[2] Louisiana State University, Baton Rouge, La. 70803

Contributed by the Heat Transfer Division for publication in the JOURNAL OF HEAT TRANSFER. Manuscript received by the Heat Transfer Division September 9, 1982.

g = acceleration due to gravity
h = porous layer height
k_m = effective thermal conductivity of porous media
Nu = Nusselt number
p = pressure
Pr = Prandtl number
q = heat flux
$\dot{Q}_v$ = internal heating rate
Ra_I = internal Rayleigh number, $g\beta Q_v h^5/k_m\alpha_m\upsilon_f$
t = time
T = temperature
T_B = lower surface temperature
T_T = upper surface temperature
$\mathbf{u}$ = vector velocity
v = y or horizontal component of velocity
w = z or vertical component of velocity
y = horizontal direction
z = vertical direction

Greek Letters

α_m = effective thermal diffusivity, $k_m/(\rho C_p)_f$
β = thermal expansion coefficient
λ = wavelength
ϕ = stability functional
ρ_f = fluid density
υ_f = fluid kinematic viscosity
Ω = heat capacity ratio $(\rho C_p)_f/(\rho C_p)_m$
ψ = permeability

Introduction

A problem of current interest is that of natural convection in a porous layer with internal heating within the layer. This problem has applications in the fields of nuclear reactor safety, solar collector design, and geothermal energy conversion. The authors' interest in this work is generated primarily from concerns about the coolability of debris beds which may form following a severe accident in a nuclear reactor. In the present work, a mixed finite difference-Galerkin procedure is used to calculate the solution to the steady, two-dimensional Darcy-Oberbeck-Boussinesq (DOB) equations for an infinite horizontal porous layer, when the wave number is prescribed. The wave number of the motion is obtained from nonequilibrium thermohydrodynamic theory. Hence, our solution yields not only velocity and temperature fields, but also the size of the convection cells.

A similar analysis has been done previously by the authors [1] for the case of no internal heating, which proved to be very successful in predicting heat transfer. When volume heating of the porous layer is considered, the problem changes slightly, primarily through the addition of a new term to the energy equation. Analysis for the onset of convection in a porous layer with volume heating have been made by Gasser and Kazimi [2] and Hwang [3]. Gasser and Kazimi employ linear stability theory and solve the perturbation equations with a Galerkin procedure. They consider both stabilizing and destabilizing temperature gradients. Hwang uses the small parameter method of Poincare but only considers stabilizing temperature gradients. Tveitereid [4] solves the heat transfer problem with an adiabatic lower surface. He uses a Galerkin method to solve the governing equations but does not state what he used to obtain the wavenumber. Hardee and Nilson [5] employ a convection roll model to obtain a relationship between the internal Rayleigh number and the Nusselt number.

A number of experimental studies have been conducted for the volume heated case. Buretta [6] and Sun [7] use Joule heating of a glass-0.01 mole percent $CuSO_4$ aqueous solution to study the heat transfer problem. The bottom surface of their experiment was thermally insulated while the top surface was cooled. Rhee [8] and Cherng [9] use induction heating of a bed of steel particles with water as the fluid.

Governing Equations and Method of Solution

The steady, two-dimensional Darcy-Oberbeck-Boussinesq equations with volume heating are

$$\frac{\partial v}{\partial y}+\frac{\partial w}{\partial z}=0 \tag{1a}$$

$$\frac{\partial^2 v}{\partial y^2}+\frac{\partial^2 v}{\partial z^2}=\frac{\partial P}{\partial y}+\left(\frac{1}{\mathrm{Da}}\right)v \tag{1b}$$

$$\frac{\partial^2 w}{\partial y^2}+\frac{\partial^2 w}{\partial z^2}=\frac{\partial P}{\partial z}+\left(\frac{1}{\mathrm{Da}}\right)w-(\mathrm{Ra}_I)T \tag{1c}$$

$$v\frac{\partial T}{\partial y}+w\frac{\partial T}{\partial z}=\frac{\partial^2 T}{\partial y^2}+\frac{\partial^2 T}{\partial z^2}+1 \tag{1d}$$

Equations (1) are made dimensionless by scaling length, velocity, temperature, and pressure with h, α_m/h, $\dot{Q}_v h^2/k_m$, and $\rho_f\nu_f\alpha_m/h^2$, respectively. This results in two dimensionless parameters, the intermal Rayleigh number, and the Darcy number

$$\mathrm{Ra}=\frac{g\beta\dot{Q}_v h^5}{k_m\alpha_m\upsilon_f},\quad \mathrm{Da}=\frac{\psi}{h^2}$$

The corresponding boundary conditions on velocity for equations (1) are

$$v(y,0)=v(y,1)=0 \tag{2a}$$

$$w(y,0)=w(y,1)=0 \tag{2b}$$

As for boundary conditions on temperature, two different cases will be considered

$$T(y,1)=0 \tag{2c}$$

and

$$T(y,0)=0 \text{ or } \left.\frac{\partial T}{\partial z}\right|_{z=0}=0 \tag{2d}$$

which correspond to a zero applied temperature gradient or an adiabatic lower surface, respectively. Additional conditions are required to obtain a well-posed boundary value problem. Experimental observations suggest that periodicity conditions should be imposed; i.e.,

$$v(y,z) = v(y+\lambda,z) \tag{3a}$$

$$w(y,z) = w(y+\lambda,z) \tag{3b}$$

$$T(y,z) = T(y+\lambda,z) \tag{3c}$$

$$P(y,z) = P(y+\lambda,z) \tag{3d}$$

Here, λ is the wavelength of the motion (i.e., twice the size of a convection cell), which in general is not known a priori.

The method used to solve equations (1-3) is the mixed finite difference-Galerkin procedure of McDonough and Catton [10], which for the present case consists of a Galerkin approximation satisfying periodicity conditions in the horizontal direction and finite differencing in the vertical direction. The details of the solution for porous layer convection can be found in [1].

A key to obtaining a valid solution using the above methodology is a correct prescription of the wave number. The authors utilize the nonequilibrium thermodydrodynamic

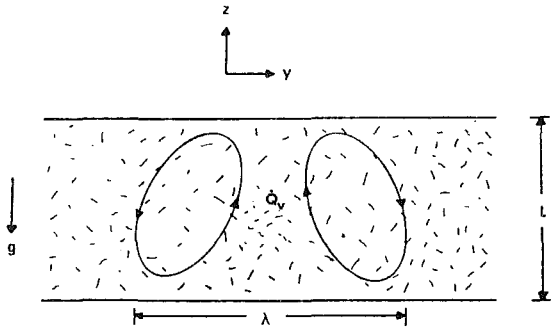

Fig. 1 The physical model

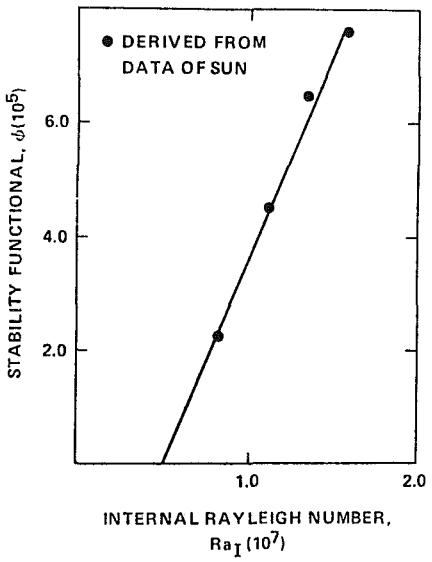

Fig. 2 Stability functional versus internal Rayleigh number for an adiabatic lower surface

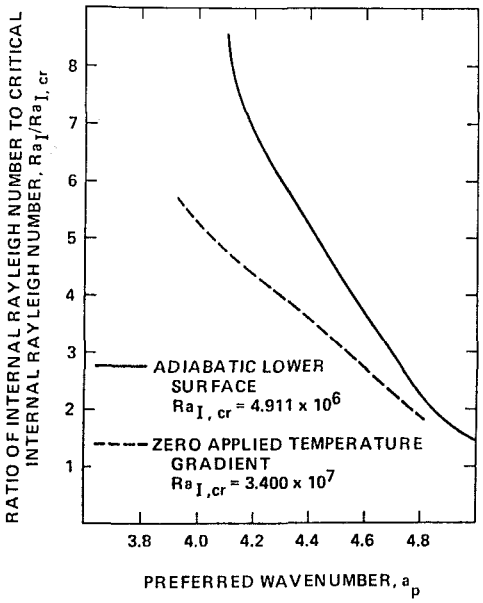

Fig. 3 Preferred wave number as a function of internal Rayleigh number

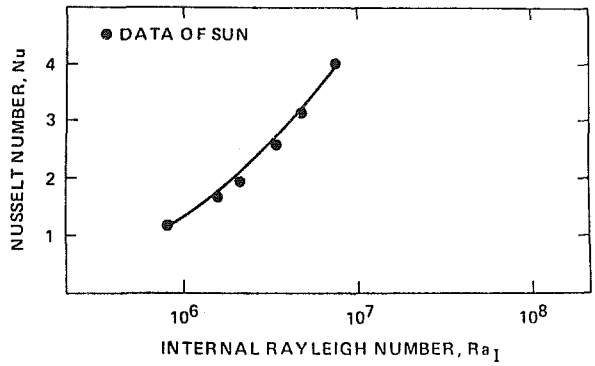

Fig. 4 Comparison of theoretical heat transfer with experimental data for adiabatic lower surface, $Da = 1.3438 \times 10^{-5}$ and $\Omega = 1.442$

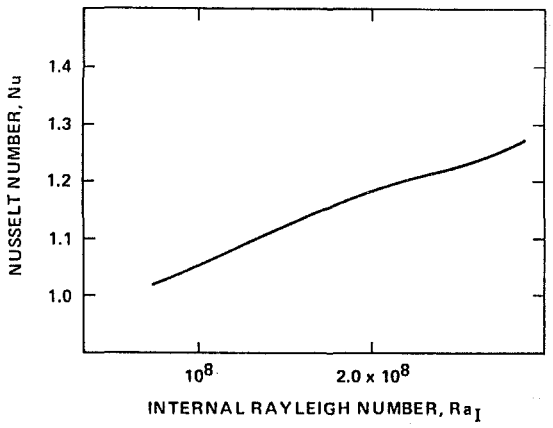

Fig. 5 Theoretical heat transfer results for zero applied temperature gradient with $Da = 1.3438 \times 10^{-5}$ and $\Omega = 1.442$

stability theory of Glansdorff and Prigogine [11] to provide the additional relationship needed to predict the wave number. The basis of the method is the observation that a certain Liapunov stability function, ϕ, which can be identified with the generalized excess entropy production of [11], varies linearly with Ra_I when evaluated at preferred wave numbers, a_p. In particular, it is seen that

$$\frac{d^2\phi}{dRa_I^2} = 0 \tag{7}$$

for $\phi\ (a,\ Ra_I) = \phi(a_p,\ Ra_I)$. This provides the additional relationship, albeit implicit, needed to predict wave numbers of two-dimensional convection.

For the porous layer problem with internal heating, the generalized excess entropy production can be expressed as

$$\phi = \int_0^1 \int_0^{\lambda/2} \left[-(Ra_I)T^* \frac{\partial T^*}{\partial t} - \left(\frac{1}{Pr}\right) T_0 \mathbf{u}^* \cdot \frac{\partial u^*}{\partial t} \right] dydz \tag{8}$$

The time derivatives where the "*" quantities are fluctuation are given by

$$\frac{\partial T^*}{\partial t} = \Omega(\nabla^2 T^* + 1 - \mathbf{u} \cdot \nabla T^*) \tag{9a}$$

$$\frac{\partial u^*}{\partial t} = Pr\left(\nabla^2 \mathbf{u}^* - \nabla P^* - \left(\frac{1}{Da}\mathbf{u}^* + (Ra_I)(T^*)\hat{e}_z\right)\right. \tag{9b}$$

where Ω is a heat capacity ratio defined as

$$\Omega = \frac{(\rho C_p)_f}{(\rho C_p)_m}$$

The fluctuating quantities can be obtained directly from the velocity, temperature, and pressure solutions with the functional obtained by the subsequent substitution into the time derivatives. A secant-chord root finding algorithm is then used to find the wave number such that (7) holds.

Results, Discussion, and Conclusions

The premise upon which we employ our wave number prediction technique is the validity of equation (7), i.e., the linearity of ϕ with Ra_I. With our solution method, it is possible to deduce wave numbers, and hence ϕ, from heat transfer data. We have done this for the data of Sun [17], and the corresponding values of ϕ are plotted versus Ra in Fig. 2. We observe that the validity of equation (7) is well supported by these data. We also observe that the line in Fig. 2 extrapolates to a critical internal Rayleigh number which is in good agreement with Sun's [10] experimental measurements.

We next use equation (7) directly, in conjunction with solutions of equations (5), to calculate theoretical wave numbers and thus obtain complete solutions to equations (1-3). Wave numbers for two cases of thermal boundary conditions, adiabatic lower surface and zero applied temperature gradient, are presented in Fig. 3. We see that the wave number decreases with increasing Ra_I as one would expect from [1].

In Figs. 4 and 5 we present the Nusselt number as a function of Ra_I for the two cases of interest. For the zero applied temperature gradient case, we define Nusselt number as

$$\mathrm{Nu} = \frac{q(h)}{\dot{Q}_v h/2} \tag{10}$$

For an adiabatic lower surface the Nusselt number becomes

$$\mathrm{Nu} = \frac{\dot{Q}_v h^2}{2k_m(T_B - T_T)} \tag{11}$$

In Fig. 6 we have compared our results with the experimental work of Sun [7]. We see that agreement between experiment and theory is good up to a Rayleigh number of 15 times critical.

In all of our calculation we have used $\mathrm{Da} = 1.3438 \times 10^{-5}$ and $\Omega = 1.442$. As seen earlier [1], the solution is independent of Ω and independent of Da for $\mathrm{Da} \leq 5 \times 10^{-4}$. These values for Da and Ω have been chosen so that they represent real systems, such as Sun's [7] glass water system. From this study, we make the following conclusions:

(*i*) The nonequilibrium thermohydrodynamic theory of Glansdorff and Prigogine [11] can be extended to the problem of natural convection in a porous layer with internal heating to predict wave numbers.

(*ii*) The results indicate that wave number decreases with increasing internal Rayleigh number.

(*iii*) Heat transfer results have been obtained for two specific cases, adiabatic lower surface and zero applied temperature gradient. Theoretical heat transfer predictions for an adiabatic lower surface are in good agreement with experiment when preferred wave numbers are used.

Acknowledgment

The authors gratefully acknowledge the support of the Department of Energy Grant #DEATO382ER12021.

References

1 Somerton, C. W., McDonough, J. M., and Catton, I., "Natural Convection in Porous Media: A Mixed Finite Difference-Galerkin Solution with Wavenumber Predictions," Paper No. 44, *Proceedings of the 7th International Heat Transfer Conference*, Munich, 1982, pp. 347-350.

2 Gasser, R. D., and Kazimi, M. S., "Onset of Convection in a Porous Medium With Internal Heat Generation," JOURNAL OF HEAT TRANSFER, Vol. 98, 1976, pp. 48-54.

3 Hwang, I., "Finite Amplitude Thermal Convection in Porous Media With Heat Source and Variable Viscosity," Ph.D dissertation, University of Minnesota, 1971.

4 Tveitereid, M., "Thermal Convection in a Horizontal Porous Layer With Internal Heat Generation," *International Journal of Heat and Mass Transfer*, Vol. 20, 1977, pp. 1045-50.

5 Hardee, H. C., and Nilson, R. H., "Natural Convection in Porous Media With Heat Generation," *Nuclear Science and Engineering*, Vol. 63, 1977, pp. 119-132.

6 Buretta, R., "Thermal Convection in a Fluid Filled Porous Layer With Internal Heat Generation," Ph.D dissertation, University of Minnesota, 1972.

7 Sun, W. J., "Convective Instability in Superposed Porous and Free Layers," Ph.D dissertation, University of Minnesota, 1973.

8 Rhee, S. J., "Natural Convection Heat Transfer in Beds of Inductively Heated Particles," M.S. thesis, University of California, Los Angeles, 1977.

9 Cherng, J. -C., "Effect of Bottom Cooling on Natural Convection in Beds of Inductively Heated Particles," M.S. thesis, University of California, Los Angeles, 1978.

10 McDonough, J. M., and Catton, I., "A Mixed Finite Difference-Galerkin Procedure for Two-Dimensional Convection in a Square Box," to appear in *International Journal of Heat and Mass Transfer*, 1982.

11 Glansdorff, P., and Prigognie, I., *Thermodynamic Theory of Structure, Stability and Fluctuations*, Wiley-Interscience, New York, 1971.

Radiation View Factors Between Axisymmetric Subsurfaces Within a Cylinder With Spherical Centerbody

B. Mahbod[1] and R. L. Adams[2]

Introduction

Radiative view factors for a number of relatively simple geometries have been documented both in text books (e.g., Sparrow and Cess [1] and Siegel and Howell [2]) as well as the recent catalog published by Howell [3]. Though a large number of planar, circular, and spherical geometries have been considered, an on-going investigation of radiative heat transfer in fluidized beds has revealed an absence of differential and finite view factors for the case of a sphere coaxially placed within a cylinder, as shown in Fig. 1. The only previous published view factors for this geometry are those of Feingold and Gupta [4], and Naraghi and Chung [9]. Feingold and Gupta [4] derived expressions for the total view factors between the sphere and surrounding surfaces, and Naraghi and Chung [9] reported view factors between disks and a class of axisymmetric bodies. However, their results do not include information for the view factors between differential and finite axisymmetric elements. The development of these additional view factors using a combination of direct application of Lambert's cosine law and the method of contour integration [5] is summarized below. Also, calculated results are presented for view factors between finite elements in which numerical integration is required.

Analysis

The view factor between two differential elements is defined by

$$F_{dA_i - dA_j} = \frac{\cos\beta_i \cos\beta_j}{\pi S^2} dA_j \tag{1}$$

where S is the length of the vector connecting the differential areas, and β_i and β_j are angles between this vector and the unit vectors normal to differential area elements dA_i and dA_j, respectively. Direct integration of equation (1) gives the view factor between the differential element and the finite area, A_j, i.e.

$$F_{dA_i - A_j} = \frac{1}{\pi} \int_{A_i} \frac{\cos\beta_i \cos\beta_j}{S^2} dA_j \tag{2}$$

[1] Research Assistant, Department of Mechanical Engineering, Oregon State University, Corvallis, Ore. 97331, Mem. ASME

[2] Associate Professor, Department of Mechanical Engineering, Oregon State University, Mem. ASME

Contributed by the Heat Transfer Division for publication in the JOURNAL OF HEAT TRANSFER. Manuscript received by the Heat Transfer Division February 25, 1983.

Results, Discussion, and Conclusions

The premise upon which we employ our wave number prediction technique is the validity of equation (7), i.e., the linearity of ϕ with Ra_I. With our solution method, it is possible to deduce wave numbers, and hence ϕ, from heat transfer data. We have done this for the data of Sun [17], and the corresponding values of ϕ are plotted versus Ra in Fig. 2. We observe that the validity of equation (7) is well supported by these data. We also observe that the line in Fig. 2 extrapolates to a critical internal Rayleigh number which is in good agreement with Sun's [10] experimental measurements.

We next use equation (7) directly, in conjunction with solutions of equations (5), to calculate theoretical wave numbers and thus obtain complete solutions to equations (1-3). Wave numbers for two cases of thermal boundary conditions, adiabatic lower surface and zero applied temperature gradient, are presented in Fig. 3. We see that the wave number decreases with increasing Ra_I as one would expect from [1].

In Figs. 4 and 5 we present the Nusselt number as a function of Ra_I for the two cases of interest. For the zero applied temperature gradient case, we define Nusselt number as

$$\mathrm{Nu} = \frac{q(h)}{\dot{Q}_v h/2} \tag{10}$$

For an adiabatic lower surface the Nusselt number becomes

$$\mathrm{Nu} = \frac{\dot{Q}_v h^2}{2k_m(T_B - T_T)} \tag{11}$$

In Fig. 6 we have compared our results with the experimental work of Sun [7]. We see that agreement between experiment and theory is good up to a Rayleigh number of 15 times critical.

In all of our calculation we have used $\mathrm{Da} = 1.3438 \times 10^{-5}$ and $\Omega = 1.442$. As seen earlier [1], the solution is independent of Ω and independent of Da for $\mathrm{Da} \leq 5 \times 10^{-4}$. These values for Da and Ω have been chosen so that they represent real systems, such as Sun's [7] glass water system. From this study, we make the following conclusions:

(*i*) The nonequilibrium thermohydrodynamic theory of Glansdorff and Prigogine [11] can be extended to the problem of natural convection in a porous layer with internal heating to predict wave numbers.

(*ii*) The results indicate that wave number decreases with increasing internal Rayleigh number.

(*iii*) Heat transfer results have been obtained for two specific cases, adiabatic lower surface and zero applied temperature gradient. Theoretical heat transfer predictions for an adiabatic lower surface are in good agreement with experiment when preferred wave numbers are used.

Acknowledgment

The authors gratefully acknowledge the support of the Department of Energy Grant #DEATO382ER12021.

References

1 Somerton, C. W., McDonough, J. M., and Catton, I., "Natural Convection in Porous Media: A Mixed Finite Difference-Galerkin Solution with Wavenumber Predictions," Paper No. 44, *Proceedings of the 7th International Heat Transfer Conference*, Munich, 1982, pp. 347-350.

2 Gasser, R. D., and Kazimi, M. S., "Onset of Convection in a Porous Medium With Internal Heat Generation," JOURNAL OF HEAT TRANSFER, Vol. 98, 1976, pp. 48-54.

3 Hwang, I., "Finite Amplitude Thermal Convection in Porous Media With Heat Source and Variable Viscosity," Ph.D dissertation, University of Minnesota, 1971.

4 Tveitereid, M., "Thermal Convection in a Horizontal Porous Layer With Internal Heat Generation," *International Journal of Heat and Mass Transfer*, Vol. 20, 1977, pp. 1045-50.

5 Hardee, H. C., and Nilson, R. H., "Natural Convection in Porous Media With Heat Generation," *Nuclear Science and Engineering*, Vol. 63, 1977, pp. 119-132.

6 Buretta, R., "Thermal Convection in a Fluid Filled Porous Layer With Internal Heat Generation," Ph.D dissertation, University of Minnesota, 1972.

7 Sun, W. J., "Convective Instability in Superposed Porous and Free Layers," Ph.D dissertation, University of Minnesota, 1973.

8 Rhee, S. J., "Natural Convection Heat Transfer in Beds of Inductively Heated Particles," M.S. thesis, University of California, Los Angeles, 1977.

9 Cherng, J. -C., "Effect of Bottom Cooling on Natural Convection in Beds of Inductively Heated Particles," M.S. thesis, University of California, Los Angeles, 1978.

10 McDonough, J. M., and Catton, I., "A Mixed Finite Difference-Galerkin Procedure for Two-Dimensional Convection in a Square Box," to appear in *International Journal of Heat and Mass Transfer*, 1982.

11 Glansdorff, P., and Prigognie, I., *Thermodynamic Theory of Structure, Stability and Fluctuations*, Wiley-Interscience, New York, 1971.

Radiation View Factors Between Axisymmetric Subsurfaces Within a Cylinder With Spherical Centerbody

B. Mahbod[1] and R. L. Adams[2]

Introduction

Radiative view factors for a number of relatively simple geometries have been documented both in text books (e.g., Sparrow and Cess [1] and Siegel and Howell [2]) as well as the recent catalog published by Howell [3]. Though a large number of planar, circular, and spherical geometries have been considered, an on-going investigation of radiative heat transfer in fluidized beds has revealed an absence of differential and finite view factors for the case of a sphere coaxially placed within a cylinder, as shown in Fig. 1. The only previous published view factors for this geometry are those of Feingold and Gupta [4], and Naraghi and Chung [9]. Feingold and Gupta [4] derived expressions for the total view factors between the sphere and surrounding surfaces, and Naraghi and Chung [9] reported view factors between disks and a class of axisymmetric bodies. However, their results do not include information for the view factors between differential and finite axisymmetric elements. The development of these additional view factors using a combination of direct application of Lambert's cosine law and the method of contour integration [5] is summarized below. Also, calculated results are presented for view factors between finite elements in which numerical integration is required.

Analysis

The view factor between two differential elements is defined by

$$F_{dA_i - dA_j} = \frac{\cos\beta_i \cos\beta_j}{\pi S^2} dA_j \tag{1}$$

where S is the length of the vector connecting the differential areas, and β_i and β_j are angles between this vector and the unit vectors normal to differential area elements dA_i and dA_j, respectively. Direct integration of equation (1) gives the view factor between the differential element and the finite area, A_j, i.e.

$$F_{dA_i - A_j} = \frac{1}{\pi} \int_{A_i} \frac{\cos\beta_i \cos\beta_j}{S^2} dA_j \tag{2}$$

[1] Research Assistant, Department of Mechanical Engineering, Oregon State University, Corvallis, Ore. 97331, Mem. ASME

[2] Associate Professor, Department of Mechanical Engineering, Oregon State University, Mem. ASME

Contributed by the Heat Transfer Division for publication in the JOURNAL OF HEAT TRANSFER. Manuscript received by the Heat Transfer Division February 25, 1983.

By using Stokes's Theorem, Sparrow [5] has shown that equation (2) can also be expressed as the contour integral

$$F_{dA_i-A_j} = \frac{1}{2\pi}\int_c \left\{ \frac{n_i(y_j-y_i)-m_i(z_j-z_i)}{S^2}dx_j + \frac{l_i(z_j-z_i)-n_i(x_j-x_i)}{S^2}dy_j + \frac{m_i(x_j-x_i)-l_i(y_j-y_i)}{S^2}dz_i \right\} \quad (3)$$

where x_i, y_i, and z_i are the coordinates of dA_i, l_i, m_i, and n_i are the direction cosines of the normal to dA_i, and x_j, y_j and z_j are the coordinates of the boundary enclosing A_j.

Differential Spherical Band to a Coaxial Finite Cylindrical Strip

With the intent of applying contour integration (equation (3)), dA_1 is located on the y-axis with its normal in the yz-plane, thus, $x_1 = 0$, $y_1 = \sin\beta$, and $Z_1 = 0$, as seen from Fig. 1 for a sphere of unit radius. Also the direction cosines are $l_1 = 0$, $m_1 = \sin\beta$, and $n_1 = \cos\beta$. The coordinates of dA_2 become $x_2 = \zeta\cos\alpha'$, $y_2 = \zeta\cos\alpha'$ and $Z_2 = Z$.

In view of the symmetry of the problem about the y-axis, the following simplification can be made. The denominator in equation (3) and the variable, y_2, i.e., $\zeta\sin\alpha'$, have the same value at points of symmetry, whereas the variable x_2, i.e., $\zeta\cos\alpha'$, reverses sign. Therefore, since the integrations are carried out proceeding in one direction around the contour, dx_2 will have the same sign at points of symmetry, whereas dy_2 will reverse sign. The net result is that the portion of the line integral on the negative side of the y-axis is equal to that on the positive side, so that only the integral on one side of the y-axis need be evaluated. The closed contour integral will be obtained by doubling the integral for the half space contour.

From Figs. 1(a) and 1(b) it is clear that the contour consists of two circular arcs with radius, ζ, at heights, Z_1 and Z_2, respectively, bounded by the intersection of a plane tangent to element, dA_1, and the cylinder, line FG in Fig. 1(a). This limit is determined by angle, α, equation (4), in a plane containing the appropriate circular arc, and perpendicular to the z-axis.

Other sections of the contour are completed by curves which are the locii of points A and C as Z changes from Z_1 to Z_2. The end points of each locus is defined in cylindrical coordinates by $\alpha(Z_1)$, Z_1 and ζ, and $\alpha_2(Z_2)$, Z_2, and ζ, where

$$\alpha_i = \sin^{-1}\left[\frac{Z_i\cos\beta+\sin^2\beta}{\zeta\sin\beta}\right] \quad i=1,2 \quad (4)$$

Integration of equation (3) along the indicated contour produces the view factor from a differential spherical element to a finite coaxial cylindrial strip in the form

$$F_{dA_1-A_2} = \frac{1}{\pi}\left\{ \tfrac{1}{4}[(\pi-2\alpha_1)(Z_1-\cos\beta) - (\pi-2\alpha_2)(Z_2-\cos\beta)] - \frac{2\zeta^2\cos\beta+(Z_1-\cos\beta)a_1}{\sqrt{a_1^2-b^2}} \left[\tan^{-1}\left(\frac{a_1+b}{a_1-b}\right)^{1/2} - \tan^{-1}\frac{a_1\tan(\alpha_1/2)+b}{\sqrt{a_1^2-b^2}}\right] + \frac{2\zeta^2\cos\beta+(Z_2-\cos\beta)a_2}{\sqrt{a_2^2-b^2}} \left[\tan^{-1}\left(\frac{a_2+b}{a_2-b}\right)^{1/2} - \tan^{-1}\frac{a_2\tan(\alpha_2/2)+b}{\sqrt{a_2^2-b^2}}\right] + \zeta\cos\beta\int_{\alpha_1}^{\alpha_2}\frac{\zeta-\sin\beta\sin\alpha'}{a_3\sin^2\alpha'+b\sin\alpha'+C}d\alpha' \right\} \quad (5)$$

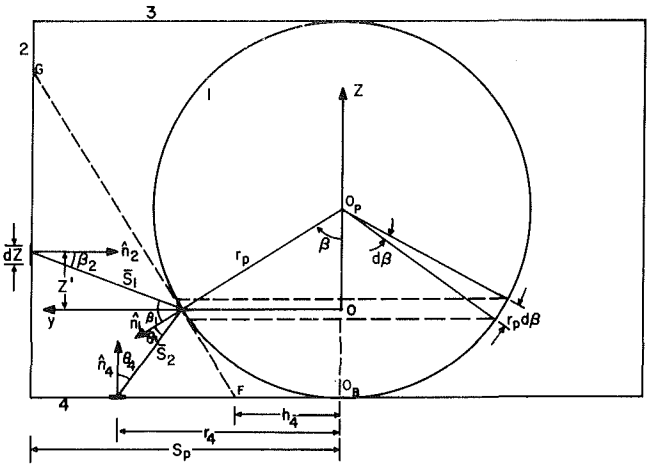

Fig. 1(a) Side view indicating the nomenclature for view factor calculations

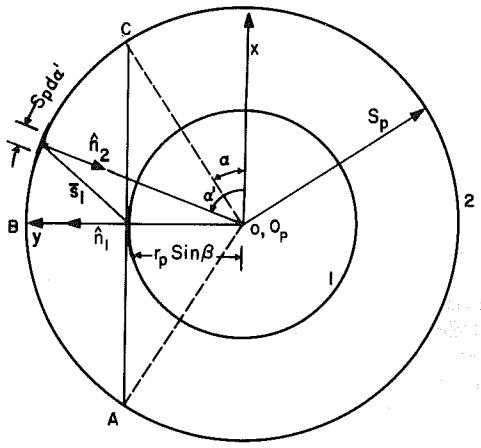

Fig. 1(b) Top view indicating the relative positions of differential elements dA_1 and dA_2

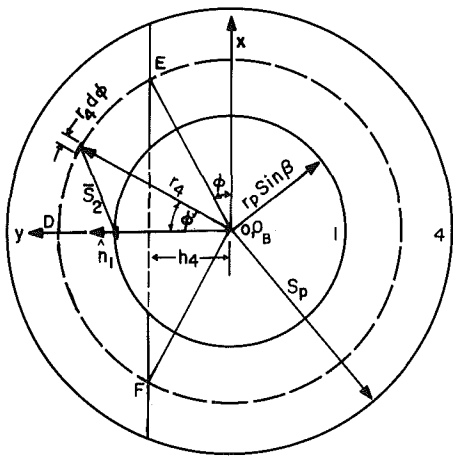

Fig. 1(c) Top view indicating the position of differential elements dA_1 and dA_4

where

$$a_i = \zeta^2 + Z_i^2 + \sin^2\beta \qquad i=1,2$$
$$b = -2\zeta\sin\beta$$
$$a_3 = \zeta^2\sin^2\beta$$
$$C = \zeta^2\cos^2\beta + \sin^2\beta$$

The last term of equation (5) must be integrated numerically.

Equation (5) represents the view factor between an element of area on a spherical centerbody and a finite cylindrical strip. Since any element, dA_1, on the spherical band, $dA_{\text{band},1}$ has the same fraction of its energy reaching strip, A_2, it follows that the fraction of energy from the entire $dA_{\text{band},1}$ that reaches A_2 is the same as the fraction for each element dA_1. Hence, the view factor between one differential width spherical band $dA_{\text{band},1}$ and cylindrical strip A_2 is F_{dA1-A2}, which is given by equation (5). Here, care must be taken to evaluate equation (5) along the cylinder, since only the portion of the cylinder which is visible by dA_1 should be taken into account. This portion can be determined by equation (6).

$$Z_{\max} = 1. + \zeta \tan\beta - \operatorname{Sec}\beta \tag{6}$$

The graphic representation of the dependence of F_{dA1-A2} on the spherical coordinate of dA_1, i.e., angle β, and on the ratio $\zeta = S_p/r_p$ is shown in Fig. 2.

Differential Spherical Band to a Differential Coaxial Annular Base Ring

For the coordinate system in Figs. 1(*a*) and 1(*c*), dA_1 is located on the y-axis with its normal in the yz-plane, $x_1 = 0$, $y_1 = r_p \sin\beta$, and $z_1 = 0$. The location of dA_1 becomes $x_4 = r_4 \sin\phi'$, $y_4 = r_4 \cos\phi'$ and $z_4 = (\cos\beta - 1)r_p$. The direction cosines remain the same as previous case. The integration of equation (3) with the above substitution is simplified by taking advantage of the symmetry about the y-axis as was done in the case with equation (5).

The contour shown in Figs. 1(*a*) and 1(*c*) consists of the two circular arcs with radii R_1 and R_2, the y-axis and the line represented by the intersection of the tangent plane to the spherical element, dA_1, with circles of radii R_1 and R_2. The remainder of the contour is the portion of the line which is described above and is bounded by arcs of radii R_1 and R_2. After some manipulation and use of existing analytical results for the integrals [6] and [7], the following relation is obtained

$$F_{dA_1-A_4} = \frac{1}{\pi}\Bigg\{ 3/2(\phi_1 - \phi_2) - \frac{2R_1^2\cos\beta - a_1}{\sqrt{a_1^2 - b_1^2}} \tan^{-1} \frac{(a_1 - b_1)\tan\left(\frac{\pi}{4} - \frac{\phi_1}{2}\right)}{\sqrt{a_1^2 - b_1^2}} - \frac{a_2 - 2R_2^2\cos\beta}{\sqrt{a_2^2 - b_2^2}} \tan^{-1} \frac{(a_2 - b_2)\tan\left(\frac{\pi}{4} - \frac{\phi_2}{2}\right)}{\sqrt{a_2^2 - b_2^2}} \Bigg\} \tag{7}$$

where

$$a_i = R_i^2 + 4\sin^2\left(\frac{\beta}{2}\right) \qquad i = 1,2$$

$$b_i = -2R_i \sin\beta$$

and

$$\phi_i = \sin^{-1}\left[\frac{\tan(\beta/2)}{R_i}\right]$$

Consistent with the argument that followed equation (5), the view factor between a differential width spherical band, $dA_{\text{band},1}$, and the finite annular base ring, A_4, is also F_{dA1-A4}, as given by equation (7).

Numerical results for the dependence of F_{dA1-A4} on the spherical coordinate of dA_1, i.e., angle β, can be determined using Fig. 2, where $F_{dA1-A4} = 1 - F_{dA1-A2}$.

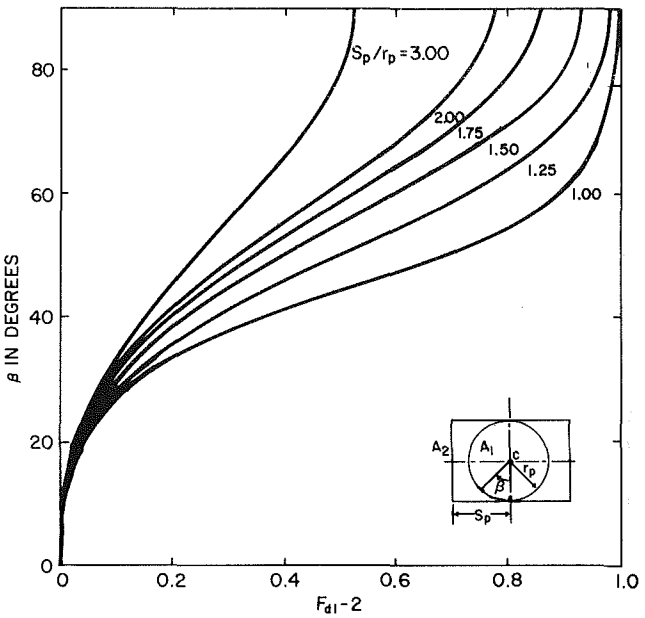

Fig. 2 View factor between a differential spherical band and coaxial cylinder wall

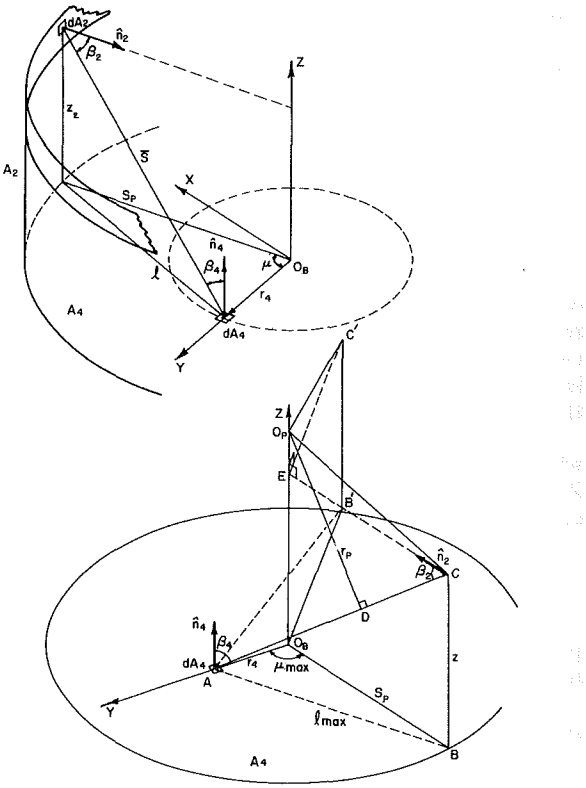

Fig. 3 (a) Geometry for derivation of view factor between differential elements dA_4 on the base and dA_2 on the cylinder wall; (b) geometry of the limit of integration for derivation of view factor between element dA_4 on the base and dA_2 on the cylindrical strip

Differential Annular Base Ring to Finite Cylindrical Strip With Spherical Blockage

According to the coordinates shown in Fig. 3(*a*), dA_4 is located on the y-axis with its normal parallel to the z-axis, $x_4 = 0$, $y_4 = r_4$, and $z_4 = 0$, so that in cylindrical coordinates, equation (3) reduces to

$$F_{dA_4-A_2} = \frac{1}{2\pi}\int_c \frac{\zeta(\zeta - R\cos\mu)}{R^2 + Z^2 + \zeta^2 - 2R\zeta\cos\mu}\, d\mu \tag{8}$$

In view of the symmetry about the y-axis the closed contour integral is established by doubling the integral for the half space contour.

The contour for integration of equation (8) is shown in Figs. 3(a) and 3(b) and consists of two circular arcs with radius ζ at heights Z_1 and Z_2. These arcs are located on disks perpendicular to the z-axis and bounded by the yz-plane and the line that makes an angle $\mu_{\max}$ with the y-axis. The limits of these arcs are shown geometrically in Fig. 3(b). The integration is to be carried out along the locus of point c on Fig. 3(b) as Z changes form Z_1, to, Z_2. Due to the implicit dependence that exists between Z and $\mu_{\max}$, the integral on this line must be numerically evaluated. Thus, the integral becomes

$$F_{dA_4-A_2} = \frac{1}{\pi}\left\{\frac{\mu_{\max_1}-\mu_{\max_2}}{2} + \frac{\zeta^2-a_1}{\sqrt{a_1^2-b^2}}\tan^{-1}\frac{(a_1-b)\tan(\mu_{\max_1}/2)}{\sqrt{a_1^2-b^2}} - \frac{\zeta^2-a_2}{\sqrt{a_2^2-b^2}}\tan^{-1}\frac{(a_2-b)\tan(\mu_{\max_2}/2)}{\sqrt{a_2^2-b^2}} + \int_{\mu_{\max_1}}^{\mu_{\max_2}} \frac{\zeta(\zeta-R\cos\mu)}{R^2+\zeta^2+Z^2-2R\zeta\cos\mu}\,d\mu\right\} \tag{9a}$$

where

$$\begin{aligned} R &= r_4/r_p \\ a_i &= R^2+\zeta^2+Z_i^2 \quad i=1,2 \\ b &= -2R\zeta \\ Z &= Z_2/r_p \\ \mu_{\max} &= \cos^{-1}\left[\frac{Z-R\sqrt{Z^2+\zeta^2-2Z}}{R\zeta}\right] \end{aligned} \tag{9b}$$

and

$$\zeta = S_p/r_p$$

For the last term, i.e., the integral term, Z, is determined by the roots of the following quadratic equation

$$(1-R^2)Z^2 - 2R(\zeta\cos\mu - R)Z - R^2\zeta^2\sin^2\mu = 0 \tag{10}$$

$$Z = \frac{-B\pm\sqrt{B^2-4AC}}{2A}$$

where

$$A = 1-R^2$$

$$B = 2R(\zeta\cos\mu - R)$$

and

$$C = R^2\zeta^2\sin^2\mu$$

For $R<1$ the plus sign is used and when $R>1$, the minus sign must be used.

Since, again, the fraction of energy from the entire ring, $dA_{\text{ring},4}$, that reaches A_2 is the same as the fraction for each element, dA_4, the view factor between the differential width annular base ring, $dA_{\text{ring},4}$, and cylindrical strip, A_2, is F_{dA4-A2}, which is given by equation (9a).

The height limitation that was discussed in the previous case also applies to this case.

The graphical representation of equation (9a) and dependence of F_{dA4-A2} on the location of annular differential base ring as a function of the parameter $\zeta = S_p/r_p$ is depicted on Fig. 4.

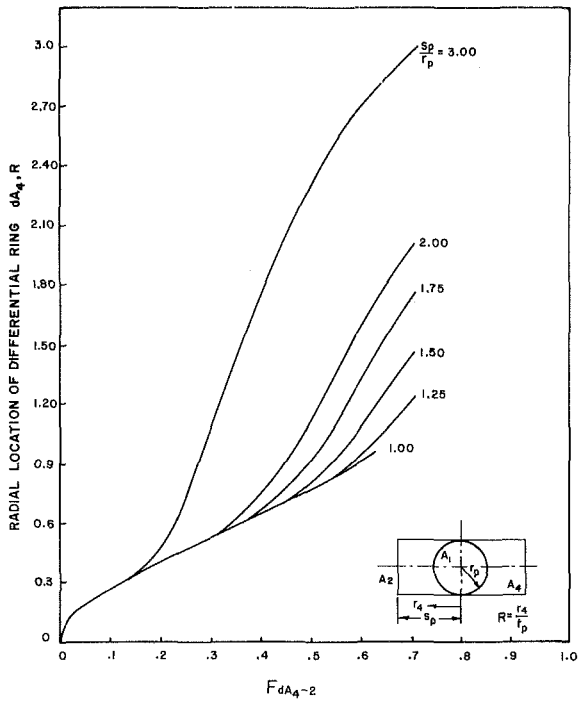

Fig. 4 View factor between a differential annular ring on the base and the cylinder wall

Relations for Finite Areas

In order to verify the results obtained by equations (5), (7), and (9a), it is necessary to integrate these relations to establish the view factors between finite areas. For the view factor between a finite spherical band and a finite area on a coaxial cylinder (annular base ring or cylindrical strip on the wall of cylinder)

$$F_{A_1-A_i} = \frac{1}{\cos\phi_2-\cos\phi_1}\int_{\phi_1}^{\phi_2} F_{dA_1-A_i}\sin\phi\,d\phi, \quad i=2 \text{ and } 4 \tag{11}$$

where angles ϕ_1 and ϕ_2 are, respectively, the spherical coordinate of the two rings establishing the band, A_1, on the sphere. For the view factor between a finite annular base ring and a coaxial band

$$F_{A_4-A_2} = \frac{2}{R_o^2-R_i^2}\int_{R_i}^{R_o} F_{dA_4-A_2}R\,dR \tag{12}$$

where R_i and R_o are, respectively, the inner and outer radii of the annular base ring.

Because of the complexity of the differential view factors as given by equations (5), (7), and (9a), numerical integration is used.

The results obtained by the foregoing numerical integration were verified using the results of Feingold and Gupta [4] for radiation from an isothermal sphere to a coaxial disk and radiation to a right cylinder from an isothermal spherical centerbody. With the use of view factor algebra and reciprocity relations, equations (9a) and (12) were also verified.

The view factor between an annular ring and a disk with spherical blockage cannot be obtained from the view factor between two parallel disks, since the sphere forms a spherical blockage to the view from any element on either disk; however, one is able to obtain this view factor by slight modification of the relations reported by Holchendler and Laverty [8].

In closing, it should be noted that within the limitations of the model other view factors may be obtained by standard view factor algebra.

Summary

Expressions and numerical results have been presented for view factors involved in the analysis of the radiative heat transfer within an enclosure formed by a sphere placed within a cylinder. The results for differential and finite strips have been checked for self consistency, and numerical integration to produce view factors for the total surfaces agree well with exact analytical results by Feingold and Gupta [4].

Acknowledgments

The support of this work by the National Science Foundation under Grant MEA 80-20781 is gratefully acknowledged. The contents of this paper do not necessarily reflect the view or policies of the Foundation.

References

1 Sparrow, E. M., and Cess, R. C., *Radiation Heat Transfer*, Books J. Cole, 1966.

2 Siegel, R., and Howell, J. R., *Thermal Radiation Heat Transfer*, McGraw-Hill, 1981.

3 Howell, J. R., *A Catalog of Radiation Configuration Factors*, McGraw-Hill, 1982.

4 Feingold, A., and Gupta, K. G., "New Analytical Approach to the Evaluation of Configuration Factors in Radiation from Spheres and Infinitely Long Cylinders," ASME JOURNAL OF HEAT TRANSFER, Vol. 92, No. 1, 1970, pp. 69–76.

5 Sparrow, E. M., "A New and Simpler Formulation for Radiative Angle Factor," ASME JOURNAL OF HEAT TRANSFER, Vol. 85, No. 2, 1963, pp. 81–88.

6 Dwight, H. R., *Tables of Integrals and Other Mathematical Data*, Macmillan, 4th ed., 1961.

7 Korn, G. A., and Korn, T. M., *Mathematical Handbook For Scientists and Engineers*, McGraw-Hill, 2nd ed., 1968.

8 Holchendler, J., and Laverty, W. F., "Configuration Factors for Radiant Heat Flux in Cavities Bounded at the Ends of Parallel Disks and Having Conical Centerbodies," ASME JOURNAL OF HEAT TRANSFER, Vol. 96, No. 2, 1974, pp. 254–257.

9 Naraghi, M. H. N., and Chung, B. T. F., "Radiation Configuration Factors Between Disks and a Class of Axisymmetric Bodies," ASME JOURNAL OF HEAT TRANSFER, Vol. 104, No. 3, Aug. 1982, pp. 426–431.

APPENDIX

The view factor between differential areas within this model can be determined by application of equations (1) and (2). The cosines in the definition of view factors are obtained by use of the dot product between two vectors normal to the surface and the position vector connecting centers of two differential elements. A list of view factors between differential subareas within the limitations applicable to the model are listed below. Equations (13–15) contain parameters and angles which are complicated functions of z and R, respectively, so that direct integration is not possible.

Differential Spherical Element to Differential Coaxial Cylinder Strip

$$F_{dA_1-dA_2}=\frac{\zeta}{\pi}\left\{\frac{(\pi-2\alpha)a}{h^2}-\left[\frac{a}{h}+\frac{h(a-c)-eb}{e^2-h^2}\right]*\right.$$
$$\frac{2\cos\alpha}{e+h\sin\alpha}+\frac{2}{\sqrt{e^2-h^2}}\left[\frac{e(a-c)-hb}{e^2-h^2}-\frac{ae}{h^2}\right]*$$
$$\left.\left[\tan^{-1}\frac{e\cot(\alpha/2)+h}{\sqrt{e^2-h^2}}-\tan^{-1}\frac{e\tan(\alpha/2)+h}{\sqrt{e^2-h^2}}\right]\right\}dz \qquad (13)$$

where

$$\alpha = \sin^{-1}\left[\frac{Z\cos\beta+\sin^2\beta}{\zeta\sin\beta}\right]$$
$$a = \zeta\sin^2\beta$$
$$b = (\zeta^2+\sin^2\beta+Z\cos\beta)\sin\beta$$
$$c = \zeta\sin^2\beta-Z\zeta\cos\beta$$
$$e = \zeta^2+Z^2+\sin^2\beta$$
$$h = -2\zeta\sin\beta$$

Differential Spherical Band to a Differential Coaxial Annular Base Ring

$$F_{dA_1-dA_4}=\frac{R}{\pi}\left\{\frac{2(ae+gb)}{(b^2-a^2)(b+a\sin\phi)}-\frac{4(ag+be)}{(b^2-a^2)^{3/2}}*\right.$$
$$\left.\tan^{-1}\left[\frac{(b-a)\tan\left(\frac{\pi}{4}-\frac{\phi}{2}\right)}{\sqrt{b^2-a^2}}\right]\right\}dR \qquad (14)$$

where

$$a = -2R\sin\beta$$
$$b = R^2+2(1-\cos\beta)$$
$$e = (1-\cos\beta)^2$$
$$g = R\sin\beta(1-\cos\beta)$$
$$R = r_4/r_p$$
$$\phi = \sin^{-1}\left[\frac{\tan(\beta/a)}{R}\right]$$

Differential Element on an Annular Base Ring to a Differential Cylindrical Strip With Spherical Centerbody

$$F_{dA_4-dA_2}=\frac{2Z\zeta}{\pi(a^2-b^2)}\left\{\frac{2(a\zeta+bR)}{\sqrt{a^2-b^2}}*\right.$$
$$\left.\tan\left[\frac{(a-b)\tan(\mu/2)}{\sqrt{a^2-b^2}}\right]-\frac{(b\zeta+aR)\sin\mu}{a+b\cos\mu}\right\}dR \qquad (15)$$

where

$$a = Z^2+\zeta^2+R^2$$
$$b = -2R\zeta$$
$$\zeta = S_p/r_p$$
$$R = r_4/r_p$$

and μ is given by equation (9b).

Determination of Angular Distribution of Radiation in an Isotropically Scattering Slab

Y. A. Cengel[1], M. N. Özişik[1] and Y. Yener[2]

Nomenclature

a = optical thickness of the slab
$E_n(x)$ = exponential integral function
$f_i(\mu)$ = intensity of externally incident radiation (i = 1, 2)
$G(x)$ = incident radiation defined by equation (2a)
$I(x,\mu)$ = radiation intensity
$I^+(x,\mu), I^-(x,\mu)$ = forward ($\mu>0$) and backward ($\mu<0$) intensity

[1]Mechanical and Aerospace Engineering Department, North Carolina State University, Raleigh, N.C. 27650

[2]Mechanical Engineering Department, Northeastern University, Boston, Mass. 02115

Contributed by the Heat Transfer Division for publication in the JOURNAL OF HEAT TRANSFER. Manuscript received by the Heat Transfer Division January 26, 1983.

Summary

Expressions and numerical results have been presented for view factors involved in the analysis of the radiative heat transfer within an enclosure formed by a sphere placed within a cylinder. The results for differential and finite strips have been checked for self consistency, and numerical integration to produce view factors for the total surfaces agree well with exact analytical results by Feingold and Gupta [4].

Acknowledgments

The support of this work by the National Science Foundation under Grant MEA 80-20781 is gratefully acknowledged. The contents of this paper do not necessarily reflect the view or policies of the Foundation.

References

1 Sparrow, E. M., and Cess, R. C., *Radiation Heat Transfer*, Books J. Cole, 1966.

2 Siegel, R., and Howell, J. R., *Thermal Radiation Heat Transfer*, McGraw-Hill, 1981.

3 Howell, J. R., *A Catalog of Radiation Configuration Factors*, McGraw-Hill, 1982.

4 Feingold, A., and Gupta, K. G., "New Analytical Approach to the Evaluation of Configuration Factors in Radiation from Spheres and Infinitely Long Cylinders," ASME JOURNAL OF HEAT TRANSFER, Vol. 92, No. 1, 1970, pp. 69–76.

5 Sparrow, E. M., "A New and Simpler Formulation for Radiative Angle Factor," ASME JOURNAL OF HEAT TRANSFER, Vol. 85, No. 2, 1963, pp. 81–88.

6 Dwight, H. R., *Tables of Integrals and Other Mathematical Data*, Macmillan, 4th ed., 1961.

7 Korn, G. A., and Korn, T. M., *Mathematical Handbook For Scientists and Engineers*, McGraw-Hill, 2nd ed., 1968.

8 Holchendler, J., and Laverty, W. F., "Configuration Factors for Radiant Heat Flux in Cavities Bounded at the Ends of Parallel Disks and Having Conical Centerbodies," ASME JOURNAL OF HEAT TRANSFER, Vol. 96, No. 2, 1974, pp. 254–257.

9 Naraghi, M. H. N., and Chung, B. T. F., "Radiation Configuration Factors Between Disks and a Class of Axisymmetric Bodies," ASME JOURNAL OF HEAT TRANSFER, Vol. 104, No. 3, Aug. 1982, pp. 426–431.

APPENDIX

The view factor between differential areas within this model can be determined by application of equations (1) and (2). The cosines in the definition of view factors are obtained by use of the dot product between two vectors normal to the surface and the position vector connecting centers of two differential elements. A list of view factors between differential subareas within the limitations applicable to the model are listed below. Equations (13–15) contain parameters and angles which are complicated functions of z and R, respectively, so that direct integration is not possible.

Differential Spherical Element to Differential Coaxial Cylinder Strip

$$F_{dA_1-dA_2}=\frac{\zeta}{\pi}\left\{\frac{(\pi-2\alpha)a}{h^2}-\left[\frac{a}{h}+\frac{h(a-c)-eb}{e^2-h^2}\right]*\right.$$
$$\frac{2\cos\alpha}{e+h\sin\alpha}+\frac{2}{\sqrt{e^2-h^2}}\left[\frac{e(a-c)-hb}{e^2-h^2}-\frac{ae}{h^2}\right]*$$
$$\left.\left[\tan^{-1}\frac{e\cot(\alpha/2)+h}{\sqrt{e^2-h^2}}-\tan^{-1}\frac{e\tan(\alpha/2)+h}{\sqrt{e^2-h^2}}\right]\right\}dz \qquad (13)$$

where

$$\alpha = \sin^{-1}\left[\frac{Z\cos\beta+\sin^2\beta}{\zeta\sin\beta}\right]$$
$$a = \zeta\sin^2\beta$$
$$b = (\zeta^2+\sin^2\beta+Z\cos\beta)\sin\beta$$
$$c = \zeta\sin^2\beta-Z\zeta\cos\beta$$
$$e = \zeta^2+Z^2+\sin^2\beta$$
$$h = -2\zeta\sin\beta$$

Differential Spherical Band to a Differential Coaxial Annular Base Ring

$$F_{dA_1-dA_4}=\frac{R}{\pi}\left\{\frac{2(ae+gb)}{(b^2-a^2)(b+a\sin\phi)}-\frac{4(ag+be)}{(b^2-a^2)^{3/2}}*\right.$$
$$\left.\tan^{-1}\left[\frac{(b-a)\tan\left(\frac{\pi}{4}-\frac{\phi}{2}\right)}{\sqrt{b^2-a^2}}\right]\right\}dR \qquad (14)$$

where

$$a = -2R\sin\beta$$
$$b = R^2+2(1-\cos\beta)$$
$$e = (1-\cos\beta)^2$$
$$g = R\sin\beta(1-\cos\beta)$$
$$R = r_4/r_p$$
$$\phi = \sin^{-1}\left[\frac{\tan(\beta/a)}{R}\right]$$

Differential Element on an Annular Base Ring to a Differential Cylindrical Strip With Spherical Centerbody

$$F_{dA_4-dA_2}=\frac{2Z\zeta}{\pi(a^2-b^2)}\left\{\frac{2(a\zeta+bR)}{\sqrt{a^2-b^2}}*\right.$$
$$\left.\tan\left[\frac{(a-b)\tan(\mu/2)}{\sqrt{a^2-b^2}}\right]-\frac{(b\zeta+aR)\sin\mu}{a+b\cos\mu}\right\}dR \qquad (15)$$

where

$$a = Z^2+\zeta^2+R^2$$
$$b = -2R\zeta$$
$$\zeta = S_p/r_p$$
$$R = r_4/r_p$$

and μ is given by equation (9b).

Determination of Angular Distribution of Radiation in an Isotropically Scattering Slab

Y. A. Cengel[1], M. N. Özişik[1] and Y. Yener[2]

Nomenclature

a = optical thickness of the slab
$E_n(x)$ = exponential integral function
$f_i(\mu)$ = intensity of externally incident radiation (i = 1, 2)
$G(x)$ = incident radiation defined by equation (2a)
$I(x,\mu)$ = radiation intensity
$I^+(x,\mu), I^-(x,\mu)$ = forward ($\mu>0$) and backward ($\mu<0$) intensity

[1]Mechanical and Aerospace Engineering Department, North Carolina State University, Raleigh, N.C. 27650

[2]Mechanical Engineering Department, Northeastern University, Boston, Mass. 02115

Contributed by the Heat Transfer Division for publication in the JOURNAL OF HEAT TRANSFER. Manuscript received by the Heat Transfer Division January 26, 1983.

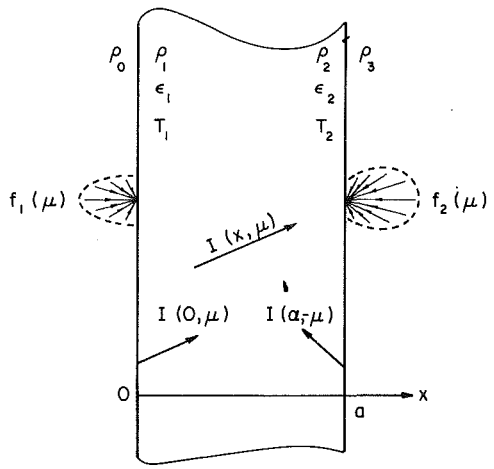

Fig. 1 The geometry and coordinates

n = refractive index
$S(x)$ = $(1-\omega)n^2\sigma T^4(x)/\pi$
T = temperature
x = optical variable
ϵ_i = emissivity ($i=1,2$)
ρ_i = reflectivity ($i=0,1,2,3$ as shown in Fig. 1)
σ = Stefan-Boltzmann constant
θ = angle between the positive x-axis and direction of intensity
μ = $\cos\theta$
ω = single scattering albedo

Introduction

In a recent work [1], the use of the Galerkin method was introduced for solving the equation of radiative transfer in an absorbing, emitting, isotropically scattering plane-parallel slab to predict radiation flux. In this work, the method is further developed to accurately determine angular distribution of radiation intensity anywhere in the medium, subject to general boundary conditions.

Analysis

We consider the radiation problem for an absorbing, emitting, isotropically scattering, plane-parallel slab of optical thickness "a" as illustrated in Fig. 1. The equation of radiative transfer and the boundary conditions are taken as

$$\mu\frac{\partial I(x,\mu)}{\partial x}+I(x,\mu)=S(x)+\frac{\omega}{4\pi}G(x),\quad \text{in } 0<x<a,\ -1\le\mu\le 1 \tag{1a}$$

$$I(0,\mu)=(1-\rho_o)f_1(\mu)+A_1+2\rho_1K_1,\quad \mu>0 \tag{1b}$$

$$I(a,-\mu)=(1-\rho_3)f_2(\mu)+A_2+2\rho_2K_2,\quad \mu>0 \tag{1c}$$

where

$$G(x)=2\pi\int_{-1}^{1}I(x,\mu')\,d\mu' \tag{2a}$$

$$A_i=\epsilon_i\frac{n^2\sigma T_i^4}{\pi},\quad i=1,2 \tag{2b}$$

$$K_1=\int_0^1 I(0,-\mu)\,\mu d\mu\equiv\frac{1}{2\pi}q^-(0) \tag{2c}$$

$$K_2=\int_0^1 I(a,\mu)\,\mu d\mu\equiv\frac{1}{2\pi}q^+(a) \tag{2d}$$

This system is transformed into the following integral equation for $G(x)$ by following a procedure discussed in [2]

$$G(x)=Y(x)+\omega\int_0^a K(x,x')\,G(x')dx' \tag{3}$$

where

$$K(x,x')=\frac{1}{2}E_1(|x-x'|)+\rho_1\beta E_2(x)[E_2(x')+\alpha_2E_2(a-x')]+\rho_2\beta E_2(a-x)[E_2(a-x')+\alpha_1E_2(x')] \tag{4a}$$

$$Y(x)=2\pi\Big\{2\int_0^a K(x,x')S(x')\,dx'+A_1\beta[E_2(x)+\alpha_2E_2(a-x)]+A_2\beta[E_2(a-x)+\alpha_1E_2(x)]+(1-\rho_0)\int_0^1 f_1(\mu)e^{-x/\mu}d\mu+(1-\rho_3)\int_0^1 f_2(\mu)e^{-(a-x)/\mu}d\mu+2\rho_2\beta[\alpha_1E_2(x)+E_2(a-x)](1-\rho_o)\int_0^1 f_1(\mu)e^{-a/\mu}\mu d\mu+2\rho_1\beta[\alpha_2E_2(a-x)+E_2(x)](1-\rho_3)\int_0^1 f_2(\mu)e^{-a/\mu}\mu d\mu\Big\} \tag{4b}$$

$$\beta=\frac{1}{1-\alpha_1\alpha_2},\quad \alpha_i=2\rho_iE_3(a),\quad i=1,2 \tag{4c}$$

To solve the integral equation (3), $G(x)$ is represented in a power series in the form

$$G(x)=\sum_{n=0}^{N}C_nx^n\quad \text{in } 0<x<a \tag{5}$$

where C_n are the unknown expansion coefficients which are yet to be determined. When the Galerkin method is applied as outlined in [1], the following matrix equation is obtained for the determination of the coefficients C_n

$$[b_{mn}]\{C_n\}=\{d_m\},\quad m,n=0,1,2,\ldots,N \tag{6}$$

where $\{C_n\}$ is the column vector of the unknown expansion coefficients C_n. The elements of the square matrix $[b_{mn}]$ and the column vector $\{b_m\}$ are given respectively by

$$b_{mn}=\frac{a^{m+n+1}}{m+n+1}-\omega\int_o^a\int_o^a K(x,x')x^m{x'}^n\,dx\,dx' \tag{7}$$

$$d_m=\int_o^a Y(x)x^m\,dx \tag{8}$$

Equations (6) provide $N+1$ algebraic equations for the $N+1$ unknown expansion coefficients C_n. It is to be noted that the matrix $[b_{mn}]$ is independent of the boundary surface intensities A_i, $f_i(\mu)$, ($i=1,2$) and the source term $S(x)$. In addition, it is a symmetric matrix.

All the integrations appearing in the elements b_{mn} are performed analytically by utilizing the integrals in [1, 3] and the resulting explicit expression for b_{mn} is determined as

$$b_{mn}=\frac{a^{m+n+1}}{m+n+1}-\omega\Big\{\frac{1}{2}T_{mn}+\beta[\rho_1T_mT_n+\alpha_1\rho_2(T_mT_n^*+T_m^*T_n)+\rho_2T_m^*T_n^*]\Big\} \tag{9}$$

where

Table 1(*a*) Angular distribution for $f_1(\mu)=1+\mu$, $a=1$, $\rho_1=\rho_2=0$, $S(x)=A_1=A_2=f_2(\mu)=0$

ω	θ	$x=0$	$x=a/2$		$x=a$	NT
		I^-	I^-	I^+	I^+	
	0	0.0	0.0	1.2131	0.7358	
	15	0.0	0.0	1.1715	0.6982	
	30	0.0	0.0	1.0476	0.5881	
0.0	45	0.0	0.0	0.8417	0.4150	1
	60	0.0	0.0	0.5518	0.2030	
	75	0.0	0.0	0.1824	0.0264	
	90	0.0	0.0	0.0	0.0	
	0	0.0243	0.0084	1.2309	0.7545	
	15	0.0249	0.0086	1.1898	0.7172	
	30	0.0269	0.0094	1.0673	0.6080	
0.100	45	0.0306	0.0110	0.8643	0.4362	9
	60	0.0372	0.0139	0.5794	0.2255	
	75	0.0490	0.0198	0.2173	0.0473	
	90	0.0763	0.0296	0.0296	0.0139	
	0	0.4350	0.1923	1.5203	1.1041	
	15	0.4449	0.1976	1.4869	1.0728	
	30	0.4767	0.2152	1.3891	0.9819	
0.900	45	0.5366	0.2504	1.2347	0.8406	10
	60	0.6368	0.3169	1.0368	0.6658	
	75	0.7890	0.4473	0.8184	0.4843	
	90	0.9725	0.6307	0.6307	0.3087	
	0	0.5488	0.2520	1.5978	1.2080	
	15	0.5611	0.2590	1.5664	1.1785	
	30	0.6006	0.2820	1.4755	1.0934	
0.995	45	0.6748	0.3281	1.3344	0.9622	8
	60	0.7975	0.4151	1.1611	0.8005	
	75	0.9773	0.5851	0.9859	0.6235	
	90	1.1560	0.8168	0.8168	0.4042	
	0	0.5557	0.2557	1.6025	1.2143	
	15	0.5682	0.2628	1.5712	1.1850	
	30	0.6081	0.2862	1.4807	1.1003	
1.000	45	0.6832	0.3329	1.3405	0.9697	8
	60	0.8072	0.4211	1.1686	0.8088	
	75	0.9886	0.5937	0.9961	0.6321	
	90	1.1667	0.8283	0.8283	0.4101	

Table 1(*b*) Angular distribution for $f_1(\mu)=\delta(\mu-1)$, $a=1$, $\rho_1=\rho_2=0$, $S(x)=A_1=A_2=f_2(\mu)=0$

ω	θ	$x=0$	$x=a/2$		$x=a$	NT
		I^-	I^-	I^+	I^+	
	0	0.0	0.0	0.6065	0.3679	
	15	0.0	0.0	0.0	0.0	
	30	0.0	0.0	0.0	0.0	
0.0	45	0.0	0.0	0.0	0.0	1
	60	0.0	0.0	0.0	0.0	
	75	0.0	0.0	0.0	0.0	
	90	0.0	0.0	0.0	0.0	
	0	0.0037	0.0016	0.6091	0.3710	
	15	0.0037	0.0017	0.0026	0.0032	
	30	0.0040	0.0018	0.0028	0.0033	
0.100	45	0.0045	0.0021	0.0033	0.0036	7
	60	0.0053	0.0027	0.0040	0.0040	
	75	0.0066	0.0038	0.0053	0.0040	
	90	0.0082	0.0052	0.0052	0.0031	
	0	0.0668	0.0344	0.6521	0.4284	
	15	0.0683	0.0353	0.0468	0.0617	
	30	0.0729	0.0385	0.0508	0.0651	
0.900	45	0.0814	0.0447	0.0586	0.0709	10
	60	0.0949	0.0564	0.0728	0.0785	
	75	0.1123	0.0789	0.0976	0.0813	
	90	0.1152	0.1060	0.1060	0.0597	
	0	0.0847	0.0445	0.6639	0.4453	
	15	0.0865	0.0458	0.0590	0.0789	
	30	0.0922	0.0498	0.0640	0.0833	
0.995	45	0.1029	0.0578	0.0739	0.0908	10
	60	0.1196	0.0730	0.0920	0.1008	
	75	0.1405	0.1021	0.1237	0.1049	
	90	0.1395	0.1364	0.1364	0.0765	
	0	0.0857	0.0451	0.6647	0.4464	
	15	0.0876	0.0464	0.0597	0.0799	
	30	0.0934	0.0505	0.0648	0.0844	
1.000	45	0.1042	0.0587	0.0748	0.0920	10
	60	0.1211	0.0740	0.0931	0.1021	
	75	0.1422	0.1035	0.1253	0.1063	
	90	0.1410	0.1383	0.1383	0.0776	

$$T_{mn} \equiv \int_o^a \int_o^a E_1(|x-x'|)x^m x'^n dx dx' \tag{10a}$$

$$T_k \equiv \int_o^a E_2(x)x^k dx \tag{10b}$$

$$T_k^* = \int_o^a E_2(a-x)x^k dx = k!\left[(-1)^{k+1}E_{k+3}(a) - \sum_{j=0}^{k} \frac{a^{k-j}}{(k-j)!}\frac{(-1)^{j+1}}{j+2}\right] \tag{10c}$$

Explicit expression for $T_{m,n}$ and T_k are given in [1], and that for d_m is determined as

$$\frac{d_m}{2\pi} = 2\int_o^a \int_o^a K(x,x')S(x')x^m dx' dx$$

$$+A_1\beta[T_m+\alpha_2 T_m^*]+A_2\beta[T_m^*+\alpha_1 T_m]$$

$$+(1-\rho_o)m!\left[\int_0^1 f_1(\mu)\mu^{m+1}d\mu - \sum_{j=0}^{m}\frac{a^{m-j}}{(m-j)!}\int_0^1 f_1(\mu)\mu^{j+1}e^{-a/\mu}d\mu\right]$$

$$+(1-\rho_3)m!\left[\sum_{j=0}^{m}(-1)^j\frac{a^{m-j}}{(m-j)!}\int_0^1 f_2(\mu)\mu^{j+1}d\mu - (-1)^m\int_0^1 f_2(\mu)\mu^{m+1}e^{-a/\mu}d\mu\right]$$

$$+2\rho_2\beta(\alpha_1 T_m+T_m^*)(1-\rho_o)\int_0^1 f_1(\mu)\mu e^{-a/\mu}d\mu$$

$$+2\rho_1\beta(T_m+\alpha_2 T_m^*)(1-\rho_3)\int_0^1 f_2(\mu)\mu e^{-a/\mu}d\mu \tag{11}$$

Once the coefficients C_n are known, the forward and backward intensities $I(x,\mu)$ and $I(x,-\mu)$ are determined, respectively, from

$$I(x,\mu) = [(1-\rho_o)f_1(\mu)+A_1+2\rho_1 K_1]e^{-x/\mu} + \frac{1}{\mu}\int_o^x S(x')e^{-(x-x')/\mu}dx' + \frac{\omega}{4\pi}\sum_{n=0}^{N} C_n n!\left\{(-1)^{n+1}e^{-x/\mu}\mu^n + \sum_{j=0}^{n}\frac{(-1)^j x^{n-j}}{(n-j)!}\mu^j\right\},\ \mu>0 \tag{12a}$$

and

Table 2(*a*) Angular distribution for $S(x)=1$, $a=1$, $\rho_1=\rho_2=0$, $A_1=A_2=f_1=(\mu)=f_2(\mu)=0$

ω	θ	$x=0$	$x=a/2$		$x=a$	NT
		I^-	I^-	I^+	I^+	
	0	0.6321	0.3935	0.3935	0.6321	
	15	0.6449	0.4041	0.4041	0.6449	
	30	0.6848	0.4386	0.4386	0.6848	
0.0	45	0.7569	0.5069	0.5069	0.7569	1
	60	0.8647	0.6321	0.6321	0.8647	
	75	0.9790	0.8551	0.8551	0.9790	
	90	1.0000	1.0000	1.0000	1.0000	
	0	0.6730	0.4194	0.4194	0.6730	
	15	0.6866	0.4307	0.4307	0.6866	
	30	0.7291	0.4676	0.4676	0.7291	
0.100	45	0.8057	0.5405	0.5405	0.8057	17
	60	0.9200	0.6743	0.6743	0.9200	
	75	1.0398	0.9134	0.9134	1.0398	
	90	1.0464	1.0721	1.0721	1.0464	
	0	1.4096	0.8877	0.8877	1.4096	
	15	1.4378	0.9119	0.9119	1.4378	
	30	1.5260	0.9909	0.9909	1.5260	
0.900	45	1.6838	1.1478	1.1478	1.6838	9
	60	1.9150	1.4383	1.4383	1.9150	
	75	2.1265	1.9724	1.9724	2.1265	
	90	1.8448	2.3970	2.3970	1.8448	
	0	1.6229	1.0236	1.0236	1.6229	
	15	1.6553	1.0515	1.0515	1.6553	
	30	1.7567	1.1428	1.1428	1.7567	
0.995	45	1.9380	1.3241	1.3241	1.9380	9
	60	2.2027	1.6602	1.6602	2.2027	
	75	2.4398	2.2807	2.2807	2.4398	
	90	2.0710	2.7856	2.7856	2.0710	
	0	1.6358	1.0320	1.0320	1.6358	
	15	1.6685	1.0602	1.0602	1.6685	
	30	1.7706	1.1523	1.1523	1.7706	
1.000	45	1.9533	1.3353	1.3353	1.9533	3
	60	2.2201	1.6745	1.6745	2.2201	
	75	2.4589	2.3019	2.3019	2.4589	
	90	2.1417	2.8219	2.8219	2.1417	

Table 2(*b*) Angular distribution for $S(x)=1+x$, $a=1$, $\rho_1=\rho_2=0$, $A_1=A_2=f_1=(\mu)=f_2(\mu)=0$

ω	θ	$x=0$	$x=a/2$		$x=a$	NT
		I^-	I^-	I^+	I^+	
	0	0.8964	0.6804	0.5000	1.0000	
	15	0.9126	0.6985	0.5138	1.0220	
	30	0.9628	0.7571	0.5588	1.0918	
0.0	45	1.0490	0.8723	0.6485	1.2217	1
	60	1.1617	1.0803	0.8161	1.4323	
	75	1.2114	1.4316	1.1338	1.7256	
	90	1.0000	1.5000	1.5000	2.0000	
	0	0.9562	0.7223	0.5359	1.0629	
	15	0.9736	0.7414	0.5507	1.0862	
	30	1.0273	0.8038	0.5989	1.1601	
0.100	45	1.1196	0.9264	0.6952	1.2975	17
	60	1.2407	1.1480	0.8749	1.5194	
	75	1.2950	1.5241	1.2160	1.8244	
	90	1.0598	1.6081	1.6081	2.0795	
	0	2.0439	1.4577	1.2055	2.1850	
	15	2.0823	1.4971	1.2388	2.2312	
	30	2.2012	1.6252	1.3476	2.3768	
0.900	45	2.4082	1.8787	1.5649	2.6433	10
	60	2.6885	2.3434	1.9715	3.0565	
	75	2.8421	3.1706	2.7465	3.5374	
	90	2.1529	3.5955	3.5955	3.3815	
	0	2.3609	1.6670	1.4037	2.5078	
	15	2.4055	1.7121	1.4425	2.5604	
	30	2.5437	1.8590	1.5693	2.7263	
0.995	45	2.7847	2.1500	1.8224	3.0292	10
	60	3.1127	2.6846	2.2962	3.4954	
	75	3.2983	3.6428	3.1992	4.0210	
	90	2.4754	4.1784	4.1784	3.7376	
	0	2.3804	1.6798	1.4159	2.5275	
	15	2.4253	1.7252	1.4550	2.5805	
	30	2.5646	1.8733	1.5829	2.7477	
1.000	45	2.8078	2.1665	1.8382	3.0528	10
	60	3.1387	2.7054	2.3161	3.5222	
	75	3.3263	3.6717	3.2270	4.0505	
	90	2.4952	4.2142	4.2142	3.7592	

$$I(x,-\mu)=[(1-\rho_3)f_2(\mu)+A_2+2\rho_2K_2]e^{-(a-x)/\mu}+\frac{1}{\mu}\int_x^a S(x')e^{-(x'-x)/\mu}dx'+\frac{\omega}{4\pi}\sum_{n=0}^{N}C_n n!\sum_{j=0}^{n}\frac{\mu^j}{(n-j)!}(x^{n-j}-a^{n-j}e^{-(a-x)/\mu}),\ \mu>0 \tag{12b}$$

where

$$K_1=\beta\Big\{\alpha_2(1-\rho_o)\int_0^1 f_1(\mu)e^{-a/\mu}\mu d\mu+(1-\rho_3)\int_0^1 f_2(\mu)e^{-a/\mu}\mu d\mu+\alpha_2E_3(a)A_1+E_3(a)A_2+\int_o^a[E_2(x)+\alpha_2E_2(a-x)]S(x)dx+\frac{\omega}{4\pi}\sum_{n=0}^{N}C_n(T_n+\alpha_2T_n^*)\Big\} \tag{13a}$$

and

$$K_2=\beta\Big\{(1-\rho_o)\int_0^1 f_1(\mu)e^{-a/\mu}\mu d\mu+\alpha_1(1-\rho_3)\int_0^1 f_2(\mu)e^{-a/\mu}\mu d\mu+E_3(a)A_1+\alpha_1E_3(a)A_2+\int_o^a[\alpha_1E_2(x)+E_2(a-x)]S(x)dx+\frac{\omega}{4\pi}\sum_{n=0}^{N}C_n(\alpha_1T_n+T_n^*)\Big\} \tag{13b}$$

It is to be noted that the angular distribution of radiation intensity given by equations (12) is applicable for all angles, including $\mu=0$.

Results and Discussion

We illustrate the application of the foregoing analysis for a slab with transparent boundaries.

Table 1(*a*) shows the angular distribution of radiation intensity within the medium and at the boundaries for an external irradiation represented by $f_1(\mu)=1+\mu$ at the boundary surface $x=0$ with $f_2(\mu)=0$ at $x=a$. The function, $f_1(\mu)$, implies that the external radiation is incident on the boundary surface in the form of cones coming from all directions in the space. A function in the form, $f_1(\mu)=\delta(\mu-\mu_o)$, however, represents beams forming a single cone in the direction, μ_o.

Table 1(*b*) shows similar results for $f_1(\mu)=\delta(\mu-1)$ at $x=0$, which implies a normal incidence of unit intensity. For this special case the terms involving the integrals of $f_1(\mu)$ should be divided by 2π since the cone reduces to a single beam.

Finally in Tables 2(*a*) and 2(*b*), we present intensity calculations for distributed volumetric sources in the medium of strengths $S(x)=1$ and $S(x)=1+x$, respectively. In both

of these cases the boundaries are transparent, and there are no externally incident radiation.

The present study provides a simple, straightforward, and highly accurate method of analysis for the determination of angular distribution of radiation anywhere in the medium. As an independent check, the results are compared with those calculated with the F_N method [4]; the agreement was very good. Computations require very little computer time. In the tables presented, the number of terms, NT, used in the calculations for convergence are also listed.

Acknowledgment

This work was supported in part by the National Science Foundation through the grant MEA 8110705.

References

1 Özişik, M. N., and Yener, Y., "The Galerkin Method for Solving Radiation Transfer in Plane-Parallel Participating Media," ASME *Journal of Heat Transfer*, Vol. 104, 1982, pp. 351–354.

2 Özişik, M. N., *Radiative Transfer*, John Wiley and Sons, New York, 1973.

3 LeCaine, J., "A Table of Integrals Involving the Functions $E_n(x)$," *National Research Council of Canada*, Report No. MT-131, 1948.

4 Garcia, R. D. M., and Siewert, C. E., "On Angular Flux Computations in Neutron-Transport Theory," *Nucl. Sci. Eng.*, Vol. 81, 1982, pp. 474–476.

The Latent Heat of Vaporization of a Widely Diverse Class of Fluids

S. Torquato[1] and P. Smith[2]

Introduction

The critical region for most fluids is known to possess nonanalytical character that prohibits a power-series expansion of thermodynamic potentials about the critical point in density and temperature [1]. Over the past two decades, an enormous effort has been made to theoretically describe the anomalous thermodynamic behavior of fluids in the vicinity of the critical point. Phenomenological scaling thoery [2–4] and, more recently, renormalization-group theory [5], for example, have illuminated our understanding of the critical-point region. In order to obtain the proper functional form of the latent of vaporization, L, of a pure fluid that is applicable throughout its entire domain of existence (i.e., from the triple point to the critical point), it is clear one must employ results of modern critical-point theories.

Various latent-heat formulae for certain fluids have previously been given, but, in almost all cases, such expressions either have not accurately described the latent heat data over the broad domain of values that is of interest here [6, 7] or are unnecessarily complex in form, often containing a large number of terms [8]. The flaws in all these empirical equations appear to be the result of failure to incorporate the aforementioned modern understanding of the critical region.

Basic Equation

Using the Clausius-Clapeyron equation and results of renormalization-group theory, Torquato and Stell [9] were able to formulate the following simple expression for the dimensionless latent heat, λ, of a fluid belonging to the same universality class as the three-dimensional Ising model

$$\lambda = a_1 t^{\beta} + a_2 t^{\beta+\Delta} + a_3 t^{1-\alpha+\beta} + a_4 t + a_5 t^2 + a_6 t^3 \qquad (1)$$

Here $\lambda = L/L_t$, L_t is the latent-heat value at the triple point, $t = (T_c - T)/T_c$, T is the absolute temperature, T_c is the critical temperature, and the a_i are system-dependent parameters. The critical exponents, β and α, describe the singularities associated with the difference in coexisting densities and the specific heat at constant volume, respectively. The exponent Δ is Wegner's first gap exponent [10]. Torquato and Stell least-squares fitted this latent-heat formula to the highly accurate latent-heat data of water obtained by Osborne, Stimson, and Ginnings (OSG) [11] and Osborne, Stimson, and Fiock (OSF) [12] for $T_t \le T \le T_c$ (T_t being the triple point temperature). Their predicted latent-heat values were found to be in excellent agreement with the OSG and OSF data.

One object of this study is to fit equation (1) to the data of a large number of different substances, such as alcohols, halogen substituted hydrocarbons (Freons), simple nonpolar fluids, polar fluids, and other hydrocarbons, in order to determine the extent of its validity. Such an inclusive tabulation of properties is given by Vargaftik [13] and is the one employed in this investigation. Second, it is of interest to determine whether a least-squares fit of the data of a particular substance may be used to numerically predict, within some acceptable error, the latent heat of another fluid. Both of these problems are addressed in the subsequent section.

Results and Discussion

Vargaftik's data are by no means the most accurate data available for the individual substances contained therein, but he does provide, in a single compilation, relatively reliable tabulations of thermodynamic properties for a widely diverse class of fluids. We consider twenty different fluids and least-squares fit each latent-heat data set associated with a particular system from the triple point to the critical point using equation (1). Following Torquato and Stell, we take $\beta = 1/3$, $\alpha = 1/8$, and $\Delta = 0.79 - \beta \approx 0.4567$ for all the substances. The justification for this is the expectation that all fluids belong to the same universality class [1]. In Table 1, we summarize the results of these fits by giving T_c, T_t, L_t, the coefficients a_i, the maximum percentage deviation $\delta_m \equiv 100 \times |\lambda_i^* - \lambda_i|/\lambda_i^*$, and the standard error

$$\sigma \equiv \left[\sum_{i=1}^{N} (\lambda_i^* - \lambda_i)^2 / N \right]^{1/2}.$$

Here N is the number of latent-heat values; λ_i^* and λ_i are the ith measured and predicted scaled latent-heat values.

The fit for carbon monoxide yields $\sigma = 0.00325$, the largest standard error for the group of fluids presented in this study. On average, the predicted scaled latent-heat values for all twenty substances are within 0.8 percent of the data, assuming an average λ value of 0.5 for the entire temperature range and $\sigma = 0.004$. The fits for most of the fluids, moveover, yield λ values that are within 0.2 percent of the data, on average. The maximum percentage deviation, δ_m, is seen to always occur in the near critical region. This result is expected in light of the experimental difficulties one is faced with in the vicinity of the critical point [9].

A plot of λ versus t for each of the twenty substances does not show universal behavior, i.e., a corresponding states principle [14] is not demonstrated. However, a plot of λ versus $\tau \equiv (T_c - T)/(T_c - T_t)$, for all fluids for which Vargaftik reports values of L_t, appears to display a corresponding states principle in that the function $\lambda = \lambda(\tau)$ is

[1] Assistant Professor, Department of Mechanical and Aerospace Engineering, North Carolina State University, Raleigh, N.C. 27650, Assoc. Mem. ASME

[2] Graduate Student, Department of Mechanical and Aerospace Engineering, North Carolina State University, Student Mem. ASME

Contributed by the Heat Transfer Division for publication in the JOURNAL OF HEAT TRANSFER. Manuscript received by the Heat Transfer Division June 22, 1983.

of these cases the boundaries are transparent, and there are no externally incident radiation.

The present study provides a simple, straightforward, and highly accurate method of analysis for the determination of angular distribution of radiation anywhere in the medium. As an independent check, the results are compared with those calculated with the F_N method [4]; the agreement was very good. Computations require very little computer time. In the tables presented, the number of terms, NT, used in the calculations for convergence are also listed.

Acknowledgment

This work was supported in part by the National Science Foundation through the grant MEA 8110705.

References

1 Özişik, M. N., and Yener, Y., "The Galerkin Method for Solving Radiation Transfer in Plane-Parallel Participating Media," ASME *Journal of Heat Transfer*, Vol. 104, 1982, pp. 351–354.

2 Özişik, M. N., *Radiative Transfer*, John Wiley and Sons, New York, 1973.

3 LeCaine, J., "A Table of Integrals Involving the Functions $E_n(x)$," *National Research Council of Canada*, Report No. MT-131, 1948.

4 Garcia, R. D. M., and Siewert, C. E., "On Angular Flux Computations in Neutron-Transport Theory," *Nucl. Sci. Eng.*, Vol. 81, 1982, pp. 474–476.

The Latent Heat of Vaporization of a Widely Diverse Class of Fluids

S. Torquato[1] and P. Smith[2]

Introduction

The critical region for most fluids is known to possess nonanalytical character that prohibits a power-series expansion of thermodynamic potentials about the critical point in density and temperature [1]. Over the past two decades, an enormous effort has been made to theoretically describe the anomalous thermodynamic behavior of fluids in the vicinity of the critical point. Phenomenological scaling thoery [2–4] and, more recently, renormalization-group theory [5], for example, have illuminated our understanding of the critical-point region. In order to obtain the proper functional form of the latent of vaporization, L, of a pure fluid that is applicable throughout its entire domain of existence (i.e., from the triple point to the critical point), it is clear one must employ results of modern critical-point theories.

Various latent-heat formulae for certain fluids have previously been given, but, in almost all cases, such expressions either have not accurately described the latent heat data over the broad domain of values that is of interest here [6, 7] or are unnecessarily complex in form, often containing a large number of terms [8]. The flaws in all these empirical equations appear to be the result of failure to incorporate the aforementioned modern understanding of the critical region.

Basic Equation

Using the Clausius-Clapeyron equation and results of renormalization-group theory, Torquato and Stell [9] were able to formulate the following simple expression for the dimensionless latent heat, λ, of a fluid belonging to the same universality class as the three-dimensional Ising model

$$\lambda = a_1 t^{\beta} + a_2 t^{\beta+\Delta} + a_3 t^{1-\alpha+\beta} + a_4 t + a_5 t^2 + a_6 t^3 \qquad (1)$$

Here $\lambda = L/L_t$, L_t is the latent-heat value at the triple point, $t = (T_c - T)/T_c$, T is the absolute temperature, T_c is the critical temperature, and the a_i are system-dependent parameters. The critical exponents, β and α, describe the singularities associated with the difference in coexisting densities and the specific heat at constant volume, respectively. The exponent Δ is Wegner's first gap exponent [10]. Torquato and Stell least-squares fitted this latent-heat formula to the highly accurate latent-heat data of water obtained by Osborne, Stimson, and Ginnings (OSG) [11] and Osborne, Stimson, and Fiock (OSF) [12] for $T_t \le T \le T_c$ (T_t being the triple point temperature). Their predicted latent-heat values were found to be in excellent agreement with the OSG and OSF data.

One object of this study is to fit equation (1) to the data of a large number of different substances, such as alcohols, halogen substituted hydrocarbons (Freons), simple nonpolar fluids, polar fluids, and other hydrocarbons, in order to determine the extent of its validity. Such an inclusive tabulation of properties is given by Vargaftik [13] and is the one employed in this investigation. Second, it is of interest to determine whether a least-squares fit of the data of a particular substance may be used to numerically predict, within some acceptable error, the latent heat of another fluid. Both of these problems are addressed in the subsequent section.

Results and Discussion

Vargaftik's data are by no means the most accurate data available for the individual substances contained therein, but he does provide, in a single compilation, relatively reliable tabulations of thermodynamic properties for a widely diverse class of fluids. We consider twenty different fluids and least-squares fit each latent-heat data set associated with a particular system from the triple point to the critical point using equation (1). Following Torquato and Stell, we take $\beta = 1/3$, $\alpha = 1/8$, and $\Delta = 0.79 - \beta \approx 0.4567$ for all the substances. The justification for this is the expectation that all fluids belong to the same universality class [1]. In Table 1, we summarize the results of these fits by giving T_c, T_t, L_t, the coefficients a_i, the maximum percentage deviation $\delta_m \equiv 100 \times |\lambda_i^* - \lambda_i|/\lambda_i^*$, and the standard error

$$\sigma \equiv \left[\sum_{i=1}^{N} (\lambda_i^* - \lambda_i)^2 / N \right]^{1/2}.$$

Here N is the number of latent-heat values; λ_i^* and λ_i are the ith measured and predicted scaled latent-heat values.

The fit for carbon monoxide yields $\sigma = 0.00325$, the largest standard error for the group of fluids presented in this study. On average, the predicted scaled latent-heat values for all twenty substances are within 0.8 percent of the data, assuming an average λ value of 0.5 for the entire temperature range and $\sigma = 0.004$. The fits for most of the fluids, moveover, yield λ values that are within 0.2 percent of the data, on average. The maximum percentage deviation, δ_m, is seen to always occur in the near critical region. This result is expected in light of the experimental difficulties one is faced with in the vicinity of the critical point [9].

A plot of λ versus t for each of the twenty substances does not show universal behavior, i.e., a corresponding states principle [14] is not demonstrated. However, a plot of λ versus $\tau \equiv (T_c - T)/(T_c - T_t)$, for all fluids for which Vargaftik reports values of L_t, appears to display a corresponding states principle in that the function $\lambda = \lambda(\tau)$ is

[1] Assistant Professor, Department of Mechanical and Aerospace Engineering, North Carolina State University, Raleigh, N.C. 27650, Assoc. Mem. ASME

[2] Graduate Student, Department of Mechanical and Aerospace Engineering, North Carolina State University, Student Mem. ASME

Contributed by the Heat Transfer Division for publication in the JOURNAL OF HEAT TRANSFER. Manuscript received by the Heat Transfer Division June 22, 1983.

Table 1 Results of least-squares analysis using equation (1) for twenty different fluids for Vargaftik's data [13]. Temperatures are given in K, latent-heat in kJ/kg.

	Ammonia	Argon	Carbon Dioxide	Carbon Monoxide	Ethane
T_c	405.55	150.86	304.19	132.92	305.50
T_t	195.42	83.78	216.55	68.14	89.88
L_t	1473.90	161.80	347.30	235.52	601.19
a_1	0.47057	0.36102	1.35069	1.45169	− 0.64121
a_2	3.04437	23.96446	−5.95311	−25.33722	36.15830
a_3	−8.04468	55.53528	−20.83607	−82.04570	66.16418
a_4	2.69778	−67.19804	21.89009	87.67934	−90.29894
a_5	5.37598	−17.88592	11.94955	32.14627	−14.05575
a_6	−2.82782	7.40818	−13.93713	−14.91833	4.03838
δ_m	0.33581	0.44605	0.15900	1.54475	0.49968
σ	0.00081	0.00085	0.00118	0.00325	0.00086
	Ethanol	Freon-12	Freon-22	Isooctane	Krypton
T_c	521.35	384.95	369.28	544.25	209.39
T_t	158.65	118.15	113.15	165.77	115.76
L_t	1187.32	207.83	294.18	351.78	109.60
a_1	1.34686	0.94297	0.72254	0.67128	1.30503
a_2	−15.85366	−4.70274	2.95824	4.96085	−10.66454
a_3	−37.48493	−11.92221	3.42752	7.92755	−32.53309
a_4	47.15897	15.46468	−5.36903	−10.87562	36.43934
a_5	7.37973	0.59654	−1.17015	− 2.43041	9.54154
a_6	− 1.70348	1.20085	0.81290	− 0.91875	−2.80368
δ_m	0.26812	0.60933	0.24399	0.03399	0.56980
σ	0.00077	0.00063	0.00020	0.00031	0.00083
	Methane	Methanol	Neon	Nitrogen	n-Nonane
T_c	190.55	513.15	44.40	126.25	595.15
T_t	91.00	175.15	24.50	63.15	219.65
L_t	543.40	1354.16	89.45	212.60	387.81
a_1	0.78206	0.29045	0.88154	1.41557	0.31647
a_2	0.84814	12.12910	9.79304	−10.94088	13.56551
a_3	−9.79152	14.11962	24.10286	−29.52156	22.12327
a_4	6.41067	−24.69802	−28.20568	34.51737	−31.61818
a_5	4.66431	1.28818	− 8.03241	8.43211	−4.26098
a_6	−2.04333	−3.46706	2.70559	−3.10147	1.05594
δ_m	1.12302	0.74542	0.03090	0.59132	1.71695
σ	0.00073	0.00105	0.00007	0.00083	0.00207
	Oxygen	Propane	1-Propanol	Water	Xenon
T_c	154.77	370.00	536.85	647.27	289.74
T_t	54.35	85.46	147.15	273.16	161.36
L_t	238.70	540.31	946.80	2501.00	96.98
a_1	1.24529	0.32838	1.15023	0.72241	1.13256
a_2	− 4.05385	13.25739	−14.07059	5.33402	− 3.08280
a_3	− 6.31829	26.78045	−31.76604	8.97347	− 8.18035
a_4	10.20602	−34.00190	40.45017	−11.93143	10.80348
a_5	−0.81329	−8.50819	− 8.64866	−3.31206	−0.91775
a_6	0.98570	3.84203	4.26884	1.63257	2.42356
δ_m	0.84017	0.25917	1.09955	1.53773	0.17028
σ	0.00074	0.00064	0.00208	0.00028	0.00099

nearly the same for each substance. By using the smallest temperature value given and the associated latent-heat value reported for this temperature, we have used this universal function $\lambda = \lambda(\tau)$ (equation (2) below) in order to estimate the value of L_t for those fluids for which Vargaftik does not provide data. Less than half of the latent-heat values at the triple point given in Table 1 were obtained in this way. In order to test the accuracy of this method, we apply the technique to estimate L_T using ammonia, a substance for which L_T is given. Using the ammonia data at 260 K and 300 K, the predicted L_T are within 0.1 and 1.3 percent of the reported L_T, respectively.

We obtain λ explicitly as a function of τ for water using the coefficients, a_i, of Table 1 for water and equation (1)

$$\lambda = b_1\tau^{\beta} + b_2\tau^{\beta+\Delta} + b_3\tau^{1-\alpha+\beta} + b_4\tau + b_5\tau^2 + b_6\tau^3 \qquad (2)$$

where

$$b_1 = 0.60176 \quad b_2 = 3.45913 \quad b_3 = 4.62671$$
$$b_4 = -6.89614 \quad b_5 = -1.10643 \quad b_6 = 0.31522$$

Clearly $b_i = a_i[(T_c - T_t)/T_c]^{\theta_i}$, where θ_i is the exponent associated with the ith term, $i = 1, \ldots, 6$. In Fig. 1, we plot equation (2) for water along with $\lambda - \tau$ values obtained from Vargaftik's data for five other respresentative fluids. Note that τ varies from zero at the critical point to unity at the triple point. The latent-heat curve for water appears to be bounded by nitrogen data from above and carbon dioxide data from below. At $\tau = 0.1$ and $\tau = 0.5$, both nitrogen and carbon dioxide data are within 2 and 5 percent of equation (2), respectively.

Conclusions

A least-squares fit of the latent-heat data of a widely diverse class of fluids is made using equation (1), yielding predicted values that are in excellent agreement with the data throughout a wide range of temperatures. Proper scaling of the temperature allowed us to obtain a universal expression for the scaled latent heat, λ, which may be used to provide good estimates of the latent heat of vaporization of any fluid, given T_c, T_t, and L_t. Equation (2) may also be used to estimate the latent heat in instances when L_t is not given by first using the universal expression to estimate L_t in the manner described above. It is important to note, however, that the universality of equation (2) does not depend upon the

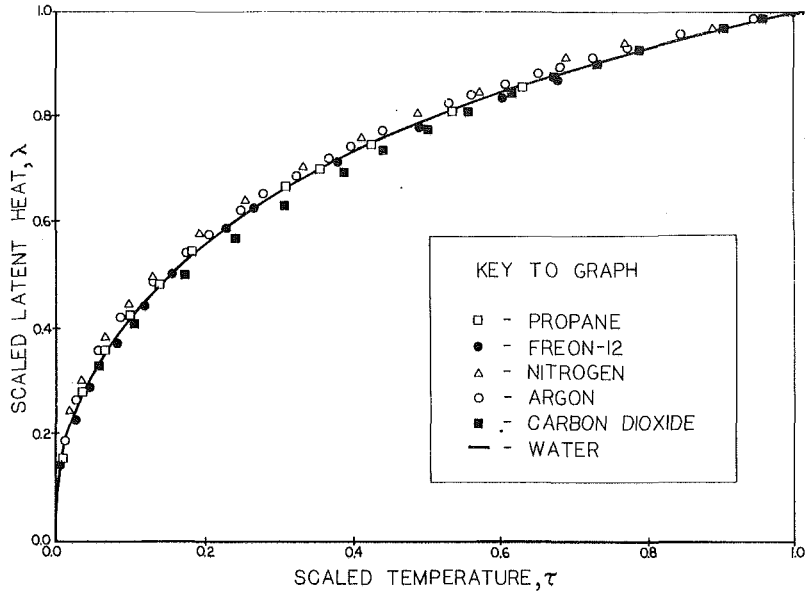

Fig. 1 A plot of the scaled latent heat, λ, versus the scaled temperature $\tau \equiv (T_c - T)/(T_c - T_t)$. The universal curve obtained from equation (1) is shown here along with data for several representative substances (from Vargaftik [13]).

constant latent heat, L_O, used to scale the actual latent-heat value, i.e., we could scale L with cL_T (where c is some constant such that $0 < c \leq 1$) instead of L_T and obtain universal behavior, but in this general case, $0 \leq L/L_0 \leq 1/c$. We have chosen $c = 1$ in this study for convenience. Although the latent-heat values provided by Vargaftik are not numerically the most accurate, the data are sufficiently reliable to demonstrate the existence of a universal equation. For future work, it is suggested that more precise correlations be obtained by using better data.

References

1 Sengers, J. V., and Sengers, J. M. M., "Concepts and Methods for Describing Critical Phenomena in Fluids," *NASA Contractor Report 149665*, 1977.

2 Widom, B., "Equation of State in Neighborhood of the Critical point," *J. Chem. Phys.*, Vol. 43, 1965, pp. 3898-3905.

3 Kadanoff, L. P., "Scaling Laws For Ising Models Near T_c," *Physics*, Vol. 2, 1966, pp. 263-272.

4 Griffiths, R. B., "Thermodynamic Functions and Ferromagnets Near the Critical Point," *Phys. Rev.*, Vol. 158, 1967, pp. 176-187.

5 Wilson, K. G., and Kogut, J., "The Renormalization Group and the ϵ Expansion," *Physics Reports*, Vol. 12c, No. 2, 1974, pp. 75-199.

6 Nutting, P. G., "Vapor Pressure and Heat of Vaporization," *Ind. Eng. Chem.*, Vol. 22, 1930, p. 771.

7 Watson, K. M., "Thermodynamics of the Liquid State," *Ind. Eng. Chem.*, Vol. 35, 1943, pp. 398-406.

8 Meyer, C. A. McClintock, R. B., Silvestri, G. J., and Spencer, R. C., *ASME Steam Tables*, 3d ed., 1977.

9 Torquato, S., and Stell, G. R., "An Equation for the Latent Heat of Vaporization," *Ind. Eng. Chem. Fund.*, Vol. 21, 1982, pp. 202-205.

10 Wegner, F., "Corrections to Scaling Laws," *Phys. Rev. B*, Vol. 5, 1972, pp. 4529-4536.

11 Osborne, N. S., Stimson, H. F., and Ginnings, D. C., "Calorimetric Determination of the Thermodynamic Properties of Saturated Water Vapor in Both the Liquid and Gaseous States from 100 to 374°C," *J. Res. Natl. Bur. Stand.*, Vol. 18, 1937, pp. 389-447.

12 Osborne, N. S., Stimson, H. F., and Fiock, E. F., "Calorimetric Determination of Thermal Properties of Saturated Water and Steam From 0 to 270°C," ASME *Trans.*, Vol. 52, 1930, pp. 191-220.

13 Vargaftik, N. B., *Tables on the Thermophysical Properties of Liquids and Gases*, 2d ed., John Wiley and Sons, New York, 1975.

14 Kestin, J., and Dorfman, J. R., *A Course in Statistical Thermodynamics*, Academic Press, New York, 1971.

Journal of Heat Transfer

Discussion

Transient Conduction with Pyrolysis (Approximate Solutions for Charring of Wood Slabs)[1]

L. T. Yeh[2] and B. T. F. Chung.[3] In their recent paper, Kanury and Holve presented approximate solutions for charring of wood slabs. It appears that the authors were not aware of some recent publications in this field. Approximate analysis of more complicated problems involving radiative and convective boundary conditions in either a semi-infinite region or a finite region have been available [1, 2]. We would like to offer the following comments.

First, the assumption of a linear temperature profile in the preheat phase by the authors is obviously oversimplified. This simplification may lead significant error in predicting the onset of melting time. Based on our previous experience [1] the assumption of linear temperature profile yields a much worse result than when a parabolic profile is used. Second, in their analysis, the authors assumed that the surface temperature at $X=0$ reached the phase change temperature, T_c, before the penetration depth, X_T, arrived at the insulated surface ($X=1$). This is not always true. The authors ignored another possibility, i.e., the penetration depth, X_T, reaches the insulated surface before the phase change takes place at the front surface ($X=0$). In this case, the thermal thickness concept is abandoned and the finite thickness of the body becomes an important factor. This time period is usually referred to as second time domain [3]. The sequence of events occurring during the melting process can be illustrated in Fig. 1, where "1" and "2" represents the old phase (wood in this case) and the newly formed phase (char), respectively. Depending on the material properties, the initial temperature, and the strength of wall heat flux, there are two possible paths that the transfer process may follow, namely, the paths A-B-D and A-C-D shown in Fig. 1. The former is the continuation of preheating phase while the latter is the one considered by the authors.

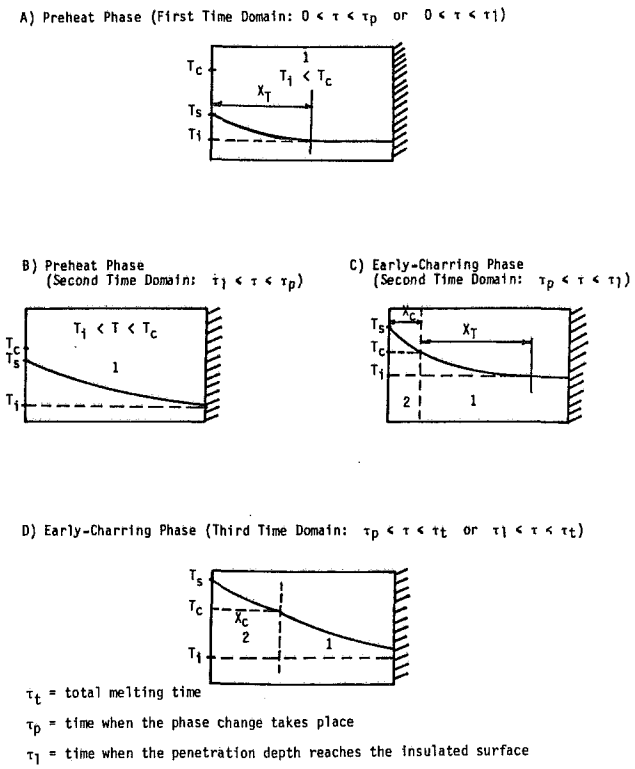

Fig. 1 Sequence of events occurring during melting (charring phase)

References

1 Chung, B. T. F., and Yeh, L. T., "Solidifications and Melting of Materials Subject to Convection and Radiation," *Journal of Spacecraft and Rockets*, Vol. 12, 1975, pp. 329–.

2 Yeh, L. T., and Chung, B. T. F., "A Variational Analysis of Freezing or Melting in a Finite Medium Subject to Radiation and Convection," ASME JOURNAL OF HEAT TRANSFER, Vol. 101, 1979, pp. 592–.

3 Arpaci, V. S., *Conduction Heat Transfer*, Addison-Wesley, Reading, Mass., 1966. p. 80–

[1] By A. M. Kanury and D. J. Holve, published in the May 1982 issue of the ASME JOURNAL OF HEAT TRANSFER, Vol. 104, No. 2, pp. 338-343.

[2] Thermal Design Section, Texas Instruments, Inc., Lewisville, Texas 75067

[3] Department of Mechanical Engineering, The University of Akron, Akron, Ohio 44325

Authors' Closure

With full appreciation of the comments of Drs. Yeh and Chung, we would like to point out that the wood-charring problem differs from the freezing/melting problem in certain significant aspects. Among the most important of these aspects are: (*a*) the volumetric nature of the pyrolytic phase-change; (*b*) the drastic differences in thermophysical properties of the old and new phases; (*c*) the internal convection of the pyrolyzates; and (*d*) the expansion effects associated with freezing. If the wood pyrolysis kinetics are simplified to be represented by an infinite activation energy, then charring occurs at a distinct temperature. The problem is then benefited by the concepts in the freezing/melting literature. But the foregoing aspects (*b*) and (*c*) persist so that one cannot draw a one-to-one correspondence between the problems of wood-charring and freezing/melting.

Specifically addressing the criticisms of Yeh and Chung, we agree that quadratic profiles are better than linear profiles. In as much as: (*a*) there exist serious ambiguities in the available thermophysical properties of wood and partially charred

wood; (*b*) assumptions of isotropy, negligible internal convection, and infinite-activation-energy-pyrolysis are made; (*c*) the relevant nondimensional variables (both dependent and independent) can be identified even with linear profiles; and (*d*) the data sought to be compared with our predictions come from experiments involving considerable practical complexity, we have deliberately chosen the simplest acceptable profiles. After all, the intended use of the results should always determine the degree of approximation.

In making the second comment, which is related to where the thermal penetration occurs on the insulated backface before the exposed front face commences to pyrolyze, Yeh and Chung have failed to notice the last paragraph of section 6 of our paper. Thus, their claim that we ignored this possibility is a hasty one. If our objective were to study the charring of thin sheets and films, we would have considered this issue in greater detail.

Design and Optimization of Air-Cooled Heat Exchangers[1]

F. L. Rubin.[2] The goal of the authors to develop a computer program to design a heat exchanger without iteration has been sought by many. However, most exchangers are designed with a fouling resistance. The writer is unaware of any computer program which can design a practical heat exchanger without iteration and yet include a fouling resistance.

The abstract of the aforementioned paper implies that the information presented in the main text is applicable to the design of commercial air-cooled heat exchangers. However, the basic assumptions used to develop the solutions are never met in commerical practice.

The program "take(s) into account the variation of heat transfer coefficients and differential pressure drop with temperature and/or length of flow path . . . " The assumption of uniform air flow across the tube bundle is indicated.

Air-cooled heat exchangers utilize circular fans and rectangular tube bundles. The plenum height rarely has one-half of a fan diameter between the top of the fan ring and the heat transfer surface. The ensuing maldistribution of air results in heat transfer coefficient variations, which are greater than those due to changes in physical properties.

Tube diameters available for heat exchanger construction do not have an infinite range of sizes. Only the first of the nine tabulated sizes is actually available; it is probably used in less than 0.1 percent of all exchangers.

Similarly only a discrete number of motor sizes is available for air-cooled heat exchangers. Bundle width is severely limited by a maximum value to permit shipment and a minimum to facilitate air distribution across the heat exchanger surface. These conditions preclude preliminary definition of air quantity and air side pressure drop when designing an optimum exchanger.

"The side constraints on the design variable are of a practical nature . . . " state the authors. However only equilateral triangular pitch can be considered "practical." The case study figure is for a tube layout, which does not have equilateral spacing.

Most heat exchangers (e.g., shell-and-exchangers, spiral plate exchangers, double-pipe sections, multitube sections, plate and frame exchangers, etc.) are purchased as such and auxilliary equipment is bought separately. Air-cooled exchangers are rarely sold commercially as heat transfer surfaces only. The supplier furnishes the tube bundle, the fan(s), the driver(s), the plenum, the fan ring, etc. The concept of "minimum volume" of heat transfer surface is meaningless when one designs an air-cooled exchanger with these components.

It is most unlikely that this computer program or any minor modification of it could be used commercially for the design and optimization of air-cooled exchangers.

Authors' Closure

In any attempt to move forward in the field of Heat Transfer, the comments and viewpoints of a practioner are always appreciated. It appears though, that some unfortunate and unwarranted implications have been drawn by Mr. Rubin. Our goal in the paper was to demonstrate the usefulness to the heat transfer designer of the optimization techniques that have been used for over a decade in structural design. Our goal is not to replace the designer with the computer—it would be foolish to try.

The following replies are offered to Mr. Rubin's specific comments:

The method proposed is *applicable* to the design of commercial air-cooled heat exchangers. It is a tool, one of many, it is hoped, that the designer will use.

Not all air-cooled heat exchangers utilize circular fans. There are many applications in the transportation industry where ram air is utilized.

Mr. Rubin's comments on the discrete sizes of components available to the designer only points out the need to extend the techniques of heat exchanger design optimization to include more advanced optimization algorithms. More to the point, the use of continuous variables is common practice early in the design process, rapidly providing a near optimum from which to discritize the actual parameters.

To reiterate: our purpose was to to eliminate the designer but to provide tools that will make the design process more efficient. As is stated in the paper's abstract, the method we have proposed "is shown to be a useful tool for heat exchanger design."

The Optimum Dimensions of Convective Pin Fins[1]

J. E. Wilkins, Jr.[2] Readers interested in this paper, or that of Sonn and Bar-Cohen [1], may wish to consult the earlier paper of Focke [2], in which the principal results for pin fins, or circular spines, with constant, triangular, and convex parabolic ($n=2$) profiles are derived. The numerical values furnished for u^*, b^*, L^*, and V^* in Table 1 of the Razelos paper are in essential agreement with those of Focke, although there are minor discrepancies (the largest is between the values 0.4400 and 0.45 for L^* for the constant profile case by Razelos and Focke, respectively). We have resolved all of these discrepancies in favor of the Razelos results.

It is also true, as claimed by Focke but not by Razelos, that the convex parabolic profile is the optimum in the class of all profiles. This result follows from a general theory [3] for optimizing circular spine profiles for arbitrary temperature-dependent heat transfer modes, when that theory is specialized to the case of convective heat transfer with constant surface heat transfer coefficient and constant thermal

[1] By C. P. Hedderich, M. D. Kelleher, and G. N. Vanderplaats, published in the November 1982 issue of the JOURNAL OF HEAT TRANSFER, Vol. 104, No. 4, pp. 683–689.

[2] Practical Heat Transfer Consultants, Houston, Texas 77036

[1] By P. Razelos, published in the May 1983 issue of the ASME JOURNAL OF HEAT TRANSFER, Vol. 105, No. 2, pp. 411–413.

[2] Deputy General Manager for Science and Engineering, EG&G Idaho, Inc., Idaho Falls, Idaho 83415. Assoc. Mem. ASME. Work performed under the auspices of the U.S. Department of Energy, Contract No. DE-AC07-76ID01570.

wood; (*b*) assumptions of isotropy, negligible internal convection, and infinite-activation-energy-pyrolysis are made; (*c*) the relevant nondimensional variables (both dependent and independent) can be identified even with linear profiles; and (*d*) the data sought to be compared with our predictions come from experiments involving considerable practical complexity, we have deliberately chosen the simplest acceptable profiles. After all, the intended use of the results should always determine the degree of approximation.

In making the second comment, which is related to where the thermal penetration occurs on the insulated backface before the exposed front face commences to pyrolyze, Yeh and Chung have failed to notice the last paragraph of section 6 of our paper. Thus, their claim that we ignored this possibility is a hasty one. If our objective were to study the charring of thin sheets and films, we would have considered this issue in greater detail.

Design and Optimization of Air-Cooled Heat Exchangers[1]

F. L. Rubin.[2] The goal of the authors to develop a computer program to design a heat exchanger without iteration has been sought by many. However, most exchangers are designed with a fouling resistance. The writer is unaware of any computer program which can design a practical heat exchanger without iteration and yet include a fouling resistance.

The abstract of the aforementioned paper implies that the information presented in the main text is applicable to the design of commercial air-cooled heat exchangers. However, the basic assumptions used to develop the solutions are never met in commerical practice.

The program "take(s) into account the variation of heat transfer coefficients and differential pressure drop with temperature and/or length of flow path . . . " The assumption of uniform air flow across the tube bundle is indicated.

Air-cooled heat exchangers utilize circular fans and rectangular tube bundles. The plenum height rarely has one-half of a fan diameter between the top of the fan ring and the heat transfer surface. The ensuing maldistribution of air results in heat transfer coefficient variations, which are greater than those due to changes in physical properties.

Tube diameters available for heat exchanger construction do not have an infinite range of sizes. Only the first of the nine tabulated sizes is actually available; it is probably used in less than 0.1 percent of all exchangers.

Similarly only a discrete number of motor sizes is available for air-cooled heat exchangers. Bundle width is severely limited by a maximum value to permit shipment and a minimum to facilitate air distribution across the heat exchanger surface. These conditions preclude preliminary definition of air quantity and air side pressure drop when designing an optimum exchanger.

"The side constraints on the design variable are of a practical nature . . . " state the authors. However only equilateral triangular pitch can be considered "practical." The case study figure is for a tube layout, which does not have equilateral spacing.

Most heat exchangers (e.g., shell-and-exchangers, spiral plate exchangers, double-pipe sections, multitube sections, plate and frame exchangers, etc.) are purchased as such and auxilliary equipment is bought separately. Air-cooled exchangers are rarely sold commercially as heat transfer surfaces only. The supplier furnishes the tube bundle, the fan(s), the driver(s), the plenum, the fan ring, etc. The concept of "minimum volume" of heat transfer surface is meaningless when one designs an air-cooled exchanger with these components.

It is most unlikely that this computer program or any minor modification of it could be used commercially for the design and optimization of air-cooled exchangers.

Authors' Closure

In any attempt to move forward in the field of Heat Transfer, the comments and viewpoints of a practioner are always appreciated. It appears though, that some unfortunate and unwarranted implications have been drawn by Mr. Rubin. Our goal in the paper was to demonstrate the usefulness to the heat transfer designer of the optimization techniques that have been used for over a decade in structural design. Our goal is not to replace the designer with the computer—it would be foolish to try.

The following replies are offered to Mr. Rubin's specific comments:

The method proposed is *applicable* to the design of commercial air-cooled heat exchangers. It is a tool, one of many, it is hoped, that the designer will use.

Not all air-cooled heat exchangers utilize circular fans. There are many applications in the transportation industry where ram air is utilized.

Mr. Rubin's comments on the discrete sizes of components available to the designer only points out the need to extend the techniques of heat exchanger design optimization to include more advanced optimization algorithms. More to the point, the use of continuous variables is common practice early in the design process, rapidly providing a near optimum from which to discritize the actual parameters.

To reiterate: our purpose was to to eliminate the designer but to provide tools that will make the design process more efficient. As is stated in the paper's abstract, the method we have proposed "is shown to be a useful tool for heat exchanger design."

The Optimum Dimensions of Convective Pin Fins[1]

J. E. Wilkins, Jr.[2] Readers interested in this paper, or that of Sonn and Bar-Cohen [1], may wish to consult the earlier paper of Focke [2], in which the principal results for pin fins, or circular spines, with constant, triangular, and convex parabolic ($n=2$) profiles are derived. The numerical values furnished for u^*, b^*, L^*, and V^* in Table 1 of the Razelos paper are in essential agreement with those of Focke, although there are minor discrepancies (the largest is between the values 0.4400 and 0.45 for L^* for the constant profile case by Razelos and Focke, respectively). We have resolved all of these discrepancies in favor of the Razelos results.

It is also true, as claimed by Focke but not by Razelos, that the convex parabolic profile is the optimum in the class of all profiles. This result follows from a general theory [3] for optimizing circular spine profiles for arbitrary temperature-dependent heat transfer modes, when that theory is specialized to the case of convective heat transfer with constant surface heat transfer coefficient and constant thermal

[1] By C. P. Hedderich, M. D. Kelleher, and G. N. Vanderplaats, published in the November 1982 issue of the JOURNAL OF HEAT TRANSFER, Vol. 104, No. 4, pp. 683–689.

[2] Practical Heat Transfer Consultants, Houston, Texas 77036

[1] By P. Razelos, published in the May 1983 issue of the ASME JOURNAL OF HEAT TRANSFER, Vol. 105, No. 2, pp. 411–413.

[2] Deputy General Manager for Science and Engineering, EG&G Idaho, Inc., Idaho Falls, Idaho 83415. Assoc. Mem. ASME. Work performed under the auspices of the U.S. Department of Energy, Contract No. DE-AC07-76ID01570.